Palaeoclimate and biotic records from the Uruguayan Margin

Andrew MacLean Mair

Submitted in accordance with the requirements for the degree of Doctor of Philosophy

The University of Leeds

Earth Surface Science Institute

School of Earth and Environment

2022

The candidate confirms that the work submitted is his own and that appropriate credit has been given where reference has been made to the work of others.

Acknowledgements

I am indebted to a great many individuals for their support, advice and encouragement throughout this PhD, particularly over the COVID19 pandemic, a time of great uncertainty for myself and this project.

First of all I would like to thank my primary supervisor Dr Tracy Aze, who set me off on this planktonic foraminiferal journey during my undergraduate studies, encouraged me to pursue a Micropalaeontology Masters, and developed my academic ability through this PhD. Without your guidance and support this project would not have evolved into the opportunity filled adventure it ultimately became. Thank you for pushing me out of my comfort zone, giving me confidence when I questioned my own ability, and celebrating my triumphs alongside me.

I would also like to recognise the support of my supervisory team, Dr Ruza Ivanovic and Dr Robert Newton. Ruza thank you for welcoming me into your research group, expanding my knowledge on the power of modelling, and for challenging my assumptions relating to research questions and my Quaternary signals. Without your guidance and comments this project would be a shadow of itself. Rob, thanks for your support and words of advice on all things elemental. The stable isotopes in these chapters definitely benefitted from your eye, and the discussions on possible drivers of ITRAX signals were key in interrogating the downcore records. I would also like to thank you for your welcome into institute meetings during my time as PGR rep, you provided me the opportunity to voice the concerns of my peers and welcomed my input on a range of ESSI issues. Thank you to you both for helping shape this project, and importantly making it an enjoyable experience.

Next, I would like to thank the technical staff whom without, this project would not be possible. Firstly, I wish to recognise the work by the BOSCORF staff whom provided support and advice on sample selection, collection and research methods during my visits to the facility. You guys do a fantastic job and never failed to answer any query relating to the Uruguayan cores. Secondly, I would like to thank the staff of the NEIF Radiocarbon facility for their training and advice on obtaining useful radiocarbon dating, critical in the temporal portions of the palaeoenvironmental study. Finally, a massive thank you must go to the staff of the Cohen Laboratories at the University of Leeds, whose experience, support

and good humour made collecting primary data a joy. In particular, I would like to thank Dr Robert Jamieson whose sage academic advice, wealth of isotope experience and dedication in the support of science, made this study. I would also like to thank him for his excellent book recommendations, frequent reminders to take a coffee break, and stalwart friendship in and outside of work.

I have found camaraderie key to getting through a PhD, and I would like to extend a special thanks to the following groups: Palaeo@Leeds, Climate-Ice, Cohen and those whom made the ESSI institute a fantastic, social research group. I would also like to specially thank those I shared “Hell Creek” office 7.130 with over the years. The advice from friends here really made my time at work a pleasure, and I wish you the best in the future. In particular, I would like to thank: Adam Woodhouse, Autumn Pugh, Bethany Allen, Carl Spence-Jones, Emma James, Frances Proctor and Grace Lamyman, for laughing with-, and putting up with me for the longest time.

To friends, both at home and abroad, thank you for your friendship, jokes and support. In particular, I want to thank the: Birmingham Boys, Leeds Lads, Lymm Lads and Undergrad Lads. Reminders that life is more than work, were always appreciated and I look forward to raising a glass with you all soon.

To my family, words cannot fully express the appreciation I feel for your unwavering support of me. You’ve always encouraged my academic pursuits from the beginning, counselled me through trying decisions, and ultimately cheered me toward the next goal or achievement. Without you this simply doesn’t happen. Thank you.

Finally, I would like to thank my fiancée Anna Bland. You committed as much to this PhD, in many ways, as I. You upended your life to move back to Leeds, enabling me pursue this course. You’ve been my rock through times of uncertainty, always quick with a laugh, a smile or an exasperated sigh to put me right. Your support, faith and optimism are the unseen foundations of this PhD, and enabled the culmination of this work. I look forward to finally opening that bottle of Urbino wine and dancing into the next chapter of life together!

Abstract

The Brazilian-Malvinas Confluence (BMC) dominates western South Atlantic margin oceanography, marking a distinct mixing region between the tropical Brazil Current and sub-polar Malvinas Current. Tracing this confluence requires a readily available proxy, sensitive to the contrasting BMC water masses. Planktonic foraminifera are unicellular marine plankton that construct a calcium carbonate test, these tests are abundant in the fossil record, enabling analysis of past environments. The BMC migrates along the margin over a range of timescales, with variation impacting wider regional oceanography and climate.

Using planktonic foraminifera, this study assesses BMC regional spatial and temporal variation, utilising: planktonic foraminiferal assemblages, single specimen stable isotope analysis, ITRAX XRF scanning and new radiocarbon dating, reconstructing modern and past Holocene signals. These techniques targeted three aims 1) assessment of spatial variability of planktonic foraminiferal core top records in relation to the modern setting, 2) investigation of BMC evolution over the last 10 Kyr, tracking confluence movement in relation to a single site, and 3) evaluation of water mass specific morphotypes and variable test encrustation states on the isotopic signals recorded by *Globoconella inflata*, a key species in oceanographic studies.

Use of high-density spatial mapping of assemblages and isotopic measurements reveals significant heterogeneity between sites, at a resolution normally unobtainable to similar studies. Assemblage and stable isotope variability continue downcore, alongside ITRAX productivity spikes, coinciding with ENSO intensification. Variation corresponds with mid-Holocene BMC southern migration, supporting Argentine and Brazilian studies. Investigation into increasing encrustation and increasing stable oxygen isotope values finds little correlation when using single specimens, contrasting previous work. However, this study provides recommendations for resolving morphotype/encrustation influences on $\delta^{18}O$ records. This study emphasises the value of high-density spatial and temporal sampling in understanding complex oceanographic regions, and promotes single specimen isotopes for fingerprinting water mass signatures and deciphering BMC morphotype/encrustation $\delta^{18}O$ signals.

Key words: Brazil-Malvinas Confluence, Planktonic Foraminifera, Uruguay, Uruguayan Margin, Holocene, Southwest Atlantic, Oceanography, Spatial Variance, Temporal Variance, Palaeoecology, Palaeoclimate.

Table of Contents

List of Tables

List of Figures

List of Equations

Abbreviations

Abbreviation	Term
AABW	Antarctic Bottom Water
AAIW	Antarctic Intermediate Water
ACC	Antarctic Circumpolar Current
AMOC	Atlantic Meridional Overturning Circulation
AMS	Accelerated Mass Spectrometer
ANCAP	Administración Nacional de Combustibles, Alcoholes y Portland
BC	Brazil Current
BMC	Brazilian-Malvinas Confluence
BOSCORF	British Ocean Sediment Core Research Facility
cal BP	Calibrated years before present
cps	Counts per second
CT	Core top
CTD	Conductivity Temperature Depth
DC	Downcore
ENSO	El Niño Southern Oscillation
GCBC	*Globoconella inflata* Brazil Current
GCMC	*Globoconella inflata* Malvinas Current
GIA	Glacial Isostatic Adjustment
GRBC	*Globorotalia truncatulinoides* Brazil Current
GRMC	*Globorotalia truncatulinoides* Malvinas Current
IDW	Inverse Distance Weighting
IODP	International Ocean Discovery Program
IPCC	International Panel on Climate Change
ITCZ	Inter-Tropical Convergence Zone
ITRAX	Name of an integrated XRF and radiograph scanning instrument
ka/kya	Thousand Years Ago
ky/kyr	Thousand Years
LCDW	Lower Circumpolar Deep Water
LGM	Last Glacial Maximum
mbsl	Meters below sea level

MC	Malvinas Current
MSE	Mean Squared Error
NADW	North Atlantic Deep Water
NBC	Northern Brazil Current
OGCM	Ocean General Circulation Model
PPW	Plata Plume Water
RSL	Relative Sea Level
S.D	Standard Deviation
SACW	South Atlantic Central Water
SACZ	South American Convergence Zone
SAMS	South American Monsoon System
SASW	Sub-Antarctic Shelf Water
SEM	Scanning Electron Microscope
SSS	Sea Surface Salinities
SST	Sea Surface Temperature
STSF	Sub-tropical Shelf Front
STSW	Sub-tropical Shelf Water
SWWB	South Westerly Wind Belt
TOC	Total Organic Content
TW	Tropical Water
UCDW	Upper Circumpolar Deep Water
VPDB	Vienna Pee Dee Belemnite
VSMOW	Vienna Standard Mean Ocean Water
WOA 18	World Ocean Atlas 18
XRF	X-ray Fluorescence
$\delta^{13}C$	Carbon Stable Isotopes
$\delta^{18}O$	Oxygen Stable Isotopes

Chapter 1 Introduction

1.1 Thesis Rationale

The Uruguayan margin, and large swathes of the Western South Atlantic, are historically understudied; with low-resolution transects and few sediment samples available to document planktonic foraminiferal communities along the continental margin. This has led to poor coverage in global datasets (i.e. ForCens/ MARGO/IODP), especially when compared to Northern Hemisphere sites at similar latitudes (Haddam et al., 2016; García Chapori and Laprida, 2021). This uneven coverage has been highlighted by the International Panel on Climate Change (IPCC) as a key area for refinement, to better capture regional variation within climate models and expand palaeoclimate records (Solomon et al., 2007; Jansen et al., 2007; Masson-Delmotte et al., 2014). The study utilises a number of cores made available by the British Ocean Sediment Core Research Facility (BOSCORF), donated by BG Group and ANCAP, from commercial petroleum explorations along the Uruguayan margin. The donation includes two hundred gravity short cores and represents a novel opportunity to expand understanding of regional, and wider South Atlantic, oceanographic changes.

This study utilises a number of core tops and high resolution sampled cores from the BOSCORF core repository, with work split into three discrete work packages to tackle the listed aims and objectives. The first package focuses on gravity core-top data, to analyse modern day planktonic foraminiferal abundances, assemblages and stable isotopes from the region. This package will set a benchmark for comparison of past communities and provide insight into regional homo/heterogeneity of records. The second will explore how planktonic foraminiferal assemblages have altered over the Holocene, with respect to the modern, recording how water column properties have changed, and the impact on species distributions accordingly in response to oceanographic change. The third package will focus on understanding morphological and isotopic change within an oceanographically complex region. Specifically, whether there is any evidence of oceanographic shifts altering the representation of planktonic foraminifera morphotypes through test parameter and isotopic changes within a species. The Brazilian Malvinas Confluence (BMC) is the meeting of two

boundary currents, and has in previous works been shown to migrate seasonally, and over longer time intervals (Figure 1.1-1) (Olson et al., 1988; Peterson and Stramma, 1991; Piola and Matano, 2019), changing the properties of water bathing the site, likely resulting in disturbances to the abiotic conditions species must tolerate (Piola and Matano, 2019). A number of contributing mechanisms for BMC migration have been proposed, over a variety of timescales, and will be discussed in detail in later chapters (Chapter 2 and Chapter 5). By sampling at high resolution downcore the project aims to distinguish whether changes in Holocene climate impact the test morphology and stable isotope values of *Globoconella inflata* and whether this can be attributed to oceanographic shifts. Clarifying recent literature assessments of the species and the application of the species in tracing oceanographic shifts (Morard et al., 2011; Morard et al., 2016; Schiebel and Hemleben, 2017; Jonkers et al., 2021).

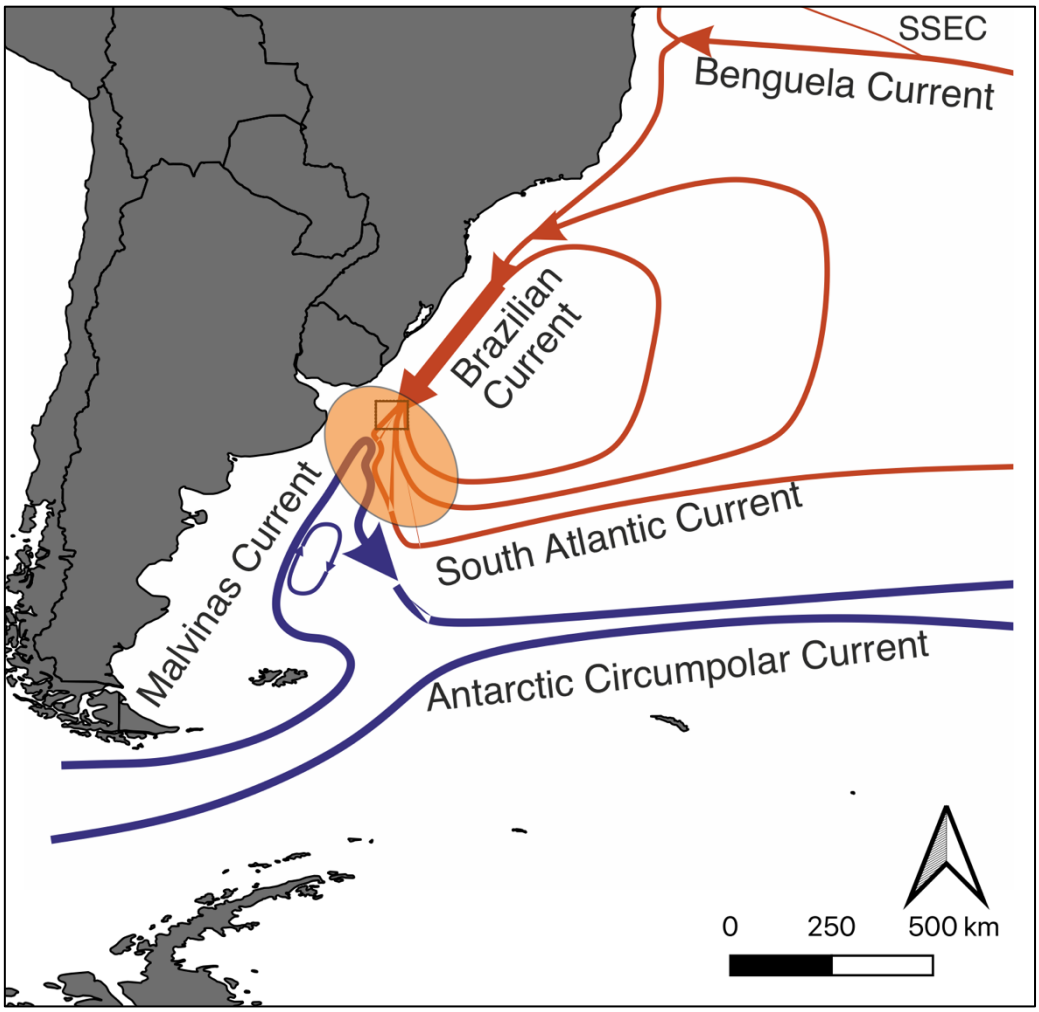

Figure 1.1-1 A simplified broad scale depiction of South Atlantic oceanography with the competing and contrasting Brazilian and Malvinas currents colliding to form Brazilian-Malvinas Confluence (BMC) (Stramma and England, 1999; Piola and Matano, 2019). This BMC region is highlighted in orange with confluence and the region from which the BOSCORF cores were donated depicted by the black box .

1.2 Aims and Objectives

This thesis aims to analyse the spatial and temporal variance in planktonic foraminiferal assemblages during the Late Quaternary, from an understudied portion of the Uruguayan margin (Hernández-Molina et al., 2016). The sediments recovered from the region were deposited within a complex oceanographic and sedimentological setting (Hernández-Molina et al., 2016). When combined with shifts during the deglaciation from the Last Glacial Maximum the margin has undergone significant changes (Lantzsch et al., 2014; Hernández-Molina et al., 2016; Warratz et al., 2017; Gu et al., 2018c), which are hypothesised to significantly impact foraminiferal assemblages.

With planktonic foraminifera being a widely utilised tool in the study of oceanography and climate change (Bé and Hutson, 1977; Pearson, 2012; Schiebel and Hemleben, 2017), the aim of this thesis is to assess how spatially variable the assemblages are within the complex modern mixing regime. The temporal aspect of these changes will be evaluated by assemblage and isotope records, alongside radiocarbon dating, to build a detailed environmental record for the region using a single core sampled in high resolution. This will be of use to regional palaeoclimate reconstructions and in understanding how Southern Atlantic oceanography altered in response to global deglaciation.

Through the tracking of an individual species morphology and isotopic variability the project aims to assess the temporal impact of the migrating BMC, the afore mentioned heat exchange or mixing zone of the Western South Atlantic, has on the species recovered from a single site. This study will expand on previous work that identified isotopic offset of morphotypes of *Globoconella inflata* across the BMC (Morard et al., 2011; Morard et al., 2016), alongside the stable isotope impact of encrustation categorisation (Jonkers et al., 2021) by analysing the stable isotopes of single specimens. It will target this question by completing a high resolution, temporal, single specimen isotope analysis to observe whether encrustation classification and BMC migration resulted in isotopic change at a single site.

1.3 Aims and research questions:

To assess the spatial variability of planktonic foraminiferal core top records across an oceanographically complex region.

- Do planktonic foraminiferal core top records reflect overlying oceanographic currents, displaying spatial heterogeneity between sites, or does the record provide a homogenous signal across the margin?

To investigate the evolution of the Brazilian-Malvinas Current over the last 10 Kyr

- How does the planktonic foraminiferal record reflect Holocene Brazilian-Malvinas Confluence evolution over the last 10 Kyr?

To assess the influence of regional oceanographic controls and test encrustation on the isotopic signals of *Globoconella inflata.*

- Is encrustation the likely dominant factor in variation of *Globoconella inflata* single specimen stable isotope values rather than regional oceanographic controls with distinct morphotype populations?

Chapter 2 Literature Review

2.1 The Uruguayan Margin

The cores in this study are located between 36-37°S latitude and 54°W30'-52°W longitude in the Punta del Este basin, from a region with complex oceanography close to the outflow of the second largest South American river (Depetris and Griffin, 1968). As the region straddles the oceanic/continental margin it is necessary to consider both continental and oceanographic climatic controls in order to understand modern day and palaeoenvironmental influences on the region.

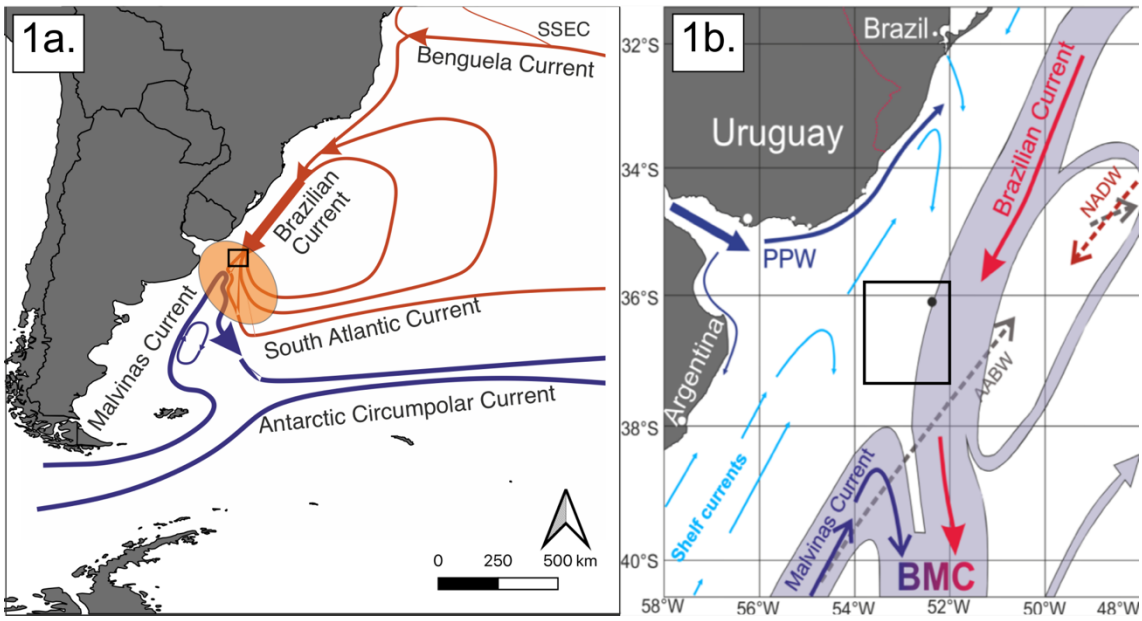

Figure 2.1-1 a) Generalised South Atlantic oceanography with the main components realised. The BMC mixing region is highlighted by the orange oval, with the study region inset highlighted back a black box. The position of currents is modified from Stramma and England, (1999). b) the regional oceanography, modified from Hernández-Molina et al., (2016) and location of core UPC028 (black dot), the core study region is also highlighted (black box). Shelf currents south of 33°S reflect the colder SASW (Piola et al., 2000).

2.2 Modern Oceanography

The modern South Atlantic oceanography, shown in Figure 2.1-1, has been extensively modelled over the last 30 years as an important part of wider ocean circulation and global heat exchange, with the Brazilian Malvinas Confluence (BMC) a key feature of the Western South Atlantic (Olson et al., 1988; Stramma and England, 1999; Wainer et al., 2000; Chiessi et al., 2007; Piola and Matano, 2008; Lumpkin and Garzoli, 2011). The influence of regional oceanography is key

in defining the sediment deposition for the study region with oceanic currents shown to limit direct fluvial delivery of sediment by directing Plata Plume Water northward (Voigt et al., 2013; Razik et al., 2015), and enabling deposition and remobilisation of sediment through contouritic processes (Hernández-Molina et al., 2009; Preu et al., 2013; Hernández-Molina et al., 2016; Warratz et al., 2017). In addition, contrasting regional oceanography impacts species presence/absence of planktonic foraminifera with species often thermally or nutrient limited, resulting in potential assemblage variations through time (Chiessi et al., 2007; Kucera, 2007; Chiessi et al., 2014; Morard et al., 2016; Schiebel and Hemleben, 2017).

Defined as a mixing region the BMC is comprised of south flowing, warm, salty waters combining to form the Brazilian Current (BC) and the northward flowing, cool, relatively fresh waters of the Malvinas current (MC) in one of the most energetic regions of the world's oceans (Gordon, 1981; Peterson and Stramma, 1991; Stramma and England, 1999; Silveira et al., 2000; Piola and Matano, 2008; Matano et al., 2010; Paniagua et al., 2018; Piola and Matano, 2019; Frozza et al., 2020). The BC is comprised of two distinct warm water packages, Tropical Water (TW) and South American Central Water (SACW), that differ in density and depth. When compared to the MC, both TW and SACW are significantly different in terms of temperature and salinity (Table 2.2-1) (Stramma and England, 1999; Piola and Matano, 2008). The joining of the BC and MC currents is marked by a sharp salinity front, projecting eastward from the margin at approximately 38°S into the Argentine Basin (Olson et al., 1988; Stramma and England, 1999; Piola and Matano, 2008; Piola et al., 2013; Guerrero et al., 2014; Matano et al., 2014; Hernández-Molina et al., 2016; Paniagua et al., 2018). In addition to contrasting thermohaline properties the MC is often cited as being significantly richer in nutrients, either through chlorophyll observations (Brandini et al., 2000; Garcia et al., 2004; Saraceno et al., 2005) or through fish catch/ecological metrics (Acha et al., 2004; Matano et al., 2010).

Below the surface waters the complexity of the BMC continues with interaction of several northward flowing, sub-/polar currents including the Antarctic Intermediate Waters (AAIW), Upper Circumpolar Deep Water (UCDW), Lower Circumpolar Deep Water (LCDW) and Antarctic Bottom Waters (AABW) coming into contact with southern flowing, and comparatively warmer, North Atlantic

Deep Water (NADW) and recirculated AAIW (Piola and Matano, 2008; Preu et al., 2013). Each of these water masses are described in the water column by salinity and temperature properties, often with sharp gradients between adjacent currents (Table 2.2-1).

Combined, the BMC represents a key feature in the thermal, salinity and nutrient exchange between the sub-tropics and sub-polar regions of the South Atlantic and results in a complex, intense mixing region on the margin (Stramma and England, 1999; Brandini et al., 2000; Piola and Matano, 2008; Paniagua et al., 2018; Piola and Matano, 2019). This intense mixing generates mesoscale eddies, alongside seasonal latitude variation of the central BMC region, derived from variable seasonal strengths of confluence currents (Olson et al., 1988; Peterson and Stramma, 1991; Hernández-Molina et al., 2016; Piola and Matano, 2019).

Table 2.2-1 Table of regional water mass temperature and salinity signatures from the literature for water mass classification.

Name	Potential Temperature (°C)	Salinity (PSU)	Reference
Plata Plume Water	20-25	<33.5	Physical properties (Piola et al., 2008)
Sub-tropical Shelf Water	<13	33.9-36	Physical properties (Piola et al., 2008)
Sub-Antarctic Shelf Water	6-16	33.4-33.8	Physical properties (Piola et al., 2008)
Tropical water	>20	>36	Physical properties (Piola and Matano, 2019)
South Atlantic Central Water	5-18	34.3-35.8	Physical properties (Emery, 2015)
Malvinas Current	5.6-15	<34.2	Physical properties (Gordon, 1981; Paniagua et al., 2018; Piola and Matano, 2019)
Antarctic Intermediate Water	2-6	33.8-34.8	Physical properties (Emery, 2015; Paniagua et al., 2018)
North Atlantic Deep Water	1.5-4	34.8-35	Physical properties (Emery, 2015)
Antarctic Bottom Water	-0.9-1.7	34.64-34.72	Physical properties (Emery, 2015)

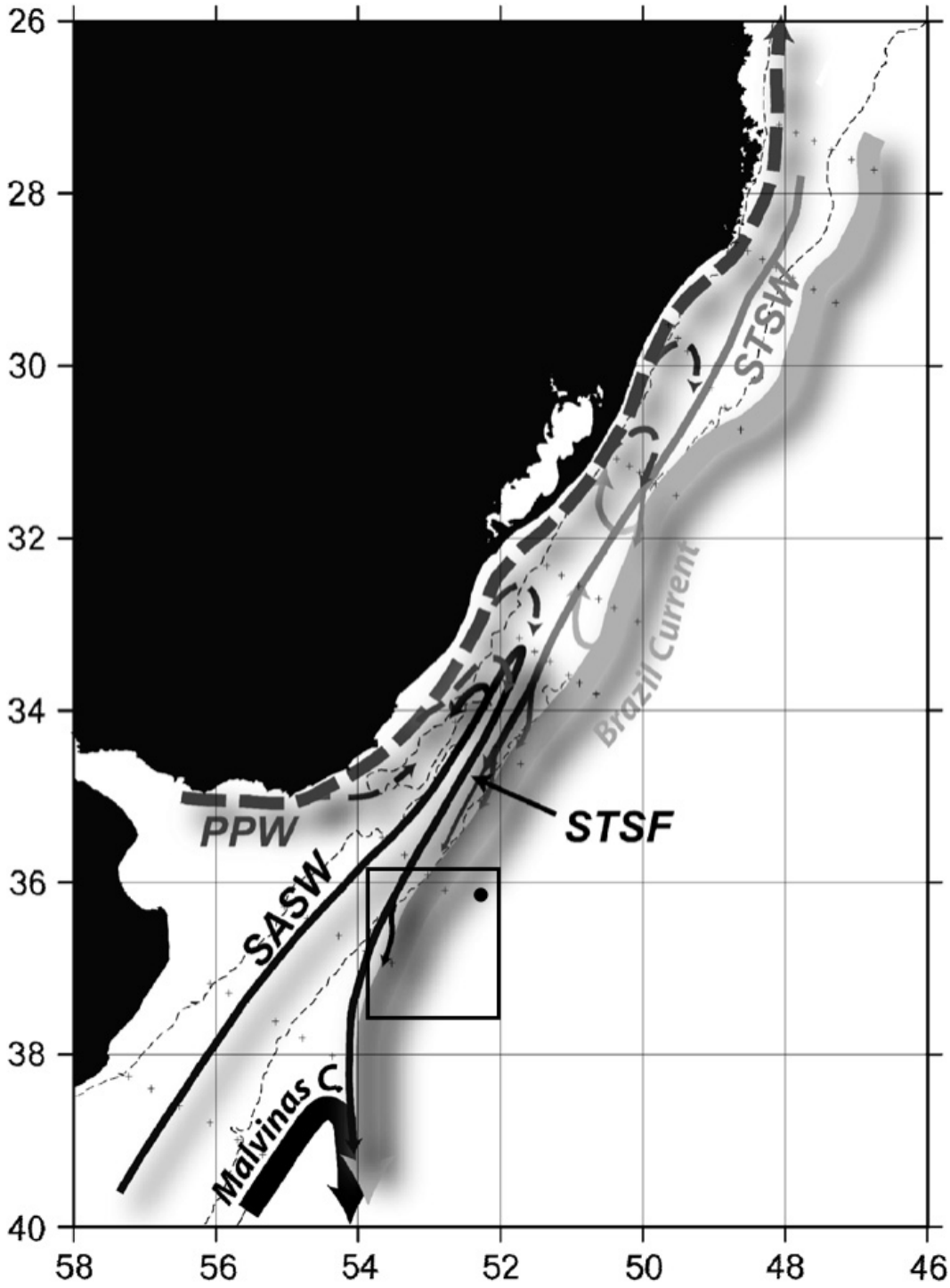

Figure 2.2-1 Schematic surface shelf currents modified from Piola et al., 2008. Black box approximates region cores were collected from, black circle represents site UPC 028. Dashed lines indicate the 40 mbsl and 200 mbsl. Plata Plume Water (PPW) is advected north, Sub-Antarctic Shelf Water (SASW) converges with Sub-Tropical Shelf Water (STSW) north of the BMC at approximately 33 ºS (Piola et al., 2008).

Whilst the BMC lies off the margin, a similar system operates in the shallow waters (~<200 m) off the continental shelf, with two opposing shelf currents converging, although evidence suggests minimal mixing (Piola et al., 2000; Piola et al., 2008). This convergence is between Sub-Antarctic Shelf Water (SASW), a cooler, fresher and nutrient enriched (T<16 °C, S<33.8) water mass originating

from the Patagonian shelf, meeting the warmer, saltier and nutrient depleted Sub-tropical Shelf Water (STSW) (T>13 °C, S<33.9) from the Brazilian margin at the Sub-tropical Shelf Front (STSF) (Piola et al., 2000; Piola et al., 2008). This front is located to the north of the study region with an average position of approximately 33 °S, with minor seasonal migration (Piola et al., 2000; Lantzsch et al., 2014). There is no firm connection certifying a coupling of the STSF and BMC, (Matano et al., 2010; Bender et al., 2013; Voigt et al., 2015), although some authors have connected the two features (Bender et al., 2013; Franco-Fraguas et al., 2014; Lantzsch et al., 2014). These water masses are unlikely to overlie any cores within the study region directly, due to the water depths involved (~>1000 mbsl), however limited indirect influence may be seen at those sites closer to shore (Piola et al., 2008).

As previously indicated the cores originate north of the Río de la Plata estuary, the outflow for the Paraná River and the Uruguay River. This estuary handles drainage from 3,100,000 km^2 of tropical and sub-tropical South America in the form of the Río de la Plata basin, with a discharge of 22,000 $m^3 s^{-1}$ (Depetris and Griffin, 1968; Acha et al., 2004; Cruz et al., 2007). The influence of the Río de la Plata outflow, sometimes termed Plata Plume Water (PPW), appears to be largely restricted to the continental shelf (<200 m) through prevailing seasonal wind directions, mixing with and freshening both the SASW and STSF nearshore (Piola et al., 2000; Palma et al., 2008; Bícego et al., 2021). The selection of cores within the study site are located on the continental slope in water depths varying from ~1100-3050 mbsl and thus unlikely to experience PPW influence. The Río de la Plata drainage basin incorporates large sections of Northern Argentina, Southern Bolivia, the entirety of Paraguay, much of Southern Brazil and most of Uruguay (Depetris and Griffin, 1968). Therefore, it stands to reason that the climate regime of these regions can be expected to influence the output of the river, influencing sedimentary outflow of the Río de la Plata and the freshwater input along the margin. However, it has been suggested that the sediments deposited on the continental slope are more likely to be sourced and under the influence of strong contouritic currents than river discharge in the modern (Krastel et al., 2001; Krastel et al., 2011).

2.3 Continental Climate

There are a number of atmospheric systems influencing South America, impacting the continental climate and offshore oceanography (Garreaud et al., 2009). Here a summary description is provided for the relevant systems likely to influence the study site, either through proximal location or through distal in/direct interaction. Schematic locations of these systems in South America are presented in Figure 2.3-1.

One of the major modern environmental phenomena affecting South America is the South American Monsoon System (SAMS), a seasonal precipitation event over the austral summer months of October-April, but most intense during December, January and February (Jones and Carvalho, 2013; Baker and Fritz, 2015). The monsoon covers a large portion of sub-/tropical South America, taking in much of the Amazon basin and extending down to the La Plata Basin, causing strong seasonal variability in precipitation across this region (Marengo et al., 2012; Baker and Fritz, 2015). The SAMS is sensitive to land-sea thermal gradients, resulting in sensitivity to changes in insolation causing migration to the SAMS north and south (Cruz et al., 2005; Vuille et al., 2012).

This system is bounded to the north by the Inter-Tropical Convergence Zone (ITCZ), a persistent global belt of converging trade winds proximal to the equator (Vuille et al., 2012; Villela, 2017). This band is key in moisture fluxes into the SAMS and is principally driven by meridional SST gradients (Vuille et al., 2012). Bounding the SAMS to the south is the South American Convergence Zone (SACZ), an elongated band of convection and associated cloud bands leading to significant precipitation (Villela, 2017). The SACZ, which like the ITCZ, shows inter-annual latitudinal positional variation, influencing the position of the SAMS, and therefore inter-annual heat transport and precipitation (Barros et al., 2000; Doyle and Barros, 2002; Vera et al., 2006; Garreaud et al., 2009; Marengo et al., 2012).

Several continental studies have analysed changes in the SAMS with a view to analyse climate and precipitation patterns over tropical/sub-tropical South America (Cruz et al., 2005; Cruz et al., 2007; Cruz et al., 2009; Bird et al., 2011; Stríkis et al., 2011; Marengo et al., 2012; Vuille et al., 2012; Kanner et al., 2013; Baker and Fritz, 2015). Changes in intensity of the monsoon has the capacity to impact agricultural land usage, hydroelectric generation and regional water

availability in the modern; thus understanding the SAMS variability is the focus of ongoing research (Sylvester, 2009; Marengo et al., 2012; Jones and Carvalho, 2013). However, changes in SAMS position, or indeed the bounding ITCZ and SACZ, over the course of the Holocene will impact the palaeoclimate and corresponding palaeo-proxy records proximal to the continental margin. Understanding the connections between the atmospheric and marine systems will be key in understanding Holocene climate shifts.

Another key atmospheric feature of South American climate is the Southern Westerly Wind Belt (SWWB), a mid-latitude (typically 40-60 °S) system that extends from the surface to the stratosphere (Thompson and Solomon, 2002; Garreaud, 2007; Garreaud et al., 2009; Razik et al., 2013; Voigt et al., 2015). This system migrates throughout the year reaching a northernmost latitude of ~30 °S during austral winter before contracting below ~40 °S during austral summer (Garreaud et al., 2009; Lamy et al., 2010). SWWB position and strength are typically controlled by meridional SST gradients (Garreaud et al., 2009; Lamy et al., 2010). SWWB and SACZ form a see-saw in their migrations with the SWWB pushing north during austral winter and retreating with SACZ advance over austral summer (Garreaud et al., 2009; Sylvester, 2009; Razik et al., 2013).

A final climate factor is the El Niño Southern Oscillation (ENSO), this is a cycle of alternating warm (El Niño) and cold (La Niña) events originating in the tropical Pacific that lead to changes in global atmospheric and ocean processes (McPhaden et al., 2006; Garreaud et al., 2009). This ENSO leads to significant precipitation and temperature variability over much of modern South America (Garreaud et al., 2009). Establishment of modern ENSO conditions likely occurred ~7-5 Kya, depending on threshold utilised, impacting the precipitation, winds and ocean currents surrounding South America (Moy et al., 2002; Wanner et al., 2008; Gyllencreutz et al., 2010; Bender et al., 2013; Voigt et al., 2013; Bícego et al., 2021). Additionally, the number of events and their amplitude increases toward the modern (Moy et al., 2002), likely having further impact on regional climate and oceanography. A full overview of the mechanisms influencing the modern continental climate of South America can be found in Garreaud et al., (2009).

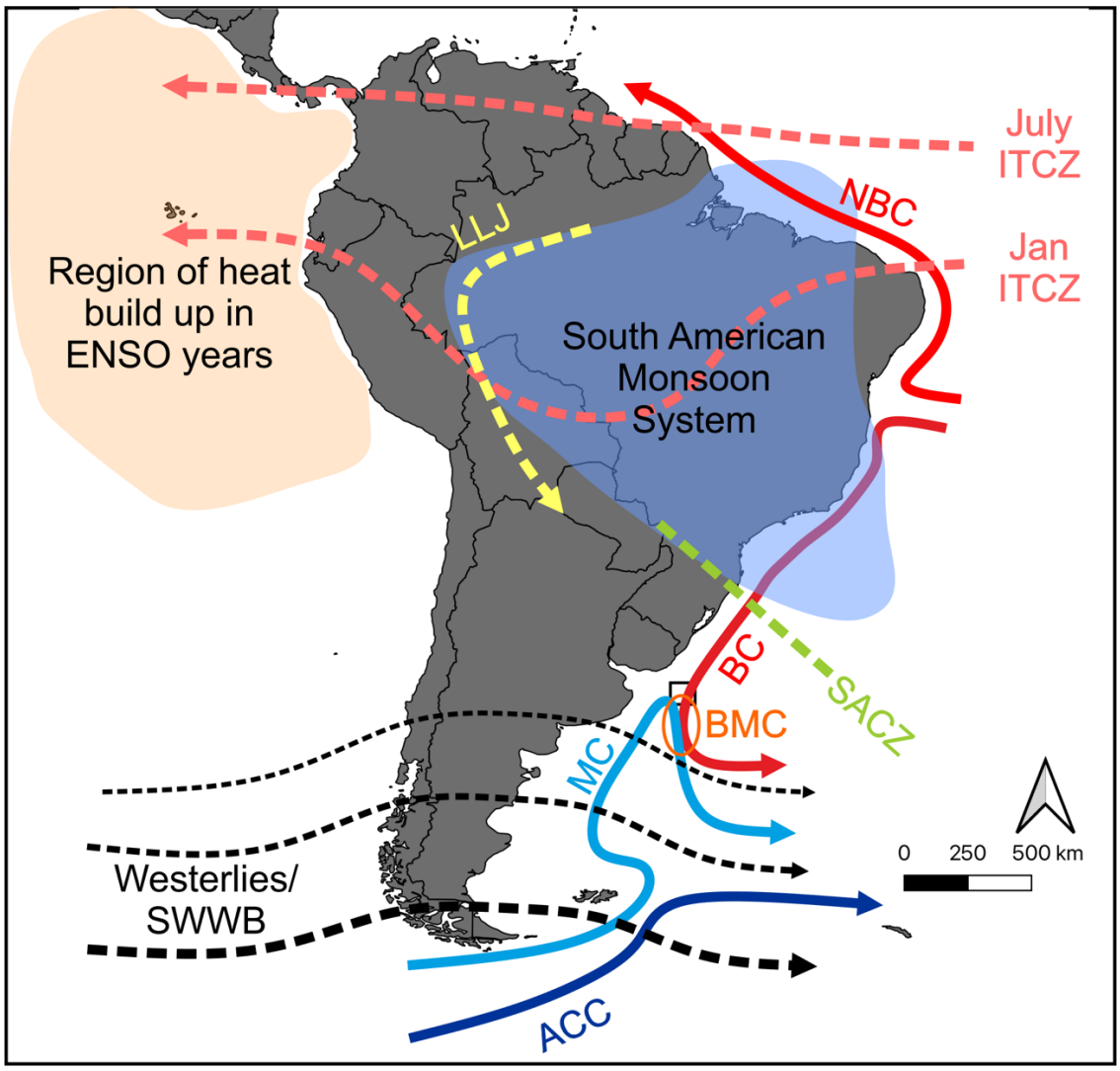

Figure 2.3-1 Schematic of the modern climatic regime over South America. Atmospheric flows are delimited by dashed lines. The Inter Tropical Convergence Zone (ITCZ) (pink) summer and winter mean positions and Low Level Jet (LLJ) (yellow) are based on Sylvester, (2009). South Atlantic Convergence Zone (SACZ) average position is detailed by a green dashed line (Sylvester, 2009; Barros et al., 2000; Villela, 2017; Pivel et al., 2010). The South Westerly Wind Belt (SWWB) position is presented by black dashed lines, with increasing weight implying greater wind strength (Sylvester, 2009; Voigt et al., 2015). The South American Monsoon System (SAMS) is a precipitation feature highlighted by the blue region, the position of this system is controlled by surrounding atmospheric patterns (Barros et al., 2000; Vera et al., 2006; Sylvester, 2009). Orange shaded region defines latitudinal location for heat build-up during El Niño Southern Oscillation (ENSO) events, with atmospheric-ocean teleconnections impacting South Atlantic systems (Marengo et al., 2012). Simplified oceanic currents on the western margin are detailed by solid lines based on Stramma and England, (1999), with the tropical Northern Brazilian Current (NBC), polar Antarctic Circumpolar Current (ACC), tropical/sub-tropical Brazilian Current (BC) and sub-polar Malvinas Current (MC) depicted. The average position of the Brazilian-Malvinas Confluence (BMC) is also illustrated with an orange oval. The black box represents the location of cores used in this study.

2.4 Atmosphere-Oceanography Interactions

The position of the BMC, and the linked ocean-atmosphere interactions, is a key tenet of regional palaeoclimate study. The combination of these systems influences continental climate, ocean circulation patterns, thermocline ventilation and sedimentary processes (Peterson and Stramma, 1991; Chiessi et al., 2007; Jullion et al., 2010; Hernández-Molina et al., 2010; Bender et al., 2013; Franco-Fraguas et al., 2014; Burone et al., 2018). However, the BMC location is not fixed, displaying latitudinal variation seasonally and the average position varying over multi-decadal and longer timescales (Olson et al., 1988; Peterson and Stramma, 1991; Garcia et al., 2004; Toledo, 2008; Lumpkin and Garzoli, 2011; Morard et al., 2016; Piola and Matano, 2019).

Numerous drivers for BMC positional variation have been suggested including: 1) changes to various wind stress curl fields within the South Atlantic, influencing the position of the SWWB and entire subtropical basin Sea Surface Temperature (SST) anomalies (Sylvester, 2009; Lumpkin and Garzoli, 2011; Bender et al., 2013; Razik et al., 2013; Voigt et al., 2015), 2) changes to ITCZ and SACZ position, influencing migration of the intervening SAMS and changing moisture and heat transport surrounding the continent (Zhou and Lau, 1998; Sylvester, 2009; Garcia and Kayano, 2010; Laprida et al., 2011), 3) variation in ENSO in the Pacific, indirectly impacting the sub-tropics of the South Atlantic and impacting currents (Garreaud et al., 2009), and 4) Atlantic Meridional Ocean Circulation (AMOC) mode switching, weakening or strengthening the BC (Chiessi et al., 2014; Chiessi et al., 2015; Mulitza et al., 2017; Santos et al., 2017). The variety of mechanisms are often interlinked and speak to the complexity of the regional climate and oceanography. However, it is important to note that this variation in position determines the water masses influencing a given site, with knock on impacts for regional climate, planktonic foraminiferal distribution and regional productivity, both in the modern and through time (Toledo, 2008; Laprida et al., 2011; Morard et al., 2016).

2.5 Current Margin Sedimentology and Processes

Contourites represent accumulations or remobilisation of sediments by persistent action of alongslope bottom-water ocean currents, contrary to turbidites which transport sediment downslope as density flows (Figure 2.5-1) (Rebesco et al., 2014). Contourites are comprised of muddy, silty or sandy sediments, typically due to the low strength bottom-water currents involved (Rebesco et al., 2014; Hernández-Molina et al., 2016). The Uruguayan margin is largely comprised of contourite deposits and intervening plastered drift deposits that extend from the Upper Slope to the Lower Slope-Rise Transition (Hernández-Molina et al., 2016). Regionally, there are multiple submarine canyon systems, that despite major riverine input from the Rio de la Plata have no clear continental shelf connection, instead propagating via head-ward slope failure (Krastel et al., 2011; Lantzsch et al., 2014).

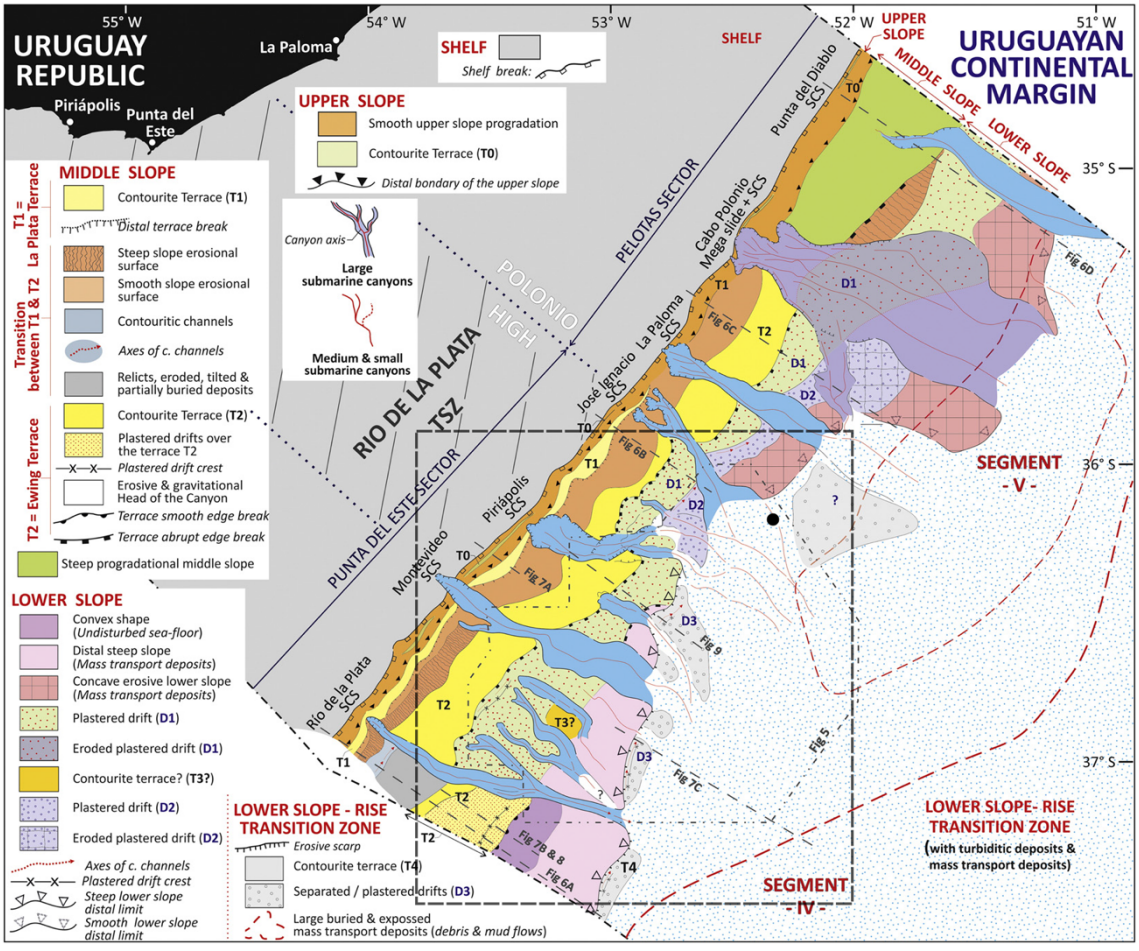

Figure 2.5-1 Modified from Hernandez-Molina et al., 2016. A morphosedimentary map displaying regions of contouritic sediment deposition (drifts and terraces) alongside erosive feature like canyons and mass transport deposits on the Uruguayan margin (Hernández-Molina et al., 2016). Dashed black box indicates the region in which cores were collected and the black circle represents the approximate location of site UPC 028.

The means through which contourite deposits form, makes them ideal for recent past climate study due to high sediment accumulation rates providing fairly continuous, high resolution records (Rebesco et al., 2014). As such, this region is an ideal location to futher investigate Late Quaternary palaeoclimate, palaeoceanographic and biotic records of the South West Atlantic. Use of contourites for palaeoclimate and palaeoceanography studies extend along the South American margin in publications on the Argentine (Hernández-Molina et al., 2009; Hernández-Molina et al., 2010; Bozzano et al., 2011; Krastel et al., 2011; Lastras et al., 2011; Preu et al., 2012; Piola et al., 2013; Preu et al., 2013; Voigt et al., 2013; Pérez et al., 2015; Warratz et al., 2017), Uruguayan (Hernández-Molina et al., 2016; Creaser et al., 2017; Morales, Chang, Soto, Corrêa, et al., 2017) and Brazilian margins (Viana and Faugères, 1998; Viana, Hercos, et al., 2002; Viana, 2002; Viana, Jr, et al., 2002; Knutz, 2008; Contreras et al., 2010; Borisov et al., 2013; Rebesco et al., 2014)

A broad summary of the contouritic and drift morpho-sedimentary facies of the Uruguayan continental margin is discussed in Burone et al., (2018), largely building on Hernández-Molina et al., (2016), Franco-Fraguas et al., (2014) and Lantzsch et al., (2014) amongst others. Dominant regional grain sizes tend to be sand and silt size with some biogenic components (Franco-Fraguas et al., 2014; Burone et al., 2018). The coverage of these studies is not entirely inclusive of the sampled area with some studies only extending to 1900 m water depth for direct sampling and relying on geophysical study for deeper depths. The above studies do however, further encourage the use of high-resolution spatial and temporal studies to expand understanding of this complex margin (Lantzsch et al., 2014; Franco-Fraguas et al., 2014; Hernández-Molina et al., 2016; Burone et al., 2018).

The upper slope of the contouritic region north of the core locations is predominantly influenced by the low energy MC, whilst regions that appear scoured and erosive are suggested to experience higher energy BC conditions (Franco-Fraguas et al., 2014). The sedimentology found in Franco-Fraguas et al., (2014) suggests a coarser grain size than that found within the studied cores, where silts and fine sands dominate alongside a small biogenic and organic component to the sediment (Franco-Fraguas et al., 2014). This is likely due to the study occupying shallower shelf waters, whereas this study deeper water depths further south on the continental slope (~1250-3000 m water depth).

2.6 Margin Geological History

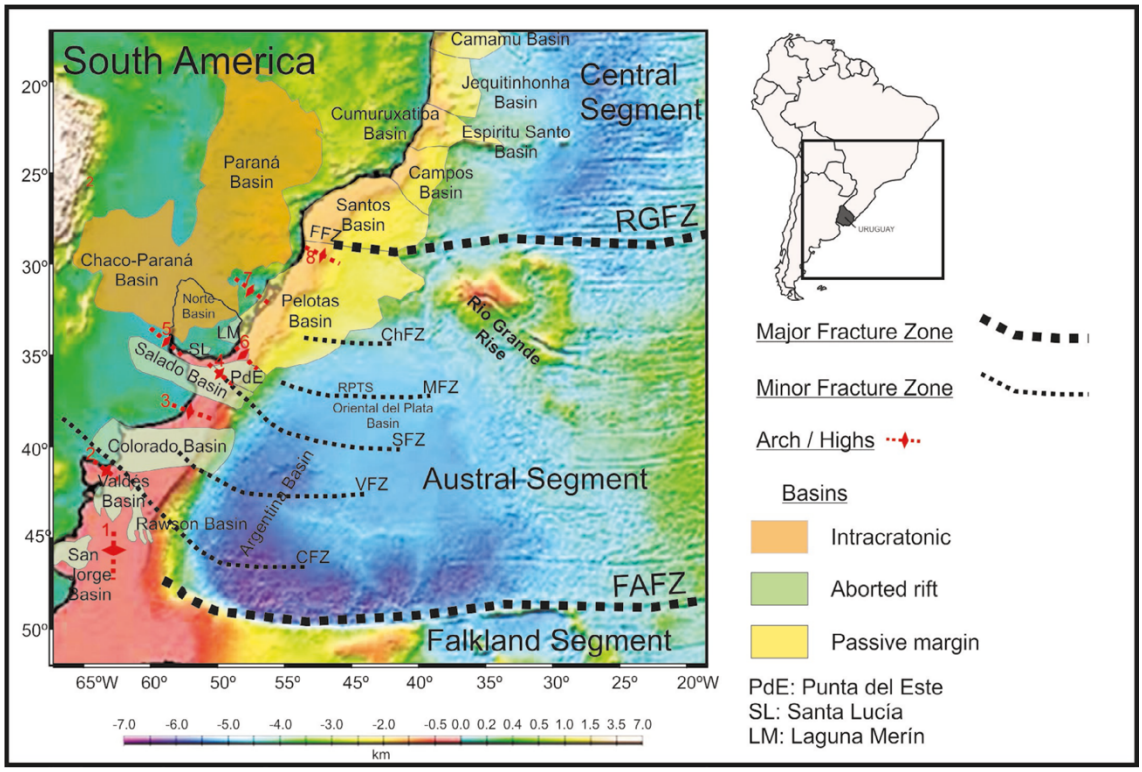

Figure 2.6-1 South American onshore and offshore sedimentary basins alongside tectonic segments and rifts, overlain on regional topography/bathymetry. Major Fracture Zones: FAFZ, Falkland-Agulhas Fracture Zone; RGFZ, Rio Grande Fracture Zone. Minor Fracture Zones: CFZ, Colorado Fracture Zone; VFZ, Ventana Fracture Zone; SFA, Salado Fracture Zone; RPTS, Rio de la Plata Transfer System; MFZ, Meteor Fracture Zone; ChFZ, Chui Fracture Zone; FFZ, Florianópolis Fracture Zone. Arch/Highs: 1. Patagonia Oriental; 2. Río Negro; 3. Tandilia; 4. Plata; 5. Martín García; 6. Polonio; 7. Rio Grande; 8. Florianópolis. This study focuses on material recovered from the Punta del Este basin (PdE), offshore Uruguay. Figure taken from Morales, Chang, Soto, Veroslavsky, et al., 2017.

Geographically the cores are located within the Punta del Este basin which, like the rest of the Uruguayan margin, has a long and complex geological history. This begins with the rifting and breakup of Gondwana and the opening of the South Atlantic Ocean, subsequently forming a passive margin during the Lower Cretaceous (137 to 126 Ma) (Blaich et al., 2009; 2013). Four segments were identified within the South Atlantic, each separated by fracture zones (Moulin et al., 2005; Morales, Chang, Soto, Corrêa, et al., 2017). These segments facilitated extension and opening of the South Atlantic, beginning in the southernmost segment (Falkland/Malvinas Segment) and propagating north through the South/Austral Segment, Central Segment and finally through the Equatorial Segment (Nürnberg et al., 1991; Hinz et al., 1999; Blaich et al., 2009; Morales, Chang, Soto, Corrêa, et al., 2017). The Punta del Este Basin is the northernmost failed rift basin of the Austral Segment, trending NW-SE and transected by the

Rio de la Plata Transfer System, offsetting several of the structures and features therein (Figure 2.6-1) (Soto et al., 2011; Morales, Chang, Soto, Corrêa, et al., 2017).

The Punta del Este basin is commonly split into four phases of tectonic and stratigraphic evolution: pre-rift, synrift, transition and post-rift or similarly named (Stoakes et al., 1991; Soto et al., 2011; Pérez, 2013; Conti et al., 2017; Morales, Chang, Soto, Veroslavsky, et al., 2017; Morales, Chang, Soto, Corrêa, et al., 2017). Much of the stratigraphy for the Punta del Este basin has been correlated between two drilled wells, the Gaviotín and Lobo wells, and correlated with horizons visible in seismic traces. Large sections of the margin evolution have been summarised in even greater detail within the following sources: Stoakes et al., (1991); Raggio et al., (2011); Pérez, (2013); Hernández-Molina et al., (2016); Morales, Chang, Soto, Corrêa, et al., (2017); Morales, Chang, Soto, Veroslavsky, et al., (2017) amongst others. Research has principally focused on three themes: the break-up of Gondwana and opening of the South Atlantic, contourite processes and morphology, and hydrocarbon exploration along the South Atlantic margin.

Due to the length of the cores in this region it is unlikely these older sediments have been sampled, unless significant erosive surfaces were encountered. The basin stratigraphy has been identified and detailed in Figure 2.6-2, split into the four phases of basin formation to provide reference of the deposited lithologies present (Figure 2.6-2).

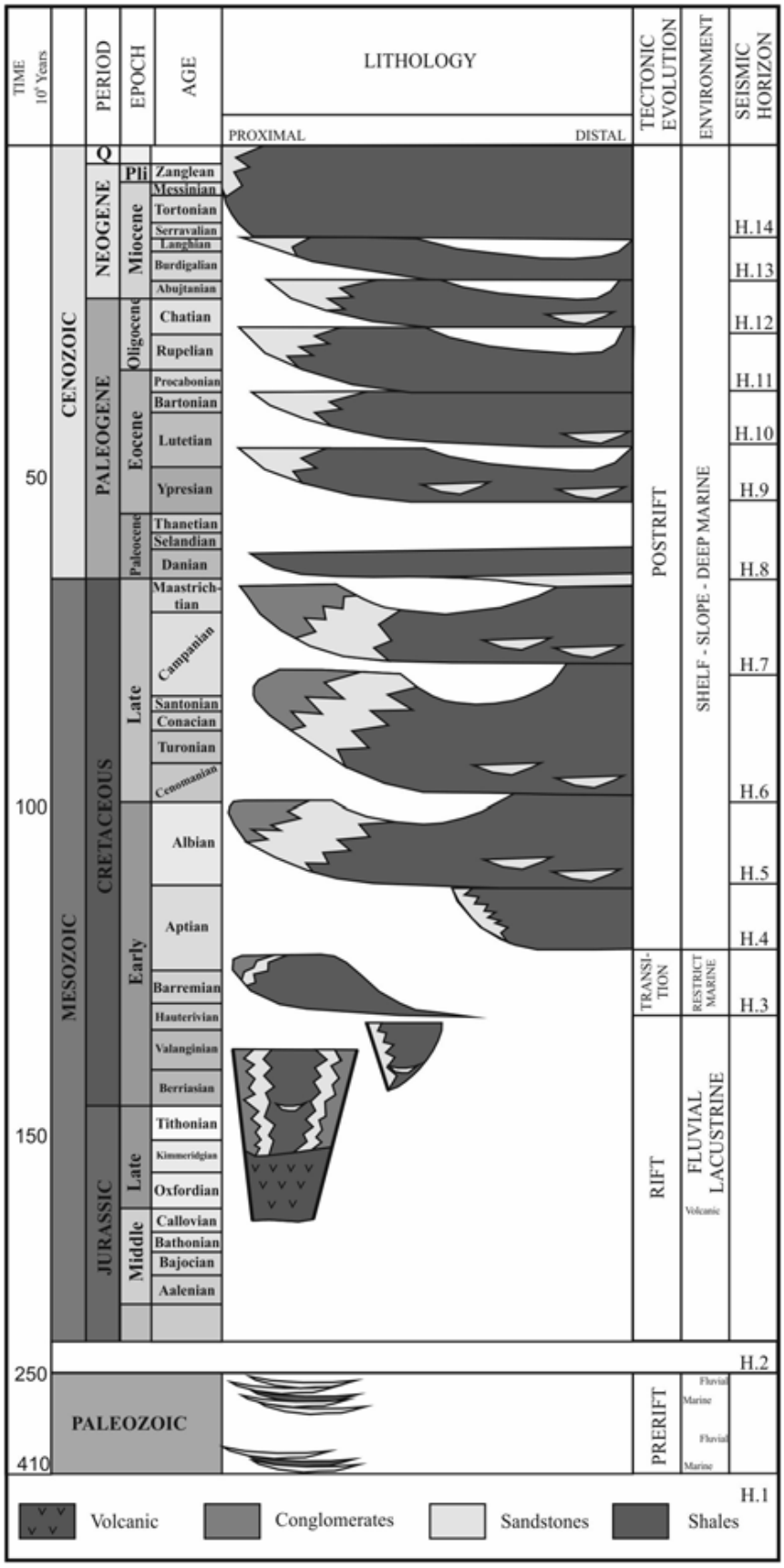

Figure 2.6-2 Stratigraphic chart for the Punta del Este basin. Lithology based on proximity, basin stage, likely environment of deposition and corresponding seismic horizon. Cores are unlikely to encounter samples older than the Quaternary and incorporate poorly/unlithified muds and sands. Taken from Morales, Chang, Soto, Corrêa, et al., 2017.

2.7 Planktonic foraminifera

Planktonic foraminifera are single-celled biomineralising marine zooplankton, prevalent from the tropics to polar latitudes with a fossil record that stretches back approximately 170 My (Bé, 1982; Sen Gupta, 2003; Schiebel and Hemleben, 2017). The highest abundances and diversity of planktonic foraminifera peak in the upper mixed-layer of the ocean (<100 m) with a few species specialised to live below the photic zone (Birch et al., 2013; Schiebel and Hemleben, 2017). During growth the organism constructs a calcium carbonate ($CaCO_3$) shell or 'test', with additional test chambers added as the individual matures, presenting a diverse array of distinct morphologies with varying degrees of ornamentation (Wolfgang H Berger, 1969; Schiebel and Hemleben, 2017). Critically for palaeoenvironmental studies, the precipitation of the $CaCO_3$ test is influenced by abiotic factors, consequently geochemical analysis of the test can shed light on the surrounding ambient seawater temperature and chemistry during growth (Aze et al., 2011; Schiebel and Hemleben, 2017; Schiebel et al., 2018). Planktonic foraminifera, along with other biomineralising planktonic organisms, contribute significantly to material exported to the sea floor, with their tests extremely abundant in calcareous biogenous sediments (Wolfgang H. Berger, 1969; Berger, 1971; Schiebel and Hemleben, 2017; Schiebel et al., 2018). The steady accumulation of these sediments, particularly in stable settings, makes it common for millions of years of evolutionary and palaeoclimatic history to be captured (Aze et al., 2011; Pearson, 2012). A remarkable fossil record, proxy hosting potential and globally ubiquitous nature make planktonic foraminifera an excellent study group for testing evolutionary theories and reconstructing marine environments.

2.8 Taxonomy

Taxonomically, the modern fauna features approximately 50 extant morphologically distinct species, with further genotypes being distinguished using genetics and molecular methods (Schiebel and Hemleben, 2017; Schiebel et al., 2018). Preservation of genotypes in the fossil record is problematic due to the loss of biological material post death, limiting fossil records to morphological distinctions (Schiebel and Hemleben, 2017; Schiebel et al., 2018). Common morphological characteristics are used to delineate existing species concepts within the literature, with examples of characteristics including: test shape, wall structure, number of chambers, aperture position and size, number of apertures,

presence/absence of spines or keels amongst other attributes (Wolfgang H Berger, 1969; Schiebel and Hemleben, 2017). The morphological taxonomy of the group has often been under revision to standardise the taxonomy globally, as species are synonymised and split from one another, altering the phylogeny of this group, as new studies incorporate additional data. This process has been ongoing in the literature for decades, but gained impetus with research community led efforts to standardise terminology through a series of atlases for the Cenozoic. To date the Palaeogene, Eocene and Oligocene Atlases have been completely revised (Olsson et al., 1999; Pearson et al., 2006; Wade et al., 2018) with a revision of the Neogene currently underway, building on the last major revision of Kennett and Srinivasan, (1983). Due to the core lengths, previous collection work (McGuire et al., 2019), and in the absence of an updated Neogene Atlas this study will rely heavily on modern texts such as Schiebel and Hemleben, (2017), and associated literature, with cores expected to be entirely Quaternary in age, unless cores pierce significantly older sediments.

2.8.1 Ecology

Modern planktonic foraminiferal species distributions have been shown to be strongly tied to ecological preferences including SST, nutrients and vertical temperature profiles (Kucera, 2007). The dominant parameter defining planktonic foraminiferal distributions is temperature (Boltovskoy et al., 1996; Boltovskoy et al., 2000; Sen Gupta, 2003; Kucera, 2007; Schiebel and Hemleben, 2017). Through analysis of modern species preferences and habitats it is possible to estimate past biogeographic and oceanographic conditions (Sen Gupta, 2003; Kucera, 2007; Schiebel and Hemleben, 2017). Estimations assume limited taphonomic reworking and that past species were similarly constrained as modern species (Schiebel et al., 2001; Kucera, 2007; Van Sebille et al., 2015; Schiebel and Hemleben, 2017). Table 2.8-1 provides eco-groups for a number of key species in this study, that will be used for isotope analysis. Expected eco-groups isotopic positions are plotted in Figure 2.8-1 and SEM images of key species to have stable isotopes conducted are presented in Figure 2.8-2.

Through planktonic foraminiferal assemblage counts this study will attempt to reconstruct the modern oceanographic assemblage and using the spatial distribution of foraminiferal abundances. Once constructed, this modern

representation will be applied to downcore samples at a single site to test whether oceanographic variations are recorded within the planktonic record.

Table 2.8-1 Key species for stable isotopes and their associated eco-groups, dwelling depths and whether they host symbionts based on the literature.

Species	Eco-group	Depth	Symbionts	Reference
Gs. ruber white	Tropical/Sub-tropical[1,4,5]	Open ocean mixed layer[1,4,5]	Yes[1,4,5]	1) Schiebel and Hemleben, 2017 2) (Darling et al., 2017) 3) (Ujiié and Asami, 2014) 4) Aze et al., 2011 5) Kucera, 2007 6) (Boltovskoy et al., 1996)
N. pachyderma	High latitude/Polar[1,2,4,5]	Mixed layer depleted, sub-surface[1,4,5]	No[1,2,4,5]	
Gc. inflata	Transitional[1,5,6]	Open ocean thermocline[1,4,5,6]	No[1,]	
Gr. truncatulinoides	Transitional[3,5,6]	Open ocean sub-thermocline[1,4,5]	No[5]	

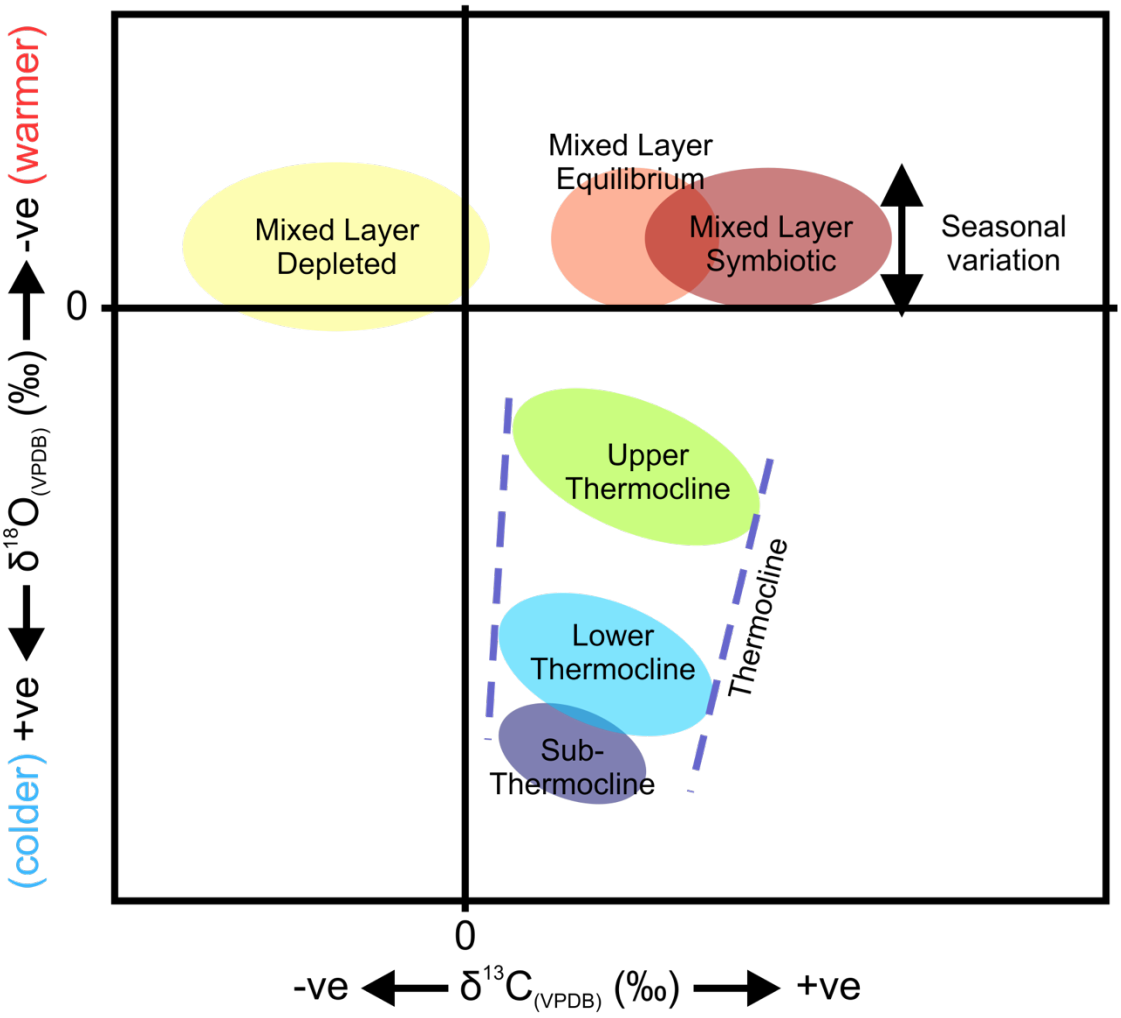

Figure 2.8-1 Expected modern relationships between known foraminiferal ecologies and isotopic signatures. Variation is expected seasonally, most notably impacting the δ $^{18}O_{(VPDB)}$ values, reflecting temperature change. Plot based on similar reproductions in Pearson et al., (2012) and Birch et al., (2013).

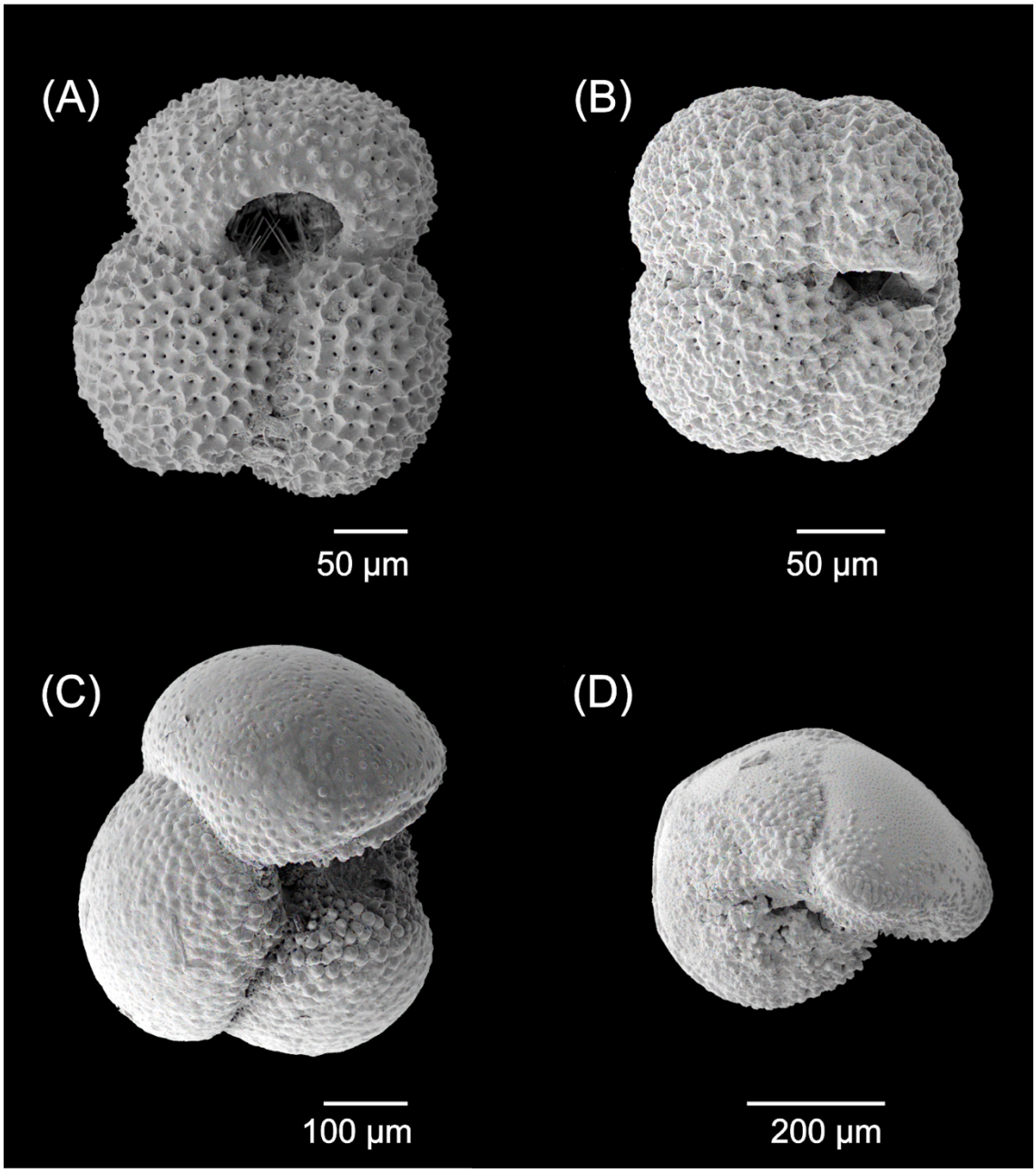

Figure 2.8-2 SEM plate with corresponding scales. A) *Gs. ruber white*, B) *N. pachyderma* C) *Gc. inflata* and D) *Gr. truncatulinoides.* Corresponding to species listed in Table 2.8-1.

2.8.2 Morphometrics

Morphometrics is the quantitative analysis of form relating to part or whole of an organism and can be utilised to study how form changes in a population through time or space. Planktonic foraminifera provide a readily available source of morphometric information, due to tests representing the whole organism, being readily preserved into the fossil record and being abundant both spatially and temporally (Schiebel and Hemleben, 2017; Schiebel et al., 2018). Body size variability is a visible proxy of an organism's life history, with changes to growth rate, maturation and death evidenced in preserved body dimensions (McKinney,

1990; Schmidt et al., 2008). Organisms should achieve peak growth under optimum environmental conditions and therefore obtain idealised body forms, with reductions in size or aberrations (i.e. deformities) occurring under more stressful parameters (Hecht, 1976; Schmidt et al., 2004; Schmidt et al., 2008). Test size and shape of planktonic foraminifera therefore reflects changes in physiology, ecology, with evolutionary change becoming apparent over greater periods of time (Schmidt et al., 2006). Whilst this study will not involve such large timescales, observation of morphometric change may be prevalent within a high-resolution study as environmental stresses change with boundary shifts between distinct neighbouring water masses.

Measuring morphometric variability of individual specimens within a species of planktonic foraminifera provides a history of response to changing environmental conditions. Application across multiple species enables an assessment of water column changes and the ecological shifts of species toward or away from optima with regard to events and trends through time. Furthermore it has been suggested that planktonic foraminifera have had stable optima for approximately the last 300 ky for most species, and the last 120 ky for all species (Schmidt et al., 2003; Schmidt et al., 2008). Thus, size shifts throughout the core are likely to be directly comparable to modern day species counterparts. Through observation of multiple species morphology and knowledge of the regions climatic/oceanographic shifts it may be possible to observe which species are pushed toward or away from their optima i.e. the winners or losers of habitat change during BMC migration at a single site.

2.8.2.1 Alternative morphometric study

The above suggested technique of measurement of quantitative morphometric characteristics of multiple species to reconstruct environmental change follows a more traditional format. However, this style of measurement would benefit from paired morphological and single specimen isotopic measurements in order to infer the potential drivers behind any change. Similar studies have been undertaken on single specimens of modern and Cenozoic planktonic foraminifera, using morphometric change alongside shifting isotope measurements to infer shifts in ecological niches (Woodhouse et al., 2021). This study demonstrated that shifts between eco-groups in both morphology and

isotopic signatures can be documented through time and across regions of complex oceanography.

Previous morphometric studies on the western South Atlantic margin have used multiple specimens per data point within their geochemical analysis (Morard et al., 2016; Jonkers et al., 2021). Morard et al., (2016), analysed *Gc. inflata* tests from across the BMC to build on findings by Chiessi et al., (2007) that a 2 ‰ $\delta^{18}O$ offset was visible in the species across the confluence. Morard et al., (2016), tested to see whether two genotypes of the species, one to the north of the boundary and one to the south (Morard et al., 2011), explained this offset using morphometric characters to split the two cryptic species alongside geochemical data. The results show some separation, however the lack of single specimen analysis hampers the study, with the authors suggesting such an approach would improve the extraction of ecological signals (Morard et al., 2016). Subsequent analysis by this study could help disentangle this signal with a BMC site.

Additional work was conducted by Jonkers et al., (2021) on the impact of encrustation on the stable isotopes, using the two morphotypes of the cryptic species to assess the regional variability. They found that specimens could be split into four extremes, encrusted and non-encrusted morphotype I from the BC and encrusted and non-encrusted morphotype II from the MC. No examples of non-encrusted specimens of morphotype II were recovered (Jonkers et al., 2021). Encrustation impacted the stable isotope signature by up to 2 ‰ $\delta^{18}O_{(VPDB)}$ compared to the non-encrusted forms within the BMC (Figure 2.8-3) (Jonkers et al., 2021). Work to disentangle the level of encrustation and its influence on cryptic species $\delta^{18}O$ values requires single specimen analysis.

This study took the extreme end members for the majority of their analysis i.e. fully encrusted or no encrustation, however they provide a means to semi-quantitatively assess encrustation into four categories (A-D) quickly (Figure 2.8-4). A study assessing spatial and temporal variability could implement this quick encrustation classification to see if it consistently explains a 2 ‰ offset in $\delta^{18}O_{(VPDB)}$ measurements alongside, or independent from, further morphometric analysis. In the absence of cryptic species analysis, the isotopic values by their associated water mass enable some classification into likely morphotypes of the cryptic species.

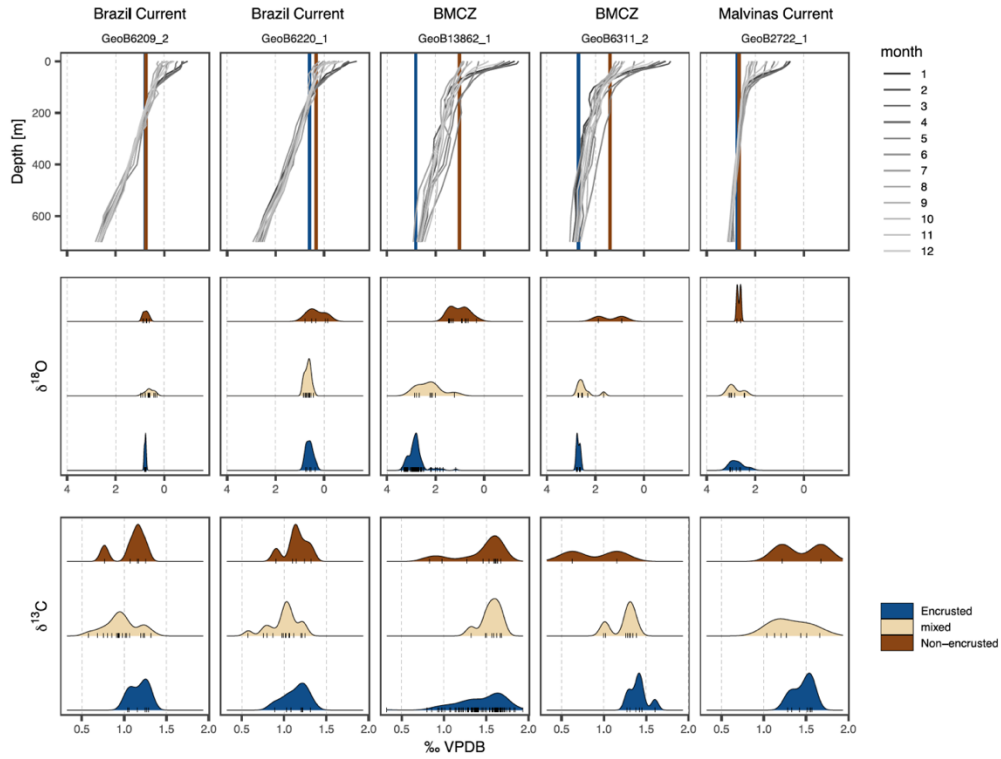

Figure 2.8-3 Results from Jonkers et al., (2021). Upper panel: water column monthly temperature/depth plots for five western South Atlantic margin sites with averaged apparent calcification depths for encrusted and non-encrusted forms. Middle panel: stable $\delta^{18}O_{(VPDB)}$ density curves. Outside the BMC encrustation shows little impact on $\delta^{18}O$ values. Lower panel: $\delta^{13}C_{(VPDB)}$ density curves, little impact of encrustation vs non-encrustation.

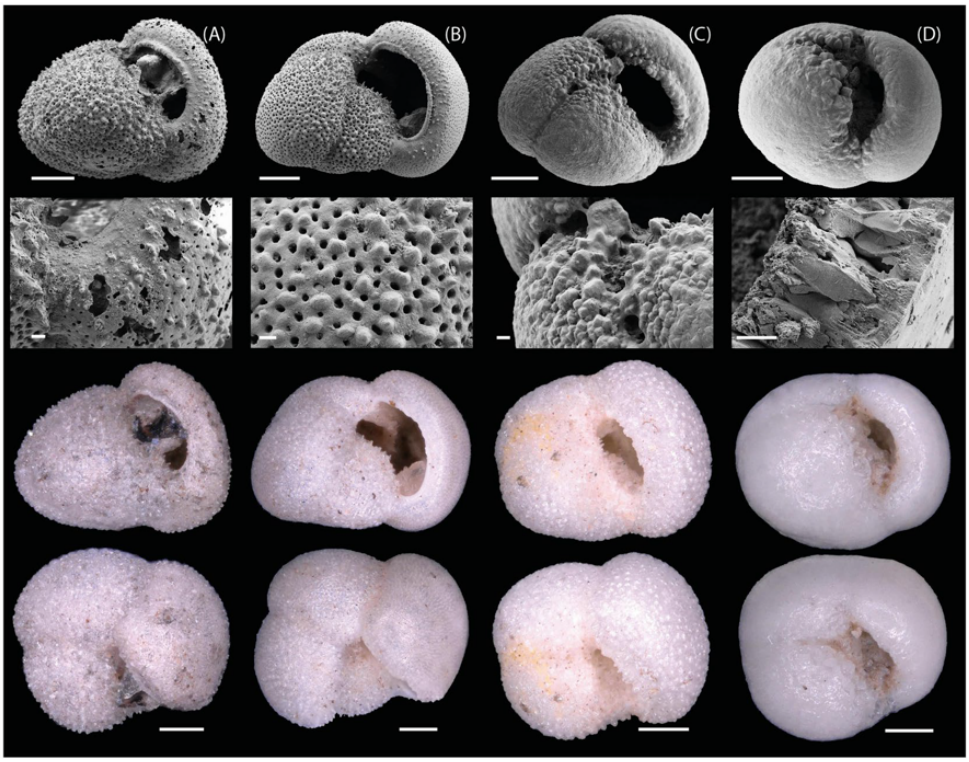

Figure 2.8-4 Taken from Jonkers et al., (2021). SEM and light microscope images of *Gc. inflata* specimens with degrees of encrustation. A) no encrustation, original test preserved. B) light encrustation, original test wall features visible. C) moderate encrustation, calcite overgrowths on test wall give shiny character. D) heavy encrustation, smooth walled specimen depicted. Scale bars: 100 μm whole tests, 10 μm wall structure SEM images.

2.8.3 Regional planktonic foraminiferal studies

Specific to this work are several relatively low resolution oceanographic investigations along the Western South Atlantic margin, broadly tracing modern water masses and relating them to planktonic foraminiferal assemblages (Boltovskoy et al., 1996; Boltovskoy et al., 2000). Boltovskoy et al., (1996), collected ninety-six plankton tows from twenty stations between 30-60°S in 1993, recreating a similar North Atlantic project (Bé and Hamlin, 1967; Boltovskoy et al., 1996). The following year Boltovskoy et al., (2000), collected thirty-eight plankton tow samples, resolving variation in the upper 100 m of the water column (Boltovskoy et al., 2000). Comparison of the data shows little interannual variability at similar latitudes of the most common species relative abundances, suggesting minor variation in distribution of surface plankton (Boltovskoy et al., 2000). Although a relatively small dataset for quantifying the whole of the South Atlantic margin, it is useful to note that species present in the plankton are indicative of SST and the water mass they occupy, and this framework will be used to underpin assemblage/water-mass associations in this thesis. A series of assemblage zones indicative of the water mass present were proposed based on the two studies with approximate latitudinal ranges (Table 2.8-2) (Boltovskoy et al., 1996).

Table 2.8-2 Approximate latitudinal Sea Surface Temperature ranges. Ranges are based on planktonic foraminiferal assemblages from two cruises conducted during the Southern Hemisphere late spring (Boltovskoy et al., 1996; Boltovskoy et al., 2000).

Zone	Approximate latitude range (°S) November 1994 (38 samples)	Approximate latitude range (°S) November 1993 (96 samples)
Subtropical	<35	<34
Cold subtropical	35-37	34-37
Transitional subtropical	37-39	
Transitional	39-47	37-49
Sub-Antarctic	47-54	49-55
Antarctic	54-60	>55

Additional studies using core top material include Chiessi et al., (2007), in which samples taken along the continental margin had oxygen and carbon isotopes run to determine whether any species record the BMC. Several species were found to depict various aspects of the water column including *Globigerinoides ruber pink*, *Globigerinoides ruber white* and *Trilobatus sacculifer/trilobus* for northern warm BMC stratified waters, *Globigerina bulloides* for southern cool subsurface

waters and *Globoconella inflata* and *Globorotalia truncatulinoides* (left and right coiling variants) indicated deeper waters across the entirety of the transect (Chiessi et al., 2007). It was in these two later species that an oxygen isotope offset of ~2 ‰ was observed across the BMC and prompted further study of *Gc. inflata* and potential genotypic and morphologic variation of the species across the BMC in the hopes of tracing past oceanographic processes by Morard et al., (2011; 2016); Jonkers et al., (2021). Whilst separate genotypes of *Gc. inflata* were indeed found either side of the BMC with subtle morphological variation (Morard et al., 2011; Morard et al., 2016) it has recently been suggested the ~2 ‰ $\delta^{18}O$ signal is a result of non-depth dependent test encrustation (Jonkers et al., 2021). The work of these authors further suggests the utility of planktonic foraminifera on the Uruguayan margin, both spatially and temporally, still has utility in tracing palaeoceanographic movements and an increase in sample density would help further resolve this.

Laprida et al., (2011), reconstructed middle Pleistocene SST (~300-120 ka) based on assemblages collected from a core from 3400 m water depth to the south of the Plata estuary, and indeed our sampling area, at 38° 29.7'S / 53° 40.7'W. Following Boltovskoy et al., (1996), the assemblages are dominated by sub-Antarctic species, with the ratio of *N. pachyderma* left coiling vs. left and right coiling used to determine colder, MC influenced conditions at the site between 300-120 ka (Boltovskoy et al., 1996; Laprida et al., 2011). The paper suggests a BMC shift north, inciting 4-6 °C cooling, as MC waters dominate the time period, explaining the shift of planktonic foraminiferal assemblages (Laprida et al., 2011). However, it should be noted the dating on this core relies on biostratigraphy, with the authors noting the potential for reworking within their site due to slumping proximal to the core (Laprida et al., 2011). However, the study dates to significantly earlier than the expected dates of this study, with no Holocene material recovered (Laprida et al., 2011).

Chapori et al., (2015; 2021), utilise planktonic foraminiferal assemblage data from a proximal site on the Argentine margin, GeoB2806-4, to reconstruct estimates of Mean Annual Temperature over the Holocene. These studies indicate an overall warming trend from the early Holocene, peaking by the mid-Holocene before a slight cooling trend to the modern, although resolution is coarse at ~1 ky. They find evidence for BMC migration across the Holocene, with a more

northerly position during the early Holocene and a migration south to a more southerly position during the mid-Holocene (Chapori et al., 2015; García Chapori and Laprida, 2021). This agrees with another study based on *Gc. inflata* isotope data from the Argentine margin, that cites a similar timing of movement in relation to changes in atmospheric patterns (Voigt et al., 2015).

Pivel et al., (2010), used $\delta^{18}O$ isotope data from *Gs. ruber white* specimens to construct a SST record offshore south-eastern Brazil, encompassing the last 20 ky at comparatively low resolution. Their findings suggest a warming trend from the early Holocene, with the largest rise occurring over the mid-Holocene (Pivel et al., 2010). Through comparison with other records they suggest SAMS activity is at its most intense during the Last Glacial Maximum (LGM) and late Holocene, aligning with changes to insolation, with the intervening period featuring a weakened monsoonal system (Pivel et al., 2010).

Portilho-Ramos et al., (2019), provides a reconstruction of productivity on the adjacent south-eastern Brazilian margin for the last 70 ky based on planktonic foraminiferal assemblages. This was done by correlating the relative abundance of upwelling favouring species, such as *Gg. bulloides*, with species known to favour oligotrophic conditions i.e. *Gs ruber*, *T. sacculifer* and *Ge. siphonifera* (Portilho-Ramos et al., 2019). They find that during the last glacial period evidence for greater upwelling is present through increased eutrophic species abundances vs. oligotrophic species and a drop in subsurface temperatures. The mechanism for this is thought to be related to oceanographic shifts, enabling a greater influx of silicic acid via SACW transport further north (Portilho-Ramos et al., 2019). A similar study was also conducted further north on the Brazilian margin by Toledo, (2008), which utilised the ratio of *Gs. ruber white* to *Gg. bulloides* to infer productivity shifts over the last 30 ky. In this instance their record also infers an increase in productivity over the last glacial as nutrient poor tropical sourced waters were impeded in favour of nutrient enriched waters sourced from further south (Toledo, 2008).

Frozza et al., (2020), primarily focus on bioerosion of planktonic foraminifera but also produce a south-eastern Brazilian margin record through assemblage analysis. This record covers the last 46 ky approximately and infers a warming signal over the Holocene alongside a decline in regional productivity (Frozza et al., 2020). An additional south-eastern Brazilian margin record, Chiessi et al.,

(2014), reconstruct BC variability during the last 5 ky, providing a late Holocene record. Through $\delta^{18}O$ isotopes and Mg/Ca data from planktonic foraminifera they infer a ~730 year cyclicity relating to BC vs. Northern Brazil Current (NBC) strength, driven by changes in AMOC, which they infer through alignment with North Atlantic records (Chiessi et al., 2014).

Wider global databases of foraminiferal assemblage and ecological data, such as the ForCens, Margo, Cortese, Neptune databases, and various combinations thereof lack the detailed coverage of the Western South Atlantic Margin (Haddam et al., 2016; Siccha and Kucera, 2017). Whilst previous planktonic foraminiferal studies from sites along the western South Atlantic margin predominantly agree on warming from the early to mid-Holocene, the temporal scale and dispersed nature of studies provides motivation to record BMC migration, on a higher spatial and temporal resolution. Further sampling on the margin would enable determination of whether observed patterns are consistent spatially across the margin, and through high-resolution sampling, temporally down core. Additionally, this warming story is not necessarily reflected in other proxies reported on the margin, which will be discussed in Section 2.8-2 (Kilian and Lamy, 2012; Varma et al., 2012; Bender et al., 2013; Razik et al., 2013; Lantzsch et al., 2014). As such the limited published data for planktonic foraminiferal assemblages enables a niche for this study to contribute new high-resolution spatial data in this oceanographically dynamic region, by taking advantage of the high-density core sampling.

2.9 Palaeoclimate Stable Isotope Geochemistry

The following section aims to briefly outline the theory behind stable isotope geochemistry in relation to palaeoclimate studies, and in particular the planktonic foraminiferal record. As previously highlighted, foraminifera precipitate a test of calcium carbonate, the isotopic composition of which is determined by the isotopic composition of surrounding seawater present during calcification (Pearson, 2012). Oxygen isotopes (with the corresponding proportions), $\delta^{16}O$ (99.757 %), $\delta^{17}O$ (0.038 %) and $\delta^{18}O$ (0.205 %) form part of this calcification process, with the relative abundance within a test controlled by fractionation processes (Pearson, 2012). A detailed review of the fractionation processes can be found in Pearson (2012), however one of the main factors impacting oxygen isotope proportions in seawater are evaporation and condensation. $\delta^{16}O$, being fractionally lighter, evaporates more readily than the heavier $\delta^{18}O$, which condenses more readily. As a result of repeated evaporation/condensation fractionation processes from low latitude oceans the poles at high latitudes, water vapour becomes increasingly depleted in $\delta^{18}O$, and thus ice sheets that form from that depleted water vapour retain a isotopically light composition (Pearson, 2012).

Over millennial timescales ice sheets wax and wane in response to climatic forcings, with growth of ice sheets concentrating $\delta^{18}O$ within the world's oceans, whilst ice sheet loss results in lower $\delta^{18}O$ values as melting of enriched $\delta^{16}O$ ice dilutes the global reservoir (Pearson, 2012). Because foraminifera, and other calcifying organisms, diagenetically preserve the ratio of oxygen isotopes at time of formation, it is possible to assess past isotope values over geological time and compare palaeoclimates of the past to the modern (Pearson, 2012). It is further possible to derive past temperatures from oxygen isotope ratios, using lab derived equations (Kim and O'Neil, 1997). A more detailed explanation of the history and processes of oxygen isotopes, in relation to foraminifera, can be found in Pearson (2012), whilst the use of isotopes by this study is discussed in Section 3.5.

2.9.1 The Holocene

2.9.1.1 Global temperature records

The Holocene palaeoclimatic story has often been cited as crucial in understanding the natural climate system variability, in order to understand and quantify the impact of anthropogenic climate change (Mayewski et al., 2004; Wanner et al., 2008; Shakun and Carlson, 2010; Marcott et al., 2013; Liu et al., 2014; Marcott and Shakun, 2015; Wanner et al., 2015). Reconstructing the degree of global Holocene palaeoclimate change, and defining the spatial and temporal extent of palaeoclimatic change, has proved difficult for the scientific community. This is in part due to apparent inconsistencies between paleo-proxy data and modelled results relating to global palaeoclimatic shifts (Liu et al., 2014). Palaeo-proxy signals indicate a global warming trend into the mid-Holocene before an apparent cooling toward the modern, this is in disagreement with model predictions which use retreating ice sheets and rising CO_2 values to predict mid-late Holocene warming (Marcott et al., 2013; Liu et al., 2014). This apparent discrepancy between measurements and modelling lead to the coining of the term Holocene Temperature Conundrum within the literature (Liu et al., 2014).

Attempts to resolve this conundrum have involved: 1) identification of seasonal and/or regional biases in proxy data, 2) factoring in the heavy northern hemisphere sampling bias for proxy data and impacts on climate models, 3) ongoing tuning of climate sensitivity within current climate models to realistically incorporate the above factors (Liu et al., 2014; Wanner et al., 2015; Bader et al., 2020; Kaufman, McKay, Routson, Erb, Dätwyler, et al., 2020; Bova et al., 2021). Recent data from IODP site 363 suggests the global Holocene Conundrum is likely a reflection of seasonality dominating records, with warming across the entire Holocene (Figure 2.9-1) (Bova et al., 2021). This was first in response to deglaciation and in the latter half of the Holocene (from 6.5 kya to the modern) a response to rising CO_2 levels (Bova et al., 2021).

Accounting for this seasonality, model estimates for global and latitudinal bands suggest minimal warming within the tropics, over the Holocene, with greater warming occurring in the mid- and high-latitudes, particularly for the northern hemisphere (Kaufman, McKay, Routson, Erb, Dätwyler, et al., 2020; Bova et al., 2021). Proxy records still suggest warming peaking during the middle Holocene, with the highest values occurring at approximately 6.5 ka, however producing

modelled seasonal SST and modelled mean annual SST suggests warming continues over the entire Holocene, driven by greenhouse gases, orbital forcing and loss of ice-sheets (Kaufman, McKay, Routson, Erb, Dätwyler, et al., 2020; Bova et al., 2021).

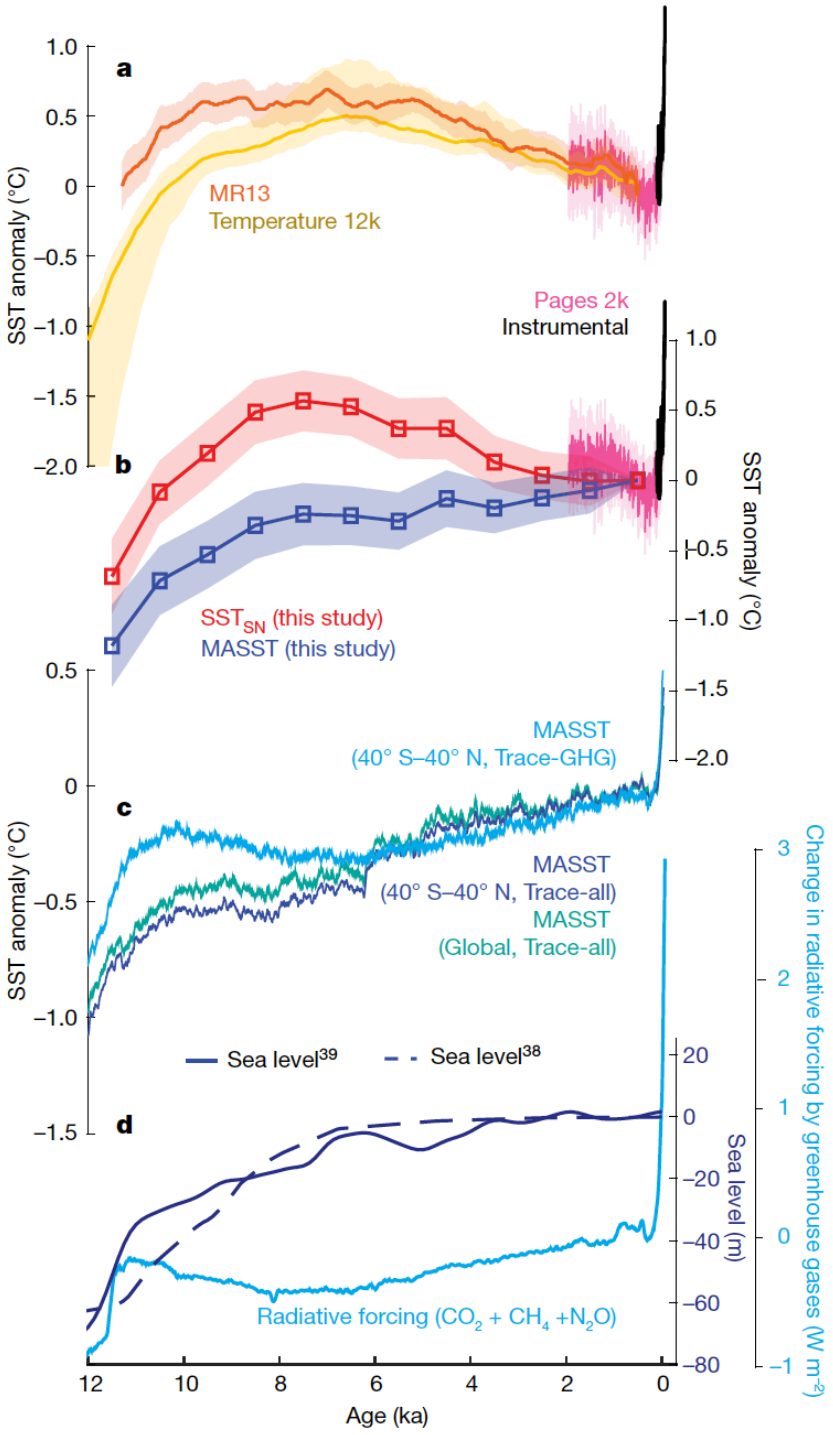

Figure 2.9-1 Holocene Temperature Conundrum global records. A) Previous global temperature proxy records with 1σ uncertainty shaded, showing warming peaking in the mid-Holocene (~6.5 ka). B) Seasonal (SST_{SN}) and Mean Annual Sea Surface Temperature records (MASST) reconstructed by Bova et al., (2021). C) A collection of simulated Holocene temperature records. D) Holocene sea level curves accounting for decreasing global ice volume and combined change in the radiative forcing from CO_2, CH_4 and NO_2. Figure taken from Bova et al., (2021) with references provided within.

2.9.1.2 Potential Holocene South American atmospheric interactions

Study of the modern system can be utilised to infer past changes over the course of the Holocene. The modern climate of South America is interconnected, both across the continent, but also tied into the regional oceanography (Peterson and Stramma, 1991; Stramma and England, 1999; Garreaud et al., 2009; Sylvester, 2009; Garcia and Kayano, 2010; Marengo et al., 2012; Razik et al., 2013; Jones and Carvalho, 2013; Voigt et al., 2015; García Chapori and Laprida, 2021). Examples of such systems include the ENSO, indirectly impacting the eastern sub-tropics in the South Atlantic from the Pacific side of the continent (Garreaud et al., 2009); the SAMS influencing heat and moisture transport, which is in turn impacted by ITCZ positional variation to the north, and the SACZ to the south (Zhou and Lau, 1998; Sylvester, 2009; Garcia and Kayano, 2010). One of the final systems impacting regional climate and oceanography is the SWWB that limits southward thermal expansion and drives polar advection northward (Sylvester, 2009; Voigt et al., 2015). Changes in latitudinal temperature gradients alter the positions of these regional climate systems, with migrations impacting the position and corresponding strength of associated oceanographic currents i.e. BC and MC, leading to north/south shifts of the BMC across the Holocene (Voigt et al., 2015; Piola and Matano, 2019). Similarly changes in ENSO frequency and amplitude through time has the potential to impact atmosphere-ocean interactions (Moy et al., 2002; McPhaden et al., 2006).

2.9.2 Holocene Continental Precipitation

Climate variability over millennia has been proposed to impact a number of factors relating to continental climate, including the position of oceanographic frontal systems (Lamy et al., 2010; Bender et al., 2013; Razik et al., 2013; Lantzsch et al., 2014; Chiessi et al., 2014; Voigt et al., 2015); the precipitation and foliage cover of the continental interior (Lamy et al., 2001; Cruz et al., 2009; Lamy et al., 2010; Stríkis et al., 2011; Kilian and Lamy, 2012; Vuille et al., 2012; Gu et al., 2017; Novello et al., 2017; Gu et al., 2018c) and the erosiveness and transport capacity of the Río de la Plata (Chiessi et al., 2009; Lantzsch et al., 2014; Razik et al., 2015). Whilst not the focus of this study, changes in the continental climate may influence the conditions planktonic foraminifera dwell in offshore and as such variability in these systems needs to be understood. A

series of papers relating to South American continental climate since the LGM can be found in Sylvester, (2009).

Evidence for climate variability has been derived from a variety of sources including modern SST and rainfall records (Robertson and Mechoso, 2000; Wainer and Venegas, 2002; Doyle and Barros, 2002; Garreaud, 2007; 2009; Marengo et al., 2012), marine (Lamy et al., 2001; Chiessi et al., 2009; Baker and Fritz, 2015), speleothems (Cruz et al., 2005; 2007; 2009; Lachniet et al., 2009; Stríkis et al., 2011; Vuille et al., 2012; Kanner et al., 2013; Baker and Fritz, 2015; Akers et al., 2016; Novello et al., 2017), ice cores (Vuille et al., 2012; Baker and Fritz, 2015), palynological records (Lamy et al., 2010; Baker and Fritz, 2015; Gu et al., 2017; 2018b; 2018c) and lake varves (Bird et al., 2011; Vuille et al., 2012; Baker and Fritz, 2015). A number of these records provide an indirect estimate of SAMS rainfall variability, chiefly the speleothem records, through $\delta^{18}O$ variability (Cruz et al., 2007). This is possible due to moisture sourcing for the SAMS having a distinct $\delta^{18}O$ signature compared to extra-tropical rainfall, meaning inference of changing seasonal relative rainfall contributions is possible based on the $\delta^{18}O$ signature preserved (Cruz et al., 2007).

Providing a broad scale overview, there are few records extending back into the Quaternary beyond the mid-Holocene, but those available show the LGM as a wetter period than the early-mid Holocene (Cruz et al., 2005; Novello et al., 2017). This is likely due to the ITCZ and SACZ being driven further south, due to the impact of orbitally driven decreased northern hemisphere insolation values and the associated cooling (Cruz et al., 2005; Novello et al., 2017). The inter-hemispheric temperature gradient is then shifted, enabling enhanced convection in the southern tropics, providing increased precipitation and a stronger SAMS (Cruz et al., 2005; Novello et al., 2017). The precipitation patterns shift during the early Holocene, with generally drier conditions in south eastern South America, as northern hemisphere warming leads to ITCZ and SACZ migration, driving the average SAMS location and corresponding precipitation northward (Cruz et al., 2005).

The majority of, but not all, studies show an increasing intensity of the SAMS over the mid to Late Holocene, with increasing aridity in Northern South America, and rising precipitation values further south, driven by increasing summer insolation values impacting SAMS and ITCZ location (Cruz et al., 2005; 2007; 2009; Chiessi

et al., 2009; Bird et al., 2011; Stríkis et al., 2011; Vuille et al., 2012; Kanner et al., 2013; Razik et al., 2013; Lantzsch et al., 2014; Baker and Fritz, 2015; Mulitza et al., 2017). This shift during the late Holocene to a more intense SAMS, and wetter conditions, has also been attributed to increased ENSO variability (Vuille et al., 2012; Kanner et al., 2013).

The result of this precipitation variation on the La Plata drainage basin is higher river discharge prior to the onset of the Holocene, tied to changes a more southward position of the SAMS (Chiessi et al., 2009; Razik et al., 2013; Lantzsch et al., 2014). This feedback is also evidenced in late Holocene records when precipitation increases after the relatively drier early-mid Holocene (Razik et al., 2013; Lantzsch et al., 2014). Such variation in discharge may impact records nearer shore, or in the likely path of the PPW on the Uruguayan and Brazilian shelves and may need to be considered when analysing productivity records.

2.9.3 Holocene oceanography

Oceanographic change is known to have occurred since the Pleistocene, and extendeding into the Holocene, reflecting a number of changes as the world warmed from the last ice age (Milne et al., 2005; Clark et al., 2009; Lambeck et al., 2014; Harrison et al., 2019). Regional records are available for offshore Argentina, Uruguay and Southern Brazil, a number of these papers suggest movement of oceanographic fronts and/or sea-level change (Isla, 1989; Milne et al., 2005; Cruz et al., 2009; Laprida et al., 2011; Razik et al., 2013; Bender et al., 2013; Chiessi et al., 2014; Lantzsch et al., 2014; Chapori et al., 2015; Voigt et al., 2015; Morard et al., 2016; Warratz et al., 2017; Prieto et al., 2017; Gu et al., 2018c; Frozza et al., 2020). This leads to uncertainty in the degree and direction of front movement, with similar contrast in the nature of relative sea-level (RSL) change. However, given the depth of sites investigated here (>1000 mbsl), it is unlikely the scopes of RSL change proposed (+/- 4-6 m) would impact these deep water sites. Through these papers a number of mechanisms are suggested and this will be explored in the later sections.

2.9.3.1 Sea level change

Sea-level change is well documented in response to global deglaciation following conclusion of the LGM, a period defined as 26-19 ka, during which global ice sheets reached maximum extents (Denton et al., 2010; Lambeck et al., 2014;

Harrison et al., 2019). From this global glacial maximum, changes in insolation, increases in meltwater input, changes to inter-hemisphere ocean and atmospheric circulation, and increases in atmospheric CO_2 causing thermal expansion, combine to cause global mean sea level rise over the remainder of the Pleistocene and into the Holocene (Denton et al., 2010; Rovere et al., 2016; Harrison et al., 2019). This rise is displayed in a global mean sea level ice-volume equivalent plot, shown in Figure 2.9-2, on which a number of Pleistocene and Holocene climatic events, that occurred during the deglaciation, are framed (Harrison et al., 2019). As the bulk of these events occur prior to the Holocene record of this study, these are not discussed in detail.

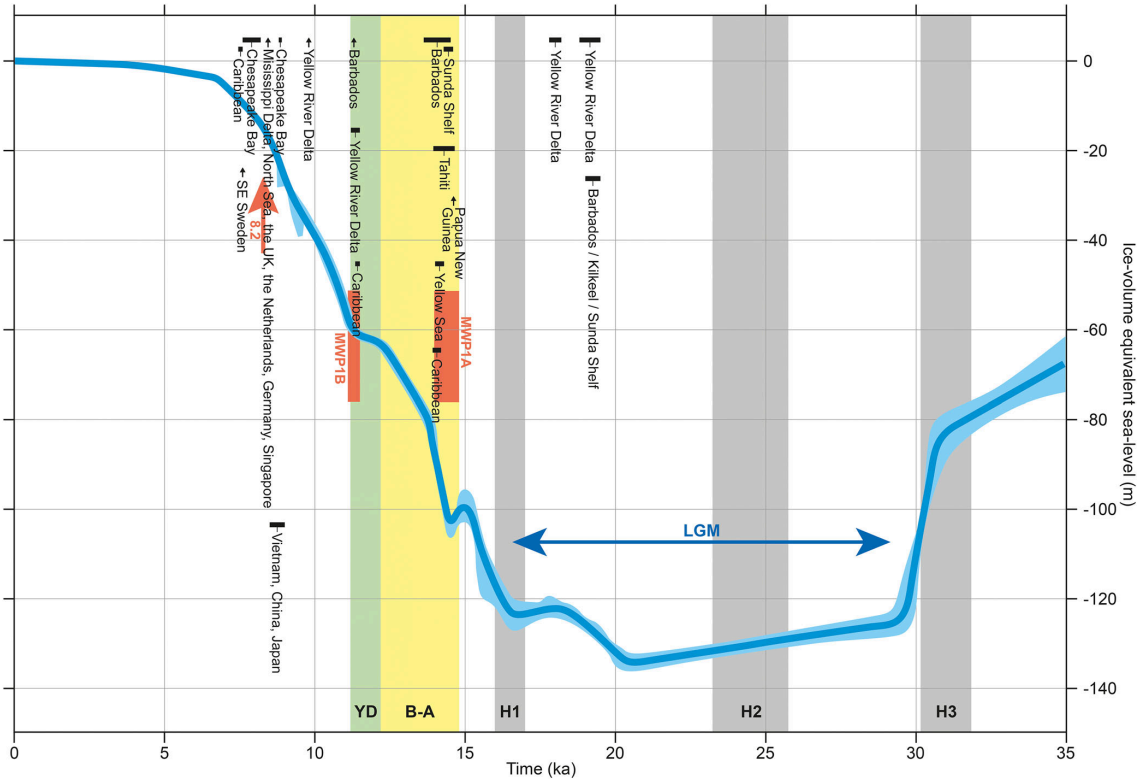

Figure 2.9-2 Global Mean Sea Level curve for the Pleistocene and Holocene, incorporating the Last Glacial Maximum (LGM), and subsequent deglaciation through a number of Melt Water Pulses (MWP). Additionally, a number of major climate events are highlighted including the Heinrich events (H1-3), the Bølling-Allerød warm period (B-A) and the Younger Dryas cold period (Y-D) for reference. The Holocene timeframe of this study is unlikely to incorporate the bulk of this sea level rise, however this does provide a wider framework. This plot was taken from Harrison et al., 2019.

Alongside this global mean sea level rise, more local and regional factors influence RSL rise. These can include isostatic uplift and subsidence, in relation to tectonics, uplift adjustment due to ice sheet unloading, and sea level change due to local gravitational factors (Guilderson et al., 2000; Denton et al., 2010; Lambeck et al., 2014; Rovere et al., 2016). Examples of these processes are detailed in Figure 2.9-3. It is important to use regional RSL curves that take account local variations. There are few reliable RSL studies proximal to the study region, however Milne et al., (2005) provide estimates for the whole of South

America, whilst Prieto et al., (2017) review those RSL records available for the neaby Río del Plata, incorporating Uruguayan and Argentine records (Milne et al., 2005; Prieto et al., 2017).

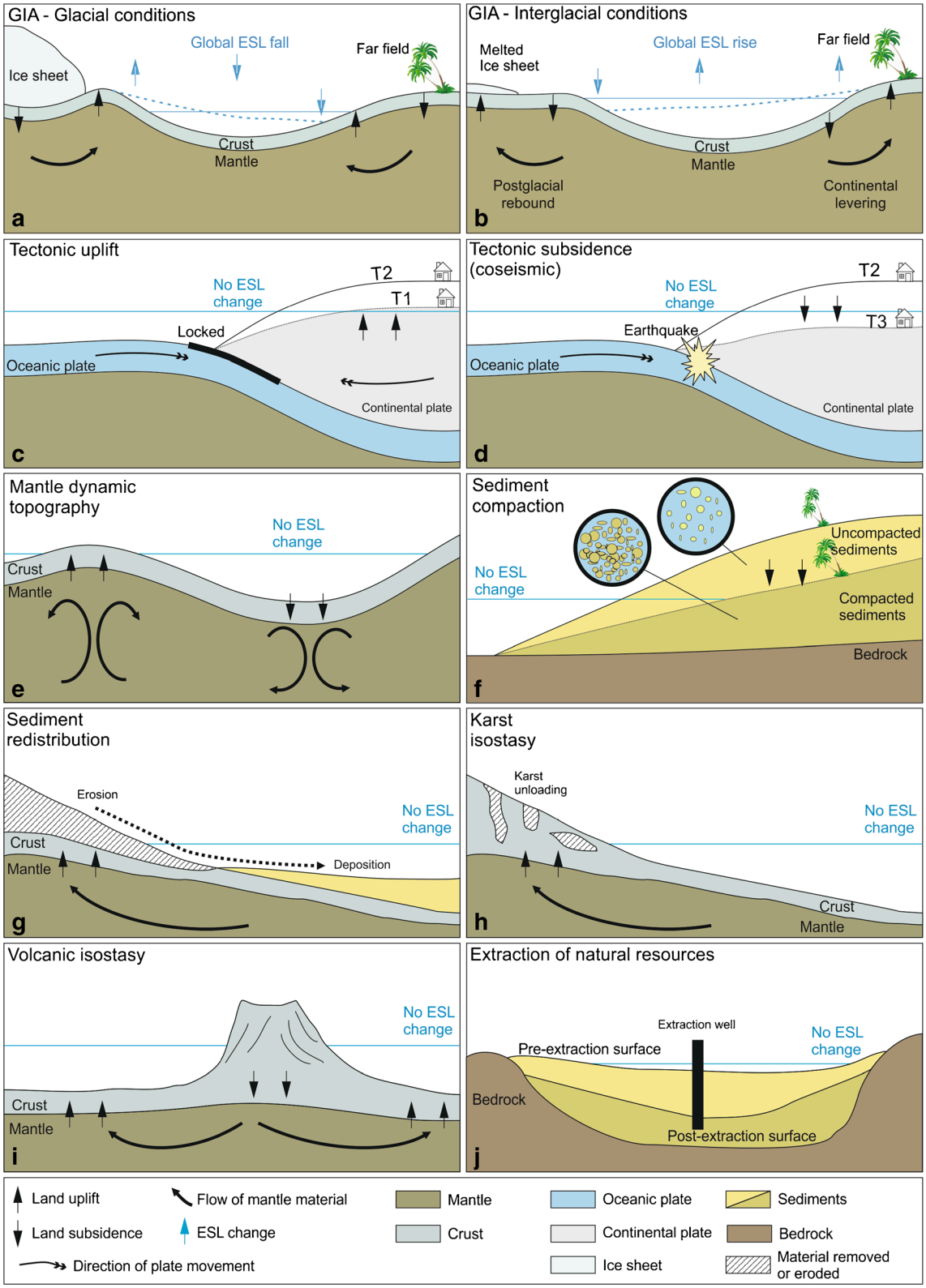

Figure 2.9-3 Examples of the local and regional processes that can impact relative sea level (RSL), on top of global changes, termed Eustatic Sea Level (ESL). GIA stands for Glacial Isostatic Adjustment. These processes can act at a site in conjunction with one another or oppose one another to impact RSL. Taken from Rovere et al., 2016.

2.9.3.2 Regional Relative Sea Level

Continuing deglacial trends from the LGM, the Holocene broadly observes global sea level rise, however the extent of this change varies regionally (Fairbanks, 1989; Pirazzoli, 1993; Mörner, 1996; Milne et al., 2005; Bracco et al., 2011; Hanebuth et al., 2011; Stanford et al., 2011; Bender et al., 2013; Lambeck et al., 2014; Prieto et al., 2017; Khan et al., 2019; Harrison et al., 2019). Regional records from along the western South Atlantic margin suggest this sea-level rise peaks within the mid-Holocene, although the exact timing and size of this highstand varies by study and latitude (Guilderson et al., 2000; Cavallotto et al., 2004; Milne et al., 2005; Angulo et al., 2006; Nagai et al., 2009; Bracco et al., 2011; Martínez and Rojas, 2013; Bender et al., 2013; Bracco et al., 2014; Castro et al., 2014; Colombo et al., 2014; Prieto et al., 2017).

Prieto et al., (2017) reviewed the data collected from the Argentine and Uruguayan margins, again finding the timing and amplitude of the mid-Holocene highstand was poorly constrained. This was in part due to the variety of methods that had previously been utilised, and because the data employed in reconstructions across the region was sourced from differing envrionments (Prieto et al., 2017). The authors conducted a thorough review of available data types, with the associated radiocarbon dating, filtering out likely erroneous data and applied consistent radiocarbon curves (Prieto et al., 2017). Data was then compared to local palynological records and predictions from Glacial Isostatic Adjustment (GIA) models, finding good agreement (Prieto et al., 2017).

The broad timing of the highstand across the literature is between 7-5 ka, with models, GIA predictions and trends inferred from the palynological/diatom records implying sea level in the Río del Plata began to fall over the last 6 ky (Prieto et al., 2017). RSL data derived from the Río del Plata region suggests, when reached, highstand was ~4-6 m above present day (Prieto et al., 2017). The total RSL change from the early Holocene to mid-Holocene highstand, given the uniform sea level rise observed, is unlikely to exceed 20 m and thus unlikely to be observed in >1000 mbsl sites (Cavallotto et al., 2004; Angulo et al., 2006; Bracco et al., 2011; Martínez and Rojas, 2013; Bender et al., 2013; Bracco et al., 2014; Lantzsch et al., 2014; Colombo et al., 2014; Prieto et al., 2017; Harrison et al., 2019).

From the highstand, the literature agrees RSL fell during the remaining mid-Holocene and late Holocene to the modern, however the nature of this fall is debated. Several authors suggest a smooth, continuous RSL decline (Cavallotto et al., 2004; Angulo et al., 2006; Gyllencreutz et al., 2010; Martínez and Rojas, 2013; Colombo et al., 2014), whilst some imply a oscillating RSL fall, with brief smaller rises offsetting the general declining RSL pattern (Gyllencreutz et al., 2010; Bracco et al., 2011; Bracco et al., 2014). As Bracco et al., (2014), point out in their reply to Martínez and Rojas, (2013), the curves are largely similar in the overall trends displayed.

However, the use of palynological and diatom records from nearby salt marsh sediments help clarify the nature of RSL fall, with Acritarchs and Dinocysts peaking during highstand (Figure 2.9-4). These are then replaced by algae and pollen as RSL falls, with limited pulses that would suggest oscilation in RSL (Prieto et al., 2017). Additionally, this palynological/diatom data is in agreement with a non-parametric “Loess” smoothing model, based on available elevation-time plots that, predicts a consistent decline in RSL (Figure 2.9-4). The alternative model Prieto et al., 2017 utilised was a Gamma model, however this does not take into account subsurface data, and thus was not favoured, additionally the Loess model was in close agreement with GIA model predictions (Prieto et al., 2017).

From this relatively proximal study (Prieto et al., 2017), it is possible to infer RSL change is similar at the UPC sites. Although given the water depths, and distance to shore from slope position, of the UPC sites it is not expected to impact this studies results, with site records maintaining marine status in entirety.

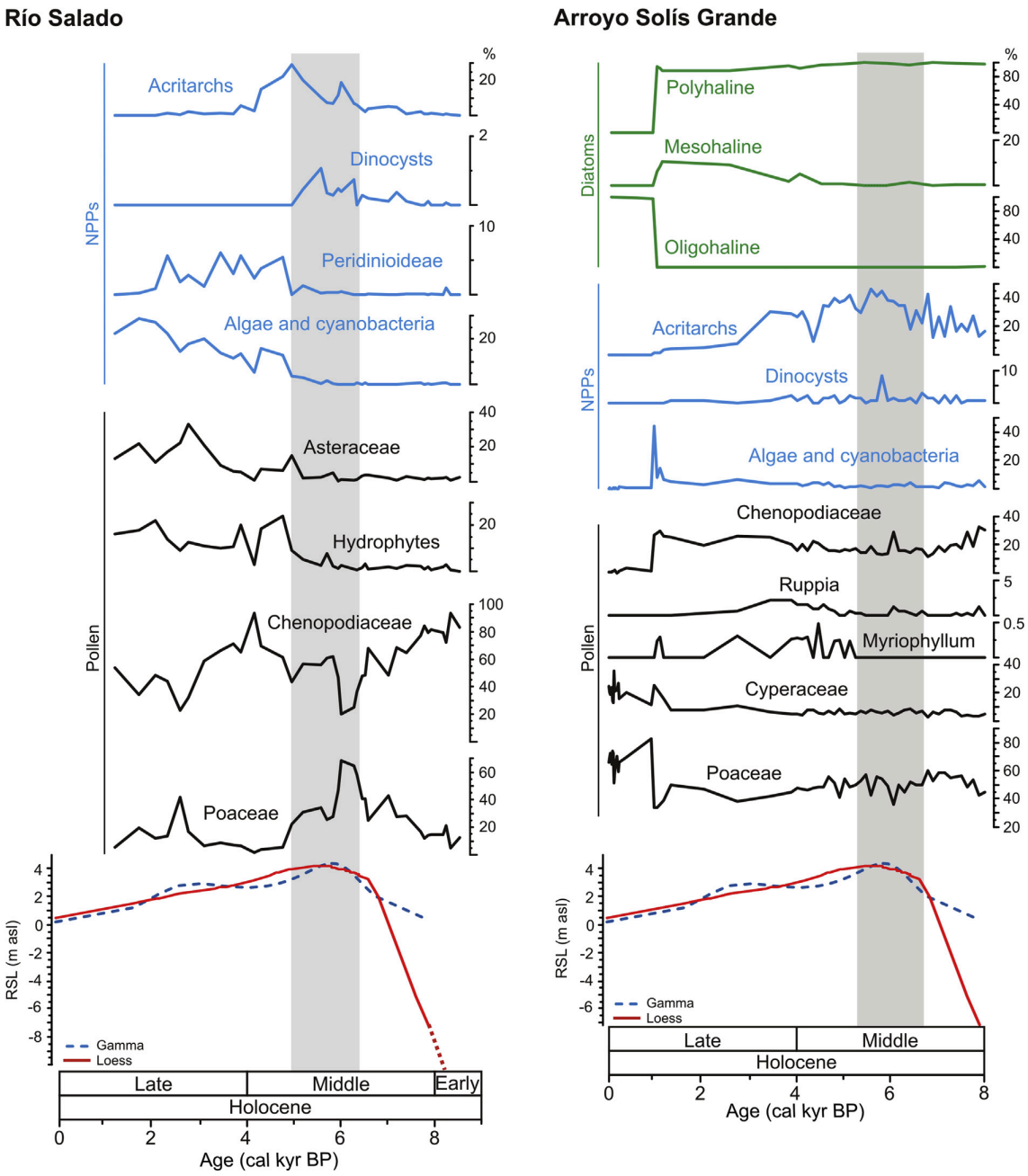

Figure 2.9-4 Palynological and Diatom data from two salt marsh sites either side of the Río del Plata estuary and utilised to reconstruct Relative Sea Level (RSL) by Prieto et al., 2017. NPPs refers to Non-Pollen Palynomorphs with the grey band indicating highstand inferred from the palynomorphs and diatoms. Loess and Gamma refer to two statistical models employed by Prieto et al., 2017 to determine RSL, with the former closely aligning with Glacial Isostatic Adjustment models, and the latter likely differing due to subsurface data omission. Taken from Prieto et al., 2017.

2.9.3.3 BMC shifts

Debate within the literature centres around the potential migration of the BMC in response to complex changing ocean-atmospheric influences. Whilst the majority agree some migration occurs, the direction, magnitude of migration and timing of movement along the margin are debated, with a number of mechanisms utilised to explain records. Additional confusion seems to come from authors coupling the

BMC with the STSF (Bender et al., 2013; Lantzsch et al., 2014; Franco-Fraguas et al., 2014). The STSF however, has not been shown to be connected with the BMC further offshore, and thus migrations suggested in this shallow, nearshore front do not necessarily reflect conditions further offshore (Piola et al., 2000; Matano et al., 2010; Voigt et al., 2015).

The prevailing process based on planktonic foraminiferal stable isotopes and palynological studies suggest BMC migration moves south from the current position over the mid-Holocene. This is linked to a weakening of the SWWB, shifting the maximum wind stress curl southward, a weakened ENSO state over the early/mid-Holocene and a strengthened BC; this enables the southward migration from ~0.75° north of the present day latitude at ~10 ka, to ~0.5° south at ~5 ka within the mid-Holocene (Figure 2.9-5) (Cane, 2005; Sylvester, 2009; Lamy et al., 2010; Lumpkin and Garzoli, 2011; Voigt et al., 2015; Gu et al., 2018c). Additional Brazilian margin records imply a weakening of westerlies during the mid-Holocene (de Mahiques et al., 2009). However, as Kilian and Lamy, (2012), point out in their collation of South American SWWB records from Patagonia, and Varma et al., (2012), also confirm, the SWWB signals are not always in agreement, with contradictory records for SWWB reconstruction over the Holocene a challenge (Kilian and Lamy, 2012; Varma et al., 2012; Voigt et al., 2015).

After the mid-Holocene, a number of changes occur impacting atmospheric patterns and oceanographic processes, complicating the potential migration of the BMC. Insolation changes result in a cooling northern hemisphere, which in turn drives the ITCZ southward, and through Hadley cell weakening translates to a stronger SWWB in the mid-latitudes (Sylvester, 2009; Lee et al., 2011). Southern hemisphere mid-latitude temperatures in the late Holocene cool slightly, causing a number of shifts to occur impacting the SWWB position (Lamy et al., 2010). This cooling is coeval with eastern tropical Pacific warming, establishing more modern like El Niño conditions, and increasing the SST meridional gradient in the low-mid latitudes, reducing the suppression of the SWWB at high latitudes enabling migration north (Lamy et al., 2001; Lamy et al., 2010; Voigt et al., 2015). This southward ITCZ movement also brings the aforementioned southern migration of the SAMS resulting in increased precipitation (Lantzsch et al., 2014).

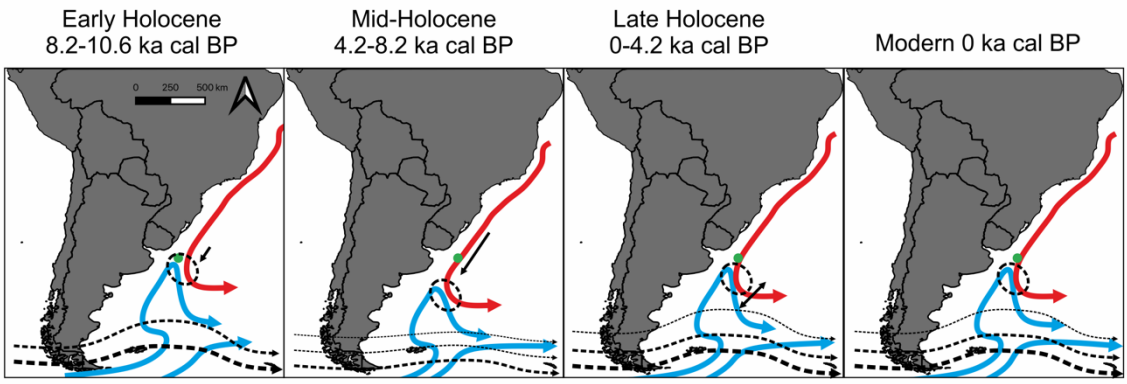

Figure 2.9-5 Schematic showing how the South Westerly Wind Belt (SWWB) may have migrated over the Holocene and impacted the BMC position based on supporting literature (Lamy et al., 2010; Voigt et al., 2015; Gu et al., 2018c). Green dot: approximate location of this studies cores. Blue line: Malvinas Current (MC). Red line: Brazilian Current (BC) Dashed oval: BMC mixing region. Black dashed arrows are the SWWB, increasing weight denotes increased wind strength. During the early Holocene the study region was likely under BMC conditions, albeit slightly cooler than present. In the mid-Holocene SWWB suppression southward results in BMC migration south, bathing the study in warmer BC waters. Late Holocene the BMC migrated further north with increasing SST meridional gradients expanding the SWWB (Lamy et al., 2010; Voigt et al., 2015), toward present BMC position. However, increased ENSO amplitude and frequency from the mid-Holocene likely resulted in increased variability in BMC position (Moy et al., 2002; Voigt et al., 2015).

Contrasting the expansion of the SWWB, a mechanism for further variability may be present in the late Holocene due to southward migration of the ITCZ. This could potentially weaken the NBC, increasing the strength of the BC, and drive the BMC position southward, although this process also seems to oscillate through the late Holocene (Chiessi et al., 2014). The increased variability of BMC positioning in the literature appears to originate from entanglement of a number of processes as mentioned above. Voigt et al., (2015), and Gu et al., (2018), capture this in two proximal records to this study, utilising planktonic foraminifera and palynology separately. They both imply a migration of the BMC north from the mid-Holocene southern position, overshooting the modern position by ~1° at 1.5 ka and then migrating south again toward the modern position of ~38 °S. (Moy et al., 2002; Voigt et al., 2015; Gu et al., 2018c). It seems likely this increase in BMC variability is tied to the ENSO increasing in variability and amplitude from ~6 ka onward (Moy et al., 2002; Cane, 2005), leading to increased variability observed in BMC position (Voigt et al., 2015).

A number of studies on the continental shelf have suggested contrary trends over the Holocene, with migrations of the STSF going in the opposite direction to studies analysing the BMC further offshore (Bender et al., 2013; Razik et al., 2013; Lantzsch et al., 2014). Those sites that imply northward STSF migration

are typically nearer shore and from water depths <700 m, commonly cite two mechanisms controlling the STSF position (Bender et al., 2013; Razik et al., 2013; Lantzsch et al., 2014). The first mechanism utilises sea-level rise over the early and mid-Holocene, all studies agree sea level rise occurs over the early to mid-Holocene on the eastern South American margin (Angulo et al., 2006; Gyllencreutz et al., 2010; Bender et al., 2013; Martínez and Rojas, 2013; Bracco et al., 2014; Colombo et al., 2014; Prieto et al., 2017). Within these STSF studies the sea level rise broadens the available shelf space and leads to an intensification of SASW pushing further north, driving the STSF northward (Bender et al., 2013; Razik et al., 2013; Lantzsch et al., 2014). The second mechanism to migrate the STSF northward over the early and mid-Holocene, is via a northward expansion of the SWWB (Bender et al., 2013; Razik et al., 2013; Lantzsch et al., 2014), counter to the studies of Voigt et al., (2015), and Gu et al., (2018). Whilst the sea level rise, and disconnected nature of the STSF and the BMC, could permit contrary directions of migration, the inferred opposite trends in SWWB is difficult to resolve and will need investigation.

Chapter 3 Methodology

3.1 Site Selection and Donation

The project aims of testing the spatial and temporal heterogeneity of planktonic foraminiferal assemblages necessitate a high density of cores. Core density is key in enabling assessment of assemblage variability between proximal sites, and in determining relationships between foraminiferal communities and complex regional oceanographic processes (Kucera, 2007; Schiebel and Hemleben, 2017). Ideally, cores will have been collected using the same methodology and during the same time interval to minimise potential biases or sedimentological/ biological events between sampling (Schiebel and Hemleben, 2017).

Few scientific expeditions can sample at the required spatial resolution due to the expense of offshore expeditions and the premium of extensively coring the seafloor. However, in 2014 ANCAP and BG Group donated over two hundred, industry-collected, sediment piston cores from the Uruguayan Margin to UK research. Over 800 m of cored material, from an area approximately 7100 km^2, collected on cruise J14092 is housed at the British Ocean Sediment Core Research Facility (BOSCORF) and provides a unique opportunity to test a variety of spatial and temporal research questions (Figure 3.1-1).

The region covers water depths from 800 to 3200 m on the continental slope and comprises a range of settings including: plastered drifts, contourite terraces, mass transport deposits, channels and erosive surfaces. For the purposes of this study regions of drift sediments were targeted to avoid sedimentary reworking and winnowing by contourite and turbiditic processes, based on previous work along the margin (Hernández-Molina et al., 2016; McGuire et al., 2019).

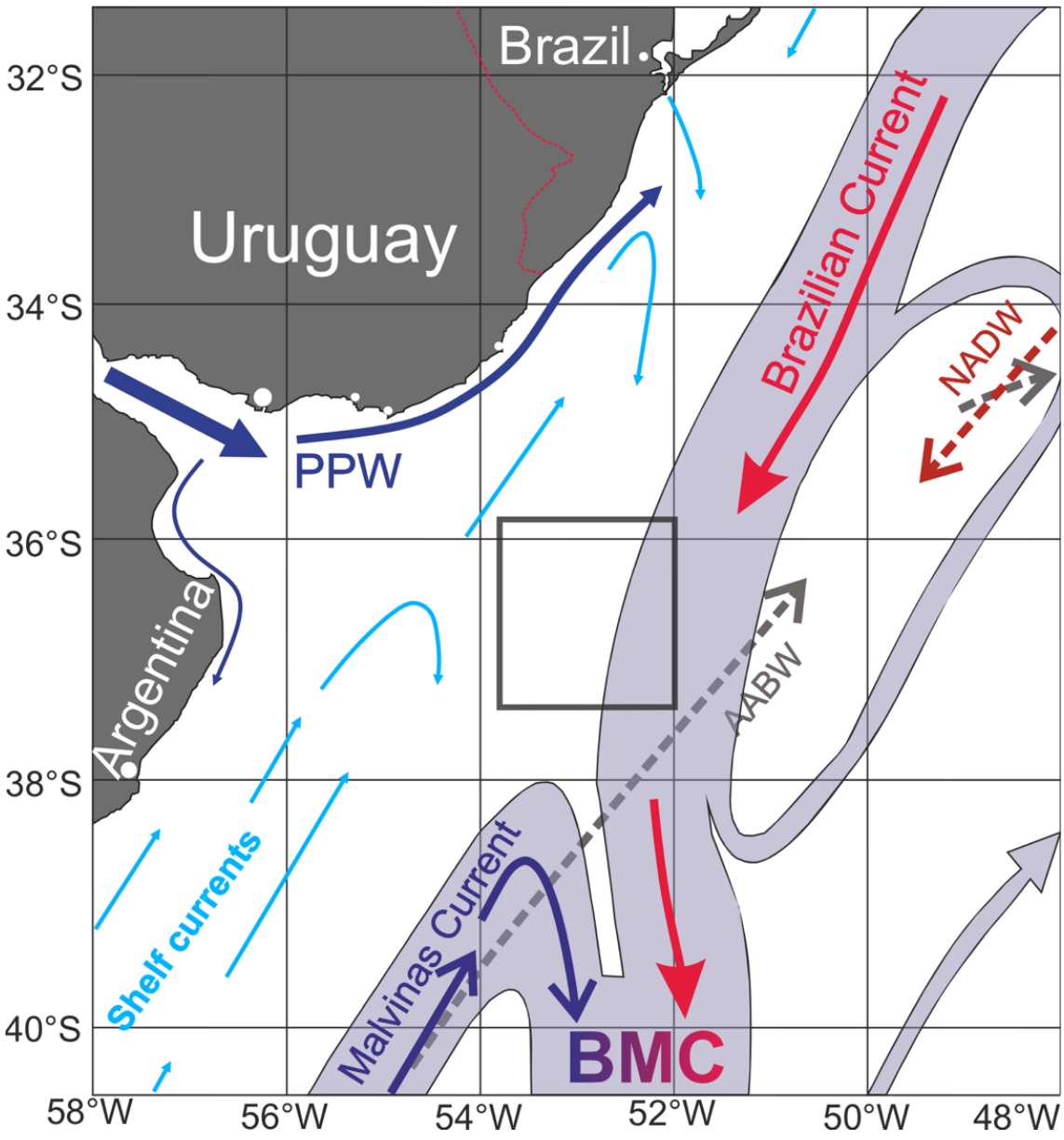

Figure 3.1-1 Site location in relation to Uruguayan coastline. Grey box defines the region from which 200 cores were collected by BG group and ANCAP. Additionally, the regional simplified oceanography is overlain. Modified from Hernández-Molina et al., 2016.

3.2 Core Selection, Sampling and Scanning

3.2.1 Core selection

From the 200 cores available several core-tops had already been sampled and thus were unavailable for study, this included many of the margin transects. An initial fifteen surface samples were requested and supplied by BOSCORF covering a variety of sub-environments within this dynamic erosive/deposition region. Cores were selected to sample the margin length (WSW-ENE) and target drifts and terraces for good preservation of foraminifera in the silts and clays. Sections including the slope base, mass transport deposits and scarps were omitted to avoid reworked material blurring the modern signal (Hernández-Molina et al., 2016). A few canyon bases were targeted to determine if these features incised into significantly older sediment. After the initial investigation a further 20 core tops were requested for the spatial study (Figure 3.2-1), covering the margin breadth and a range of water depths, increasing sampling resolution.

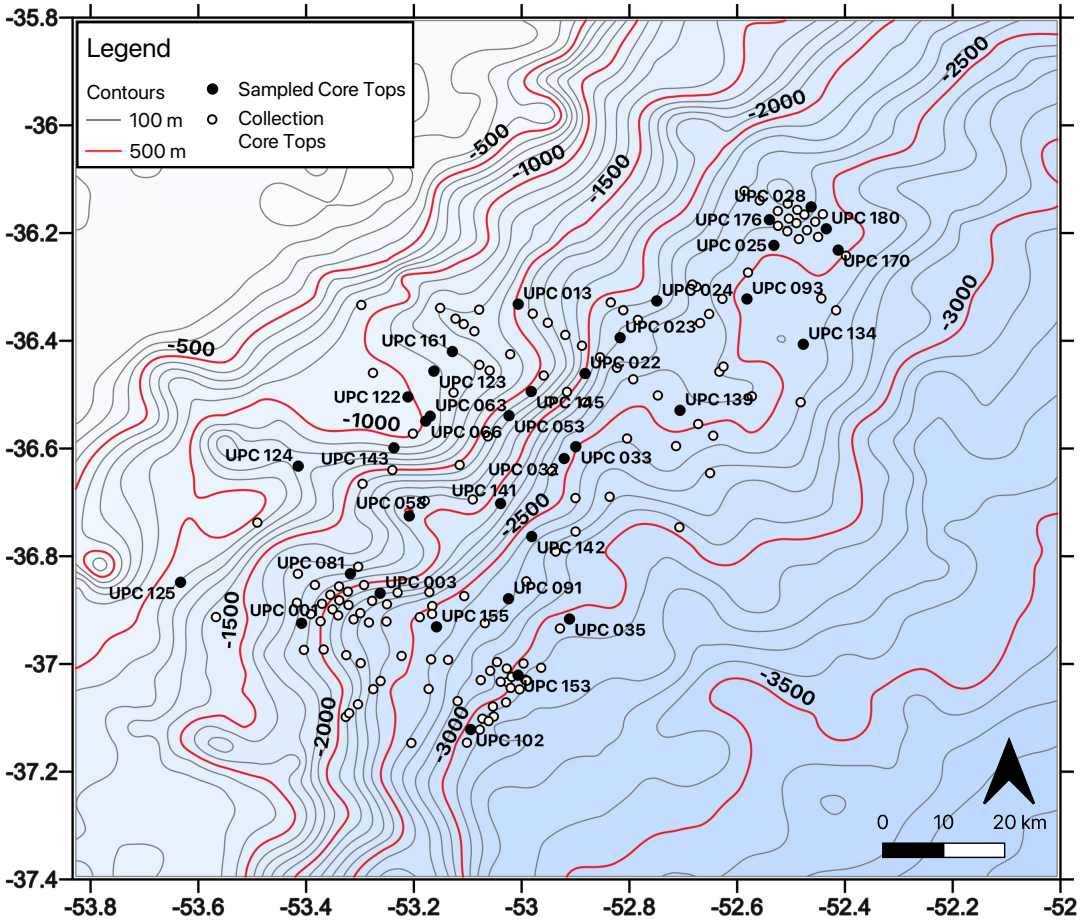

Figure 3.2-1 Site bathymetry and Core selection. Black circles denote cores for which a core top was acquired. White circles display additional sites within the collection. In total 35 sites have been sampled for core tops, these cores are listed in Table 3.2-1. Bathymetric data modified from Hernández-Molina et al., 2016 and McGuire et al., 2019.

Table 3.2-1 Core tops selected for analysis listed by core identifier. Thirty-five core tops were selected to cover the length, breadth and depth of the margin. Latitude and longitude are given in decimal degrees and water depth is in meters.

Cruise	Core Number	Latitude (°N)	Longitude (°E)	Water depth (m)
J14092	UPC 001	-36.92448	-53.40836	-2053.05
J14092	UPC 003	-36.86874	-53.26260	-2205.15
J14092	UPC 013	-36.33201	-53.00631	-1574.92
J14092	UPC 022	-36.46070	-52.88230	-2027.53
J14092	UPC 023	-36.39428	-52.81722	-2046.34
J14092	UPC 024	-36.32602	-52.74928	-2252.95
J14092	UPC 025	-36.22284	-52.53185	-2445.71
J14092	UPC 028	-36.15147	-52.46271	-2353.00
J14092	UPC 032	-36.61858	-52.92106	-2513.29
J14092	UPC 033	-36.59669	-52.89966	-2582.33
J14092	UPC 035	-36.91654	-52.91118	-3026.75
J14092	UPC 053	-36.53901	-53.02343	-2115.24
J14092	UPC 058	-36.72520	-53.20857	-2255.28
J14092	UPC 063	-36.54007	-53.16968	-1255.00
J14092	UPC 066	-36.54913	-53.17811	-1257.00
J14092	UPC 081	-36.83252	-53.31780	-1895.64
J14092	UPC 091	-36.87895	-53.02436	-2644.10
J14092	UPC 093	-36.32239	-52.58188	-2572.48
J14092	UPC 102	-37.12170	-53.09456	-2933.09
J14092	UPC 122	-36.50425	-53.21101	-1154.19
J14092	UPC 123	-36.45636	-53.16293	-1194.30
J14092	UPC 124	-36.63271	-53.41462	-1710.71
J14092	UPC 125	-36.84831	-53.63301	-1121.22
J14092	UPC 134	-36.40651	-52.47728	-2731.00
J14092	UPC 139	-36.52917	-52.70616	-2499.00
J14092	UPC 141	-36.70213	-53.03904	-2431.08
J14092	UPC 142	-36.76356	-52.98125	-2682.11
J14092	UPC 143	-36.59872	-53.23702	-1356.17
J14092	UPC 145	-36.49421	-52.98218	-1595.39
J14092	UPC 153	-37.02070	-53.00667	-3046.37
J14092	UPC 155	-36.93111	-53.15800	-2557.21
J14092	UPC 161	-36.42000	-53.12850	-1241.64
J14092	UPC 170	-36.23158	-52.41256	-2535.00
J14092	UPC 176	-36.17517	-52.54017	-2351.00
J14092	UPC 180	-36.19210	-52.43453	-2433.00

Three cores were selected for downcore appraisal and sampling. These were selected to obtain good coverage in the northeast (UPC 028), centre (UPC 023) and southwest (UPC 122) of the margin, to cover the extent of the oceanographic mixing within the region. The cores, in drift sediment, all penetrated at least 3.5

m into the sea floor with variable recovery rates and breaks between core casings, as shown in Table 3.2-2. UPC 028 was selected for further assessment due to high sedimentation recovery and few core breaks, providing the most continuous record to assess oceanographic and ecological changes.

Table 3.2-2 Cores selected for downcore sampling with location, approximate seafloor depth penetration and sediment recovery.

Core Number	Latitude (˚N)	Longitude (˚E)	Approx. Depth penetrated (cm)	Sediment recovered (%)
UPC 023	-36.39428	-52.81722	470	86
UPC 028	-36.15147	-52.46271	489	86
UPC 122	-36.50425	-53.21101	367	78

3.2.2 Core sampling and scanning

Core top samples comprising of 20 cm^3 of sediment were taken from the first core section, sampling the centre of the core barrel to minimise core contamination from sediment smearing from the casing walls. Downcore sampling involved core sections being individually split along the longest axis using a Geotek core splitter, one half was preserved as an archive section and the other set aside for sampling. Immediately after splitting and prior to sampling one of the two halves was placed through a Multi-Sensor Core Logger XYZ scanner, imaging the core and measuring magnetic susceptibility, before the core was substantially degraded. Core photos are shown in Appendices (Appendix H.1). Downcore sampling involved taking 20 cm^3 of sediment from the centre of the core barrel every 5-7 cm, where the core permitted. In total 175 samples were taken (Table 3.2-2), in addition to 35 core tops. Due to high demand for core top samples only one sample was permitted regardless of section length/ quantity of core top material. Post sampling samples were further processed in the Micropalaeontology Laboratory at the University of Leeds. All samples were placed into sealed plastic bags to prevent sample mixing and inhibit drying on shipping/transport back to the University of Leeds.

Table 3.2-3 Total number of 20 cm^3 samples taken from the three cores, split by section.

Number of samples from cores			
Sections	**UPC 023**	**UPC 028**	**UPC 122**
1	1	1	1
2	13	14	14
3	12	12	8
4	20	15	11
5	9	9	10
6	10	18	N/A
Totals	65	69	44

3.3 Washing

The wet samples were weighed using a Fisherbrand SG-402 top pan balance in the original pot/bag to obtain a wet weight for each sample and an associated empty 500 ml plastic beaker was weighed. The wet samples were removed from the travel pots/plastic bags and washed using distilled water into the empty plastic beakers. During washing the samples were disaggregated by hand until the sediment was primarily suspended in the distilled water, following this samples were placed into an oven at 60 °C to dehydrate the sample. This stage used as little water as possible to speed up the drying process typically taking approximately two to three days.

Once dry, samples were reweighed to obtain a dry weight before a final wash with distilled water. For this final wash the samples were rinsed out of the plastic beakers over a large 63 μm sieve removing the finest fractions, predominantly organics, silts and clays, from the sample. The >63 μm fraction was then rinsed back into the beaker and dried in the oven at 60 °C. Once dry, the sample was weighed a final time before splitting. The dried residue was sieved over a 125 μm dry sieve with the <125 μm put aside. The remaining >125 μm portion was split into two equal parts using a micro-splitter, the first part is labelled as assemblage split and the second as an isotope split. These splits are stored separately in glass phials and provide a representative subsample of the whole sample.

3.4 Microscopy and foraminiferal identification

The assemblage was further split, typically to an eighth or quarter split before analysis under a Zeiss Stemi 305 binocular reflected light microscope. Entire splits were counted, aiming for a minimum of 300 individuals, as a representative subset of the wider population (Patterson and Fishbein, 1989; Flores et al., 2016). Additionally, forams per gram were calculated using the dry sample weights to assess variability in population between sites and downcore utilising the following equation (Equation 3.2.2-1). A table of foraminifera dried weights, splits and number of individuals from which the Foraminifera per gram was calculated is provided in the appendix for core tops and downcore samples.

$$Foraminifera\ per\ gram = \frac{N^o individuals}{total\ dry\ weight * sample\ split}$$

Equation 3.2.2-1 Equation for foraminifera per gram of sample. Total number of foraminifera, benthic and planktonic, was divided by dry sample weight of split counted.

Species taxonomy was classified using Schiebel and Hemleben Planktic Foraminifers in the Modern Ocean (Schiebel and Hemleben, 2017). Key characteristics utilised in species identification include: overall test shape, number and arrangement of chambers, test colouring, wall texture, presence/absence of spines, number and position of apertures, presence/absence of other features such as bullas and keels as described within relevant atlases and literature (Kennett and Srinivasan, 1983; Schiebel and Hemleben, 2017). The >125 μm fraction was selected for assemblage analysis to remove most juvenile foraminifera, aid in taxonomic identification and capture an approximation of maximum diversity (Al-Sabouni et al., 2007; Schiebel and Hemleben, 2017).

3.4.1 Foraminiferal temperature groupings and palaeo-depth

The assemblage data for all samples was logged for inter-sample comparison, with species classified for temperature preference using modern planktonic tows data from the Southern Atlantic and previous core top databases (Boltovskoy et al., 1996; Boltovskoy et al., 2000; Kucera, 2007; Schiebel and Hemleben, 2017). Based on the water masses within the region, five temperature preference sub-groupings were used to provide three groupings for analysis, incorporating known latitudinal displacement and depth habitats occupied during life (Table 3.4-1). These were grouped as follows: warm – comprising any tropical to sub-tropical

species, cold – comprising any polar or sub-polar species, and transitional – known species associated within mixing regions of water masses i.e. the Brazilian Malvinas Confluence (BMC).

Table 3.4-1 Species classification into temperature groupings. Groupings based on previous South Atlantic plankton tow data from 1. Boltovskoy et al. (1996), 2. Boltovskoy et al. (2000) and from ecological descriptions in 3. Schiebel and Hemleben (2017).

Water mass groupings	Temperature Sub-groupings	Planktonic foraminiferal species
Warm water mass	Tropical	*Globigerinoides ruber* (pink)[1,2], *Globorotalia crassaformis*[3], *Globorotalia menardii*[3], *Globorotalia tumida*[3], *Trilobatus sacculifer*[1,2]
	Sub-tropical	*Candeina nitida*[3], *Globigerina falconensis*[1,2,3], *Globigerinella calida*[3], *Globigerinella siphonifera*[1,2], *Globigerinita minuta*[3], *Globigerinoides conglobatus*[1,2], *Globigerinoides conglobatus*[1,2], *Globigerinoides ruber* (white) [1,2], *Globorotalia hirsuta*[3], *Globoturborotalita rubescens*[1,2], *Neogloboquadrina dutertrei*[1,2], *Orbulina universa*[1,2], *Tenuitella clarkei*[3], *Tenuitella parkerae*[3]
Transitional	Transitional	*Globoconella inflata*[1,2], *Globigerinita glutinata*[1,2], *Globigerina bulloides*[1,2], *Globorotalia scitula*[1,2], *Globorotalia truncatulinoides*[1,2]
Cold water mass	Sub-polar	*Neogloboquadrina incompta*[1,2], *Tenuitella quinqueloba*[1,2]
	Polar	*Neogloboquadrina pachyderma*[1,2]

Using the above groupings foraminiferal assemblages were compiled for both the core top data set and the down core analysis of UPC 028. This comprised of individual species relative abundance as percentages within the sample being summed into temperature sub-groupings. From this information an individual site can be classified into one of the five sub-groups and an inference on which water mass is likely influencing the site can be made.

In order to assign individual sites to one of the five sub-groups a series of rules based on the summed assemblage percentages was utilised, these are listed in Table 3.4-2. These rules were determined using knowledge of species temperature preferences and based on the principal that if species preferences are not met at a given water depth colder favouring species may sink to a cooler water depth (Rebotim et al., 2017). This possibility requires additional ecological constraints to be met i.e. light, nutrients, salinity etc. Species requiring warmer conditions are limited to the maximum surface water temperature, and therefore cannot occupy alternate water depths in cooler conditions (Schiebel and Hemleben, 2017; Rebotim et al., 2017). Transitional taxa were given the lowest priority due to their generalist nature and known favouring of the BMC, rather than either the BC or MC, as seen in other studies (Boltovskoy et al., 1996; Boltovskoy et al., 2000; Chiessi et al., 2007; Schiebel and Hemleben, 2017).

Table 3.4-2 Rules for classifying a given sample based on planktonic foraminiferal assemblage percentages. Rules are applied sequentially until a sample fits the given classification, warm water species are favoured due to strictest temperature requirements, followed by cooler water species before the generalist transitional taxa are considered. A sample can have ≥40% transitional taxa and still be classed otherwise if one of the earlier rules is also true.

Order applied	Site classification	Assemblage percentage
1	Tropical	If Tropical ≥18
2	Sub-tropical	If Tropical + Sub-tropical ≥18
3	Polar	If Polar ≥40
4	Sub-polar	If Polar + Sub-polar ≥40
5	Transitional	If ≥40 and previous rules are not true

3.4.1.1 Palaeo-depth (P %)

In addition to reporting individual assemblage compositions benthic foraminifera were tallied to provide a crude water depth indicator through the relative abundance of planktonic foraminifera. This equation is given as Equation 3.4.1-1:

$$P\ (\%) = \left(\frac{Total\ number\ of\ planktonic\ foraminifera}{Total\ number\ of\ foraminifera}\right) * 100$$

Equation 3.4.1-1 The relative abundance of planktonic foraminifera. A means to derive an estimate to relative sea-level between samples.

This equation provides the percentage of planktonic foraminifera in relation to all foraminifera within the sample and can be used to infer water depth, with increasingly open marine systems displaying higher planktonic percentages. Approximate percentage planktonic values >50% likely indicate outer neritic water depths (100-150 m), ~80% indicates upper bathyal depths (150-500 m, depending on productivity) and >80% is indicative of open marine conditions (Culver, 1988; Gibson, 1989; Leckie and Olson, 2003; Toledo, 2008).

3.4.1.2 Benthic percentages

The relative benthic percentage can be similarly be calculated and can be utilised to assess palaeo-depth (van der Zwaan et al., 1990; Toledo, 2008) and palaeo-productivity (Berger and Diester-Haass, 1988; Toledo, 2008; Frozza et al., 2020). This presented alongside other palaeo-productivity metrics can be used to infer shifts in overlying water column conditions (Equation 3.4.1-2).

$$B\ (\%) = \left(\frac{Total\ number\ of\ benthic\ foraminifera}{Total\ number\ of\ foraminifera}\right) * 100$$

Equation 3.4.1-2 The relative abundance of benthic foraminifera. As with Equation 3.4.1-1 provides a means to derive palaeo-depth estimates relating to relative sea-level and/or used in conjunction with other proxies to asses palaeo-productivity.

3.4.1.3 Gs. ruber white:Gg.bulloides ratio

The ratio of Gs. ruber white to Gg. bulloides was compiled from assemblage counts for use as a productivity indicator (Toledo, 2008; Frozza et al., 2020). Gs. ruber white has been shown to favour oligotrophic states (Kroon et al., 1991; Toledo, 2008), whilst Gg. bulloides prefers eutrophic conditions (Kroon et al., 1991; Toledo, 2008) resulting in an inverse relationship between the two species. This is a relatively simple metric to calculate from the relative assemblage information, and the ratio can inform on the palaeo-productivity of a region, showing good agreement with the relative abundance of benthic foraminifera (Toledo, 2008; Frozza et al., 2020).

3.4.1.4 *Gr. truncatulinoides* coiling direction ratio

Gr. truncatulinoides is a deep dwelling, sub-thermocline species that has five genotypes globally (de Vargas et al., 2001; Ujiié et al., 2010; Ujiié and Asami, 2014). Whilst the fossil record does not permit ready analysis of genetic material, certainly not within the scope of this study, the genotypes are hydrographically limited and manifest as two easily identifiable morphotypes (Ujiié et al., 2010; Ujiié and Asami, 2014). This is primarily based on the coiling direction of the test, with left coiling forms dominating southern sourced waters in the South Atlantic and right coiling specimens occurring alongside left coiling specimens in the mid-latitudes ~20-40 °S (Ujiié et al., 2010). Using knowledge of the modern latitudinal dominance of coiling directions, presented in Ujiié and Asami (2014) and Ujiié et al., (2010) and based on the MARGO core top database assemblage counts (Kucera et al., 2005), assessment of palaeo-oceanographic migration through time can be made.

3.4.2 Mapping and Inverse Distance Weighting Interpolation of analysis

In order to estimate the likely spatial variability in and around individual core tops and interpolate between sites Inverse Distance Weighting (IDW) was applied. IDW is a widely used non-geostatistical interpolator that estimates the value of an attribute of an unsampled location based on values of nearby sampled sites. The values of sampled sites are inversely weighted based on the distances between sites with nearer locales having a greater influence on the estimation than more distal sites (Li and Heap, 2008). An example of how IDW works and the calculations utilised is presented in Figure 3.4-1.

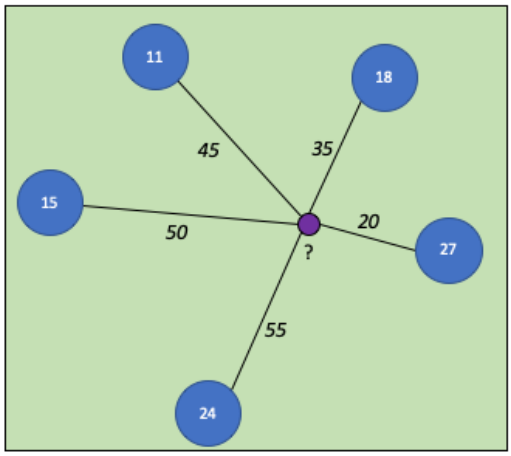

$$?= \frac{\sum_{i=1}^{n}(z_i/d_i^p)}{\sum_{i=1}^{n}(1/d_i^p)}$$

$p = 2$

$$? = \frac{(27/20^2)+(18/35^2)+(11/45^2)+(15/50^2)+(24/55^2)}{(1/20^2)+(1/35^2)+(1/45^2)+(1/50^2)+(1/55^2)}$$

$$? = \frac{0.10155986}{0.00454073}$$

$? = 22.366$

Figure 3.4-1 Schematic of Inverse Distance Weighting (IDW) Interpolation calculation and associated formula complete with example. z_i is the attribute measured, for this study either relative abundance, $\delta^{18}O$, or derived temperature (ºC). d_i is the distance from the unknown location to the sampled site. p is the power parameter responsible for weighting the samples proximal to distal, based on the assumption that samples proximal to the unknown site will be a better estimation (Mitas and Mitasova, 2005; Li and Heap, 2008).

For assemblage counts IDW interpolation was applied to species relative abundances to infer species abundances and eco-group patterns of unsampled regions. IDW was selected due to the preservation of site values through interpolation, the ability to handle irregularly spaced Uruguayan Margin samples, its local focus in weighting and its univariate nature (Shepard D, 1968; Li and Heap, 2008). IDW interpolation was run in QGIS mapping software, using a point shape file containing the assemblage/isotope data split by site and species to produce rasters limited in extent to the study regions bathymetry. The power value used was two, the default value for IDW interpolation (Figure 3.4-2) (Li and Heap, 2008). This power level, combined with a pixel size of 0.001 in the X and Y direction for the raster, ensures a smooth plot whilst maintaining computational run speed.

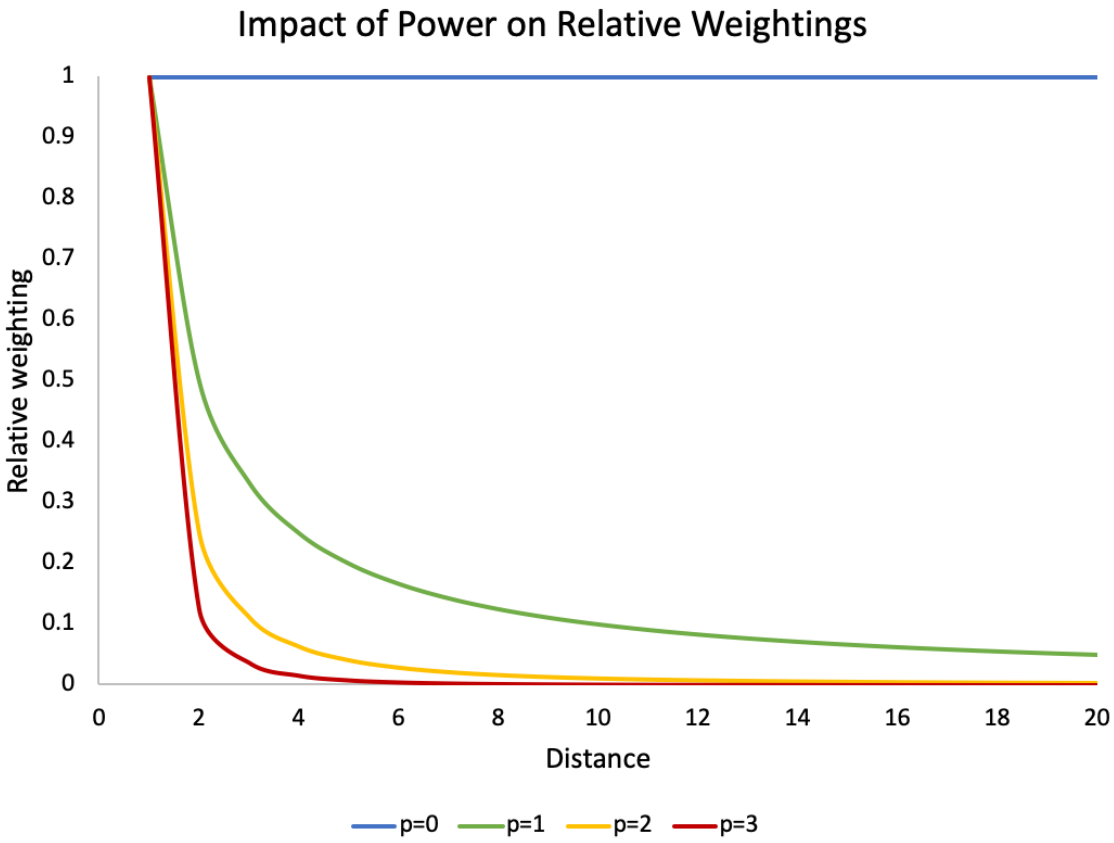

Figure 3.4-2 Effect of altering the power value for IDW interpolation calculation and the impact on the relative weighting of sampled sites, with increasing distance from the unknown site.

Once the individual raster file was produced a contouring equation was employed to define regions based on the interpolated parameter i.e. relative abundance, temperature or $\delta^{18}O$ stable isotope values. Contour spacing was determined from the range of attribute values interpolated and kept consistent intervals where possible. These contour IDW interpolation plots provide a heat map of estimated regional heterogeneity for the given parameter, and can be used to determine relationships with oceanographic water masses.

Using IDW interpolation does contain some caveats, chief among them being values outside the maximum and minimum values cannot be interpolated, leading to under- and over-estimation at the extremes of the interpolation. For example, if peak or minimum relative abundances have not been sampled by the selected sites the interpolation can only estimate values between the maximum and minimum relative abundance, a greater sampling level will reduce the likelihood of this significantly impacting the data. Similarly, whilst IDW can be employed in regions with irregular spacing it provides the best estimations when clustering of sample sites is at a minimal as this permits better estimates of samples proximal or distal to such clusters (Li and Heap, 2008).

3.4.3 Statistical analysis of assemblages

Diversity analysis of all assemblages utilised PAST statistical software in order to obtain metrics for inter-sample comparison. The first metric is richness, a simple count of taxa within an assemblage and defined by *S*. The total number of individuals within a sample is given as *n* and the total number of individuals within a taxon is given as n_i.

3.4.3.1 Dominance and Simpsons Index of Diversity

The first formula used is Dominance, measuring whether taxa are equally represented within a sample, with values 0≤ x ≥1. A value of zero indicates all taxa are equally present whilst a value of 1 indicates the community is dominated by a single taxon (Magurran, 2004). Dominance is given using Equation 3.4.3-1.

$$D = \frac{\sum_i n_i(n_i - 1)}{n(n-1)}$$

Equation 3.4.3-1 Equation for calculating Dominance within a sample.

Simpson's index of diversity, 1-D, inverts dominance and forms a clearer diversity index with values approaching zero indicating low diversity, whilst those approaching 1 tend toward infinite diversity (Equation 3.4.3-2) (Simpson, 1949; Magurran, 2004; Hammer and Harper, 2007).

$$Simpson's\ index = 1 - \frac{\sum_i n_i(n_i - 1)}{n(n-1)}$$

Equation 3.4.3-2 Simpsons index equation for measuring diversity of a sample.

3.4.3.2 Shannon-Wiener Index

Shannon-Wiener index (*H'*) is a widely used metric for measuring diversity that considers the number of taxa and the relative abundance of each taxa. The lowest *H'* value is zero, when only one taxon is present in a sample and thus no/low diversity. The maximum value is given as H_{max} = ln*S* and has no upper limit, being the log of the number of species, assuming all species have the same number of individuals (Hammer and Harper, 2007). However, given communities have a limited number of species, values typically fall between 1.5-3.5 (Gaines et al., 1999). Shannon-Wiener values were calculated due to the prevalence in diversity studies, although the metric is biased if all species in a community are not accounted for (Magurran, 2004). The Shannon-Wiener index suffers from

combining richness and evenness, but can make interpretation of change difficult with either component impacting the index (Magurran, 2004). That said it is possible to further use Shannon-Wiener index in the calculation of additional parameters, provided natural logs are used, to decompose and better interpret whether changing evenness, richness or both are the contributing factor to changing diversity (Magurran, 2004). Equation 3.4.3-3 gives the formula for calculating *H'* is as follows:

$$H' = \left(- \sum_{i} \frac{n_i}{n} \ln \frac{n_i}{n} \right) - \frac{S-1}{2n}$$

Equation 3.4.3-3 Shannon-Wiener index diversity equation for considering number and abundance of taxa.

3.4.3.3 Pielou's Equitability

Pielou's equitability is an index of evenness applied to the Shannon-Weiner index and is normalised for species richness, meaning it measures the evenness of individuals divided by the taxa present (Equation 3.4.3-4) (Pielou, 1966; Magurran, 2004; Hammer and Harper, 2007). Values range from zero, where there is no evenness, to one, where there is total evenness (Help et al., 1998). Its formula is as follows:

$$J' = \frac{H'}{\ln S}$$

Equation 3.4.3-4 Pielou's measure of population evenness for large collections. This formula enables estimations of population evenness from average conditions and can be calculated using Shannon-Wiener index (H') and the log of the total number of species (lnS) (Pielou, 1966; Magurran, 2004).

3.4.3.4 Fisher's Alpha Index

Fisher Alpha is a diversity index that provides a test of species richness of a given site. It follows a log distribution and can be used to estimate the number of additional species that would be found with increased sampling effort (Equation 3.4.3-5) (Magurran, 2004; Hammer and Harper, 2007). It can be calculated using the following formula:

$$S = \alpha \ln(1 + \frac{N}{\alpha})$$

Equation 3.4.3-5 Fisher's Alpha Index, S is the total number of species, α is the alpha index a calculated constant, N is the number of individuals sampled (Magurran, 2004; Hammer and Harper, 2007).

3.4.3.5 K-means Analysis

K-means cluster analysis is a statistical method that iteratively enables unlabeled data to be clustered into a set number of groups, based on similarity and the number of expected groupings. The process aims to find the lowest variance within the assigned number of groupings, a useful analysis for confirming suspected groupings within morphometric data (Hammer and Harper, 2007). K-means clustering was performed on extracted stable isotope data to statistically assess clustering relationships of *Gc. inflata* data. This was completed within the R statistical software, using the cluster and clValid packages to complete the analysis. For k-means cluster analysis the number of clusters must be preset to determine association of data points to individual clusters. In order to establish the optimal number of clusters the NbClust R package was used, comparing the results of 26 indices. This analysis was set between two and fifteen clusters to determine the minimal number of clusters each index recommended. Once number of clusters was defined the same starting point for the iterative cluster analysis was used, enabling results to be repeated, with 50 iterations run to ensure reliability of the clusters produced.

3.5 Stable Isotope analysis

3.5.1 Sample Preparation

In order to better reconstruct the oceanography of each site and build up a history of the oceanography of the region, the oxygen ($\delta^{18}O$) and carbon ($\delta^{13}C$) stable isotopes of planktonic foraminiferal calcite were analysed. The isotope split was sieved using a sieve stack comprising of 125-250 µm, 250-300 µm and 300-600 µm size fractions. Individual specimens were picked preferentially from the larger size fractions, in line with published literature suggesting species best represent ambient conditions at certain size fractions, typically 212-350 µm (Birch et al., 2013). Four species were chosen to represent distinct layers in the water column with a minimum of at least five individuals from each species picked and set aside for washing (Table 3.5-1). Where possible individuals were visually examined, using optical light microscopy, to avoid any obvious diagenetic overgrowths which would impact oxygen and carbon isotope measurements (Pearson, 2012; Birch et al., 2013; Ezard et al., 2015; Schiebel and Hemleben, 2017).

Table 3.5-1 Species used for isotope analysis to obtain a water column profile, including temperature grouping and whether species do/do not host symbionts.

Planktonic Foraminifera Species	Temperature Grouping	Symbiont/Non-Symbiont Hosting	Depth
Globigerinoides ruber white	Warm	Symbiont Hosting	Surface Waters
Neogloboquadrina pachyderma	Cold	No Symbionts	Surface Waters
Globoconella inflata	Transitional	No Symbionts	Thermocline
Globorotalia truncatulinoides	Cold	No Symbionts	Sub-thermocline

Once picking was completed each individual foraminiferal test was placed into a glass v-bottomed phial filled with deionised water and placed into a rack within an ultrasonic bath. Once full the bath was switched on for a period of no more than ten seconds, if the foraminifera being washed were delicate this may be as little as five seconds. This process was employed to remove any surface organics or detrital material stuck to the surface of the tests. Following washing the tests were extracted and dried in the oven at 60 ºC for twenty-four hours.

After drying the forams were individually weighed using a Sartorius ME5 microbalance before being placed in a mass spectrometer v-bottomed vial and sealed. The weight and position of each sample was recorded for use with the mass spectrometer and standards of Carrara Marble of similar mass were also prepared. For each run a maximum of 60 tubes could be processed requiring an initial three standards and a further two for each five foraminiferal samples ran.

3.5.2 Mass Spectrometry

Stable isotope data was generated using an Elementar Isoprime 100 with Dual Inlet and Multicarb sample preparation device in the Cohen Laboratories, at the University of Leeds. Single specimen samples were reacted with anhydrous phosphoric acid at 90 ºC. Samples were calibrated relative to Carrara Marble calcite standard (Elemental Microanalysis – B2214) with mean values of $\delta^{13}C_{VPDB}$ +2.10‰ (σ‰ 0.07) and $\delta^{18}O_{VPDB}$ -2.01 (σ‰ 0.1). Repeatability of standards is generally better than 0.05‰ (1 S.D) for $\delta^{13}C$ and 0.1‰ (1 S.D) for $\delta^{18}O$. Data is reported to the Vienna Pee Dee Belemnite (VPDB) scale.

$\delta^{18}O$ data was converted to temperature using the Kim and O'Neil (1997) equation for synthetic calcite with the caveat that symbiont hosting forms may require offsetting (Equation 3.5.2-1) (Kim and O'Neil, 1997; Pearson, 2012). This equation was selected as the temperature range of 10-40 ºC represents a suitable range for expected water mass temperatures (Pearson, 2012). Defined as follows:

$$T(ºC) = 16.1 - 4.64(\delta^{18}O_{cc} - \delta^{18}O_{SW}) + 0.09(\delta^{18}O_{cc} - \delta^{18}O_{SW})^2$$

Equation 3.5.2-1 Simplified oxygen isotope Palaeo-temperature conversion equation. $\delta^{18}O_{cc}$ represents foraminiferal test calcium carbonate oxygen isotope value, $\delta^{18}O_{SW}$ is the oxygen isotope value of surrounding seawater, remaining values are constants (Pearson, 2012).

In order to parameterise $\delta^{18}O_{SW}$ two values must be known, interaction of these two values is shown in Equation 3.5.2-2. The components of $\delta^{18}O_{SW}$ are δw and c. δw is the local water mass value of $\delta^{18}O$, from global modelling, with a value of 0.51 ‰ $\delta^{18}O$ calculated for offshore Uruguay (LeGrande and Schmidt, 2006; Chiessi et al., 2007; Rohling, 2013). Parameter c, is a conversion factor to transform Vienna Standard Mean Ocean Water (VSMOW), the universal seawater standard, to VPDB, the universal carbonate standard, with a value of 0.27 (Kim and O'Neil, 1997; Bemis et al., 1998; Pearson, 2012).

$$\delta^{18}O_{SW} = \delta w - c$$

Equation 3.5.2-2 Equation to determine $\delta^{18}O_{SW}$ for Uruguayan Margin. δw is the ratio of ^{16}O to ^{18}O local to sample sites. c is the conversion factor to convert $\delta^{18}O_{VSMOW}$ to $\delta^{18}O_{VPDB}$ (Kim and O'Neil, 1997; Bemis et al., 1998; Pearson, 2012).

3.6 Particle transport modelling

In a bid to quantify the impact planktonic foraminiferal post-mortem transport may incur on assemblage and isotopic analysis, particle transport modelling was employed to reconstruct potential settling trajectories of planktonic foraminifera from the seabed, back to the surface waters the species occupied during their lifecycle. This enabled analysis of where core top sediment foraminifera may have originated to see whether conditions were dissimilar to those reported immediately above the core site. The model itself was written and run by a masters student from the University of Utrecht as part of a masters research project (Kruijt, 2019). Project involvement was significant and centred around supplying core locations, literature on the basin and oceanographic processes within, advising on foraminifera species selection, size, weight and likely sinking velocities. It also required this project's core top counts and isotope values to compare with modelled results, refine the process and assess reliability of the model. Species selected, and properties assigned, for the model are listed in Table 3.6-1, with further information available in Kruijt, 2019.

The model utilised an Ocean General Circulation Model (OGCM) with a resolution of ~0.1 ° across 54 depth layers between 75 °S to 75 °N. This output was in the form of an OGCM for the Earth Simulator, utilised to map the impact of eddies within the energetic BMC region. The project used a hindcast simulation based on historical daily mean atmospheric data from the second half of the twentieth century (Kruijt, 2019). Parcels software in Python was utilised to track particles along settling trajectories. Particles used to represent sinking planktonic foraminifera were released from a central site to the margin (36.5 °S, 52.5 °W) and back-tracked to the surface, this central site was taken to broadly represent the portion of the margin from which cores were recovered (36-37 °S, 52-53.5 °W). Additionally, from the deepest known dwelling depths published in the literature particles were assumed to be alive and traced for a further period of time representative of the foraminifera's lifespan (~15-30 days typically, depending on species), a table of these properties is provided (Table 3.6-1) (Schiebel and Hemleben, 2017; Kruijt, 2019). On the timing of particle release Kruijt, 2019 state "particles are released every three days over a time span of ten model years and their location and local conditions are stored every model day". Through this work particles were tracked back, taking snapshots of water column

properties, mapping potential origin locations and SSTs of foraminifera. Example of model process is shown in Figure 3.6-1.

$\delta^{18}O$ isotope values acquired at the University of Leeds (Section 3.5) were compared to modelled $\delta^{18}O$ values to assess offsets that could be the result of transport and expatriation of foraminifera, within this complex oceanographic setting (Van Sebille et al., 2015; Kruijt, 2019). Modelled $\delta^{18}O$ values used temperature and salinity assessments from the model to construct calculated $\delta^{18}O_w$ values based on known fractionation processes, before this $\delta^{18}O_w$ is fed into a $\delta^{18}O_c$ equation to predict the likely $\delta^{18}O$ value recorded by a particle (LeGrande and Schmidt, 2006; Kruijt, 2019). Assemblages were also utilised in the model/empirical data comparison through assessment of the dominant water mass signal recorded in the thermally limited planktonic foraminifera. Combined with modelled temperature ranges and known foraminiferal preferences (Kucera, 2007; Schiebel and Hemleben, 2017), it was possible to estimate which eco-groups should be present given average dwelling conditions vs. the relative eco-group dominance the assemblages presented (Kruijt, 2019).

Table 3.6-1 Modified table of species specific values used within the model from Kruijt, 2019, further information can be found within the volume. References within the table are as follows 1) Takahashi and Be, 1984, 2) Gyldenfeldt et al., 2000, 3) Rebotim et al., 2017, 4) Schiebel and Hemleben, 2017, 5) Bijma et al., 1990, 6) Groeneveld and Chiessi, 2011, 7) Boltovskoy et al., 2000.

Species Name	**General**	***Gs. ruber white***	***N. pachyderma***	***Gc. inflata***
Sinking speed (m/day)	200[1]	200[1]	250[2]	250[4]
Dwelling depth (m)	50[3]	50[3]	100[3]	300[6]
Lifespan (days)	30[4]	15[5]	30[4]	30[4]
Growth rate	Linear	Linear	Linear	Linear
Ecology		Sub-tropical[4,7]	Sub-polar[4,7]	Transitional[4,7]

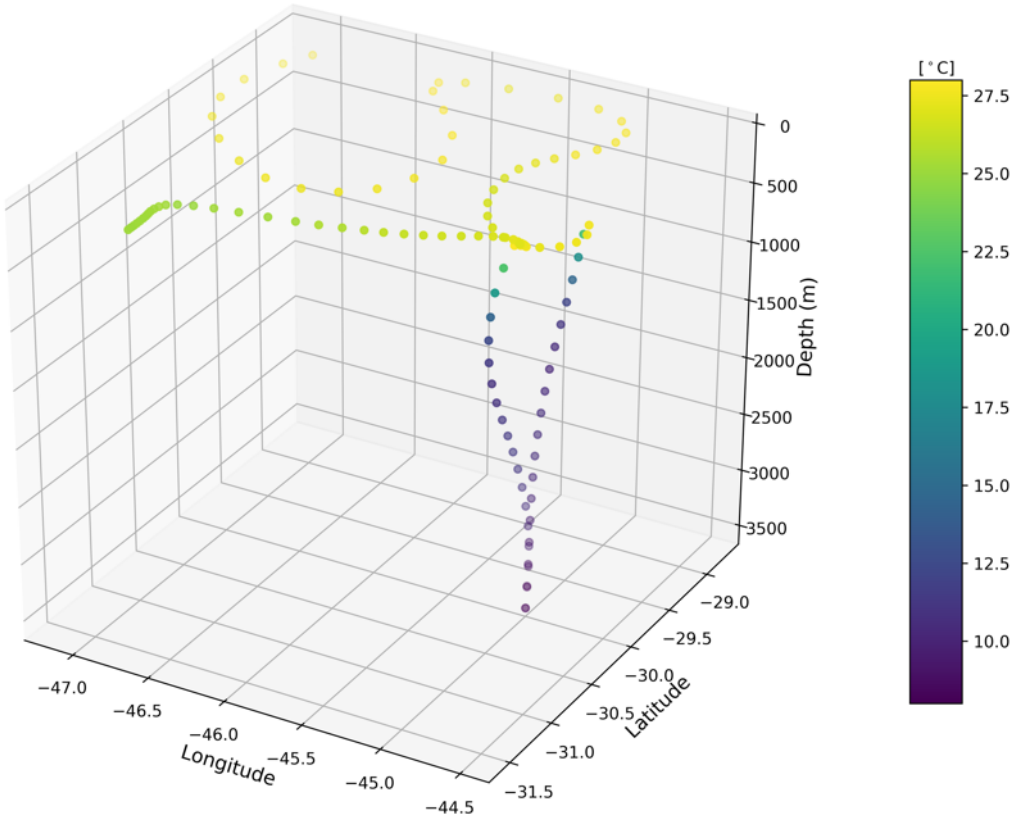

Figure 3.6-1 Illustration of the particle back-tracking model. The model takes snapshots from the particle's original location on the seafloor, and using ocean currents, calculates potential sinking trajectories alongside water temperatures experienced. We can thereby trace likely location origins of planktonic foraminifera and compare isotope measurements to evaluate expatriation potential (Modified from Kruijt, 2019).

3.7 ITRAX scanning

Knowledge of elemental variations down core through construction of chemostratigraphic records are valuable in the reconstruction of local and regional environmental reconstructions, including sediment providence studies. ITRAX is a commercial scanner, with scans providing optical and radiographic imaging, in addition to elemental variations from sediment cores. The use of an ITRAX scanner permits collation of these records without disturbing or destroying sediment cores, whilst analysing element variations at up to 200 μm intervals (Croudace et al., 2006; Croudace and Rothwell, 2015).

Elemental variations are obtained through excitement of materials when exposed to incident x-rays, in this case from a radioactive Molybdenum source. This excites individual atoms with electrons lost from inner atomic shells, and the created vacancies filled by electrons from outer shells. The subsequent electromagnetic radiation emitted is dependent on the atomic number and thus each element releases a characteristic wavelength (Croudace and Rothwell, 2015). The x-ray source can be varied for analysis of different elements, but the standard is Molybdenum at 30 kV and 30 mA for most environmental analysis as this captures a significant portion of elements (Croudace et al., 2006).

Three cores were ITRAX scanned in their entirety at BOSCORF, these cores were UPC 023, UPC 028 and UPC 122.

3.7.1 Core preparation

To obtain the scanned data recently split archive half barrel cores were removed from the core repository. These archive cores were allowed to warm to room temperature, as they had been stored in refrigeration, and had the split surfaces smoothed to remove undulations and ensure distance to the detector was as uniform as possible. Additionally, a 1.5-6.0 μm polypropylene film was placed on the core surface to prevent dehydration, prior to loading onto the ITRAX sample cradle (Croudace and Rothwell, 2015).

3.7.2 Scanner and Scanning process

The split core is slowly fed into the scanner using a motorised transport bed, passing the core past four sensors in the central measuring tower. These include an optical-line camera, a laser topographic scanner, an X-ray line camera and a high count-rate XRF detection system (Croudace et al., 2006). The operating

system follows a procedure in which the core length, voltage for the X-ray tube and initiation of the topographic scan of the core are input and initiated. The topographic scan is important to ensure the XRF sensor remains at a constant distance to the core surface and the instrumentation is not damaged during scanning. The next step involves selecting likely elements present in the sample and choosing a best-fit spectral peak, calibrating against reference regions of the core (Croudace et al., 2006). Similarly, the radiographic camera must be referenced by removing the core from the X-ray beam. Once this is all complete the data storage location is selected and the XRF count time is set and the instrument can commence scanning (Croudace et al., 2006).

The settings selected for the running of UPC 023, UPC 028 and UPC 122 was a voltage of 45 kV with a current of 40 mA for the X-ray. The measurement interval was set at 0.5 cm intervals with an XRF exposure time of 30 seconds to the Molybdenum source under 30 kV and 30 mA. The process of running three complete cores took approximately 72 hours of machine run time. Figure 3.7-1 details a schematic of the scanner and examples of the equipment and cores processed.

3.7.3 Data processing

Data was outputted as comma delimited text files for each core section and stitched together using Microsoft excel, forming a record for core. Section numbers, section depths and total depths were calculated and added. For each core section the validity column was checked and if data rows equalled zero the data was removed, values of zero correspond to sections of core below detector tolerance limits. This was typically only found at section tops and bottoms, or within significant cracks where the underlying core liner was visible. Values of Mean Squared Error (MSE) were checked and if greater than five the corresponding elemental values were removed. This can be caused by counts per second (cps) varying due to reference materials differing to those measured, uneven cut core surfaces and crack related effects (Croudace et al., 2006).

Elemental data with low or excessively high cps were removed, this was defined by cps values being two standard deviations from the section mean. Instances of data removal were low, typically occurring where the scanner interacted with the core caps. Similarly, values were investigated where the core topography significantly changed i.e. around section breaks or significant cracks.

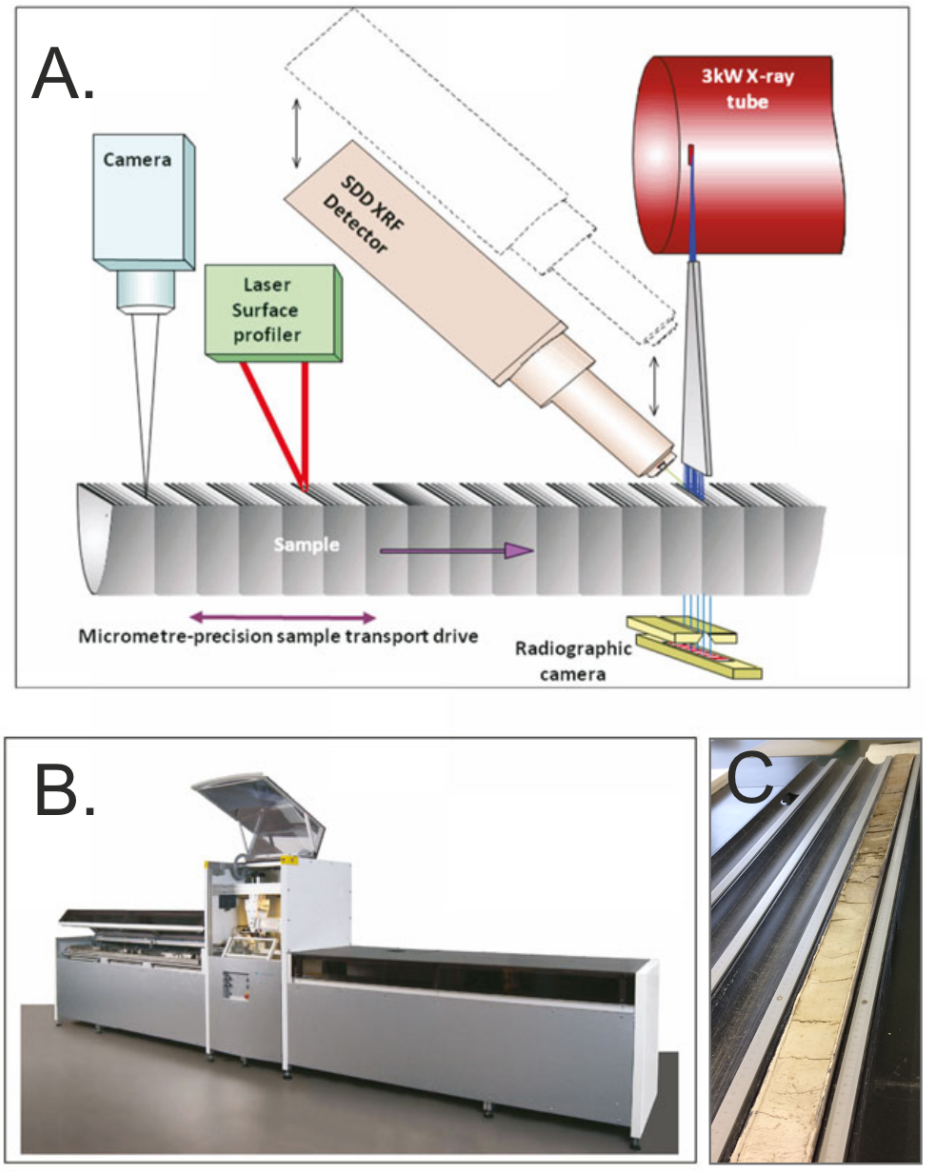

Figure 3.7-1. A) Schematic of ITRAX scanner instrumentation and main components. B) ITRAX Scanner similar to that housed at BOSCORF, with sensor housing and sample loader open. C) Example of an archive half barrel core.

3.7.4 Elements for Analysis

Elements of interest include those whose interpretation relates to the production of biogenic carbonate, productivity measures and ratios that can infer production of organic matter. The following ratios and raw element count information were selected based on the literature (Table 3.7-1). Counts were compared to Titanium (Ti), a conservative element compared to redox sensitive elements i.e. Iron (Fe) (Croudace and Rothwell, 2015), where possible to enable comparison between data. Elemental data is presented as log ratios to reduce error in interpretation of intensities (Weltje and Tjallingii, 2008), with the exception of Calcium (Ca) and Strontium (Sr). This raw data is plotted to show the co-varying nature, a signal for biogenic carbonate production (Croudace and Rothwell, 2015).

Table 3.7-1 ITRAX XRF element counts and element ratios with palaeoenvironmental implications.

Element/ratio	Importance	Relevant literature
Ba/Ti	Palaeo-productivity marker, Ba has been shown to be associated with organic matter.	Thomson et al., 2006; Croudace et al., 2006; Croudace and Rothwell, 2015
Br/Cl	Peaks indicate organic rich layers, deviating from salinity ratio expected in marine sediments as Br is associated with photosynthetic processes.	Thomson et al., 2006; Rothwell et al., 2006; Croudace and Rothwell, 2015
Br/Ti	Br/Ti is a organic productivity indicator, particularly in margin environments.	Agnihotri et al., 2008; Croudace and Rothwell, 2015
Ca and Sr	Co-variance of element counts implies biogenic carbonate source. Deviation suggests terrestrial input of Ca to system.	Croudace and Rothwell, 2015
Ca/Fe	Used for quantifying marine vs. terrigenous sediment input to a site.	Rothwell and Rack, 2006; Marsh et al., 2007; Voigt et al., 2013; Croudace and Rothwell, 2015
Ca/Ti	Biogenic vs. lithogenic sediment, less likely than Ca/Fe to be impacted by redox influences.	Piva et al., 2008; Croudace and Rothwell, 2015
Fe/Ca	Ratio used to assess terrigenous vs. biogenic sediment input.	Rogerson et al., 2006; Dickson et al., 2010; Croudace and Rothwell, 2015
Fe/K	Continental rainfall proxy, high values indicate wet conditions vs. low values relating to dust and more arid states. Used as a cross core correlator.	Blanchet et al., 2009; Croudace and Rothwell, 2015; Warratz et al., 2017
Fe/Ti	Changes in terrigenous input and potential Fe mobilisation due to diagenesis i.e. the formation of pyrite.	Thomson et al., 2006; Marsh et al., 2007; Blanchet et al., 2009; Croudace and Rothwell, 2015
S/Ti	Presence of pyrite or increased organic matter.	Moreno et al., 2007; Croudace and Rothwell, 2015
S/Cl	A proxy used to assess pyrite authigenesis and/or organic matter compared to sea-salt ratios.	Passier et al., 1999; Thomson et al., 2006; Croudace et al., 2006; Croudace and Rothwell, 2015; Shi et al., 2016
Si/Ti	Used in preference to Si/Al ratios due to low counts, a proxy for siliceous productivity.	Rothwell and Rack, 2006; Marsh et al., 2007; Moreno et al., 2007; Agnihotri et al., 2008; Croudace and Rothwell, 2015

3.8 Radiocarbon dating

Radiocarbon, ^{14}C, is a naturally occurring radioactive carbon isotope and the product of Nitrogen atoms in the upper atmosphere interacting with cosmogenic rays (Anderson, 1953). The abundance of the radioisotope declines following a half-life of 5,730±40 years, as the radioisotope decays into a stable isotope of nitrogen (^{14}N) (Hajdas et al., 2008; Fabel, 2015). ^{14}C is quickly oxidised in the atmosphere to either CO or CO_2 and through photosynthesis ^{14}C enters the food chain. As such radiocarbon is incorporated into living organisms through food chains, an organisms death stops the intake of ^{14}C and thus marks the start of the radiocarbon clock from which subsequent ^{14}C activity is counted (Hajdas et al., 2008). Radiocarbon dating measures the abundance of ^{14}C radioisotope in relation to the more common stable carbon isotopes (^{12}C and ^{13}C). Limits to radiocarbon dating are based on the 5,730±40 years half-life, with an upper age limit of 50,000 BP (Hajdas et al., 2008) (Figure 3.8-1).

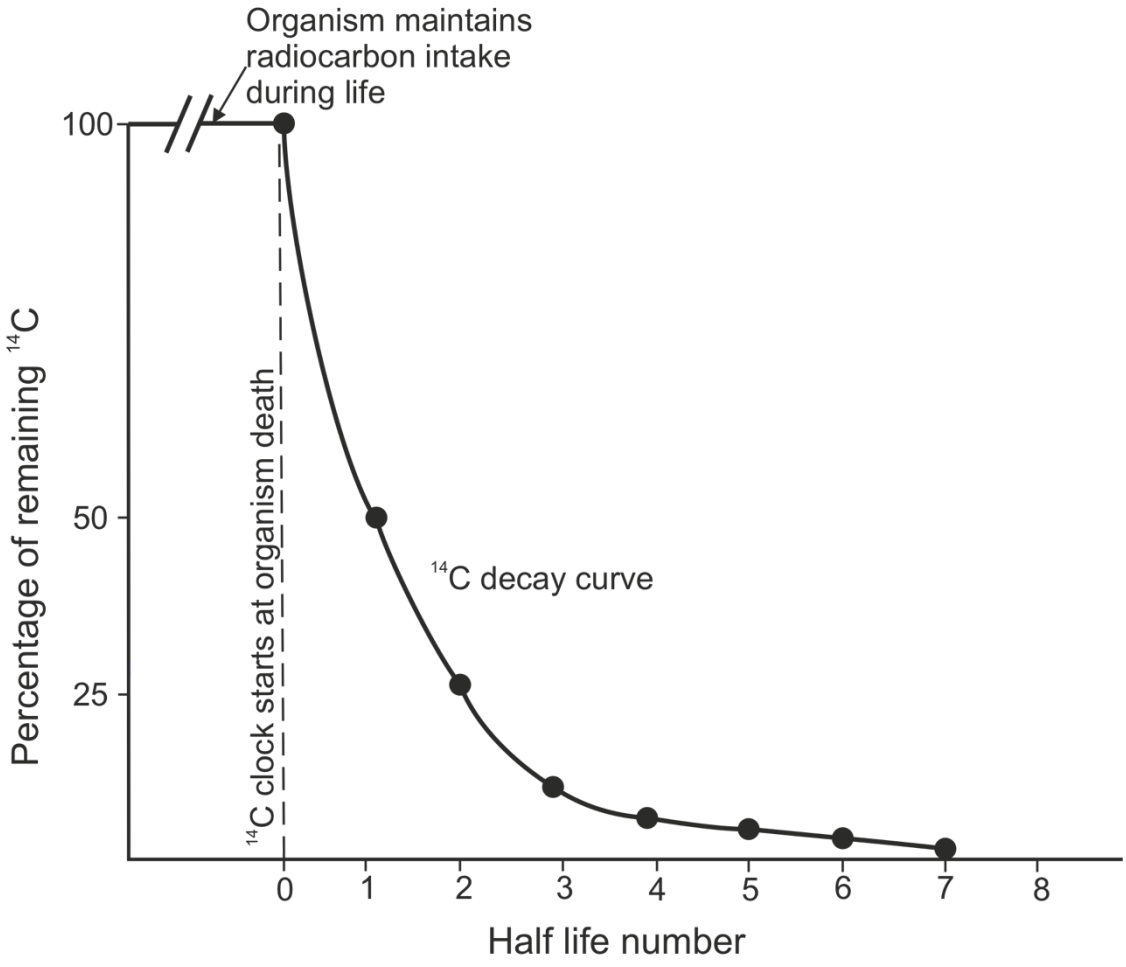

Figure 3.8-1. Radioactive decay of Radiocarbon. Post death radiocarbon present within an organism/fossil declines following a set half-life of 5730 years. Through this process age can be determined using the ratio of ^{14}C to the more stable ^{13}C and ^{12}C isotopes.

Radiocarbon dating was deemed necessary for this study due to a number of reasons. Firstly, the record was deemed likely to only incorporate Holocene material, meaning biostratigraphic dating was unfeasible due to a lack of extinctions and first occurrences of species. Secondly, to track possible BMC migrations and relate these to Holocene events, and other Holocene records, required reliable dating.

3.8.1 Sample preparation (University of Leeds)

Five range finding dates were awarded from the NERC Radiocarbon Facility amounting to £2510 for core UPC 028. These dates were at the following specific horizons: 97 cm, 197 cm, 310 cm, 400 cm and 487 cm. Each of the five samples required a minimum of 4 mg of planktonic foraminifera picked to obtain 1 mg of carbon post processing, as such each of the five samples was picked clean of planktonic foraminifera. Ideally the sample would have produced enough individuals of a single species to meet the required weight, however this was not possible, and all five samples have a mix of species.

Once picked all foraminifera were ultrasonically washed to clean the tests and remove as much organic/detrital material as possible before being dried in an oven at 60 °C. These samples were placed into a weighed labelled Exetainer® before being reweighed using a Fisherbrand SG 402 balance to acquire sample weight.

3.8.2 Processing at Radiocarbon Facility

Standards of similar weight to the foraminifera samples were weighed out and composed of Carrara Marble at the National Environment Isotope Facility Radiocarbon (Environment) in East Kilbride. The samples and standards were converted to graphite cathodes at the NEIF Radiocarbon (Environment) laboratory before being passed, due to the low yield weights, to Dr Xiaomei Xu of the Keck Carbon Cycle AMS Facility at the University of California, Irvine, USA for ^{14}C analysis.

3.8.3 Radiocarbon Measurement

Radiocarbon measurements were carried out using an Accelerated Mass Spectrometer and results reported as conventional radiocarbon years BP (relative to AD 1950). Sample $^{13}C/^{12}C$ ratio was also simultaneously measured to

in correct for isotopic fractionation during graphitization and Accelerated Mass Spectrometer (AMS) measurement processes.

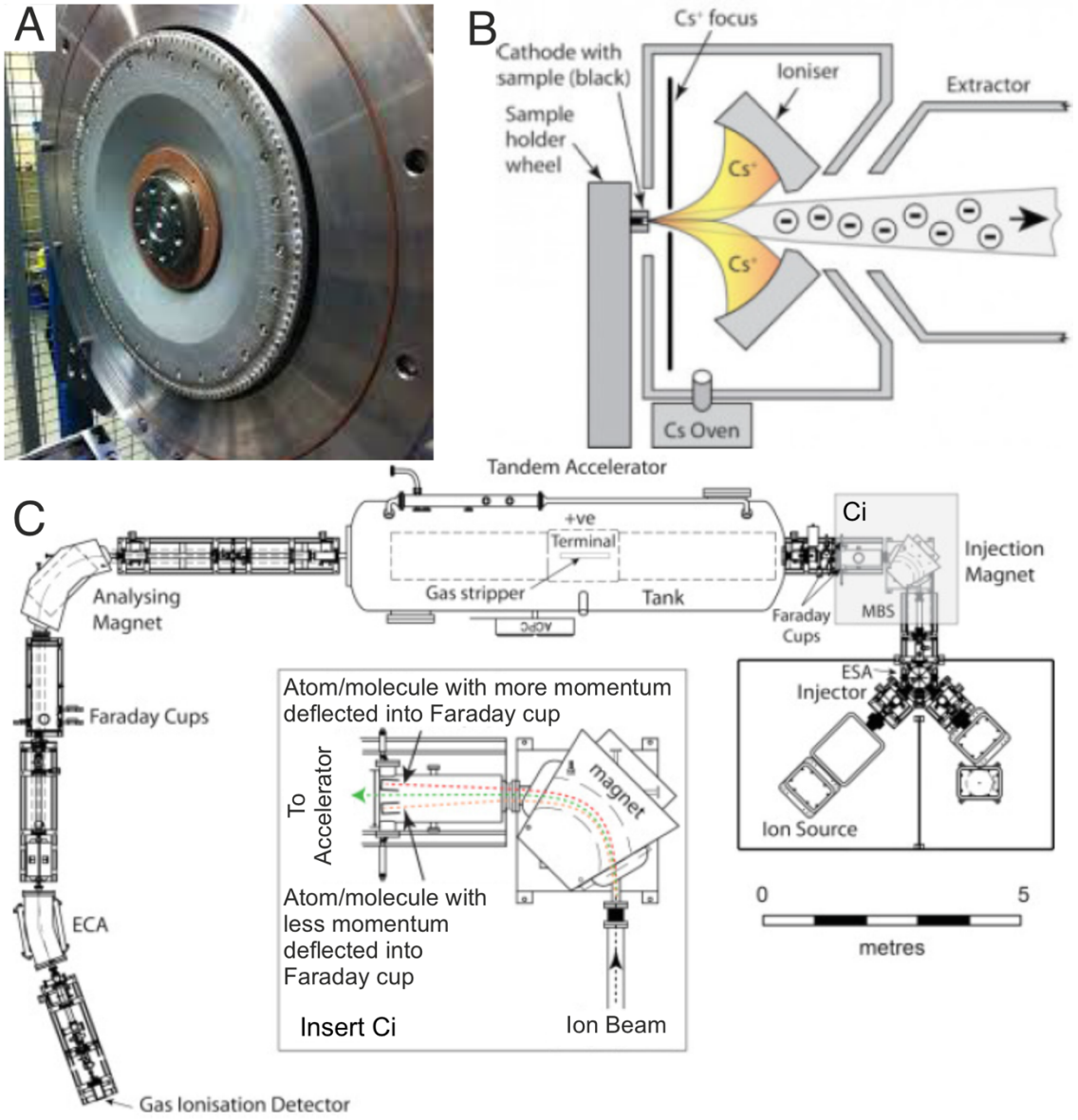

Figure 3.8-2 Simplified schematic of an Accelerated Mass Spectrometer. A) shows the loaded sample wheel graphite cathodes. B) process of creating negative ions from the graphitised sample for acceleration. C) schematic for the entire AMS with the accelerator, injector, stripper and sensors for analysis. Ci) injection magnet for removing molecules that are heavier or lighter than the target molecule. Modified from Fabel, 2015.

3.8.3.1 Accelerated Mass Spectrometer process

The graphite cathode samples are inserted onto an AMS sample wheel alongside standards and loaded into an ion source, which is then closed and pumped down to vacuum (Figure 3.8-2 A). The cathode is bombarded with positive Caesium ions, these are then focussed into the beam line and extracted (Figure 3.8-2 B). The now negative sample ions are accelerated through an injector to 66 keV (~1000 km/s) using electrodes and magnets separating particles by mass through

velocity, targeting particles with a mass of fourteen (Figure 3.8-2 Ci) (Fabel, 2015).

The ions pass through an accelerator tank accelerating to ~7500 km/s and exposed to a positive charge in a gas stripper (Figure 3.8-2 C). Collisions strip the ions of electrons converting them to a positively charged particle. The settings of the terminal voltage are key in removing a minimum of three electrons, destroying other molecular ions other than ^{14}C, which can be separated based on differing mass charge ratios (Fabel, 2015).

Out of the gas stripper the ions are further accelerated reaching speeds in excess of 17000 km/s. At this point it is possible to separate the C^+ ions according to momentum, with $^{12}C^+$ and $^{13}C^+$ ions collected in faraday cups. The $^{14}C^+$ gas continues onto the gas ionisation detector where the particles are slowed using a gas, each atom ionises with the gas with the resulting electrons counted. The $^{14}C/^{13}C$ ratio is used to calculate the radiocarbon age of a sample when compared to the standards in the sample wheel (Fabel, 2015).

3.8.3.2 Calibration and reservoir effects

OxCal program version 4.4 was used to correct conventional radiocarbon age to calibrated BP and produce a corresponding age depth plot (Ramsey, 2008; Ramsey, 2009). Due to location of the core and composition of the sample the Marine20 calibration curve was selected, which incorporated a reservoir age of 500 years (Heaton et al., 2020). This reservoir age is slightly larger than previous studies, which used regional estimates from Marine13 of 405 years (Bender et al., 2013; Reimer et al., 2013). A Poisson sequence, or P_Sequence, was used to interpolate deposition for estimating deposition rates with an intial k value of 1 with variance of the k value permitted to two $\log_{10}$ either side. This method assumes random deposition with approximate proportionality to depth, given the variable methods of deposition within the area (i.e. contourites, turbidites and pelagic settling) this seemed the most appropriate when compared to a Uniform Sequence model (Ramsey, 2008; Rebesco et al., 2014). The resulting age depth model was set to provide interpolated dates between samples at a 0.5 cm resolution for the length of the core from an assumed sampling date of 2013.5, approximately when the cores were sampled on the Uruguayan margin. Output dates were converted to calibrated years before present (cal BP) within the OxCal software.

3.9 SEM imaging

Scanning Electron Microscope (SEM) imaging was utilised to confirm species concepts and provide high resolution imagery for the purposes of this thesis.

3.9.1 Sample preparation

Individuals were picked from core tops to minimise the potential for overgrowths and ensure best preservation based on visual comparison with individuals further downcore. Where possible multiple individuals were selected to capture several viewing angles on the SEM. Tests were picked initially using distilled water onto a slide that was dried overnight in an oven at 60 ºC. The following day individuals were mounted onto SEM stubs using ethanol to ensure specimens were dry prior to coating.

Samples were taken to the Leeds Electron Microscopy & Spectroscopy Centre and sputter coated in ~10 nm of gold, samples were then loaded into the Tescan VEGA3 XM SEM and pumped down to vacuum. Stubs were coated in gold to minimise the impact of charging i.e. electrons accumulating due to Calcium Carbonate foraminiferal tests being non-conductive, and preserve the quality of images collected.

3.9.2 SEM imaging and processing

Images were captured at magnifications appropriate to the test size, with contrast and image brightness adjusted to preserve image quality and reduce effects of electron backscatter. Voltage was kept constant at 10 kV for all images to ensure resolution. Captured images were exported as TIFF files for manipulation in graphics software, captured images contain the image scale and SEM settings.

3.10 CTD data and processing

Historical CTD data for the study site is available due to a single CTD transect bisecting the region from March 2009, collected by the RRS James Cook on cruise JC032 (King et al., 2010). This data is comprised of pressure (equivalent to depth below sea level), temperature, potential salinity and oxygen datasets and was available for download from the National Oceanography Centre British Oceanographic Data Centre (BODC). Of the nine CTD stations available, six stations were within the study region and from depths comparable to the core top sites. These six stations were processed initially in excel before the R ggplot2 package was utilised for plotting of temperature-salinity plots.

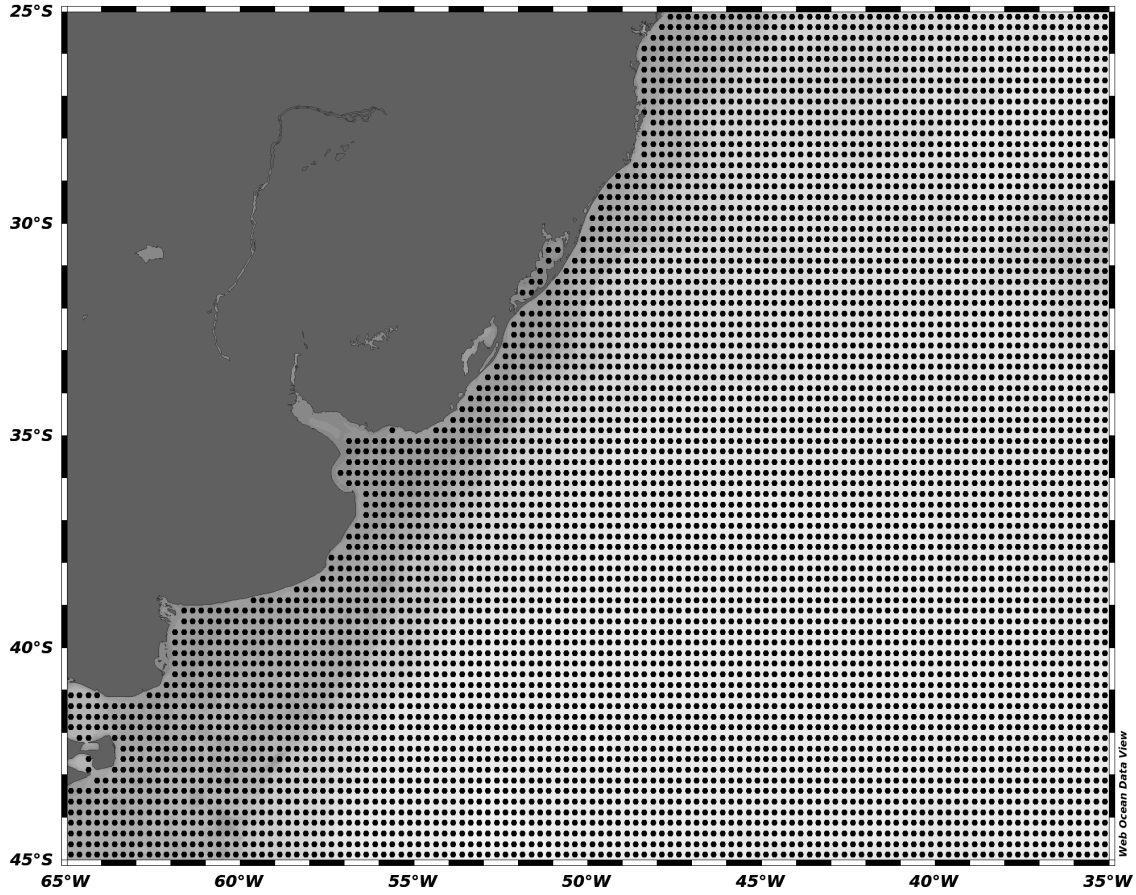

Figure 3.10-1 Grid of interpolated stations used in webODV online software to generate seasonal and annual regional SST plots in the absence of local CTD data for multiple seasons or years. Grid provides 0.25 degree coverage across the study region and supplements acquired CTD data where possible (Locarnini et al., 2019; Schlitzer and Mieruch-Schnülle, 2021).

In order to obtain additional water column data, to capture margin seasonality and annual averages, the World Ocean Atlas 18 (WOA18) datasets were accessed through the webODV platform (www.explore.webodv.awi.de). This uses modelled ocean variables over the last 62 years to provide an estimate on

a variety of parameters such as sea surface temperatures (SSTs), sea surface salinities (SSS) and temperatures/salinities at regular depth intervals (Locarnini et al., 2019; Schlitzer and Mieruch-Schnülle, 2021). The 0.25-degree grid was utilised for all figures representing SSTs, either on a seasonal or annual basis, using the WOA18 dataset. A gridded field using weight-average gridded was utilised to produce figures, incorporating all available stations. Figure 3.10-1 presents the spacing of stations utilised in the weight-average gridding. In the absence of in-situ measurements this provides a means of comparison for planktonic foraminiferal isotope results and analysis relating to the seasonal and inter-annual variability of Uruguayan margin oceanographic variability.

3.11 Morphological imaging and analysis

For assessment of *Gc. inflata* morphospecies in Chapter six, individual specimens were required to be imaged and a number of parameters digitally parameterised in order to distinguish between two distinct morphotypes, based on aperture size (Morard et al., 2011; Morard et al., 2016; Jonkers et al., 2021) (Figure 3.11-1). Imaging would utilise a Zeiss Axio Zoom V16 microscope with attached Cannon EOS 100D camera at 19.4x magnification. A minimum of 25 individuals of foraminifera were to be imaged in umbilical and side views for robust statistical analysis (Brombacher et al., 2017). The images would then subsequently be analysed using ImagePro Premier software collecting measurements on test area, perimeter, length of major axis in edge view, aspect ratio, aperture size and terminal chamber major axes (Figure 3.11-2). These measurements would be taken largely automatically with images checked by eye to ensure entire tests are measured correctly. Each foraminifer is allocated a number so as all measurements are assigned to the correct specimen, this is key as it would enable subsequent isotope analysis to be assigned to the digital parameters per specimen.

Analysis beyond collation of parameters would use landmark analysis on the terminal chamber of the foraminifera test with TPS and MorphoJ, following Morard et al. (2016) in order to split the two morphotypes (Morard et al., 2016).

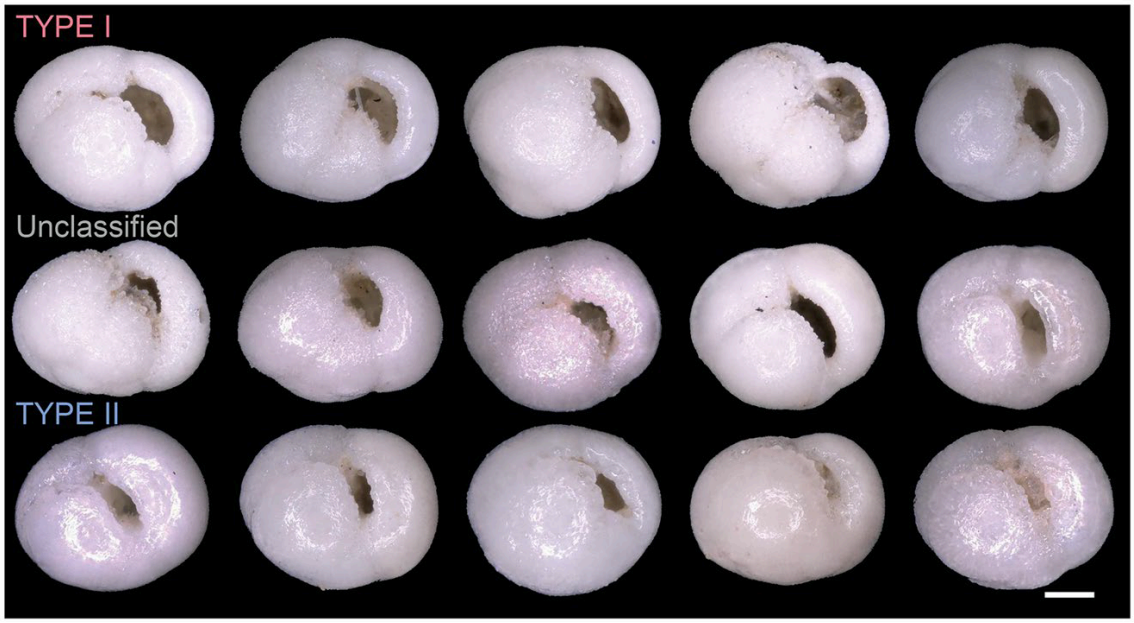

Figure 3.11-1 Visual delineation of the two *Gc. inflata* morphotypes from Core GeoB13862-1, with Type I typically displaying a larger, more open aperture than Type II. Image is taken from Jonkers et al., 2021 and the scale bar is 100 µm.

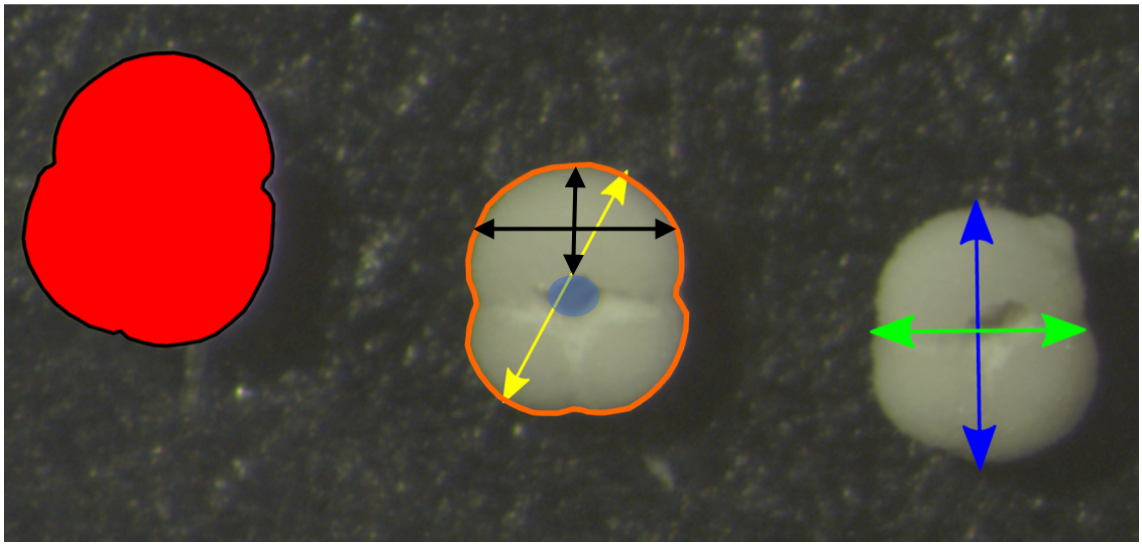

Figure 3.11-2 Example measurements that would have been collected. Red denotes test area, orange line is test perimeter, yellow arrow is maximum diameter, blue area is aperture size, black arrows show measurements of the terminal chamber. Blue arrow shows length, green arrow shows width, which combined can provide the test aspect ratio.

Chapter 4 Uruguayan Margin spatial variability of planktonic foraminifera

4.1 Aim

In this chapter I will investigate planktonic foraminifera assemblage compositions, the stable carbon and oxygen isotopes values of species representing different ecological niches, and modelled planktonic foraminifera settling trajectories, to establish whether it is possible to identify the complexity of the overlying oceanography in core top sediments distributed across the Punta del Este Basin.This chapter aims to assess the spatial variability of planktonic foraminiferal core top records across an oceanographically complex region to investigate how faithfully foraminiferal assemblages record overlying water masses. Answering the broader question:

- Do planktonic foraminiferal core top records reflect overlying oceanographic currents, displaying spatial heterogeneity between sites, or does the record provide a homogenous signal across the margin?

The Brazilian-Malvinas Confluence (BMC) is a key feature of South Atlantic circulation with heat, salinity and nutrient exchange between the sub-tropics and sub-polar regions (Stramma and England, 1999; Brandini et al., 2000; Piola and Matano, 2008; Paniagua et al., 2018; Piola and Matano, 2019). This meeting of two contrasting surface currents, the sub-tropical, southward flowing Brazilian Current (BC) transporting heat and high salinity waters interacts with the sub-polar derived and northward flowing Malvinas Current (MC), a comparatively nutrient rich and colder water mass. The result is a complex mixing region with intense eddy generation, and a migratory oceanographic front that shifts seasonally and inter-annually based on the competing strength of the two currents (Figure 4.1-1) (Olson et al., 1988; Peterson and Stramma, 1991; Hernández-Molina et al., 2016; Piola and Matano, 2019).

Tracing this important, but highly variable oceanographic feature requires reliable proxies and extensive spatial sampling. This study uses core top records, across one degree of latitude along the Uruguayan Margin, and planktonic foraminiferal ecological preferences, to test whether this overlying oceanography is preserved

in the sedimentary record, or whether this signature is obscured through mixing within the confluence. I will use known planktonic foraminiferal assemblage ecological affinities for regional water masses, stable isotopic analysis of planktonic foraminiferal tests, and, where present, regional CTD data to align converted $\delta^{18}O$ foraminiferal values to regional water masses. Additional work with colleagues at the University of Utrecht employs particle transport models to trace whether transport of foraminiferal tests is likely to impact assemblage and isotope data in such an oceanographically dynamic region.

Aims and questions:

1. Assess the spatial variability of planktonic foraminiferal assemblages and stable oxygen and carbon isotopes across the margin.
- Are proximal sites variable in the recovered assemblage and stable isotope results?
2. Correlate with overlying oceanography to assess how reliably core top data corresponds to major oceanographic features.
- Do the recovered results reliably reflect modern oceanographic settings?
3. Utilise transport modelling to determine the likely transport distances for planktonic foraminifera and whether this is to impact the reliability of assemblage and isotope data in an oceanographically dynamic region.
- Is transport a significant factor influencing results and blurring signals recorded?

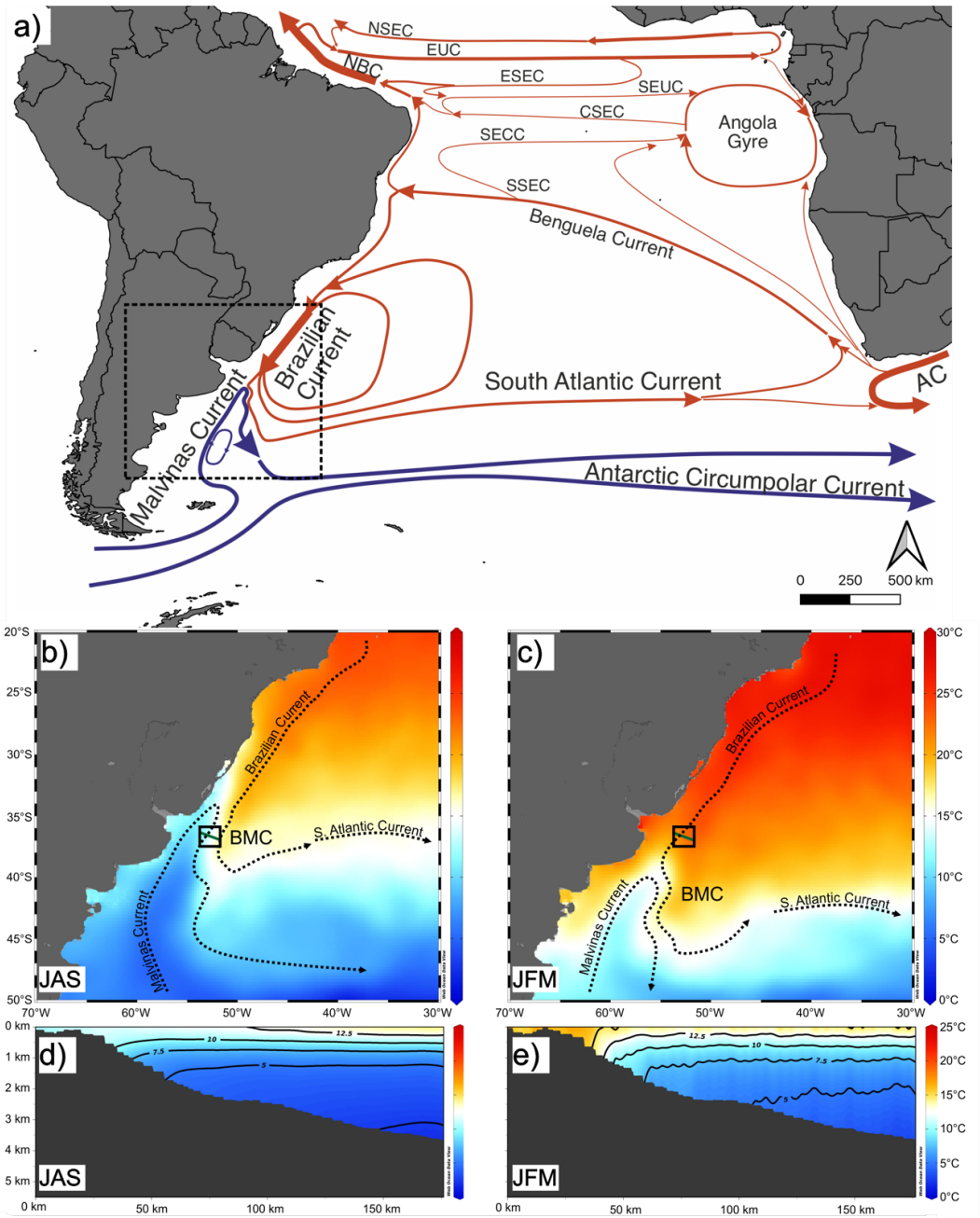

Figure 4.1-1 Southwestern Atlantic oceanography is dominated by the Brazilian Malvinas Confluence (BMC), the meeting of counter flowing surface currents (Piola and Matano, 2019). a) southern hemisphere ocean circulation reproduced from Stramma and England, (1999). The BMC migrates within this framework seasonally and inter-annually. b) sea surface temperature austral winter months of July to September show BMC equatorward migration, with nearshore MC expansion and offshore BC overshoot influencing the study region. c) warm austral summer months of January to March show a more poleward BMC position, with the site experiencing more BC influence. The studied region straddles this seasonal and inter-annual BMC shift on the Uruguayan margin, (black solid box, panels b and c). d) and e) are temperature transects (green line) across the study region displaying seasonal temperature depth changes. Panels b-e were constructed using the online Ocean Data Viewer from the seasonal 0.25 degree World Ocean Atlas 18 (WOA18) dataset (Stramma and England, 1999; Schlitzer and Mieruch-Schnülle, 2021).

4.2 Materials and Methods

Of the 200 cores sampled in the Punta del Este basin a sub-set of 35 core top sediments were selected for direct sampling across the margin length (SW-NE) at a variety of water depths (800-3200 m) (Figure 4.2-1). Each core top comprised of 20 cm^3 of sediment, principally composed of fine sands, silts, bioclastic carbonates and organic sediments. Core top samples represent an inter-decadal (~13.5 years/cm) record based on downcore work.

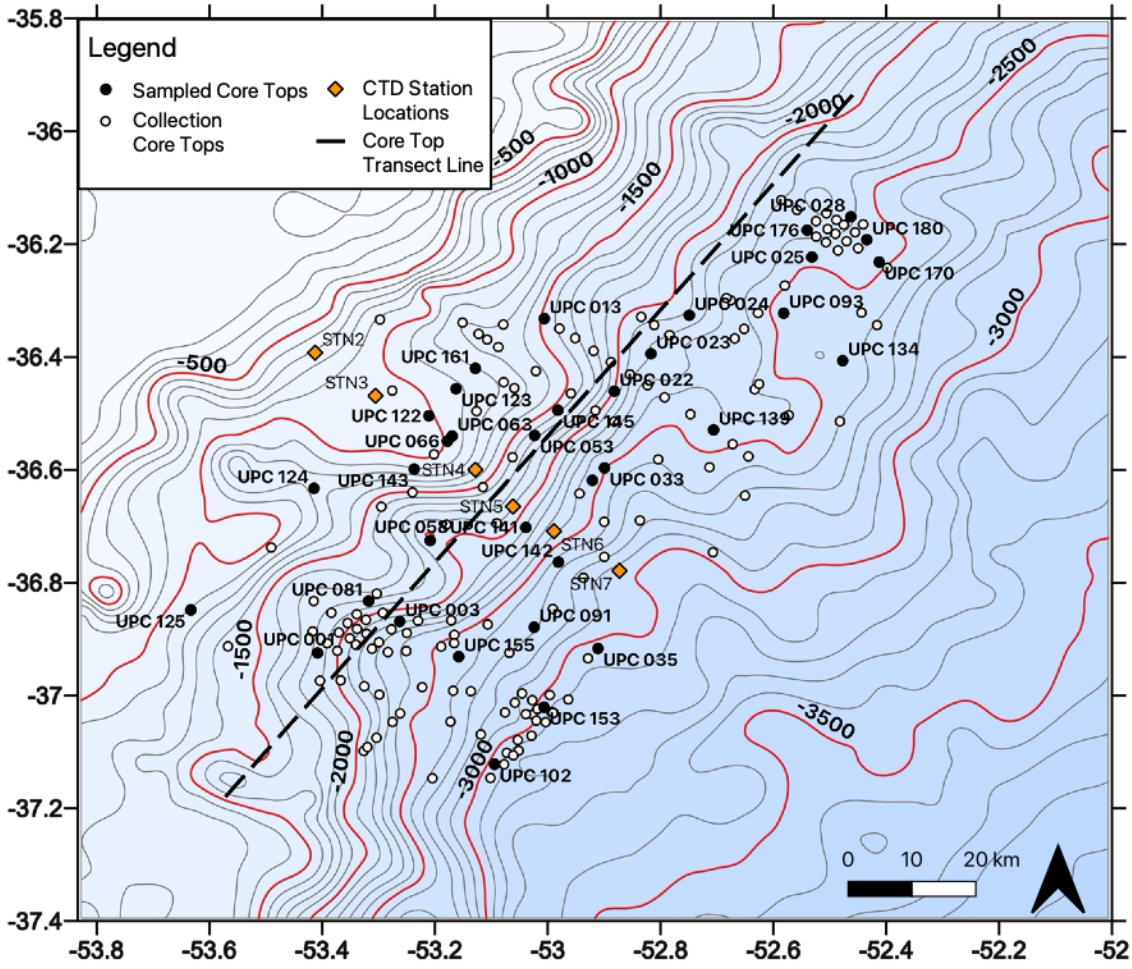

Figure 4.2-1 Bathymetric map showing the spatial distribution of the cores within the British Ocean Sediment Core Research Facility (BOSCORF) collection along the Uruguayan margin. The collection comprises some 200 cores of which 35 core tops (black circles) were sampled for assemblage and isotope analysis along the margin length. The core top sampling followed a SW-NE transect as represented by the dashed line. A Conductivity Temperature Depth (CTD) hydrographic line runs through the study area in a NW-SE direction as indicated by the orange diamonds. Blue colouring relates to depth. Bathymetric data modified from Hernández-Molina et al., 2016 and McGuire et al., 2019.

Each of these samples were analysed for assemblage counts, planktic:benthic ratios and a number of diversity metrics. Spatial interpolation was employed to observe regional patterns and predict likely patterns for unsampled areas, constructing a core top ecological model for comparison with the known surface

oceanography on the margin. Additionally, a subset of samples had stable oxygen and carbon isotope analysis performed on four species for water column properties reconstruction. Where possible this involved the use of single specimen isotope analysis in order to interrogate the per mil averages reported in broader latitude multi-specimen studies, and to discern foraminiferal end-member isotope measurements with water masses spatially (Chiessi et al., 2007; Morard et al., 2016).The methods utilised in this chapter are detailed in the methods chapter and cross-referenced here (Table 4.2-1). Samples for which assemblage and isotope analysis was conducted are listed in Table 4.2-2.

Table 4.2-1 List and location of methods utilised for analysis in Chapter 4.

Method	**Section #**	**Sample material**	**Sites analysed**	**Species targeted**
Foraminiferal sample preparation & assemblage ecological analysis	3.4	Core top sediments	35	All
Stable isotope preparation and analysis	3.5	Single and multi-specimen foraminifera	15	*Globigerinoides ruber, Globoconella inflata, Globorotalia truncatulinoides, Neogloboquadrina pachyderma*
Digital Spatial Mapping and Interpolation	3.4.2	Data	All	All

Table 4.2-2 List of sites sampled for core top assemblages, and stable isotope analysis of four planktonic foraminiferal species. The isotope analysis is for the purpose of reconstructing water column properties within the study region.

Site	Latitude (°)	Longitude (°)	Depth (m)	Assemblages	Isotopes
UPC 125	-36.85	-53.63	-1121.22	Yes	No
UPC 001	-36.92	-53.41	-2053.05	Yes	Yes
UPC 102	-37.12	-53.09	-2933.09	Barren	Barren
UPC 081	-36.83	-53.32	-1895.64	Yes	Yes
UPC 003	-36.87	-53.26	-2205.15	Barren	Barren
UPC 155	-36.93	-53.16	-2557.21	Yes	No
UPC 153	-37.02	-53.01	-3046.37	Yes	No
UPC 124	-36.63	-53.41	-1710.71	Yes	No
UPC 058	-36.73	-53.21	-2255.28	Yes	Yes
UPC 091	-36.88	-53.02	-2644.10	Yes	No
UPC 035	-36.92	-52.91	-3026.75	Barren	Barren
UPC 143	-36.60	-53.24	-1356.17	Yes	No
UPC 142	-36.76	-52.98	-2682.11	Yes	Yes
UPC 141	-36.70	-53.04	-2431.08	Yes	Yes
UPC 063	-36.54	-53.17	-1255.00	Yes	Yes
UPC 066	-36.55	-53.18	-1257.00	Yes	Yes
UPC 122	-36.50	-53.21	-1154.19	Yes	Yes
UPC 123	-36.46	-53.16	-1194.30	Yes	No
UPC 053	-36.54	-53.02	-2115.24	Yes	Yes
UPC 032	-36.62	-52.92	-2513.29	Yes	No
UPC 161	-36.42	-53.13	-1241.64	Yes	No
UPC 033	-36.60	-52.90	-2582.33	Yes	Yes
UPC 145	-36.49	-52.98	-1595.39	Yes	Yes
UPC 022	-36.46	-52.88	-2027.53	Yes	Yes
UPC 013	-36.33	-53.01	-1574.92	Yes	No
UPC 139	-36.53	-52.71	-2499.00	Yes	No
UPC 023	-36.39	-52.82	-2046.34	Yes	Yes
UPC 024	-36.33	-52.75	-2252.95	Yes	No
UPC 093	-36.32	-52.58	-2572.48	Yes	Yes
UPC 134	-36.41	-52.48	-2731.00	Yes	No
UPC 025	-36.22	-52.53	-2445.71	Yes	No
UPC 176	-36.18	-52.54	-2351.00	Yes	No
UPC 170	-36.23	-52.41	-2535.00	Yes	No
UPC 180	-36.19	-52.43	-2433.00	Yes	No
UPC 028	-36.15	-52.46	-2353.00	Yes	Yes

4.3 Results

4.3.1 Assemblage counts and regional diversity

Of the 35 sites selected for analysis, 32 provided ≥300 individual planktonic foraminifera to reliably conduct assemblage analysis representative of the population (Schiebel and Hemleben, 2017), with the remaining three sites subsequently classified as barren. In total 13,213 planktonic foraminifers were counted and classified into 24 species, additionally 11,351 individual benthic foraminifera were logged to enable planktic:benthic ratios to be calculated for each site (Appendices B.1).

The number of species found at each site was mapped and interpolated as an initial estimator for margin diversity. The aim was to identify geographical regions of low or high diversity of species and correlate with oceanography, based on previous literature linking a higher number of species to warmer water masses (Kucera, 2007; Schiebel and Hemleben, 2017). Species numbers are illustrated in Figure 4.3-1 with the maximum number of taxa recorded at a given site being 22 at UPC 093 and a minimum number of 10 at UPC 124, the average across all sites was 17. Interpolating species richness between sites and plotting alongside the bathymetric contours, shows sites in shallower water have lower numbers of taxa present (<17 species) versus those in deeper waters. The selected transect route across the margin lies between 1500 and 2000 mbsl, the result of which is sites at comparable latitude but in differing water depths display differing numbers of species. Analysis of these species ecologies is required to assess whether this is the result of water mass variability or purely water depth.

Based on the assemblage counts, the fragmentation of the sample and the diversity metrics seen below, UPC124 was removed from further eco-group analysis due to suspected taphonomic processes that have resulted in preferential preservation of a single species (>76% of the assemblage). This is likely the result of being located in a canyon base, with erosion and transport activity favouring preservation of the robust *Globoconella inflata* over other contemporaneous more fragile species.

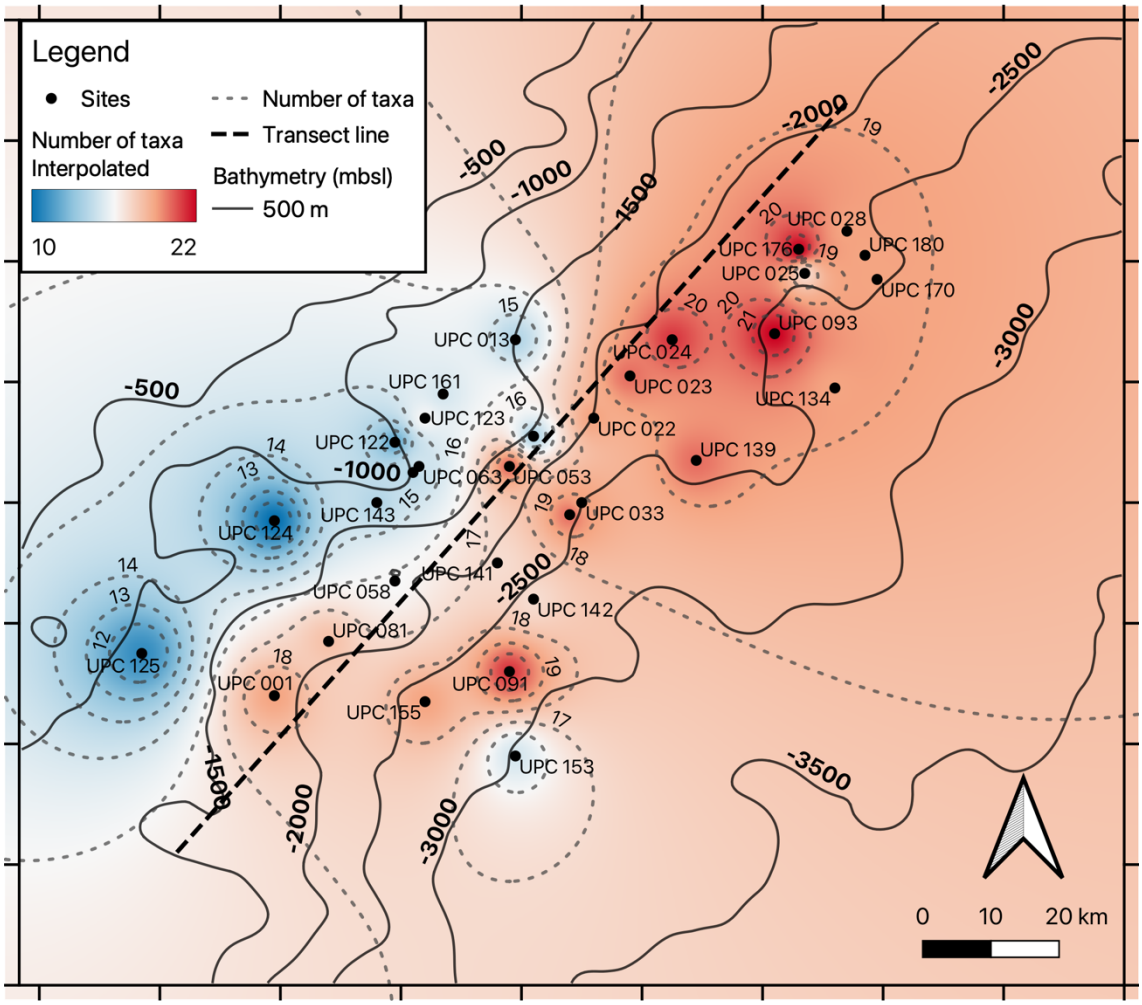

Figure 4.3-1 The number of species recorded at each site is mapped with major bathymetry lines overlain. Interpolation between sites produces grey dashed contour lines that indicate number of taxa recorded, with the blue-red colouring similarly based on number of taxa present to distinguish areas of low diversity (blue) versus more diverse regions (red). Initial analysis shows concentration of low diversity sites to the West/Northwest, above 1500 mbsl, whilst sites toward the east show higher diversity of taxa. Bathymetric data modified from Hernández-Molina et al., 2016 and McGuire et al., 2019.

Relative abundance data collected for the remaining 31 sites is detailed below (Figure 4.3-2). As outlined in the methods, the assemblages were split by eco-groups. A spatial plot of the study region is presented with sites classified according to procedures outlined in the methods (Figure 4.3-3). Assemblage data shows a trend of increasing tropical and sub-tropical species to the northeast, with an associated drop in polar and sub-polar species. Transitional forms largely remain consistent between 40-60% of the assemblage. The transect shows significant spatial variability between sites, with changeable proportions of the five groups within a single degree of latitude. Combining the tropical and sub-tropical groups into a warm water species group, the increasing influence of warmer waters to the northeast is clear. The decline of polar and sub-polar species is matched by increases in warm water forms at more northerly sites.

The most prevalent species across all sampled sites along the margin (with average relative abundances) are: *Gc. inflata* (~31.1%), *N. pachyderma* (~18.6%), *Gt. glutinata* (~13.2%), *N. incompta* (~8.8%), *Gg. bulloides* (~6.4%) and *Gs. ruber white* (~5.0%). Proportions of these taxa at each site vary significantly over the margin, in the case of *Gc. inflata* by up to 30%, impacting the overall eco-group composition of individual sites significantly, and leading to heterogeneous site classification.

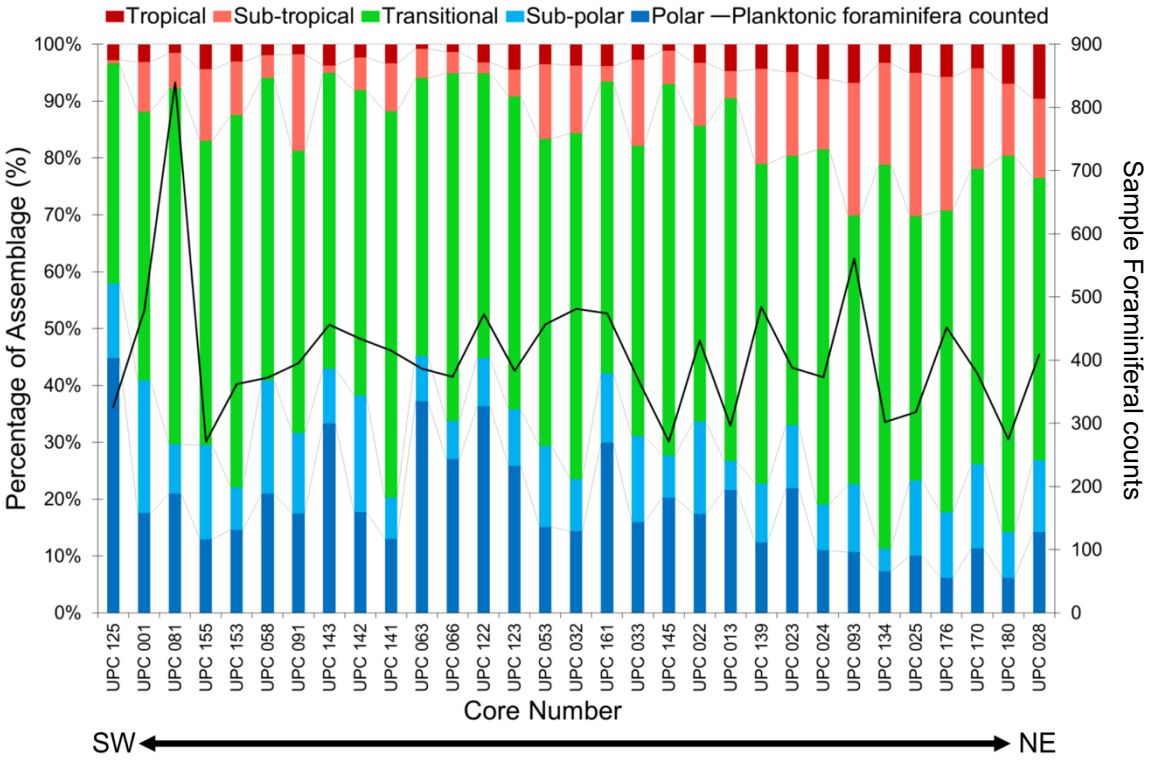

Figure 4.3-2 Assemblage groupings based on temperature eco-groups for 31 sites, ordered on the transect from SW (left) to NE (right). The assemblages show significant margin-wide variation, with a trend of increasing relative abundance of species favouring warmer waters toward the northeast of the transect, and a notable decline in polar taxa.

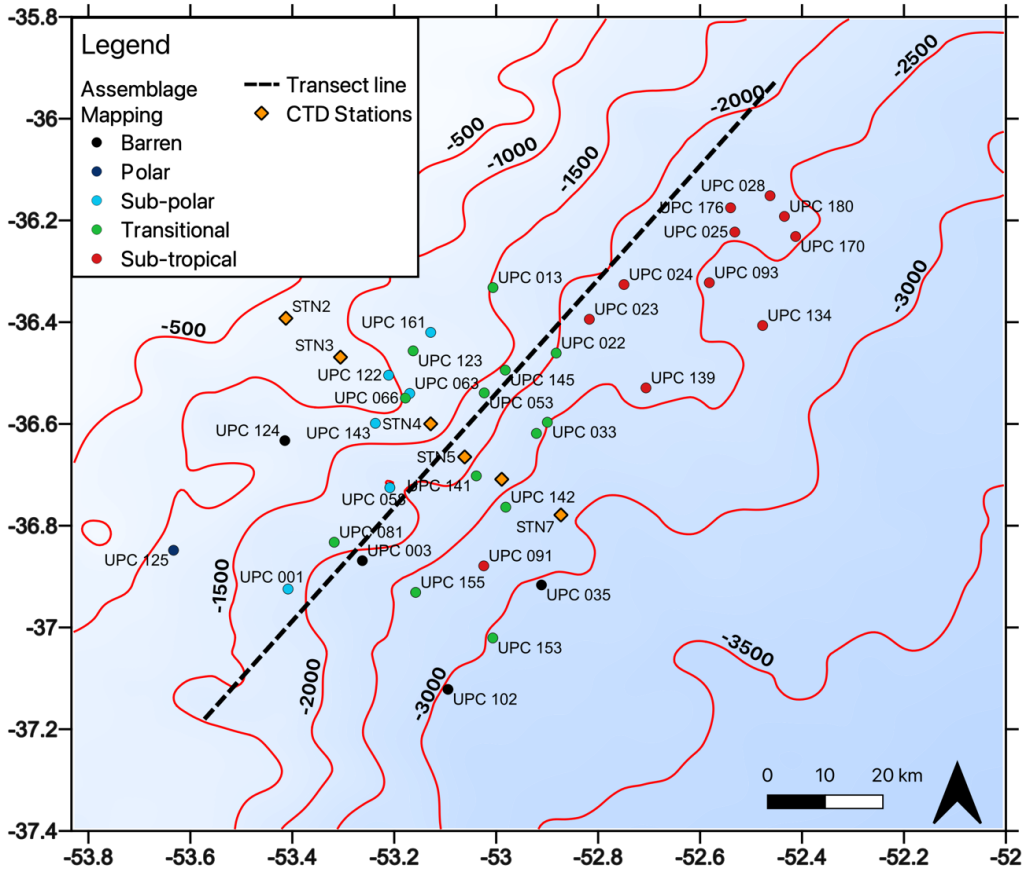

Figure 4.3-3 Sites categorised into temperature regimes based on the eco-groups of the species found at each site. There is a clear transition from sub-tropical to transitional/sub-polar at approximately 52.8° longitude. Bathymetric data modified from Hernández-Molina et al., 2016 and McGuire et al., 2019.

4.3.1.1 Diversity Metrics

Diversity metrics, on the collected assemblages, were calculated for all remaining samples. Calculated Fisher alpha values suggest an increase in species richness moving along the transect to the northeast, with values typically above three. This increase in species richness corresponds with increases in warmer water taxa in the more northerly sites. Simpsons Index of Diversity (Figure 4.3-4) indicates that all sites show a diverse assemblage of planktonic foraminifera, producing high values between 0.7-0.9, suggesting no one species dominates the assemblages and that the sampled region is typical of an open ocean setting (e.g. Armstrong and Brasier, 2005). As this metric is the inverse of dominance it also implies samples are comparatively even, becoming more so toward the east, and northeast of the transect. This is with the exception of UPC 124 that is dominated by *Gc. inflata* resulting in a Simpsons Index value approaching 0.4. This dominance of one species and the deviation from local sites lead to the removal of this site from subsequent analysis and the sites omittance from Figure 4.3-2 and Figure 4.3-3.

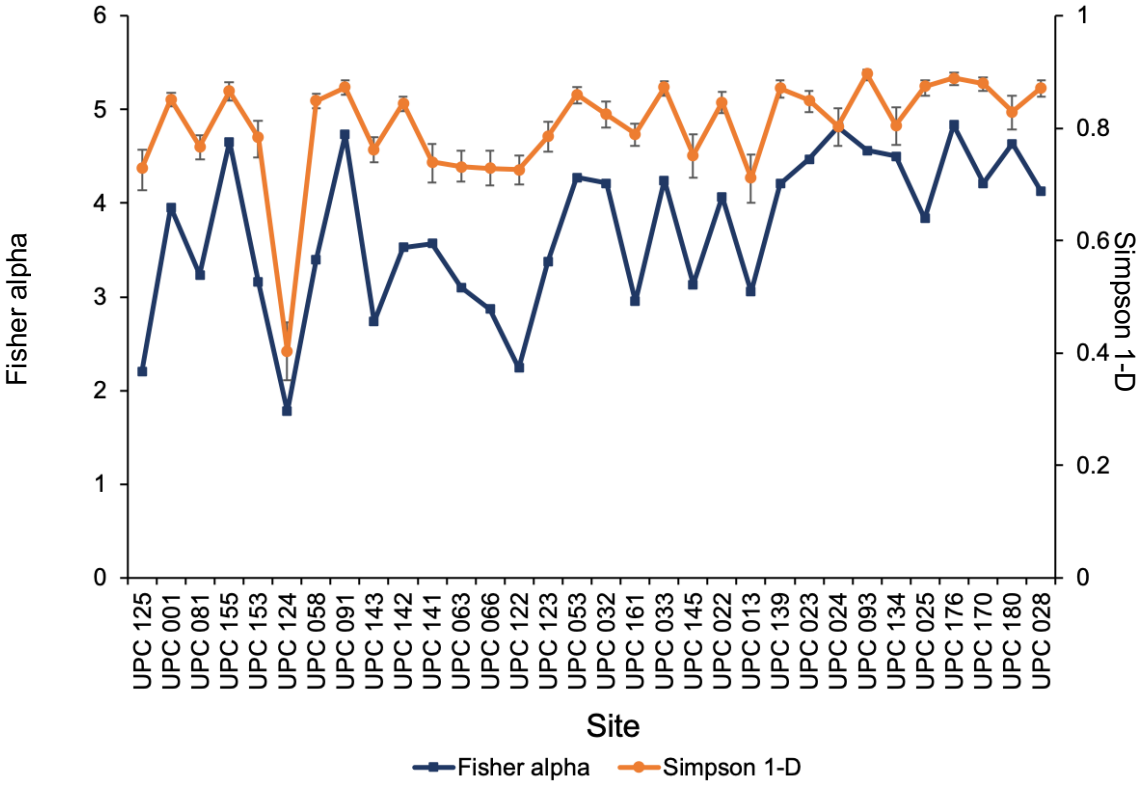

Figure 4.3-4 Calculated Fisher alpha diversity and Simpson 1-D values are plotted above for each site in the transect. Fisher alpha suggests an increase in species richness moving toward the northeast, or righthand side, of the transect. Simpson 1-D provides an assessment of species evenness across the transect and whether samples are dominated by a singular species or record an even assemblage. Within both metrics UPC 124 deviates from surrounding samples, particularly Simpsons Index of diversity, where the value of 0.4 suggests dominance of a single species.

4.3.1.2 Wider South Atlantic

To test whether eco-group classification was not significantly biased by expected conditions and could be utilised outside the region, the same species classifications were applied to counts across the South Atlantic Ocean. This involved using a subset of a pre-existing database, the Southern Hemisphere Ocean Database, which had collated a number of global databases between the latitudes of 15-64°S (Haddam et al., 2016). Additionally, a number of western South Atlantic margin counts became available during the course of this analysis and were subsequently classified in this study (García Chapori and Laprida, 2021). Results are presented in Figure 4.3-5, in which all available counts outside of the Uruguayan Margin, within the Southern Atlantic have been categorised following the same procedures. Clear latitudinal separation of a tropical/sub-tropical band, a transitional band and a sub-polar/polar band is apparent. The sites of this study straddle the tropical/sub-tropical transitional boundary with some evidence of cooler sub-polar waters present at similar latitudes in the South Atlantic.

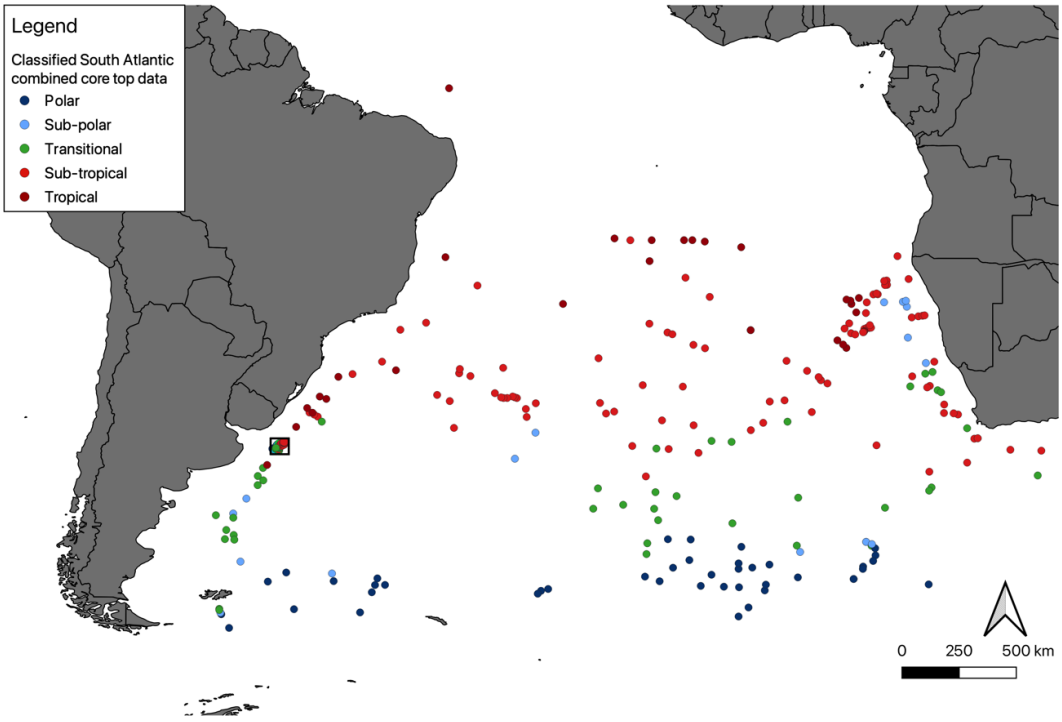

Figure 4.3-5 Classification of published census count data for the South Atlantic combining numerous datasets from Haddam et al., 2016 and South Atlantic margin study sites from Chapori et al., 2021. Study region (black box) with this studies data within.

4.3.2 Spatial mapping of species distributions

Using the relative abundance values determined from assemblage counts at the 31 remaining sites it was possible to plot the regional distribution of species to resolve where significant variation occurred between sites. Species distributions were plotted using inverse distance weighting (IDW) interpolation to extrapolate regional signals from the sampled locations to the wider margin. Through contour mapping on top of the generated raster files it is possible to interpolate to the unsampled regions between sites and make inference on the margin-wide variability.

Both species specific and grouped plots were generated with groups following the Transitional, Warm (sub-tropical and tropical) and Cold (sub-polar and polar) groupings outlined within the methods. Within the results section, only the grouped plots are displayed, however, plots for the ten most common species found across the margin are contained within the Appendices (Appendix G.1-G.10). All interpolations were conducted within the same area to provide consistency in the calculation with the contouring scale changing to reflect the varying relative abundances. Single band colouring was utilised to better identify hotspots with known tropical and sub-tropical species displayed in white-red, sub-polar and polar species in white-blue and transitional taxa in white-green.

4.3.2.1 Species plots

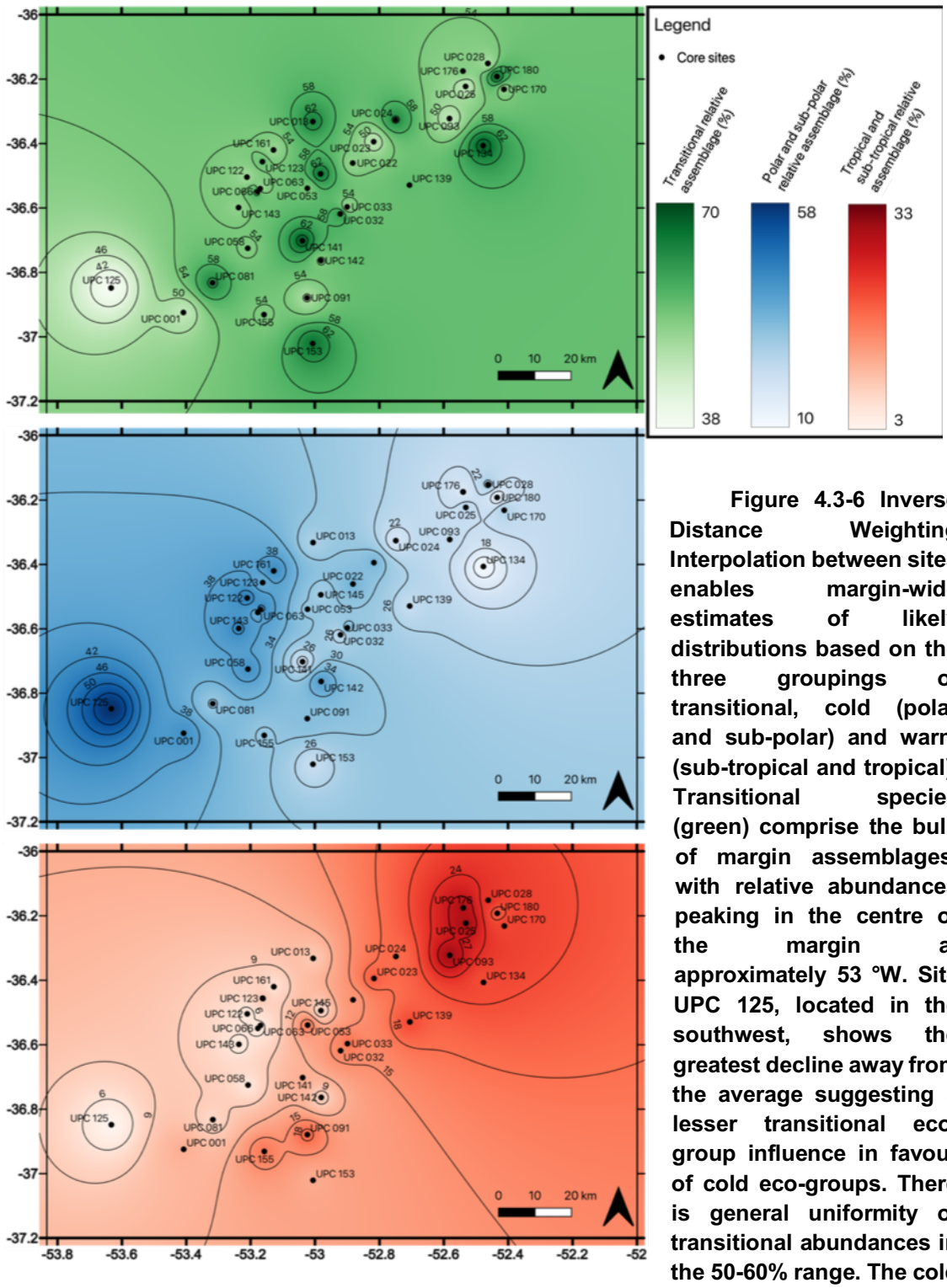

Figure 4.3-6 Inverse Distance Weighting Interpolation between sites enables margin-wide estimates of likely distributions based on the three groupings of transitional, cold (polar and sub-polar) and warm (sub-tropical and tropical). Transitional species (green) comprise the bulk of margin assemblages, with relative abundances peaking in the centre of the margin at approximately 53 °W. Site UPC 125, located in the southwest, shows the greatest decline away from the average suggesting a lesser transitional eco-group influence in favour of cold eco-groups. There is general uniformity of transitional abundances in the 50-60% range. The cold species IDW interpolation plot (blue) is based on relative abundances of three species: *N. pachyderma*, *N. incompta* and *T. quinqueloba*. UPC125 dominates the plot in the southwest with decreasing abundance to the northeast, where the lowest value at UPC134 is found. All sites show at least 10% of cold-water taxa, even in the northernmost sites. The warm species IDW plot (red) displays the greatest relative abundance concentrations in the northeast, in particular the eastern slope portion (UPC025, UPC028, UPC093, UPC134, UPC 170, UPC176 and UPC180) and slope bases (UPC091 and UPC155). There is contrast when comparing warm and cold groupings with transition between the two occurring at the centre of the margin.

Transitional: The summed transitional species found across the 31 sites within the region present spatial patterns that only differ slightly between species. For instance, higher relative abundances further offshore in the mid-slope and lower slope/terrace are recorded for *Gg. bulloides* and *Gt. glutinata.* Comparatively *Gc. inflata* shows higher values nearer shore on the upper slope/terrace portion of the margin, whilst *Gr. truncatulinoides* is largely consistent across the studied area (Figure 4.3-6). Species plots are available in the appendices (Appendix G.6-G.8). The transitional fauna is dominated by *Gc. inflata* and to a lesser extent *Gt. glutinata* and this is seen when analysing all transitional fauna together (Figure 4.3-6). The resulting spatial pattern is comparatively smooth when compared to warmer and cooler taxa with few sites exhibiting less than 50% transitional forms. Regions where this value drops can be seen to the southwest of the study area (UPC001 and UPC125) and to a lesser extent in the northeast (UPC023, UPC025 and UPC091). Variability is observed between adjacent sites, particularly in the central and north-eastern portions, with a bullseye effect indicating sites with increased transitional taxa dominance when compared to their immediate neighbours (UPC134, UPC141 and UPC180).

Polar and sub polar: The diversity of species that comprise the polar and sub-polar groups is low, however, the relative abundance is higher than some transitional, sub-tropical and tropical forms. Of the three species present in the cold grouping, two species (*N. pachyderma* and *N. incompta*) comprise the bulk of the polar and sub-polar relative abundances (Figure 4.3-6). Individual plots available in Appendices (Appendix G.9-G.10).

All sites have some cold-water species component to the assemblage, however, the site with the highest proportion of cold taxa is UPC 125 (>54%), the furthest west site sampled. The western portion of the margin sees a number of sites with relative abundances >34%, encompassing much of the upper terrace section and western slope within the study area. To the east and northeast cold-water proportions drop in samples from below 1500 m water depth, compared to those from sites nearer shore on the upper slope and terraces. A clear decline is seen in the relative abundance of cold-water favouring species toward the east or east-northeast when compared to the west or west-southwest. This change is driven by significant loss of *N. pachyderma*, and to a lesser extent *N. incompta*.

Tropical and sub-tropical: The warm water grouping is comprised of two diverse sub-groups, the tropical and sub-tropical groupings. Tropical and sub-tropical planktonic foraminifera found within the Uruguayan margin contain five and fourteen species respectively, with a diverse array of morphologies displayed. Despite the range of species present, the relative abundance of such species is often found to be low. IDW plots for the four most prevalent species along the Uruguayan margin; sub-tropical taxa *Gs. ruber* (white) and *Gr. hirsuta,* and tropical taxa *Gs. ruber* (pink) and *T. sacculifer* can be found in the appendices (Appendix G.1-G.5). A combined warm-water IDW plot is provided for summary as the pattern of sub-tropical and tropical taxa are broadly similar, showing higher relative abundances in the northeast of the margin at sites UPC025, UPC028, UPC093 and UPC134 (Figure 4.3-6). The highest warm water values are found in the north-eastern section of the margin, below 2000 m water depth on a lower terrace, with values >30% of the total relative abundance at sites UPC025 and UPC093. This is in direct contrast to the summed cold species plot marking an adjustment of assemblage composition along the margin, from cold prevalent in the southwest to greater warm species influence in the northeast.

Removing the transitional taxa present in both the BC and MC, and summing the remaining cold and warm water species, the relative abundances of the two can be directly compared. Dividing the warm water species by this new summed grouping gives the warm water species contribution. The warm water species were chosen as cold-water species are present at every site, and potentially able to persist at depth in their preferred cooler temperatures (Schiebel and Hemleben, 2017; Rebotim et al., 2017). An IDW plot of warm species contribution shows increasing relative influence of warm water species from less than 10% at UPC125 to highs greater than 50% at a number of sites in the northeast (Figure 4.3-7). The distribution of sites shows a clear shift between sub-tropical and sub-polar sites, with an intermediary boundary in between, demarked at approximately -53 °W longitude on the continental slope. This is principally driven by a loss of *N. pachyderma* moving from the southwest toward the northeast and an increasingly diverse and numerous tropical and sub-tropical fauna.

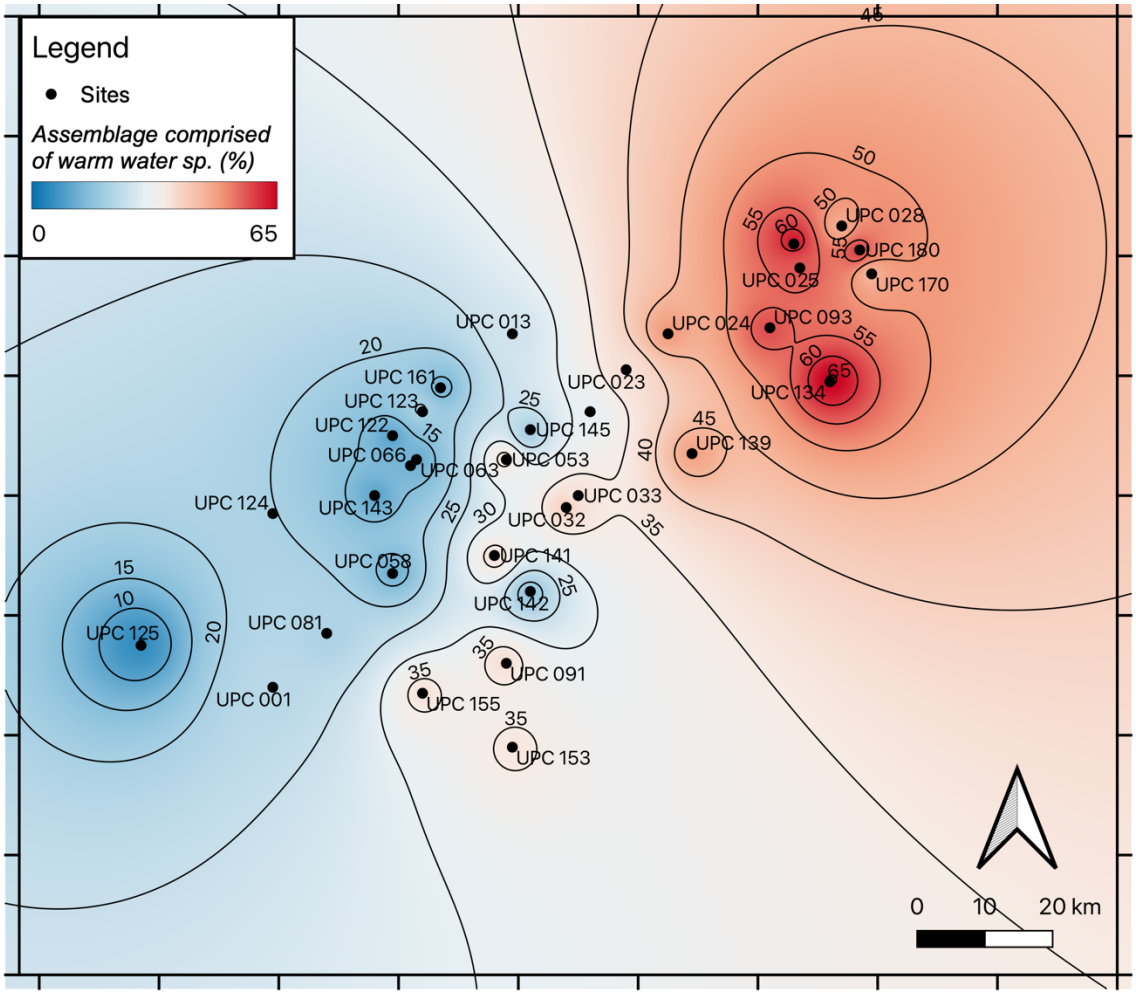

Figure 4.3-7 The relative contributions of warm vs. cold species to individual core sites. Through removal of Transitional species and subsequent calculation of the remaining summed assemblages, warm species influence is determined, providing a measure of the competing BMC currents. The northeast and eastern portions of the margin reflect a greater number of warmer taxa, suggesting a greater BC influence. The southwest and west of the margin, and the bulk of the shallower water sites, show a greater number of polar and sub-polar taxa supporting greater MC influence.

4.3.3 CTD data

Concurrent CTD data was not collected during the sediment core sampling along the Uruguayan margin however, there is a profile bisecting the study region (Figure 4.3-8), that was collected in March 2009 by the RRS James Cook research cruise JC032 (King et al., 2010). The timing of sampling was during Southern Hemisphere late summer/early Autumn and as such it only provides a snapshot of the region and does not account for seasonality. A number of water masses can be characterised based on published properties, and using the CTD temperature and salinity data for several of the stations proximal to the core top transect. For the purposes of this study six of the CTD stations (STN 2-8) proved relevant for the region and are displayed in Figure 4.3-9 with overlying water masses.

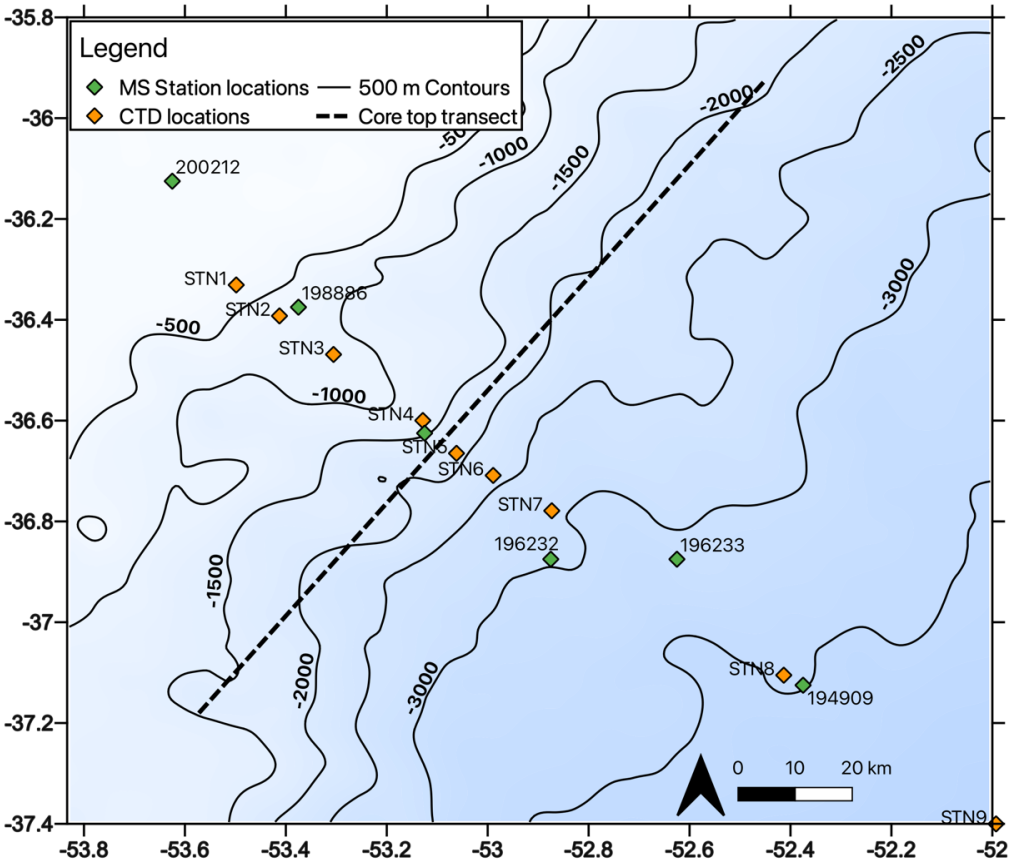

Figure 4.3-8 Location of CTD stations displayed in orange and WOA18 stations utilised for Austral Summer/Winter Temperature-Salinity plots in Figure 4.3-11. Bathymetric data modified from Hernández-Molina et al., 2016 and McGuire et al., 2019.

The water masses identified are as follows: Tropical water (TW), the shallow surface component of the BC, South Atlantic Central Water (SACW), the deeper component of the BC, the MC which is the cold surface waters flowing from the Antarctic, Antarctic Intermediate Water (AAIW), an intermediate depth water mass sourced from Antarctica, North Atlantic Deep Water (NADW), a comparatively warmer deep water mass originating in the Northern Hemisphere and Antarctic Bottom Water (AABW), a cold deep bathyal water mass formed in Antarctica. River Discharge Influence (RDI) is potentially observed in the shallower two stations and is marked by a maintenance of high temperatures but fresher salinities before mixing with the aforementioned water masses, chiefly TW (Piola et al., 2008). La Plata River discharge is usually confined to the shelf (200 mbsl) and advected northward along the Uruguayan and Brazilian Margins. During Austral winter months whilst river discharge is flowing northward the shelf experiences lower salinity waters from the Patagonian shelf. However, during Austral Summer south-westerly winds limit this movement north and instead direct riverine outflow into the BMC. As seen in the CTD data (Figure 4.3-9), the

maintenance of higher temperatures indicates the water was sourced from the La Plata River rather than the cooler temperatures associated with the Patagonian shelf (Combes and Matano, 2014; Guerrero et al., 2014; Matano et al., 2014).

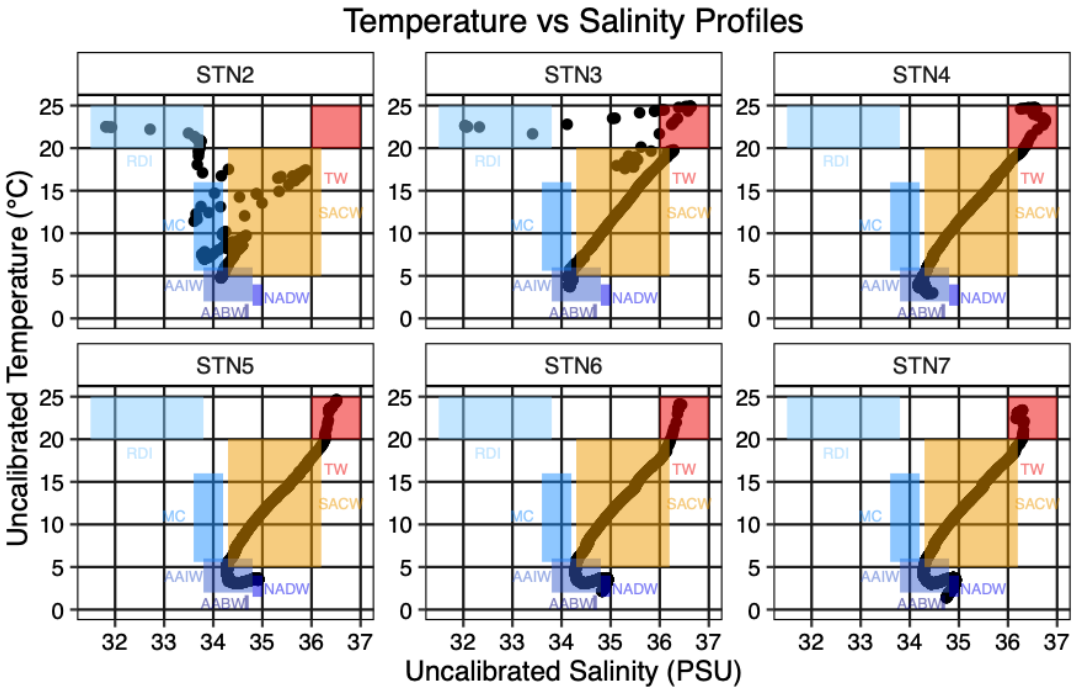

Figure 4.3-9 CTD drop data displaying Temperature vs Salinity curves for a subset of stations relevant to the study. See Figure 4.3-3 for station locations to assemblage sites. Water mass values presented: TW – Tropical Water, SACW – South Atlantic Central Water, MC – Malvinas Current, AAIW – Antarctic Intermediate Water, NADW – North Atlantic Deep Water, AABW – Antarctic Bottom Water, RDI River Discharge Influenced. SACW, AAIW, NADW and AABW values from Emery, 2015 and Piola and Matano, 2019. MC values from Gordon, 1981; Paniagua et al., 2018 and Piola and Matano, 2019, TW values from Piola and Matano, 2008 and Piola and Matano, 2019. RDI is inferred due to the station's coastline proximity and low salinity values suggesting runoff-surface water mixing. TW and SACW are two BC components cited in the literature, TW is the immediate surface waters and SACW the BC extension to depth (Piola and Matano, 2019). Majority of stations show similar profiles, with BC conditions heading offshore during late summer. Nearshore (STN 2 and 3) show colder MC currents and TW and RDI mixing (Piola et al., 2008).

World Ocean Atlas 2018 (WOA18) data provides an approximation for seasonal CTD values through use of interpolated data, enabling estimation of winter water column temperatures. Values are presented as shaded regions in Figure 4.3-10 from 0.25-degree gridded seasonal datasets of austral summer (January to March) and austral winter (July to September). Data is interpolated and averaged over 62 years and as such provides an array of potential values, showing good alignment with summer CTD curves (Locarnini et al., 2019; Schlitzer and Mieruch-Schnülle, 2021). Additionally, it is possible to produce Temperature-Salinity plots based on the interpolated data in the absence of austral winter CTD casts. This data is similarly averaged but provides an indication of potential water masses present during the winter months (Figure 4.3-11).

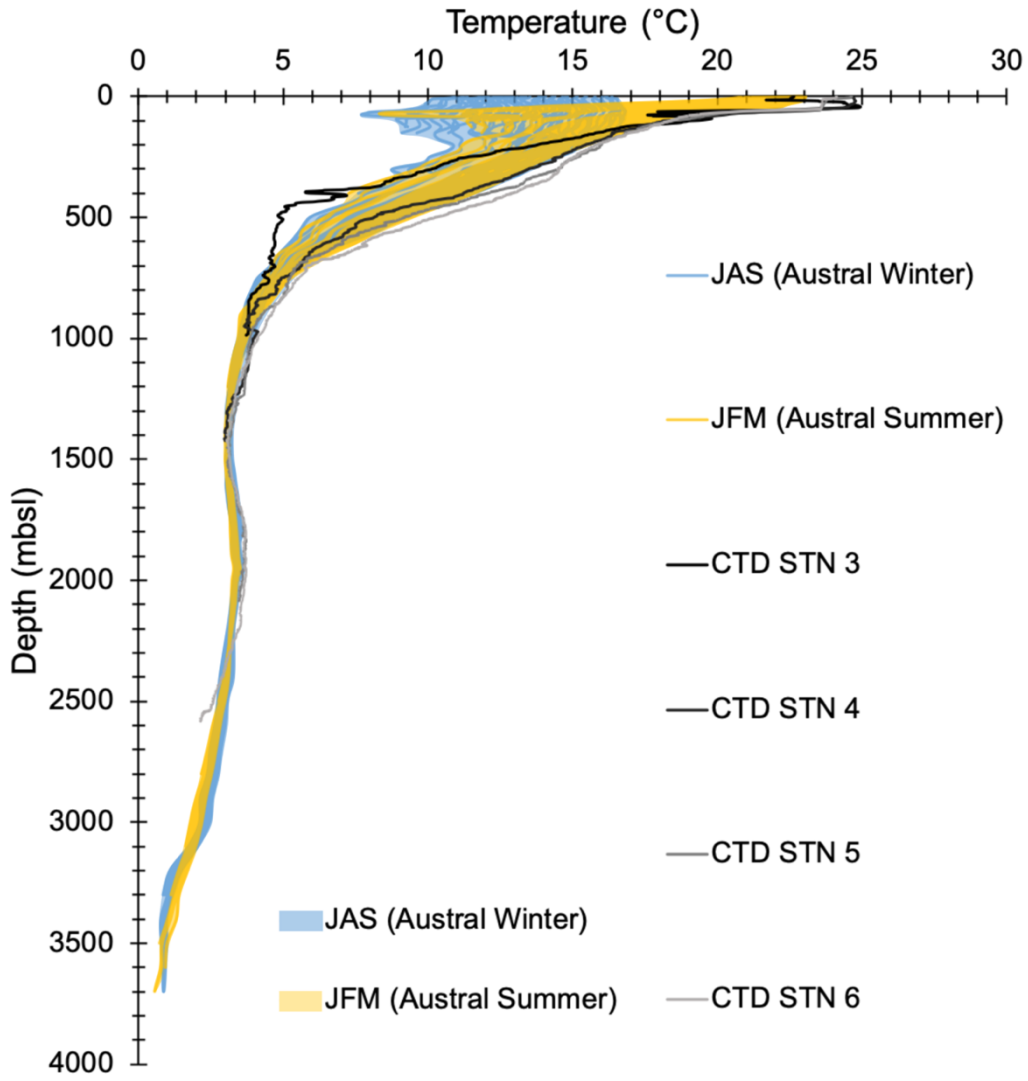

Figure 4.3-10 CTD data from a number of stations across the study area (CTD 3-6) collected in March 2009 by the RRS James Cook research cruise JC032 (King et al., 2010). This data is presented alongside WOA18 modelled data interpolated over 62 years to provide averaged CTD data on a 0.25-degree grid. The WOA18 data provides an approximation of summer (yellow) and winter (blue) CTD temperature values, beyond the March 2009 dataset (Locarnini et al., 2019; Schlitzer and Mieruch-Schnülle, 2021).

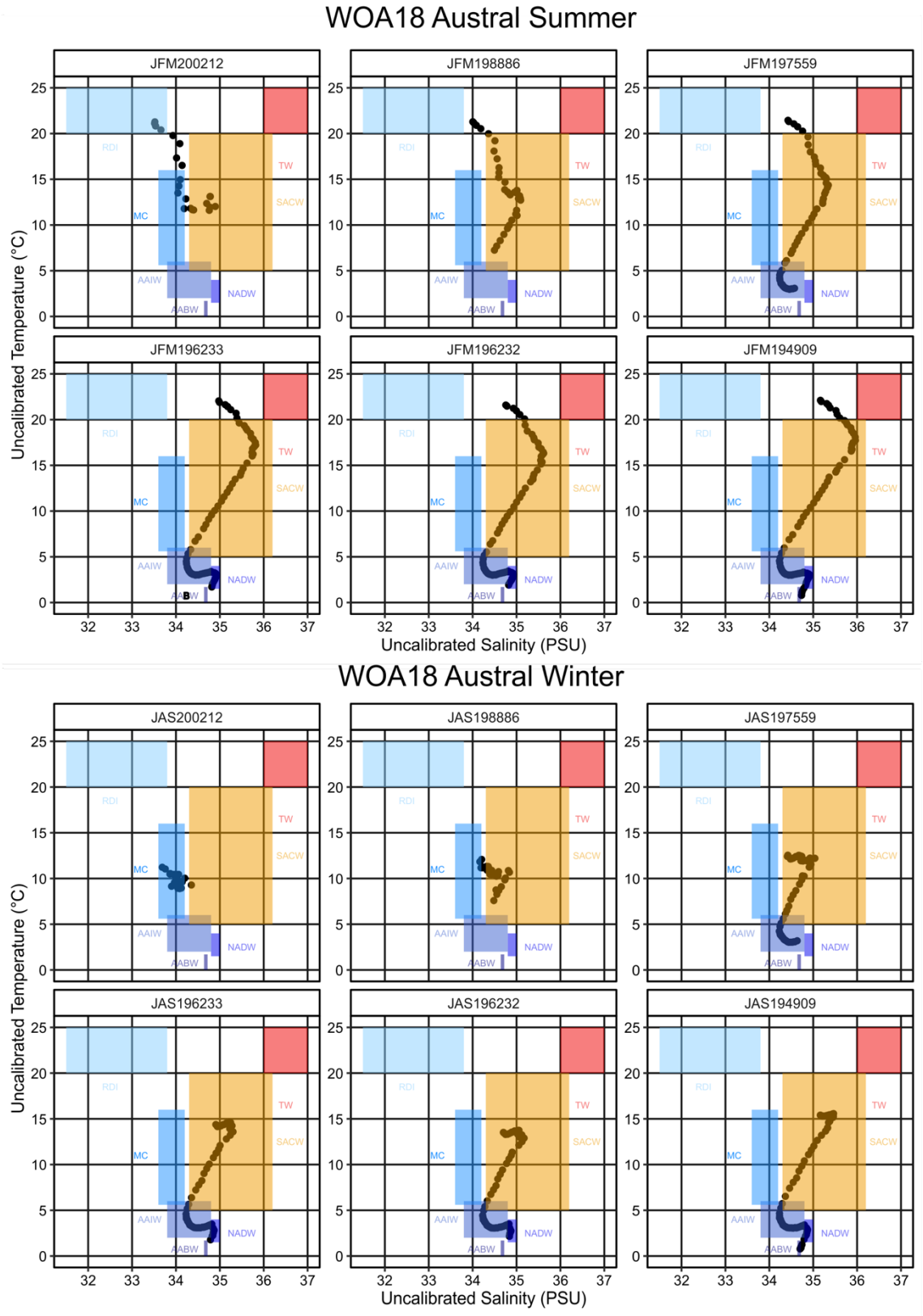

Figure 4.3-11 Temperature-salinity plots for MS stations displayed in Figure 4.3-8, data in Austral Summer is comparable with CTD stations displayed in Figure 4.3-9. Summer values suggest warm SACW dominance, a component of the BC. Austral winter temperature values are reduced, backing cooling and an increased MC presence on the margin, particularly to the NW, whereas stations further offshore largely maintain a warmer SACW signature (Locarnini et al., 2019; Zweng et al., 2019; Schlitzer and Mieruch-Schnülle, 2021).

4.3.4 Spatial Isotopic Variation

Stable oxygen and carbon isotopic analysis were conducted on four species for 15 of the studied sites from a transect along the margin breadth and length (Figure 4.2-1). The four selected species each represent distinct portions of the water column and correspond to differing water masses. *Gs. ruber white*, the shallowest dwelling species, favours the warmer waters of the BC with individual measurements preformed on 2-3 specimens to obtain enough sample. *N. pachyderma* was utilised to assess cooler shallow waters of the MC and typically required seven or more individuals to generate a single data point. The deeper water dweller of *Gc. inflata* was selected to track the thermocline properties across the sites, whilst *Gr. truncatulinoides* was the deepest dweller, anticipated to record the sub-thermocline properties. *Gc. inflata* and *Gr. truncatulinoides* measurements were conducted on single specimens, with the latter species further categorised by coiling direction to determine whether differing properties were being recorded by different morphotypes. Raw isotope data provided in Appendix C.1.

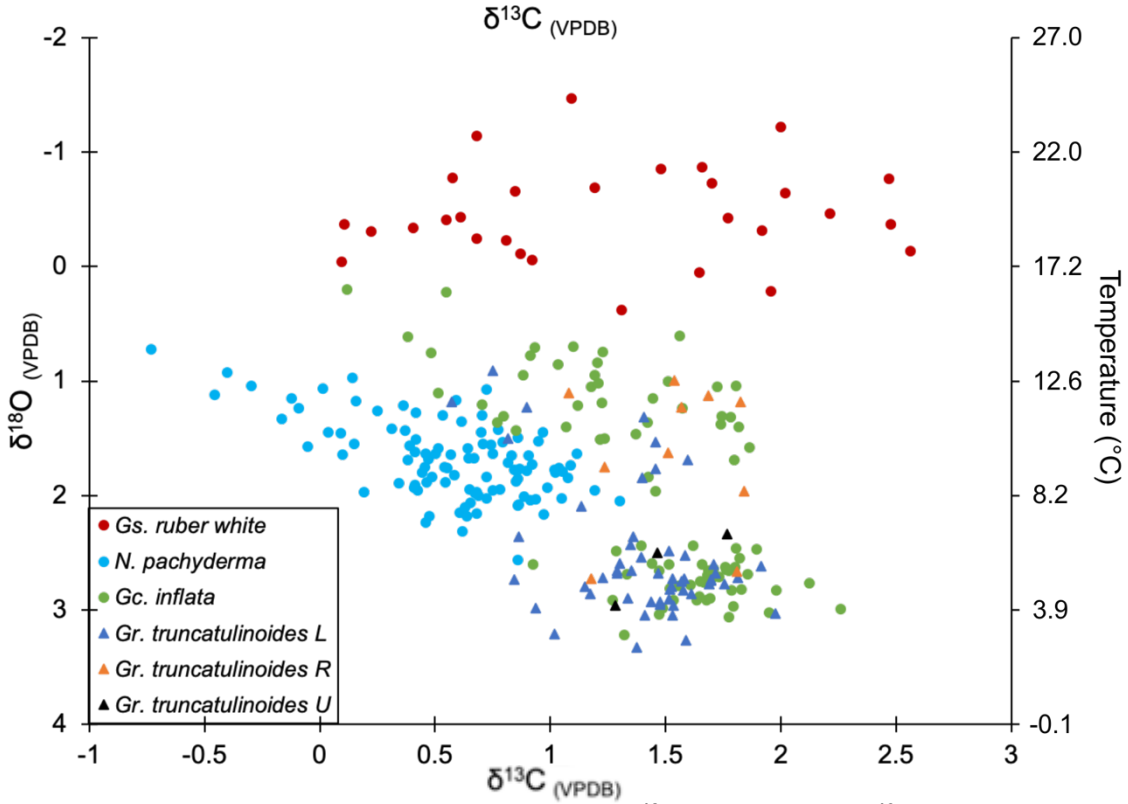

Figure 4.3-12 Stable oxygen and carbon isotope ($\delta^{18}O_{(VPDB)}$ (‰) and $\delta^{13}C_{(VPDB)}$ (‰)) cross-plot of the four species investigated. *Gs. ruber* white (red dots), *N. pachyderma* (light blue dots), *Gc. inflata* (green dots), *Gr. truncatulinoides* Right coiling (orange triangles), *Gr. truncatulinoides* Left coiling (blue triangles) and *Gr. truncatulinoides* Unclassified (black triangles). Measurement uncertainty based on standard repeatability is generally better than 0.05‰ (1 S.D) for $\delta^{13}C$ and 0.1‰ (1 S.D) for $\delta^{18}O$.

The geochemical records obtained provide insight into the aforementioned water column properties, $\delta^{18}O$ values have been converted into temperature values for ease of comparison using the palaeotemperature conversion equation of Kim and O'Neil (1997) (Figure 4.3-12). Plotted together we see *Gs. ruber* (white) consistently plots with values lower than 0.5 ‰ $\delta^{18}O_{(VPDB)}$, which, when converted to temperature, equates to values between 17-25 °C, these values are the highest recorded of any of the species studied. *Gs. ruber* (white) records a range of $\delta^{13}C_{(VPDB)}$ values (~0 - 2.5 ‰), but still form a distinct cluster due to the $\delta^{18}O_{(VPDB)}$ separation from other taxa. *N. pachyderma*, a shallow water, high latitude species, has values that chiefly plot between 7-14 °C (1.0-2.2 ‰ $\delta^{18}O_{(VPDB)}$) and record some of the lowest carbon isotope values, forming a cluster that is distinct from the deeper species it plots proximal to.

Gc. inflata, the most abundant species on the margin, shows a range of carbon and oxygen values. This species forms two clusters, largely separated in terms of $\delta^{18}O_{(VPDB)}$ values, the first cluster plots with lower oxygen isotope values (Group I) (~0.0-2.0 ‰ $\delta^{18}O_{(VPDB)}$ or ~8-16 °C) and the second provides oxygen values typically between 2.5-3.0 ‰ $\delta^{18}O_{(VPDB)}$ (~3-7 °C) (Group II). This separation has been reported across the BMC in previous studies utilising multiple specimen samples (Chiessi et al., 2007; Morard et al., 2016). Reported carbon values see little offset with the warmer Group I, displaying a wider range of values (~0.25-2.0 ‰ $\delta^{13}C_{(VPDB)}$) compared to the colder Group II (~1.0-2.25 ‰ $\delta^{13}C_{(VPDB)}$). These two clusters are labelled on the provided figure (Figure 4.3-13)

The final species for which isotope records were compiled was *Gr. truncatulinoides*, this species has been shown to have two coiling types which can occupy different portions of the water column (Ujiié et al., 2010), as such these were run with the coiling direction noted. *Gr. truncatulinoides* (right coiling) were less numerous within samples for analysis, only being present at eight sites, but where present, this group produces values similar to those of the first *Gc. inflata* group. The lower $\delta^{18}O$ values suggest calcification at a warmer, shallower dwelling depth than the left coiling morphotype. The more numerous *Gr. truncatulinoides* (left coiling) is present in both *Gc. inflata* Groups I and II, although the majority can be found in the colder second group. The *Gr. truncatulinoides* (left coiling) has some of the highest $\delta^{18}O$ values, in line with cooler waters at depth. The unclassified *Gr. truncatulinoides* were run early on in

the project and coiling direction was not noted, based on the isotope values returned, and values aligning with the second group. It is likely these specimens were left coiling variants, due to the predominance of left coiling forms in comparison to right coiling forms.

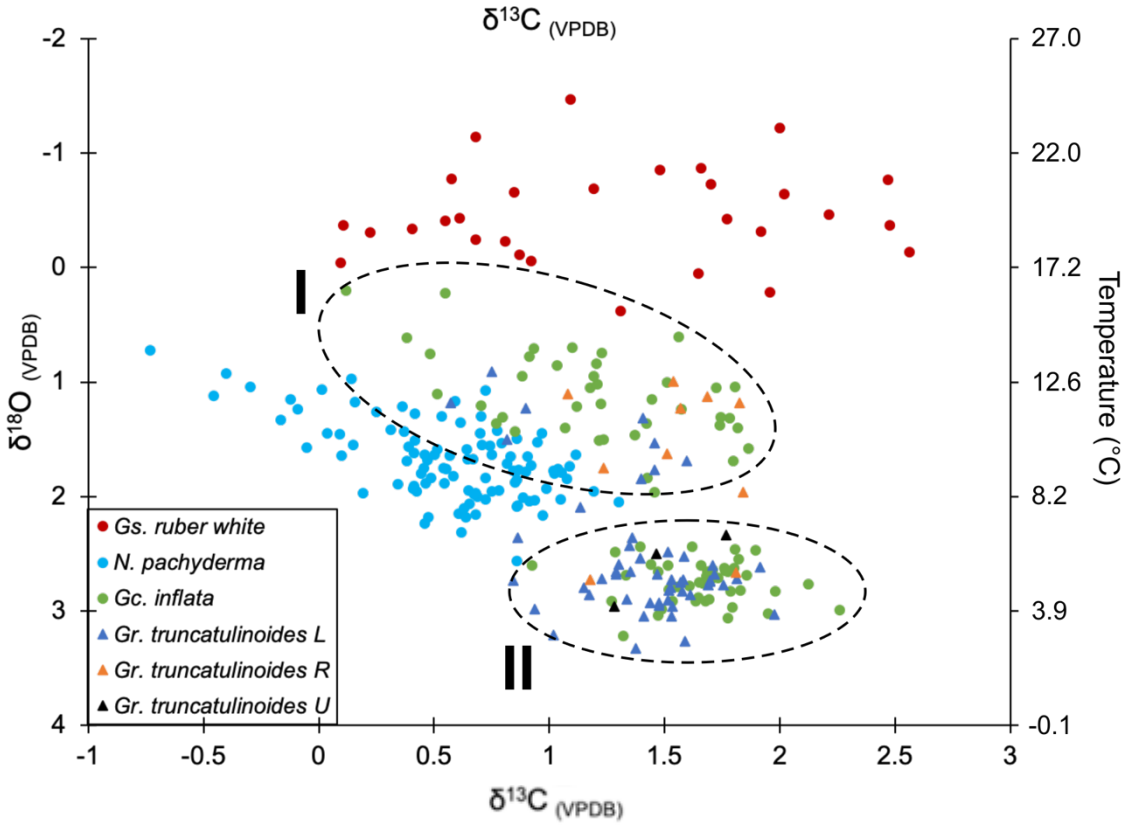

Figure 4.3-13 *Gc. inflata* isotope groupings are encircled and labelled, Grouping I is comprised of individuals with $\delta^{18}O_{(VPDB)}$ values <2 ‰ and typically lower, <2 ‰, $\delta^{13}C_{(VPDB)}$ values. Group II displays cooler values, isolated with higher $\delta^{18}O_{(VPDB)}$ values than the other grouping, typically these are >2 ‰ $\delta^{18}O_{(VPDB)}$.

Inter- and intra-species isotopic heterogeneity is present across the margin with *Gc. inflata* and *Gs. ruber white* showing the largest variation of $\delta^{13}C$ and $\delta^{18}O$ values. All of the sampled sites are found within a single degree of latitude, showing the potential for hydrological heterogeneity at the given sites. Placing the sites in transect order does not show a consistent increase in temperature values in the surface dwellers (*Gs. ruber white* and *N. pachyderma*) or the deeper dwellers (*Gc. inflata* and *Gr. truncatulinoides*), instead species display consistent values across the margin (Figure 4.3-14). There is a higher propensity for *Gs. ruber white* individuals in the northeast, reflected in the higher number of available samples, although reported values are similar.

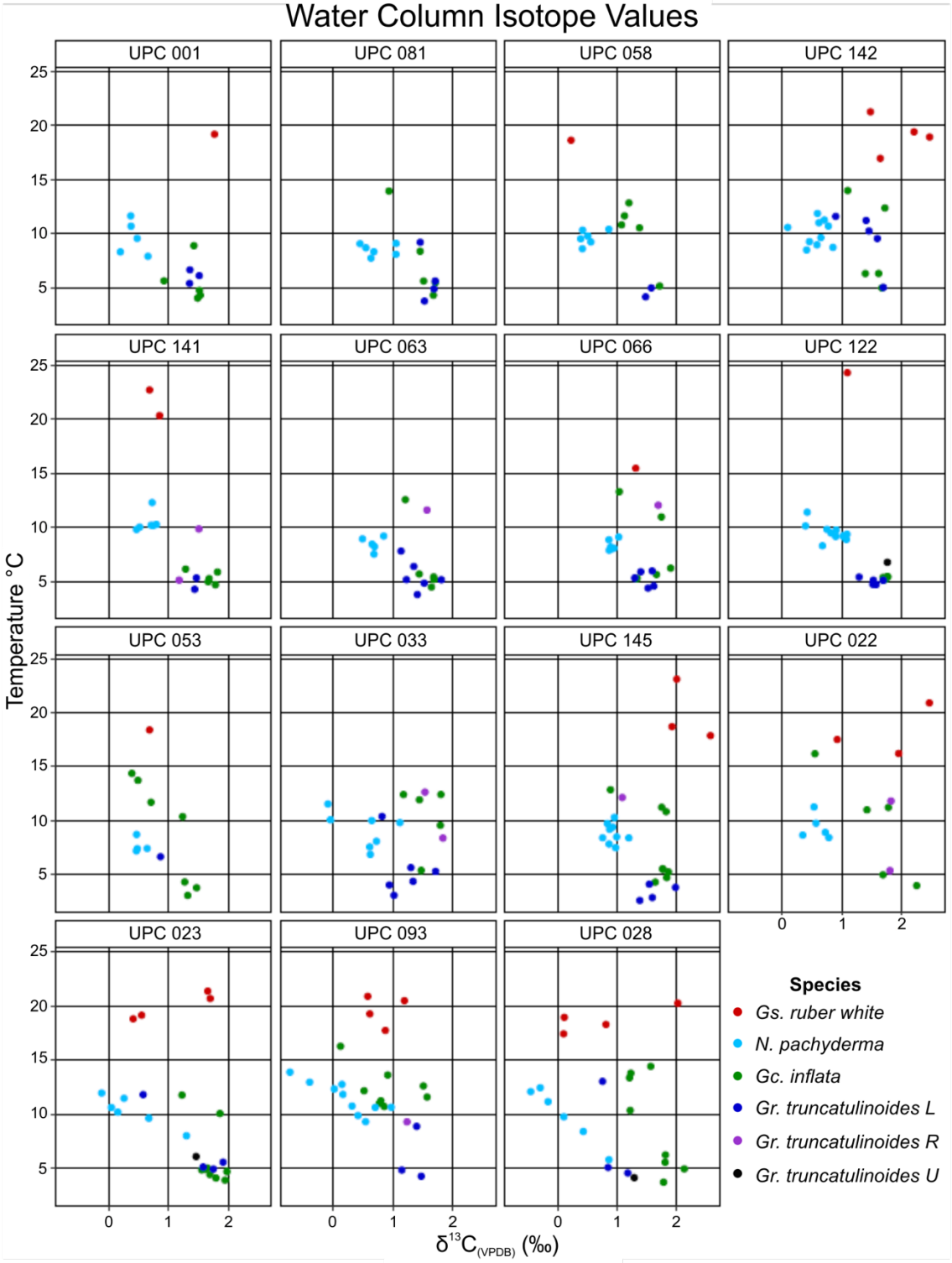

Figure 4.3-14 Geochemical values replotted with $\delta^{18}O$ values converted to temperature (°C) and plotted on a roughly SW-NE transect from top left to bottom right. Temperature shows little variation between sites across the margin with persistent separation of *Gs. ruber (white)* from the other species. *N. pachyderma, Gr. truncatulinoides R* and approximately half the *Gc. inflata* plot between seven- and fourteen-degrees Celsius. The remaining *Gc. inflata* and *Gr. truncatulinoides L* plot cluster around five-degrees Celsius. Splitting of *Gc. inflata* is likely a reflection of two distinct groupings. Position on the margin transect does not appear to influence likelihood of colder *Gc. inflata* or *Gr. truncatulinoides* L values. North-eastern sites show a slightly higher propensity for *Gs. ruber white*, potentially reflecting greater BC involvement.

Temperature depth profiles are overlain with foraminiferal derived temperatures and assigned literature reported depth ranges in Figure 4.3-15 (Anand et al., 2003; Ujiié et al., 2010; Rebotim et al., 2017; Rebotim et al., 2019), resulting in estimated depth habitats for the four species. Three of the species (*Gs. ruber white, Gc. inflata and Gr. truncatulinoides*) show good agreement for at least part of the possible depths and derived temperatures, with *N. pachyderma* the only species not to fit to any of the surrounding CTD stations. All four species record temperatures that skew colder than the CTD stations implying *N. pachyderma* poor fit is not species limited, but more pronounced than in the other species.

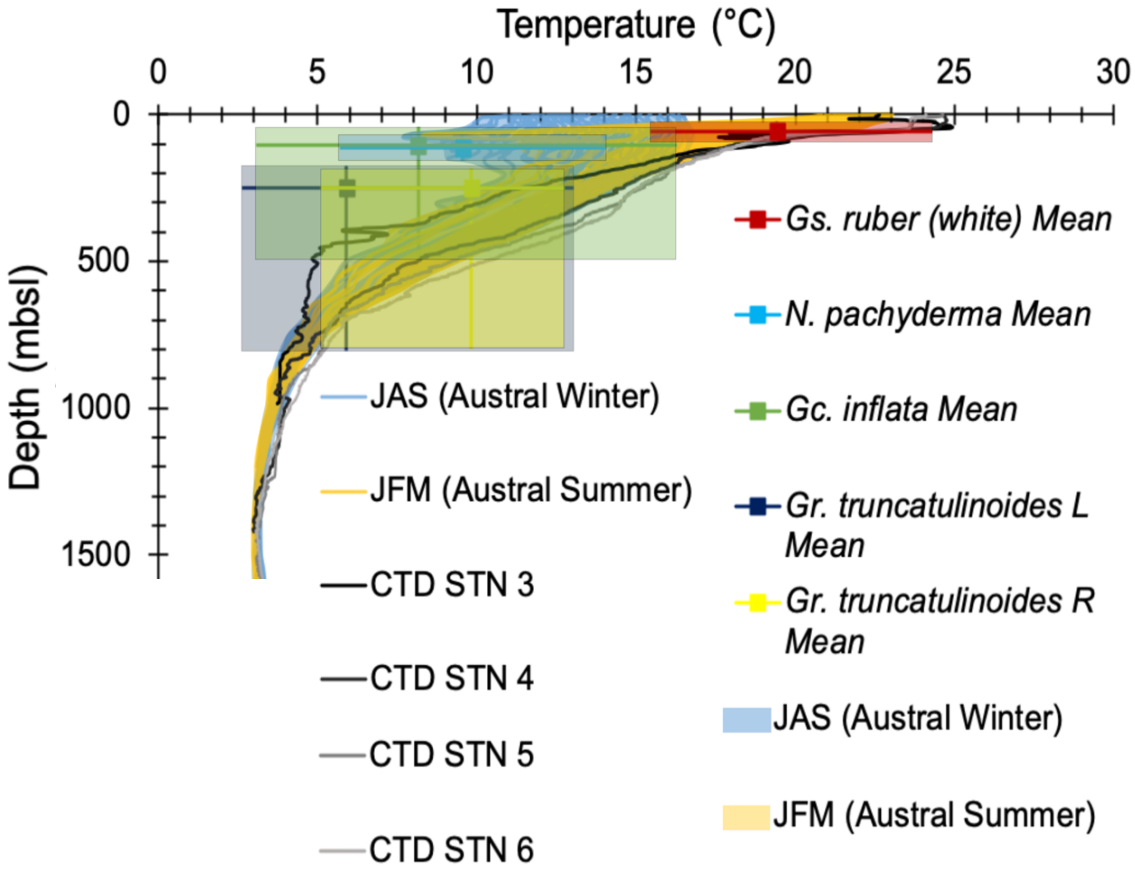

Figure 4.3-15 Four CTD sections with proximal foraminiferal isotope data for four recorded species overlain. Horizontal ranges comprise temperatures recorded by species foraminiferal calcite converted to temperature using Kim and O'Neil (1997) palaeotemperature conversion. Vertical ranges are based on published living depths of foraminifera, over which calcification occurs and within recorded temperatures are likely in equilibrium to surroundings. A series of CTD casts are available and proximal to isotope sites, see Figure 4.3-8 for locations, CTD profiles collected in austral summer (March 2009) (King et al., 2010). WOA18 data of interpolated stations is provided to estimate winter temperatures with good agreement between summer temperatures and measured CTD profiles (Locarnini et al., 2019; Schlitzer and Mieruch-Schnülle, 2021).

4.3.5 Particle Transport

In order to address the impact of planktonic foraminifera geographic ranges and post mortem transport on their contribution to sediments across this margin particle sinking models were used to predict settling trajectories (modelling performed by Anne Kruijt). (Figure 4.3-16). The model utilised an Ocean General Circulation Model (OGCM) with a horizontal resolution of ~0.1 ° across 54 depth layers between 75 °S to 75 °N, based on a hindcast simulation of twentieth century atmosphere data (Kruijt, 2019). This output was in the form of an OGCM for the Earth Simulator, utilised to map the impact of eddies within the energetic BMC region. A horizontal resolution of ~0.1 ° was used as this was deemed to accurately predict the location of the fronts and shedding of eddies Kruijt, 2019

Parcels software in Python was utilised to track particles along settling trajectories. Particles were released over ten model years, with particles released every third day, particles then have their location and surrounding conditions logged every model day. This resulted in over a thousand released particles, with roughly 50 measurements per particle. The particles were released from a central site within the core sampling area (36.5 °S, 52.5 °W), which was taken to be broadly representative of the study area. The details of this modelling methodology are in the methods chapter.

Pathways for planktonic foraminifera settling predominantly remained proximal, within several degrees latitude of the sites, or followed the Brazilian coastline to the site. The SST values typically showed a ~0.7 °C offset in the reported ranges between local properties and potential origin locations (12.5-25 °C). Results relating to distances transported showed the average particle would travel approximately 1053 km, with most of this distance covered during the foraminifer's life prior to sinking. Whilst there is potential for greater transport distances of planktonic foraminifera, to distances of 3000 km, the vast majority of these model simulations had foraminifera being entrained in eddies that retain the water mass properties of their source within the BMC, proximal to the sampling region. This is seen in the direct travel distances reported, with most particles travelling between 200-600 km, with an average straight-line distance of ~408 km. The chief direction of travel was north to south with foraminifera transport driven by the BC, before entrainment and deposition within the study region (Figure 4.3-16).

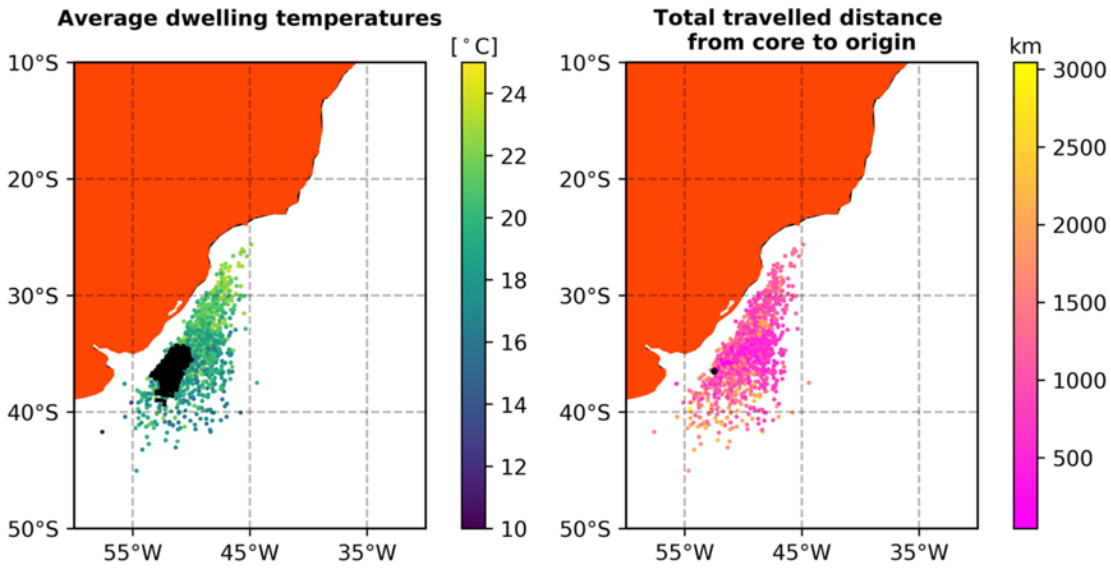

Figure 4.3-16 Plots from Kruijt (2019) the left-hand plot shows the range of average surface temperatures experienced by particles at their origin locations. Black dots signify location from which the particle sinks to the seafloor. The right-hand plot shows the distance travelled from origin location to the black dot on the sea floor. Distances are mostly below 500 km, however higher distances can be observed proximal to the particle release site (black dot), suggesting entrainment and circulation in eddies within the BMC.

4.4 Discussion

4.4.1 CTD data

The available CTD data for the region is sparse, only providing a snapshot of water column properties at a given point in time. The data was collected in early March 2009, which is late Austral summer (King et al., 2010). As such, water column properties are likely closer to the warmest annual temperatures recorded on the margin. The site was not revisited after the coring cruise and as such there is no additional CTD data to assess seasonal trends from the margin throughout the year. The CTD data collected shows sites in shallower water and nearer shore experience cooler waters. At STN2, and to a lesser extent STN3, there is evidence for limited MC involvement above 1500 mbsl, with cooler Temperature-Salinity values plotting and corresponding well with modelled data for the South American Margin (Combes and Matano, 2014; Piola and Matano, 2019). Additionally, the Temperature-Salinity data display a drop in salinities at these two stations (Figure 4.3-9), that is likely the diminishing offshore riverine input of the La Plata River mixing with TW, which would be warmer than the Patagonian shelf waters present during Austral Winter (Piola et al., 2008; Guerrero et al., 2014; Matano et al., 2014). By STN4, values indicative of the BC are recorded with influence of MC and potential riverine input being greatly diminished. This warmer pattern continues further offshore, where the core of the BC flows south to collide with the MC.

Additional CTD data for early spring would enable determination of whether the MC current has a significant presence in cooler months and whether cooler Patagonian shelf waters are observed when La Plata discharge is deflected northward. Nevertheless, the CTD data indicates a number of water masses are present within the region with MC likely more prevalent nearshore, and as depth increases further offshore the TW and SACW of the BC dominate. Additionally, the CTD data also picks up the deeper, cooler, water masses of the AAIW (below 500 m), NADW (below 2500 m) and AABW (below 2900 m). Planktonic foraminifera are not typically known to dwell deep enough that they would inhabit NADW and AABW in this locality, however it is possible some deeper dwelling species may be found at the periphery of the AAIW based on published literature (Schiebel and Hemleben, 2017; Rebotim et al., 2017). As such we would expect to see the MC, the TW and SACW of the BC, and, potentially, AAIW water

masses. These water masses provide a range of temperatures (5-16 °C) for the MC, a wider range (5-20 °C for SACW, 20-25 °C for TW) for the combined BC and a cold but tight range (2-6 °C) for AAIW influencing our assemblages across the site.

In the absence of additional CTD data, it is possible to obtain estimates for water column properties using the Ocean Data Viewer (ODV) software and the World Ocean Atlas 2018 data (WOA18) (Locarnini et al., 2019; Zweng et al., 2019; Schlitzer and Mieruch-Schnülle, 2021). This provides aggregated seasonal data, interpolated to standard depths for the margin, as presented in Figure 4.1-1, Figure 4.3-10, and Figure 4.3-11, see Chapter 3 for further detail on ODV data. Within this dataset we see significantly cooler surface waters (10-16 °C) bathing the margin in austral winter (Figure 4.3-10), which is likely indicative of northern migration of the BMC and a stronger winter MC influence. Comparing the CTD (Figure 4.3-9) and WOA18 (Figure 4.3-11) Temperature-Salinity plots there is notable similarity between the austral summer values, with comparable water masses represented at depth, enabling this dataset to be utilised for mapping foraminiferal temperature estimates onto water masses. The Temperature-Salinity plots for austral winter typically show fresher and cooler values, with greater involvement of MC waters during the winter months (Figure 4.3-11).

It is important to stress however that, whilst provided on a 0.25-degree station grid, the data from these ODV stations is interpolated from a range of available data from the World Ocean Database (Boyer et al., 2018; Locarnini et al., 2019; Zweng et al., 2019). The station grid resolution does provide a number of temperature depth profiles along the margin, however the seasonal data is averaged through time, as such it may not fully encapsulate the range of inter-annual variability along the margin, smoothing more extreme end-members, which may be represented in planktonic foraminiferal isotope data. Whilst the Modelled Stations (MS) of the WOA18 dataset approximate the CTD data, there is a noticeable underestimation when comparing the summer temperatures of MS to the CTD data. This is clearest in the surface waters, where a ~3 °C offset can be seen, between MS and CTD data, but shows reasonable alignment below 300 m depth. This is likely due to two reasons 1) the MS vs CTD stations are not taken in the exact same location and thus some offset is expected due to spatial variability of the margin and 2) the seasonal MS are the mean across three

months and additionally averaged over several years. CTD stations may occur on a warmer/colder day within this three-month interval on a warmer/colder year, hence some offset is expected, so although the WOA18 data is unlikely to display the full range of values it does provide an approximation in the absence of more CTD data. It is likely the winter MS would similarly be impacted were they to be compared to winter CTD sections, and thus should be similarly viewed as a guide for temperature values.

4.4.2 Relation of oceanography to assemblages

The bulk of published literature states the core of the northward flowing MC meets the BC at 38°S (Olson et al., 1988; Piola and Matano, 2008; Preu et al., 2013; Piola et al., 2013; Combes and Matano, 2014; Guerrero et al., 2014; Matano et al., 2014; Hernández-Molina et al., 2016; Paniagua et al., 2018; Piola and Matano, 2019), however, this latitude is an average and the confluence position can vary seasonally extending north of 37°S in winter (Olson et al., 1988; Garcia et al., 2004; Piola and Matano, 2019). This seasonal latitudinal variation in BMC position also varies inter-annually resulting in a significant range of temperatures bathing the study region, the WOA18 data sets suggest an average annual SST variation of ~10 °C when using interpolated data from the past 62 years (Locarnini et al., 2019).

With this in mind the diversity metrics and assemblage mapping show that the western portions of the study area, particularly the shallower north-western portions, have fewer species and have the highest numbers of polar and sub-polar species. Due to the greater flow of the BC (70-80 Sv at 36°S) versus the MC (~50-70 Sv) into the BMC, an overshoot forms offshore resulting in eddy formation and pinning of the MC nearshore by the southward flowing BC (Saraceno et al., 2005; Paniagua et al., 2018; Piola and Matano, 2019). Further to this, the MC varies in strength on a sub-annual timescale, resulting in variable penetration northwards, with some instances resulting in 1.5° latitude alteration (Piola et al., 2013; Paniagua et al., 2018). This is seen within the study region with cooler winter SSTs present in the WOA18 dataset as the BMC migrates north. Cooler favouring taxa and lower numbers of species are typical of waters sourced from polar regions (Schiebel and Hemleben, 2017), this suggests that sites located in the west of the region above 1500 mbsl are influenced by the

northernmost penetration of the MC, and seasonally associated cooler Patagonian shelf waters (Figure 4.4-1).

Contrastingly, in the eastern section of the margin, an increasing proportion of tropical and sub-tropical taxa is observed, combined with a taxa diversity increase (Figure 4.4-1). These changes in assemblage composition indicate increasing influence of the BC compared with nearshore and western portions of the margin. Increasing diversity and warmer taxa in offshore sections of the margin fits SST and Sea Surface Salinities (SSS) modelled and observed in previous studies, with the core of the BC flow detaching from the shelf at ~36°S, moving further offshore (Olson et al., 1988; Combes and Matano, 2014; Guerrero et al., 2014; Matano et al., 2014; Hernández-Molina et al., 2016; Piola and Matano, 2019). Unlike the nearshore sites the distance from shore means there is no impact from Patagonian shelf waters or the northernmost extent of the MC (Guerrero et al., 2014; Matano et al., 2014). Additionally, the offshore sites are more likely to be influenced by the BC overshoot (Figure 4.1-1, and Figure 4.4-1), resulting in a lack of cooler sourced water seasonally and inter-annually, reflected by the reduction in cooler taxa present (Saraceno et al., 2005; Paniagua et al., 2018; Piola and Matano, 2019; Locarnini et al., 2019; Schlitzer and Mieruch-Schnülle, 2021). Across all sites the transitional species assemblage proportion remains comparatively stable, and the fluctuations in other eco-groupings to the northeast and southwest suggest the study region is within the BMC mixing zone, with sites further to the northeast or southwest showing increasing contributions from the BC or MC respectively. Given the transitional nature of the mixing zone this is to be expected, with transitional species adaptable to wider temperature and nutrient conditions, and thus able to tolerate the range in conditions across the margin (Figure 4.4-1) (Lončarić et al., 2007; Schiebel and Hemleben, 2017).

The influence of these distinct water masses, the BC and the MC, can be picked out through planktonic foraminifera eco-group assemblage analysis. However, it should be noted that inter-annual variation of the BMC is likely to be smoothed out within the foraminiferal test assemblages, with the core top material sampled in this study not representing a single year. Rather the sedimentation rate for the core tops is ~0.074 cm/year, resulting in a 2 cm core top encapsulating ~27 years. As such, even though we can clearly pick out the influence of the different water masses at a very high spatial resolution, it would not be possible to determine

seasonal shifts in the BMC across this zone with any confidence. The structures suggested by the assemblage data align well with WOA 2018 SST data, showing that foraminiferal assemblages record average annual BMC positions likely over a decadal timescale, with dominance of the BC offshore and greater influence of MC faunas nearshore and to the west of the margin (Figure 4.4-1).

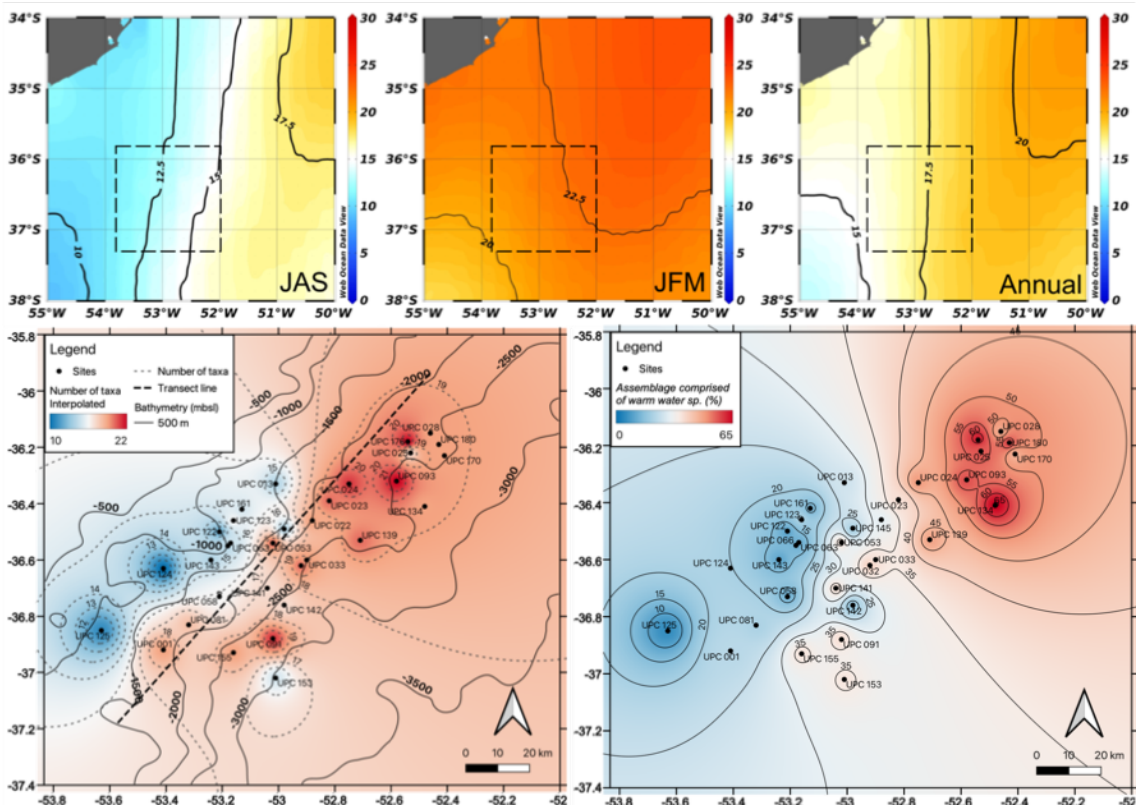

Figure 4.4-1 WOA 2018 average winter (July, August, September), average summer (January, February, March) and average annual temperature data from 1955-2017 (Locarnini et al., 2019), with study area highlighted by dashed black box. For comparison, species richness (bottom left) and warm versus cold (bottom right) plots from assemblage studies. The planktonic foraminiferal data clearly record the overlying water masses influence with colder fauna to the southwest/west and warmer fauna dominating the east/northeast. Note scales are different due to WOA interpolation constraints (Locarnini et al., 2019; Schlitzer and Mieruch-Schnülle, 2021).

The results of the assemblage profiling produced a colder signal versus the expected data from model results, as produced in conjunction with a masters student. Based on the origin locations of particle tracking, the trajectory model predicted particles (foraminiferal tests) would be transported a relatively small distance from the north, and thus within the warmer water of the BC. Analysis of the assemblages shows higher than expected abundances of *N. incompta* and *N. pachyderma*, are responsible for the colder than expected signal, with both species known to favour colder water masses (Boltovskoy et al., 1996; Kucera, 2007; Schiebel and Hemleben, 2017). Explaining the higher abundances of polar

and sub-polar species within the BMC is possible using satellite and in-situ data; these data show high seasonal chlorophyll values, with the energetic mixing of the stable BC and the nutrient rich MC, through the winter months alongside seasonal variations in temperature (Figure 4.4-2) (Brandini et al., 2000; Garcia et al., 2004; Saraceno et al., 2005; Locarnini et al., 2019).

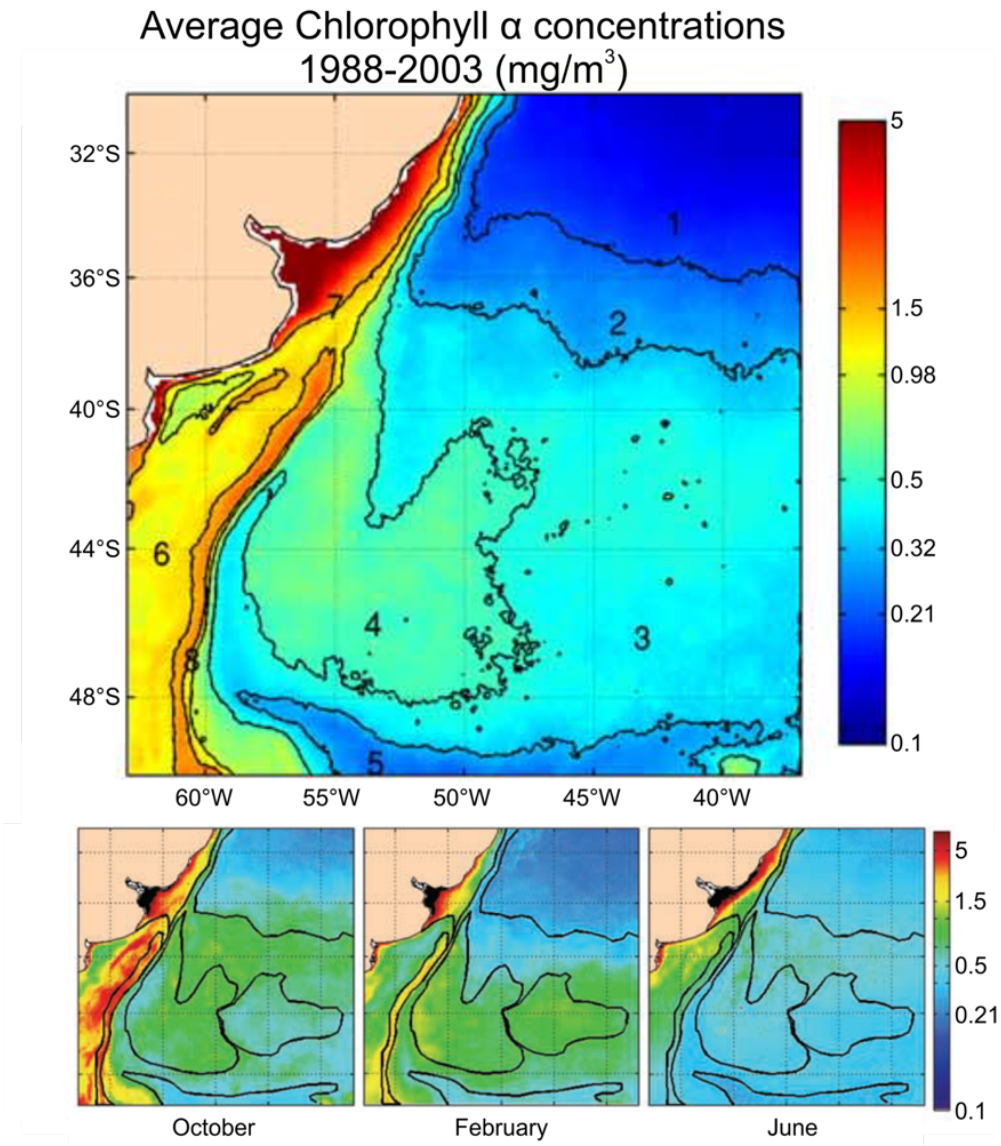

Figure 4.4-2 Average Chlorophyll α values for the western South Atlantic derived from satellite imagery. Modified from Saraceno et al., 2005. Seasonal variation is observable, with the highest concentrations in October, shortly after the peak austral winter months. Black contour lines reflect Chlorophyll groupings from Saraceno et al., 2005.

The higher nutrients and seasonally low temperatures likely aid *N. pachyderma,* and the sub-polar taxa, which have been shown to tolerate higher temperatures in nutrient rich waters i.e. Benguela Current, with specific genotypes developing to niche conditions (Darling et al., 2017; Schiebel and Hemleben, 2017). Identifying specific genotypes requires sampling genetic material of otherwise morphologically identical species and is beyond the scope of this project.

4.4.2.1 Interpretation of the South Atlantic Dataset

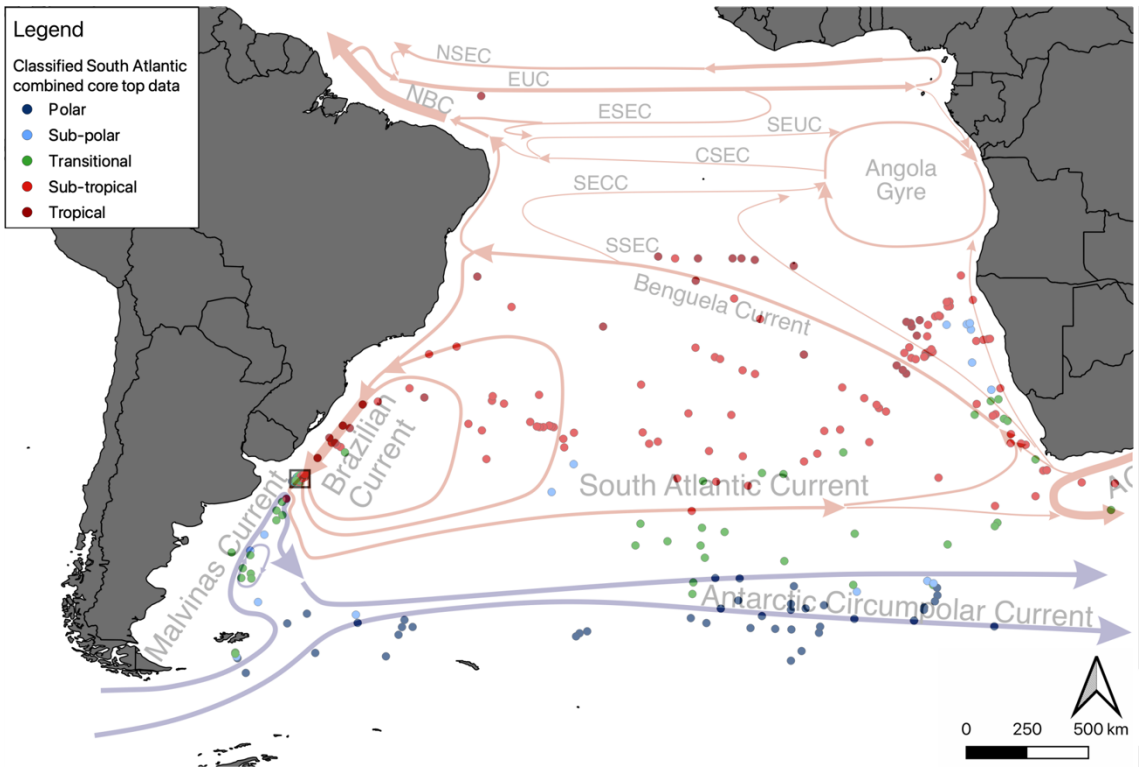

Figure 4.4-3 Macroscale ocean currents overlain on classified South Atlantic core top assemblages. Assemblage classifications record overlying oceanography well with good agreement for the majority of currents. Only areas of upwelling, in which nutrient supply becomes a greater forcing than temperature, provide anomalies on the Argentine and Namibian coastlines.

The classification system used in this study was applied to other published South Atlantic planktonic foraminiferal databases to characterise and compare a wider set of core top samples (Haddam et al., 2016; García Chapori and Laprida, 2021). Interpretation of these results, with published overlying macroscale South Atlantic oceanographic currents (Stramma and England, 1999), show good agreement between sites and expected overlying currents (Figure 4.4-3). There are regions where it is apparent temperature is not the dominant driver, i.e. sub-polar sites on the Namibian coastline. However, these counts are often borderline to other eco-groups. Additionally, these sites are likely under the influence of significant upwelling, resulting in low abundance of species not adapted to a unique, nutrient-rich system (Giraudeau, 1993; Sakko, 1998) and potential presence of differing genotypes exploiting nutrient rich environments (Darling et al., 2017; Schiebel and Hemleben, 2017). Overall agreement with the main oceanographic systems indicates planktonic foraminiferal eco-group assemblages can be utilised to reliably assess local overlying oceanography, and fit sites into a regional framework, even within oceanographically complex systems.

4.4.3 Planktonic foraminifera isotopes

Stable oxygen isotope analysis was used to align sampled species with water column depths based on the CTD profiles, and determine which species were recording which water mass properties. The inter- and intra-species variability in carbon and oxygen isotope values also provide insight into the potential effects of seasonal and inter-annual variation across the margin. As previously discussed, there is only CTD data available for Austral summer when temperatures are higher in the surface waters due to seasonal strengthening of the BC and a dominance of La Plata river discharge (Combes and Matano, 2014). This river discharge in the nearshore region mixes with strengthened BC components, TW and SACW currents, whilst cooler Patagonian Shelf waters and MC influenced surface waters are inhibited flowing north (Combes and Matano, 2014; Guerrero et al., 2014). During austral winter and early spring however, colder Patagonian shelf waters and the MC strengthen, pushing further north, influencing and cooling the study region, and this should be considered when investigating CTD and isotope data (Olson et al., 1988; Saraceno et al., 2004; Saraceno et al., 2005; Combes and Matano, 2014; Guerrero et al., 2014; Matano et al., 2014; Paniagua et al., 2018).

WOA18 data was utilised to provide additional interpolated water column temperatures for Austral summer, and importantly winter months, lacking in the CTD data (Locarnini et al., 2019; Schlitzer and Mieruch-Schnülle, 2021). Whilst not in-situ measurements, this data enables species isotope records to be compared to an approximation of seasonal water column properties, particularly useful for species that see a bulk of their test flux to the seafloor during winter. These species include *N. pachyderma*, *Gc. inflata* and *Gr. truncatulinoides* (Jonkers and Kučera, 2015; Kretschmer et al., 2018).

Core top assemblages at best represent an inter-decadal (~13.5 years/cm) record based on downcore work. The standing stock of a species can vary widely throughout the year depending on the species' optimal conditions (Kretschmer et al., 2018). Such seasonal turnover was observed in a number of studies globally (Fairbanks and Wiebe, 1980; Eguchi et al., 1999; Mohiuddin et al., 2002; Wilke et al., 2009; Jonkers et al., 2013; Jonkers and Kučera, 2015). As species are most likely to bloom and contribute to the test flux during optimal conditions within

a season, variation is most likely the result of inter-annual BMC positional variation.

4.4.3.1 Surface Dwellers

Gs. ruber white: The *Gs. ruber* white results display a wide array of stable isotope values, and are both the shallowest and warmest plotting species on the margin. Temperature values obtained via conversion from $\delta^{18}O$ align well with the available CTD data for the region, although the values also cover cooler than expected ranges. This cooler portion of the range is likely due to the inter-seasonal and inter-annual variability from years when BC currents are weaker during summer months, particularly as *Gs. ruber white* is unlikely to change depth habitat significantly (Figure 4.3-15) (Rebotim et al., 2017; Kretschmer et al., 2018). Another factor to consider might be the input of freshwater from the La Plata River. However, river discharge is unlikely to significantly impact the sites $\delta^{18}O$ values, and thus converted temperatures, with published literature showing minimal impact on modern SSS beyond the shelf (200 mbsl) (Palma et al., 2008; Matano et al., 2010; Combes and Matano, 2014). Additionally, the CTD data displays negligible RDI involvement beyond station 2 and 3 at ~700 m and ~900 m respectfully, implying a more typically open ocean $\delta^{18}O$ signature for this study's deeper sites (Figure 4.3-9). Based on the temperatures preserved (>16 °C) *Gs. ruber* white records temperature ranges of the TW (>20 °C) and the upper SACW (>10 °C) across the margin (Piola and Matano, 2019).

The *Gs. ruber white* values cover a significant part of all available summer CTD curves, and summer WOA18 interpolations, in the upper 120 m of the water column, suggesting good alignment (Figure 4.3-15). Despite this, a small proportion of the *Gs. ruber* white isotope data record temperatures <16 °C. *Gs. ruber white* taxon is known to be thermally limited (Jonkers and Kučera, 2015; Schiebel and Hemleben, 2017), and these outliers were likely expatriated leading to calcification outside of optimal thermal conditions. Evidence of *Gs. ruber white* expatriation and survival outside known ecological preferences has previously been suggested by Mojtahid et al., (2013) in palaeoclimatic records in the Bay of Biscay. Overall, the *Gs. ruber white* data supports the late summer CTD data. The test flux to the seafloor in the sub-tropics/temperate zones peaks in late summer when temperatures are highest and closest to optima for warmer favouring species, such as *Gs. ruber white* (Kretschmer et al., 2018). This would

explain differences in recorded temperatures from *N. pachyderma,* despite both being surface dwellers (Jonkers and Kučera, 2015).

N. pachyderma: *N. pachyderma* data covers a 6-14 °C temperature range and provides some of the more negative $\delta^{13}C$ values on the margin. The cooler temperatures align with published MC temperature ranges of 5-16 °C (Piola and Matano, 2019), however this also aligns with SACW values (5-20 °C (Emery, 2015; Piola and Matano, 2019)). For *N. pachyderma,* the greatest abundance of living individuals occurs when surface ocean is cooler (0-10 °C (Kretschmer et al., 2018)) leading to a higher flux of tests to the seafloor, with numbers diminishing during summer. This can cause a skewed record with a greater number of winter representatives calcifying in cold waters contributing to the shell flux (Jonkers and Kučera, 2015; Kretschmer et al., 2018). We see good alignment with winter averaged records from the WOA18, however some of the colder values do not overlap (Figure 4.3-12).

The low $\delta^{13}C$ values of *N. pachyderma* imply a nutrient rich water mass. When compared, the nearshore water masses of the MC and Patagonian shelf waters are higher in nutrients than the BC, providing suitable habitat for the asymbiotic *N. pachyderma* reliant on phytoplankton blooms (Brandini et al., 2000; Jonkers and Kučera, 2015; Paniagua et al., 2018; Piola and Matano, 2019). The $\delta^{13}C$ values, cooler $\delta^{18}O$ values and likely austral winter test flux suggest *N. pachyderma* are more likely to represent MC properties than SACW (Brandini et al., 2000; Saraceno et al., 2005; Jonkers and Kučera, 2015; Piola and Matano, 2019). In Figure 4.3-12 we see some variation in recorded *N. pachyderma* oxygen isotopic values, but clear and distinct separation from the other surface dweller, *Gs. ruber white.* This implies the two are recording separate water mass properties, representing intra-annual variation in water masses bathing each site. This and the contrasting seasonal fluxes explains the misalignment with the summer CTD records available to this study in Figure 4.3-15, however there are a number of alternative explanations to explain the colder skew.

The implications of the skew and poor fit of some of the *N. pachyderma* isotopes on temperatures recorded by the foraminiferal calcite are 1) the aforementioned result of species occupying a water mass only seasonally present over the study area, as suggested in the literature i.e. *N. pachyderma* represents MC conditions and presence seasonally 2) the species are living at significantly greater depth

than suggested in the literature 3) the tests were transported further north from where the individuals lived. This latter point would mean tests originate in cooler MC waters to the south and are transported northward, by the MC, to the margin, resulting in higher $\delta^{18}O$ values, and would have to be transported during austral winter months when BMC position migrates northward.

The most likely reason for poor fit of CTD profiles to the high $\delta^{18}O$, low temperature, *N. pachyderma* values is margin seasonality. These lower temperatures would represent peak margin cooling, during a time when intra-annual migration of the BMC northward permits greater influence of the MC (Olson et al., 1988; Piola and Matano, 2019). As the CTD casts were collected during summer months, the temperature/depth relationship in Figure 4.3-15 does not reflect the calcifying conditions of these individuals (Jonkers and Kučera, 2015; Kretschmer et al., 2018). Similarly, the winter WOA18 records are average winter interpolated profiles, utilising data from 1955-2017 to provide a seasonal record, and thus likely do not represent the full range of possible margin conditions in which *N. pachyderma* may calcify, potentially explaining the slight skew observed in Figure 4.3-15 (Boyer et al., 2018; Locarnini et al., 2019).

A significant deviation in living depth for all species is unlikely, especially as *N. pachyderma* would have to descend approximately 300 m in water depth taking it significantly below other reported values (Anand et al., 2003; Rebotim et al., 2017; Kretschmer et al., 2018; Rebotim et al., 2019). *N. pachyderma* have, in a rare case, been reported at depths down to 700 m, however the authors note it was not clear whether the foraminifera were living and feeding at depth, or were simply empty/sinking tests collected in deep sea nets in the isolated Arabian Sea (Darling et al., 2017). The mechanism by which these planktonic organisms would descend to greater depths locally is not immediately apparent either, thus, depth migration is unlikely to be the cause of the isotope-CTD temperature mismatch and will not be discussed further.

The impact of transport is assessed in more detail in section 4.4.4. However, the overall results suggest transport is predominantly from proximal origin locations, with a mean travel distance of 408 km, and limited variation in overlying water mass temperature ranges, which struggles to explain the colder skew of *N. pachyderma* temperatures. Additionally, the direction of travel is primarily north

to south resulting in warmer BC conditions likely to be expatriated in rather than colder conditions associated with *N. pachyderma* (Kruijt, 2019).

Surface dwelling summary: The differing records between two surface dwelling species indicates some aspect of regime variation within these averaged inter-annual records. With a core top expected to encapsulate foraminiferal accumulations of ~30 years, the core top will be an averaged record impacted by seasonal variations in surface water, foraminiferal species abundances and inter-decadal oceanographic change. Whilst the $\delta^{18}O$ and $\delta^{13}C$ surface-dwelling foraminifera can be assigned to specific water masses, the intra-species variation is likely a mix of this seasonality and inter-decadal oceanographic change. From the lack of $\delta^{18}O$ data overlap it appears that the two species are recording differing signals, likely the two BC components (TW and SACW) are recorded by *Gs. ruber white* and MC presence from *N. pachyderma*. These seasonal and oceanographic factors contribute to a complex heterogenous signal within a single degree of latitude in the core top isotope record, but imply BMC migration within the surface waters of the region. Further analysis of intra- and inter-annual CTD data, alongside sediment trap data, would be required to disentangle seasonality from longer-term BMC migration within this setting. Expatriation of foraminiferal tests, and thus the isotopic values, is another factor that will be analysed in section 4.4.4 Transport.

4.4.3.2 Deep Dwellers

Gc. inflata and *Gr. truncatulinoides* are the two species analysed to reconstruct the thermocline and sub-thermocline conditions respectively. All data points originate from single foraminifer tests, with the aim being: 1) to record the full range of stable isotope values that are otherwise lost by averaging over multiple specimens per data point (Chiessi et al., 2007; Morard et al., 2016). 2) Observe whether the individual sites enabled spatial variation of the $\delta^{18}O$ to be visible along the margin within a single degree of latitude (Chiessi et al., 2007).

Gc. inflata: *Gc. inflata* is a known deep dwelling herbivorous species that exhibits opportunistic behaviour within changeable conditions, such as oceanographic fronts (Schiebel and Hemleben, 2017). In particular *Gc. inflata* has been shown to avoid oligotrophic conditions, favouring mesotrophic environments (Eguchi et al., 1999; Lončarić et al., 2006; Storz et al., 2009; Schiebel and Hemleben, 2017; Portilho-Ramos et al., 2019). Additionally, *Gc inflata* is known to live at different

water depths throughout the year in search of nutrient rich waters, following the chlorophyll maxima, which in turn is related to temperature and turbidity (Lončarić et al., 2007; Storz et al., 2009; Retailleau et al., 2011). Similar to *N. pachyderma*, sediment flux studies have suggested peak annual test flux to the seafloor for *Gc. inflata* occurs in winter/spring, potentially creating a seasonal signal in the properties recorded (Lončarić et al., 2006; Jonkers and Kučera, 2015).

Gc. inflata $\delta^{18}O_{(VPDB)}$ measurements have previously reported 2.5 ‰ ranges across the BMC, from offshore transects of the South Atlantic margin, with a switch to higher $\delta^{18}O_{(VPDB)}$ values south of 37 °S (Chiessi et al., 2007; Voigt et al., 2015; Morard et al., 2016). This shift in $\delta^{18}O_{(VPDB)}$ values has been suggested as a useful tracer for the BMC and a mechanism to derive whether a site is influenced by BC or MC currents (Chiessi et al., 2007; Voigt et al., 2015; Morard et al., 2016). *Gc. inflata* values from this study display a 3 ‰ range in $\delta^{18}O_{(VPDB)}$, with a slightly higher proportion plotting in a cluster >2.5 ‰ $\delta^{18}O_{(VPDB)}$ and a slightly smaller cluster found <2.0 ‰ $\delta^{18}O_{(VPDB)}$ (Figure 4.3-13). The smaller range of the aforementioned studies is likely due to averaging isotope measurements over ten individuals resulting in homogenisation, instead of the individual specimen analysis we performed.

The <2 ‰ $\delta^{18}O_{(VPDB)}$ values (Group I) equate to a temperature range of ~8-16 °C, whilst the >2.5 ‰ $\delta^{18}O_{(VPDB)}$ (Group II) convert to ~3-6.5 °C. The warmer group accounts for roughly 44 % of measurements and aligns with both MC (5-16 °C) and SACW (5-20 °C) temperature ranges. This makes determining the water mass for Group I difficult, however a wider scatter of $\delta^{13}C_{(VPDB)}$ (~0-2 ‰) suggests this grouping predominantly relates to nutrient depleted SACW (Figure 4.3-13). This aligns well with the literature, which reports lower $\delta^{18}O$ values, and a wider range of $\delta^{13}C$ values to the north of the confluence (Chiessi et al., 2007; Morard et al., 2016). Within the BMC the BC and MC, with their contrasting nutrient profiles and temperature gradients, mix on the mesoscale, inter-weaving with one another and producing large phytoplankton blooms (Brandini et al., 2000; Saraceno et al., 2005; Piola and Matano, 2019). The potential for change in the chlorophyll maxima, in addition to the inter-weaving nature of the MC and BC currents, is likely the reason for the spread of isotope values within Group I (Brandini et al., 2000; Saraceno et al., 2005; Combes and Matano, 2014; Paniagua et al., 2018; Piola and Matano, 2019).

Group II (>2.3 ‰ $\delta^{18}O_{(VPDB)}$) cluster temperature values fall within the lower extremes of MC and SACW, along with the AAIW range (2-6 °C). CTD profiles do feature AAIW water mass properties nearshore (~>400 m), at STN2 and STN3, within the depth range of *Gc. inflata* during the summer months, making this a possibility. *Gc. inflata* has been shown to alter its dwelling depth depending on food availability to maintain more mesotrophic conditions, and thus could lead to an array of recorded temperatures depending on the season and extent of BMC mixing, including the colder AAIW temperatures (Retailleau et al., 2011; Retailleau et al., 2012; Schiebel and Hemleben, 2017). The lower, larger cluster (Group II on Figure 4.3-13) values are likely representative of deeper, colder conditions with elevated nutrients, aligning well with other $\delta^{18}O$ records from the Argentine margin (Chiessi et al., 2007; Morard et al., 2016). Combined with the slightly elevated, and less variable (~1.0-2.0 ‰ $\delta^{13}C_{(VPDB)}$), $\delta^{13}C$ data suggests nutrient rich MC/AAIW water mass properties are captured, over SACW values. Additionally, *Gc. inflata* test fluxes are typically higher in the winter months, timing with BMC northward migration (Olson et al., 1988; Piola and Matano, 2019). The tests are likely recording annual cooler water mass properties, with variation depending on inter-annual variability of BMC location (Saraceno et al., 2005; Lončarić et al., 2006; Jonkers and Kučera, 2015; Voigt et al., 2015).

Single specimen isotope analysis from each site enables a latitudinal comparison of the two *Gc. inflata* groupings (Figure 4.4-4). It would be reasonable to expect the colder Group II representatives and their MC preference, like the assemblage data, to show a greater preference for the SW. However, whilst a slight preference may be visible between the two groups latitudinally, this does not appear to be consistent implying both SACW and MC/AAIW water masses are present. Further single specimen sampling is required to fully assess this; however, this was not possible given the constraints placed on this study.

Gr. truncatulinoides: Often cited as a deep dwelling sub-thermocline species, *Gr. truncatulinoides* specimens have been found living down to 2000 m water depth (Darling and Wade, 2008; Schiebel and Hemleben, 2017). However, the depth of calcification is debated within the literature, with some authors arguing calcification in equilibrium ceases below 500 m (Wilke et al., 2009; Birch et al., 2013; Rebotim et al., 2017; Reynolds et al., 2018; Rebotim et al., 2019), and that secondary calcification may occur down to 800 m depth (Ujiié et al., 2010). This

range in potential dwelling depths is significant, however temperature variation over the sub-thermocline is minimal (~4 °C). For the purposes of this study, to avoid overinterpretation but encompass potential secondary calcification, the depth range was limited to 800 m, placing *Gr. truncatulinoides* at the lower thermocline/upper sub-thermocline (Figure 4.3-15).

Additionally, *Gr. truncatulinoides* has a number of genotypes, covering differing biogeographical ranges, that manifest differing coiling directions (Darling and Wade, 2008; Ujiié et al., 2010; Ujiié and Asami, 2014). The boundary between two of these biogeographic ranges is proximal to the study region with Type III, a dominantly left coiling morphotype, in the southern cooler waters and a mixed assemblage of Type III, the predominantly right coiling Type II and left coiling Type I in the warmer northern waters (Darling and Wade, 2008; Ujiié et al., 2010; Ujiié and Asami, 2014). Coiling direction is argued to be a genetically controlled phenomena rather than the direct influence of temperature (Ujiié and Asami, 2014). However, the literature suggests a lack of wider gene flow throughout the world's oceans between populations is tied to oceanographic circulation inhibiting mixing of populations, thus indirectly linking to temperature and salinity parameters, with the ability of water masses to mix (Ujiié and Asami, 2014). Within our study region this enables coiling direction to be indicative of regional influence, with right coiling morphs implicating influence of warmer, sub-tropical masses on the margin (Ujiié and Asami, 2014). Through separation of the coiling morphotypes and knowledge of the genotypes present within the varying nutrient contents and thermally contrasting South Atlantic water masses, isotopic variation within the species can be accounted for based on oceanographic changes. As such, we would expect the presence of right coiling variant of *Gr. truncatulinoides* to be specifically linked to the sub-tropically sourced BC, likely in the form of the SACW, whilst the left coiling form could be indicative of either the BC or MC based on current knowledge of morpho-group spatial distributions (Ujiié et al., 2010; Ujiié and Asami, 2014).

The two variants of *Gr. truncatulinoides* have been observed in living plankton tows and react differently in terms of seasonality. The right coiling forms are restricted to winter months, whereas the sinistral form is predominantly found to calcify during winter months, but has been observed during summer months too (Lončarić et al., 2006). Right coiling *Gr. truncatulinoides* were considerably less

common for isotope analysis in the core top studies, with warmer values suggesting expatriation of tests, or rare periods of winter BC dominance (Renaud and Schmidt, 2003; Darling and Wade, 2008; Ujiié et al., 2010; Ujiié and Asami, 2014). Variation in the left coiling form could be accounted for by expatriation of tests out of a warmer climate, or seasonal site variation based on BC dominance during the summer months versus winter MC dominance, when test flux to the seafloor is high (Jonkers and Kučera, 2015).

Gr. truncatulinoides results produced ~2.5 ‰ variation in $\delta^{18}O$ and ~1.5 ‰ $\delta^{13}C$ values across the margin when combining both coiling variants. The isotope values split into two clusters, the first is comprised of both left and right coiling variants with $\delta^{18}O_{(VPDB)}$ values <2 ‰, aligning with the Group I values of *Gc. inflata*. Additionally, the converted temperature values reported fall between ~8-12.5 °C, but maintain the ~1.5 ‰ $\delta^{13}C$ spread (Figure 4.3-13). Occurrence of the left coiling variants in this group may reflect a minority of summer calcifying individuals, during a time in which SACW is likely to bath the margin, whilst the right coiling individuals may represent winter calcifying individuals, from either a winter SACW presence or expatriation from further north. An alternative suggestion involves shifts in dwelling depth within the species to find suitable conditions, over an annual cycle (Rebotim et al., 2017). However, this has been linked to seasonal temperature change, with *Gr. truncatulinoides* shoaling during winter months, and thus this seems an unlikely explanation for the $\delta^{18}O$ offset if the species is seeking to maintain temperature. As such the Group I represents either intra-annual presence of both SACW and MC waters, during winter months due to BMC migration, or more likely a purely sub-tropical SACW grouping, with some minor examples of expatriation.

The bulk of the *Gr. truncatulinoides* data, and majority of the left coiling variant values are >2‰ $\delta^{18}O_{(VPDB)}$, aligning with MC/AAIW *Gc. inflata* temperatures in Group II. Given the species deep dwelling depths and upper boundary depth of AAIW, this aligns well. The $\delta^{13}C$ results are more tightly constrained in this grouping, largely falling within a ~0.75 ‰ range that is higher than that of Group I (Figure 4.3-13). This implies a more nutrient rich baseline and provides further credence to MC/AAIW influence. Additionally, Group II comprises of a greater number of individuals, reporting colder, more nutrient rich values, aligning with the greater winter test flux reported in the literature (Jonkers and Kučera, 2015).

The $\delta^{18}O_{(VPDB)}$ and $\delta^{13}C_{(VPDB)}$ values additionally align with modern latitudinal *Gr. truncatulinoides* from south of the BMC, in MC waters (Chiessi et al., 2007; Morard et al., 2016), alongside the left coiling dominance in sub-polar waters repeated here (Ujiié et al., 2010; Ujiié and Asami, 2014).

One aspect that may impact all *Gr. truncatulinoides* values is secondary encrustation, with studies reporting a secondary phase of calcification at greater depths, leading to higher $\delta^{18}O$ values recorded (Rebotim et al., 2019). This calcification appears to still be in line with $\delta^{18}O$ temperature equilibrium equations, but may mean recorded temperatures are slightly deeper than observed dwelling depths (Rebotim et al., 2019). This study attempted to avoid where possible overly encrusted tests through visual inspection, but is unable to definitively investigate this potential encrustation phenomenon further, without appropriate tools to analyse specific portions of individual tests i.e. using Secondary Ion Mass Spectrometry (Schiebel and Hemleben, 2017; Wycech et al., 2018). Investigation of encrustation and $\delta^{18}O$ values on the other deep dwelling species, *Gc. inflata*, can be found in Chapter 6, with the likelihood of impact discussed further.

There is also the possibility the colder Group II values may be the result of expatriation and transport of tests north from colder MC waters to the south. This too seems unlikely given the prevailing strengths of currents involved in the BMC, with the BC principally being the stronger, the large number of colder individuals recovered, and modelling of transport implying a predominant transport direction of NE to SW (Figure 4.3-16) (Piola and Matano, 2019; Kruijt, 2019). Should this process be occurring, it would likely be a minor component of this grouping.

Assessing the latitudinal variation of *Gr. truncatulinoides* the colder Group II again supports MC/AAIW influence at all sites. Perhaps more so than the *Gc. inflata* groupings, additional sampling is required to assess the spatial variability, with a number of sites lacking data points. Further sampling might enable a better assessment of the relative importance of each water mass latitudinally.

<u>*Deep dwelling summary:*</u> The two groups within the two species, *Gc. inflata* and *Gr. truncatulinoides,* are able to be disentangled from one another within isotopic space (Figure 4.3-13). Typically, this involves separation around 2 ‰ $\delta^{18}O$, with values <2 ‰ $\delta^{18}O$ indicative of the warmer BC and those >2 ‰ $\delta^{18}O$ aligning with more MC conditions. This further fits with the >2 ‰ $\delta^{18}O$ groupings having tighter,

and higher, $\delta^{13}C$ values, indicating more nutrient rich waters than the more variable <2 ‰ $\delta^{18}O$ groupings for each species. The presence of these two groupings within both deep dwelling species implies two water masses are interacting above the sites, at least inter-annually if not intra-annually. Single specimen analysis of both species does not show a clear latitudinal preference for groupings i.e. *Gc. inflata* Group I favouring the NE and Group II the SW or vice versa (Figure 4.4-4), however there may be a slight preference for fewer Group I (warmer) individuals at sites to the SW. The cooler Group II specimens appear to be present at all sites regardless of latitude (Figure 4.4-4). This suggests that all sites experience conditions associated with the BC and MC within the region, albeit to varying extents. Further isotopic measurements would help corroborate this, with certain sites lacking high numbers of data points, particularly in relation to *Gr. truncatulinoides* i.e. UPC 053 and UPC 022.

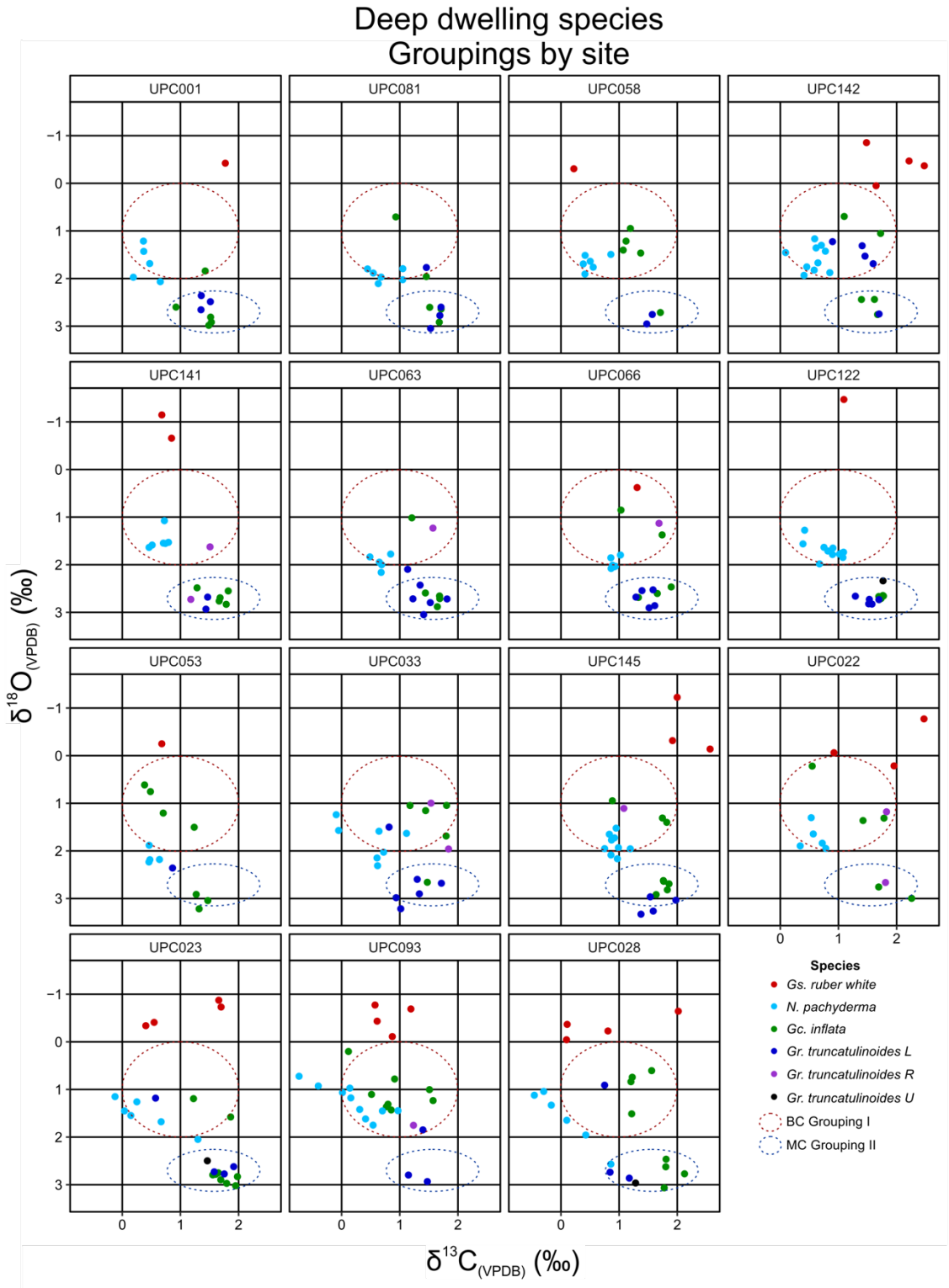

Figure 4.4-4 $\delta^{18}O_{(VPDB)}$ and $\delta^{13}C_{(VPDB)}$ isotopes plotted by site organised on the SW-NE transect displayed in Figure 4.2-1. Groupings from Figure 4.3-11 are approximated on each site's plot. There is a slight preference for Grouping I, the warmer grouping, to sites in the NE versus the SW, however both groupings are represented across the transect, implying presence of corresponding water masses on at least an inter-annual scale if not intra-annually.

4.4.4 Transport

Expatriation of foraminifera has been mentioned as a possible mechanism for anomalous isotope values. Planktonic foraminifera are free floating and as such their final resting locations on the sea floor are determined by a number of factors: 1) the speed of the water currents they inhabit during life before post-mortem transport 2) the post-mortem sinking speed of the test to the sea floor and 3) the depth to the seafloor (Schiebel and Hemleben, 2017). For a significant proportion of the world's oceans conditions are regionally similar over vast distances, and thus this potential transport effect has minimal impact on the recorded water column properties within foraminiferal tests for palaeoceanographic reconstructions. However, within oceanographically complex regions of the world's oceans i.e. confluences of currents in marginal settings, the difference in water mass properties over short distances can be significant, and transport of plankton within these regions could significantly impact the palaeoceanographic record (Van Sebille et al., 2015; Lange and Sebille, 2017; Nooteboom et al., 2019). Despite these challenges, planktonic foraminifera represent the best proxy for palaeoceanographic reconstructions, as the greater mass and sinking speeds result in a smaller footprint in terms of their origin locations, this is especially true when compared to organic walled plankton (Van Sebille et al., 2015; Schiebel and Hemleben, 2017; Nooteboom et al., 2019).

Working with colleagues at Utrecht University, the aim was to investigate the potential transport effect on the Uruguayan margin and directly compare model outcomes with the data derived from foraminiferal studies. Designing the project and building the model required input on the regional oceanographic framework (Chapter 2), the foraminiferal life cycle for species selection, and the foraminiferal assemblage and isotope data acquisition conducted in Leeds (Chapter 3). The transport model predicted warmer assemblages than the core top studies, which contained more *N. pachyderma* and *Gc. inflata* than the model predicted, suggesting there is still some room for refinement. This may be related to factors not modelled, such as elevated nutrient/food availability within the mixing region (Brandini et al., 2000; Garcia et al., 2004), which may favour transitional to polar eco-groups, both species are known to favour such conditions (Lončarić et al., 2007; Schiebel and Hemleben, 2017). Whilst warmer, sub-tropical species, such as the modelled *Gs. ruber white*, show preference for oligotrophic conditions, potentially influencing assemblage proportions and explaining model offset from

colder foraminiferal assemblages (Toledo, 2008; Pivel et al., 2013; Schiebel and Hemleben, 2017; Frozza et al., 2020).

The findings illustrated that most foraminifera originated proximal to core sites, with direct travel distances typically between 200-600 km, and on average ~408 km away. However, there was a likelihood that a minority of foraminifera would be expatriated to the study site from further afield. Some of the potential travel distances modelled are large (500-1500 km), but it should be noted these distances are often the result of eddy entrainment rather than straight line distances (Figure 4.3-14), and thus are still within the ~408 km average direct distance radius of the final resting place. In the modelling, the expatriated foraminifera most often originated from further north to the studied region (Figure 4.3-16), transported south by the BC. The ranges reported for transported particles and overlying water masses are remarkably similar, reporting an average dwelling temperature of ~19.5 °C for waters directly above the site to ~19.6 °C for particles travelling to the site (Kruijt, 2019). Indeed the temperature distributions also show minor offsets with a ~0.7 °C difference impacting the temperature range of transported particles, when compared to the temperature range of water masses overlying the core site (12.5-25 °C) (Kruijt, 2019). This suggests expatriated particles to the site show little deviation in the recorded temperature ranges, enabling confidence in the reported $\delta^{18}O$ values being indicative of overlying water mass temperature, and expatriation having only a minor effect at this site.

Comparing to previous plankton transport studies, we see slightly smaller straight line transport distances to those within the Agulhas Current, with a lower average transport distance of 408 km versus 713 km in the Agulhas Current, and 533 km for the Agulhas Leakage (Van Sebille et al., 2015). This is likely a result of the greater strength of the Agulhas Current (~84 -/+11 Sv) compared to the BC (70-80 Sv) or MC (50-70 Sv), with depths of comparative sites roughly equivalent (this study 2,578 m versus Agulhas Leakage 2,440 m, Agulhas Current 3,090 m) (Beal et al., 2015; Van Sebille et al., 2015; Piola and Matano, 2019; Kruijt, 2019). Dinoflagellate estimates for the Uruguayan margin estimate between 800-1200 km of lateral transport, with sinking speed, current strength and water depth the largest factors dictating the lateral distances (Nooteboom et al., 2019). Clearly, transport remains a factor of concern for local environmental

reconstructions however, the proposed travel distances and temperature offsets on the Uruguayan Margin are on a scale comparable to the approximately two degrees latitude annual migration of the core BMC (Olson et al., 1988; Schmid and Garzoli, 2009; Franco-Fraguas et al., 2014; Piola and Matano, 2019). This enables confidence in the ability of planktonic foraminifera to reliably record proximal water mass properties within the migrating confluence i.e. Figure 4.3-16. Expatriation of foraminifera into the study region is a clear possibility, but unlikely to significantly impact the majority of isotope measurements, or drastically alter assemblage counts, it may explain some of the more extreme outliers.

4.5 Conclusions

Do planktonic foraminiferal core top records reflect overlying oceanographic currents, displaying spatial heterogeneity between sites, or does the record provide a homogenous signal across the margin?

This chapter set out to outline and assess the variability of planktonic foraminiferal assemblages and isotope records across the Uruguayan margin, in a known oceanographically complex region. Assemblage data allows for spatial mapping of species distributions, and their reflected ecological associations, across the margin with a distinct western and shoreward cooler fauna contrasting the deep water, distal warmer dominated faunas of the east. This heterogeneity aligns with the complex overlying oceanography, with the higher propensity for cooler assemblages reflecting MC conditions, whilst those warmer sites further offshore align with BC settings. Evidence for significant variation was not entirely unexpected within the mixing zone of the BMC, but taking individual core sites in isolation would fail to delineate the complex oceanographical interactions present offshore Uruguay. This is evidenced by the diversity of assemblage classifications within the study region, resulting in significant variation across just <1° latitude and longitude (~7100 km^2). This variation suggests that in regions of known complex oceanography planktonic foraminiferal assemblages can capture overlying oceanography, but a high density of sampling is required to reasonably quantify the regional complexity within foraminiferal core top assemblages.

Variability in planktonic foraminiferal isotopes is evident across the region, and enables the separation of water masses based on the clusters presented. *Gs. ruber* white tracks the sub-tropical BC and shows clear separation from the remaining species. *N. pachyderma* is correlated to the surface waters of the sub-polar MC, with its low $\delta^{13}C$ values indicative of a nutrient rich water mass from upwelling on the Patagonian shelf (Matano and Palma, 2008; Paniagua et al., 2018; Piola and Matano, 2019). *Gc. inflata*, often the most abundant in assemblages, splits into two clusters with Group I representing the nutrient variable and warm SACW (a BC component) and Group II the nutrient enriched and cold MC/AAIW. Finally, the deepest dwelling taxa, *Gr. truncatulinoides*, similarly splits into two groupings, with a smaller Group I identifying with a warmer water mass likely to be the SACW and Group II the colder, nutrient rich MC and AAIW. The multi-core approach taken in this study provides insight into the

complexity of this region that would not be replicated by a single “representative” site for the margin, and is further evidence of the heterogeneity recorded. As such future studies in regions of known oceanographic complexity (e.g. The Benguela Current (Garzoli and Gordon, 1996), Agulhas Current (Van Sebille et al., 2015), Southern and Eastern Australian Margins (Li and McGowran, 1998; Nelson and Cooke, 2001), The Northwest Atlantic Shelf (Bé and Hamlin, 1967)) should aim to apply similar sampling strategies in order to better resolve spatial variation. This study further differentiated itself from previous South Atlantic studies by attempting, where possible, to use single specimen isotopes to identify complexity that can be lost by averaging over significant numbers of specimens (Chiessi et al., 2007; Morard et al., 2016). In doing so, intra-site variations are identified that likely reflect site inter-annual, and potentially some inter-seasonal, variation of overlying water mass properties. Inter-site variation of isotopes did not readily identify significant spatial offsets across the core-top transect, compared to the spatial variability in assemblage data classifications, where patterns reflective of overlying oceanography are more readily apparent. However, sites approaching the furthest SW of the study region seemingly displayed less influence of warmer water masses. Further isotope analyses and additional sites may aid in testing the spatial variability, with a focus on the proximal vs. distal, west vs. east, cool vs. warm trends identified in this study. Additionally, sediment trap experiments across multiple seasons and inter-annually may help better resolve seasonal and inter-annual differences between sites, but is beyond the scope of this project.

Transportation is a factor to consider with some expatriation of foraminifera likely occurring along the South Atlantic Margin, however the magnitude is modelled and shows limited impact on the extremities of water column records (Figure 4.3-16). The likelihood of test transport explaining all margin wide variability is low given the distances required to significantly warm the dataset and dominance of transport coming from the north versus the contrasting MC to the south (Figure 4.3-16). Parameter refinements within the model to include water mass nutrients, species survival capabilities outside preferential temperature ranges, potential variable dwelling depths or variable genotype ecologies within species i.e. *N. pachyderma* or *Gr. truncatulinoides* (Darling and Wade, 2008; Ujiié et al., 2010). Such parameters inclusion was beyond the scope of the project at present but may reveal greater ramifications of expatriation to assemblage data and isotopic

results. However, at present this is seen as unlikely to significantly impact the particle transport reconstructions with this setting, but may have an impact on the survival capacity of individual foraminifers and may explain the discrepancy between model results and recovered data. Transport should be more widely considered in future studies, both within the region studied here and in similarly complex ocean environments outside open ocean conditions.

4.5.1 Key take away messages

- Are proximal sites variable in the recovered assemblage and stable isotope results?

- Yes, assemblage mapping highlights the variability in planktonic foraminiferal distributions across a marginal transect, displaying additional complexities between sites accounted for by oceanographic constraints.
- Similarly, stable isotope records are variable between sites and at the same site. Inter-annual and seasonal variability of records explains correlation of CTD and isotope data and is likely the reason for the clustering of multiple taxa within the same sites.

- Is transport a significant factor influencing results and blurring signals recorded?

- No, whilst transport and expatriation of foraminifera by the BC is a possibility, transport from warmer SSTs likely results in a small (~0.7 °C) offset on the temperature ranges. This is unlikely to significantly impact isotope results but may explain some significant outliers.

- Do the recovered results reliably reflect modern oceanographic settings?

- Yes, however within complex oceanographic settings a dense sampling strategy enables reconstruction of overlying oceanographic spatial structures. Use of fewer sites as representative of a larger region is likely to introduce error in understanding local oceanographic frameworks, resulting in simplification of regional systems.

4.5.2 Limitations and further work

There are aspects to this study that require reflection and should be considered as areas for future focus. The first is the availability of material for study. Core tops from the region are a limited resource, and as such difficult to obtain in sufficient number to fully quantify the margin. Locations of the core tops were also

pre-determined given the cores were donated to the scientific community, ideally additional sites would be available further to the NE and SW, and preferably on a complete grid to aid interpolation. A number of cores were unavailable for study due to extensive sampling of previous researchers, dictating sample density. Additional assemblage counts to the SW and NE would enable a greater density of sampling, the opportunity to determine whether barren sites are a local phenomenon or more widely spread at depth and the prospect of clarifying the extremities of polar and sub-tropical faunas. Finally, to improve the assemblage counts a number of surface dates would be useful to confirm core top samples are approximately contemporaneous, but due to the limited material available for sampling this was not possible.

As mentioned within the text, additional repeat CTD profiles, particularly of the winter months, would help match the isotope data, modelled oceanography and observed satellite data to resolve potential margin seasonality. World Ocean Atlas data presents a good assessment in the absence of CTD data but averaging can leave significant offset to CTD data. The final area for additional work is the collection of more isotope data for 1) a number of additional species at all sites and 2) collection of data from additional sites to improve the spatial density of results. This was not possible due to machine time and cost constraints, but combined with further CTD data would aid in defining seasonality of foraminiferal stock associated to water masses, enabling assessment of margin wide spatial heterogeneity. It is likely the study would also benefit from seasonal sediment trap data to test the regional flux of planktonic foraminiferal tests to the margin. This would provide a greater handle on the seasonality of these fluxes and their impact on both the assemblage datasets, but more significantly the isotope datasets to better resolve reconstructions. However, such an undertaking is not without significant expense of both time and financial resources, which represent significant barriers to obtaining this data at the present time.

Chapter 5 Palaeoceanographic, palaeoenvironmental and palaeobiotic Holocene records from the Uruguayan margin.

5.1 Aim

This chapter will investigate the changing downcore signals from the Uruguayan Margin core UPC 028, examining the nature of Brazilian-Malvinas Confluence (BMC) migration and evolution over the last 10 Kyr.

The South Atlantic, and southern hemisphere broadly, remains an under-sampled region of the world's oceans, particularly when comparing available palaeoclimate archives to the number of northern hemisphere records (Masson-Delmotte et al., 2013; Haddam et al., 2016; Siccha and Kucera, 2017; Kaufman, McKay, Routson, Erb, Zhilich, et al., 2020; García Chapori and Laprida, 2021). Recent IPCC reports have highlighted the need to increase the number of available southern hemisphere data sets, to improve the spatial resolution of archives, and better develop understanding of past climates to aid predictions of future change (Masson-Delmotte et al., 2013).

The importance of this study lies in 1) generating a new southern hemisphere climate and oceanographic record, and 2) contributing to the understanding of Holocene oceanographic variation relating to the BMC, a significant ocean mixing zone in relation to thermohaline transport and South American climate (Piola and Matano, 2008; Matano et al., 2010; Piola and Matano, 2019).

The BMC is known to migrate latitude annually, responding to seasonal variation in relative strength of the two currents that make up the confluence, the Brazilian Current (BC) and Malvinas Current (MC) (Olson et al., 1988; Peterson and Stramma, 1991; Wainer et al., 2000; Hernández-Molina et al., 2016; Piola and Matano, 2019). Over longer timescales changes in climate are thought to shift the average BMC latitude, enabling current migration up and down the western South Atlantic margin (Olson et al., 1988; Wainer and Venegas, 2002; Bender et al., 2013; Razik et al., 2013; Voigt et al., 2015; Gu et al., 2018c; García Chapori and Laprida, 2021). Understanding this movement has remained a challenge, and the existing literature is marred with inconsistency observed in the direction of migration over the Holocene (Bender et al., 2013; Razik et al., 2013; Pivel et al.,

2013; Lantzsch et al., 2014; Chapori et al., 2015; Voigt et al., 2015; Gu et al., 2018c; Frozza et al., 2020; García Chapori and Laprida, 2021). This is particularly evident in determining the nature of the mid-Holocene, with some authors suggesting a warming trend for the margin (Pivel et al., 2013; Voigt et al., 2015; Gu et al., 2017; Gu et al., 2018c; Frozza et al., 2020; García Chapori and Laprida, 2021), whilst others indicate a cooling signal (Gyllencreutz et al., 2010; Bender et al., 2013; Razik et al., 2013; Lantzsch et al., 2014).

With this study we aim to improve on previous work by utilising a range of high-resolution records including: planktonic foraminiferal assemblages, planktonic foraminiferal $\delta^{18}O$ and $\delta^{13}C$ single specimen isotopes covering the water column, planktonic and benthic ratios, assemblage diversity metrics, ITRAX elemental core scans and radiocarbon dating. The high-resolution assemblage studies, building on the findings of the previous chapter, will enable eco-group classification and assessment of palaeo-oceanographic shifts. Additionally, using planktonic foraminifera single specimen isotopes for reconstructing past water column properties facilitates a deeper interrogation of BMC variability. By using single specimens we are able to improve on previous studies in observing BMC position temporal variation, in comparison to modern planktonic foraminiferal $\delta^{18}O$ and $\delta^{13}C$ values, through limitation of data loss seen in multi-specimen analyses and enable better understanding of end member signals (Chiessi et al., 2007; Morard et al., 2016). Using a multiproxy approach, we will quantify the overlying oceanographic front migration, along the western South Atlantic margin, assessing Holocene change at higher resolution and with more fidelity than previous studies.

Research questions

- What are the overall BMC migratory trends documented by site UPC 028 over the last 10 Kyr? Is latitudinal variation observed and does site UPC 028 display signs of mid-Holocene warming?
- Do single specimen stable isotopes and assemblage records suggest changes in BMC mixing over the Holocene?

5.2 Summary of Materials and Methods

5.2.1 Core location and assemblage work

The cores sampled from the margin were part of a scientific donation to UK research by ANCAP and BG group in 2014. Cores sample a maximum depth of around five meters and sample a variety of seafloor terrains on the contouritic margin. Site selection was key, requiring near continuous sedimentation to provide a complete margin record, with little evidence of recent disturbance. Visible scarps, slips and erosive terraces were avoided with drift sediments preferred. The piston core for this study, UPC 028, was taken from 2,353 mbsl at -36.15147°S latitude and -52.46271°W longitude from plastered drift sediments, primarily comprising of silts and muds, with some fine sands, organics and carbonate content. Core photos are provided within Appendix H.1.The core location is displayed in Figure 5.2-1 alongside additional sites utilised for regional palaeoclimate comparisons. A total retrieved length of 489 cm, with 424 cm of sediments, was recovered. Samples comprising of 20 cm^3 of sediment were taken at five-centimetre intervals, where sediments permitted, and processed in the Micropalaeontology Laboratory at the University of Leeds, with the >125 μm portion split into two parts, using a micro-splitter, for assemblage counts and isotope analysis respectively.

Assemblage portions were split to obtain counts of approximately 300 specimens under a Zeiss Stemi 305 binocular reflected light microscope. Species taxonomy was classified using Schiebel and Hemleben Planktic Foraminifers in the Modern Ocean (Schiebel and Hemleben, 2017). SEM plates are provided in Appendices (Appendix I 1-7). The >125 μm fraction was selected for assemblage analysis to remove juvenile foraminifera and aid in taxonomic identification (Schiebel and Hemleben, 2017). Planktonic foraminiferal assemblage data was logged for inter-sample comparison, with species classified by temperature preference using modern South Atlantic planktonic tow data and previous core top databases (Boltovskoy et al., 1996; Boltovskoy et al., 2000; Kucera, 2007; Schiebel and Hemleben, 2017). Based on regional water masses five temperature preference groupings were identified, incorporating known latitudinal displacement and depth habitats occupied during life. These were grouped as follows: tropical, sub-tropical, polar, sub-polar and a transitional grouping, comprised of species associated within ocean mixing regions i.e. the BMC. Alongside assemblage

counts, diversity metrics were used to assess planktonic foraminiferal community responses to BMC migration. Further information on methods can be found in the Chapter 3.

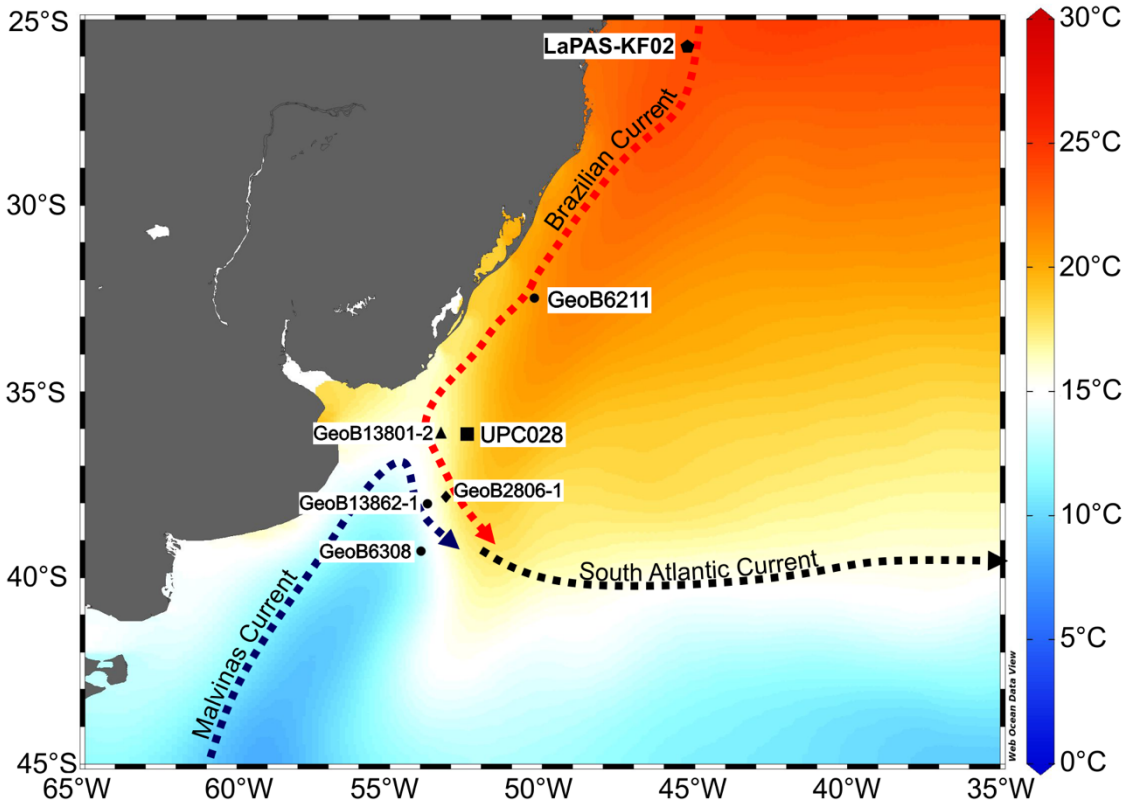

Figure 5.2-1 Annual sea surface temperatures off the western South Atlantic margin. UPC 028 record, this study, identified with a black square. Comparable literature records are identified as follows: planktonic foraminifera palaeotemperature transfer function record (black diamond) (Chapori et al., 2015), three *Gc. inflata* $\delta^{18}O_{(VPDB)}$ records (black circles) and a dinoflagellate/pollen record (GeoB13862-1) (Voigt et al., 2015; Gu et al., 2018c), a shelf Holocene reconstruction (black triangle) (Bender et al., 2013). LaPAS-KF02 faunal and isotopic record (black pentagon) (Pivel et al., 2013). Broad scale oceanographic currents are denoted by labelled dashed lines from Stramma and England, 1999. Regional map was constructed using the online Ocean Data Viewer from the annual 0.25 degree World Ocean Atlas 18 dataset (Schlitzer and Mieruch-Schnülle, 2021).

5.2.2 Isotopes

Oxygen ($\delta^{18}O$) and carbon ($\delta^{13}C$) stable isotope records were compiled for four species downcore to reconstruct water column properties through time. The species used are displayed in Table 5.2-1, alongside water column properties they represent and whether they host symbionts. This study improved on previous literature though the use of single specimen analysis, with all measurements collected in the Cohen Laboratories at the University of Leeds and relative to the Carrara Marble Standard, reported to the Vienna Pee Dee Belemnite (VPDB) scale, see methods for Standard values. $\delta^{18}O$ data was

converted to palaeo-temperature using the Kim and O'Neil (1997) equation for synthetic calcite (Kim and O'Neil, 1997; Pearson, 2012).

Based on previous literature, deep dwelling species (*Gc. inflata* and *Gr. truncatulinoides*) were split into BC and MC groupings using $\delta^{18}O$ values (Chiessi et al., 2007; Voigt et al., 2015; Morard et al., 2016). Individuals originating north of the BMC (BC) typically have lower, warmer values (<1.70 ‰), versus those south of the BMC (MC), which show higher, colder $\delta^{18}O_{(VPDB)}$ values (>2.33 ‰) (Chiessi et al., 2007; Morard et al., 2016). Water mass properties derived from the literature were used to assign individuals to distinct water masses, with separate means constructed for each grouping, to assess changing palaeoceanography. An overall mean was produced to detail mixing of the two water masses through time, to compare with previous studies methodologies (Voigt et al., 2015 and Chiessi et al., 2007). Movement of this mid-latitude front impacts water masses to considerable depth (~400-500 m), falling within associated depths of *Gc. inflata* calcification and a significant portion of reported *Gr. truncatulinoides* depths (Lončarić et al., 2006; Ujiié et al., 2010; Groeneveld and Chiessi, 2011; Rebotim et al., 2019). Complete information on the instrument utilised and processing procedure is found in Chapter 3.

Table 5.2-1 Species for stable isotope analysis to reconstruct water column properties.

Planktonic Foraminifera Species	Symbiont Hosting	Water Column Depth
Globigerinoides ruber white	Symbiont Hosting	Surface Waters
Neogloboquadrina pachyderma	Non-Symbiont Hosting	Surface Waters
Globoconella inflata	Non-Symbiont Hosting	Thermocline
Globorotalia truncatulinoides	Non-Symbiont Hosting	Sub-thermocline

5.2.3 Radiocarbon dating

Five radiocarbon dates for core UPC 028 were acquired at the following horizons: 97 cm, 197 cm, 310 cm, 400 cm and 487 cm. Samples contained all planktonic foraminifera above 125 µm to obtain sufficient mass for ^{14}C analysis (4 g). Samples were compared to Carrara Marble standards at the National Environment Isotope Facility Radiocarbon (NEIF Environment) in East Kilbride. Samples and standards were converted to graphite cathodes at the NEIF Radiocarbon Environment Laboratory and run at the Keck Carbon Cycle AMS Facility at the University of California, Irvine, USA for ^{14}C analysis due to low masses obtained.

From the dates provided, the OxCal program version 4.4 was utilised to correct and convert conventional radiocarbon age into calibrated BP and produce an associated age depth plot (Ramsey, 2009). The Marine20 calibration curve, incorporating a reservoir age of 500 years was used (Heaton et al., 2020). A P_Sequence model was used for estimating deposition rates with an intial k value of 1 with variance of the k value permitted to two $\log_{10}$ either side. This variation was used in the absence of confirmed uniform deposition and known variability of deposition processes within the region (i.e. contourites, turbidites and pelagic settling) (Ramsey, 2008; Rebesco et al., 2014). Interpolated dates were modelled at 0.5 cm resolution for the length of the core. More detailed information on how measurements were obtained see Chapter 3.

5.2.4 ITRAX

Non-destructive chemo-stratigraphic records were acquired using an ITRAX XRF scanner at the British Ocean Sediment Core Research Facility (BOSCORF). Archive sections were scanned to acquire optical and elemental data at 0.5 cm intervals for each core section. The output provides semi-quantitative assessment of sediment elemental concentrations based on X-Ray Fluorescence (XRF) counts. This was used alongside assemblage, isotope and radiocarbon data to access temporal variance on the margin. Chapter 3 provides in-depth analysis on preparation and process for data acquisition and utility of an XRF machine. Alongside the scanning data, core photos split by section were captured and are displayed in the Appendices (Appendix H.1).

5.3 Results

5.3.1 Radiocarbon

Radiocarbon dating was conducted on $CaCO_3$ samples composed of mixed planktonic foraminifera, due to insufficient mass for single species dating. Radiocarbon dates indicate this record covers the bulk of the Holocene epoch to the modern (Table 5.3-1). A sedimentary deposition model was constructed in OxCal using a P_Sequence model based on these five dates and a sixth assumed date for the core top. The core top date was taken as 2013, the year cores were sampled. Subsequent interpolation provided mean dates at 0.5 cm intervals across the cores. No age reversals were detected and all dates were accepted. An age/depth plot is presented in Figure 5.3-1 with the one and two standard errors plotted for all interpolated dates. Additionally, Figure 5.3-2 provides a simplified Age/Depth curve and sedimentation rates for site UPC 028. Appendix D.1 contains acquired dates and Appendix D.2 the interpolated dates.

Table 5.3-1 C^{14} dates for chronology acquired using AMS on samples derived from planktonic foraminifera. C^{14} converted to calibrated years using updated Marine20 curve to obtain years before present (cal BP).

Publication code	Sample identifier	Material (Planktonic foraminifera)	Depth (cm)	C^{14} Radiocarbon Age (years BP ± 1 σ)	Marine20 Calibrated Age median (cal BP)	1 σ error (years)	2 σ error (years)
UCIAMS-228257	UPC028 97-99 cm	$CaCO_3$	97-99	1830 ± 25	1235.9	119	248
UCIAMS-228258	UPC028 197-199 cm	$CaCO_3$	197-199	3560 ± 30	3280.7	150	301
UCIAMS-228259	UPC028 310-312 cm	$CaCO_3$	310-312	5170 ± 40	5359.4	160	355
UCIAMS-228260	UPC028 400-402 cm	$CaCO_3$	400-402	7550 ± 60	7819.9	177	338
UCIAMS-228261	UPC028 487-489 cm	$CaCO_3$	487-489	9340 ± 70	9944.3	280	503
Core top age was assumed based on known sampling date in 2013 and required to assess upper sections of the core.			Depth (cm)	Assumed C^{14} Radiocarbon Age (years BP ± 1 σ)	Marine20 Calibrated Age median range (cal BP)	1 σ error (years)	2 σ error (years)
			0	-62.5 ± 1	-62.5	10	10

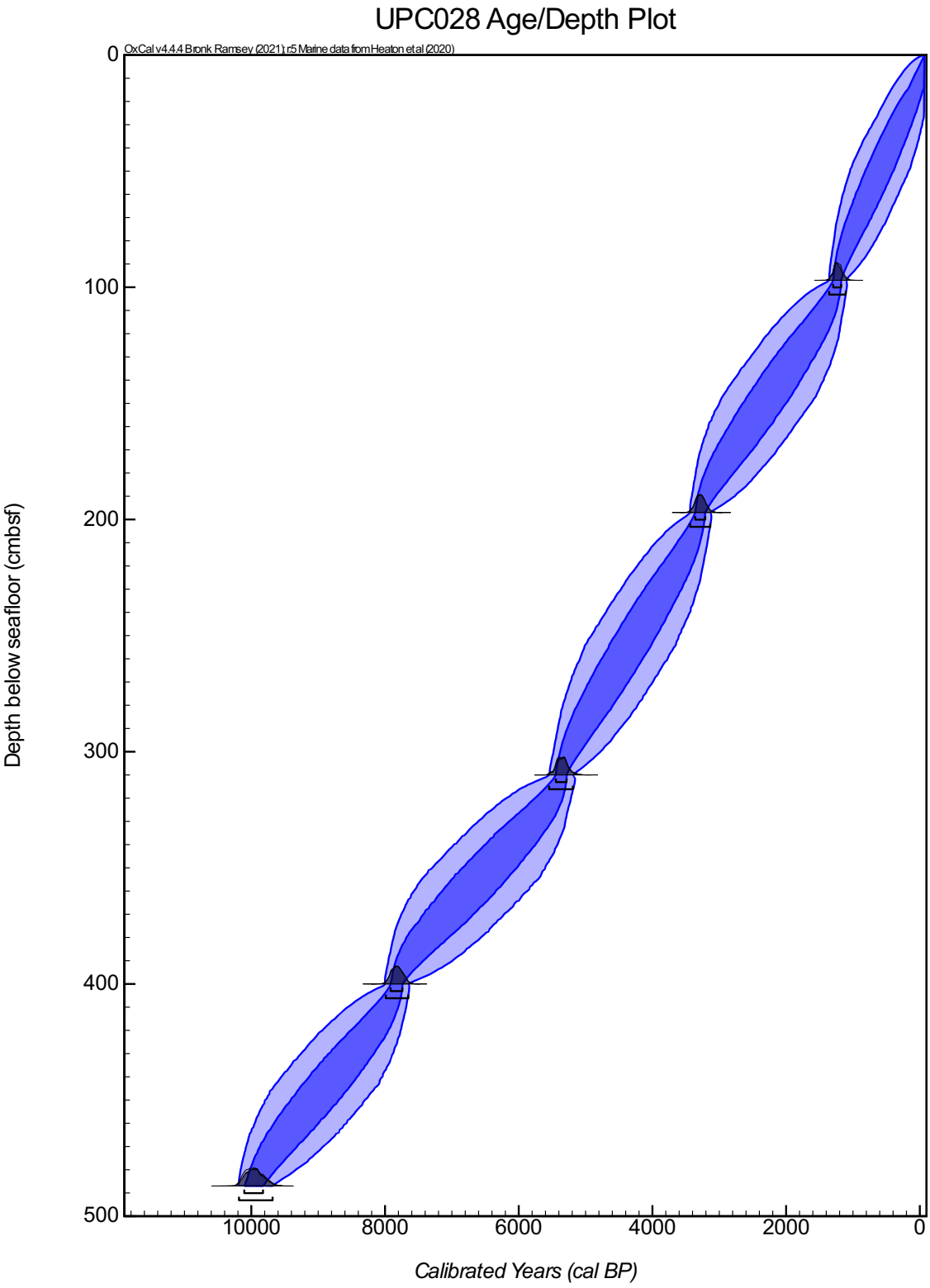

Figure 5.3-1 UPC 028 age/depth plot based on obtained radiocarbon dates and calibrated using Marine20 curve. Dark blue delimits one σ error, light blue marks two σ error.

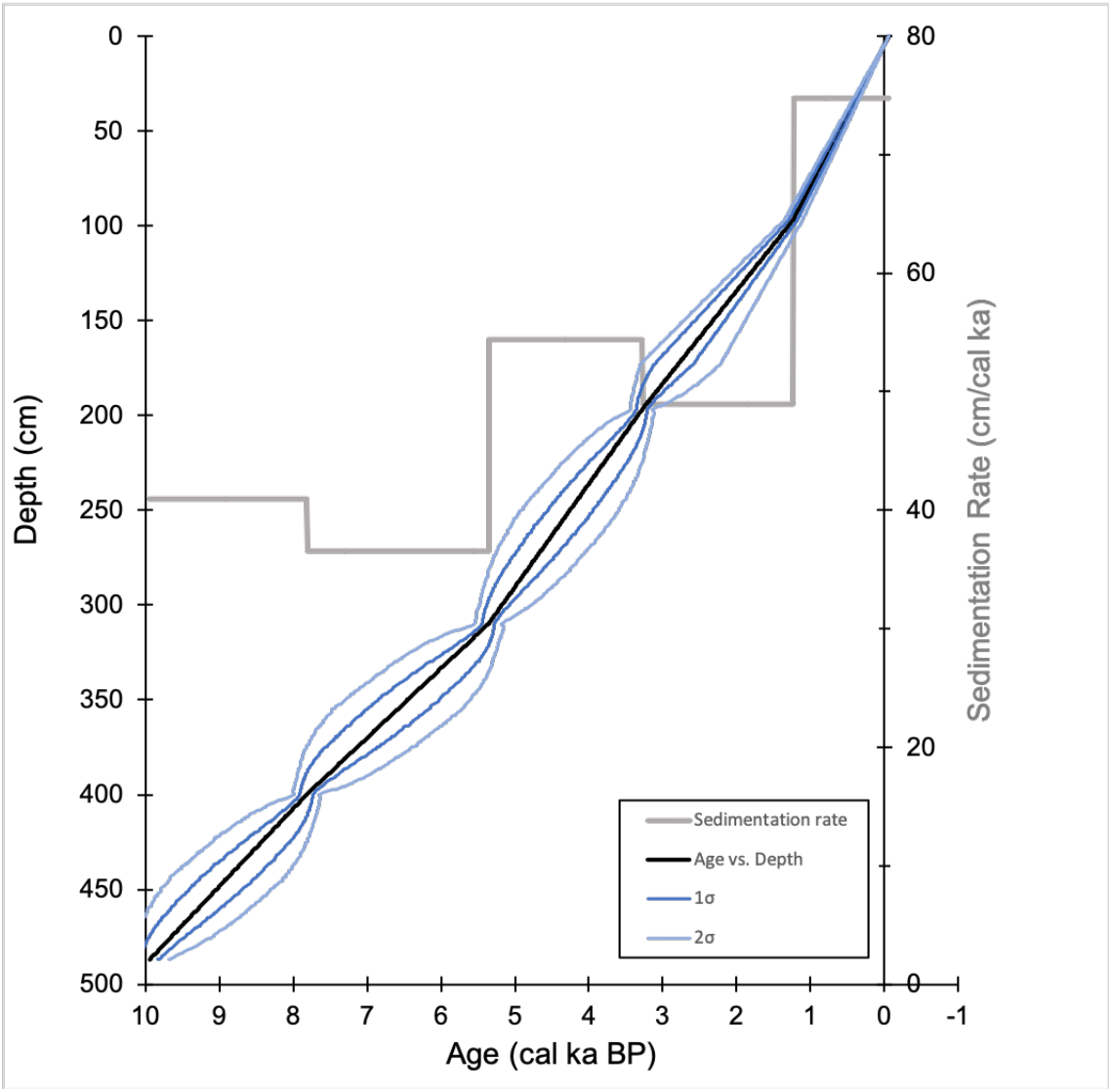

Figure 5.3-2 Simplified Age/depth (black) and sedimentation rate (grey) curves based on acquired conventional radiocarbon dates, utilising the Marine20 curve, for UPC 028. One sigma and two sigma radiocarbon age error are shown in dark blue and light blue respectfully.

5.3.2 Assemblage and diversity metrics

In total assemblage counts for 69 samples from core UPC028 were taken, with a <200-year resolution for the majority of the core. The exception is between section three and four where 40 cm, and ~900 years, were not recovered. 26 individual species were identified from 29,493 planktonic foraminifera counted, a further 5579 benthic foraminifera were counted for the purpose of relative abundance ratios. All counts provided enough taxa for assemblage counts, with splits ranging between 1/2 and 1/8 in order to provide ~300 planktonic foraminiferal specimens. Raw count data is provided within Appendix B.2. Across five eco-groups a single polar species, two sub-polar species, five transitional species, thirteen sub-tropical and five tropical species were recorded. The most

prevalent species averaged were *N. pachyderma* (16.6%), *Gc. inflata* (15.8%), *Gt. glutinata* (13.4%), *N. incompta* (12.9%), *Gs. ruber white* (9.6%) and *Gg. bulloides* (9.2%). Figure 5.3-3 displays the relative abundance of all 69 assemblages categorised by eco-group, with the interpolated radiocarbon age.

Polar and sub-polar species:

An overall decline in abundance of the combined cold species grouping, comprised of sub-polar and polar species, is observed across the 10 ky interval, with values dropping from ~40-60% in the early Holocene to ~20-30% for the late Holocene. The overall declining trend is broken down to show average polar assemblage contributions decreasing from ~30 % to ~20 % at the onset of the mid-Holocene and sub-polar species assemblage contributions fluctuating between ~13-26 %, before averaging out at ~20 % by the end of the early Holocene. Both polar and sub-polar species combine to see a recovery of the cold eco-group immediately prior to the end of the early Holocene at ~8.2 ka.

The mid-Holocene sees resumption of polar species decline, with continued loss of polar taxa between 8.2 and 6.6 ka and average proportions approaching ~10 %. This decrease is due to loss of *N. pachyderma* from assemblages over this interval. The polar eco-group has a slight resurgence between 6.6-4.2 ka, reaching average values of ~17 % by the end of the mid-Holocene. Sub-polar species initially decrease in relative abundance in the mid-Holocene before steadily increasing between 7.8-6.8 ka, where they peak at ~30 %. From ~6.8 ka values decline, with a brief increase at ~6 ka, before a continued decline to ~10 % at the end of the mid-Holocene. This general decline coincides with onset of a surge in transitional forms at ~5.8 ka.

The record resumes in the late Holocene after a ~900-year gap in the record. The cold species grouping, the summed polar and sub-polar eco-groups, resumes at approximately 30 % and continues to decline over the remaining ~3.3 ky. For this interval the sub-polar component consistently remains around the 10 % mark, whilst the polar species component fluctuates between 10-18 %. Between ~2.5-1.9 ka the cold eco-group sees a slight increase at the expense of warm and transitional eco-groupings, chiefly driven by an increase in polar species (Figure 5.3-3). From ~1-0.3 ka the polar portion of the cold grouping declines, coeval with warm species increases. Between ~0.3 ka and the modern both polar and sub-

polar species increase in proportion, with the combined value jumping ~9 % to 27 % in the core top, primarily driven by a polar increase of ~6 %.

Tropical and sub-tropical species:

Tropical and sub-tropical species are components of the warm species grouping. The warm species grouping increases in abundance over 10-8.5 ka, with a sharp peak at ~9.5 ka. This ~19 % rise occurs in approximately 0.3 ka and is largely driven by sub-tropical species. After this peak the warm species component fluctuates between 15-25 %. Immediately prior to, and across, the early/mid-Holocene boundary (~8.4-7.8 ka) the combined warm eco-group averages hold at ~20 %, whilst cold and transitional eco-groups increase (Figure 5.3-3).

In the mid-Holocene, and after ~7.8 ka, tropical species average values rise from 3 % to 6 % alongside sub-tropical increases of ~7 %. This results in average warm species proportions approaching 27 % between 7.8 ka and 6 ka. This shift sees the warm species eco-group form approximately 20 % of the assemblage for the remainder of the mid-Holocene, with variations chiefly driven by the sub-tropical species. Coinciding with a transitional species surge at ~5.8 ka, the warm eco-group displays a slight drop in the assemblage percentage, driven by a drop in sub-tropical species (~10 % decrease).

The late Holocene portion of the record resumes with low overall warm species percentages, rising from ~17 % to ~27 % ~300 years later. This recovery is almost entirely driven by an increase in sub-tropical species, with tropical species dropping slightly during this time. With warm species recovered to mid-Holocene levels the next notable decrease in the proportion of warm species occurs between 2.5 ka and 1.9 ka, this is again driven by a decline in sub-tropical species (drop of ~15 %), before a brief rise in values at ~1.7 ka. Another increase in polar species leads to the warm eco-group to decrease between ~1.7-1.3 ka. Tropical values show a record peak at ~1.3 ka (~10 %), signifying an increase in the warm eco-group from the previous dip, and begins a warming signal to ~0.5 ka, with sub-tropical species driving the sustained rise. Warm species peak at ~35 % at ~0.5 ka with values fluctuating rapidly to ~22 % at ~0.4 ka and ~32 % at ~0.3 ka, with both sub-tropical and tropical components fluctuating coevally. From ~0.3 ka to the modern tropical values are maintained at ~9 %, whilst sub-tropical percentages drop ~10 % in response to cold species increases, leading to a slightly cooler modern signal.

Transitional species:

Average transitional species percentages fluctuate between ~30-40 % across much of the early and mid-Holocene (10-6 ka), with a drop to ~24 % occurring at ~8.8 ka aligning with a sharp rise in polar species. From ~6 ka transitional species relative abundance increases until ~4.2 in the mid-Holocene, establishing a new average relative abundance of >50 %. This increase in assemblage proportion is largely accounted for by a decline in cooler water taxa and a slight drop in sub-tropical forms. Moving past the core break and into the late Holocene, values fluctuate between ~50-60 % right up to the modern core top sample with slight variation due to increases/decreases aligned with warm species fluctuations.

Assemblage Planktonic percentage

The planktonic percentage (Figure 5.3-3) provides a proxy for relative sea-level change (RSL) through time (van der Zwaan et al., 1990; Leckie and Olson, 2003; Olson and Leckie, 2003; Toledo, 2008). Starting with the oldest portion of the record we see a rise from <60 % around 9.8 ka to ~88 % at approximately 8.4 ka. A subsequent drop to 75 % at 8.2 ka is followed by a rise in values to >90 % at ~6.2 ka. From here a fluctuation in values (80-95 %) occurs to ~2.2 ka. Over the next 300 years the planktonic percentage drops to ~76% at 1.9 ka. From ~1.9 ka a sharp rise in planktonic percent occurs, with values re-established above 80 % for the next 1.4 ky, typically between 82-90 %. The core top value provides a sharp drop in planktonic percent from ~93 % at ~0.3 ka to ~75% in the modern.

Gr. truncatulinoides coiling direction

Gr. truncatulinoides coiling directions are associated to differing genotypes known to favour differing water masses, whilst not definitive, the ratio between the two coiling directions can provide an indication of water mass dominance (Ujiié et al., 2010; Ujiié and Asami, 2014). The record (Figure 5.3-3) shows a dominance of left coiling forms for the majority of the core, with a sustained period of right coiling individuals between ~9.5-8.5 ka. A brief spike at ~8 ka aligns with a decline in cold eco-group species following a cold eco-group resurgence post ~8.4 ka. Additionally, peaks at ~2.5 ka and ~1.1 ka bracket a brief rise in cold eco-groups during the intervening period. A final peak at ~0.3 ka aligns with elevated warm eco-group relative abundances.

Gg. bulloides/Gs. ruber white ratio

The ratio between *Gg. bulloides*, a eutrophic favouring species, and *Gs. ruber white*, an oligotroph species, can be utilised to infer water mass nutrient content (Toledo, 2008). Increased values signify a greater proportion of *Gg. bulloides* within the assemblages and thus more eutrophic conditions (Toledo, 2008). The *Gg. bulloides/Gs. ruber white* ratio shows a fluctuating trend throughout the record and broadly follows changes seen in the relative abundances of benthic species (Figure 5.3-3).

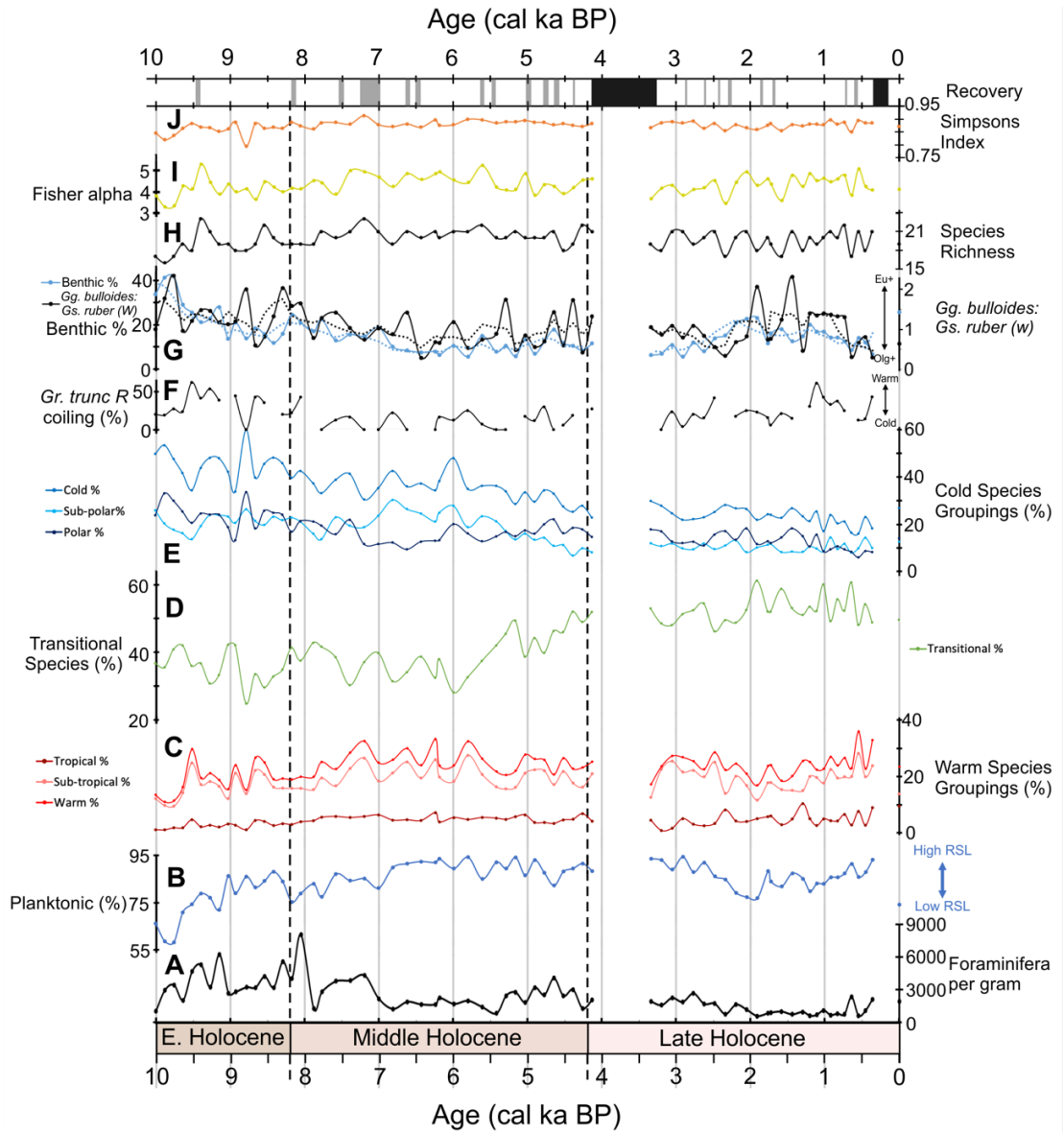

Figure 5.3-3 Downcore assemblage groupings. A) Sample foraminifera per gram values. B) Percentage of total foraminifera that are planktonic. C) Warm species percentage, combing the tropical and sub-tropical species, monitoring warm water influence. D) Variation in the relative abundance of transitional species. E) Cold species percentage, combining polar and sub-polar species groupings, monitoring cold water influence. F) *Gr. truncatulinoides* right coiling proportion, with higher percentages equating to warmer water influence. G) Ratio of *Gg. bulloides* to *Gs. ruber white*, a productivity indicator alongside the change in relative abundance of benthic species. H) Variation in species richness downcore. I) Fisher alpha values. J) Simpsons Index values.

Over the early Holocene the average ratio broadly declines to the early/mid-Holocene boundary at 8.2 ka, shifting to more oligotrophic conditions. In the samples immediately surrounding the boundary however, the average ratio rises for a period of ~500 years, extending into the mid-Holocene, shifting to more eutrophic conditions. During the mid-Holocene, from ~8-6.5 ka the ratio fluctuates but declines, indicating a decline toward more oligotrophic conditions. However, from ~6.5 ka the ratio fluctuates and rises slightly, most notably between 6-5 ka and between ~4.7-4.1 ka, suggesting a shift from the declining state. Into the late Holocene, the ratio drops between ~3.3-2.3 ka, before a sharp rise between ~2.3-0.5 ka to an increased nutrient state. This increase in the ratio is pulsed, with large peaks occurring at ~1.9 and ~1.4 ka, prior to establishment of an elevated plateau between ~1.2-0.7 ka. From ~0.7 ka values then decline to more oligotrophic conditions approaching the modern.

From the base of the record we see a fluctuating rise in foram/gram values to 9.1 ka at ~6,200. A drop to ~2,700 at 9 ka begins a new rise, to a peak value of ~8000 forams/gram at ~8 ka. From this peak, values drop sharply down to 7.8 ka before rebounding to values between 3,000-4,000 forams per gram for the next ~600 years. From ~7-5.8 ka the forams per gram remains relatively steady around ~2000 forams per gram, before a series of sharp fluctuations between 5.8-4.1 ka and the core break. These fluctuations continue into the late Holocene to ~2.5 ka, before numbers decline to <1000 forams per gram. At ~0.7 ka there is a sharp jump to ~2300, with another peak of ~2100 at 0.3 ka, a value similar to that reported within the core top.

5.3.2.1 Diversity metrics

Diversity downcore remains stable across the 10 ky interval with an average of 20 species recorded per sample, and a range of values encompassing 16-23 species (Figure 5.3-3). Fisher alpha values fluctuate between ~3.6-5.0 for the length of the core (Figure 5.3-3). Fisher alpha has the lowest values at ~9.8 ka before rising from 3.3 to 5.3 in 400 years. From here it drops sharply, and between ~9.2-7.5 ka Fisher values fluctuate between 4-4.5, before rising at 7.4 ka where the average values fluctuate between 4.5-5 until 5.6 ka. After 5.6 ka Fisher values return to fluctuating between 4-4.5 for the most part until the core section break at 4.1 ka. Above the core break the fluctuation in Fisher alpha values continues between 4-4.5, with a slight increase in values between ~1.4-0.5 ka years ago.

For this final 500 years to the core top there is a slight decrease in Fisher alpha to 4.1. The Simpson's index values are high across all samples (~0.8-0.9) and largely show little variation between samples (Figure 5.3-3). The exception occurs at ~8.8 ka where values temporarily drop by ~0.1, before returning to steady levels. The steady state and high Simpson's Index imply high diversity and a lack of dominance by one species over the others throughout the record.

5.3.3 Foraminiferal Stable Isotopes

Spacing of samples provides a resolution of ~581 years, with four species analysed to represent differing water column parameters over the 10 ky interval. These four species are the surface dwellers *Gs. ruber white* and *N. pachyderma,* and deeper dwellers *Gc. inflata* and *Gr. truncatulinoides*, with the latter split into differing coiling directions. Downcore isotope values are plotted in Figure 5.3-4 and raw data is provided in Appendix C.2.

5.3.3.1 Surface dwellers:

Both surface dwelling species record average warming trends with decreases in $\delta^{18}O$ values, although values are offset from one another by approximately 2 ‰ $\delta^{18}O_{(VPDB)}$, equating to ~9 °C difference (Figure 5.3-4). *Gs. ruber white* records the most negative $\delta^{18}O$ values, indicative of the warmest temperatures on the margin, these values range between -1.2 and 0.2 ‰ $\delta^{18}O_{(VPDB)}$ (16-23 °C), with mean $\delta^{18}O_{(VPDB)}$ values varying between -1.0 and -0.2 ‰ (18-22 °C). *Gs. ruber white* temperature rises occur in pulses, the first pulse occurs between ~9.8-9.5 ka with an average decline of $\delta^{18}O_{(VPDB)}$ values of ~0.4 ‰, equating to a temperature rise of ~1.8 °C. After this peak, values return to ~-0.2 ‰, with temperatures dropping to ~18 °C for approximately 1.25 ky. The next warming pulse begins at ~7.7 ka, peaking at ~6.8 ka with ~-0.7 ‰ $\delta^{18}O_{(VPDB)}$, or ~20.7 °C. A sharp drop to ~-0.2 ‰ $\delta^{18}O_{(VPDB)}$ (~18.4 °C) occurs at 6.4 ka and begins a new phase of warming continuing to the core break at ~4.4 ka, when values reach ~-0.8 ‰, or ~21.1 °C. On resumption of the record in the late Holocene $\delta^{18}O_{(VPDB)}$ values maintain values <-0.6 ‰ averaging temperatures of approximately 20.9 °C to ~0.5 ka. Modern temperatures show a drop to ~-0.3 ‰ (~18.7 °C) returning to similar values pre-7.2 ka.

Gs. ruber white mean $\delta^{13}C_{(VPDB)}$ values vary by approximately 1.5 ‰ over the 10 ky interval, starting at the lowest value of ~0.1 ‰ at ~9.9 ka (Figure 5.3-4). Over the next 4 ky, to ~5.8 ka, the overall trend shows increasing $\delta^{13}C_{(VPDB)}$ values, peaking at 1.6 ‰. After this peak the values return to ~1.1 ‰ at ~4.4 ka prior to the core break. The record resumes at ~2.9 ka, and running up to modern, the $\delta^{13}C_{(VPDB)}$ signal shows a slight decline from ~1.1 ‰ to ~0.8 ‰.

N. pachyderma values record an average warming trend from 10 ka to ~5.8 ka, declining from ~1.8 ‰ $\delta^{18}O_{(VPDB)}$ (~9.0 °C) at ~9.9 ka to ~1.0 ‰ (~12.7 °C) at

~5.8 ka. From ~5.8 ka there is an increase in values to ~4.4 ka, where ~1.7 ‰ $\delta^{18}O_{(VPDB)}$ (~9.7 °C) values are recorded, equivalent to a temperature decrease of ~3 °C. After the core break mean $\delta^{18}O_{(VPDB)}$ values fluctuate between~1.3 and 1.8 ‰ (~9.0-11.2 °C), remaining warmer than in the 10.0-8.0 ka portion of the record, but on average colder than the 8.0-6.0 ka portion of the record. Similar to the *Gs. ruber white* record, the modern $\delta^{18}O_{(VPDB)}$ value is colder than the late Holocene average at ~1.6 ‰ (~9.9 °C), but is not as significantly offset to records in the last 3 ka (Figure 5.3-4).

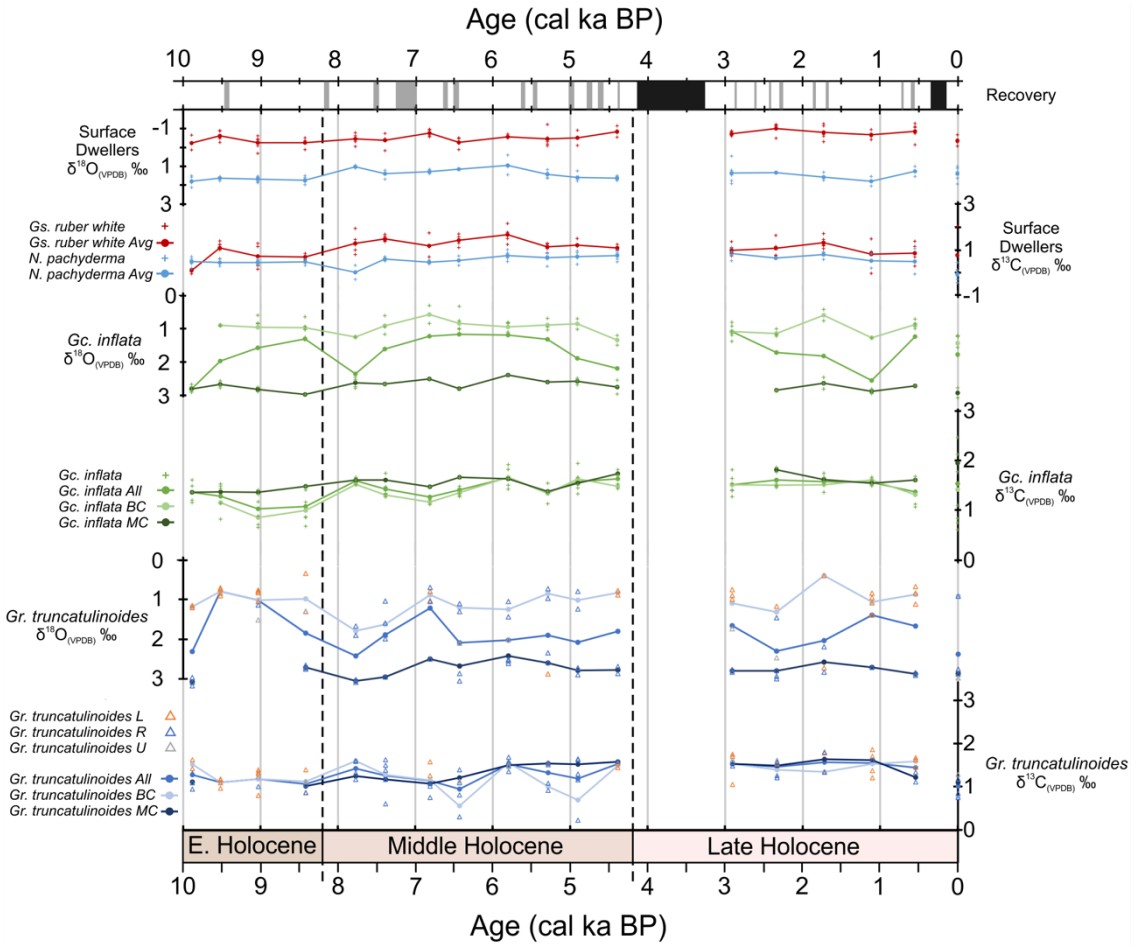

Figure 5.3-4 Downcore $\delta^{18}O_{(VPDB)}$ and $\delta^{13}C_{(VPDB)}$ isotope analyses of four species representative of differing water column depths. Two surface dwellers, the warm water *Gs. ruber white*, and the cold-water *N. pachyderma*. Both species show slight warming trends across the Holocene whilst the $\delta^{13}C$ values for both species increase and peak during the mid-Holocene. The remaining two species are deeper dwelling with *Gc. inflata* a thermocline dweller and *Gr. truncatulinoides* a sub-thermocline species. Both species were split into two groupings likely representative of differing water mass conditions due to the significant offsets between individuals, see text for details on BC/MC classification. Trends over the Holocene show a warming signal predominantly, peaking in the mid-Holocene.

N. pachyderma $\delta^{13}C_{(VPDB)}$ values fluctuate between 0.0 and 0.9 ‰ and form a fairly stable record across the 10 ky interval (Figure 5.3-4). For the first 1.5 ky (~10.0-8.5 ka) the record sees values of ~0.5 ‰ after which there is a significant drop to ~0.0 ‰ at ~7.8 ka. Values immediately rebound to ~0.5 ‰ for approximately 1 ky, before steadily increasing to ~0.7 ‰ at ~4.4 ka. The record resumes at ~2.9 ka with values of ~0.8 ‰, before declining toward the modern, decreasing to ~0.5 ‰ at ~0.5 ka. The modern average value is significantly lower still at 0.07 ‰ and more akin to values seen at ~7.8 ka.

5.3.3.2 Deeper dwelling species:

Following findings of chapter four results were split into groups greater than and less than 2.0 ‰ $\delta^{18}O_{(VPDB)}$, with clustering of the deep dwelling species isotope results into two groups, replicating surface observations by Chiessi et al., (2007) (Figure 5.3-4). *Gc. inflata* downcore groupings are offset by ~1.5 ‰ in $\delta^{18}O_{(VPDB)}$. Two separate means are calculated due to this offset, one tracking $\delta^{18}O_{(VPDB)}$ values >2 ‰ and the second for values <2 ‰. To aid referencing these two groups are called *Gc. inflata* MC (GCMC) and *Gc. inflata* BC (GCBC) respectively. The GCMC record is remarkably stable across the 10 ky record, with values fluctuating between ~2.4 and 3.0 ‰ $\delta^{18}O_{(VPDB)}$, displaying an average of 2.7 ‰ $\delta^{18}O_{(VPDB)}$. This equates to temperature fluctuations between 4.1-6.6 °C, with an average of ~5.2 °C. GCBC shows slightly more variability, ~0.6 and 1.4 ‰ $\delta^{18}O_{(VPDB)}$, displaying an average value of 1.0 ‰ $\delta^{18}O_{(VPDB)}$. Converted, this is approximately 10.7-14.6 °C, with an average of ~12.7 °C. The two ranges are distinct from one another and show no overlap.

An overall average curve marks shifting influence between BC and MC groupings, and is reflective of BMC movement (Chiessi et al., 2007; Voigt et al., 2015). Results show warming in the early Holocene, before a sharp rise in isotope values at ~7.8 ka. Over the mid-Holocene $\delta^{18}O$ values fall and a warming period of at least 2.5 ky occurs, until rising $\delta^{18}O$ values indicate cooling to the end of the mid-Holocene (Figure 5.3-4). The late Holocene record is interrupted by a 40 cm core break and resumes at 2.9 ka, with a BC dominated average value of ~1.1 ‰ $\delta^{18}O_{(VPDB)}$, equating to ~12.3 °C. Late Holocene combined average $\delta^{18}O_{(VPDB)}$ values for the whole of the interval are approximately 1.7 ‰, equivalent to ~9.6 °C, producing a signal similar to those of the mid-Holocene (~1.6 ‰ $\delta^{18}O_{(VPDB)}$ or ~10.0 °C). However, this averaging belies a swing to higher values

within the interval and some large shifts in $\delta^{18}O_{(VPDB)}$. Over the remainder of the late Holocene overall mean (BC+MC) $\delta^{18}O$ values rise in two pulses to a maximum of ~2.5 ‰ $\delta^{18}O_{(VPDB)}$ (~5.9 °C) at ~1.1 ka, reporting similar values to ~7.8 ka, before sharply declining to 1.2 ‰ $\delta^{18}O_{(VPDB)}$ (~11.6 °C) by 0.5 ka. $\delta^{18}O_{(VPDB)}$ values rise to ~1.8 ‰ (~9.3 °C) in the modern, indicating slight cooling in the UPC 028 record.

$\delta^{13}C$ records for *Gc. inflata* has been similarly split into GCBC and GCMC groupings, however the split is less significant than the $\delta^{18}O$ values, corroborating the findings of Chiessi et al., (2007). GCMC average values are typically higher than GCBC average values, however both fluctuate between ~1.0 and 2.0 ‰ $\delta^{13}C_{(VPDB)}$ (Figure 5.3-4). Between 10 and 8 ka there is ~0.5 ‰ offset, until ~7.8 ka when the two records converge briefly, with a minor ~0.1 ‰ difference between GCBC (~1.5 ‰ $\delta^{13}C_{(VPDB)}$) and GCMC (~1.6 ‰ $\delta^{13}C_{(VPDB)}$). Records then diverge, with a ~0.3 ‰ offset prior to convergence at 5.8 ka. The two records remain converged until ~4.9 ka, where they display ~0.3 ‰ difference, just before the core break. From 2.9 ka the GCBC record resumes at ~1.5 ‰ $\delta^{13}C_{(VPDB)}$, showing minor variation until ~1.1 ka. The GCMC record restarts at 2.3 ka at ~1.8 ‰ $\delta^{13}C_{(VPDB)}$, trending toward the GCBC profile until 1.1 ka. Thereafter GCBC and GCMC records diverge with modern values of ~1.4 ‰ and ~2.0 ‰ $\delta^{13}C_{(VPDB)}$ respectively.

Gr. truncatulinoides downcore data comprises of both left and right coiling variants. $\delta^{18}O_{(VPDB)}$ data is split with two groupings visible and delimited either side of 2 ‰, as with *Gc. inflata*, with a 1.5 ‰ offset (~8 °C). The >2 ‰ $\delta^{18}O_{(VPDB)}$ grouping was termed *Gr. truncatulinoides* MC (GRMC) and the <2 ‰ $\delta^{18}O_{(VPDB)}$ grouping designated *Gr. truncatulinoides* BC (GRBC). The GRMC grouping is predominantly represented by the left coiling variant and the GRBC by a mix of right and left coiling individuals. The GRMC record starts at ~9.8 ka with a value of ~3.1 ‰ (~3.7 °C), there is then a 1.4 ky interval comprising the bulk of the early Holocene, before the next measurement of ~2.7 ‰ $\delta^{18}O_{(VPDB)}$ (~5.2 °C) at ~8.4 ka (Figure 5.3-4). Over the mid-Holocene the record fluctuates between 2.4 and 3.0 ‰ $\delta^{18}O_{(VPDB)}$ (~3.8-6.5 °C), with values warming particularly between 7.3-5.3 ka. After the core break the record resumes with similar $\delta^{18}O_{(VPDB)}$ values at ~2.9 ka of ~2.8 ‰ (~4.9 °C), with a slight warming trend peaking at ~2.6 ‰ (~5.8 °C) at ~1.7 ka, before increasing and cooling to ~2.9‰ $\delta^{18}O_{(VPDB)}$ (~4.6 °C) in the

modern. The average $\delta^{18}O_{(VPDB)}$ value for the GRMC record is ~2.8 ‰, equating to ~5.0°C.

The GRBC record is more variable, with average values ranging between 0.4 and 1.8 ‰ $\delta^{18}O_{(VPDB)}$ (~9.2-15.4 °C), with a Holocene average of ~1.1 ‰ $\delta^{18}O_{(VPDB)}$ (~12.4 °C) (Figure 5.3-4). Starting at ~9.8 ka and a value of ~1.2 ‰ $\delta^{18}O_{(VPDB)}$ (~11.9°C), we see warming to ~0.8 ‰ (~13.6 °C) at ~9.5 ka. Over the next 1 ky $\delta^{18}O_{(VPDB)}$ values rise to ~1.0 ‰ (~12.8 °C) at ~8.4 ka. From this point the $\delta^{18}O_{(VPDB)}$ signal increases sharply to ~1.8 ‰ (~9.2 °C) at ~7.8 ka, and then warms back to ~0.9 ‰ $\delta^{18}O_{(VPDB)}$ (~13.2 °C) at 6.8 ka. The record rises again to ~1.2 ‰ (~11.6 °C) at 5.8 ka, albeit less extreme than previously. Warmer values return for the period of 5.3-4.4 ka, varying between 0.8 and 1.0 ‰ $\delta^{18}O_{(VPDB)}$ (~12.6-13.5 °C). Resuming in the late Holocene at ~2.9 ka, with a $\delta^{18}O_{(VPDB)}$ value of ~1.1 ‰ (~12.3 °C) the record sees some significant fluctuations over the next 1.8 ky. Cooling to 1.3 ‰ $\delta^{18}O_{(VPDB)}$ (~11.3 °C) before warming to 0.4 ‰ $\delta^{18}O_{(VPDB)}$ (~15.4 °C) in a period of ~600 years, before returning to a more moderate value of 1.1 ‰ $\delta^{18}O_{(VPDB)}$ (~12.4 °C) by 1.1 ka. The final 1 ky of the record sees minor fluctuation heading toward the modern value of 0.9 ‰ $\delta^{18}O_{(VPDB)}$ (~13.0 °C) for the GRBC grouping.

The resulting overall average combining GRBC and GRMC groupings aims to indicate dominance between BC and MC associated values. A sharp warming signal at the record onset is observed, with values reaching 0.8 ‰ $\delta^{18}O_{(VPDB)}$ (~13.6 °C) at ~9.5 ka (Figure 5.3-4). This sharp rise in average values is due to a lack of GRMC data points over a ~1 ky interval. $\delta^{18}O_{(VPDB)}$ values then increase to a maximum of ~2.4 ‰ (~6.5 °C) at ~7.8 ka, marking a distinct cooling trend following the end of the early Holocene. Over the next 1 ky average $\delta^{18}O_{(VPDB)}$ values drop, warming to a peak at 6.8 ka of ~1.2 ‰ (~11.8 °C). This pattern largely follows the *Gc. inflata* data however, from ~6.8 ka onward *Gr. truncatulinoides* $\delta^{18}O_{(VPDB)}$ values rise and diverge from *Gc. inflata* averages, fluctuating around 2.0 ‰ (~8.2 °C). This cooling continues to the end of the mid-Holocene with a slight decrease in $\delta^{18}O_{(VPDB)}$ to ~1.8 ‰ (~9.2 °C). Record resumption in the late Holocene at ~2.9 ka sees comparatively warmer values of 1.7 ‰ $\delta^{18}O_{(VPDB)}$ (~9.8 °C). The available late Holocene combined average fluctuates, with a cooling trend to ~2.3 ‰ $\delta^{18}O_{(VPDB)}$ (~7.0 °C) at 2.3 ka, before warming over the next ~1.2 ky to ~1.4 ‰ $\delta^{18}O_{(VPDB)}$ (~11.0 °C). From 1.1 ka to

the modern, average *Gr. truncatulinoides* $\delta^{18}O_{(VPDB)}$ values cool quickly, rising to ~2.4 ‰ $\delta^{18}O_{(VPDB)}$ (~6.7 °C) in the modern. Over the last 2 ky the records of *Gc. inflata* and *Gr. truncatulinoides* appear out of sync, with peak late Holocene warming for *Gr. truncatulinoides* coinciding with peak *Gc. inflata* cooling.

The $\delta^{13}C_{(VPDB)}$ trend for *Gr. truncatulinoides* is similar to *Gc. inflata* in that both the GRBC and GRMC groupings average values fall within a ~0.6 and 1.7 ‰ range, and at times the offset in mean $\delta^{13}C_{(VPDB)}$ values is within ~0.1 ‰ (Figure 5.3-4). The GRMC values steadily rise from ~1.0 ‰ at ~8.4 ka to ~1.6 ‰ at ~1.1 ka before dropping quickly to modern values of 1.1 ‰. The GRBC, whilst similar in the value range shows a slightly more erratic trend, with notable rises in $\delta^{13}C$ above GRMC values at ~7.8 ka (~1.6 ‰ $\delta^{13}C_{(VPDB)}$) and ~0.5 ka (~1.6 ‰ $\delta^{13}C_{(VPDB)}$). Additionally, there are significant drops in $\delta^{13}C_{(VPDB)}$ values at ~6.4 ka and between 5.8-4.3 ka with values reaching as low as ~0.7 ‰ $\delta^{13}C_{(VPDB)}$. After the core break, in addition to the divergence at ~0.5 ka there is another divergence at ~1.7 ka with a ~0.3 ‰ offset between GRMC and GRBC values. Similar to GRMC values, GRBC see a drop in average $\delta^{13}C_{(VPDB)}$ values in the modern to ~0.8 ‰.

5.3.4 ITRAX and XRF scanning data

Non-destructive core scanning techniques, XRF and ITRAX XRF, were employed to obtain greyscale reflectance and semi-quantitative data of elemental variations within the core (Croudace and Rothwell, 2015). Raw ITRAX XRF data for UPC 028 is provided in Appendix F.2. Regarding the ITRAX elemental data, raw counts are typically not utilised due to factors like dilution and calibration issues, instead data is presented as log-ratios to negate such issues (Weltje and Tjallingii, 2008; Croudace and Rothwell, 2015). The raw data has been presented in Figure 5.3-5 to aid determination of which element drives log-ratio change. Key sedimentary and productivity metrics in (Figure 5.3-6), and summary ITRAX figures are utilised in this section (Figure 5.3-7).

Greyscale variance measures sediment lightness and correlates with sediment composition. Brighter, higher values are often associated with carbonate content, whilst lower values are attributed to darker, potentially organic rich sediments (Giosan et al., 2002; Rothwell and Rack, 2006). Results show that between ~10-8.6 ka there is minor variation, before a sharp rise over ~400 years to the early/mid-Holocene boundary (Figure 5.3-5). During the mid-Holocene minor variation is observed, however the record is patchy from ~8.0-6.5 ka, seemingly the result of cracking in the core. Where present values appear similar to those recorded between 10-8.6 ka, suggesting similar sediment composition. This pattern is largely continued to ~5.8 ka. After ~5.8 ka variability increases slightly, with a smaller set of peaks visible between ~5.3-4.2 ka, signifying a lightening of the core to the end of the mid-Holocene. Late Holocene trends see greyscale values decline, with peaks similar in size to those between ~4.5-4.2 ka at ~2.2-1.8 ka. A sawtooth pattern persists to the modern, with a slight peak at ~0.4 ka.

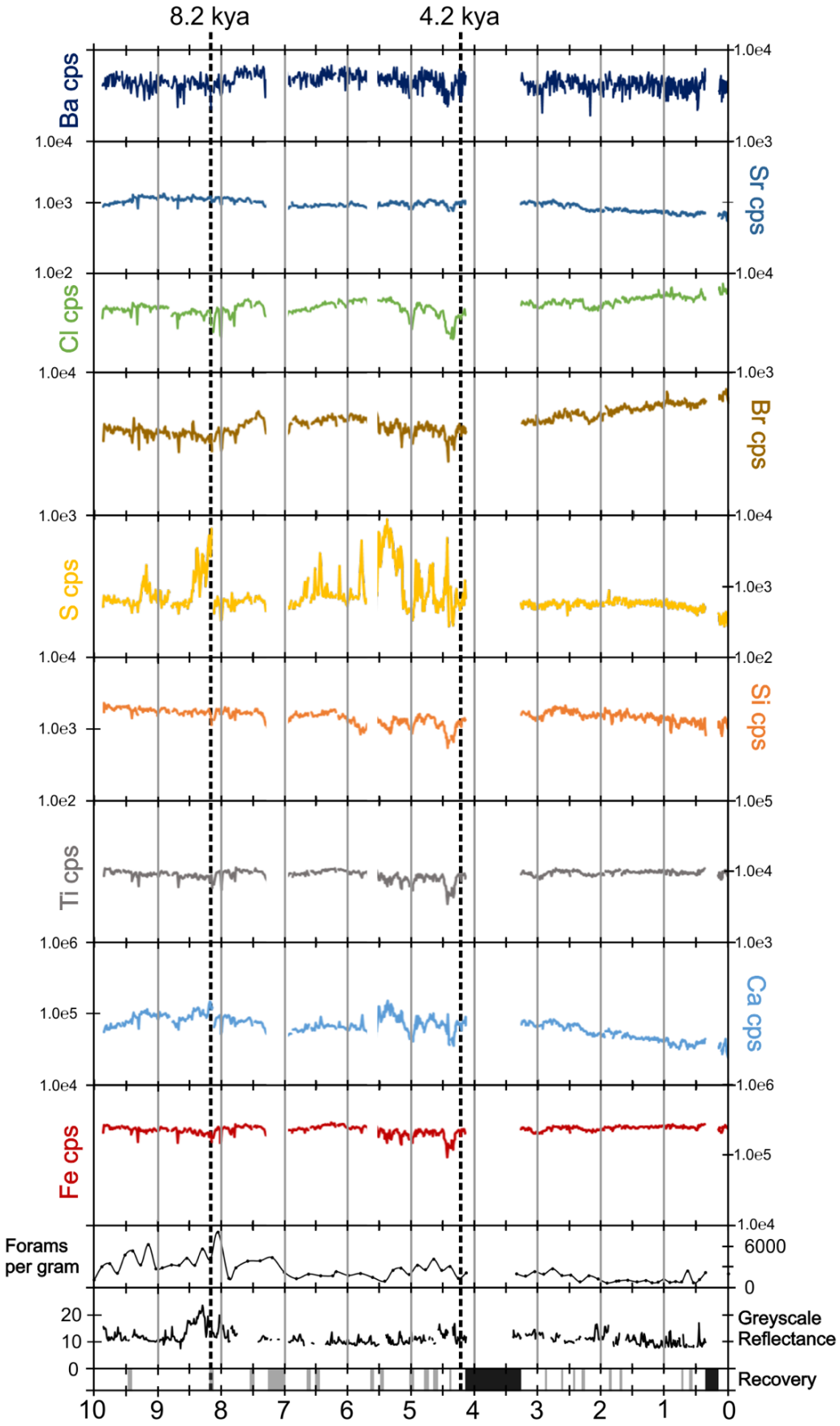

Figure 5.3-5 Core greyscale reflectance, foraminifera per gram counts and raw ITRAX counts of the main elements utilised by this study. ITRAX counts are presented on log scales. Core recovery is shaded on the left-hand side of the plot with black sections indicating missing material and grey bars areas of cracking in the core.

Raw counts of calcium (Ca) and strontium (Sr) are displayed together (Figure 5.3-5). Sr is prevalent within the marine realm and readily incorporated into biogenic calcium carbonate vs inorganic derived calcite (Hodell et al., 2008; Croudace and Rothwell, 2015). Co-variance of these elements is used to indicate Ca is predominantly marine sourced, via biological production, rather than from inorganic terrestrial inputs (Carlson et al., 2008; Croudace and Rothwell, 2015). The UPC 028 record sees Ca-Sr co-variance, despite differing scales, implying a marine signature for the Ca present. Between ~5.5-5.2 ka the raw counts record may differ, with Ca counts showing a slightly larger peak than Sr. This episode is brief, also containing moderate Sr increases, implying part biogenic influence still.

Fe/Ti is used to assess the terrestrial input to the region and can be utilised to assess Fe remobilisation during the formation of pyrite (Croudace and Rothwell, 2015). The UPC 028 Fe/Ti record in comparison to the Fe/Ca record sees comparatively little variation (Figure 5.3-6). Drops in the Fe/Ti ratio occur prior to the 8.2 ka boundary at ~8.4 ka and, in conjunction with minor peaks in the Fe/Ca and Ca/Ti curves, between 7.0-6.5 ka. Slightly elevated peaks during the mid-Holocene portion occur at ~5.7 and ~4.4 ka, although variation is modest. For the late Holocene the Fe/Ti record shows a slightly increasing trend, however the scale of variation does not suggest significant pyrite formation in the core.

Ca/Ti is another method of analysing terrigenous versus biogenic input to the site, however unlike Fe/Ca, Ti is less likely to be impacted by redox influences (Croudace and Rothwell, 2015). UPC 028 Ca/Ti has elevated values in the early Holocene, with a steady rise in values to ~9.2 ka, following similar trends to the S/Ti curve, and anti-phased to the Fe/Ca curve (Figure 5.3-6). From 9.2-8.7 ka values decline before rising again between 8.7-8.2 ka. At ~8.2 ka Ca/Ti values reach a high for the early Holocene before declining sharply across the early/mid-Holocene boundary. After this, mid-Holocene values decline with minor variation between 6.8-6.0 ka, that are similarly anti-phased to Fe/Ca ratios. A more significant set of excursions occur between 6.0-4.2 ka, with 5.5-5.1 ka showing elevated Ca/Ti ratios. Into the late Holocene the Ca/Ti ratio values resume and begin a steady decline toward the modern, with comparatively minor fluctuations compared to the mid-Holocene. The anti-phasing of the Ca/Ti record with the Fe/Ca record, further reinforces dominance of Ca between 8.5-8.2 ka and 5.5-4.2 ka. The late Holocene record shows a declining trend, with some fluctuation

during 1.0-0.5 ka, aligning with minor increased greyscale reflectance over the same interval. Perhaps unsurprisingly the foraminifera per gram values previously described, closely follow the Ca/Ti curve, suggesting Ca in the core is linked to foraminifera per gram abundances.

Ba/Ti is a productivity measure utilised within the literature and shown to associate with organic matter (Thomson et al., 2006; Croudace and Rothwell, 2015). Ba/Ti ratios consistently display a saw-tooth nature, however within this there are a number of trends. During the early Holocene, mean values rise to ~9.2 ka and then drop at ~9.1 ka, from this point the Ba/Ti values rise to ~8.2 ka before dropping slightly across the early/mid-Holocene boundary (Figure 5.3-6). During the mid-Holocene the Ba/Ti ratios show a rise in values from ~8.1-7.0 ka, before levelling to ~5.5 ka with sawtooth variation. From ~5.5 ka, coinciding with other proxies (Ca/Ti, Si/Ti, S/Cl and S/Ti), the Ba/Ti ratio rises, peaking at ~5.3 ka. Elevated values largely continue to the end of the mid-Holocene, with an additional peak at ~4.4 ka. Over the late Holocene Ba/Ti values drop and decline to the modern, similar to S/Cl, S/Ti and Si/Ti records.

Si/Ti ratios can depict changing siliceous productivity and is used over Si/Al due to the low counts recovered at UPC 028 (Croudace and Rothwell, 2015). During the early Holocene records are relatively high and steady with minor saw tooth fluctuations up to the early/mid-Holocene boundary, where there is a slight rise in values (Figure 5.3-6). However, from the onset of the mid-Holocene Si/Ti values decline, reporting increasingly negative ratio values to ~7.0 ka. Between ~6.9-6.2 ka log-ratio values obtain a relatively steady state before dropping sharply at ~5.8 ka. Values then steadily increase over the next ~1.2 ky to ~4.6 ka before decreasing slightly to the end of the mid-Holocene. Over the late Holocene a general steady decline is observed with less significant variation in the saw-tooth pattern. There are a few punctuated decreases at ~0.9 and ~0.4 ka but these are on a less than centennial scale.

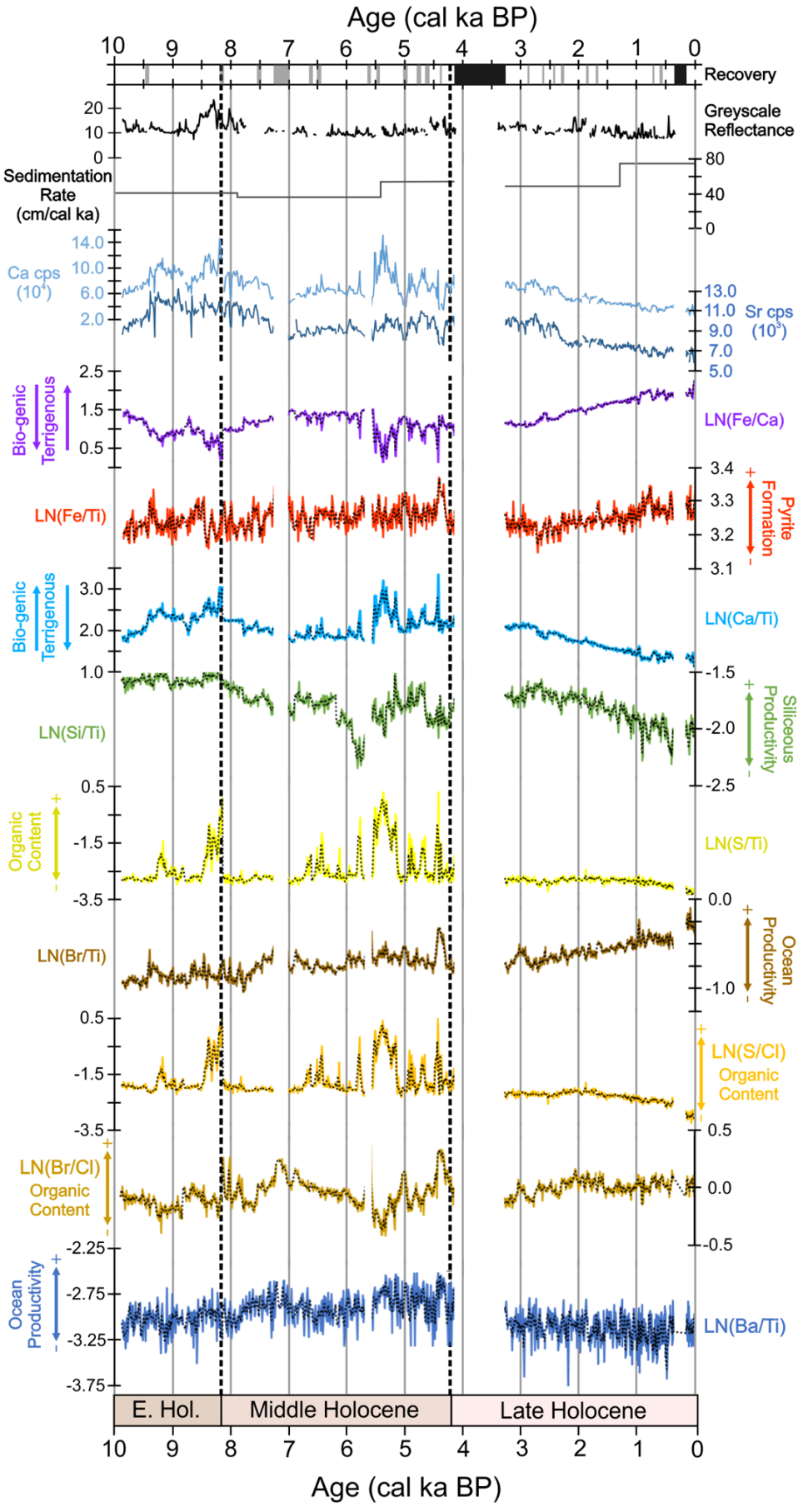

Figure 5.3-6 Greyscale reflectance, sedimentation rate based on radiocarbon dating, alongside ITRAX counts and ratios pertinent to sediment changes (Ca, Sr, Fe/Ca, Fe/Ti, Ca/Ti) and productivity changes (Si/Ti, S/Ti, Br/Ti, S/Cl, Br/Cl and Ba/Ti).

S/Ti and S/Cl records provide an indication on potential organic matter within the sediment, or possible pyrite preservation/formation (Thomson et al., 2006; Moreno et al., 2007; Croudace and Rothwell, 2015). S/Ti compares S to the clastic component, whilst S/Cl compares to sea-salt ratios within these marine cores (Passier et al., 1999; Thomson et al., 2006; Moreno et al., 2007; Croudace and Rothwell, 2015). The two records are dominated by the S signal, thus show almost identical curves, and will be discussed together. During the early Holocene a number of peaks are observed, the first is at approximately 9.2 ka, with a second larger series of peaks between 8.4 and 8.2 ka, coeval with Ca/Ti ratio peaks and rises in Ba/Ti ratios (Figure 5.3-6). At the onset of the mid-Holocene S/Ti and S/Cl ratios drop to pre-peak levels until approximately 6.8-6 ka, where the curves show a series of punctuated peaks, similar in scale to the peak at 9.2 ka, and again coeval with Ca/Ti. Over the remainder of the mid-Holocene, from 6.0-4.2 ka, there are numerous large spikes in S/Ti and S/Cl, with the most sustained falling between 5.5-5.0 ka. The shift in ratios is similar to those seen prior to the end of the early Holocene at 8.4-8.2 ka. Punctuated peaks continue beyond 5.0 ka to the core break, and end of the mid-Holocene, although at reduced magnitude with a notable peak at ~4.4 ka, aligning with Ca/Ti, Ba/Ti and the Br/Ti and Br/Cl records. After the core break at approximately 4.2 ka there is a ~900-year interval for which there was no available core. However, on the resumption of the record at ~3.3 ka the S/Ti and S/Cl values return to background levels, declining toward the modern and displaying little variation.

Br/Ti and Br/Cl log-ratios (Figure 5.3-6) provide insight into the preservation of organic carbon due to enrichment of Br alongside organic carbon, with the latter much like for S/Cl, used to highlight increases in Br relative to Cl found in seawater (Thomson et al., 2006; Agnihotri et al., 2008; Ziegler et al., 2008; Croudace and Rothwell, 2015). Early Holocene Br/Ti record observes some of the lowest values in the core, with slight increases in the log-ratio preceding S/Ti and S/Cl peaks at ~9.2 ka and ~8.5 ka. After ~8.0 ka Br/Ti values increase over a ~600-year interval, levelling out at ~7.0 ka. From 7.0-5.7 ka the record remains relatively stable before peaking at ~5.6 ka immediately prior to increases in Ca/Ti, Ba/Ti, S/Ti and S/Cl log-ratios. From ~5.6-4.2 ka Br/Ti values are slightly elevated, coinciding with the interval S/Ti and S/Cl are elevated significantly. The largest peak in Br/Ti ratio data is at ~4.4 ka and coincides with peaks in all productivity/organic content ITRAX log-ratios displayed in Figure 5.3-6. Into the

late Holocene, Br/Ti values increase steadily with shallowing depth to the core top, reflecting increasing Br counts to the surface, observed in Figure 5.3-5. Outside of a minor peak at 3.0 ka and 1.0 ka the profile shows little variation away from the increasing trend.

The Br/Cl record (Figure 5.3-5) shows little variation in the early Holocene with a slight decline in values to ~9.0 ka, before rising to a peak following the end of the early Holocene at ~8.0 ka. During the mid-Holocene the ratio fluctuates, showing an increasing trend to ~6.8 ka. Over the next 1 ky, values decline slightly before a sharp peak at ~5.6 ka, similar to the Br/Ti curve, and just prior to the Ca/Ti, S/Ti and S/Cl curves. An increasing trend in Br/Cl begins at ~5.4 ka, coeval with S/Ti and S/Cl peaks, and largely continues to the peak at ~4.4 ka seen also in the other productivity records. Values then drop to the end of the mid-Holocene and across the core break, on resumption of the record Br/Cl ratio values show an increasing trend to the modern, similar to that observed in the Br/Ti record.

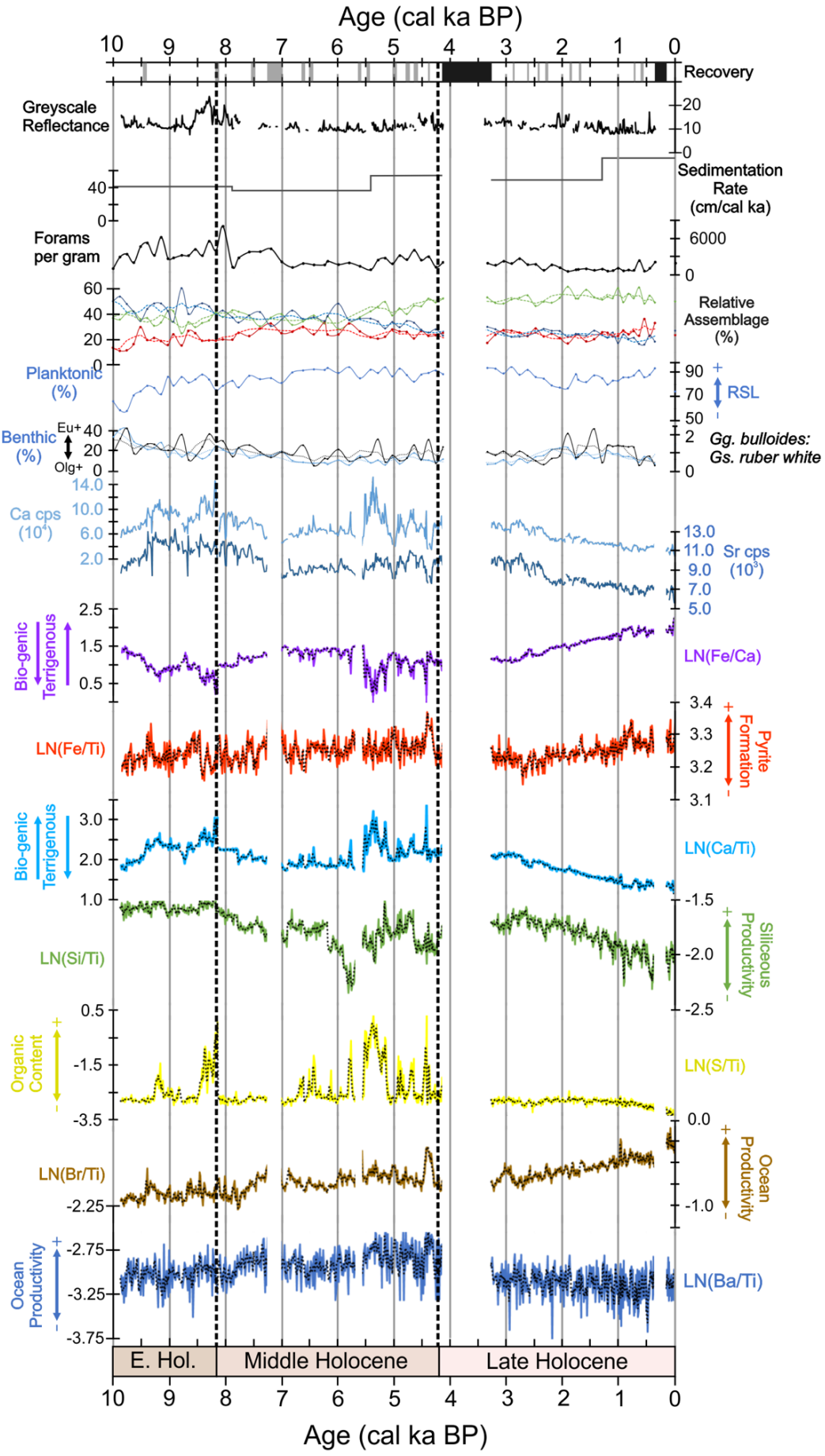

Figure 5.3-7 Summary figure of key ITRAX records, containing both sedimentary and productivity metrics, alongside the summary foraminifera information previously supplied.

5.4 Discussion

5.4.1 Palaeo-oceanography and palaeo-temperature record

As suggested by recent global modelling of southern hemisphere sub-tropical and temperate latitudes (Kaufman, McKay, Routson, Erb, Dätwyler, et al., 2020; Bova et al., 2021), a warming signal is observed over much of the Holocene, with early Holocene palaeotemperatures rising from the deglacial. Using Holocene proxies from the length and breadth of the western South Atlantic margin, and those generated by this study, we identify number of trends relating to changes in temperature and oceanography. This is key as it enables study of palaeo-BMC migration, a key mixing region for ocean circulation, with converging thermally contrasting currents (Stramma and England, 1999; Hernández-Molina et al., 2016; Piola and Matano, 2019). This was investigated using planktonic foraminiferal eco-groups and ratios, with strong species thermal latitudinal correlation originating from modern core top and plankton tow studies (Boltovskoy et al., 1996; Boltovskoy et al., 2000; Kucera, 2007). Additionally, $\delta^{18}O$ values are extracted from foraminiferal calcite, providing insight into past water column temperatures based on modern observations of dwelling depths (Birch et al., 2013). Used in conjunction these records enable reconstruction of palaeotemperature and palaeoceanography on the margin (Figure 5.4-1).

5.4.1.1 Early Holocene

During the early Holocene, a time of RSL rise globally and on the Uruguayan margin (Fairbanks, 1989; Bard et al., 1990; Pirazzoli, 1993; Mörner, 1996; Guilderson et al., 2000; Cavallotto et al., 2004; Stanford et al., 2011; Bender et al., 2013; Lantzsch et al., 2014; Prieto et al., 2017), a number of records suggest palaeotemperatures rise. The literature on the early Holocene suggests global warming, with the scale varying latitudinally and a stronger signal in the mid-high latitudes, particularly in the Northern Hemisphere (Kaufman, McKay, Routson, Erb, Dätwyler, et al., 2020; Bova et al., 2021).

The UPC 028 early Holocene record broadly shows decline in cold eco-group (polar and sub-polar species), alongside a drop in transitional species, with a doubling of warm eco-group individuals (i.e. sub-tropical and tropical species) (Figure 5.4-1). Simultaneous with the rapid increase in the number of warm eco-groups individuals, is a rapid rise in the proportion of right coiling *Gr.*

truncatulinoides occurs during the early Holocene. This sharp increase may imply a rapid transition during the early Holocene, with increasing dominance of warmer waters, sourced from the sub-tropical South Atlantic, to the site (Ujiié et al., 2010; Ujiié and Asami, 2014). This likely indicates a predominant migration of the BMC southward during the early Holocene, bathing the site in increasingly warmer BC waters.

Comparison with Brazilian assemblage studies within the early Holocene (Pivel et al., 2013; Portilho-Ramos et al., 2019; Frozza et al., 2020), sees loss or significant reduction of transitional or cold-water preference species, such as *Gc. inflata, N. incompta* and *N. pachyderma*. These species are replaced over this interval by tropical and sub-tropical forms including *Gr. menardii* and *Ge. calida*, species typically absent or in low abundances at UPC 028 (Pivel et al., 2013). The warming signal is not entirely unexpected after the transition from the deglaciation of the late Pleistocene into the early Holocene and this is reflected in the assemblage and isotope records of such sites (Pivel et al., 2013; Portilho-Ramos et al., 2019; Frozza et al., 2020). Consistency in the increasing warming trends coincides with a decrease in the productivity along the South Brazilian margin, observed through declining relative abundances of *Gg. bulloides* and *Gc. inflata,* that typically favour nutrient rich conditions (Lončarić et al., 2007; Storz et al., 2009; Schiebel and Hemleben, 2017), and coinciding with increases in oligotrophic forms like *Gr. menardii*, *Ge. calida/Ge. siphonifera* and *Gs. ruber* (Toledo, 2008; Pivel et al., 2013; Portilho-Ramos et al., 2019; Frozza et al., 2020). The mechanism for such a decline is changes to South Atlantic wind patterns, in particular a weakened Southern Westerly Wind Belt (SWWB), resulting in a strengthening of the BC, which in turn forces the BMC poleward and results in nutrient depleted waters on the South Brazilian margin (Toledo, 2008; Pivel et al., 2013; Portilho-Ramos et al., 2019). These records would seemingly agree with a strengthening of the BC and therefore a southern migration of the BMC over much of the Holocene, with associated impacts to the planktonic foraminifera assemblages and the ambient water temperature at site UPC 028.

Based on $\delta^{18}O$ measurements, mean SSTs at UPC 028 increase over the early Holocene (Figure 5.4-1), with a decrease in *Gs. ruber white* $\delta^{18}O$ values indicating rising temperatures. The *N. pachyderma* $\delta^{18}O$ values similarly show a large decline over the same interval, implying rising temperatures. In the modern these

two species have been shown to favour differing SSTs, leading to different timings of peak test fluxes to the seafloor, potentially explaining the large offsets between surface dweller values (Jonkers and Kučera, 2015; Kretschmer et al., 2018). Whilst it is not possible to directly measure seasonality, or annual variability, on this scale, the decreasing $\delta^{18}O$ values recorded by these two species suggest a shift to warmer surface waters across the early Holocene. Deeper dwelling species $\delta^{18}O$ values (Figure 5.4-1) also show a warming pattern, with average *Gc. inflata* $\delta^{18}O$ values declining (warming) to the early/mid-Holocene boundary, despite slight increases in the average MC and BC $\delta^{18}O$ values. A similar story is observed in the sub-thermocline species of *Gr. truncatulinoides*, average $\delta^{18}O$ values decline despite slight increases in the BC average. The MC specific average shows a $\delta^{18}O$ decrease (warming) between the two early Holocene averages, but a lack of data points between 9.8-8.4 ka makes assessment of this trend difficult. This overall trend in warming likely reflects increasing BC dominance over much of the early Holocene, potentially suggesting a shift in the BMC southward leading to less frequent incursions of MC over the location of UPC 028 during this interval.

Comparison with other $\delta^{18}O$ high-resolution datasets covering the early Holocene is possible by using the three *Gc. inflata* $\delta^{18}O_{(VPDB)}$ isotope curves taken from the Argentine and Brazilian margins (Figure 5.4-1) (Voigt et al., 2015). The first of the three sites, GeoB6211, is taken from the Brazilian margin at ~32.5 °S and is known to only experience BC conditions during the Holocene. GeoB6308 collected on the Argentine margin at ~39.3 °S, experiences only MC conditions during the Holocene. The most proximal site to this study, is core is GeoB13862-1 which sits within the modern BMC mixing regime on the Argentine margin at ~38 °S (Voigt et al., 2015). Comparison to these three datasets identifies uniform warming throughout the early Holocene, with all sites showing declining $\delta^{18}O$ values, implying warming of both the BC and MC. The UPC 028 *Gc. Inflata* $\delta^{18}O$ averages are similar in value to those of GeoB13862-1 at the beginning of the early Holocene, but approaching the 8.2 ka boundary, values are more comparable with GeoB6211. This shift indicates that on top of the early Holocene warming observed in the BC (GeoB6211) and MC (GeoB6308) records, UPC 028 also warms due to increasing influence of BC waters at this latitude. This is likely to a greater extent than the warming seen at GeoB13862-1, amplifying the warming toward the end of the early Holocene (Voigt et al., 2015). Additionally, a

palynological record from GeoB13862-1 (Gu et al., 2018c), shows broad agreement with Voigt et al., (2015) *Gc. inflata* records and the record from Site UPC 028. Their study suggests a generally stable position of the BMC at the beginning of the early Holocene, with decreasing presence of polar species over the early Holocene indicating southward shifts in BMC position, and increasing regional BC dominance (Gu et al., 2018c).

5.4.1.1.1 End early Holocene cooling

Northern hemisphere records show significant evidence for a cooling event at 8.2 ka, involving large volumes of meltwater entering the North Atlantic ocean and impacting thermocline circulation (Bond et al., 2001; Morrill et al., 2013; Aguiar et al., 2021). Wider South American records contain inconsistent evidence relating to the southern hemisphere response to northern hemisphere cooling surrounding 8.2 ka, indeed the response appears not to be ubiquitous across the South Atlantic (Ljung et al., 2008; Kilian and Lamy, 2012; Morrill et al., 2013; Pivel et al., 2013; Voigt et al., 2015; Gu et al., 2018c; García Chapori and Laprida, 2021; Aguiar et al., 2021). Within the UPC 028 record there is evidence for cooling around the 8.2 ka boundary, with warmer eco-groupings showing little variation, and temporary increases in colder and transitional eco-groups (Figure 5.4-1). Within productivity markers, discussed in the following section, *Gg. bulloides:Gs. ruber white* ratios increase alongside increases in benthic relative abundances, a rise in greyscale reflectance and foraminifera per gram numbers. Additionally, the proportion of right coiling *Gr. truncatulinoides* drops prior to the boundary (Figure 5.4-1). Combined, this indicates a brief cooling at the site based on assemblage data between the early and mid-Holocene.

Previous publications have presented evidence, utilising planktonic foraminiferal assemblage transfer functions on the proximal core GeoB2806-4, to generate western South Atlantic seasonal SST estimates (Chapori et al., 2015; García Chapori and Laprida, 2021). However, the low resolution record (~1 ky) means event confirmation is speculative (Chapori et al., 2015; García Chapori and Laprida, 2021). The high-resolution $\delta^{18}O$ record from GeoB13862-1 (Voigt et al., 2015), another proximal site with a wider interval surrounding the boundary, suggests cooling. Comparison within the study invokes BMC migration, with a brief BMC equatorward excursion occurring over ~8.7-7.8 ka, to enable cooling through greater MC influence. This cooling reverses the otherwise warming

trajectory, with a mechanism involving SWWB change to temporarily shift the BMC from its poleward migration (Voigt et al., 2015; Gu et al., 2018c). Critically, the cooling trends are not visible in the $\delta^{18}O$ records of GeoB6211 or GeoB6308, further north and south, suggesting cooling relates to confluence migration specifically (Voigt et al., 2015). GeoB13862-1 also has an associated palynological record in which eutrophic palynomorphs spike coevally with cooling, whilst freshwater algae remain low, implying a shift in nutrient state is related to cooler MC migration equatorward rather than terrigenous input (Gu et al., 2018c).

A final core suitable for evaluating the event is the LaPAS-KF02 record from the Brazilian margin (Pivel et al., 2013). The record, like GeoB6211, is under BC conditions entirely, however it shows cooling from ~10 ka to 8.2 ka before abrupt warming begins (Pivel et al., 2013). The authors attribute this cooling to upwelling within the South Brazil Blight, using shifts in wind forcing as a mechanism rather than thermocline circulation changes (Pivel et al., 2013). However this cooling does not align with GeoB6211, also under BC conditions and located to the south of LaPAS-KF02, which shows a distinct warming signal over the same interval suggesting this signal is localised (Pivel et al., 2013; Voigt et al., 2015).

Whilst a potential mechanism to explain all changes and their relative timings would be desirable, many complexities remain. Based on the data previously outlined from UPC 028 it is likely cooling is linked to changes in atmospheric circulation, potentially invoking localised upwelling and/or altering BMC locations briefly. These teleconnections would see variation in atmospheric structure and strength i.e. ITCZ position, trade wind strength and SWWB position, and would be impacted by meltwater events in the northern hemisphere (Alley et al., 1997; Bond et al., 2001; Debret et al., 2009; Stríkis et al., 2011; Morrill et al., 2013). Regional alteration to wider Atlantic Meridional Overturning Circulation (AMOC) cannot be ruled out, but this would likely to lead to a strengthened BC and warming along the western South Atlantic margin not seen in our site or others (Bond et al., 2001; Stríkis et al., 2011; Morrill et al., 2013; Chapori et al., 2015; Voigt et al., 2015; García Chapori and Laprida, 2021; Aguiar et al., 2021). Identifying with confidence the cooling within the UPC028 $\delta^{18}O$ isotopes is difficult due to the event lasting <1 ky and the isotopes achieving a ~0.6 ka resolution. A broader study could interrogate numerous Southern Atlantic records, which unlike the Northern Atlantic, has a heterogeneous response across the 8.2 ka

event, with some sites showing an increase in SSTs, or little to no change (Ljung et al., 2008; Morrill et al., 2013; Aguiar et al., 2021). Further interpretation of the UPC 028 record and this potential event will follow in the productivity section.

The proxy data generated suggests an overall warming occurs throughout the early Holocene, likely driven by Site UPC 028 experiencing increasing BC influence on top of global early Holocene warming (Figure 5.4-2) (Chapori et al., 2015; Voigt et al., 2015; Dauner et al., 2019; Kaufman, McKay, Routson, Erb, Dätwyler, et al., 2020; García Chapori and Laprida, 2021; Bova et al., 2021). There is some evidence of temperature decline prior to the 8.2 ka boundary in the higher resolution records, responding to northern hemisphere meltwater forcing (Stríkis et al., 2011; Morrill et al., 2013; Aguiar et al., 2021), which may involve a greater MC influence for a short period (Figure 5.4-2). However, resolving the short-term mechanism behind the cooling signal observed was beyond the scope of this study.

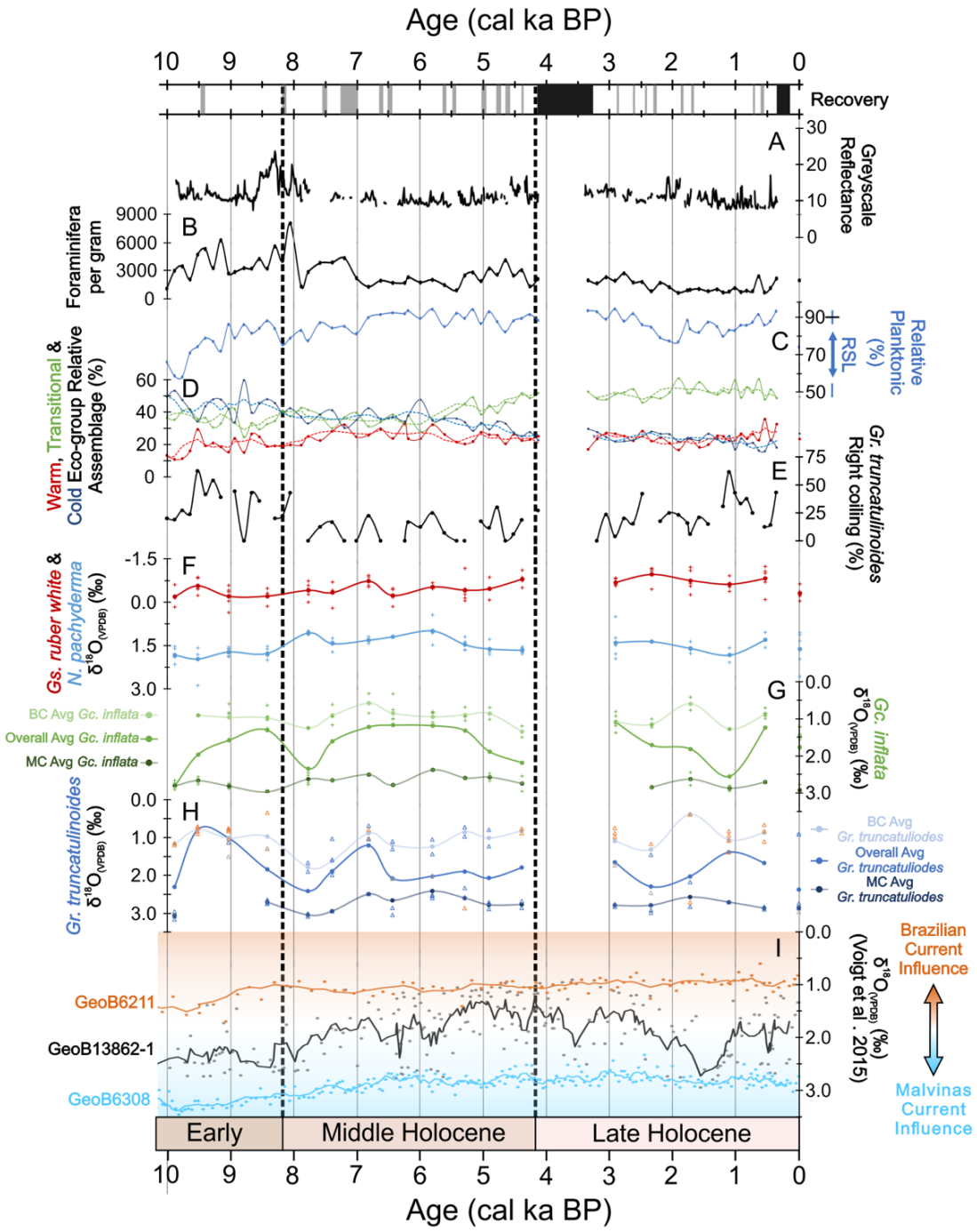

Figure 5.4-1 UPC 028 downcore records relating to oceanographic shifts. A) Greyscale core reflectance, with higher values indicating lighter colouring and likely increased carbonate content. B) Foraminifera per gram numbers, shifts to higher values indicate potential increases in productivity. C) Planktonic species %, a relative abundance metric and the inverse of benthic relative abundance. D) Relative abundance of warm (red), transitional (green) and cold (blue) planktonic foraminiferal eco-groups from assemblage counts, dashed lines are 3-point running average. E) Percentage of right coiling specimens of *Gr. truncatulinoides*. F) Surface dwelling species $\delta^{18}O_{(VPDB)}$ values: *Gs. ruber white* (red) and *N. pachyderma* (blue), raw data (points), mean values (line). G) *Gc. inflata* $\delta^{18}O_{(VPDB)}$, raw data (points) average MC data (>2 ‰, dark green line), BC data (<2 ‰, light green line), combined average (all data, mid-green line). H) *Gr. truncatulinoides* $\delta^{18}O_{(VPDB)}$ data, raw point data is split: right coiling (orange triangles), left coiling (blue triangles) and unclassified coiling (grey triangles). Average curves are similarly split to *Gc. inflata*. I) Voigt et al., 2015, isotope data for three sites with 5-point average lines. Dates recalibrated to the marine20 curve to align with dates for this study. BC influenced signified by orange colouring and blue for MC.

5.4.1.2 Mid-Holocene

The nature of mid-Holocene climate is debated within the literature, with competing theories on the occurrence of a potential Holocene Climatic Optimum. This optimum is postulated to involve a global warming signal prior to late Holocene cooling, however the extent of warming and its ubiquity across latitudes is contested (Mojtahid et al., 2013; Bader et al., 2020; Kaufman, McKay, Routson, Erb, Dätwyler, et al., 2020; Bova et al., 2021). The timing of this event, starting in the early Holocene and concluding within the mid-Holocene, is commonly inferred to fall between 10.0-6.0 ka BP (Marcott et al., 2013; Liu et al., 2014; Kaufman, McKay, Routson, Erb, Zhilich, et al., 2020; Kaufman, McKay, Routson, Erb, Dätwyler, et al., 2020; Bova et al., 2021). From this optimum, temperatures are inferred to cool over the remaining mid-Holocene and into the late Holocene, prior to anthropogenic warming (Marcott et al., 2013; Liu et al., 2014; Kaufman, McKay, Routson, Erb, Dätwyler, et al., 2020; Bova et al., 2021).

The UPC 028 record does suggest the early Holocene warming trend continues into the mid-Holocene, with a sustained decline of cold eco-groups across the 4-ky interval (Figure 5.4-1). This decline initially favours warm eco-groups, showing relative abundance increase until ~6.0 ka. However, from ~6.0 ka the transitional eco-group begins a sustained rise (~12 % between ~6.0-4.2 ka), to comprise half the relative abundance. Whilst this rise takes place, warm eco-groups are maintained, with continued loss of cold eco-groups implying mid-Holocene warming, and potential shifts in nutrient states to favour the nutrient-favouring, transitional species rise. Alongside the transitional species rise, increases in foraminifera per gram values and fluctuations in planktonic foraminifera percentage during a highstand period (Guilderson et al., 2000; Cavallotto et al., 2004; Angulo et al., 2006; Bracco et al., 2011; Bender et al., 2013; Martínez and Rojas, 2013; Bracco et al., 2014), indicate increases in the proportion of benthic foraminifera and imply more nutrient rich waters from BMC variability (Figure 5.4-2). The *Gr. truncatulinoides* record, where available, contrasts assemblage eco-groups indicating a cooler state over much of the mid-Holocene, with right coiling percentages often less than 25 %. The two opposing trends are difficult to reconcile, the eco-groups suggesting increasing temperatures and/or BC influence, whilst coiling implies greater involvement of MC at UPC 028. Left coiling variants occur within the BC alongside right coiling forms, raising the possibility that another variable causes diminished numbers of the right coiling

form during a BC dominant phase (Ujiié and Asami, 2014). Determining the nature of this shift requires further investigation.

In agreement with the warmer eco-group assemblage in the mid-Holocene, $\delta^{18}O$ records of *Gs. ruber white*, *N. pachyderma*, *Gc. inflata* and *Gr. truncatulinoides* broadly decrease in values, implying warming over the mid-Holocene (Figure 5.4-1). The surface dweller *Gs. ruber white* records average mid-Holocene $\delta^{18}O_{(VPDB)}$ values of ~-0.5 ‰, increasing from early Holocene average values of ~-0.3 ‰, the equivalent of ~0.9 °C increase. *N. pachyderma* increases in average $\delta^{18}O_{(VPDB)}$ values from an early Holocene value of ~1.8 ‰ to mid-Holocene values of ~1.3 ‰, an increase of ~2.1 °C. Both values suggest significant average warming for species known to seasonally favour differing times of year and SSTs (Jonkers and Kučera, 2015; Kretschmer et al., 2018). Whilst the $\delta^{18}O$ averages decrease (warm) in both species the trends observed are slightly different, with deviation of these two SST tracers displaying a greater $\delta^{18}O$ offset from ~5.8 ka into the late Holocene.

Looking to the thermocline dwelling *Gc. inflata*, the changes over the mid-Holocene see an average warming pattern from early Holocene average values ~1.9 ‰ $\delta^{18}O_{(VPDB)}$ declining to ~1.6 ‰ $\delta^{18}O_{(VPDB)}$, warming ~1.3 °C (Figure 5.4-1). Overall, isotopes suggest BC dominance over the mid-Holocene, with a higher proportion of data points dragging the average $\delta^{18}O$ values lower. However, toward the end of the mid-Holocene, and after ~6.0 ka, increasing MC influence is apparent with rising $\delta^{18}O$ values. Overall, the warming trend would agree with the mid-Holocene findings of Voigt et al., (2015). Within their study a similar shift in $\delta^{18}O_{(VPDB)}$ values of *Gc. inflata* specimens was observed at site GeoB13862-1, roughly two degrees to the south of UPC 028 (Voigt et al., 2015). This increase in BC influence is explained by a ~1-1.5° shift of the BMC southward, compared to the early Holocene, using a weakening of the SWWB to permit BMC migration (Figure 5.4-2) (Voigt et al., 2015). After ~6.0 ka increased isotopic variability suggests increased MC involvement, potentially triggered by greater dynamism of the BMC along the margin to maintain both warm and cold temperatures, potentially akin to modern seasonality/inter-annual variation (Olson et al., 1988; Voigt et al., 2015; Gu et al., 2018c; Piola and Matano, 2019).

Comparisons between early and mid-Holocene *Gr. truncatulinoides* averages is difficult due to the limited number of MC representatives in the early Holocene.

This lack of MC values is likely the reason for the apparent rise in in $\delta^{18}O_{(VPDB)}$ values from ~1.5 ‰ in the early Holocene, to 1.9 ‰ in $\delta^{18}O_{(VPDB)}$ in the mid-Holocene, cooling by ~1.9 °C. The *Gr. truncatulinoides* BC and MC $\delta^{18}O$ isotope records, as with the *Gc. inflata* records, show an overall warming trend throughout the mid-Holocene. This is apparent in the BC and MC curves, although the mean curve shows a significant $\delta^{18}O$ shift, in part due to the number of individuals with a BC signature. This signature would largely agree with greater BC involvement over the site during the mid-Holocene fitting with the afore mentioned ~1-1.5° poleward BMC shift (Figure 5.4-2) (Voigt et al., 2015).

In all of the isotope records produced by this study there is a shift from roughly 6.0 ka. The trend of divergent $\delta^{18}O$ values first observed between the two surface dwelling species at ~5.8 ka is also present between the specific BC and MC curves of *Gc. inflata*, and again seen in the *Gr. truncatulinoides* data (Figure 5.4-1). This deviation of *N. pachyderma* from the continually warming *Gs. ruber white*, and the MC classified *Gc. inflata* and *Gr. truncatulinoides* from their BC equivalents, suggests increasing temperature variability over the site. This wider range of recorded $\delta^{18}O$ values between species and within species indicates increasing oceanographic dynamism on the western South Atlantic margin. Timing of this $\delta^{18}O$ widening of values is coincident with a rapid increase in transitional foraminifera at ~6.0 ka, giving further credence to establishment of more intense BMC mixing over the site (Figure 5.4-2).

Similar findings have been made at GeoB13862-1 using dinoflagellates to assess surface waters, with increased dynamism in surface waters from ~6.3 ka, evidenced by the dominance of cosmopolitan species (Gu et al., 2018c). Additional evidence for this establishment comes from the near shore site GeoB13801-2, which records a high-energy shelf regime beginning after ~7.2 and continuing across the mid-Holocene (Bender et al., 2013). The mechanism behind the increased variation in isotope components, and rapid rise in transitional relative abundance is unclear, but aligns well with records of increasing ENSO variability (Moy et al., 2002; Gu et al., 2018c). This combined with a fluctuating SST gradient over the mid-late Holocene would enable shifts in the SWWB to impact the BMC position, migrating further southward with increases in the meridional temperature gradient and similarly northward with decreases to the gradient (Varma et al., 2012; Voigt et al., 2015). This increased

ENSO variability would potentially impact these SST gradients, and increase BMC position variability or increase the seasonal migration distances of the BMC from ~6.0 ka (Figure 5.4-2). The latter position would enable a wider range of temperatures and eco-groups to be recorded, but would particularly favour transitional species, like *Gc. inflata*, *Gt. glutinata* and *Gg. bulloides*, suited to a wider set of regional environmental characters across seasons, as seen in modern transects (Boltovskoy et al., 1996; Boltovskoy et al., 2000).

5.4.1.3 Late Holocene

The global trends within the late Holocene proxy record for the southern mid-latitudes show a cooling trend from the Holocene Climatic Optimum (Kaufman, McKay, Routson, Erb, Dätwyler, et al., 2020; Bova et al., 2021). This trend continues until anthropogenic CO_2 emissions rise, reversing this long term trend causing warming in the industrial era (Marcott et al., 2013; Bender et al., 2013; Liu et al., 2014; Kaufman, McKay, Routson, Erb, Dätwyler, et al., 2020; Bova et al., 2021). The variability of the BMC during the late Holocene has previously been highlighted, with position of this confluence more volatile during this interval (Bender et al., 2013; Voigt et al., 2015; Gu et al., 2018c).

The UPC 028 record provides further evidence of variability with the maintenance of high abundance of transitional species throughout the period (Figure 5.4-1). The warm and cold eco-groups show minor fluctuations, showing inverse relationships with one another. Similarly, the *Gr. truncatulinoides* coiling direction displays elevated variability when compared to the mid-Holocene record (Figure 5.4-1). Combined with the isotope records we see continuation of surface dweller values separation from the end of the mid-Holocene (Figure 5.4-1). Maintaining separation between the values of surface dwelling species and between BC and MC representatives of deep dwelling species, implies mid-Holocene BMC variability continues into the late Holocene (Figure 5.4-2). Similar variability has been suggested in the Sub-Tropical Shelf Front (STSW) for the last 4 ka (Bender et al., 2013), and within the BMC from the mid-Holocene onward (Chiessi et al., 2014; Voigt et al., 2015; Gu et al., 2018c).

Both surface dwelling species indicate a slight cooling (~0.3 ‰ $\delta^{18}O_{(VPDB)}$ or ~2 °C in surface dwellers) between ~2.3-1.0 ka (Figure 5.4-1), potentially implying a short northward migration of average BMC position, coeval with cold eco-groups showing higher abundance than the warmer counterparts (Figure 5.4-2).

Similarly, the deeper dwelling species averages shift to values more representative of MC conditions. This is also seen in GeoB13862-1 records from Voigt et al., (2015) and Gu et al., (2018), which both imply wider MC influence on the western South Atlantic margin during this interval, perhaps linked to a weakening BC current reported from sites on the Brazilian margin (Figure 5.4-2) (Chiessi et al., 2014; Voigt et al., 2015; Gu et al., 2018c). Following this late Holocene cooling interval, the majority of isotope records return to warmer values and cold eco-groups decline in favour of warm eco-groups, whilst the transitional eco-group is maintained (Figure 5.4-1). This indicates poleward migration of BMC average position over the last 1.0 ka to south of the present-day position, before a slight migration north and establishment of modern conditions in the core top data (Figure 5.4-2). This latter movement is indicated by loss of warm eco-group abundance and increases in the cold eco-group, alongside average isotopes showing a cooling pattern over the final ~300 years to the modern (Figure 5.4-1).

As stated within the mid-Holocene, from ~6.0 ka it appears the BMC mixing zone expands influencing a greater area seasonally, or remains the same size but migrates its average position further in a more vigorous manner enabling sites to experience BC or MC end members settings on a seasonal or inter-annual basis (Figure 5.4-2). This explains the elevated transitional eco-group, limited change in warm and cold eco-groups, and separation between *Gs. ruber white* and *N. pachyderma* $\delta^{18}O$ isotopes, alongside the BC and MC isotopes of *Gc. inflata* and *Gr. truncatulinoides*. There appears to be a northward BMC migration during the late Holocene, between 2.3-1.0 ka, supported by similar findings in the literature (Chiessi et al., 2014; Voigt et al., 2015; Gu et al., 2018c), before a generally southward migration in the last 1.0 ka.

5.4.1.4 Holocene Palaeotemperature summary

The overall palaeo-oceanographic and palaeotemperature Holocene trends discerned from site UPC 028 are schematically visualised in Figure 5.4-2. Initially, this involves early Holocene BMC poleward shifts into the mid-Holocene, leading to greater influence of the warmer BC at the site, likely driven by a reduction in SWWB strength (Pivel et al., 2013; Voigt et al., 2015; Gu et al., 2018c). At the end of the early Holocene (~8.2 ka), there is evidence of brief cooling within the proxies, likely triggered by Northern Hemisphere meltwater impacting AMOC and atmospheric teleconnections (Bond et al., 2001; Debret et al., 2009; Stríkis et al.,

2011; Morrill et al., 2013; Chapori et al., 2015; Voigt et al., 2015; García Chapori and Laprida, 2021; Aguiar et al., 2021). However, definitive event determination requires increasing UPC 028 record resolution and additional analyses.

Mid-Holocene results suggest warming continues from the early Holocene, with further decline of cold eco-groups and the continued BC dominance. During this interval the BMC likely reached its most southerly position, due to a weakened SWWB (Voigt et al., 2015; Gu et al., 2018c). However, from ~6.0 ka a change is observed with increasing transitional eco-group dominance and separation of $\delta^{18}O$ records, implying a change in oceanographic conditions. Surrounding studies suggest increased oceanic dynamism and the intensification of oceanic mixing (Bender et al., 2013; Voigt et al., 2015; Gu et al., 2018c). This boosts MC influence on UPC 028, enabling establishment of conditions favourable to transitional species and a broadening range of $\delta^{18}O$ values. The timing of this mixing intensification is coeval with increased ENSO intensity and variability (Moy et al., 2002). This is the likely mechanism driving change over the end of the mid-Holocene, impacting SST gradients that determine the SWWB strength and position, and thus enabling greater seasonal and inter-annual variability within the BMC (Moy et al., 2002; Voigt et al., 2015; Gu et al., 2018c).

The late Holocene UPC 028 record continues the mid-Holocene trends, with transitional eco-group dominance maintained over the period. $\delta^{18}O$ isotopes remain offset from one another, implying the volatility and variability of BMC position continues. There are some subtle variations in the warm and cold eco-groupings, showing inverse changes indicating late Holocene cooling, and a northward BMC shift between 2.3-1.0 ka. This aligns with cooling in the Voigt et al., (2015) and UPC 028 $\delta^{18}O$ isotope records, alongside palynological shifts that corroborate cooling and northward BMC shift between 2.3-1.0 ka (Gu et al., 2018c). The mechanism behind this migration may be linked to a weakening BC, possibly tied to ocean circulation periodicity as hypothesised by Chiessi et al., (2014), enabling the northward migration of the BMC. Similarly, the coincident increase in ENSO events may have enabled a northward migration of the average BMC with decreased meridional SST gradients, through a brief equatorward shift of the annual mean SWWB position (Moy et al., 2002; Varma et al., 2012; Voigt et al., 2015; Gu et al., 2018c). After ~1.0 ka, a warming trend returns to the UPC 028 isotope record, with rising warm eco-group abundances, implying southward

BMC migration once again (Bender et al., 2013; Voigt et al., 2015; Gu et al., 2018c; García Chapori and Laprida, 2021).

The complex palaeo-oceanographic Holocene history of UPC 028 sees numerous BMC migrations, likely influenced by multiple changing atmospheric-ocean processes that facilitate confluence movement. These processes are often interlinked in the global atmospheric-ocean circulation system and add complexity to the oceanographic setting of UPC 028. Reconstructions utilising planktonic foraminiferal assemblages and isotopes do present a readily available proxy to track BMC movements. However, a higher density of sampling along the South Atlantic margin would enable better disentanglement of the palaeotemperature and palaeo-oceanographic signals of this highly variable confluence.

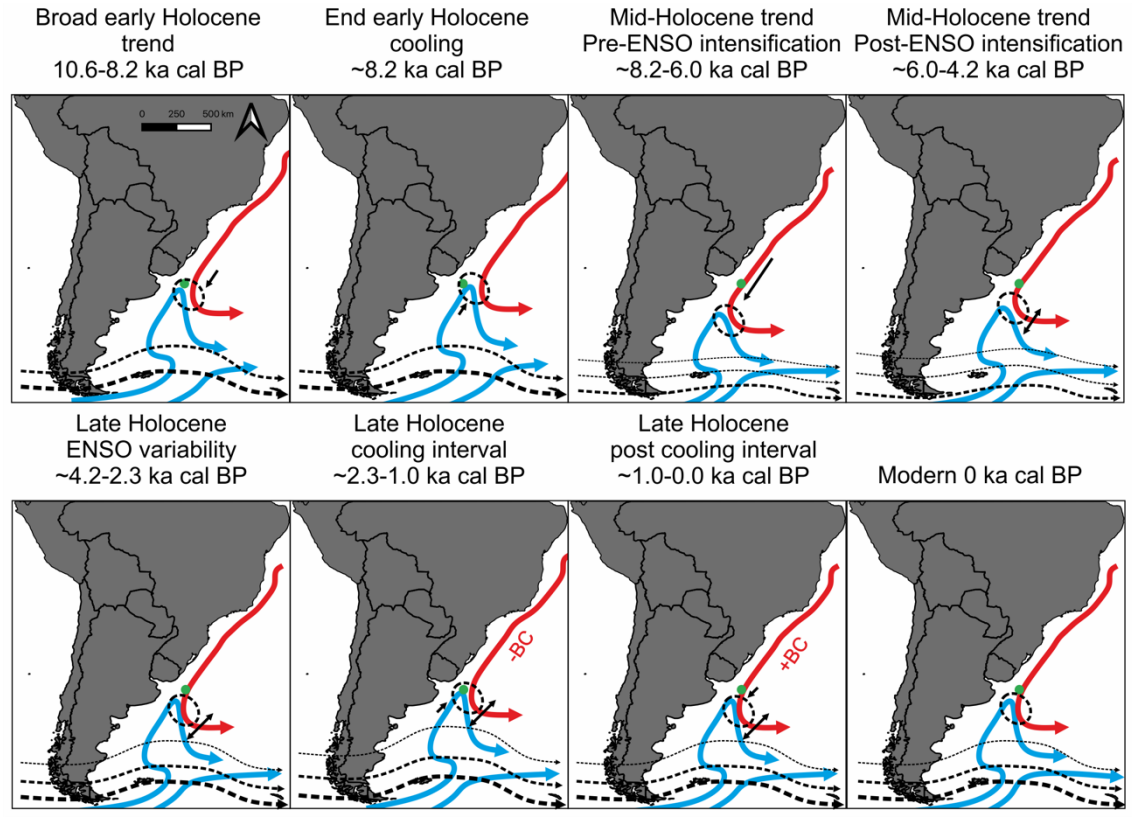

Figure 5.4-2 Schematic storyboard for BMC migration over the Holocene. General early Holocene trend is for southward BMC migration as UPC 028 warms. Immediately prior to the early-mid-Holocene boundary some northward migration and cooling is suggested. The first half of the mid-Holocene sees South Westerly Wind Belt (SWWB) suppression, leading to further BMC southward migration. From ~6.0 ka, increasing El Niño Southern Oscillation (ENSO) drives increased seasonal position variability. Into the late Holocene variability continues, with a lowering of the SST gradient resulting in SWWB expansion. Combined with BC weakening between ~2.3-1.0 ka leads to cooling at UPC 028 and brief northward BMC migration, prior to establishment of modern conditions from ~1.0 ka.

5.4.2 Holocene productivity signals

The BMC is comprised of two water masses that contrast in temperature and salinity, but also in their nutrient content (Boltovskoy et al., 2000; Brandini et al., 2000; Garcia et al., 2004; Saraceno et al., 2005; Piola and Matano, 2008). This influence of nutrients, alongside temperature, is a factor that leads to differing faunas dominating either side of the BMC (Boltovskoy et al., 1996; Boltovskoy et al., 2000). Changes in BMC location therefore will impact the nutrient availability, and thus the faunas present. Here we seek to understand this impact and the effect this has on associated overlying faunas at UPC 028, recording these shifts over the Holocene. Figure 5.4-3 provides a summary of the main productivity proxies alongside reference to a plot in the ITRAX summary (Figure 5.3-7).

5.4.2.1 Productivity prior to 6.0 ka

Previous studies on the western South Atlantic margin have utilised a number of records to infer shifts in productivity through time (Toledo, 2008; Portilho-Ramos et al., 2015; Gu et al., 2017; Gu et al., 2018c; Gu et al., 2018b; Gu et al., 2018a; Portilho-Ramos et al., 2018; Portilho-Ramos et al., 2019; Frozza et al., 2020). Broad scale records extending back into the Pleistocene show faunal turnover from more eutrophic conditions in the glacial periods compared to more nutrient depleted records during the inter-glacials right along the margin (Portilho-Ramos et al., 2015; Gu et al., 2017; Pereira et al., 2018; Portilho-Ramos et al., 2018; Gu et al., 2018a; Lessa et al., 2019; Portilho-Ramos et al., 2019; Frozza et al., 2020). As such it is clear over long timescales the margin displays shifts between eutrophic and oligotrophic states, with past studies implying a number of mechanisms including oceanographic migration (Toledo, 2008; Gu et al., 2018c; Frozza et al., 2020), onset of shelf break upwelling (Portilho-Ramos et al., 2015; Gu et al., 2017; Pereira et al., 2018) and the intrusion of PPW (Gu et al., 2018c; Portilho-Ramos et al., 2019). The nature of these mechanisms is invariably interlinked with changes in atmosphere circulation influencing shifts in oceanographic currents, alongside RSL rise, meaning sites previously under one nutrient regime will switch to a new set of conditions.

These shifts are not entirely coeval along the western South Atlantic margin, with decline from a eutrophic state first observed at ~11.0 ka in some Brazilian margin planktonic foraminiferal assemblages, and continuing to the end of the mid-Holocene (Toledo, 2008; de Oliveira Lessa et al., 2014; Portilho-Ramos et al.,

2019; Frozza et al., 2020). This is evidenced in records by relative abundance losses of eutrophic favouring *Gg. bulloides* whilst the oligotrophic favouring *Gs. ruber white* increases, implying a shift toward more oligotrophic states north of the study region over the Holocene. Looking to other proxies there appears to be consensus in dinoflagellate records from nearby sites, indicating eutrophic conditions for much of the early Holocene, before eutrophic dinocyst decline in the mid-Holocene (Gu et al., 2017; Gu et al., 2018c). The proximal site, GeoB13862-1 dinoflagellate record, suggests eutrophic conditions were present as late as ~5.7 ka, with a particularly highly eutrophic environment between 6.3-5.7 ka, on the Argentine margin south of the study region (Gu et al., 2018c). This site also provides biogenic opal and Si/Al records that decline over much of the early Holocene, prior to spikes in the mid-Holocene roughly coeval to the high eutrophic period (Voigt et al., 2013; Gu et al., 2018c). Within the UPC 028 record, a background of largely declining eutrophic conditions is observed in numerous proxy records over the course of the early and mid-Holocene to ~6.0 ka. This is seen most clearly in the declining cold eco-groups, increasing warm eco-groups, the decline in the *Gg. bulloides:Gs. ruber white* ratio, drops in the relative abundance of benthic foraminifera and drops in the siliceous productivity indicators from the beginning of the record to ~6.0 ka (Figure 5.4-3).

UPC 028 *Gs. ruber white* $\delta^{13}C$ records over the early and mid-Holocene involve a rise in values coeval with reported warming, before declining into the late Holocene (Figure 5.4-3). This suggests decline in available nutrients alongside warming, from a more eutrophic state as oligotrophic BC waters become more prevalent, particularly over warmer months during peak test production (Brandini et al., 2000; Kretschmer et al., 2018; Piola and Matano, 2019). *N. pachyderma* produces a lower average set of $\delta^{13}C$ values than *Gs. ruber white*, which indicates greater influence of the nutrient enriched MC during test production in seasonally cooler months, alongside the cooler recorded temperatures (Jonkers and Kučera, 2015; Kretschmer et al., 2018; Paniagua et al., 2018; Piola and Matano, 2019). The *N. pachyderma* record shows little variability over the early Holocene prior to a drop in $\delta^{13}C$ values into the mid-Holocene (Figure 5.4-3), possibly linked to a reported 8.2 ka temperature minima (Chapori et al., 2015; García Chapori and Laprida, 2021). This could indicate a brief increase in seasonal MC influence, increasing nutrient availability. Despite this brief dip in values, *N. pachyderma* $\delta^{13}C$ values slightly increase over the mid-Holocene, suggesting a decrease in

nutrient availability throughout the interval, and probable move to more mesotrophic conditions.

Fe/Ca is a widely used ratio of biogenic carbonates against detrital clays to determine terrigenous sediment input to a site (Rogerson, Rohlin, et al., 2006; Rogerson, Weaver, et al., 2006; Govin et al., 2012; Croudace and Rothwell, 2015). Values are typically higher near the continental shelf due to influence of siliciclastic content and proximity to fluvial sources, versus the biogenic calcium carbonate dominance found further offshore (Govin et al., 2012). Increases in the ratio value on the continental shelf imply increasing terrestrial input, with invariant Fe counts coinciding with decreasing Fe/Ca, suggesting increasing biogenic carbonate dominance (Croudace and Rothwell, 2015). The trend in UPC 028 sees increasing biogenic influence over the early Holocene, particularly approaching the mid-Holocene boundary at 8.2 ka, and following the trend in foraminifera per gram and greyscale reflectance, implying greater biogenic carbonate content. The ratio value then returns to pre-event levels and largely is maintained to ~6.0 ka. Another biogenic/terrigenous indicator is the Ca/Ti ratio, Ti is used in preference to Fe in some studies due to the inert nature of Ti compared to Fe, which can be remobilised (Piva et al., 2008; Croudace and Rothwell, 2015). Within the South Atlantic Ocean Ca/Ti (inverse of Ti/Ca in Govin et al., 2012) and Fe/Ca ratio trends are similar in surface sediments, Ca/Ti ratios display lower values proximal to the continents and higher values approaching the mid-Atlantic ridge with decreasing siliciclastic input (Govin et al., 2012). The early and mid-Holocene variance in Ca/Ti mirrors the Fe/Ca values, with increasing biogenic influence to the 8.2 ka boundary, potentially indicating increases in surface productivity, before declining to pre-event levels toward 6.0 ka.

The cores show a number of spikes in the S/Ti, S/Cl and Br/Cl values during the early Holocene, indicating potential increases in organic content within the core. Both S/Ti and S/Cl ratios can be used as markers for the presence of authigenic pyrite and/or an increase in the deposition of organic matter (Thomson et al., 2006; Croudace et al., 2006; Moreno et al., 2007; Croudace and Rothwell, 2015; Shi et al., 2016). A lack of significant variation in the Fe/Ti suggests little enrichment in Fe expected alongside pyrite formation, implying that whilst organic matter content increases during these peaks, associated pyrite is not formed (Thomson et al., 2006; Moreno et al., 2007; Croudace and Rothwell, 2015). It is

also possible the covarying peaks of Ca/Ti and S/Ti reflect the formation of gypsum ($CaSO_4 \cdot 2H_2O$). Gypsum has been found in marine settings associated with evaporitic brines, volcanogenic material, methane hydrate settings, the sulphate-methane transition in deep water systems, and tied to the dissolution of foraminifera (Blanchet et al., 2012; Lin et al., 2016). The first three settings seem unlikely for UPC 028 based on the core locale, with the latter requiring further investigation using a full suite of geochemical analyses including: Total Organic Carbon and Total Organic Sulphur amongst others. Gypsum may also form as a result of core storage, when reduced sulphur is oxidised, alongside organic matter, potentially leading to dissolution of susceptible planktonic foraminifera (Blanchet et al., 2012). Formation in core storage is unlikely as would likely involve oxidation of pyrite, preserving the Fe and S relationships, with the core not seeing coeval spikes in Fe (Figure 5.3-5 and Figure 5.3-6) (Blanchet et al., 2012). Definitively determining whether gypsum is present would require resampling of the core as washed samples are unsuitable for such analyses, however no gypsum crystals were visible during counts. Species diversity also appears to be maintained, with dissolution of susceptible species expected to reduce diversity (Figure 5.3-3) (Schiebel and Hemleben, 2017). Additionally, foraminiferal counts per gram increase alongside the Ca/Ti and S/Ti peaks, and planktonic percentages are maintained, suggesting dissolution is not significant enough to cause loss of foraminifera (Figure 5.3-7) (Blanchet et al., 2012).

Ocean productivity measures like Ba/Ti and Br/Ti show some coeval fluctuations and are contemporaneous with spikes in Ca/Ti and declines in Fe/Ca (Figure 5.3-7), suggesting marine biogenic involvement rather than terrestrial input (Croudace and Rothwell, 2015). The increase in S/Cl and S/Ti ratio values alongside foraminifera per gram values, Ca/Ti ratio increases, and TOC and $CaCO_3$ % from proximal sites (Voigt et al., 2013), suggest an increase in overlying surface productivity to the end of the early Holocene, before reverting back after the 8.2 ka cooling. Interestingly the Si/Ti values, a siliceous productivity metric (Marsh et al., 2007; Agnihotri et al., 2008; Croudace and Rothwell, 2015), decline after the early-mid-Holocene boundary, indicating less siliceous productivity, and a shift away from eutrophic conditions over the mid-Holocene.

Despite declining nutrient trends between 10.0-6.0 ka, coeval spikes in greyscale reflectance, foraminifera per gram values, and ITRAX ratios indicate an increase in carbonate content in a potential eutrophic event surrounding the early-mid-

Holocene boundary, (~8.4-8.0 ka) (Figure 5.4-3) (Morrill et al., 2013; García Chapori and Laprida, 2021; Aguiar et al., 2021). This would tie with the short-lived cooling interval discussed above and hypothesised in a number of papers (Pivel et al., 2013; Chapori et al., 2015; García Chapori and Laprida, 2021). Similarly, there is evidence of a brief BMC northward migration, bringing increased MC nutrient rich waters, before persistent southward displacement of the BMC into the mid-Holocene (Voigt et al., 2015; Gu et al., 2018c). Other evidence for this 8.2 ka cooling, but nutrient rich, event from UPC 028 proxies include: increases in benthic relative abundances, cold eco-groups briefly resurging before declining in the mid-Holocene, and sustained high *Gg. bulloides:Gs. ruber white* values. Combined this implies a more eutrophic state (Figure 5.4-3). Aforementioned shifts in planktonic foraminiferal $\delta^{13}C$ values, notably the cooler temperature favouring *N. pachyderma* and the two deeper dwelling taxa (*Gc. inflata and Gr. truncatulinoides*), potentially signify a temporary shift toward eutrophic conditions during this period. This combined with the contrary trend observed in *Gs. ruber white* $\delta^{13}C$ isotopes may signify influx of nutrients, possibly through increased MC influence, outside of peak *Gs. ruber white* fluxes during summer months (Figure 5.4-3) (Jonkers and Kučera, 2015; Kretschmer et al., 2018). The spikes in numerous ITRAX elemental ratios i.e. Ca/Ti, S/Ti, Si/Ti and Ba/Ti and support from surrounding studies (Pivel et al., 2013; Voigt et al., 2015; Gu et al., 2018c; García Chapori and Laprida, 2021), imply an influx of nutrients and increase in surface productivity, suggesting brief MC dominance at the site.

This shift from eutrophic states occurs during a time of relative sea level rise, and typically continental shelf flooding would decrease the nutrient content reaching the site, as terrestrial sources become more distal (Bender et al., 2013; Prieto et al., 2017; Gu et al., 2018a). Additionally, the predominant direction of BMC migration observed throughout the early and mid-Holocene is southward, increasing dominance of the warmer, nutrient poor BC current over the site and wider Uruguayan margin (Voigt et al., 2015; Gu et al., 2018c). As such the prevailing move away from eutrophic conditions, with the exception of a brief resurgence of eutrophy and MC influence (8.4-8.0 ka), follows reconstructed southward BMC migratory patterns.

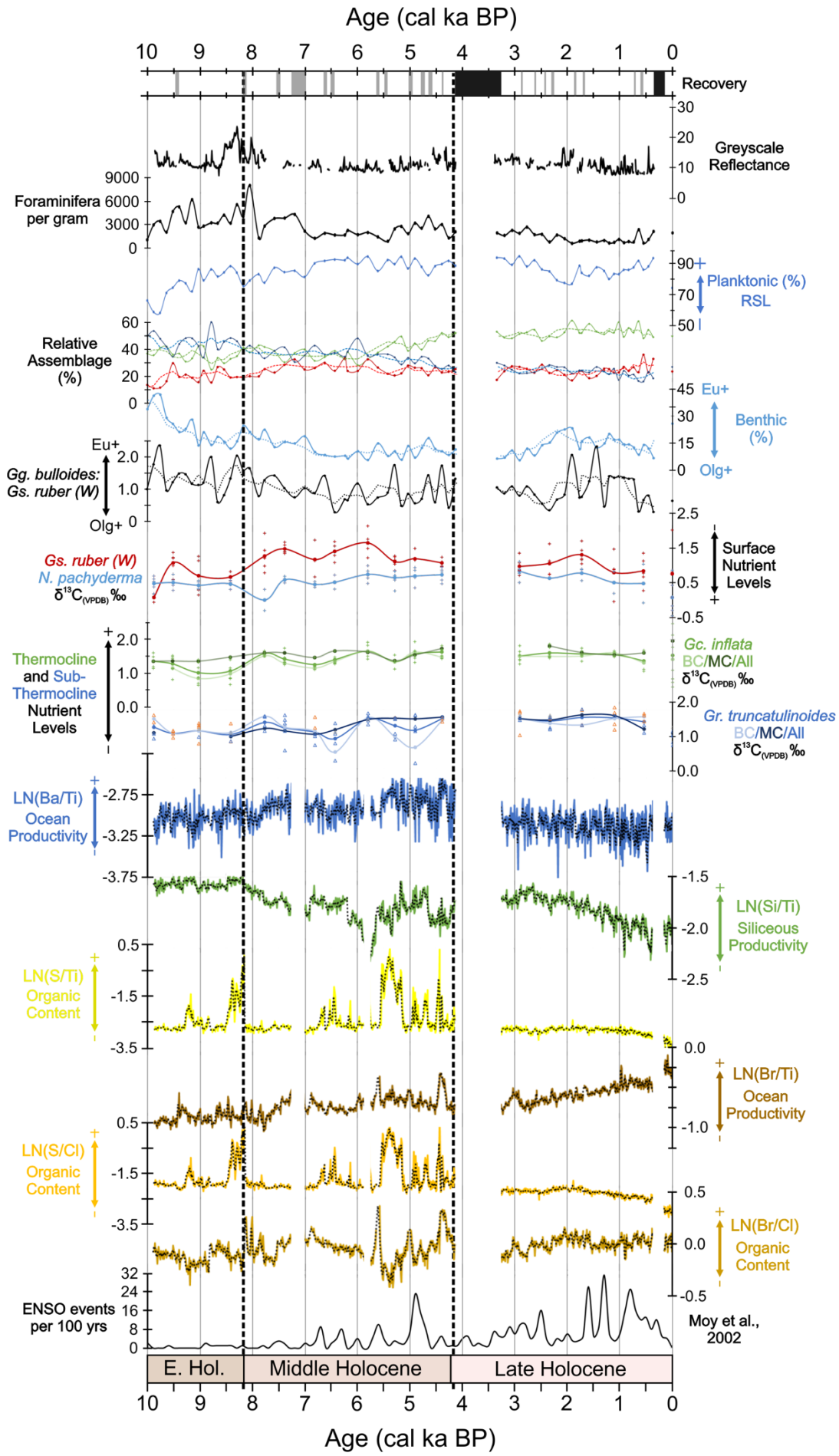
Age (cal ka BP)
10 9 8 7 6 5 4 3 2 1 0
Recovery
Greyscale Reflectance
Foraminifera per gram
Planktonic (%) RSL
Relative Assemblage (%)
Benthic (%)
Eu+
Olg+
Gg. bulloides: Gs. ruber (W)
Gs. ruber (W)
N. pachyderma
δ13C(VPDB) ‰
Surface Nutrient Levels
Thermocline and Sub-Thermocline Nutrient Levels
Gc. inflata
BC/MC/All
Gr. truncatulinoides
LN(Ba/Ti)
Ocean Productivity
LN(Si/Ti)
Siliceous Productivity
LN(S/Ti)
Organic Content
LN(Br/Ti)
LN(S/Cl)
LN(Br/Cl)
ENSO events per 100 yrs
Moy et al., 2002
E. Hol.
Middle Holocene
Late Holocene
Age (cal ka BP)

Figure 5.4-3 Compilation of Holocene productivity records for UPC 028. Greyscale reflectance details the brightness of the core with higher values likely indicative of increased carbonate content. Foraminifera per gram numbers, shifts to higher values indicate potential increases in productivity. Planktonic species % is a relative abundance metric indicative of Relative Sea Level rise. The relative abundance of warm (red), transitional (green) and cold (blue) planktonic foraminiferal eco-groups from assemblage counts, dashed lines provide a 3-point running average. Benthic %, is a relative abundance metric, used as a productivity indicator. *Gg. bulloides:Gs. ruber white* is a productivity indicator based on the species preference for trophic states. Surface dwelling species $\delta^{13}C_{(VPDB)}$ values for *Gs. ruber white* (red) and *N. pachyderma* (blue), single specimen (points) is plotted alongside mean values (line). *Gc. inflata* $\delta^{13}C_{(VPDB)}$ are presented, single specimen (points), average MC data (dark green line) and BC data (light green line) based on $\delta^{18}O_{(VPDB)}$ classifications and a combined average (all data, mid-green line). *Gr. truncatulinoides* $\delta^{13}C_{(VPDB)}$ data, single specimen data is split with right coiling specimens (orange triangles), the left coiling (blue triangles) and unclassified coiling (grey triangles). The average curves are similarly split to *Gc. inflata*. ITRAX log ratios are also presented, Ba/Ti is an ocean productivity indicator, alongside Si/Ti and Br/Cl ratios. Additionally, S/Ti, S/Cl and Br/Cl ratios are organic content indicators. The ENSO Holocene frequency data from Moy et al., 2002, is presented for correlation with UPC 028 data.

5.4.2.2 Productivity 6.0-4.2 ka

At ~6.0 ka a number of events co-occur on the margin and globally. These include RSL reaching highstand, ~4-6 m higher than modern sea level (Angulo et al., 2006; Bender et al., 2013; Bracco et al., 2014; Prieto et al., 2017), and the shift from a primarily insolation driven system to an internal climate driven system i.e. stabilisation of thermocline circulation and development of ENSO (Bond et al., 2001; Moy et al., 2002; Debret et al., 2009; Bender et al., 2013; Voigt et al., 2015; Kaufman, McKay, Routson, Erb, Dätwyler, et al., 2020; Bova et al., 2021). A number of changes occur from ~6.0 ka within the UPC 028 record, the most obvious change occurs within the planktonic foraminiferal eco-groups. Here the transitional grouping begins a sharp rise in abundance from 6.0 ka to the end of the mid-Holocene, largely driven by abundance increases in the mesotrophic favouring *Gc. inflata*, but also increases in *Gt. glutinata*, whilst warm eco-groups are maintained and cold eco-groups are diminished (Figure 5.4-3). This marks a shift in the assemblage eco-groups that are maintained to the modern. Similarly patterns have been reported from sites shifting from eutrophic conditions to mesotrophic states previously (Lončarić et al., 2007). Alongside this increase in transitional fauna the greyscale reflectance and foraminifera per gram values rise moderately from 6.0 ka to 4.2 ka (Figure 5.4-3). This combines with a slight rise in benthic foraminifera relative abundances and *Gg. bulloides:Gs. ruber white* ratio increases (Figure 5.4-3). The latter two show lower values than the ~8.2 ka

eutrophic event, potentially indicating a more mesotrophic system, but still not favouring the oligotrophic *Gs. ruber white*.

Analysing the $\delta^{13}C$ isotopes over the 6.0-4.2 ka interval sees two contrasting signals in the surface dwellers. *Gs. ruber white* $\delta^{13}C$ values transition from a maximum at ~6.0 ka, indicative of the lowest nutrient levels recorded, falling rapidly between ~5.8-5.3 ka, suggesting increased nutrients during warmer months (Figure 5.4-3). *N. pachyderma*, a species that prefers cooler waters by comparison, sees values rise slightly from pre-6.0 ka, implying a loss of nutrients within surface waters during cooler months, before stabilising post-6.0 ka (Figure 5.4-3). These two trends suggest a move from a declining eutrophic state to more mesotrophic conditions present on the margin. Within the deeper dwelling species there is a slight increase in the $\delta^{13}C$ values of both *Gc. inflata* and *Gr. truncatulinoides*, particularly in MC variants, implying a slightly more nutrient enriched system (Figure 5.4-3). Combined with the diverging BC/MC $\delta^{18}O$ records, it would seem that mixing from 6.0 ka onward intensifies, permitting a range of $\delta^{18}O$ and $\delta^{13}C$ values to be recorded at UPC 028. Aligning with the literature, Gu et al., (2018c) suggest a stable phase in the BMC position between 5.7-4.5 ka, although they note a stronger influence of colder water masses over the margin from ~5.7 ka to 0.66 ka. This may result in increased and stronger mixing from ~5.7 ka onward and facilitate the move to a mesotrophic state through BC/ MC waters mixing as a long term average (Voigt et al., 2015; Gu et al., 2018c).

The ITRAX data over this 6.0-4.2 ka period sees some striking shifts. Ba/Ti and Br/Ti show increases in ratio values compared to earlier in the mid-Holocene, implying an increase in productivity (Figure 5.4-3) (Croudace and Rothwell, 2015). Meanwhile, the Si/Ti values recover after a significant drop prior to 6.0 ka, inferring an increase in siliceous productivity toward the end of the mid-Holocene (Figure 5.4-3) (Voigt et al., 2013; Croudace and Rothwell, 2015). This would tie with an increase in MC influence from wider mixing, bringing more nutrient rich waters to the margin (Voigt et al., 2015; Gu et al., 2018c). Further evidence for a rise in nutrients on the nearby Argentine margin is elevated biogenic opal and Si/Al ratios recorded at GeoB13862-1, and additional Mar del Plata Canyon records (Figure 5.4-4) (Voigt et al., 2013). Voigt et al., (2013), cite increases in fluvial discharge from the La Plata River over the shelf, caused by intensified

precipitation anomalies. This combined with ENSO north-easterly winds impeded PPW spread along the Brazilian shelf, and lead to fertilising of the Uruguayan margin, increased phytoplankton production and biogenic opal deposition (Figure 5.4-4) (Moy et al., 2002; Voigt et al., 2013). Our study site, UPC 028, is located further north along the slope in comparison to the Mar del Plata records (Figure 5.4-4). Determining whether the site is influenced by PPW expansions is difficult but based on correlation between Ca and Sr counts a marine signal is largely maintained (Figure 5.3-7). Terrestrial input would lead to deviation in the covariance of these two counts, and whilst there is evidence for brief terrestrial input around ~5.4 ka, this is certainly not maintained over the whole interval and is not replicated in the Fe/Ca record (Figure 5.3-7), which suggests biogenic dominance (Carlson et al., 2008; Croudace and Rothwell, 2015).

One potential indicator for increased fluvial and terrestrial input is the rise in sedimentation rates during the interval, from ~37 cm/ky to ~54 cm/ky, at a time when the site is at RSL highstand (Figure 5.3-7). However, this may be due to increased biogenic input, with slight increases in greyscale reflectance, foraminifera per gram values and peaks in the Ca/Ti ratio implying increasing carbonate content rather than terrestrial material. Additional dating and integration of sedimentary grainsize records may clarify this further. Interestingly, a number of proxies (S/Ti, S/Cl and Br/Cl) suggest increasing organic content between 6.0-4.2 ka (Figure 5.4-3). The timing of S/Ti and S/Cl ratio peaks alongside increases in ocean productivity metrics and sedimentation increases potentially indicates greater deposition of organic matter during the interval. Additionally, alignment alongside the overall shift to mesotrophic states and the intensification of BMC mixing is correlated with ENSO intensification from ~5.7 ka (Moy et al., 2002; Voigt et al., 2013; Gu et al., 2018c). Total Organic Content (TOC) analysis should be considered as a potential future verification of increasing organic matter.

The timing of these assemblage and ITRAX trends within this record, and the palynological shifts and biogenic opal of adjacent sites (Voigt et al., 2013; Gu et al., 2018c), suggests the margin moved to a mesotrophic state. This is in conjunction with intensification of BMC mixing, correlated with intensification of ENSO from ~5.7 ka, and stabilising of thermocline circulation, impacting the

position of atmospheric belts over the end of the mid-Holocene prior to the core break (Moy et al., 2002; Debret et al., 2009; Voigt et al., 2013; Gu et al., 2018c).

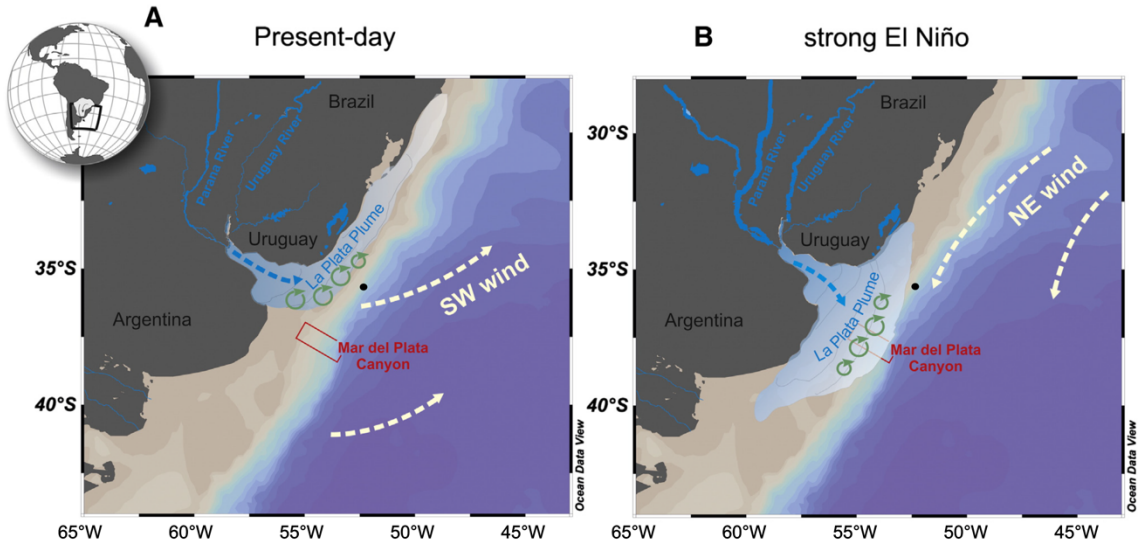

Figure 5.4-4 Modified figure from Voigt et al., 2013, detailing Mar del Plata Canyon sites locations and the suggested varied outflow of the La Plata river under modern conditions and strong El Niño conditions. Site UPC 028 (black dot) is on the fringe of influence for any Plata Plume Waters and thus is unlikely to be significantly impacted by terrestrial input, unless unusually strong El Niño conditions were to occur. The green arrows indicate regions of increased phytoplankton biomass (Voigt et al., 2013).

5.4.2.3 Productivity post core break to the modern

Into the late Holocene, upper sections of core show continuations of the mesotrophic state established in the mid-Holocene. The record resumes shortly before 3.3 ka, and shows slightly elevated foraminifera per gram numbers and maintains the elevated transitional eco-group fauna (Figure 5.4-3). Co-incident with a cooling interval between 2.3-1.0 ka there appears to be elevated benthic relative abundances and *Gg. bulloides:Gs. ruber white* ratios (Figure 5.4-3). $\delta^{13}C$ isotopes show little variation in the late Holocene, with the exception of slight increases in nutrients between 2.3-1 ka, coinciding with a slight cooling recorded in the two species (Figure 5.4-3). The 2.3-1.0 ka cooling period is coeval with high frequency ENSO events and evidence of BMC northward migration, bringing cold, nutrient rich MC waters to the site (Moy et al., 2002; Voigt et al., 2013; Chiessi et al., 2014; Voigt et al., 2015; Gu et al., 2018c). These fluctuations and pulses over the Holocene fit with wider reported late Holocene centennial variability, with the influence of the nutrient rich MC increasing post mid-Holocene (Debret et al., 2009; Voigt et al., 2013; Chiessi et al., 2014; Chapori et al., 2015; Voigt et al., 2015; Portilho-Ramos et al., 2018; García Chapori and Laprida, 2021). For the remaining 1.0 ky of the record, particularly after ~800 years ago,

warm eco-groups increase at the expense of cold eco-groups, whilst transitional species are maintained (Figure 5.4-3). Combined with declines in benthic relative abundance, *Gg. bulloides:Gs. ruber white* ratios and slight shifts in $\delta^{13}C$ isotopes to lower nutrient states suggests BC southward migration and greater BC involvement at the site and establishment of modern conditions (Figure 5.4-3).

Meanwhile the ITRAX data typically shows little variation from ~3.3 ka to the modern, this is unexpected given the significant variation in proxies during the 6.0-4.2 ka interval (Figure 5.4-3). Reasons for muted, or even declining signals, in the Ca/Ti, S/Ti and Si/Ti ratios are likely due to dilution effects closer to the core top, resulting from factors such as increased porosity, increased porewater and increased organic matter (Croudace et al., 2006; Rothwell et al., 2006; Rothwell and Rack, 2006; Thomson et al., 2006; Weltje and Tjallingii, 2008; Croudace and Rothwell, 2015). Dilution through organic matter is seen within rising Br/Ti values, to a lesser extent the Br/Cl ratio, declining Ca/Ti values and suppressed greyscale reflectance, implying a darkening of the core, this is to be expected as core age decreases. Decline in Ca/Ti values has been seen at nearer shore sites and attributed to increased terrestrial input (Bender et al., 2013). Whilst sedimentation rates rise to the top of the core and Fe/Ca ratios increase (Figure 5.3-7), indicating increased terrestrial input, the covarying Ca and Sr counts still show a marine signal rather than significant terrigenous input (Figure 5.3-7). Determining whether this distal, deeper site experiences greater terrestrial input over the late Holocene requires further investigation, chiefly on the nature of the sediment, sediment porosity and sediment organic content to assess signal dilution.

5.5 Summary

- What are the overall BMC migratory trends documented by site UPC 028 over the last 10 Kyr? Is latitudinal variation observed and does site UPC 028 display signs of mid-Holocene warming?

This study aimed to produce a palaeoceanographic record using planktonic foraminifera and sedimentary analysis to document BMC migratory shifts over the Holocene; a period of time when atmospheric and oceanographic systems were responding to the deglaciation following the Last Glacial Maximum (Rühlemann et al., 1999; Bond et al., 2001; Moy et al., 2002; Debret et al., 2009; Voigt et al., 2015; Santos et al., 2017). Building on the work presented in chapter four which established the modern ecological and oceanographic setting for UPC 028, the variation visible within the record implies shifts from a system dominated by the BC in the present-day. Assemblages derived from UPC 028 cover the last 10 ka, encompassing the majority of the Holocene, and providing a <200-year resolution, enabling identification of phases of change in the thermal and nutrient qualities of overlying water masses. This was evident in the species abundances, in addition to planktonic foraminiferal stable isotopes of four species indicative of distinct water column depths, and the ITRAX XRF core scanning semi-quantitative elemental ratios. Combined, a high-resolution reconstruction of the Uruguayan margin documenting the temporal record of BMC latitudinal migration is provided, with supporting literature and studies to understand the complex mechanisms behind this oceanographic confluence.

The prevailing signal throughout the early and mid-Holocene involves increases in warm water favouring species, and the corresponding decline in cold water representatives. Simultaneous with this eco-group change is the transition from species with eutrophic preferences to an increasing number of oligotrophs, likely sourced from the BC, a sub-/tropical water mass known to be nutrient depleted. This suggests the BMC migrated southward, decreasing the influence of MC waters across seasons, in response to SWWB constrictions to higher latitudes, driven by SST meridional gradients and orbital forcing in insolation values (Varma et al., 2012; Voigt et al., 2015). Interrupting this trend is a brief cooling event surrounding 8.2 ka, and evidenced in the assemblage and isotope data. This event sees a dip in the warm eco-group relative assemblages and a jump in cold representatives, alongside spikes in foraminiferal and ITRAX productivity metrics.

The short-term nature of the event means single specimen stable isotope data brackets the event, this is a limitation for quantifying the scale of change before pre-event warming and nutrient decline resumes.

- Do single specimen stable isotopes and assemblage records suggest changes in BMC mixing over the Holocene?

Midway through the mid-Holocene (from ~6.0 ka) a marked shift occurs in a number of proxies, including a sustained increase in the transitional eco-group, divergence of surface species $\delta^{18}O$ values, changes in surface dweller $\delta^{13}C$ values, and spikes in ITRAX productivity metrics. These changes reflect greater dynamism in the BMC confluence, likely in response to increasing ENSO conditions altering atmospheric conditions and impacting the ocean circulation (Moy et al., 2002; Voigt et al., 2015; Gu et al., 2018c). This leads to greater variability on the margin, with mixing establishing more mesotrophic conditions and a greater involvement of cooler MC waters annually (Gu et al., 2018c). The clearest evidence for greater mixing within the UPC 028 record is the rise of the mesotrophic *Gc. inflata*, driving the transitional surge, and a broader range of *Gs. ruber white* and *N. pachyderma* $\delta^{18}O$ ranges, implying presence of BC and MC waters. This establishes a new state for site UPC 028 on the margin with the core of the BMC likely remaining to the south of the site, having reached its furthest extent around 6.0 ka, however greater dynamism results in more vigorous BMC movements, exposing the site to both BC and MC conditions as seen in the assemblage and isotope data.

An example of this movement is the late Holocene northward BMC migration (2.3-1.0 ka), in which warm water eco-groups dip in favour of colder species, and nutrient levels seemingly increase across the interval. At other western South American margin sites this trend has been tied to a weakening BC, related to shifts in thermohaline circulation, or to changes in meridional temperature gradients impacting the average SWWB location (Chiessi et al., 2014; Voigt et al., 2015; Gu et al., 2018c). Both of these scenarios have the potential to cause northward BMC migration, influencing the planktonic foraminiferal eco-groups. Coincident with this BMC migration are significant peaks in the number of ENSO events, this would alter SST meridional gradients, as has been seen during modern ENSO events, potentially impacting BMC movement (Moy et al., 2002;

Barreiro et al., 2002; Münnich and Neelin, 2005; Chiessi et al., 2014; Gu et al., 2018c).

The remaining 1.0 ky of the record sees a poleward migration of the BMC toward the present location. A number of proxies detail this with a reversal of the cold and warm eco-groups, signifying warming, and a drop in nutrient rich conditions as seen in the *Gg. bulloides:Gs ruber white* ratio. This also fits with surrounding studies suggesting predominantly poleward migration over the last millennium, linked to the SWWB migrating southward (Lamy et al., 2010; Varma et al., 2012; Kilian and Lamy, 2012; Bender et al., 2013; Voigt et al., 2013; Voigt et al., 2015; Gu et al., 2018c; Pereira et al., 2018).

5.5.1 Key take away messages

- Site UPC 028 documents a number of proxies that largely concur on latitudinal migration of the BMC. This is summarised by a southward shift of the confluence over the majority of the early and mid-Holocene, established through a weakening of the SWWB, and leading to warming and decreasing eutrophic conditions as BC begins to dominate.
- This dominance of the BC is broken by a short-term cooling event between 8.4-8.0 ka in which cold eco-groups dominate, isotopes shift to more eutrophic conditions and carbonate production seemingly increases. This brief event sees more MC influence, and is likely triggered by freshwater entering the North Atlantic.
- The maximum southward extent of the BMC is reached during the mid-Holocene (~6.0 ka) where establishment of ENSO conditions in the Pacific drive atmospheric and oceanographic processes to enable greater dynamism on the margin. From this point onward, greater mixing occurs between BC and MC currents over Site UPC 028, favouring the establishment of transitional eco-groups and a mesotrophic system.
- Late Holocene is characterised by a continuation of mid-Holocene trends until a cooling interval between 2.3-1.0 ka, with a northward shift of the BMC potentially linked to a weakening of the BC and/or SST gradients influencing the SWWB annual position northward. This is evidenced in isotope records, an increase in cold eco-groups and a potential shift back to more eutrophic records recorded by the *Gg. bulloides:Gs. ruber* white ratio.

- Establishment of modern conditions occurs after 1.0 ka with a slight southward migration of the BMC to the present location, visible in the reversal of cold eco-groups in favour of warmer species, the return to more mesotrophic conditions and stable isotope shifts.

5.5.2 Limitations and further work

As with the previous chapter there are aspects to this study that require reflection and should be considered as areas for future focus. A number of constraints have restricted the level of analysis available to this study, in large part due to the time to conduct additional analyses and the Coronavirus Pandemic delaying subsequent work.

This study benefited from the acquisition of five preliminary radiocarbon dates, enabling dating of the core and interpolation of intervening samples. Additional radiocarbon dating would help better constrain some of the proxies, particularly concerning the timing of the three significant events: The 8.2 ka cooling period at the end of the early Holocene, the onset of Mesotrophic conditions and excursions of Ca/Ti and S/Ti ratios during the mid-Holocene, and the late Holocene cooling event between 2.3-1.0 ka. Future work would aim to not only better constrain the dating on these events, but also the extent of excursion from the background. This would ideally be achieved through increasing the resolution of the stable isotope record, both in terms of number of samples but also the number of analyses per interval, to approach that of the assemblage data. This would enable a greater confidence in the trends between samples and better identification of outliers/potential analytical error.

Uncertainty surrounds the nature of the large Ca/Ti and S/Ti excursions found in the mid-Holocene, post ENSO intensification. There is the potential that these reflect deposition of organic material, however this study lacks the ability to discern with certainty whether this is the case. Employing TOC analyses on fresh samples from within this region may aid in answering this question. This was not initially considered due to delay in ITRAX scanning the archived cores, resulting in samples being washed, processed and assemblage analysis started. Future work could also encompass analysis of the sediment composition, measuring silt, clay and sand content to determine sediment sourcing to UPC 028. This would help determine whether the site is completely under the influence of the marine

system throughout geological history, or with terrestrial climate regime shifts, sees greater fluvial input.

Samples from two additional cores are washed and processed for subsequent planktonic foraminiferal investigations at the University of Leeds. Provided suitable dating was available, these records could expand the understanding of Uruguayan margin processes spatially, as well as temporally. A benthic foraminiferal and contourite study, conducted by Cían McGuire as part of his PhD thesis, found cores within the collection had the capability to extend records back into the late Pleistocene. Through exploitation of samples already present at the University of Leeds, or housed within the BOSCORF repository in Southampton, there is the potential to obtain palaeoceanographic and palaeoclimatic reconstructions across Last Glacial Maximum, within an unstudied portion of the world's oceans.

Chapter 6 Discerning the impact of calcite encrustation on *Gc. inflata* isotopic and morphological signatures with respect to Brazilian- Malvinas Confluence migration

6.1 Background and Aims:

Across the western South Atlantic margin, a number of records comprising *Globoconella inflata* isotopes have been published (Chiessi et al., 2007; Morard et al., 2011; Voigt et al., 2015; Morard et al., 2016; Jonkers et al., 2021). *Gc. inflata* is a widely utilised oceanographic tracer, in part due to its high fossilisation potential, but particularly as a tracer of fronts (Schiebel and Hemleben, 2017). Thus, interest in the species analysing its morphotype variation, cause of encrustation and impact the on $\delta^{18}O$ records has increased in recent years (Morard et al., 2011; Morard et al., 2016; Rebotim et al., 2019; Jonkers et al., 2021).

Amongst them several have observed the roughly 2 ‰ $\delta^{18}O_{(VPDB)}$ offset across the Brazil-Malvinas Confluence (BMC), first presented in Chiessi et al., (2007). More recent authors have correlated this with *Gc. inflata* genotype population and/or encrustation differences, across the confluence (Morard et al., 2011; Morard et al., 2016; Jonkers et al., 2021). The differing genotypes were first described in Morard et al., 2011, whom used DNA sequencing to delinate the two cryptospecies and suggested morphological differences in size of the terminal chamber. Later Morard et al., 2016 applied these differences in morphotype character, which whilst subtle are observable using light microscopy, to attempt to trace oceanographic boundaries (Morard et al., 2011; Jonkers et al., 2021). Two main morphological types are identified; Type I specimens are generally larger, with larger apertures, whilst Type II are more diminutive with a smaller aperture compared to the size of the final chamber (Figure 6.1-1) (Jonkers et al., 2021).

Figure 6.1-1 Light microscopy images of the two *Gc. inflata* morphotypes found in the Southern Atlantic, taken from site GeoB13862-1 as part of the Jonkers et al., 2021 study. Type I individuals have a larger aperture relative to final chamber size than Type II individuals. Classification of morphotype is difficult, with the previous study finding difficulties classifying all morphotypes (Jonkers et al., 2021). Scale bar is 100 µm.

Previous studies have suggested the distributions of the two morphotype populations of *Gc. inflata* are allopatric, isolated and separated from one another, by the BMC (Morard et al., 2011; Morard et al., 2013; Morard et al., 2016). This is expressed with the more widely distributed Type I found in both hemispheres of the Pacific, Indian and Atlantic Oceans (Morard et al., 2011). Type II, by comparison is much more restricted, being confined to the Southern Hemisphere, and specifically Polar and Sub-Polar water masses (Morard et al., 2011). Margin plankton tow and core top data have suggested a link between these two morphotypes and investigated $\delta^{18}O$ values from the foraminiferal tests (Morard et al., 2016). Type I display lower $\delta^{18}O_{(VPDB)}$ (warmer) values north of the BMC and Type II have higher $\delta^{18}O_{(VPDB)}$ values (colder) south of the BMC (Chiessi et al., 2007; Morard et al., 2016) (Figure 6.1-2). Morard et al., (2016) utilised this relationship and historical isotopic data from three cores straddling the BMC (Voigt et al., 2015) to construct a model defining likely morphotypes, attempting to track population shifts along the western South Atlantic margin, and infer migration of the BMC through time (Morard et al., 2016) (Figure 6.1-2). The results of this present study fill a gap in previous transects, and unlike previous studies, the high spatial density enables assessment of isotopic variation within a region that experiences BMC conditions (Chiessi et al., 2007; Morard et al., 2011; Voigt et al., 2015; Morard et al., 2016; Piola and Matano, 2019).

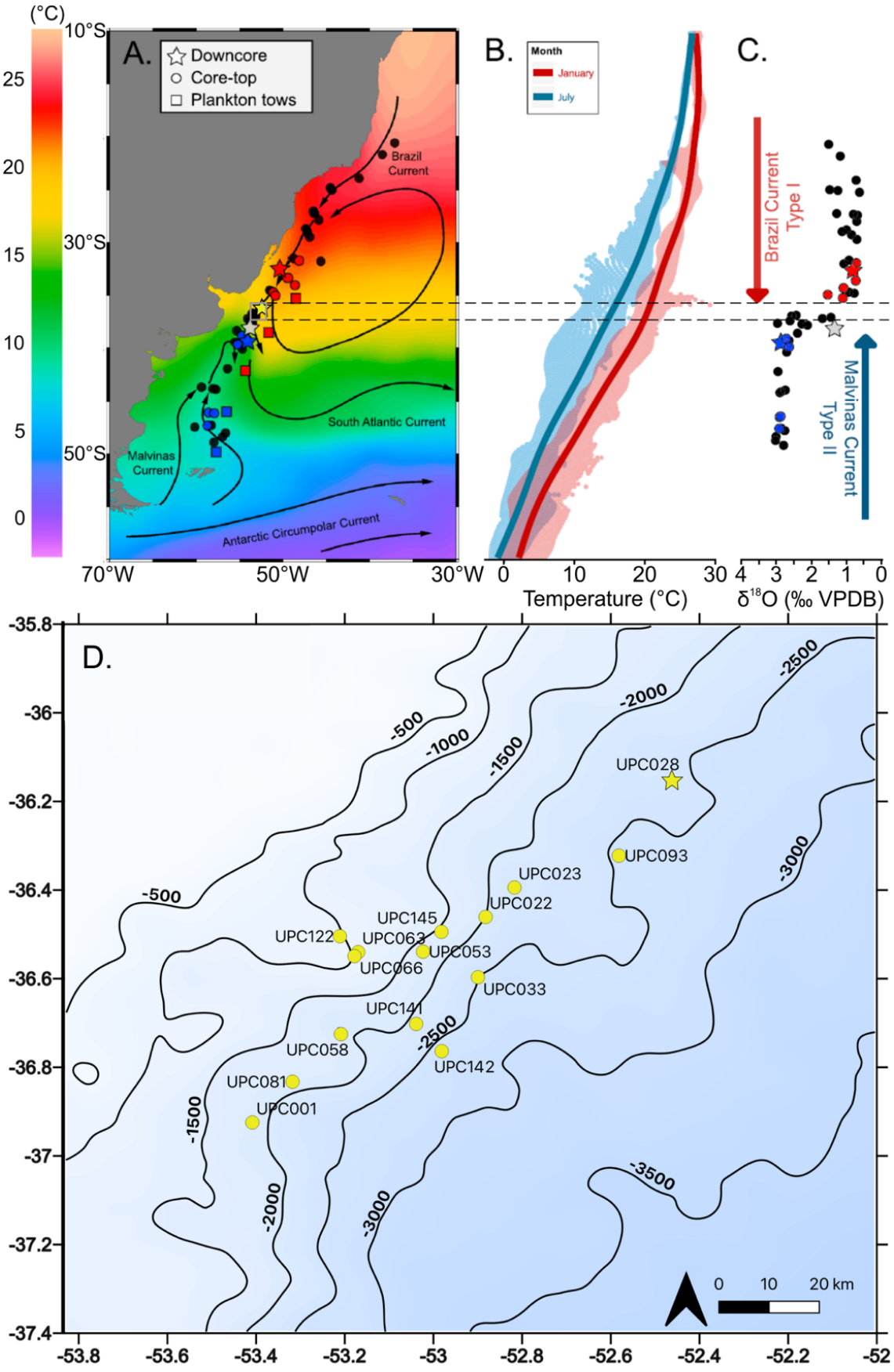
(°C)
25
20
15
10
5
0
10°S
30°S
50°S
70°W
50°W
30°W
A.
Downcore
Core-top
Plankton tows
Brazil Current
South Atlantic Current
Malvinas Current
Antarctic Circumpolar Current
B.
Month
January
July
0
10
20
30
Temperature (°C)
C.
Brazil Current Type I
Malvinas Current Type II
4
3
2
1
0
δ18O (‰ VPDB)
D.
-35.8
-36
-36.2
-36.4
-36.6
-36.8
-37
-37.2
-37.4
-53.8
-53.6
-53.4
-53.2
-53
-52.8
-52.6
-52.4
-52.2
-52
-500
-1000
-1500
-2000
-2500
-3000
-3500
UPC028
UPC093
UPC023
UPC022
UPC145
UPC122
UPC063
UPC053
UPC066
UPC033
UPC141
UPC058
UPC142
UPC081
UPC001
0
10
20 km

Figure 6.1-2 A) Location of stations utilised in Morard et al., (2016), core top data originally from Chiessi et al., (2007) (circles), downcore samples from Voigt et al., (2015) (stars), black stations were not considered in this study. Background colour is mean annual SST from Locarnini et al., (2013). Red symbols: Type I exclusivity, blue symbols: Type II exclusivity, grey symbols: Type I and Type II present. Yellow star is UPC 028, this study. Black arrows represent main surface currents. B) SST variability plotted against latitude for austral summer (January) and winter (July), shading reflects monthly average SSTs derived from the World Ocean Atlas 2013 on a 0.25° grid, a smoothed averaged curve is presented (Morard et al., 2016). C) Chiessi et al., (2007) *Gc. inflata* $\delta^{18}O_{(VPDB)}$ values, dashed lines are the sample latitudinal range recovered in this study. D) This study's region, inset of the grey box in panel A. Yellow circles denote sites where new core top *Gc. inflata* $\delta^{18}O_{(VPDB)}$ data was acquired, yellow star is site UPC 028 where downcore *Gc. inflata* $\delta^{18}O_{(VPDB)}$ data was also acquired. Panels A, B and C are modified from Morard et al., (2016). Bathymetric data modified from Hernández-Molina et al., 2016 and McGuire et al., 2019.

Variable BMC position has been observed with migration of the front occurring on seasonal time-frames, and wider movement of the migration zone suggested over longer inter-annual, decadal and geological timescales (Olson et al., 1988; Voigt et al., 2015; Gu et al., 2018; Piola and Matano, 2019, Chapters 4 and 5 herein). This migration is typically thought to result from changes in wind stress curl dictating relative transport strength of the two currents, with the BC strengthening in summer months pushing the confluence to its southern extent and retreating north during winter months (Olson et al., 1988; Piola and Matano, 2019). Changes to these winds, and regional oceanography, over longer periods of time are thought to influence BMC position though the geological record (Voigt et al., 2015, Chapters 4 and 5 herein). Within the core top samples this seasonal BMC migration will impact the morphotype occurrences present in overlying water masses, and thus the assemblage composition at each site inside the migration zone (Morard et al., 2013; Morard et al., 2016). With the age of core tops estimated to represent ~30 years based on radiocarbon dating, grouped samples are likely to incorporate individuals from multiple migrations, thus single specimen analysis enables high fidelity analysis of isotopic values and morphotypes.

Jonkers et al., (2021) assessed the impact of encrustation and morphotype variation on stable isotope values within plankton tow and sediment samples. Encrustation of *Gc. inflata* is a commonly observed phenomena, with adult specimens showing pustules coalescing during ontogeny to form a calcite crust covering the underlying lamellar calcite (Schiebel and Hemleben, 2017; Rebotim et al., 2019; Jonkers et al., 2021). Crust formation, when present, alters the test appearance with a smooth shiny cortex enveloping pustules and pores, smoothing the test surface and forming a diagnostic feature in identifying *Gc. inflata* from other globorotaliids (Schiebel and Hemleben, 2017; Jonkers et al.,

2021). The trigger for crust development is still unclear, with encrusted specimens present in surface and sub-surface waters, implying water depth migration and temperature do not instigate encrustation (Rebotim et al., 2019; Jonkers et al., 2021). The aim of their study was to ascertain whether either morphotypes or encrustation impacted $\delta^{18}O$, $\delta^{13}C$ and Mg/Ca measurements from the western South Atlantic margin. Jonkers et al., (2021) previously analysed encrustation impact on $\delta^{18}O$ and $\delta^{13}C$, finding minimal $\delta^{18}O$ variation between encrusted and non-encrusted forms at sites under the exclusive influence of BC or MC water masses. However, $\delta^{18}O$ variation between encrusted and non-encrusted forms increased at sites within the confluence zone (Jonkers et al., 2021). From multi-specimen data, broad $\delta^{18}O$ ranges within the confluence develop between encrusted and non-encrusted samples, seemingly the result of wider seasonal BMC thermal ranges (Jonkers et al., 2021). A broad range of $\delta^{13}C$ values is maintained regardless of encrustation state or geographical locale, suggesting this factor is not impacted by encrustation (Jonkers et al., 2021). In this chapter I aim to assess whether encrustation plays a role, both spatially and temporally, in the isotopic and morphological variation of *Gc. inflata* on the Uruguayan margin. This study will employ the isotopic-morphotype relationship of Morard et al., (2016) to discern whether spatial and temporal patterns are present within encrustation classifications.

The chapter plans to build on the aforementioned studies in a number of ways. Firstly, this study will make use of novel single specimen *Gc. inflata* isotope measurements, a technique unavailable to previous studies for $\delta^{18}O$ and $\delta^{13}C$ measurements. This enables individual foraminifers to be assigned to morphotype through inferred $\delta^{18}O$ ranges, permitting this chapter to assess whether Type I or Type II specimens show spatial or temporal variations on the margin. Secondly, individual foraminifera will be classified based on the level of encrustation, following Jonkers et al., (2021) recommendations for visual inspection and categorisation. This will enable *Gc. inflata* spatial and temporal encrustation distributions to be determined and observe whether level of encrustation is variable in space and time. Combined this will facilitate variation in encrustation and isotopic values, of this palaeoceanographically important species, to be constrained spatially in the modern, and enable assessment of this species to trace BMC migration temporally over the Holocene.

6.1.1 Aims and research questions:

- To apply the isotope-morphotype relationship of Morard et al. (2016) to assess the spatial and temporal occurrences of Type I and Type II *Gc. inflata* across the BMC.

How is the isotope-morphotype relationship of *Gc. inflata,* highlighted in previous work, expressed in the spatial and temporal distributions of Type I and Type II individuals across the BMC?

- To quantify the encrustation types of *Gc. inflata* (Jonkers et al., 2021) to assess the spatial and temporal occurrences of encrustation type across the BMC.

Do *Gc. inflata* encrustation classifications exhibit spatial and temporal variations over the BMC?

- To assess whether the encrustation impacts on *Gc. inflata* $\delta^{18}O$ values as indicated by Jonkers, et al. (2021) are still present when using single specimen analyses rather than multiple specimen analyses.

Through use of single specimen isotopic analyses, are $\delta^{18}O$ values impacted by encrustation state on the Uruguayan margin?

6.2 Materials and methods

6.2.1 Samples and *Gc. inflata* Encrustation Assessment

Fifteen core top samples (Table 6.2-1) (Figure 6.2-1) in addition to seventeen down core samples from core UPC 028 (Table 6.2-2), utilised in Chapter Four and Five, had individual *Gc. inflata* tests picked and cleaned for isotope analysis following methods outlined in Chapter 3. Prior to isotope analysis these specimens were visually inspected using a Zeiss Stemi 305 binocular reflected light microscope and classified based on the level of visual encrustation into four categories: non-encrusted (A), minor encrustation (B), moderate encrustation (C) and heavy encrustation (D). This was done following Jonkers et al., (2021), relating to the preservation of spines and pores on the test surface.

Non-encrusted specimens showed the highest preservation of such features, whilst heavily encrusted specimens had developed a smooth cortex, with the loss of detailed test wall features. An example of this gradient is extracted from Jonkers et al., (2021) in Figure-6.2-2, the light microscopy images were used for direct comparison and classification of specimens. Additional *Gc. inflata* specimens that were utilised for Radiocarbon analysis prior to encrustation classification, were categorised as Unknown (U) and numbered seven individuals.

Table 6.2-1 List of samples available for spatial assessment of *Gc. inflata* morphotypes and encrustation levels on the Uruguayan margin.

Site	Latitude (°)	Longitude (°)	Depth (m)	Number of specimens
UPC 001	-36.92	-53.41	-2053.05	5
UPC 022	-36.46	-52.88	-2027.53	5
UPC 023	-36.39	-52.82	-2046.34	9
UPC 028	-36.15	-52.46	-2353.00	9
UPC 033	-36.60	-52.90	-2582.33	5
UPC 053	-36.54	-53.02	-2115.24	7
UPC 058	-36.73	-53.21	-2255.28	5
UPC 063	-36.54	-53.17	-1255.00	5
UPC 066	-36.55	-53.18	-1257.00	5
UPC 081	-36.83	-53.32	-1895.64	5
UPC 093	-36.32	-52.58	-2572.48	8
UPC 122	-36.50	-53.21	-1154.19	5
UPC 141	-36.70	-53.04	-2431.08	5
UPC 142	-36.76	-52.98	-2682.11	5
UPC 145	-36.49	-52.98	-1595.39	8
			Total	**91**

Table 6.2-2 Samples from which isotopic measurements were acquired down core, with associated depth and age. All specimens were classified for encrustation prior to analysis.

Site	Depth in Core (cm)	Calibrated Age (cal BP)	Number of Specimens
UPC 028	0-2	0	9
UPC 028	41-43	548.6	5
UPC 028	83-85	1110.6	5
UPC 028	118-120	1727.3	5
UPC 028	148-150	2340.7	6
UPC 028	176-178	2913.3	6
UPC 028	254-256	4390.5	5
UPC 028	282-284	4905.9	5
UPC 028	303-305	5292.5	4
UPC 028	324-326	5803.7	6
UPC 028	347-349	6433.7	6
UPC 028	361-363	6815.3	3
UPC 028	382-384	7390.1	5
UPC 028	396-398	7772.2	5
UPC 028	422-424	8419.5	6
UPC 028	447-449	9029.8	6
UPC 028	467-469	9518.3	5
UPC 028	482-484	9884.5	5
		Total	**97**

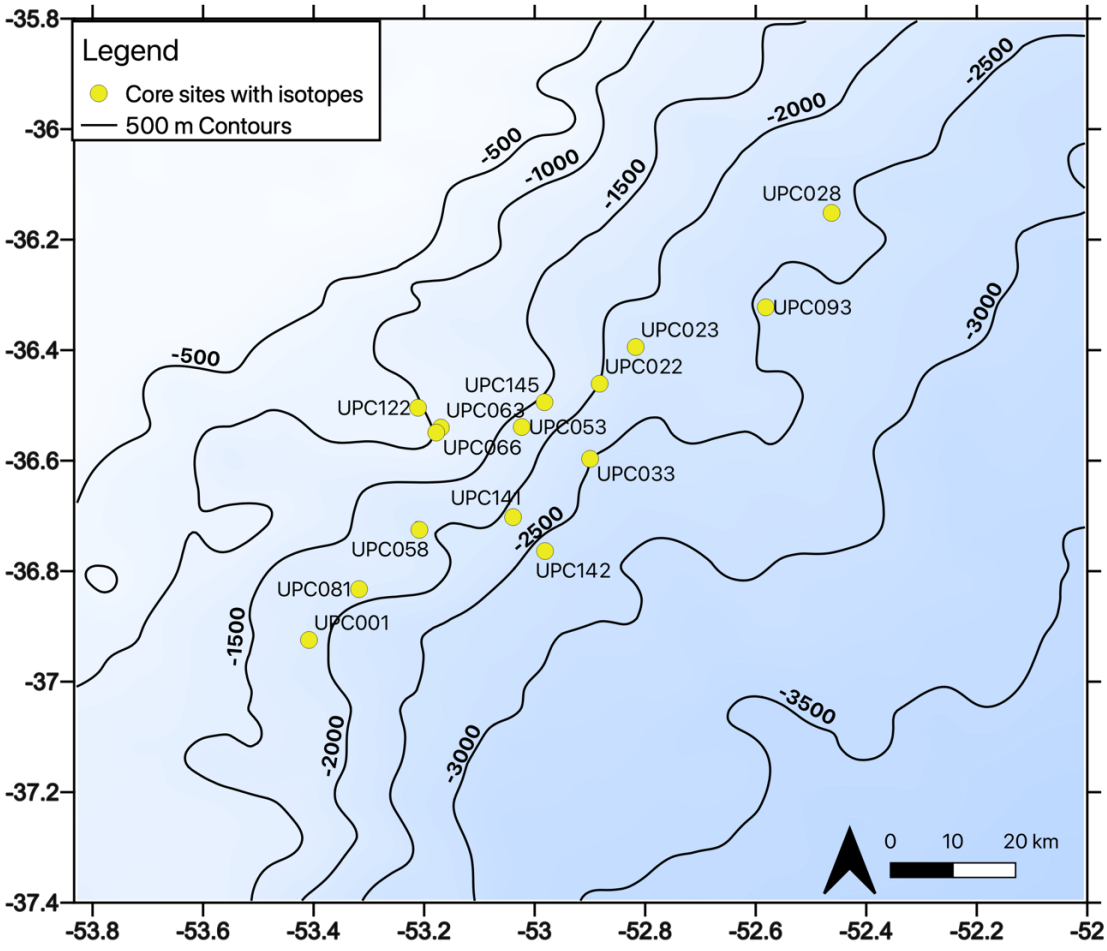

Figure 6.2-1 Spatial distribution of core topes from which *Gc. inflata* specimens were obtained for encrustation classification and stable isotope analysis on the margin. Bathymetric data modified from Hernández-Molina et al., 2016 and McGuire et al., 2019.

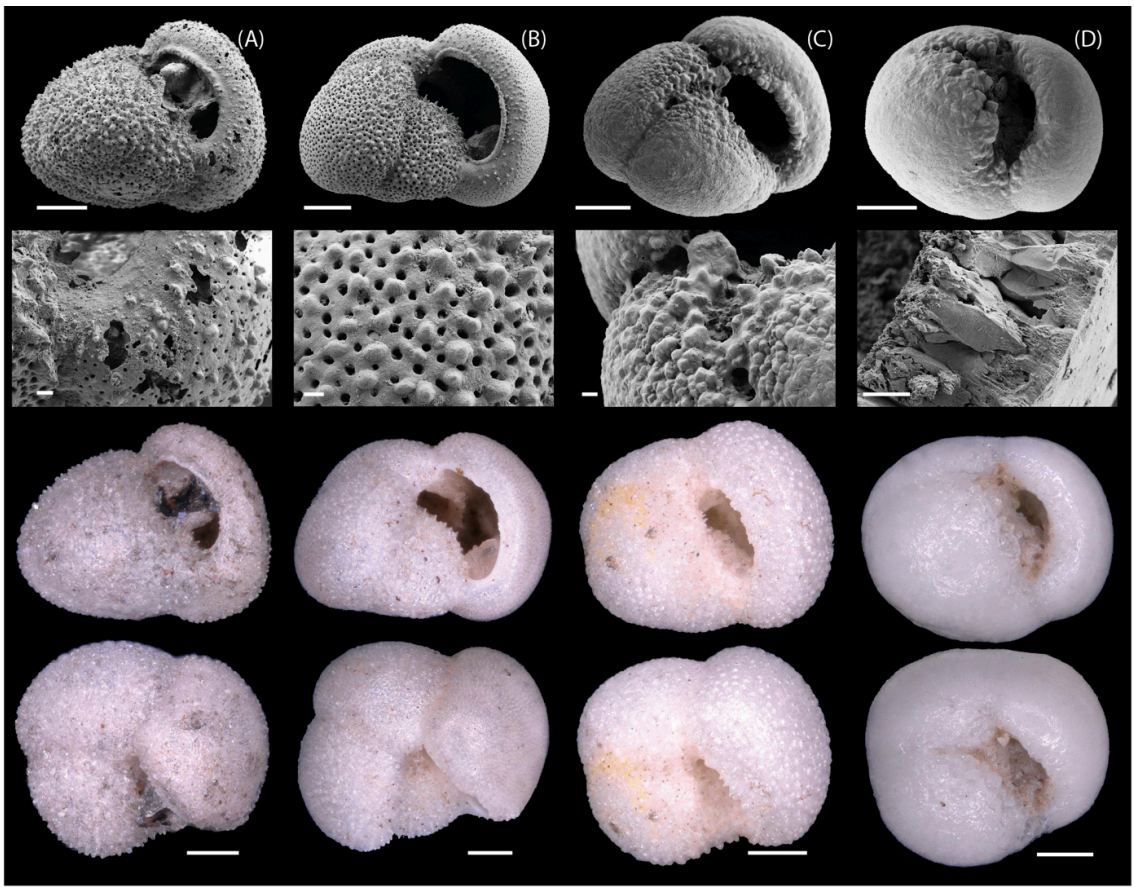

Figure-6.2-2 SEM and light microscopy images of *Gc. inflata* from Jonkers et al., (2021), used for classification of encrustation. Several degrees of encrustation are classified as follows: (A) Non-encrusted, (B) minor, (C) moderate and (D) heavy encrustation. Images display the same specimen in two views for light microscopy, an SEM image and a SEM magnification of the test wall. Scale bars are 100 µm for the full specimens, SEM and light microscopy, and 10 µm for details of the test wall ultrastructure (Jonkers et al., 2021). Preservation of this study was found to be similar to the images presented here, hence the A-D classifications were utilised.

6.2.2 $\delta^{18}O$ and $\delta^{13}C$ isotopes

Single specimen *Gc. inflata* stable isotope data ($\delta^{18}O$ and $\delta^{13}C$) was generated on an Elementar Isoprime 100 with Dual Inlet and Multicarb sample preparation device in the Cohen Laboratories, at the University of Leeds. Samples were calibrated relative to Carrara Marble calcite standard (Elemental Microanalysis – B2214) and data was reported to the Vienna Pee Dee Belemnite (V-PDB) scale. Repeatability of standards is generally better than 0.05‰ (1 S.D) for $\delta^{13}C$ and 0.1‰ (1 S.D) for $\delta^{18}O$. See Chapter 3 for further information on isotope methods.

6.2.3 Morphometric and Isotopic classification

Two morphotypes of *Gc. inflata* are able to be distinguished from one another under light microscopy based on the relative size of the aperture to the final chamber size (Figure 6.1-1) (Morard et al., 2011; Jonkers et al., 2021). Type I

typically display a large aperture relative to the final chamber and are normally larger, compared to Type II specimens, that are more diminutive in overall test size and feature a smaller aperture relative to the final chamber (Morard et al., 2011; Morard et al., 2016; Jonkers et al., 2021). Figure 6.2-3 provides some historical data collected by Morard et al., 2011 that aims to depict the observable differences in morphotypes, chiefly through size (Specimen Major Axis) and the ratio between the aperture and terminal chamber.

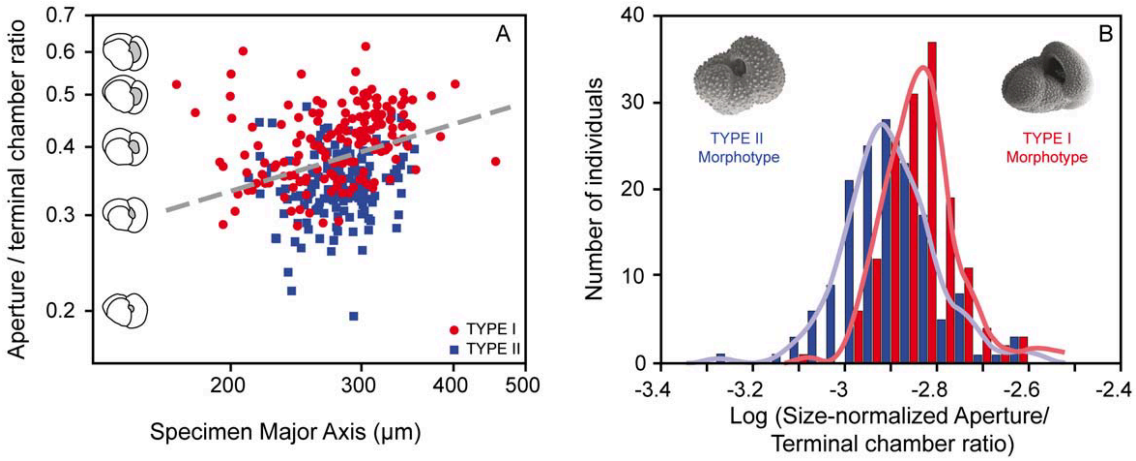

Figure 6.2-3 Previous morphometric work by Morard et al., 2011 is displayed. Plot A shows 306 specimens classified by geographic position when sample was taken. Those collected by cruise AMT-5 above the Sub-Polar front were given a Type I classification, whilst those below the front were categorised as Type II. This is a Log-Log Biplot of aperture/terminal ratio vs. specimen major axis with illustrations provided for aperture/terminal chamber ratio. The grey dashed line depicts the boundary of maximum separation between the two genotypes. Plot B are histograms and Gaussian kernel densities showing the log-ratio between aperture/terminal chamber length and specimen major axis, alongside SEM images of two example morphotypes. This figure and caption are taken/modified from Morard et al., 2011 to show the potential overlap in size ranges between morphotpyes.

In the absence of direct morphological measurement studies have utilised isotope measurements to classify individuals into the two morphotypes. This is based on past western South Atlantic margin transects of core tops and plankton tows that indicate the two morphotypes are offset in $\delta^{18}O$ values, due to contrasting water masses occupied (Chiessi et al., 2007; Morard et al., 2016). The reported mean $\delta^{18}O_{(VPDB)}$ values for Type I range between 0.61 to 1.70 ‰ and Type II mean values between 2.33 to 3.06 ‰ (Morard et al., 2016). This provides a tool to estimate a specimens morphotype, when test morphological analysis is not possible. Although this method is not necessarily definitive it may enable extraction of morphotype in this oceanographically mixed setting.

Individual specimens were to be imaged prior to isotope analysis, in both lateral and umbilical views, using a Zeiss Axio Zoom V16 microscope with attached Cannon EOS 100D camera at 19.4x magnification. A minimum of 25 individuals

of foraminifera would have been imaged for robust statistical analysis in addition to isotopic analysis (Brombacher et al., 2017). Images would then subsequently be analysed using ImagePro Premier software. Collecting measurements on test area, perimeter, length of major axis in edge view, aspect ratio, aperture size and terminal chamber major axes, with the latter two measurements key in providing metrics for morphotype classification. Due to the COVID19 pandemic reducing laboratory time and access, this portion of the methods was unable to be utilised, with constraints requiring a more expedient process for data collection for previous chapters. As such only the visual encrustation classification of *Gc. inflata* tests was feasible, prior to the reduced single specimen isotopic analysis.

6.2.4 Statistical Analysis

K-means clustering was performed on the extracted stable isotope data to statistically assess clustering relationships of *Gc. inflata* data. This was completed within the R statistical software, using the cluster and clValid packages for the analysis. For k-means cluster analysis the number of clusters must be preset to determine association of data points to individual clusters. In order to establish the optimal cluster number, the NbClust R package was used, comparing results of 26 indices. This analysis was set between 2-15 clusters to determine the minimal number of clusters each index recommended. The same starting point for the iterative cluster analysis was used, enabling results to be repeated, with 50 iterations run to ensure reliability of the clusters produced.

6.3 Results

6.3.1 Stable Isotope data

Single specimen stable isotope analysis was conducted on 179 *Gc. inflata* tests. This was comprised of a spatial dataset of 91 individual measurements encompassing a transect running SW-NE, sampling a range of water depth from ~1200-2700 meters below sea level (Figure 6.2-1); and a temporal dataset of 97 individuals collected to assess variation in stable isotopes at a single site. This was conducted on samples from site UPC 028, for which new radiocarbon dating was available from analyses in Chapter 5 (this study), providing a record over the last ~10 ky, with a resolution of less than 600 years. The $\delta^{18}O_{(VPDB)}$ and $\delta^{13}C_{(VPDB)}$ data is displayed in Figure 6.3-1, with data tagged to indicate whether present in the core top (CT), downcore (DC) or both datasets. It is clear there is significant overlap between the core top and downcore data, with a split in the $\delta^{18}O_{(VPDB)}$ values at ~2.00 ‰.

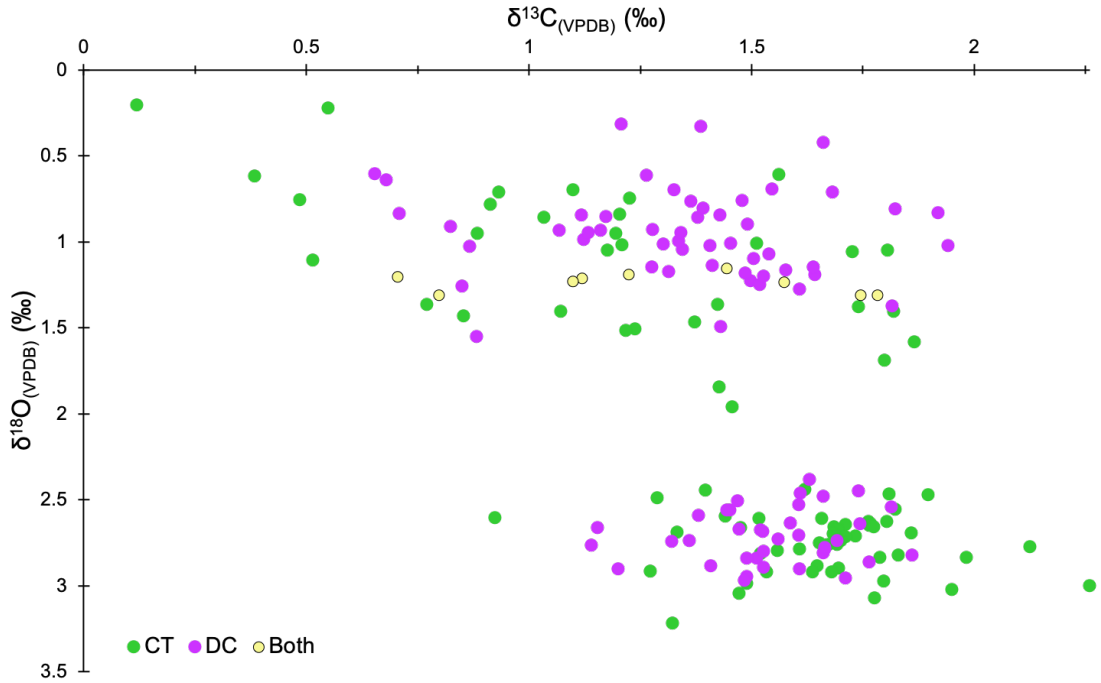

Figure 6.3-1 Stable isotope data from the spatial core top study (CT, green) on the margin and downcore temporal UPC 028 study (DC, purple), with UPC 028 core top data present in both studies highlighted (Both, yellow).

6.3.2 Density distribution plots and morphotype allocation

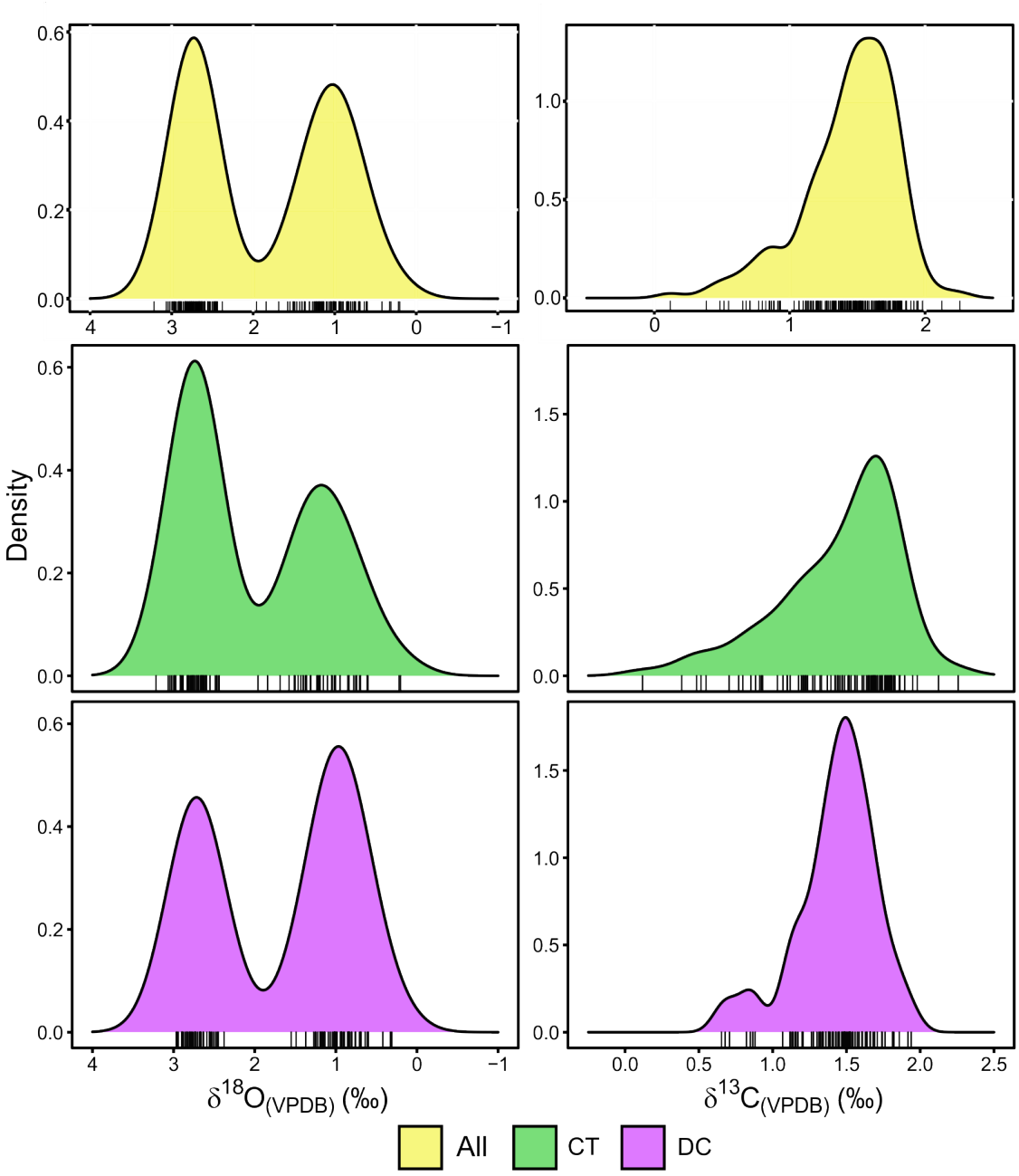

Figure 6.3-2 Density distributions of all *Gc. inflata* results from core top and downcore samples (yellow), black tick marks indicate individual data. $\delta^{18}O_{(VPDB)}$ data displays bimodal peaks, the largest centred on ~2.8 ‰, whilst the smaller, broader peak is centred on ~1 ‰. Two peaks suggest two populations within the $\delta^{18}O$ data. $\delta^{13}C_{(VPDB)}$ data displays one large peak at ~1.6 ‰ and the majority of results fall between 1-2 ‰ $\delta^{13}C_{(VPDB)}$. Core top (CT, green) vs. downcore (DC, purple) stable isotope data distribution, x-axis tick marks identify individual data. Bimodal $\delta^{18}O_{(VPDB)}$ nature is preserved in both CT and DC. CT $\delta^{13}C_{(VPDB)}$ data produces a broad unimodal peak with a skew toward higher values, DC data suggests a minor bimodal distribution.

Density distribution plots are produced for $\delta^{18}O$ and $\delta^{13}C$ isotopes, showing the range of values recorded on the margin and the potential clustering of isotope values. The results of this are displayed in Figure 6.3-2. The $\delta^{18}O_{(VPDB)}$ data displays two peaks, broadly similar in size, with the larger and slightly narrower

peak centred ~2.8 ‰, and the second broader and shorter peak centred on ~1.0 ‰. These bimodal peaks suggest two populations in the $\delta^{18}O$ data. The $\delta^{13}C$ data does not replicate the two peaks seen in the $\delta^{18}O$ dataset, instead a single broader peak between 1-2 ‰ $\delta^{13}C_{(VPDB)}$ is displayed, roughly centred on 1.6 ‰ $\delta^{13}C_{(VPDB)}$. There is a larger tail <1 ‰, creating a slope from the peak, this is not recreated on the >2 ‰ portion of the data, which shows a sharper slope from the peak. The lack of bimodality within the $\delta^{13}C$ data implies continuity across this data set, with the previously observed clustering being driven by the $\delta^{18}O$ isotope data. These trends in the $\delta^{18}O$ and $\delta^{13}C$ data remain when categorised into core top and downcore samples, with the twin peaks clearly visible in the $\delta^{18}O$ data and broad single peak for the $\delta^{13}C$ data (Figure 6.3-2). The distributions of stable isotope values are consistent between the modern core top records and the temporal record of UPC 028, over the last ~10 ka.

6.3.3 K-means clustering analysis

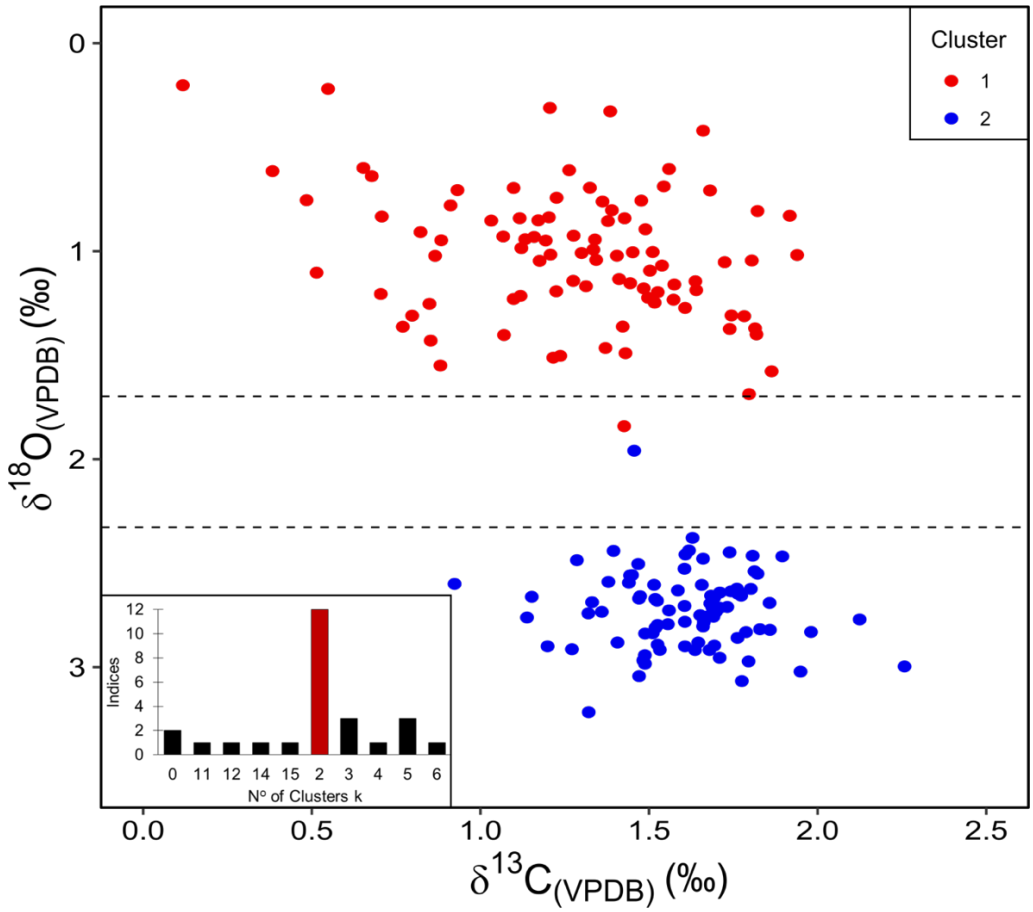

Figure 6.3-3 K-means cluster analysis for *Gc. inflata* when all data are incorporated. Two clusters were used for the analysis based on NbClust assessment (see inset). Clusters derived appear to be divided based on $\delta^{18}O_{(VPDB)}$ as the principal factor. Cluster 1 predominantly falls <1.70 ‰ $\delta^{18}O_{(VPDB)}$ whilst Cluster 2 predominantly lies >2.33 ‰ $\delta^{18}O_{(VPDB)}$ aligning with Morard et al., (2016).

K-means cluster analysis was utilised to mathematically delineate groupings, with two clusters calculated to be the best fit for the data, based on 26 indices (Methods 3.2.4) (Figure 6.3-3). Comparison between Figure 6.3-1 and Figure 6.3-3 identifies presence of both clusters in the core top and downcore record.

Cluster 1 features all specimens with values with <2 ‰ $\delta^{18}O_{(VPDB)}$ values and a large variation in $\delta^{13}C_{(VPDB)}$ values, with a range of ~0.11-2.26 ‰ $\delta^{13}C_{(VPDB)}$ (Figure 6.3-3). Cluster 2 meanwhile is comprised of individuals with $\delta^{18}O_{(VPDB)}$ values >2 ‰ and a range of $\delta^{13}C_{(VPDB)}$ values between ~0.65-1.94 ‰ $\delta^{13}C_{(VPDB)}$ (Figure 6.3-3). Combined with the density distribution data this further suggests the two clusters are linked to the $\delta^{18}O_{(VPDB)}$ split, and may indicate an isotopic signature between two separate morphotypes. Further comparison with Figure 6.3-4 corroborates the value of isotopic boundaries laid out in Morard et al., (2016).

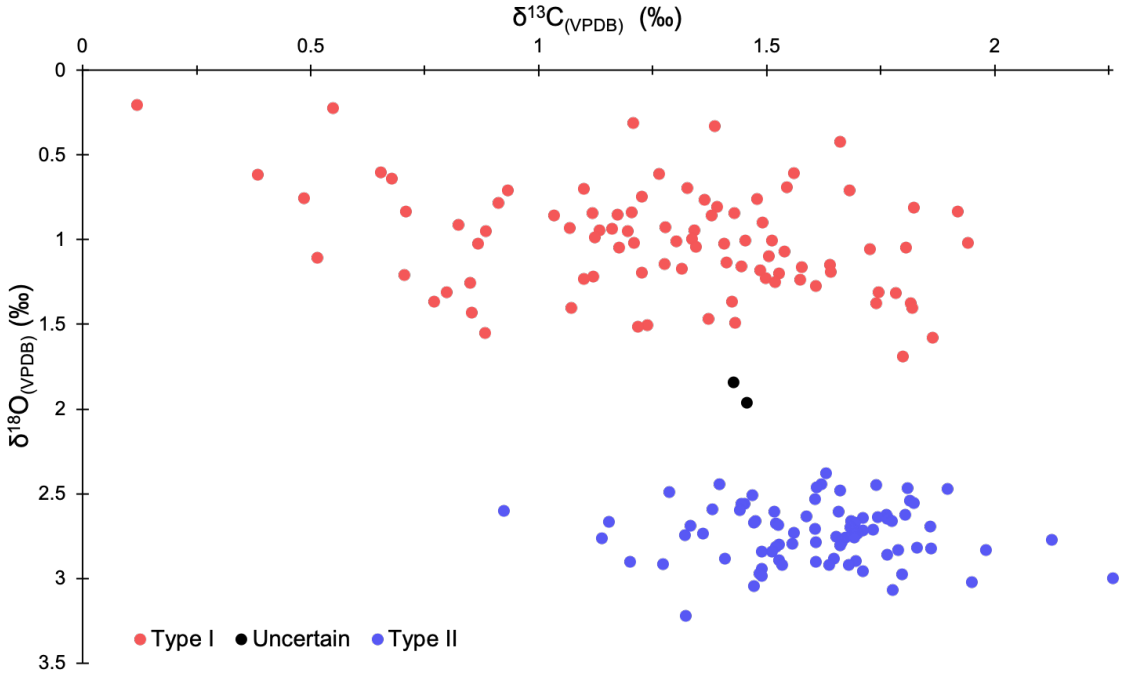

Figure 6.3-4 *Gc. inflata* likely morphotypes estimated based on $\delta^{18}O_{(VPDB)}$ limits set in Morard et al., (2016). Compared to Figure 6.3-1 it appears both the core top and downcore data comprise of morphotype I (Type I, <1.70 ‰ $\delta^{18}O_{(VPDB)}$) and morphotype II (Type II, >2.33 ‰ $\delta^{18}O_{(VPDB)}$), two data points are ascribed as uncertain, falling between the ranges of Type I and Type II of Morard et al., (2016).

From previous margin studies employing multi-specimen stable isotope analysis, only Chiessi et al., (2007) and Jonkers et al., (2021) provide both $\delta^{18}O$ and $\delta^{13}C$ values for samples, with Voigt et al., (2015) and Morard et al., (2016) only making $\delta^{18}O$ data available. Whilst this enables an estimate of morphotype to be inferred following ranges in Morard et al., (2016), it limits the ability to perform cluster

analysis. Despite this, the multi-specimen averaged data has been plotted for the Chiessi et al., (2007) and Jonkers et al., (2021) datasets, alongside the UPC spatial and temporal data (Figure 6.3-5). Data broadly follow trends observed in UPC results, with two distinct groupings visible, between Type I (<1.70 ‰ $\delta^{18}O_{(VPDB)}$) and Type II (>2.33 ‰ $\delta^{18}O_{(VPDB)}$), in which a minority of data fall, implying clear isotopic separation between groupings (Figure 6.3-5).

Comparison between Figure 6.3-3 and Figure 6.3-5 see minor differences between the positioning of the two K-means cluster results, with the slight encroachment of cluster two.

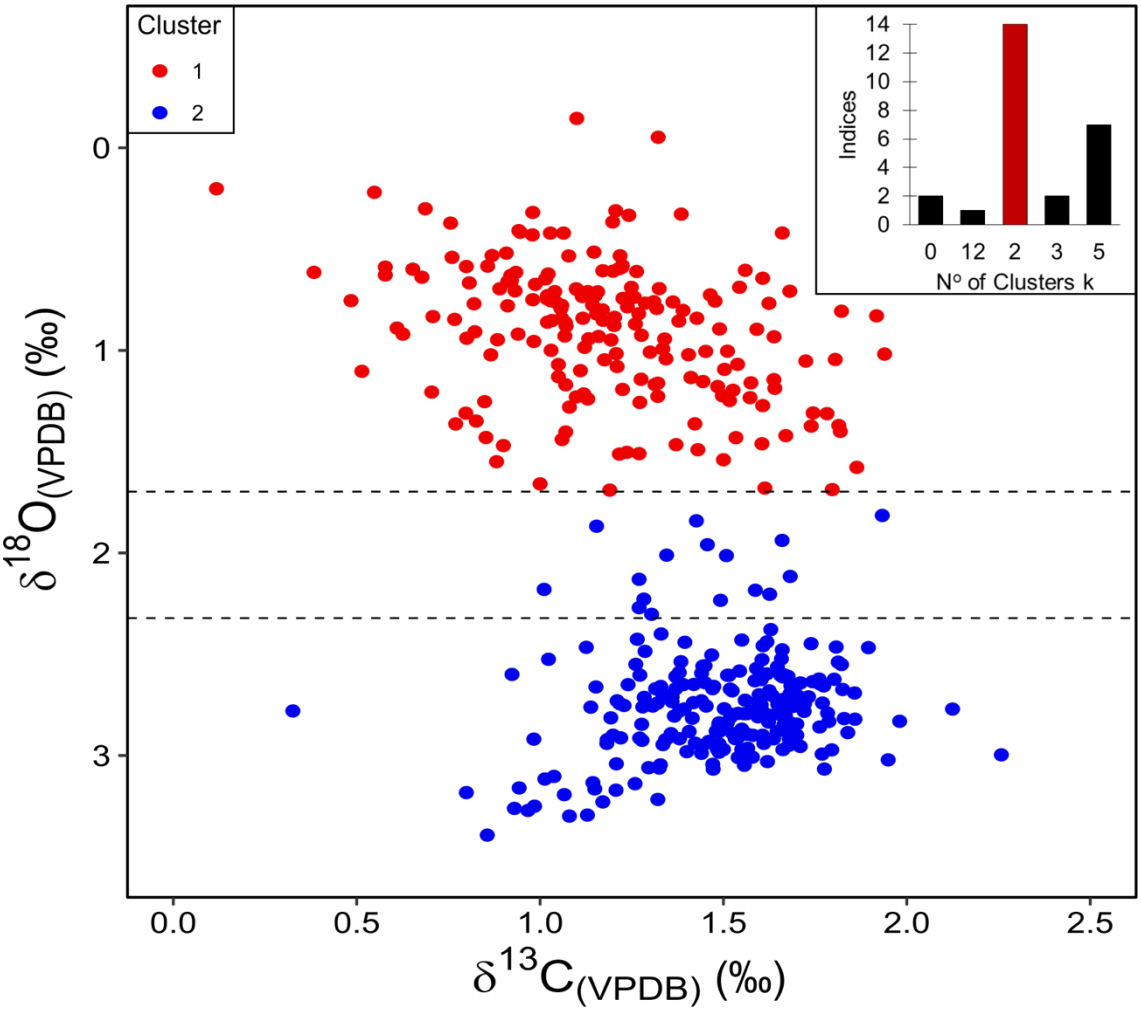

Figure 6.3-5 K-means cluster analysis of all *Gc. inflata* stable isotope data for the western South Atlantic margin. Two clusters form, corroborating results in Figure 6.3-4. Dashed lines indicate $\delta^{18}O_{(VPDB)}$ limits for inference of Type I (<1.70 ‰) and Type II (>2.33 ‰), as published in Morard et al., (2016). Inset shows results of multiple indices approach to determine optimal number of clusters for K-means analysis. Using all UPC, Chiessi et al., (2007) and Jonkers et al., (2021) data.

6.3.3.1 Spatial morphotype distribution

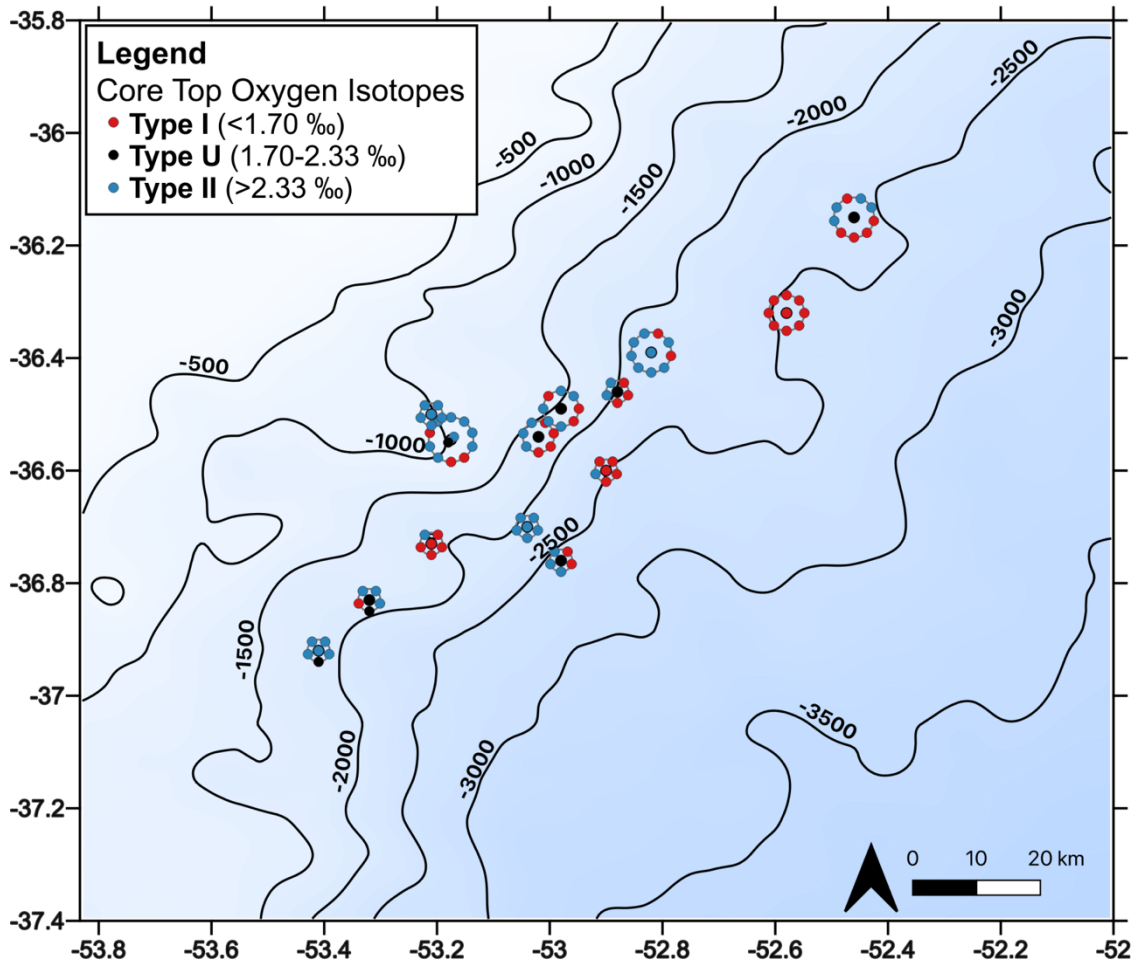

Figure 6.3-6 Spatial distribution of morphotypes using $\delta^{18}O_{(VPDB)}$ ranges from Morard et al., (2016) for classification. A majority of individuals are classified as Type II (50 specimens) versus Type I (39 specimens) with the remainder classified as Uncertain (2 individuals). Type II individuals predominate sites in the shallower northwest of the study area, with increasing proportions of Type I specimens to the east of the margin. Central circle indicates the site classification if all individual points were averaged, through this method comparison with historical studies is possible. It is clear that a number of sites would produce a Type U average signal, not representing individuals recovered from the site. Bathymetric data modified from Hernández-Molina et al., 2016 and McGuire et al., 2019.

Mapping the spatial distribution of potential morphotypes using the $\delta^{18}O_{(VPDB)}$ isotopic results obtained for individual tests, enables analysis geographic patterns to be analysed (Figure 6.3-6). All sites have a minimum of five data points with initial observations indicating the majority of sites show a mix of morphotypes, based on the $\delta^{18}O_{(VPDB)}$ isotopes. Within the spatial core top study 39 individuals are classified as morphotype Type I, 50 individuals are classified as Type II, whilst two are recorded as Uncertain morphotype. Three sites feature only one morphotype, with UPC 093 recording only Type I individuals from the northeast of the margin, while UPC 122, the shallowest site, and UPC 141 both featuring only Type II specimens in the centre/southwest of the margin. The two

individuals classified as Uncertain, with values approaching ~2 ‰ $\delta^{18}O_{(VPDB)}$, are located in the southwest of the margin at sites UPC 001 and UPC 081 respectfully. This visualisation in Figure 6.3-6 shows a dominance of the Type II form in the northwest of the margin, and increasing numbers of Type I individuals further offshore and to the east of the margin. In addition to the individual measurements, overall site average $\delta^{18}O_{(VPDB)}$ were classified, displayed as the central circle in Figure 6.3-6. This produces a number of sites with average Type U classification despite individuals classifying as either Type I or Type II and should be considered when comparing with multi-specimen data (Chiessi et al., 2007; Voigt et al., 2015; Morard et al., 2016; Jonkers et al., 2021).

6.3.3.2 Temporal morphotype distribution

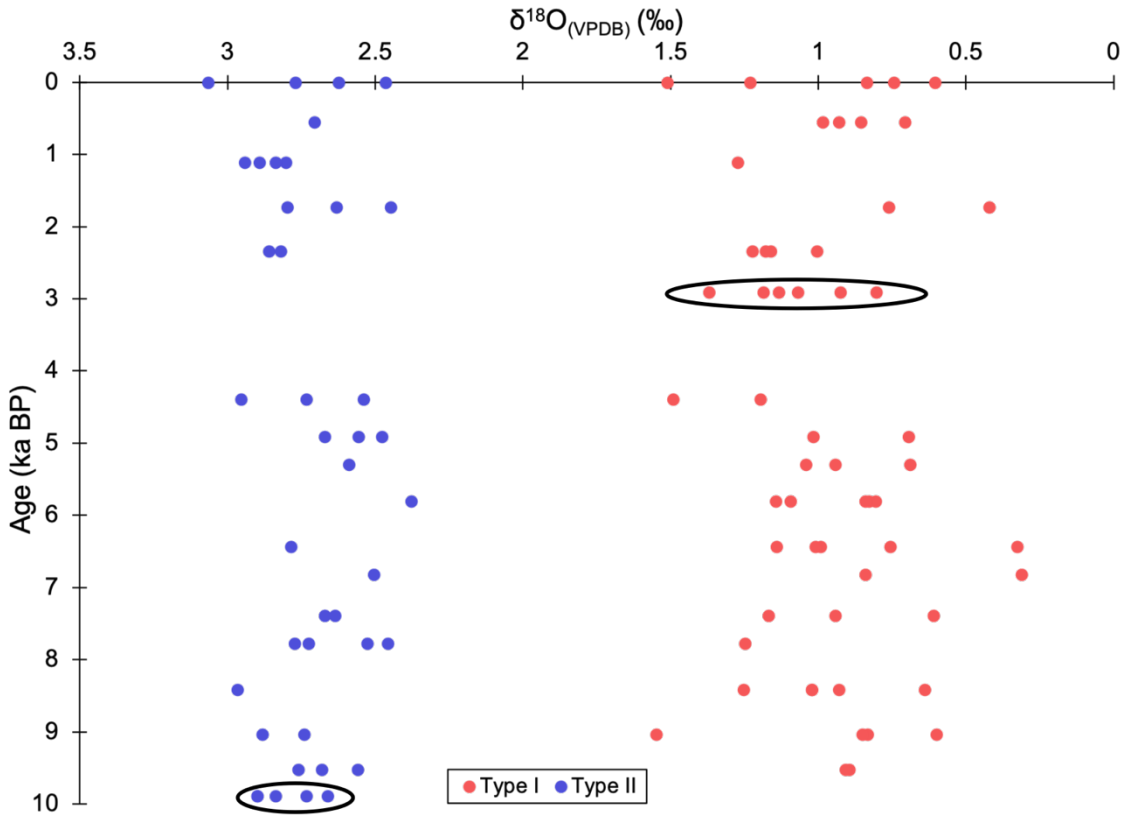

Figure 6.3-7 UPC 028 temporal single specimen $\delta^{18}O_{(VPDB)}$ data for *Gc. inflata*, separated isotopically into the two likely morphotypes represented. Coeval samples record individuals of both morphotypes inferring water mass migration is common through geological time, with the isotopic offset between populations preserved. Two samples are identified which display only one morphotype.

Temporal variation in morphotype can be similarly described to the spatial assessment using the $\delta^{18}O_{(VPDB)}$ values of core site UPC 028. All individual data points are classified with 56 individuals classified as Type I and 41 classified as Type II, covering a roughly 10 ky interval (Figure 6.3-7). As with the spatial

dataset, the temporal samples of the same age are frequently composed of both morphotypes suggesting the site experienced both water masses. Two sample horizons appear entirely composed of a single morphotype, circled on Figure 6.3-7.

6.3.4 Encrustation

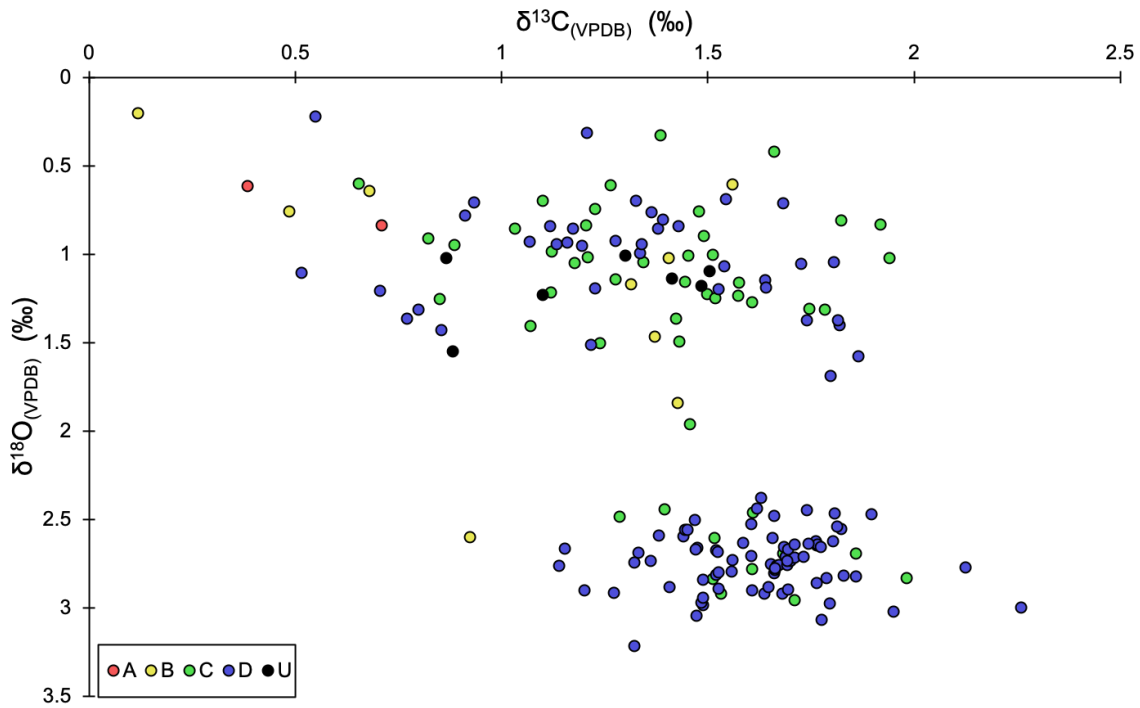

Figure 6.3-8 $\delta^{18}O_{(VPDB)}$ and $\delta^{13}C_{(VPDB)}$ individual *Gc. inflata* results categorised by degree of encrustation, both core top and downcore data. Visually, two clusters are present, split by $\delta^{18}O$, with the grouping >2 ‰ $\delta^{18}O_{(VPDB)}$ dominated by more heavily encrusted individuals.

Classification of encrustation types (A-D, and U) resulted in 179 individual *Gc. inflata* specimens categorised with single specimen stable isotopes acquired. Percentages of the total collected is provided, composed of two non-encrusted (A) class specimens (1.12 %), nine minor encrusted (B) classified individuals (5.03 %), 48 (C) medium encrusted specimens (26.82 %), 113 heavily encrusted (D) individuals (63.13 %), and seven (U) unknown individuals (3.91 %). The latter U classified group were run prior to publishing of papers investigating encrustation classification. Core top samples comprise 91 individual paired measurements, with 88 downcore samples from UPC 028, providing 97 measurements for temporal assessment. Data is categorised by encrustation and displayed in Figure 6.3-8 showing the spread of $\delta^{18}O_{(VPDB)}$ and $\delta^{13}C_{(VPDB)}$ values, with category D dominating individuals >2 ‰ $\delta^{18}O_{(VPDB)}$. All *Gc. inflata* data were visually categorised for encrustation type following methodology of Jonkers et al., (2021) as discussed above. Distributions are visualised in Figure 6.3-9.

6.3.4.1 Density Distributions of encrustation types

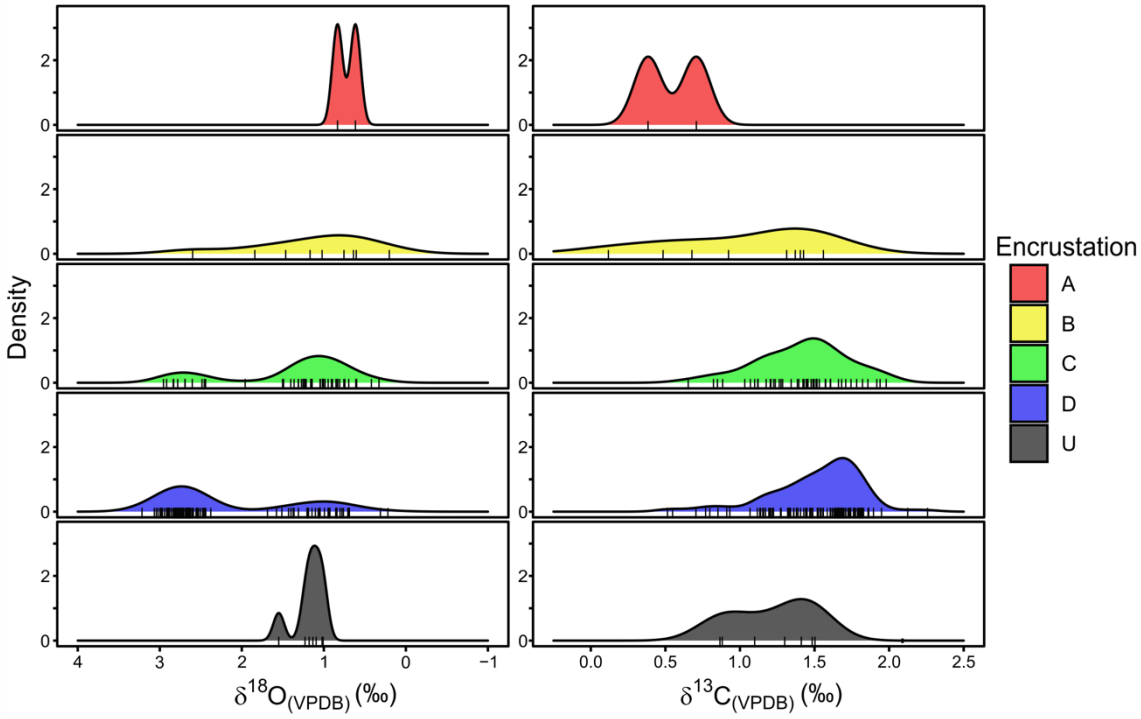

Figure 6.3-9 Stable isotope value distributions categorised for encrustation level following Jonkers et al., (2021) scheme. Plot features all recorded *Gc. inflata* values obtained by this study. Note encrustation level A (non-encrustation) features only two representatives, whilst D (heavily encrusted individuals) accounts for 113 individuals.

Relatively few non-encrusted (A) individuals are available, resulting in a twin pair of peaks in the $\delta^{18}O$ and $\delta^{13}C$ data. $\delta^{18}O_{(VPDB)}$ values report a tight range between 0.61-0.84 ‰, whilst the $\delta^{13}C_{(VPDB)}$ range is slightly broader between 0.38-0.71 ‰. Minorly encrusted (B) individuals produce a single flatter peak for both $\delta^{18}O$ and $\delta^{13}C$. The range of $\delta^{18}O_{(VPDB)}$ values is 0.20-2.60 ‰, with the majority of values falling <2 ‰. Minor encrusted $\delta^{13}C_{(VPDB)}$ values fall between 0.11-1.55 ‰, with the slight peak located at approximately 1.40 ‰.

Moderately encrusted (C) individuals show two peaks in the $\delta^{18}O_{(VPDB)}$ data, with the larger peak centred at ~1.0 ‰ with a range of ~0.32-1.51 ‰, the second, more subdued peak is centred 2.70 ‰ with a range of 2.44-2.96 ‰ (Figure 6.3-9). One individual falls between these two obvious peaks at ~1.96 $\delta^{18}O_{(VPDB)}$ ‰ and is not easily prescribed into either grouping. For the $\delta^{13}C_{(VPDB)}$ data a single, normally distributed peak is visible centred at ~1.42 ‰, with a broad range of 0.65-1.99 ‰ largely consistent with peaks (Figure 6.3-2).

Majorly encrusted (D) individuals are by far the most numerous grouping, showing two peaks in the $\delta^{18}O_{(VPDB)}$ data similar to C (Figure 6.3-9). Unlike the C grouping however, the heavier $\delta^{18}O_{(VPDB)}$ grouping is more numerous with 75 individuals forming a peak centred on ~2.74 ‰, with a range of 2.37-3.22 ‰. The smaller peak centres on ~1.02 ‰, with a range of 0.21-1.69 ‰ and comprises of 38 individual measurements, producing two populations in $\delta^{18}O$ space. For $\delta^{13}C_{(VPDB)}$ a single large peak is produced, which skews to the right, toward higher $\delta^{13}C$ values. The peak is centred at ~1.70 ‰, with a range of $\delta^{13}C_{(VPDB)}$ values encompassing 0.51-2.26 ‰. The U encrustation grouping shows two peaks in the $\delta^{18}O_{(VPDB)}$ data, with the main peak centred at ~1.11 ‰, total data range is relatively compact (1.00-1.55 ‰). $\delta^{13}C_{(VPDB)}$ data by comparison forms a broader peak with a range of 0.86-1.50 ‰ (Figure 6.3-9).

Density plots accounting for encrustation level, splitting data into core top samples or downcore samples enabled interrogation of data in a spatial and temporal sense to observe whether the stable isotopic trends were present (Figure 6.3-10). In both instances category A does not feature enough individuals to plot, whilst only the downcore dataset has enough U categorised individuals for them to be included.

Overall, plots produced for core top individuals classified by encrustation (Figure 6.3-10) produce largely similar profiles to when all data was plotted (Figure 6.3-9). Category B shows a single broad peak for both $\delta^{18}O_{(VPDB)}$ and $\delta^{13}C_{(VPDB)}$ values, with slight right skews to lower $\delta^{18}O_{(VPDB)}$ and higher $\delta^{13}C_{(VPDB)}$ values respectively. Twin peaks in category C $\delta^{18}O_{(VPDB)}$ values remains, with a greater number of individuals at <1.7 ‰. $\delta^{13}C_{(VPDB)}$ values show a similar single peak to category B, albeit with a slight left skew to lower $\delta^{13}C_{(VPDB)}$ values. Category D also shows broadly similar bimodal peaks to all *Gc. inflata* $\delta^{18}O_{(VPDB)}$ data, with a skew to higher $\delta^{18}O_{(VPDB)}$ values. $\delta^{13}C_{(VPDB)}$ data is bimodally distributed, with the main mode around ~1.70 ‰, and the bulk of reported values between 1.2-2.0 ‰. The second smaller mode is ~0.8 ‰ with a range of ~0.5-0.94 ‰ $\delta^{13}C_{(VPDB)}$.

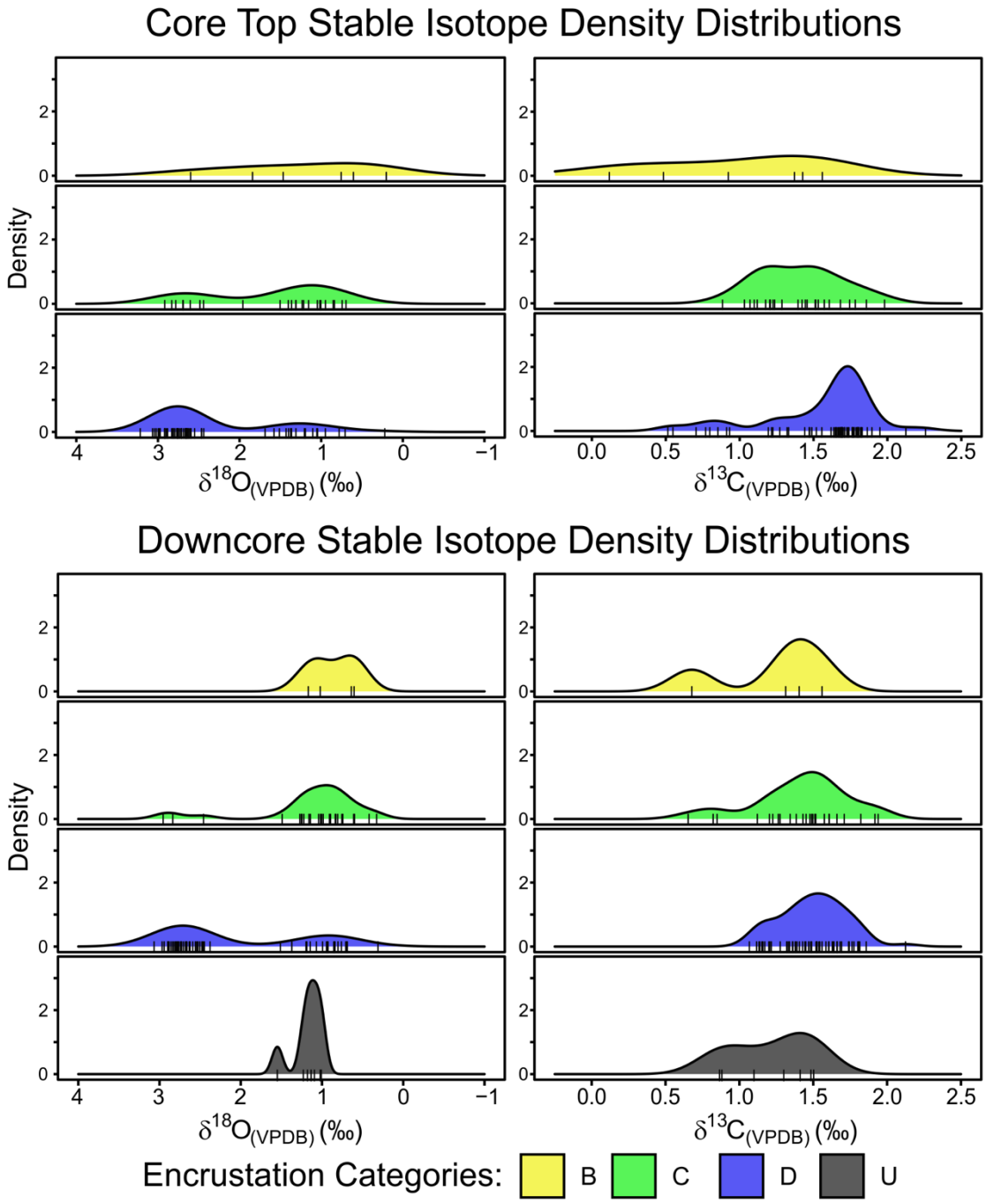

Figure 6.3-10 Distribution of core top and downcore encrusted individuals for both $\delta^{18}O_{(VPDB)}$ and $\delta^{13}C_{(VPDB)}$ values. Top panels: Total number of core top specimens is 91 measurements, the individual representatives for categories A and U respectively were removed due to too few data points for distribution plotting. Lower panels: Total number of downcore specimens is 97 measurements, including core top measurements for site UPC 028. The one category A representative was removed, insufficient for distributions.

Downcore encrustation data density curves for four categories are displayed in Figure 6.3-10. Category B sees the spread of the $\delta^{18}O_{(VPDB)}$ values concentrated around ~1.00 ‰, with a range of 0.60-1.17 ‰, displaying a shorter range of values than the core top record. $\delta^{13}C_{(VPDB)}$ data meanwhile has a bimodal peak with the larger peak centred around ~1.40 ‰ and the second peak at ~0.67 ‰, a range from ~0.67-1.56 ‰. Downcore category C encrustation record features bimodal $\delta^{18}O_{(VPDB)}$ peaks, with a smaller peak falling between ~2.40-3.00 ‰. The second larger peak spans ~0.30-1.50 ‰ $\delta^{18}O_{(VPDB)}$, with the peak centring at ~1.00 ‰. Downcore category C $\delta^{13}C_{(VPDB)}$ distributions are similar to those seen in downcore category B data, with a slightly broader range of ~0.63-1.94 ‰, the dominant peak centres on ~1.50 ‰ whilst the secondary peak lies at ~0.80 ‰. Category D encrusted individuals represent the largest group in the downcore record and form a clear set of bimodal peaks, separated from one another in $\delta^{18}O_{(VPDB)}$ space at approximately 1.80 ‰. The larger peak centres at ~2.70 ‰ $\delta^{18}O_{(VPDB)}$, ranging from 2.37-3.07 ‰, the smaller peak has a wider range, between 0.31-1.51 ‰, centred at ~0.90 ‰. Compared to category B and C in the downcore record, category D shows a more unimodal normal distribution of $\delta^{13}C_{(VPDB)}$ values, ranging from ~1.06-2.13 ‰ and centred on ~1.55 ‰. The final category U reflects the same profiles as the overall plot in Figure 6.3-9 as all unknown encrusted specimens originate from UPC 028.

6.3.4.2 Spatial and temporal variation of encrustation

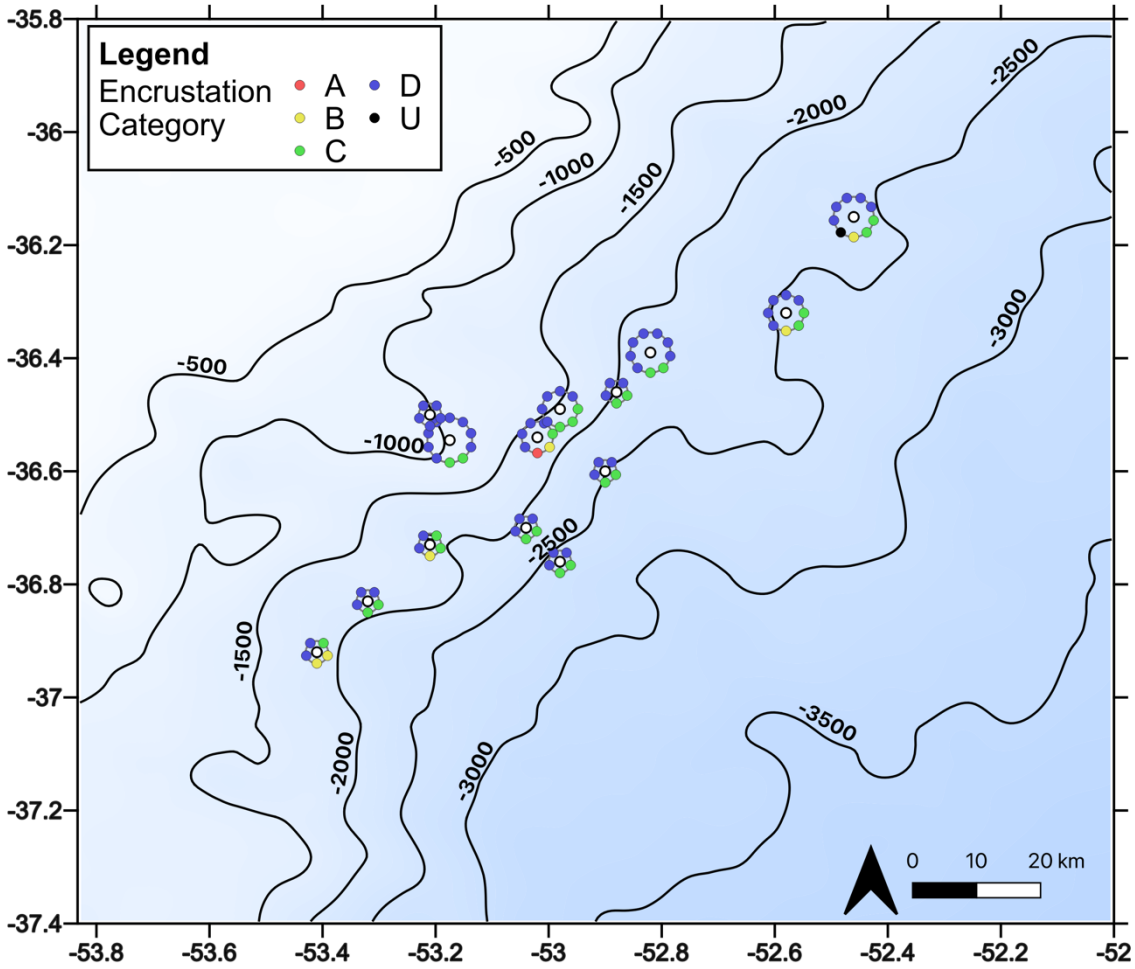

Figure 6.3-11 Spatial dispersion of *Gc. inflata* encrustation states, higher levels of encrustation observed in northern and northwest sections, whilst southern sites, and those further offshore, have higher proportion of individuals with lower levels of encrustation. Bathymetric data modified from Hernández-Molina et al., 2016 and McGuire et al., 2019.

Spatially mapping the categorisation of *Gc. inflata* data by encrustation state sees the majority of sites dominated by heavily encrusted D individuals (Figure 6.3-11). Few sites record individuals with no or minor (A and B) encrustation. Most sites show variation in encrustation state, with only one site reporting a single encrustation type. Study region sites within shallower waters and in the northwest show greater propensity for more heavily encrusted individuals however, sites in the southern portion of the margin show fewer heavily encrusted individuals.

Analysing the UPC 028 downcore record for encrustation classification a couple of trends are visible (Figure 6.3-12). Firstly, samples of the same age frequently contain individuals of multiple encrustation types, with Category D the most common. Individuals >2 ‰ $\delta^{18}O_{(VPDB)}$ are pre-dominantly heavily encrusted, with a subset of individuals categorised as medium encrusted, and no individuals

showing no or minor encrustation. The <2 ‰ $\delta^{18}O_{(VPDB)}$ dataset shows a more varied set of classifications, with fewer relative numbers of heavily encrusted individuals, and a higher proportion of medium encrusted individuals. Unlike the >2 ‰ $\delta^{18}O_{(VPDB)}$ dataset there is a small proportion of no and minor encrusted individuals, and all of the unknown encrustation individuals. Additionally, sample age does not appear to have an impact on encrustation state, with examples of no, minor and medium encrustation occurring at all depths within the core.

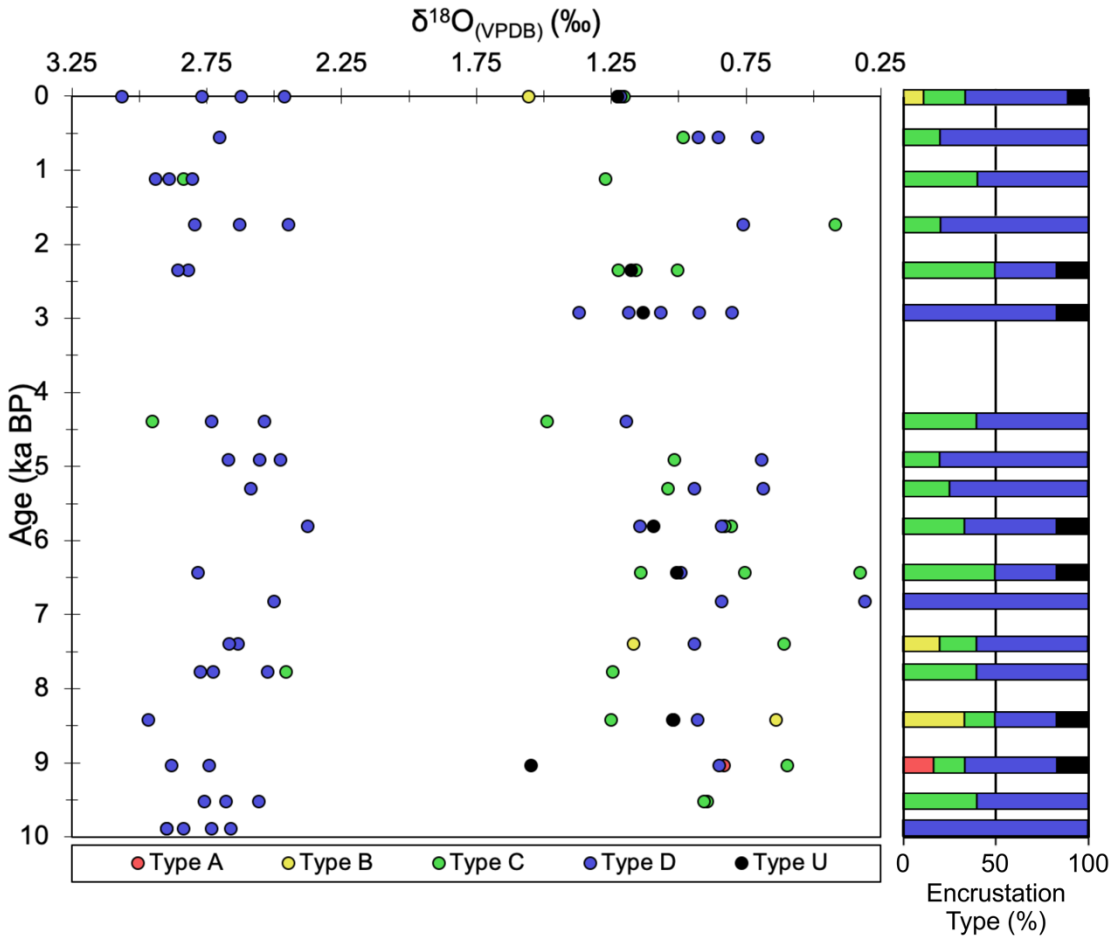

Figure 6.3-12 Downcore $\delta^{18}O_{(VPDB)}$ data categorised by encrustation level. >2 ‰ $\delta^{18}O_{(VPDB)}$ measurements dominated by heavily (D) and medium encrusted specimens (C). <2 ‰ $\delta^{18}O_{(VPDB)}$ measurements show more varied encrustation states, with higher proportions of C and instances of minor or no encrustation. Proportion of encrustation type by sample interval is provided.

6.3.5 Encrustation and Morphotype

Morphotype $\delta^{18}O_{(VPDB)}$ classifications alongside encrustation categorisations within $\delta^{18}O$ and $\delta^{13}C$ space are displayed in Figure 6.3-13. Type I morphotypes display a wider range of encrustation states. Proportionally, Type I is comprised of 2.2 % category A encrusted individuals, 7.8 % of category B encrusted specimens, 40 % of category C encrusted individuals, 42.2 % of category D encrusted examples and 7.8 % with an Unclassified encrustation level (Figure 6.3-14). Type II by comparison is much less cosmopolitan, composed of 1.1 % category B individuals, 12.6 % category C specimens and dominated by 86.2 % category D individuals (Figure 6.3-14). Two datapoints with unassigned morphotypes from $\delta^{18}O$ values (Type U) comprise a category B and category C example each (Figure 6.3-14).

Category A comprises of only Type I individuals (Figure 6.3-13), B sees highest occurrences in Type I also, with 77.8 % of individuals present and one specimen each for Type II and Type U. C, comprising of its 48 individual data, has 75 % located in the lighter $\delta^{18}O$ cluster, whilst 22.9 % reside within the heavier $\delta^{18}O$ Type II cluster, and a single specimen remains unclassified. D is by far the most numerous category within this study at 113 individuals, and of all the categories shows the most even distribution between the morphotypes. Type I accounts for 33.6 % of all D individuals recovered, but Type II dominates with 66.4 % of specimens showing heavy encrustation. The remaining seven Uncategorised individuals are all present within Type I.

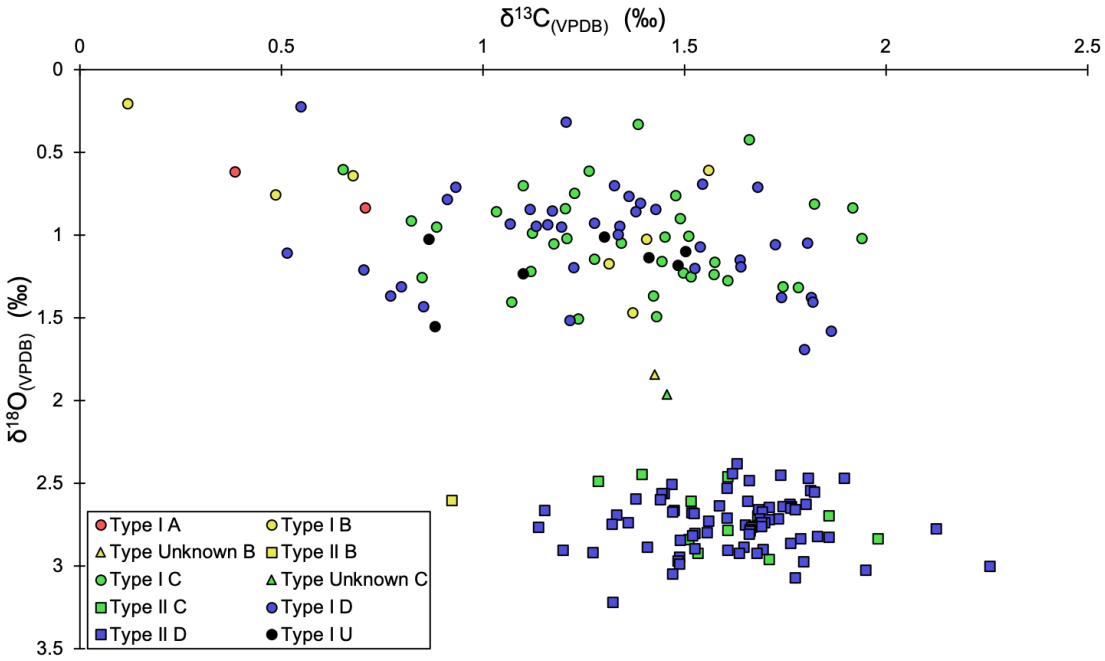

Figure 6.3-13 $\delta^{18}O_{(VPDB)}$ and $\delta^{13}C_{(VPDB)}$ plot of data categorised for assumed morphotype based on previously published expected ranges of $\delta^{18}O_{(VPDB)}$ (Morard et al., 2016). Circles = Type I, squares = Type II and triangles = Type U. Colours denote encrustation state, red = A, no encrustation, yellow = B, minor encrustation, green = C, medium encrustation, blue = D, heavily encrusted, black = U, encrustation unknown.

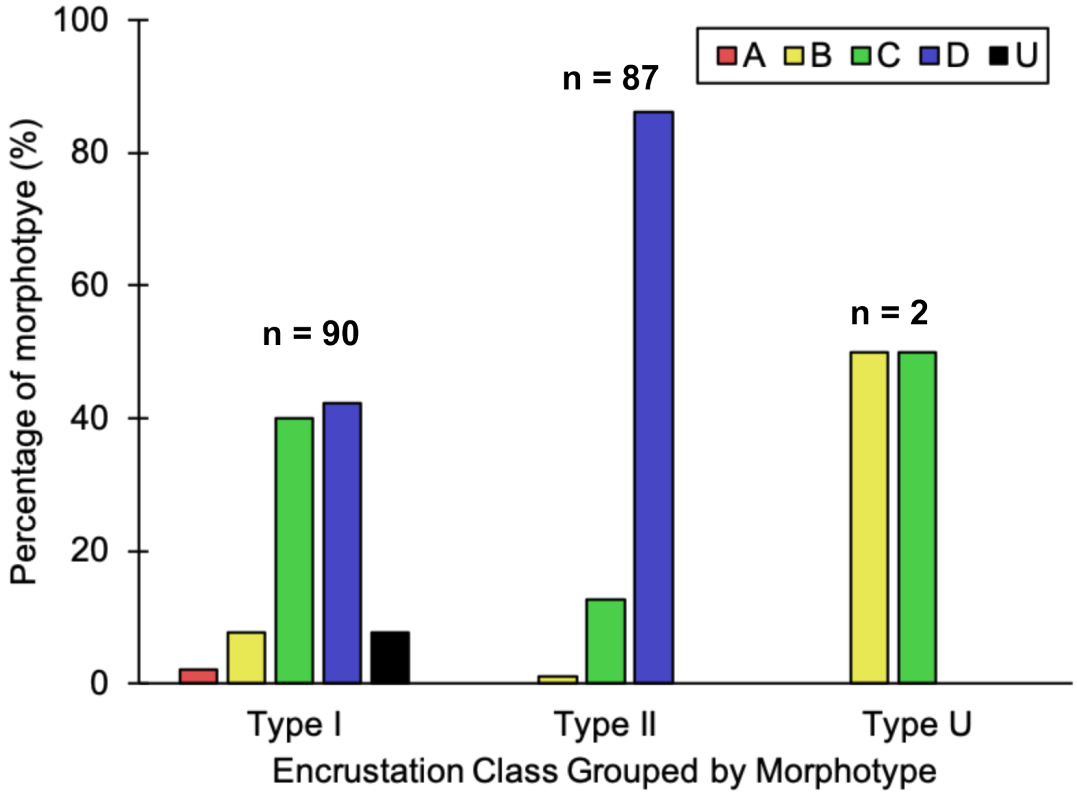

Figure 6.3-14 Composition of each morphotype by classification of encrusted individuals. Type II individuals display an 86.6 % propensity for heavily encrusted individuals, twice that of Type I. Whilst Type I is dominated by Medium (C) and Heavily (D) encrusted individuals, the type records higher proportions of lesser encrusted and unknown categorisations.

6.4 Discussion

6.4.1 Previous studies

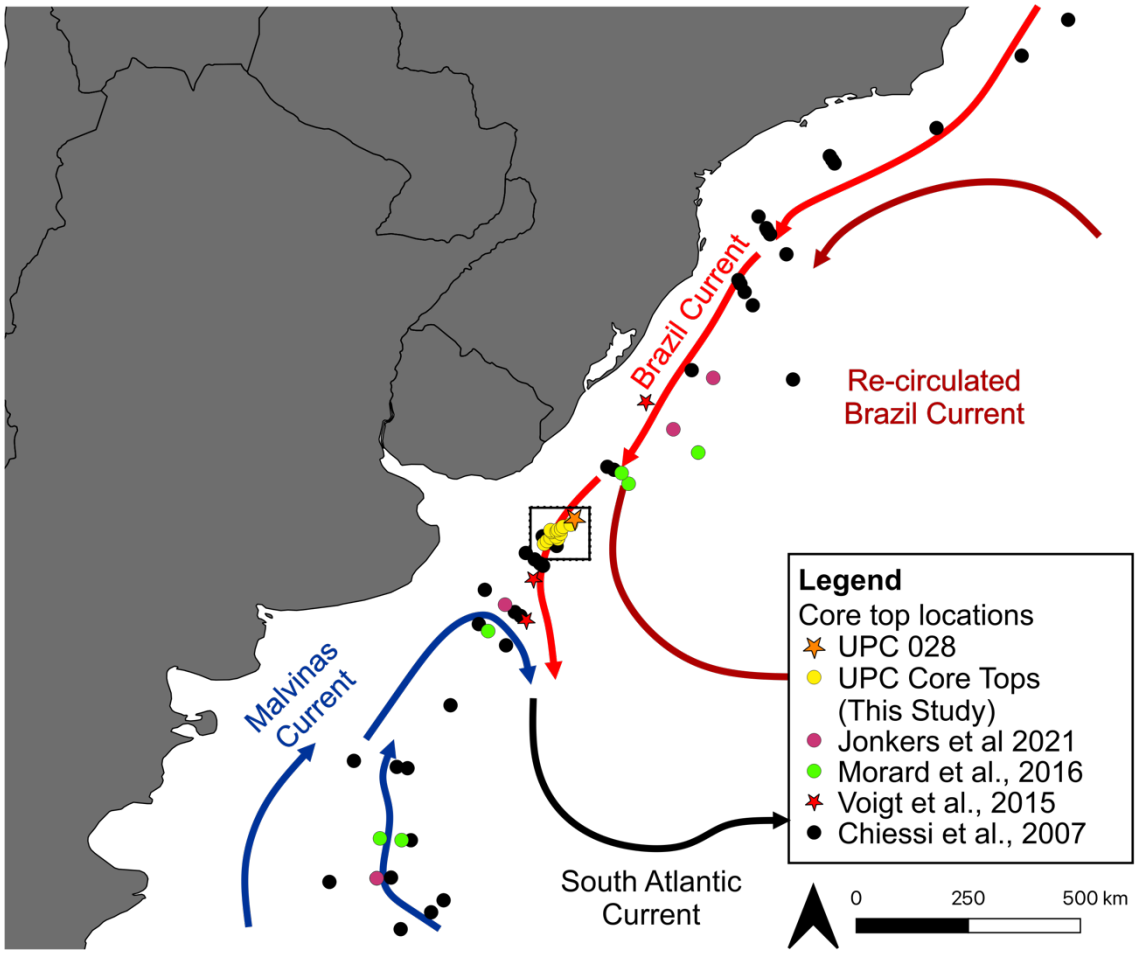

Figure 6.4-1 Location of previous *Gc. inflata* core studies relating to BMC migration (Chiessi et al., 2007; Voigt et al., 2015), morphotype classification (Morard et al., 2016; Jonkers et al., 2021), and encrustation impact (Jonkers et al., 2021). Location of this study is highlighted (Black Box, containing UPC cores) alongside broad position of regional ocean currents (Peterson and Stramma, 1991), UPC sites lie on the southern Brazil Current limb and is seasonally influenced by northern Malvinas Current intrusion (Chapter 4).

As previously mentioned, a number of *Gc. inflata* studies have been conducted on the western South Atlantic margin (Chiessi et al., 2007; Voigt et al., 2015; Morard et al., 2016; Jonkers et al., 2021). A majority of these sites originate from the Chiessi et al., (2007) core top margin transect, which collected limited multi-specimen stable isotope data, with no morphotype or encrustation classification data (Figure 6.4-1). This data first highlighted the ~2 ‰ $\delta^{18}O_{(VPDB)}$ offset observed latitudinally (Chiessi et al., 2007). However, lack of morphotype and encrustation data, combined with the multi-specimen $\delta^{18}O$ averaging, limited the investigation of morphotype and/or encrustation parameters on foraminiferal isotope values. Similar constraints limit the three downcore sites where *Gc. inflata* $\delta^{18}O$ records

were recovered (Voigt et al., 2015), alongside a lack of published $\delta^{13}C$ records (Figure 6.4-1).

Morphotypes were first classified in the isotopic records of Morard et al., (2016). The authors estimated morphotype classifications on observed plankton morphotype-isotope relationships, and through this method inference of morphotype was made on the existing isotope data (Chiessi et al., 2007; Voigt et al., 2015) through use of average isotope ranges (Morard et al., 2016). Isotope ranges utilised by Morard et al., (2016) are used in the present study to estimate morphotype in the absence of direct morphometric measurement of individual foraminifers. See methods for stated ranges (Section 3.2.3).

Jonkers et al., (2021) utilised data from the above-mentioned studies, and was the first study to introduce an encrustation framework to attempt to explain the isotope offset observed at the BMC. Whilst a step forward, this study lacks a single specimen approach that could help disentangle morphotype and/or encrustation signals through specimen mixing. Expanding this framework to include single-specimen data is the focus of the present work, enabling the spatial and temporal variability of encrustation to be analysed within a spatially and temporally dense context, within a known BMC mixing region. The distribution of this data is displayed in Figure 6.1-2, whilst the core tops are classified by study in Figure 6.4-1.

All of the *Gc. inflata* data from the western South Atlantic margin, for which both $\delta^{18}O_{(VPDB)}$ and $\delta^{13}C_{(VPDB)}$ is available, is summarised by study in Figure 6.4-2. From this summary plot it is clear that two clusters are principally maintained, aligning well with results of this study. It is important to note that both the Voigt et al., (2015) and Jonkers et al., (2021) data comprise of multi-specimen datasets, this likely accounts for values found between the morphotype $\delta^{18}O_{(VPDB)}$ ranges suggested by Morard et al., (2016).

Comparison of the cluster analysis with the literature assessing morphotypes latitudinally, shows broad agreement for the majority of $\delta^{18}O$ values reflecting the expected morphotypes. The exception to this is some Type I data (29 data points - Jonkers Type I?) from BMC classified site GeoB13862-1, this data was visually categorised as Type I, but produces comparatively high $\delta^{18}O$ values (Figure 6.4-3) (Jonkers et al., 2021). Type I is thought exclusive to the BC but the $\delta^{18}O$ values of this Jonkers Type I? grouping are more similar to Type II MC

categorised results. The site lies to the south of this study, within the BMC, with the other BMC site (GeoB6311-2) from Jonkers et al., (2021) seemingly not corroborating this finding. However, the number of Type I? individuals GeoB13862-1 produces raises questions on origin/classification of these specimens within the BMC and/or the reliability of morphotype inference based on $\delta^{18}O$ values.

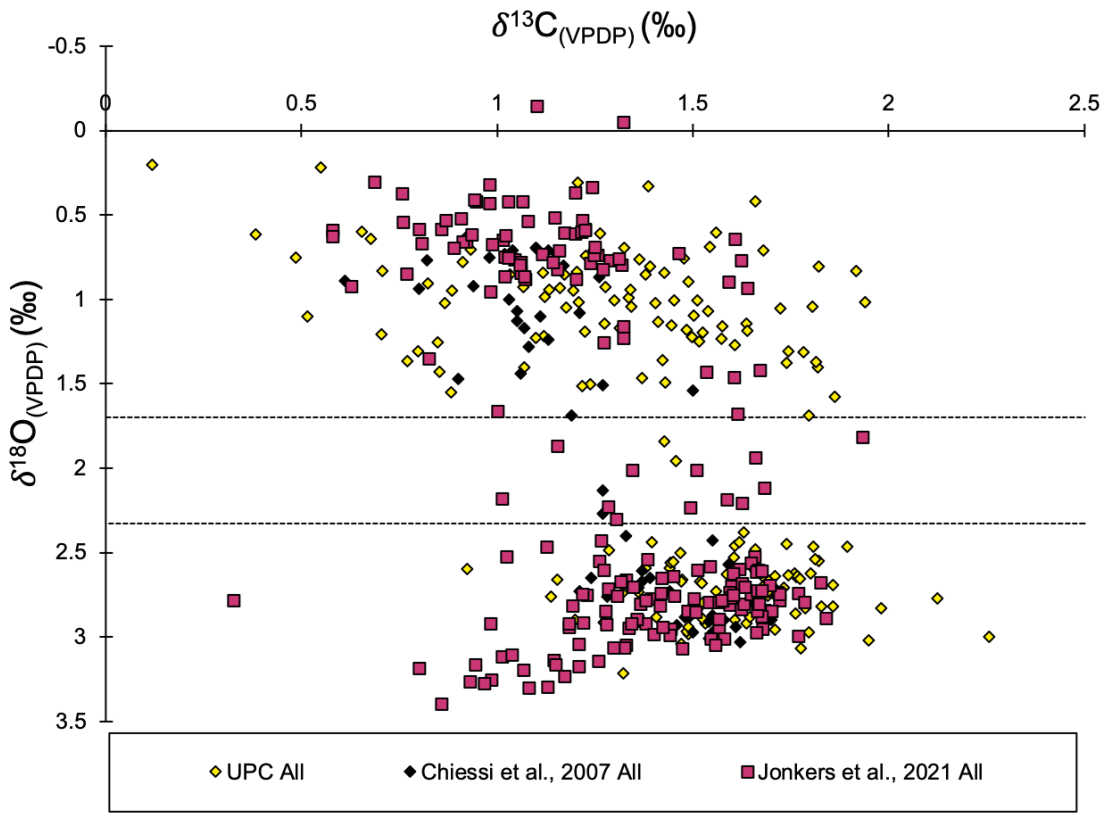

Figure 6.4-2 All available *Gc. inflata* $\delta^{18}O_{(VPDB)}$ and $\delta^{13}C_{(VPDB)}$ isotope data for the western South Atlantic margin classified by study. UPC All (yellow diamonds) represents core top and downcore isotope data from this study, Jonkers et al., (2021) data (pink squares) comprises core top and downcore data, Chiessi et al., (2007) comprises core top only data (black diamonds). Dashed lines denote Morard et al., (2016) $\delta^{18}O_{(VPDB)}$ range for Type I specimens (<1.70 ‰ $\delta^{18}O_{(VPDB)}$) and Type II (>2.33 ‰ $\delta^{18}O_{(VPDB)}$), with few data falling between, clustering is observed despite multi-specimen averaged *Gc. inflata* data.

Explaining the deviation of this southerly BMC site from the morphotype-isotope relationship established by Morard et al., (2016) presents four possibilities. The first, and most likely explanation, is a number of individuals/samples were incorrectly categorised as Type I, resulting in a higher than expected (>1.70 ‰ $\delta^{18}O_{(VPDB)}$) average for the multi-specimen samples. This seems particularly plausible, as delimiting Type I and Type II specimens from one another can a qualitative practice. In the case of Jonkers et al., (2021) this assessment was done “by eye” rather than using morphometric software such Image Pro Premier,

which can quantitatively delimit morphotypes based on aperture/final chamber size ratios, as was the intended approach of this study prior to laboratory time restrictions being imposed. Other possibilities that should not be discounted but that seem less likely based on the wealth of end member isotope data produced by the single-specimen analysis of this study are: that samples were infilled at this site altering the sample average, hence not impacting other BMC sites. A third possibility is the isotope limits suggested by Morard et al., (2016) do not perfectly delineate morphotypes present on the margin. A final possibility is that within the BMC region populations are not entirely allopatric, contrary to Morard et al., (2011), creating a narrow zone in which Type I morphotype occupies MC waters. This last suggestion seems unlikely, but cannot be completely disregarded without further morphotype and genotype profiling of Southern Ocean and South Atlantic samples. Definitively determining which explanation is most likely would require further sampling on the western South Atlantic, benefiting from paired single specimen isotopic and morphotype measurements.

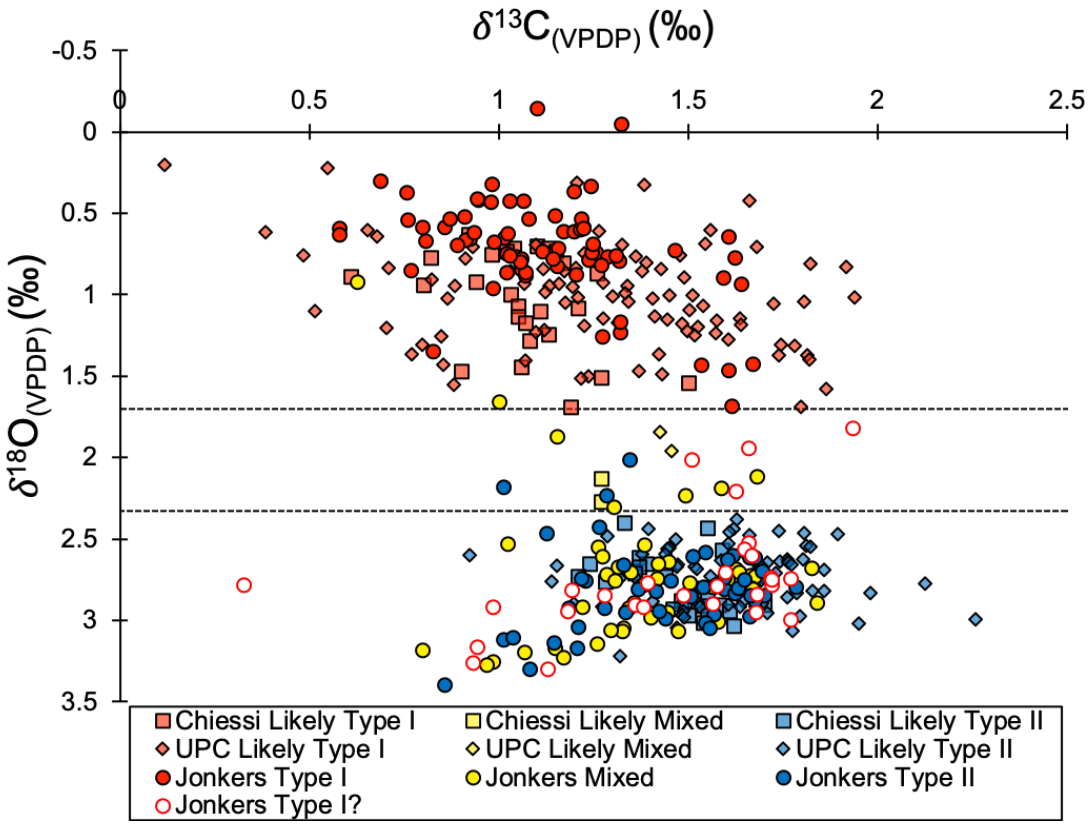

Figure 6.4-3 Isotope inferred morphotype classifications. Chiessi et al., (2007) and results from this study (UPC) based on $\delta^{18}O$ values, following Morard et al., (2016) ranges. Jonkers et al., (2021) visually categorised samples before $\delta^{18}O$ values derived. Majority of samples align with the $\delta^{18}O$ values. Exception is Type I? values which originate from core GeoB13862-1 (grey star Figure 6.4-2), represented by empty red circles.

6.4.2 Spatial and temporal morphometric relationships

6.4.2.1 Spatial morphometric relationships

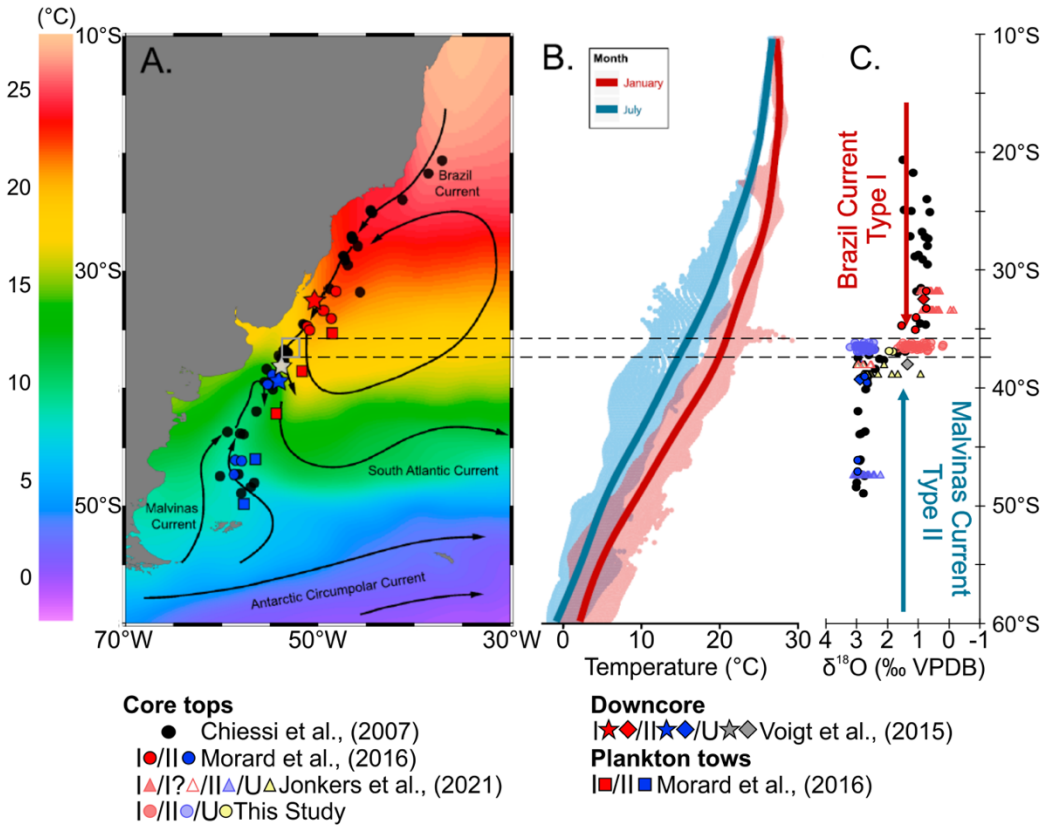

Figure 6.4-4 Modified figure from Morard et al., (2016). A) Spatial distribution of literature core top *Gc. inflata* data from Morard et al., (2016). Red symbols represent Type I morphotypes, blue symbols signify Type II morphotypes, grey star indicates a mix of morphotypes. Grey box represents this studies area. Black arrows detail main oceanographic processes from Chiessi et al., (2007), background colour is mean annual SST from Locarnini et al., (2013). B) Taken from Morard et al., (2016), SST variability plotted against latitude for austral summer (January) and austral winter (July), shading corresponds to monthly average SSTs from the World Ocean Atlas 2013 on a 0.25° grid with a smoothed averaged curve. C) Core top $\delta^{18}O_{(VPDB)}$ isotope results categorised for inferred morphotype plotted for this study (transparent circles) alongside data compiled within Morard et al., (2016) (solid circles), and Jonkers et al., (2021) (triangles). Type I (Red), Type II (Blue) and Type U (Yellow). Diamond symbols reflect stars in Panel A and are from the Voigt et al., (2015) study. Black circles indicate Chiessi et al., (2007) core top data with no morphotype classification in Morard et al., (2016). Type I? individuals from Jonkers et al., (2021) show higher than expected $\delta^{18}O_{(VPDB)}$ morphotype values. Dashed black lines indicate latitudinal range of UPC core top study area.

Mapping data from published literature it is possible to broadly estimate potential morphotypes along the western South Atlantic margin, observing $\delta^{18}O$ offsets between the two genotypes of *Gc. inflata* (Figure 6.4-4). The latitudinal trend down the margin previously suggested that the ~2 ‰ $\delta^{18}O_{(VPDB)}$ offset and morphotype transition co-occurred in line with the BMC average position, at approximately 38 °S (Chiessi et al., 2007; Morard et al., 2016; Piola and Matano, 2019).

Comparing recently published multi-specimen morphotype and isotope data from Jonkers et al., (2021), $\delta^{18}O_{(VPDB)}$ data from historical studies (Chiessi et al., 2007; Voigt et al., 2015; Morard et al., 2016), and single specimen isotope data from this study, it appears the multi-specimen isotope values mask a broader region that is occupied by these two morphotypes, with no statistically significant population of isotopic "intermediates" between Type I and Type II as shown in Jonkers et al. (2021). This mixing of morphotypes seems likely the result of seasonality and inter-annual variation within the BMC region (Olson et al., 1988; Voigt et al., 2015; Piola and Matano, 2019). If this site experienced a relatively equal exposure to both BC and MC currents hosting *Gc. inflata* specimens, it could be expected that the average of a multi-specimen approach would result in data smearing that would produce $\delta^{18}O$ values toward the middle of the Morard et al., (2016) morphotype end member ranges, smoothing out the distinct isotopic value ranges expressed by these two morphotypes. Analysing this on a more local scale, results of this study show a mixed population of the two morphotypes, with the presence of both morphotypes found in the majority of core top assemblages. It had not been possible to quantify and map this distribution in the previous multi-specimen analyses of populations of *Gc. inflata* (Chiessi et al., 2007; Morard et al., 2016; Jonkers et al., 2021) due to isotopic data averaging.

Comparison to previous results of assemblage studies (Chapter 4) are depicted in Figure 6.4-5. Assumed morphotype distributions largely follow trends observed in the Warm versus Cold species, with more northern and eastern sites displaying higher numbers of Type I, associated with BC waters, whilst the western sites typically see the MC correlated Type II predominate (Figure 6.4-5). Another indicator of water mass distribution, impacting occurrence of the two morphotypes, is number of species recorded, with higher diversity linked to warmer water masses (Figure 6.4-5) (Kucera, 2007; Schiebel and Hemleben, 2017). Again, the eastern portion of the margin with deeper water depths, see higher proportions of inferred Type I morphotypes present alongside increased species richness. Similarly, higher numbers of predicted Type II *Gc. inflata* coincide with lower diversity on the western portion of the margin and in shallower water depths. Whilst single specimen isotopes identify mixed assemblages of morphotypes, the proportions of these morphotypes recovered align with suggested average BMC positioning from Chapter 4. If the single-specimen data is averaged per site there is a prevalence of intermediary values (Type U),

obscuring the end-member variability present at individual sites (Figure 6.4-6). Seven of fifteen stations yield a Type U value, five Type II and the remaining three sites a Type I result. This is despite individuals from the isotope clusters of Type I and II known to be present across much of the margin.

With the grouped averaged isotopic analysis a more intermediary oceanographic picture is created, rather than the detail provided by single specimen analysis, identifying isotopic test variability within the BMC (Morard et al., 2016).

The limited number of individuals recording $\delta^{18}O_{(VPDB)}$ values between 1.70-2.33 ‰ (Type U) from UPC sites imply a lack of tests produced in a truly transitional mixed water mass within the BMC, instead clusters predominate either side of this range (Figure 6.4-2). Two UPC recorded instances are found in the southwest of the margin, proximal to the potential boundary between BC and MC waters as defined by species richness, and to a lesser extent the Warm vs. Cold species plots (Figure 6.4-5). Whilst they may represent a true mixing value for the BC and MC during calcification within the BMC, the fact these Type U specimens are a marked minority suggests there are no true water mass intermediates, with it more likely these specimens are impacted by processes such as infilling or contamination.

To summarise, the overwhelming majority of specimens $\delta^{18}O$ values can be used to assign specimens into morphotype Type I or II (Morard et al., 2016), with sites more often than not containing individuals of both inferred morphotypes. Placing the results of this study alongside the latitudinal findings of Chiessi et al., (2007) and Voigt et al., (2015), as displayed in Morard et al., (2016), the UPC core top data maintains associated water mass and morphotype signatures (Figure 6.4-4). Presence of both isotopically distinct morphotype populations at any given site implies variable overlying water mass signatures from BMC migration over the site to enable allopatric populations to be maintained, rather than a true intermediary water mass signature related to intense BMC mixing.

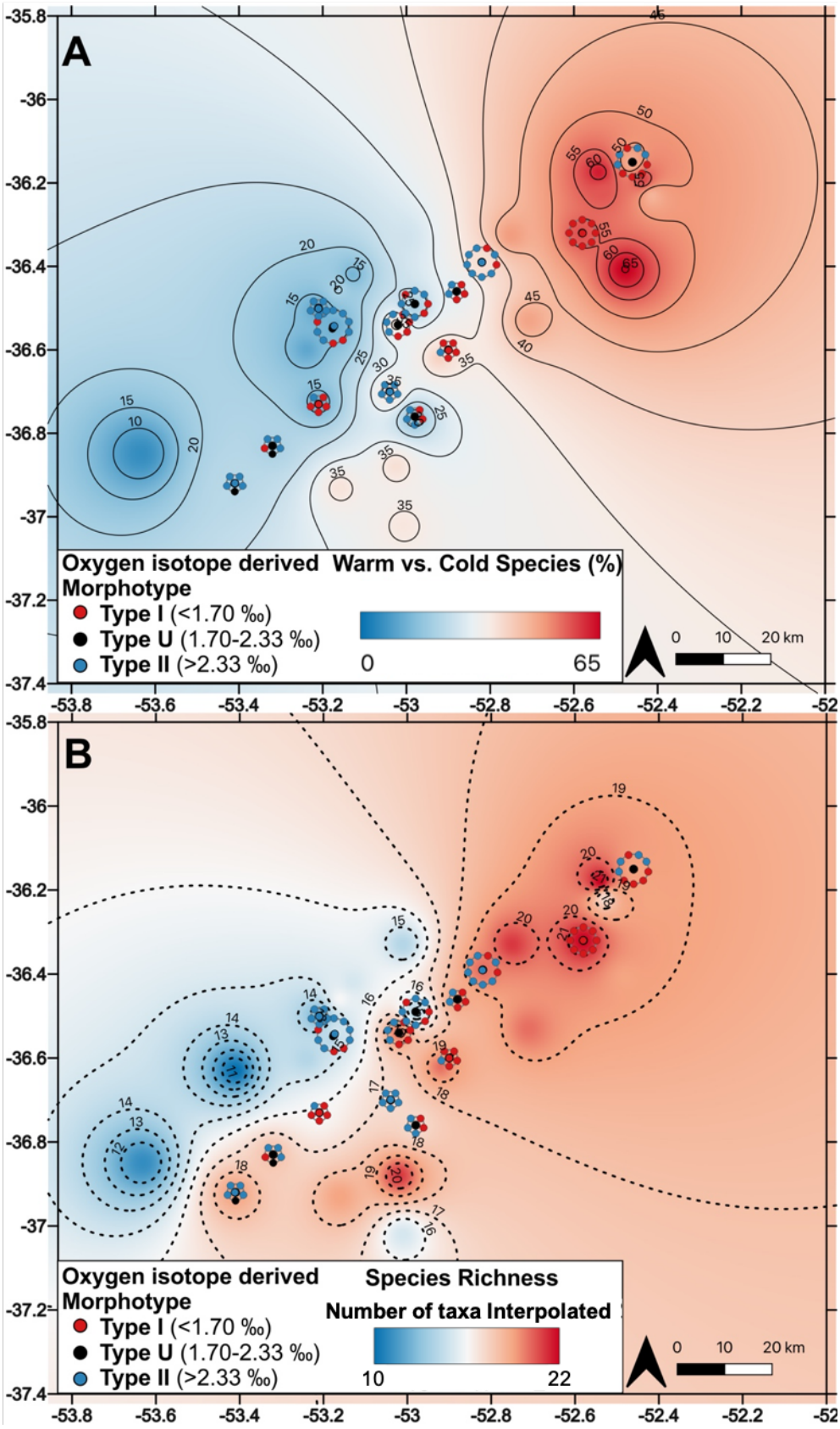

Figure 6.4-5 Overview of morphotype distributions according to $\delta^{18}O_{(VPDB)}$ classification ranges from Morard et al., (2016). Comparison with Chapter 4 assemblage mapping results shows comparable distributions of inferred Type I with (A) higher percentages of warmer species and (B) increased species diversity, associated with the BC. Inferred Type II predominance aligns with lower warm water species occurrences on the west of the margin (A), and lower diversity of species in shallower waters (B), associated with the MC.

6.4.2.2 Temporal morphometric relationships

As with the spatial morphometric analysis, the same inferred morphotype classification was applied to the downcore record of UPC 028 (Figure 6.1-2, yellow star). Previous temporal $\delta^{18}O_{(VPDB)}$ isotope work using *Gc. inflata* on the South Atlantic margin is documented in Voigt et al., (2015) and Morard et al., (2016). These studies utilised three cores to display BMC migration through time, the core locations are represented by stars in Figure 6.1-2 and Figure 6.4-1. A northern core experiences BC conditions and a southern core MC conditions exclusively, the intermediary core monitoring BMC migration, experiences both water masses and is thought to comprise of mixed morphotypes (Voigt et al., 2015; Morard et al., 2016). UPC 028 is a downcore record proximal to the Voigt et al., (2015) intermediary core (GeoB13862-1). UPC 028 samples almost exclusively infer mixed morphotype groupings, utilising single specimen analysis, with only two samples suggesting either purely Type I or Type II specimens, as shown in Figure 6.3-7, inferring influence of both BMC water masses at UPC 028 through time. No Type U individuals are recorded, with all data split into either inferred morphotype, based on Morard et al., (2016) ranges, suggesting no intermediary mixed water mass occurs at site UPC 028 through time.

Classification of averaged GeoB13862-1 data from Voigt et al., (2015) is split into likely morphotypes based on $\delta^{18}O$ values, enabling comparison with UPC 028 data. One noticeable difference between the data is the narrower range of $\delta^{18}O$ values produced by the averaged isotope values in GeoB13862-1 (~2 ‰ $\delta^{18}O_{(VPDB)}$) compared to UPC 028 (~2.75 ‰ $\delta^{18}O_{(VPDB)}$) (Figure 6.4-6). This is explained through differing methodologies used; Voigt et al., (2015) data was averaged over approximately ten specimens in comparison to the single specimen methods used in this study, accordingly that data likely represents averaging of the $\delta^{18}O$ values between the two end-member populations observed in this study, rather than individuals that were calcifying in waters that could be considered an intermediate “blend” of BC and MC $\delta^{18}O$ values.

Secondly, the Voigt et al., (2015) data produces a significant number of unclassified data points (~74 instances), whilst UPC 028 has no occurrences of Type U (mixed) individuals. This abundance of Type U data likely reflects the averaging process rather than representing true water mass conditions. When UPC 028 data is similarly averaged, results typically produce more moderate

$\delta^{18}O$ values, bringing ranges in line with GeoB13862-1 Type U and Type I samples (Figure 6.4-6).

Higher numbers of inferred Type I individuals observed in both downcore records is consistent with published BMC migration during the mid-Holocene, to the south of this study region, as discussed in Chapter 5 (Voigt et al., 2015; Gu et al., 2018c). However, the inferred morphotypes remaining mixed in the UPC 028 core implies at least some cooler MC associated Type II specimens arrived at the site, even during the warmer mid-Holocene (Figure 6.4-6). This suggests that while BMC migration moved south, MC influence was not totally removed, enabling the populations to remain allopatric through time (Morard et al., 2011; Morard et al., 2016).

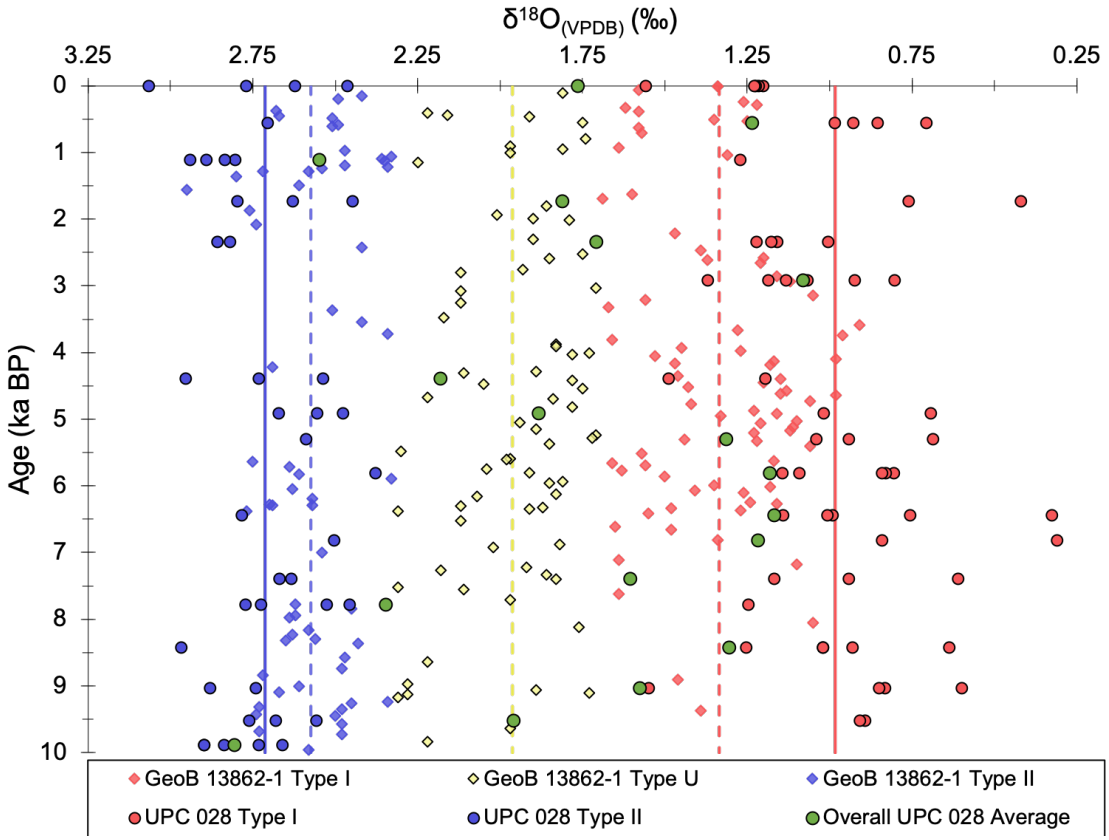

Figure 6.4-6 UPC 028 downcore *Gc. inflata* $\delta^{18}O_{(VPDB)}$ data classified into inferred morphotypes show a clear separation. Plotted alongside is the nearby downcore record of GeoB13862-1 (Voigt et al., 2015). GeoB13862-1 record produced $\delta^{18}O_{(VPDB)}$ values by averaging ten individual foraminifera per data point, results of which have been used to obtain likely morphotype. Dashed lines denote averages for Type I (pink), Type U (yellow) and Type II (blue). Voigt et al., (2015) data produces significant numbers of Type U morphotypes likely the result of averaging of data (yellow diamonds). Averaged UPC 028 samples (green dots) produce similar $\delta^{18}O_{(VPDB)}$ values, suggesting Voigt et al., (2015) data was derived from mixed morphotype populations. Solid lines are the average UPC Type I (red) and Type II (blue), with averages notably lower and higher respectively, than the Voigt et al., (2015) multi-specimen averages, implying multi-specimen approaches smear the data, likely creating more intermediary Type U values.

Unlike the averaged data, use of single specimen analysis provides additional complexity to the regional picture, showing clear separation between inferred morphotypes consistently downcore, and implying no intermediary water mass presence. Using multi-specimen data likely still enables the overall trends of BMC migration to be observed, at sites such as UPC 028 and GeoB13862-1 across the Holocene, through average isotope and morphotype population shifts. However, it may present a false image of intermediary values and omits identification of minor morphotype populations that inform on water mass temporal variation. An ideal situation would utilise significant (>10) numbers of visually and isotopically classified *Gc. inflata* morphotypes to enable morphotype temporal dominance to be assessed, provide an average for BC (Type I), MC (Type II), alongside an overall signatures per sample for comparison with past BMC migration studies.

6.4.2.3 Mechanism for site morphotype variability

Mechanistically a number of scenarios can explain how two morphotypes may occupy the same site spatially, yet remain allopatric and not display significant quantities of intermediary isotope values. Figure 6.4-7 shows four scenarios accounting for mixed morphotype site populations, whilst preserving allopatric associations (Morard et al., 2011; Morard et al., 2013; Morard et al., 2016). The first scenario depicted assumes both water masses have a similar sized morphotype populations, and an even amount of time overlying the site, (Figure 6.4-7 A). In this first instance the resulting assemblage produces an even split between morphotype and the corresponding isotopic signature. Performing grouped analysis on *Gc. inflata* tests from this site produces an average value, likely between the two populations and omits seasonal/inter-annual variation. The second scenario (Figure 6.4-7 B) shows one current dominating for longer periods, however the foraminiferal population size is diminished compared to the secondary water mass, as such morphotype assemblages remain evenly split. Using grouped specimen analysis, signatures obtained from such sites are averaged between populations, despite experiencing one water mass condition for longer time periods. In this scenario *Gc. inflata* records may differ from other proxies, showing differing foraminiferal populations between water masses i.e. a BC dominated situation may produce higher sub-tropical species population but cooler *Gc. inflata* signals.

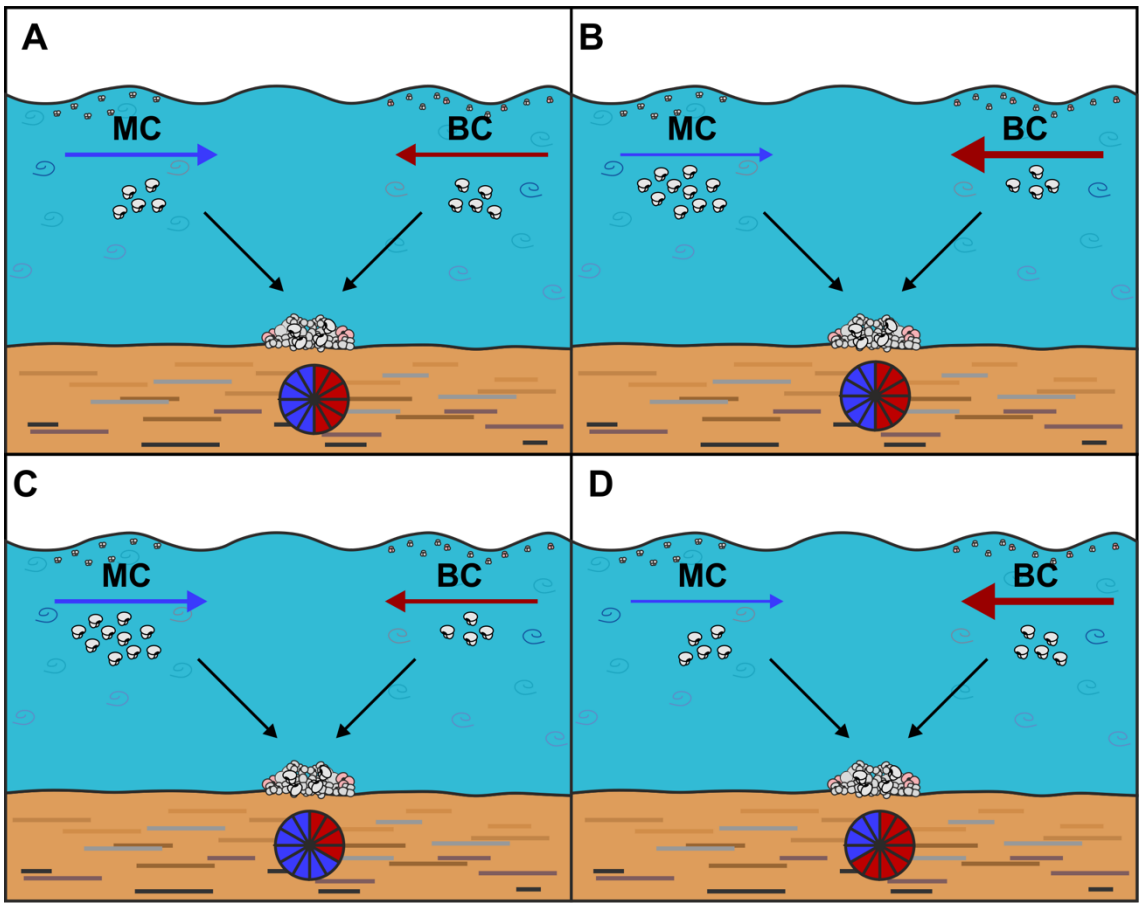

Figure 6.4-7 Schematic representations of possible morphometric assemblages based on overlying water mass dominance and relative *Gc. inflata* populations. Number of foraminifera represent population size, weight of coloured arrow indicates relative dominance of labelled water mass. Coloured chart indicates recorded assemblage proportions. A) Equal distribution of foraminifera within water masses and equal water mass dominance provides equal morphotype assemblage representation. B) Equal assemblage proportions resulting from higher population in the less dominant water mass. C) Equal dominance of competing water masses, but higher populations within one promotes assemblage dominance of one morphotype. D) Equal foraminiferal populations but greater dominance of one water mass produces assemblage dominated by one morphotype. Grouped isotopic analysis and averaged results negate identification of subsidiary populations within assemblages, smoothing over recorded complexity.

Scenario C depicts a situation where the overlying water mass is split evenly but foraminifera populations heavily favour one water mass, leading to one morphotype dominating assemblages (Figure 6.4-7 C). Grouped isotopic analysis swings in favour of this morphotype, implying the site only experiences one water mass. Single specimen analysis however, enables this smaller population to be recognised, capturing variation otherwise omitted. The final scenario (Figure 6.4-7 D) sees comparable populations of morphotypes between water masses, but one water mass dominates through time. In this scenario one morphotype dominates the assemblage and thus the recorded signal, grouped analysis would

again miss the variation of the minor morphotype component and thus the overlying water mass variability and complexity.

Applying these four models to the spatial portion of this study suggests either process B or D are most likely to explain the resulting core top data. The reasoning for this is the prevailing oceanography of the region. The BMC is known to migrate over a significant portion of the region, encompassing the study UPC sites (Olson et al., 1988; Matano et al., 2010; Hernández-Molina et al., 2016; Paniagua et al., 2018; Piola and Matano, 2019). Scenarios B and D provide examples where one current, in this case the BC, is the dominant current through time. The UPC cores sit to the north of the BMC region and thus it could be expected that the BC would likely dominate temporally, either seasonally or on an inter-annual basis (Olson et al., 1988; Matano et al., 2010; Hernández-Molina et al., 2016; Piola and Matano, 2019).

Observations from previous plankton tow data sets have suggested large populations of *Gc. inflata* both within the BMC and northern MC water masses (Boltovskoy et al., 1996; Boltovskoy et al., 2000). These populations are likely linked to the high nutrient and chlorophyll concentrations within these regions, with *Gc. inflata* known to favour more mesotrophic states compared to the oligotrophic BC (Brandini et al., 2000; Lončarić et al., 2007; Matano et al., 2010; Schiebel and Hemleben, 2017). As such the most likely scenario from Figure 6.4-7 to explain the spatial core top data, that provides a roughly even split of morphotypes derived from $\delta^{18}O$ data is scenario B, given modern oceanography.

The temporal story likely shifts through several scenarios with changing BMC position, impacting water mass presence temporally and thus the morphotypes and recorded isotope signatures. During the early Holocene (pre-9 ka) the higher proportion of MC Type II specimens likely indicates scenario C is occurring, with a less dominant BC. As proportions of Type I increase across the mid-Holocene an extreme scenario B may be said to occur, with increasing BC strength producing assemblages that reflect a more equal distribution and then a dominance of Type I (Figure 6.4-7). The peak of this is likely seen around 6 ka. Thereafter proportions migrate to a more even split over the mid- and late-Holocene, before shifting back to a Type II and MC dominated system perhaps indicative of scenario C between ~2.0-0.8 ka. From this cooling pulse values shift back to a more even, or BC dominated, split to the modern (Figure 6.4-7). This

interpretation principally uses the UPC isotope data, both as a proportion of the individual data points per time-slice, but also as an overall average for comparison with Voigt et al., (2015) multi-specimen averaged data, to suggest mechanisms through time. Ideally, a larger number of individuals per time-slice would enable greater confidence in interpreting BMC migrations.

6.4.3 Encrustation

This study derived the encrustation classification system from the previously mentioned work however, subtle differences are noted. Jonkers et al., (2021) classify specimens into non-encrusted, encrusted and mixed for stable isotope measurements. It is not made clear whether this mixed category comprises of samples composed of non-encrusted and encrusted specimens, or specimens showing minor to moderate encrustation i.e. B+C. Additionally, Jonkers et al., (2021) data is multi-specimen and it is unclear whether all individuals within a measurement are similarly encrusted. As a result, direct comparison is difficult regarding distribution of stable isotope data in relation to encrusted forms.

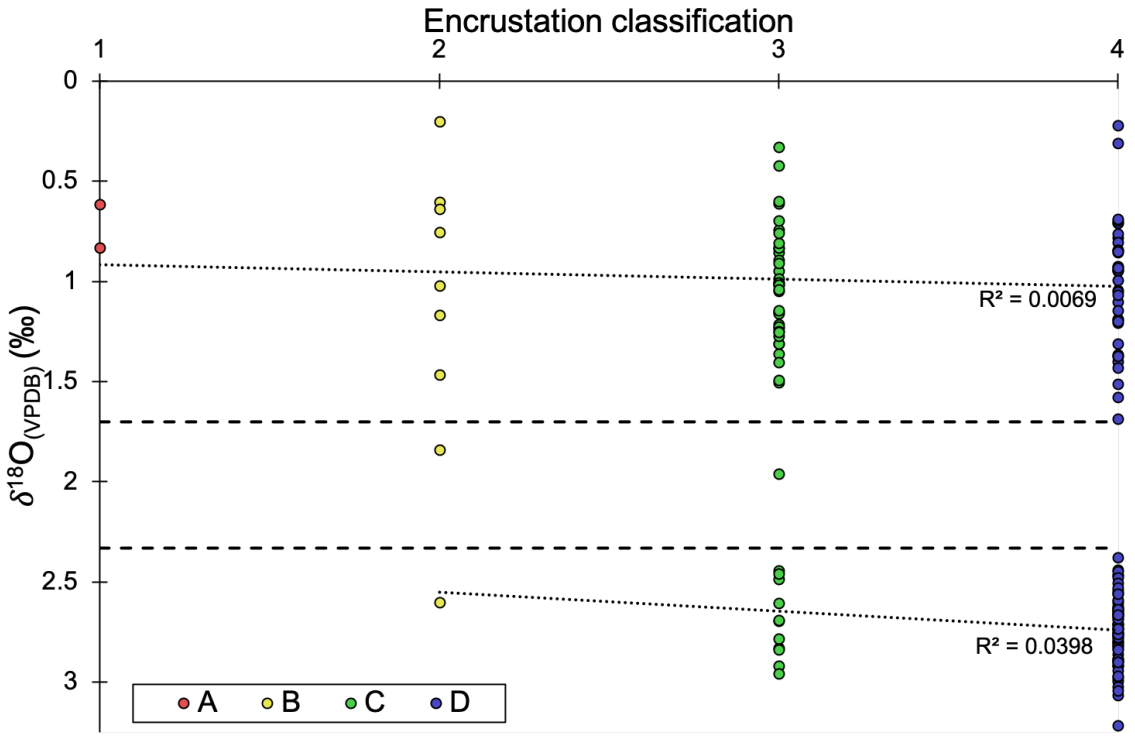

Figure 6.4-8 $\delta^{18}O_{(VPDB)}$ values plotted with encrustation state to determine whether encrustation systematically increases recorded $\delta^{18}O_{(VPDB)}$ values. Whilst encrustation appears minorly correlated (thin dashed lines) with increasing $\delta^{18}O$ values, when split into the two morphotype groupings, it is unlikely the sole cause for increasing $\delta^{18}O$ values. Morphotype $\delta^{18}O_{(VPDB)}$ boundaries (thick dashed lines) <1.70 ‰ (Type I) and >2.33 ‰ (Type II). Category U values removed due to uncertain encrustation state.

Results from UPC cores located within the BMC show an extremely weak correlation between encrustation state and more positive $\delta^{18}O$ values (Figure 6.4-8). However, this trend is likely driven by the lack of specimens that account for the less encrusted individuals, and as such the data is skewed at the "least encrusted" end towards the few specimens that happened to have been recovered. It would appear that encrustation level actually has little impact on $\delta^{18}O$ values in the BMC, as the Type I morphotypes, which are well represented in encrustation categories B, C and D, all show a full spread of data over the same $\delta^{18}O_{(VPDB)}$ range of 0.2 – 1.7 ‰. A similar pattern is seen for Type II morphotypes in the encrustation categories, being well represented in C and D, with largely overlapping $\delta^{18}O_{(VPDB)}$ ranges between 2.3 – 3.3 ‰. If there was a systematic offset in $\delta^{18}O$ values between different encrustation types, we would not expect to see such extensive overlap in the full range of $\delta^{18}O$ values across the different encrustation types between the two different morphotype groups.

Despite the aforementioned difficulties in encrustation classification systems findings for this study were placed alongside the results of Jonkers et al., (2021) to compare density distributions across the BMC (Figure 6.4-9). There are a number of similarities between the Jonkers et al., (2021) data and the UPC collection. Both studies display multiple encrustation states and a range of associated $\delta^{18}O$ and $\delta^{13}C$ values, with the distribution of individuals being uneven between encrustation states (Figure 6.4-9). Non-encrusted forms are a rarity in both the UPC cores and the Jonkers et al., (2021) data, whom similarly report low $\delta^{18}O$ values corresponding with non-encrusted forms observed at BC and BMC sites, and a lack of higher $\delta^{18}O$ non-encrusted forms recovered from MC sites (Figure 6.4-9). Alongside the few individuals showing no encrustation, comparatively few individuals show minor encrustation levels, implying moderate to heavy encrustation is the norm, spatially and temporally. Both $\delta^{18}O$ clusters comprise a number of encrusted states, and despite dominance of heavy encrustation at higher $\delta^{18}O$ values it is clear this does not exclude more encrusted forms from lower $\delta^{18}O$ values. This trend is visible in both UPC and Jonkers et al., (2021) BMC sites with available encrustation data (Figure 6.4-8 and Figure 6.4-9).

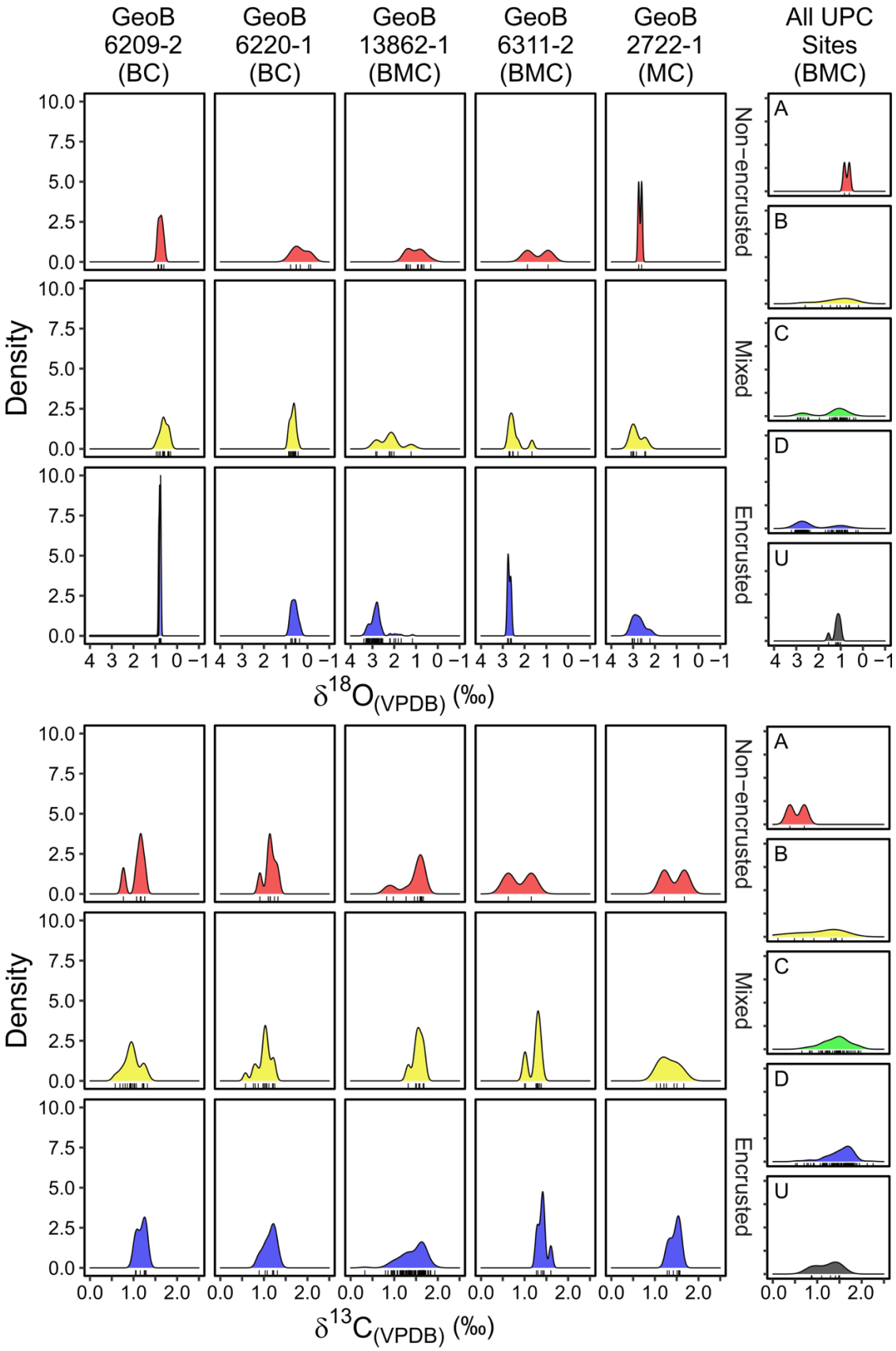

Figure 6.4-9 Replotted Jonkers et al., (2021) encrustation categorised $\delta^{18}O_{(VPDB)}$ and $\delta^{13}C_{(VPDB)}$ data replotted with all UPC data. UPC data is further categorised from Non-encrusted (A), light- (B), medium- (C) and heavily-encrusted (D) specimens, and unclassified data (U). All density scales are the same. UPC sites show broader $\delta^{18}O$ ranges, likely due to single specimen approach. Heavily encrusted forms show propensity for higher $\delta^{18}O$ values, whilst less encrusted states skew to lower $\delta^{18}O$ values.

6.4.3.1 Spatial representation

The spatial distribution of encrustation is variable both between encrusted states at individual sites and between proximal locales. The distribution of heavily encrusted individuals (D) suggests encrustation is present and impacting all sites, often dominating shallower sections of the margin to the west/northwest. Alongside high numbers of heavily encrusted individuals are the large number of medium encrusted individuals, which often form the second largest proportion at sites. Dominance of these two states is in line with the findings of Jonkers et al., (2021) regarding the abundance of encrusted forms when compared to the number of non-encrusted individuals. Within the spatial study, the few instances of non-/minor encrustation tend to fall along the SW-NE transect across the study region (Figure 6.4-10). Encrustation categorisations, when compared to assemblage data from Chapter 4, show less encrusted individuals aligning with the potential BC/MC boundary, with the BC likely the dominant water mass based on assemblage mapping (Figure 6.4-10). Similarly, sites where heavily encrusted individuals dominate are more prevalent in shallower sites to the west and northwest, where cooler MC waters have greater impact seasonally (Saraceno et al., 2005; Paniagua et al., 2018; Piola and Matano, 2019).

This spatial assessment of encrustation provides a snapshot of the variable encrustation state on both the intra- and inter-site level. Encrustation categorisations for this study were only conducted on individuals used for single specimen isotope analysis. These individuals typically originate from the >212 μm size fractions used to attempt water column reconstructions as suggested in Birch et al., (2013). As such this may enter a size specific bias into the variability of encrustation and further work would be required to assess this, and entire sample encrustation variability. However, given this study similarly encountered a rarity of non-encrusted specimens (<2 % this study vs. <3 % Jonkers et al., (2021)) it would appear fairly representative of margin encrustation states, and provide a more detailed assessment of individual test encrustation state.

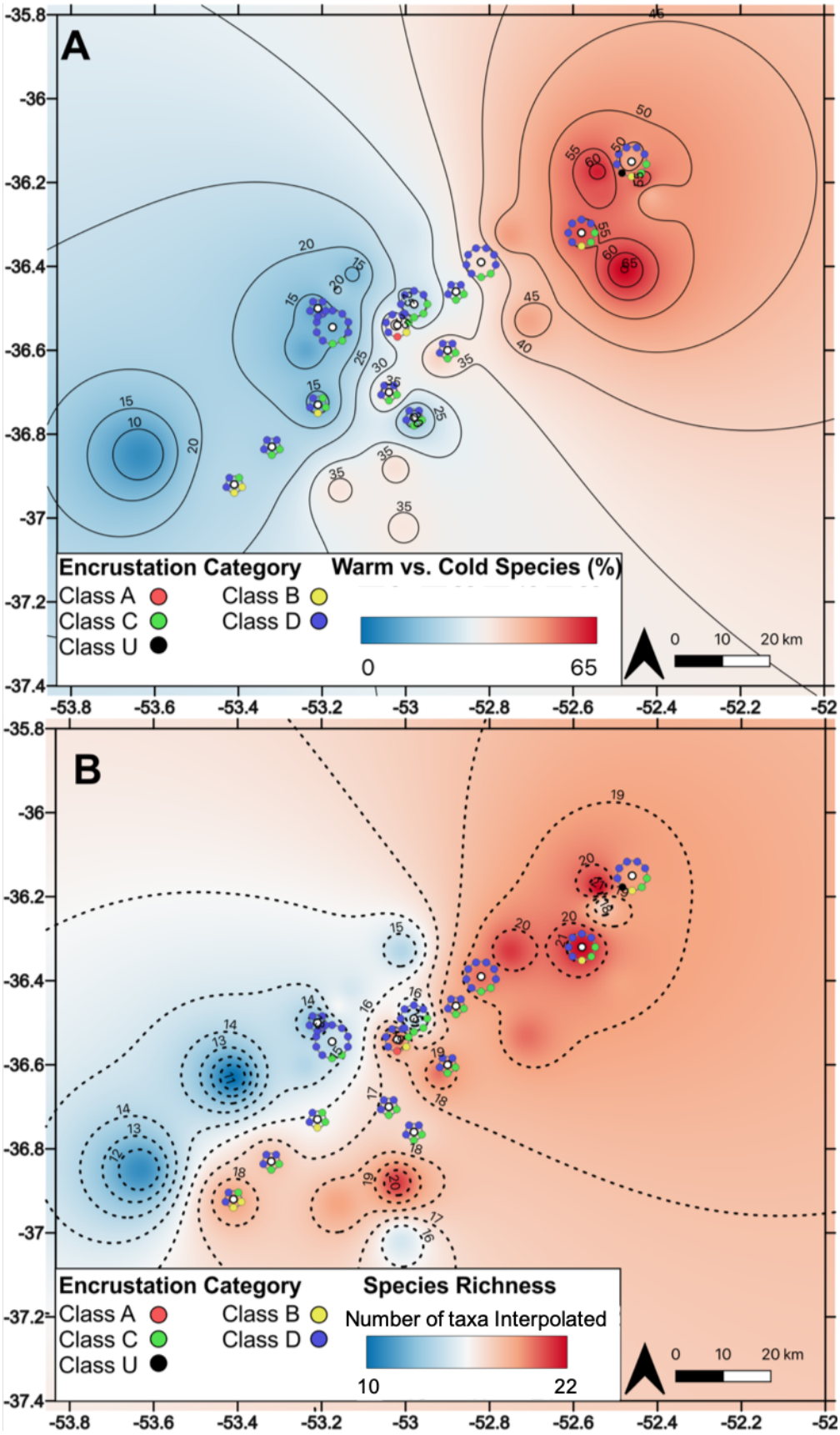

Figure 6.4-10 A) Encrustation distributions overlain on warm species assemblage data percentages, cooler assemblages in shallower waters are dominated by heavily encrusted specimens i.e. Category D. B) Encrustation categories and species richness shows shallower MC dominated regions contain higher frequencies of heavily encrusted specimens, whilst warmer BC waters align with lower encrustation occurrences.

6.4.3.2 Temporal representation

Encrustation history is analysed at site UPC 028 through the downcore record. As with the spatial study, the record shows variability with all encrustation types represented. Importantly, encrustation level does not increase with burial depth, with some of the least encrusted specimens occurring below ~7 ka, or ~380 cm (Figure 6.4-11). This suggests encrustation is unlikely to be occurring within the sediment, instead occurring prior to deposition, likely within the water column (Jonkers et al., 2021).

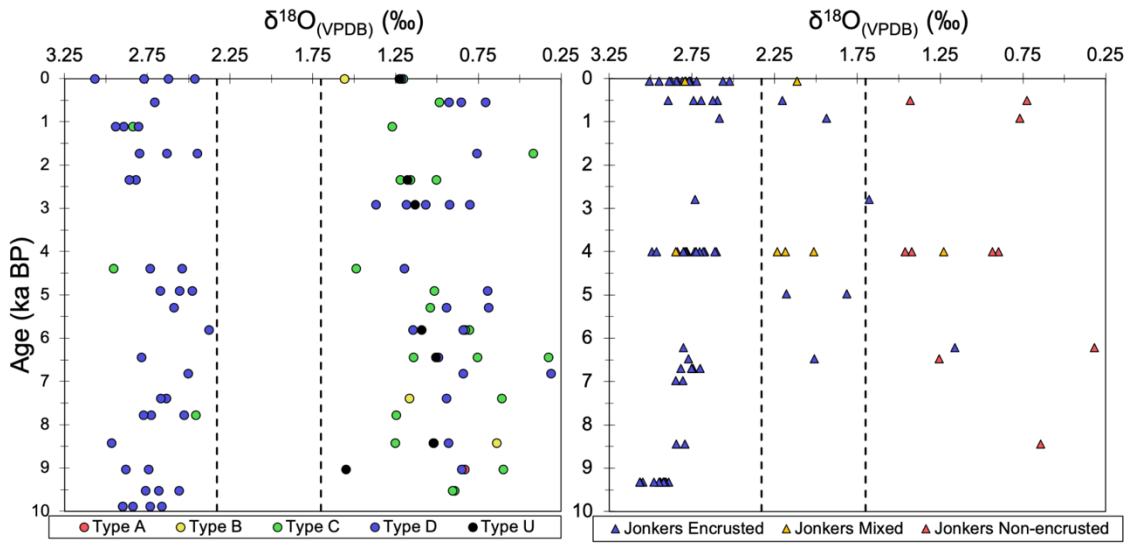

Figure 6.4-11 Classified temporal data from this study (UPC categories: A, non-encrusted, red circles; B, minor encrusted, yellow circles; C, medium encrusted, green circles; D, heavy encrustation, blue circles; U, unclassified encrustation, black circles) and GeoB13862-1 downcore encrustation data (Jonkers encrusted, blue triangles; Jonkers mixed encrusted, orange triangles; Jonkers non-encrusted, red triangles) (Jonkers et al., 2021). In both datasets, heavily encrusted forms predominate higher $\delta^{18}O$ values. Additionally, both sites record a variety of encrustation states at depth. This study (circles) reports higher encrustation variability <1.7 ‰ $\delta^{18}O_{(VPDB)}$ values and at greater proportions, whilst the GeoB13862-1 displays a number of values between morphotype ranges (dashed lines, Type I <1.7 ‰ $\delta^{18}O_{(VPDB)}$ and Type II >2.33 ‰ $\delta^{18}O_{(VPDB)}$ (Morard et al., 2016).

Additionally, the propensity for higher levels of encrustation to coincide with higher $\delta^{18}O$ values is also evident (Figure 6.4-11), furthering the association of more heavily encrusted forms with cooler MC waters (Jonkers et al., 2021). This is also seen in the Jonkers et al., (2021) data, with encrusted specimens more frequently, but not systematically, displaying >2 ‰ $\delta^{18}O_{(VPDB)}$ values (Figure 6.4-11). However, observations suggest this study reports a greater proportion of <1.7 ‰ $\delta^{18}O_{(VPDB)}$ heavily encrusted states, and a greater frequency of lower encrusted individuals, albeit Jonkers et al., (2021) typically only report non-encrusted or encrusted rather than categorising for level of encrustation (Figure

6.4-8 and Figure 6.4-11). This shows lower $\delta^{18}O$ values can occur alongside heavily encrusted forms, providing evidence that $\delta^{18}O$ values are not systematically impacted by increasing encrustation state.

To surmise a higher proportion of encrusted specimens being coincident with higher $\delta^{18}O$ values, and the temperatures of the two BMC contrasting water masses, infers a thermal influence on the likelihood of *Gc. inflata* crusts developing. This is observed in the spatial proportions of encrusted individuals recovered by this limited study, with higher proportions of encrusted individuals occurring at sites that produced cooler assemblage signals (Figure 6.4-10). The temporal signal observes representation of both encrusted and non-encrusted states at all depths, indicating encrustation, as a process, happens prior to deposition. It also signals that encrustation is occurring at the site through time despite southward BMC migration through the mid-Holocene (Voigt et al., 2015; Gu et al., 2018c). However, a larger investigation would be required to identify whether this impacts the proportion of encrusted individuals through time.

The thermal influence on likelihood of encrustation is further corroborated by the lack of non-encrusted specimens south of the BMC, and the reported increase in proportion of encrusted specimens with increasing water depth (Jonkers et al., 2021). Increasing water depth, and cooling temperatures, does not fully explain the encrustation mechanism, with encrusted specimens reported alongside non-encrusted forms from plankton tows (Rebotim et al., 2019; Jonkers et al., 2021). This suggests that dwelling depth and vertical migration are not the primary trigger of crust development, instead only increasing the chance of crust development. Determining the driver of crust formation is beyond the scope of this study, but defining the cause of encrustation will require a spatially and temporally dense sampling program, alongside further plankton nets, sediment traps and in-situ water column profiles. Whilst intensive, this would enable a better understanding of the ecology of this species and the oceanographic meaning of recorded stable isotopes in the fossil record.

6.4.4 Morphotype and encrustation signals

This study has shown the variability of encrustation state, both temporally and spatially, and the range of associated $\delta^{18}O$ signatures aligned with those encrustation states. It is clear that more heavily encrusted forms have a propensity for higher $\delta^{18}O$ values, but this is not exclusive in the UPC data, with the inferred Type I (<1.7 ‰ $\delta^{18}O_{(VPDB)}$) cluster featuring significant numbers of medium-heavily encrusted forms (Figure 6.3-14 and Figure 6.4-12). The presence of heavily encrusted specimens within the isotopically lighter grouping, alongside minor and medium encrusted Type II (>2.33 ‰ $\delta^{18}O_{(VPDB)}$) forms, suggests encrustation does not systematically increase $\delta^{18}O$ values.

Whilst morphotypes cannot be definitively stated, utility of estimations based on the Morard et al., (2016) isotopic ranges is valid, given the clear clustering of data observed in Figure 6.4-3, with the stated boundaries. This permits comparison of encrustation and morphotype for the Jonkers et al., (2021) BMC site data (Figure 6.4-13), and this studies data (Figure 6.4-12), with those assumptions in mind.

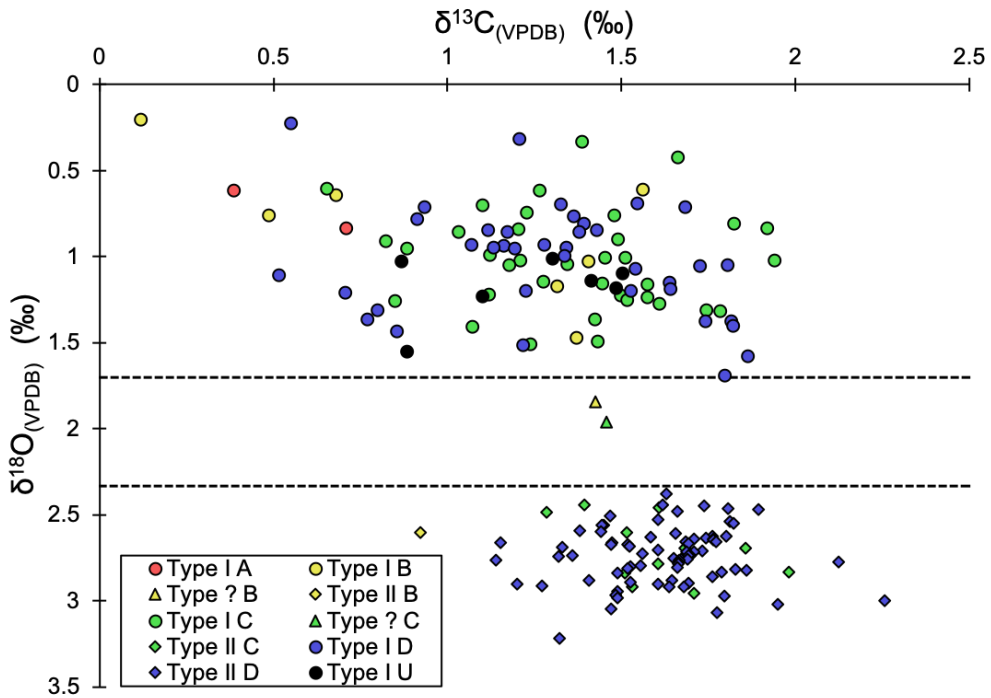

Figure 6.4-12 Encrustation and assumed morphotype classification data for UPC cores. More heavily encrusted specimens (D) are found with higher $\delta^{18}O$ values, suggesting possible Type II correlation and alignment with MC $\delta^{18}O$ values. Although heavy encrustation is visible in either assumed morphotype, the <1.7 ‰ $\delta^{18}O_{(VPDB)}$ Type I grouping shows higher proportions of lower encrustation, aligning with Type I assignment and BC $\delta^{18}O$ values of Jonkers et al., (2021).

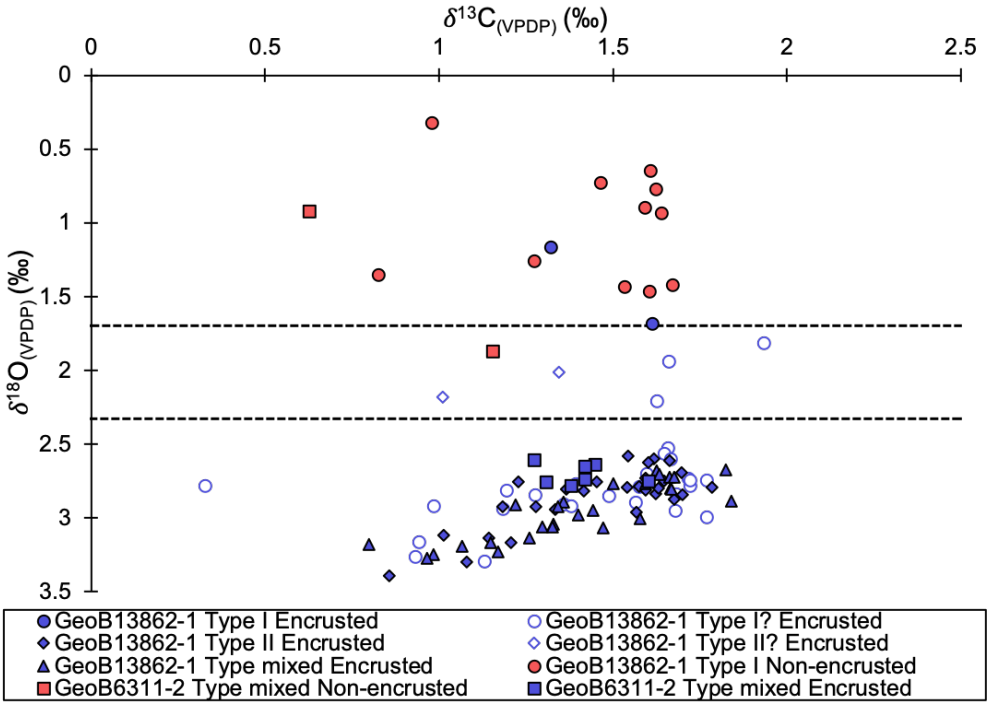

Figure 6.4-13 BMC sites (GeoB13862-1 and GeoB6311-2) from Jonkers et al., (2021), south of this study. Classified by morphotype and encrustation state show variable encrustation states with δ^{18}O values. A high number of Type I? data points >2.33 ‰ δ^{18}O$_{(VPDB)}$ all originating from the same site may suggest encrustation plays a role in increasing δ^{18}O values, occupying space previous studies would expect indicative of Type II morphotypes (Morard et al., 2016). However, given the difficulty in visually discerning morphotypes, all Type I? specimens originate at site GeoB13862-1 and the examples of encrusted forms at lower δ^{18}O values, it seems encrustation does not uniformly cause the isotope offset.

Figure 6.4-13 presents all available Jonkers et al., (2021) BMC site encrustation data coded by morphotype. Mixed encrustation data was removed due to the lack of clarity on what mixed encrustation entails. Analysis identifies a large number of Encrusted Type I? classified individuals with >1.7 ‰ δ^{18}O$_{(VPDB)}$, all originating from site GeoB13862-1 (Figure 6.4-13). These values show higher than expected δ^{18}O values given the assigned morphotype classification. This could either suggest encrustation within the BMC region may impact δ^{18}O signatures, raising δ^{18}O values, rather than the morphotype offset as stated by Jonkers et al., (2021). Alternatively, and more likely, it may reflect a number of parameters including misidentification of morphotype/averaging of multiple specimens within the multi-specimen approach, or site-specific impacts not accounted for by encrustation i.e. infilling. Further outliers remain relating to: low δ^{18}O Type I Encrusted samples, lower than expected δ^{18}O Type II? Encrusted samples and higher than expected δ^{18}O mixed morphotype non-encrusted specimens (Figure 6.4-13). Jonkers et al., (2021) utilised a visual inspection to determine morphotype, with the subtle morphometric differences between the two genotypes known to

intersect (Morard et al., 2011; Morard et al., 2016; Jonkers et al., 2021). These outliers, combined with the Type I? data, are more likely a product of the multi-specimen analyses method used, either through misidentification, or through the qualitative categorisation of encrustation, rather than an intermediary water mass signature or significant $\delta^{18}O$ increases relating to encrustation. Unfortunately, this present study can only speculate over the morphotype of individual foraminifera using isotopic measurements, however no strong correlation is reported between encrustation and increasing $\delta^{18}O$ values that would indicate a systematic process impacting the record (Figure 6.4-8).

Understanding the morphotype-encrustation relationship on $\delta^{18}O$ values is complex and is likely further exacerbated by temporal BMC migration over seasonal, and longer timescales leading to mixed morphotype samples (Olson et al., 1988; Saraceno et al., 2004; Voigt et al., 2015; Paniagua et al., 2018; Gu et al., 2018c; Piola and Matano, 2019). Determining cause of the BMC $\delta^{18}O$ offset therefore requires single specimen samples to attempt to disentangle these factors. In conjunction with increasing sample resolution within the BMC region and utilising seasonal sediment trap and/or plankton net data. This would facilitate definitively tying morphotype and encrustation to water column data, and mitigate mixing of morphotypes potentially seen in multi-specimen data.

6.5 Conclusions

Gc. inflata is an important species in the tracing of hydrographic fronts and through its fantastic fossilisation potential, remains a key tool in understanding past and present oceanography (Schiebel and Hemleben, 2017). Previous studies have reported $\delta^{18}O$ differences along the western South Atlantic margin correlating with morphotype, and thereby genotype, shifts across the oceanographically variable BMC region (Chiessi et al., 2007; Morard et al., 2013; Morard et al., 2016). Subsequent work analysed this isotope-morphometric relationship and found little impact, relating the ~2 ‰ $\delta^{18}O_{(VPDB)}$ shift to variable encrustation states, with little variation between encrusted morphotypes within the BMC (Jonkers et al., 2021). The aims for this study were to resolve these morphotype and encrustation relationships and are listed below with the relevant findings of this study:

- How is the isotope-morphotype relationship of *Gc. inflata,* highlighted in previous work, expressed in the spatial and temporal distributions of Type I and Type II individuals across the BMC?

Results of this study have highlighted the variability of *Gc. inflata* in core top samples spatially, and downcore samples temporally, particularly in regards to stable isotope results. Classification of morphotype through $\delta^{18}O$ values shows distinct clustering into groupings aligning with previously published morphotype ranges (Morard et al., 2016). From the single specimen isotope data presented here, there is a lack of evidence for an intermediary water mass with associated intermediate $\delta^{18}O$ values within the BMC, inferring morphotype ranges are upheld within the confluence. This is contrary to other studies employing multi-specimen averages, whom observed $\delta^{18}O$ values between the morphotype Type I and Type II ranges (1.70-2.33 ‰ $\delta^{18}O_{(VPDB)}$) (Chiessi et al., 2007; Voigt et al., 2015; Morard et al., 2016; Jonkers et al., 2021). Intermediary results from previous work are likely due to averaging of individuals from both BC and MC water masses, and thus representatives from the two distinct morphotypes. However, within the BMC this study suggests further combined morphotype-isotope single specimen analysis is needed to determine whether the isotope ranges proposed by Morard et al., (2016) encapsulate morphotype reliably. This is based on UPC single specimen isotope data aligning well with the Morard et al., (2011) and Morard et al., (2016) boundaries seen elsewhere on the western South Atlantic margin.

- Do *Gc. inflata* encrustation classifications exhibit spatial and temporal variations over the BMC?

It is evident from the UPC cores that medium and heavily encrusted states are prevalent within the confluence, with this study similarly reporting a rarity of non-encrusted forms, and no instances of non-encrustation with high $\delta^{18}O$ values (Jonkers et al., 2021). Spatial variation is common within the core top samples on both intra- and inter-site level, with few sites displaying a single encrustation state. Comparison with previous assemblage studies (Chapter Four) sees a slight propensity for higher encrustation states aligning with cooler water assemblages, however further isotope data is needed to confirm this trend. Temporally, encrustation states remain mixed in core UPC 028, with few samples showing exclusivity of encrustation state. Additionally, encrustation does not appear to increase with burial depth, suggesting encrustation is occurs prior to deposition, corroborating previous studies findings (Jonkers et al., 2021). Wider implementation of encrustation methodology would enable assemblage level variations to be properly understood, spatially and temporally, which would aid in understanding the prevalence of non-encrusted and minor encrusted forms more broadly.

- Through use of single specimen isotopic analyses, are $\delta^{18}O$ values impacted by encrustation state on the Uruguayan margin?

This study disputes previous work to suggest encrustation is a dominant factor in explaining the $\delta^{18}O$ offset linked to BMC position, but rather may be a factor in explaining variation within a region of dynamic oceanography (Jonkers et al., 2021). Observations of this study show distinct clustering of stable isotopes, in line with previous isotope-morphotype ranges, with a variety of encrustation states present in both groupings (Morard et al., 2011; Morard et al., 2016). Whilst higher $\delta^{18}O$ values show a greater propensity for more heavily encrusted states, there are numerous heavily encrusted single specimens within the lower $\delta^{18}O$ Type I cluster. Additionally, the lower encrusted states (B and C) report similar $\delta^{18}O$ ranges to the heavily encrusted forms (D), with the exception of non-encrusted (A), which is likely due to the limited number of specimens recovered. Thus, UPC data suggest no systematic increase in $\delta^{18}O$ values with encrustation.

Previous multi-specimen studies encrustation Type I? results are explained through likely miss-identification and mixing of intersecting morphotypes when

judged “by eye”, or site-specific impacts on $\delta^{18}O$ values. However, should the Jonkers et al., (2021) Type I? data be replicated in a broader study, then isotopically determining morphotype may in future require accounting for potential encrustation offsets. If encrustation state was systematically impacting $\delta^{18}O$ values, rather than strictly the host water mass temperature, this could have implications for regional oceanographic studies connected to ocean fronts (Chiessi et al., 2007; Voigt et al., 2015; Morard et al., 2016; Jonkers et al., 2021). This clarification in the relationship between $\delta^{18}O$ values, morphotype and encrustation is therefore key to identifying water mass associations within the seasonal BMC context, and should be the focus of future work. Regardless, this study recommends single specimen isotope analysis, to investigate morphotype and encrustation impacts within the BMC and wider South Atlantic margin, but also to capture the spatial and temporal variability of this species, in order to fully understand the impact on *Gc. inflata*.

Further work to continue to fully examine whether a relationship between morphotype and $\delta^{18}O$ value exists within the BMC region is required. Morphotype analysis undertaken with awareness of encrustation as a factor would enable resolution of the morphotype-isotope association further, building on previous work which used averaged multi-specimen isotope data, by utilising single specimen data to aid in identifying the cause of variability (Morard et al., 2016; Jonkers et al., 2021). Variability necessitates the need for paired morphotype identification and single specimen stable isotope analysis to ensure true representation of assemblage proportions, relating to both encrusted state and morphotype identification. Additionally, greater categorisation of encrustation data is required to understand the range of $\delta^{18}O$ values produced. Whilst qualitative this data would provide further context for sites, particularly when comparing sites within and external to the BMC. All of these factors will aid in the representation of modern oceanographic systems and the reconstruction of past BMC migrations. This was the original aim for the study however, constraints relating to the COVID19 pandemic and the time-consuming nature of such a study, resulted in the reconsideration of aims to enable data critical for other chapters to be collected.

6.5.1 Key take away messages

- Applying previously published morphotype $\delta^{18}O$ ranges to *Gc. inflata* data produces two clear clusters, following similar patterns observed in BC and MC water masses on the western South Atlantic margin (Morard et al., 2011; Morard et al., 2016).
- Spatially, core top sites display both intra- and inter-site variation in inferred morphotype, displaying a high degree of variation within the BMC that would be lost without use of single specimen stable isotopes. Temporally this variation is also seen with the majority of samples containing a mixture of both morphotypes.
- Encrustation, when categorised qualitatively, displays significant spatial and temporal variation. Higher encrustation states seemingly have a higher propensity for higher $\delta^{18}O$ values.
- However higher encrustation does not always equate to a higher $\delta^{18}O$ value with numerous examples of heavily encrusted forms associated with lower $\delta^{18}O$ values and Type I classified individuals. This would indicate that encrustation does not systematically result in higher $\delta^{18}O$ values within the BMC UPC cores.

6.5.2 Limitations

As previously mentioned, this study suffered from a number of constraints, chief among them was the COVID 19 pandemic, shutting laboratories and limiting the time for, and quantity of, single specimen stable isotope data able to be acquired. This required isotope data was targeted to serve multiple chapters, as such detailed morphotype visual categorisation of *Gc. inflata* specimens was unfeasible and necessitated use of $\delta^{18}O$ ranges to attempt to categorise morphotype. Additionally, the number of specimens categorised for encrustation and analysed using single specimen stable isotope analysis, was significantly reduced. Ideally, a minimum of 25 specimens would have been morphometrically measured and classified before single specimen isotope analysis was performed, with wider assemblages classified visually (for encrustation and morphotype) to ensure representation (Brombacher et al., 2017).

Visual encrustation inspection was possible immediately prior to stable isotope analysis, through comparison with previously published work, however by its nature, this data is qualitative (Jonkers et al., 2021). To maintain consistency in

classification this was conducted by one individual, but is more broadly a limitation in the assessment of encrustation and limited in the ability to assess internal encrustation/infilling. The final limitation of this study is the spatial coverage of the study region, and more broadly the western South Atlantic margin. The availability of margin material was pre-determined by cores utilised for industrial processes prior to donation, and subsequent sampling by previous scientific studies. This is particularly pertinent to the availability of core tops, with material for a number of sites unavailable or unsuitable due to previous sampling efforts. Whilst previous studies targeting *Gc. inflata* were available from the western South Atlantic margin, the lack of published $\delta^{13}C$ data from historical studies inhibited inter-site comparison (Voigt et al., 2015). Ideally, this study would have sampled from sites outside of the BMC region to verify encrustation and morphotype distributions, to fully assess the value gained from single specimen stable isotope analysis over multi-specimen averaging.

6.5.3 Future Work

Future work should aim to ground truth the relationship between isotopic value and morphotype on a single specimen basis. To do this the original methodology, as outlined in Section 2.8.2, would be employed to obtain morphometric data for Type I and Type II, alongside continued use of single specimen isotopes to pair data. This could further expand the use of single specimen morphotype and stable isotope analysis to target causation of encrustation in *Gc. inflata*, the distribution of morphotypes, and the wider influence on $\delta^{18}O$ signatures. This work would require measurement of ocean column properties alongside analyses of modern plankton tow and sediment trap data, from outside and within the BMC, to target what causes the $\delta^{18}O$ offset on the western South Atlantic margin. These efforts, whilst time-consuming, would better enable assessment of *Gc. inflata* morphotype and encrustation assemblage proportions within the mixing zone, and permit use of *Gc. inflata* more confidently to trace the margins complex oceanography temporally. Similarly, the use of single specimen analysis permits a greater complexity and fidelity of data to be acquired, enabling 'mixed' assemblages resulting from BMC seasonality and/or migration to be thoroughly investigated. Such work would ideally be collected concurrently with water column properties, particularly for identifying potential conditions that trigger encrustation in the species. Finally, increasing spatial resolution of core top

studies, and the number of dated temporal records, both within and external to the BMC, would enable a detailed picture of Holocene western South Atlantic oceanography to be reconstructed. This latter point is useful to compare how modern anthropogenic induced climate change impacts regional oceanography.

Chapter 7 Conclusions and further work

7.1 Conclusions

This project aimed to answer a number of research questions relating to the spatial and temporal variability of samples collected from a relatively understudied region in which complex oceanography dominates the surface waters (Solomon et al., 2007; Jansen et al., 2007; Masson-Delmotte et al., 2014; Piola and Matano, 2019). Through use of planktonic foraminiferal assemblages, single specimen isotopes (where possible i.e. for *Gc. inflata* and *Gr. truncatulinoides*), radiocarbon dating and ITRAX XRF data this variability was highlighted across the margin (Chapter 4), through time (Chapter 5), and within individual species (Chapter 6). This study exemplifies the merits of high resolution sampling programs and multi-proxy approaches, in assessing complex oceanographic interactions on the continental margin. Particularly spotlighting the variability of assemblages and stable isotopes, both inter-sample and intra-sample, within such oceanographically complex sites.

This study has also facilitated wider comparisons with published literature (Chiessi et al., 2007; Voigt et al., 2015; Morard et al., 2016; Gu et al., 2018c; Jonkers et al., 2021), through contemporenity of dated studies, to better constrain the temporal and spatial significance of margin oceanography change, and quantify the magnitude of such shifts (Chapter 4 and Chapter 5). Understanding the detail of these ocean mixing zones is a key component in comprehending broader questions relating to modern, and past, South American oceanographic and continental climate systems. This feeds into predictions for future regional climate change, and provides knock on implications to the global system (Chapter 2). As noted in Chapter 1 and Chapter 2, this study samples a region of relatively poor global oceanographic data coverage for the last 10 ky, which has been highlighted in previous literature and IPCC reports (Solomon et al., 2007; Jansen et al., 2007; Masson-Delmotte et al., 2014; Piola and Matano, 2019). Thus this thesis has aimed to contribute in closing these data gaps, improving our knowledge on the direction and size of BMC latitudinal migrations during the Holocene in response to changing atmospheric and ocean circulation patters, facilitating a better understanding of global climate.

Colloaborative modelling work, with partners at the University of Utrecht (Kruijt, 2019), was also used to confirm planktonic foraminiferal data collated in this study is unlikely the product of significant transport prior to deposition (Chapter 4). Based on previous studies relating to the transport potential of plankton groups, concerns were raised on the reliability of these proxies to record local/regional past climates (Van Sebille et al., 2015; Lange and Sebille, 2017; Nooteboom et al., 2019). However, based on the modelled data, transport appears to have minimal impact on the $\delta^{18}O$ estimates, with particles travelling the greatest distances often the result of entrainment within eddies rather than single straight line transport (Kruijt, 2019). Transport may be a factor to consider in other marginal settings, and should be a consideration for future studies.

Additional work on certifying the morphotype-isotope-encrustation record of *Gc. inflata* aimed to build on previous work to determine the relationship between readily observable factors, and confirm the species place as an oceanographic front tracer (Chiessi et al., 2007; Morard et al., 2011; Morard et al., 2016; Jonkers et al., 2021) (Chapter 6). Within this package of work, and through use of single-specimen stable isotope analysis, it was clear the margin showed spatial and temporal variation in $\delta^{18}O$ values recorded, and a propensity for higher levels of encrustation. The use of single-specimen isotope permitted a disentangling of samples that would otherwise have been classified as containing a mixed $\delta^{18}O$ signal. Instead, this study was able to show the composition of a 'mixed sample' breaking down the individual specimens that contributed, and inferring movement of currents across sites through time. Encrustation did not seem to be impacted by spatial location of burial, with some of the best preserved samples originating at depth in the core, in agreement with previous work that suggests encrustation occurs prior to deposition (Jonkers et al., 2021). Due to factors outside this studies control, no new morphometric data was collected, restricting opportunities to fully integrate paired morphometric and single-specimen isotope data. However, this does permit future work to build on this thesis and aid in the determination of the role *Gc. inflata* plays in recording Southern Hemisphere oceanographic fronts over the Holocene.

Lessons learned from this study for other regions and studies fall into a few key areas summarised in greater detail in the following sections of this chapter. From an overview this thesis has illustrated the high degree of variability margin sites

can offer, particularly when adjacent to complex oceanographic structures like the BMC. This is observed both spatially and temporally, in the assemblage and isotopic data provided. Sampling, where possible, should take this into account and may also have to model transport potential of proxies utilised. The second takeaway from this study is the dynamism of these confluences, and their potential fingerprint in the geological record. Extracting such information remains a challenge but can benefit from high resolution studies, and implementation of single-specimen stable isotope analysis. These techniques, combined with non-destructive ITRAX XRF scanning for downcore records, permit greater volumes of data to be extracted from the geological record, uncovering additional complexities. The third application from this study relates to the utility of *Gc. inflata* in tracing oceanographic fronts. This study agrees with previous work that there is likely a $\delta^{18}O$ offset across the BMC, however notes that intermediary isotope values are more likely a result of multi-specimen averaging within the mixing zone samples. Determining whether the $\delta^{18}O$ split is purely related to encrustation or morphotype requires further research and there is still remaining work on this key species.

The following sections will summarise the findings of each data chapter.

7.1.1 Uruguayan Margin planktonic foraminiferal spatial variability

Spatially mapped assemblage data reveals variable species distributions, and their reflected ecological associations. Across the margin, a distinct western and shoreward cooler fauna contrasts the distal eastern, deep water, warmer dominated faunas. This variation was not unexpected within the Brazilian-Malvinas Confluence (BMC), however this work demonstrates that using isolated individual sites, as is typical of palaeoceanographic research, would fail to capture the complex oceanographical interactions present offshore Uruguay. This is evidenced by the diversity of assemblage classifications within the study region, resulting in significant variation across just <1° latitude and longitude (~7100 km^2). Similarly, planktonic foraminiferal isotopes show variability across the region, enabling the fingerprinting of distinct water masses. The multi-core approach of this study provides insight into regional complexity that would not be replicated by a single “representative” site. As such future studies in regions of known oceanographic complexity should apply similar sampling strategies to better resolve spatial variation.

This study utilised, where possible, single specimen isotopes, identifying complexity lost by averaging over significant numbers of specimens (Chiessi et al., 2007; Morard et al., 2016). Employing this method identified intra-site variations, likely reflective of site inter-annual, and potentially some inter-seasonal, variation of overlying water mass properties. Isotope inter-site variation did not readily identify significant spatial offsets across the core-top transect, when compared to assemblage classifications. However, sites in the furthest southwest seemingly displayed less influence of warmer water masses.

Modelling the transport history of "foraminifera-like particles" on the western South Atlantic margin suggests the magnitude of test transport has limited impact on the extremities of water column records. Therefore, the likelihood of test transport explaining all margin wide variability is low. Future parameter refinements within the model could include water mass nutrients, species survival capabilities outside preferential temperature ranges, potential variable dwelling depths or variable genotype ecologies within species. Such parameters may reveal greater ramifications of expatriation to assemblage data and isotopic results. Transport should be more widely considered in future studies, both within the studied region, and in similarly complex ocean environments outside open ocean conditions.

7.1.1.1 Key take away messages

- Assemblage mapping highlights the variability in planktonic foraminiferal distributions across a marginal transect, displaying additional complexities between sites accounted for by oceanographic constraints.
- Inter-annual and seasonal variability of records explains correlation of CTD and isotope data and is likely the reason for the clustering of multiple taxa within the same sites. Single specimen stable isotopes present a tool to investigate this further, fingerprinting water masses within the region.
- Transport and expatriation of foraminifera shows BC transport from warmer SSTs is a possibility although a small (~0.7 °C) offset is expected on the temperature ranges. This is unlikely to significantly impact isotope results but may explain some significant outliers.
- Within complex oceanographic settings a dense sampling strategy enables reconstruction of overlying oceanographic spatial structures. Use of fewer sites

as representative of a larger region is likely to introduce error in understanding local oceanographic frameworks, resulting in simplification of regional systems.

7.1.2 Palaeoceanographic, palaeoenvironmental and palaeobiotic Holocene records from the Uruguayan margin.

A new <200-year resolution Holocene record for the Uruguayan margin was produced from UPC 028 covering the last 10 ka, based on new radiocarbon dating. This record included data that enabled identification of changing thermal and nutrient qualities of overlying water masses. This was evident in species abundances, the planktonic foraminiferal stable isotopes of four species, and the ITRAX XRF semi-quantitative elemental ratios. Combined, a high-resolution reconstruction of the Uruguayan margin is provided, documenting the temporal record of BMC latitudinal migration south during the early to mid-Holocene, before a shift to a more dynamic state likely driven by the onset of ENSO conditions impacting atmosphere-ocean processes. This is supported by a detailed review of nearby terrestrial and oceanic proxies from the literature to understand the complex mechanisms behind this oceanographic confluence.

7.1.2.1 Key take away messages

- Site UPC 028 documents a number of proxies that largely concur on latitudinal migration of the BMC. This is summarised by a southward shift of the confluence over the majority of the early and mid-Holocene, established through a weakening of the SWWB, and leading to warming and decreasing eutrophic conditions as BC begins to dominate.
- This dominance of the BC is broken by a short-term cooling event between 8.4-8.0 ka in which cold eco-groups dominate, isotopes shift to more eutrophic conditions and carbonate production seemingly increases. This brief event sees more MC influence, and is likely triggered by freshwater entering the North Atlantic.
- The maximum southward extent of the BMC is reached during the mid-Holocene (~6.0 ka) where establishment of ENSO conditions in the Pacific drive atmospheric and oceanographic processes to enable greater dynamism on the margin. From this point onward, greater mixing occurs between BC and MC currents over Site UPC 028, favouring the establishment of transitional eco-groups and a mesotrophic system.

- The Late Holocene is characterised by a continuation of mid-Holocene trends until a cooling interval between 2.3-1.0 ka, with a northward shift of the BMC potentially linked to a weakening of the BC and/or SST gradients influencing the SWWB annual position northward. This is evidenced in isotope records, an increase in the presence of cold eco-groups and a potential shift back to more eutrophic records following the *Gg. bulloides:Gs. ruber* white ratio.
- Establishment of modern conditions occurs after 1.0 ka with a slight southward migration of the BMC to the present location, visible in the reversal of cold eco-groups in favour of warmer species, a shift to warmer conditions as indicated by stable isotopes, alongside the return to more mesotrophic conditions.

7.1.3 Impact of encrustation on *Gc. inflata* isotopic and morphological signatures with respect to BMC migration

Results of this study highlight the variability of *Gc. inflata* in core top and downcore samples, particularly in regards to stable isotope results and encrustation factors. Classification of morphotype through $\delta^{18}O$ values shows distinct clustering into two groupings aligning with previously published morphotype ranges (Morard et al., 2016). However, the single specimen results obtained indicate previous studies intermediary values likely represent smearing of multi-specimen cross-morphotype averaging, rather than true intermediary water masses from BMC mixing.

It is evident from the UPC cores that medium and heavily encrusted states are prevalent within the confluence, with this study similarly reporting a rarity of non-encrusted forms, and no instances of non-encrustation with high $\delta^{18}O$ values (Jonkers et al., 2021). Spatial variation of encrustation is common within the core top samples on both intra- and inter-site level, with few sites displaying a single encrustation state. Temporally, encrustation states remain mixed in core UPC 028, with limited examples of encrustation state exclusivity in samples. Additionally, encrustation does not increase with burial depth, suggesting encrustation occurs prior to deposition, corroborating previous studies (Jonkers et al., 2021).

This study disputes previous work to suggest encrustation is the dominant factor explaining the $\delta^{18}O$ offset linked to BMC position, but rather may be a factor in explaining variation, within a region of dynamic oceanography (Jonkers et al.,

2021). Observations of this study show distinct clustering of stable isotopes, with a variety of encrustation states present in both groupings (Morard et al., 2011; Morard et al., 2016). Whilst higher $\delta^{18}O$ values show a greater propensity for more heavily encrusted states, there are numerous heavily encrusted single specimens within the lower $\delta^{18}O$ Type I cluster. Thus, UPC data suggests there is no systematic increase in $\delta^{18}O$ values with encrustation.

Further work should be undertaken to fully examine relationships between morphotype, encrustation and $\delta^{18}O$ values, by employing single specimen paired isotope-morphotype analysis. Undertaken with awareness of potential encrustation effects this would resolve associations further, clarify regional variability, and enable representation of morphotype and encrustation assemblage proportions. Additionally, greater categorisation of encrustation data is required to understand the relationship with $\delta^{18}O$ values. Whilst categorical this data provides further context for sites, particularly when comparing sites within, and external to, the BMC. Combined, these factors will aid in the representation of modern oceanographic systems, understanding the role of *Gc. inflata* in recording these systems, and reconstruction of past BMC migrations.

7.1.3.1 Key take away messages

- Isotopic variability is considerable in both the core top and downcore records, with a split into two distinct clusters at approximately 2 ‰ $\delta^{18}O_{(VPDB)}$.
- When mapped, most core top samples display spatial heterogeneity regarding morphotype classification, temporal samples also display variability. This suggests samples comprise individuals from both BC and MC water masses both spatially and temporally.
- Encrustation, when categorised qualitatively, displays significant spatial and temporal variation. Higher encrustation states seemingly have a higher propensity for higher $\delta^{18}O$ values and dominate the margin.
- However, higher encrustation does not always equate to higher $\delta^{18}O$ values, with numerous examples of heavily encrusted forms associated with lower $\delta^{18}O$ values and Type I classified individuals. This indicates encrustation does not systematically result in higher $\delta^{18}O$ values, within the BMC UPC cores.
- This study due to COVID-19 was restricted to inferring morphotype through $\delta^{18}O$ values. Thus, further work should look to corroborate the allopatric

nature of *Gc. inflata* within the BMC to aid in understanding the morphotype relationship to encrustation and $\delta^{18}O$ values, by employing paired single specimen morphotype-isotope analyses.

7.2 Outlook and suggestions for future work

The work of this study has raised several questions on the spatial and temporal variability recorded within oceanographically complex basins, such as the BMC. There are several aspects to this study that require reflection and should be considered as areas for future focus.

1. Impact of seasonality on spatial assemblage and isotope studies.

Identifying the modern seasonal depositional trends and the signals they preserve over an annual cycle would aid in understanding the preserved core top signals. In order to achieve this, numerous seasonal sediment traps would need to be deployed and recovered, ideally across a regularly spaced gird. This would enable assessment of the composition of winter vs. summer assemblages within the BMC region, and alongside seasonal CTD profiles and plankton tows permit association of BC vs. MC input to sites. An extensive programme of single specimen isotope analysis from plankton tows, sediment traps and core tops would allow species potentially present in both BMC water masses to be recovered, with isotopic ranges better constrained to observed water mass properties, and the variation therein recorded. Finally, an expanded core top study, with radiocarbon dating to ensure contemporaneity, could then understand the relative proportions of BC vs. MC planktonic foraminifera contributing to each site, enabling greater confidence in understanding how overlying water masses are recorded on the seafloor. However, such an undertaking is not without significant expense of both time and financial resources, which represent significant barriers to obtaining this data at the present time.

2. Corroboration of UPC 028 events through further downcore dating and additional site studies. Building a spatially and temporally extensive understanding of Holocene palaeoceanography.

Five preliminary radiocarbon dates provided the temporal context for this study, with interpolation enabling dating of intervening samples. Additional radiocarbon dating would help better constrain the proxies, particularly concerning timing of three significant events: The 8.2 ka cooling period at the end of the early

Holocene, the onset of Mesotrophic conditions and excursions of Ca/Ti and S/Ti ratios during the mid-Holocene, and the late Holocene cooling event between 2.3-1.0 ka. Future work would aim to not only better constrain the dating on these events, but also the extent of excursion from the background. Alongside increasing the resolution of the stable isotope record, both in terms of number of samples but also the number of analyses per interval, would enable increased confidence in trends between samples and identifying causation of excursions.

Uncertainty surrounds the nature of large Ca/Ti and S/Ti excursions found in the mid-Holocene, post ENSO intensification. There is the potential that these reflect deposition of organic material, however this study lacked the ability to discern this, with certainty. Employing TOC analyses on fresh samples, and from proximal cores, may aid in answering this question. Future work could also encompass analysis of the sediment composition, in terms of silt, clay and sand content to determine sediment sourcing to UPC028. Aiding determination of whether core sites are purely influenced by the marine system throughout geological history, or with relative sea level change and terrestrial climate regime shifts, see greater fluvial input.

Samples from two additional cores were washed and processed for subsequent planktonic foraminiferal investigations at the University of Leeds. Provided suitable dating was available, these records could expand the understanding of Uruguayan margin processes spatially, as well as temporally. A benthic foraminiferal and contourite study, conducted by Cian McGuire as part of his PhD thesis, found cores within the collection had the capability to extend records back into the late Pleistocene. Through exploitation of samples already present at the University of Leeds, or housed within the BOSCORF repository in Southampton, there is the potential to obtain palaeoceanographic and palaeoclimatic reconstructions across Last Glacial Maximum, within an unstudied portion of the world's oceans.

3. Encrustation-morphotype impact on $\delta^{18}O$ values and their wider distribution across the margin, investigating possible seasonal signals.

This study echoes calls for future studies to source further plankton tow studies, and sediment trap data, clarifying cause of encrustation to fully understand its impact on recorded $\delta^{18}O$ signature (Jonkers et al., 2021). Additionally, this study was unable to acquire morphometric data for paired single-specimen stable

isotope and morphometric analysis, future work should seek to acquire this data. By making an extensive single-specimen paired morphometric-isotope record of data sourced from seasonal plankton tows, sediment traps and core tops, the encrustation-morphotype impact on isotope signatures can be fully quantified. This is essential work for quantifying the $\delta^{18}O$ offsets found across the BMC, and critical for understanding how morphometric, and by extension genotypic, variability is recorded within this extensively-used oceanographical front marker (Morard et al., 2011; Morard et al., 2016; Schiebel and Hemleben, 2017). A similar study on core top material was the original aim for the study however, constraints relating to the COVID-19 pandemic and the time-consuming nature of isotope and morphometric work, resulted in the reconsideration of aims to enable data critical for other chapters to simultaneously be collected.

References

Acha, E.M., Mianzan, H.W., Guerrero, R.A., Favero, M. and Bava, J. 2004. Marine fronts at the continental shelves of austral South America: Physical and ecological processes. *Journal of Marine Systems*. **44**(1–2), pp.83–105.

Agnihotri, R., Altabet, M.A., Herbert, T.D. and Tierney, J.E. 2008. Subdecadally resolved paleoceanography of the Peru margin during the last two millennia. *Geochemistry, Geophysics, Geosystems*. **9**(5).

Aguiar, W., Meissner, K.J., Montenegro, A., Prado, L., Wainer, I., Carlson, A.E. and Mata, M.M. 2021. Magnitude of the 8.2 ka event freshwater forcing based on stable isotope modelling and comparison to future Greenland melting. *Scientific Reports*. **11**(1), pp.1–10.

Akers, P.D., Brook, G.A., Railsback, L.B., Liang, F., Iannone, G., Webster, J.W., Reeder, P.P., Cheng, H. and Edwards, R.L. 2016. An extended and higher-resolution record of climate and land use from stalagmite MC01 from Macal Chasm, Belize, revealing connections between major dry events, overall climate variability, and Maya sociopolitical changes. *Palaeogeography, Palaeoclimatology, Palaeoecology*. **459**, pp.268–288.

Al-Sabouni, N., Kucera, M. and Schmidt, D.N. 2007. Vertical niche separation control of diversity and size disparity in planktonic foraminifera. *Marine Micropaleontology*. **63**(1–2), pp.75–90.

Alley, R.B., Mayewski, P.A., Sowers, T., Stuiver, M., Taylor, K.C. and Clark, P.U. 1997. Holocene climatic instability: A prominent, widespread event 8200 yr ago. *Geology*. **25**(6), pp.483–486.

Anand, P., Elderfield, H. and Conte, M.H. 2003. Calibration of Mg/Ca thermometry in planktonic foraminifera from a sediment trap time series. *Paleoceanography*. **18**(2), n/a-n/a.

Anderson, E.C. 1953. The Production and Distribution of Natural Radiocarbon. *Annual Review of Nuclear Science*. **2**(1), pp.63–78.

Angulo, R.J., Lessa, G.C. and Souza, M.C. De 2006. A critical review of mid- to late-Holocene sea-level fluctuations on the eastern Brazilian coastline. *Quaternary Science Reviews*. **25**(5–6), pp.486–506.

Armstrong, H.A. and Brasier, M.D. 2005. *Microfossils* 2nd Editio. (B. P. Ltd, ed.).

Aze, T., Ezard, T.H.G., Purvis, A., Coxall, H.K., Stewart, D.R.M., Wade, B.S. and Pearson, P.N. 2011. A phylogeny of Cenozoic macroperforate planktonic foraminifera from fossil data. *Biological Reviews*. **86**(4), pp.900–927.

Bader, J., Jungclaus, J., Krivova, N., Lorenz, S., Maycock, A., Raddatz, T., Schmidt, H., Toohey, M., Wu, C.J. and Claussen, M. 2020. Global temperature modes shed light on the Holocene temperature conundrum. *Nature Communications*. **11**(1), pp.1–8.

Baker, P.A. and Fritz, S.C. 2015. Nature and causes of Quaternary climate variation of tropical South America. *Quaternary Science Reviews*. **124**, pp.31–47.

Bard, E., Hamelin, B., Fairbanks, R.G. and Zindler, A. 1990. Calibration of the

14C timescale over the past 30,000 years using mass spectrometric U-Th ages from Barbados corals. *Nature*. **345**(6274), pp.405–410.

Barreiro, M., Chang, P. and Saravanan, R. 2002. Variability of the South Atlantic convergence zone simulated by an atmospheric general circulation model. *Journal of Climate*. **15**(7), pp.745–763.

Barros, V., Gonzalez, M., Liebmann, B. and Camilloni, I. 2000. Influence of the South Atlantic convergence zone and South Atlantic Sea surface temperature on interannual summer rainfall variability in Southeastern South America. *Theoretical and Applied Climatology*. **67**(3–4), pp.123–133.

Bé, A.W.H. 1982. Biology of Planktonic Foraminifera. *Notes for a Short Course: Studies in Geology*. **6**, pp.51–89.

Bé, A.W.H. and Hamlin, W.H. 1967. Ecology of recent planktonic foraminifera: Part 3: Areal distribution in the North Atlantic during the summer of 1962. *Micropaleontology*. **13**(1), pp.87–106.

Bé, A.W.H. and Hutson, W.H. 1977. Ecology of planktonic foraminifera and biogeographic patterns of life and fossil assemblages in the Indian Ocean. *Micropaleontology*. **23**(4), pp.369–414.

Beal, L.M., Elipot, S., Houk, A. and Leber, G.M. 2015. Capturing the transport variability of a western boundary jet: Results from the Agulhas Current time-series experiment (ACT). *Journal of Physical Oceanography*. **45**(5), pp.1302–1324.

Bemis, B.E., Spero, H.J., Bijma, J. and Lea, D.W. 1998. Reevaluation of the oxygen isotopic composition of planktonic foraminifera: Experimental results and revised paleotemperature equations. *Paleoceanography*. **13**(2), pp.150–160.

Bender, V.B., Hanebuth, T.J.J. and Chiessi, C.M. 2013. Holocene shifts of the Subtropical Shelf Front off southeastern South America controlled by high and low latitude atmospheric forcings. *Paleoceanography*. **28**(3), pp.481–490.

Berger, Wolfgang H. 1969. Ecologic patterns of living planktonic Foraminifera. *Deep-Sea Research and Oceanographic Abstracts*. **16**(1), pp.1–24.

Berger, Wolfgang H 1969. Planktonic Foraminifera : Basic Morphology and Ecologic Implications Author (s): Wolfgang H . Berger PLANKTONIC FORAMINIFERA : BASIC MORPHOLOGY AND ECOLOGIC IMPLICATIONS. *Journal of Paleontology*. **43**(6), pp.1369–1383.

Berger, W.H. 1971. Sedimentation of planktonic foraminifera. *Marine Geology*. **11**(5), pp.325–358.

Berger, W.H. and Diester-Haass, L. 1988. Paleoproductivity: The benthic/planktonic ratio in foraminifera as a productivity index. *Marine Geology*. **81**(1–4), pp.15–25.

Bícego, M.C., Santos, F.R., de Aandrade Furlan, P.C., Lourenço, R.A., Taniguchi, S., de Mello e Sousa, S.H., Nagai, R.H., Cavalcante, A.B.L., Figueira, R.C.L., Wainer, I.K.C. and de Mahiques, M.M. 2021. Mid- to late-Holocene analysis of the influence of the La Plata River plume on the southwestern Atlantic shelf: A paleoenvironmental reconstruction based on lipid biomarkers and benthic foraminifera. *Holocene*.

Bijma, J., Erez, J. and Hemleben, C. 1990. Lunar and Semi-Lunar reproductive cycles in some spinose planktonic foraminifers. *Journal of Foraminiferal Research*. **20**(2), pp.117–127.

Birch, H., Coxall, H.K., Pearson, P.N., Kroon, D. and O'Regan, M. 2013. Planktonic foraminifera stable isotopes and water column structure: Disentangling ecological signals. *Marine Micropaleontology*. **101**, pp.127–145.

Bird, B.W., Abbott, M.B., Vuille, M., Rodbell, D.T., Stansell, N.D. and Rosenmeier, M.F. 2011. A 2,300-year-long annually resolved record of the South American summer monsoon from the Peruvian Andes. *Proceedings of the National Academy of Sciences*. **108**(21), pp.8583–8588.

Blaich, O.A., Faleide, J.I., Tsikalas, F., Franke, D. and León, E. 2009. Crustal-scale architecture and segmentation of the Argentine margin and its conjugate off South Africa. *Geophysical Journal International*. **178**(1), pp.85–105.

Blaich, O.A., Faleide, J.I., Tsikalas, F., Gordon, A.C., Mohriak, W.U., Pasteur, A., Janeiro, R. De and O, E.P. 2013. Crustal-scale architecture and segmentation of the South Atlantic volcanic margin. *Geological Society, London, Special Publications*. **369**(1), pp.167–183.

Blanchet, C.L., Kasten, S., Vidal, L., Poulton, S.W., Ganeshram, R. and Thouveny, N. 2012. Influence of diagenesis on the stable isotopic composition of biogenic carbonates from the Gulf of Tehuantepec oxygen minimum zone. *Geochemistry, Geophysics, Geosystems*. **13**(4), pp.1–20.

Blanchet, C.L., Thouveny, N. and Vidal, L. 2009. Formation and preservation of greigite (Fe3S4) in sediments from the Santa Barbara Basin: Implications for paleoenvironmental changes during the past 35 ka. *Paleoceanography*. **24**(2), pp.1–15.

Boltovskoy, E., Boltovskoy, D. and Brandini, F. 2000. Planktonic Foraminifera from south-western Atlantic epipelagic waters: Abundance, distribution and year-to-year variations. *Journal of the Marine Biological Association of the United Kingdom*. **80**(2), pp.203–213.

Boltovskoy, E., Boltovskoy, D., Correa, N. and Brandini, F. 1996. Planktic foraminifera from the southwestern Atlantic (30 °–60 °S): species-specific patterns in the upper 50 m. *Marine Micropaleontology*. **28**(1), pp.53–72.

Bond, G., Kromer, B., Beer, J., Muscheler, R., Evans, M.N., Showers, W., Hoffmann, S., Lotti-Bond, R., Hajdas, I. and Bonani, G. 2001. Persistent solar influence on north atlantic climate during the Holocene. *Science*. **294**(5549), pp.2130–2136.

Borisov, D.G., Murdmaa, I.O., Ivanova, E. V, Levchenko, O. V, Yutsis, V. V and Frantseva, T.N. 2013. Contourite systems in the region of the southern São Paulo Plateau escarpment, South Atlantic. *Oceanology*. **53**(4), pp.460–471.

Bova, S., Rosenthal, Y., Liu, Z., Godad, S.P. and Yan, M. 2021. Seasonal origin of the thermal maxima at the Holocene and the last interglacial. *Nature*. **589**(7843), pp.548–553.

Boyer, T.P., Baranova, O.K., Coleman, C., Garcia, H.E., Grodsky, A., Locarnini, R.A., Mishonov, A. V, Paver, C.R., Reagan, J.R., Seidov, D., Smolyar, I. V, Weathers, K.W. and Zweng, M.M. 2018. *World Ocean Database 2018*

NOAA Atlas. (A. V. Mishonov, ed.).

Bozzano, G., Violante, R.A. and Cerredo, M.E. 2011. Middle slope contourite deposits and associated sedimentary facies off NE Argentina. *Geo-Marine Letters*. **31**(5–6), pp.495–507.

Bracco, R., García-Rodríguez, F., Inda, H., del Puerto, L., Castiñeira, C. and Panario, D. 2011. Niveles relativos del mar durante el Pleistoceno final-Holoceno en la costa de Uruguay. *El Holoceno en la zona costera de Uruguay*. (January), pp.65–92.

Bracco, R., Inda, H., del Puerto, L., Capdepont, I., Panario, D., Castiñeira, C. and García-Rodríguez, F. 2014. A reply to 'Relative sea level during the Holocene in Uruguay'. *Palaeogeography, Palaeoclimatology, Palaeoecology*. **401**, pp.166–170.

Brandini, F.P., Boltovskoy, D., Piola, A.R., Kocmur, S., Röttgers, R., Cesar Abreu, P. and Mendes Lopes, R. 2000. Multiannual trends in fronts and distribution of nutrients and chlorophyll in the southwestern Atlantic (30–62°S). *Deep Sea Research Part I: Oceanographic Research Papers*. **47**(6), pp.1015–1033.

Brombacher, A., Wilson, P.A. and Ezard, T.H.G. 2017. Calibration of the repeatability of foraminiferal test size and shape measures with recommendations for future use. *Marine Micropaleontology*. **133**(January), pp.21–27.

Burone, L., Franco-Fraguas, P., Mahiques, M. and Ortega, L. 2018. GEOMORPHOLOGICAL AND SEDIMENTOLOGICAL CHARACTERIZATION OF THE URUGUAYAN CONTINENTAL MARGIN: A REVIEW AND STATE OF ART / CARACTERIZAÇÃO GEOMORFOLÓGICA E SEDIMENTOLÓGICA DA MARGEM CONTINENTAL DO URUGUAI: UMA REVISÃO E ESTADO DA ARTE. *Journal of Sedimentary Environments*. **3**(4), pp.253–264.

Cane, M.A. 2005. The evolution of El Niño, past and future. *Earth and Planetary Science Letters*. **230**(3–4), pp.227–240.

Carlson, A.E., Stoner, J.S., Donnelly, J.P. and Hillaire-Marcel, C. 2008. Response of the southern Greenland Ice Sheet during the last two deglaciations. *Geology*. **36**(5), pp.359–362.

Castro, J.W.A., Suguio, K., Seoane, J.C.S., Da Cunha, A.M. and Dias, F.F. 2014. Sea-level fluctuations and coastal evolution in the state of Rio de Janeiro, southeastern Brazil. *Anais da Academia Brasileira de Ciencias*. **86**(2), pp.671–683.

Cavallotto, J.L., Violante, R.A. and Parker, G. 2004. Sea-level fluctuations during the last 8600 years in the de la Plata river (Argentina). *Quaternary International*. **114**(1), pp.155–165.

Chapori, N.G., Chiessi, C.M., Bickert, T. and Laprida, C. 2015. Sea-surface temperature reconstruction of the Quaternary western South Atlantic: New planktonic foraminiferal correlation function. *Palaeogeography, Palaeoclimatology, Palaeoecology*. **425**, pp.67–75.

Chiessi, C.M., Mulitza, S., Groeneveld, J., Silva, J.B., Campos, M.C. and Gurgel, M.H.C. 2014. Variability of the Brazil Current during the late Holocene. *Palaeogeography, Palaeoclimatology, Palaeoecology*. **415**,

pp.28–36.

Chiessi, C.M., Mulitza, S., Mollenhauer, G., Silva, J.B., Groeneveld, J. and Prange, M. 2015. Thermal evolution of the western South Atlantic and the adjacent continent during Termination 1. *Climate of the Past*. **11**(6), pp.915–929.

Chiessi, C.M., Mulitza, S., P??tzold, J., Wefer, G. and Marengo, J.A. 2009. Possible impact of the Atlantic Multidecadal Oscillation on the South American summer monsoon. *Geophysical Research Letters*. **36**(21), pp.1–5.

Chiessi, C.M., Ulrich, S., Mulitza, S., Pätzold, J. and Wefer, G. 2007. Signature of the Brazil-Malvinas Confluence (Argentine Basin) in the isotopic composition of planktonic foraminifera from surface sediments. *Marine Micropaleontology*. **64**(1–2), pp.52–66.

Clark, P.U., Dyke, A.S., Shakun, J.D., Carlson, A.E., Clark, J., Wohlfarth, B., Mitrovica, J.X., Hostetler, S.W. and McCabe, A.M. 2009. The Last Glacial Maximum. *Science*. **325**(5941), pp.710–714.

Colombo, F., Serra, J. and Rivero, L. 2014. Río de la Plata inner estuary (Argentina): Main forms, sedimentary infill and Holocene evolution. *Geological Society Special Publication*. **388**(1), pp.305–331.

Combes, V. and Matano, R.P. 2014. A two-way nested simulation of the oceanic circulation in the Southwestern Atlantic. *Journal of Geophysical Research: Oceans*. **119**(2), pp.731–756.

Conti, B., Perinotto, J.A. de J., Veroslavsky, G., Castillo, M.G., de Santa Ana, H., Soto, M. and Morales, E. 2017. Speculative petroleum systems of the southern Pelotas Basin, offshore Uruguay. *Marine and Petroleum Geology*. **83**, pp.1–25.

Contreras, J., Zühlke, R., Bowman, S. and Bechstädt, T. 2010. Seismic stratigraphy and subsidence analysis of the southern Brazilian margin (Campos, Santos and Pelotas basins). *Marine and Petroleum Geology*. **27**(9), pp.1952–1980.

Creaser, A., Hernández-Molina, F.J., Badalini, G., Thompson, P., Walker, R., Soto, M. and Conti, B. 2017. A Late Cretaceous mixed (turbidite-contourite) system along the Uruguayan Margin: Sedimentary and palaeoceanographic implications. *Marine Geology*. **390**(February), pp.234–253.

Croudace, I.W., Rindby, A. and Rothwell, R.G. 2006. ITRAX: Description and evaluation of a new multi-function X-ray core scanner. *Geological Society Special Publication*. **267**, pp.51–63.

Croudace, I.W. and Rothwell, R.G. 2015. *Micro-XRF Studies of Sediment Cores* [Online] (I. W. Croudace & R. G. Rothwell, eds.). Dordrecht: Springer Netherlands. Available from: http://link.springer.com/10.1007/978-94-017-9849-5.

Cruz, F.W., Burns, S.J., Jercinovic, M., Karmann, I., Sharp, W.D. and Vuille, M. 2007. Evidence of rainfall variations in Southern Brazil from trace element ratios (Mg/Ca and Sr/Ca) in a Late Pleistocene stalagmite. *Geochimica et Cosmochimica Acta*. **71**(9), pp.2250–2263.

Cruz, F.W., Burns, S.J., Karmann, I., Sharp, W.D., Vuille, M., Cardoso, A.O.,

Ferrari, J.A., Silva Dias, P.L. and Viana, O. 2005. Insolation-driven changes in atmospheric circulation over the past 116,000 years in subtropical Brazil. *Nature*. **434**(7029), pp.63–66.

Cruz, F.W., Vuille, M., Burns, S.J., Wang, X., Cheng, H., Werner, M., Lawrence Edwards, R., Karmann, I., Auler, A.S. and Nguyen, H. 2009. Orbitally driven east-west antiphasing of South American precipitation. *Nature Geoscience*. **2**(3), pp.210–214.

Culver, S.J. 1988. New Foraminiferal Depth Zonation of the Northwestern Gulf of Mexico. *Palaios*. **3**, pp.69–85.

Darling, K.F. and Wade, C.M. 2008. The genetic diversity of planktic foraminifera and the global distribution of ribosomal RNA genotypes. *Marine Micropaleontology*. **67**(3–4), pp.216–238.

Darling, K.F., Wade, C.M., Siccha, M., Trommer, G., Schulz, H., Abdolalipour, S. and Kurasawa, A. 2017. Genetic diversity and ecology of the planktonic foraminifers Globigerina bulloides, Turborotalita quinqueloba and Neogloboquadrina pachyderma off the Oman margin during the late SW Monsoon. *Marine Micropaleontology*. **137**(October), pp.64–77.

Dauner, A.L.L., Mollenhauer, G., Bícego, M.C., de Souza, M.M., Nagai, R.H., Figueira, R.C.L., de Mahiques, M.M., Sousa, S.H. de M. e. and Martins, C.C. 2019. Multi-proxy reconstruction of sea surface and subsurface temperatures in the western South Atlantic over the last ~75 kyr. *Quaternary Science Reviews*. **215**, pp.22–34.

Debret, M., Sebag, D., Crosta, X., Massei, N., Petit, J.R., Chapron, E. and Bout-Roumazeilles, V. 2009. Evidence from wavelet analysis for a mid-Holocene transition in global climate forcing. *Quaternary Science Reviews*. **28**(25–26), pp.2675–2688.

Denton, G.H., Anderson, R., Toggweiler, J., Edwards, R., Schaefer, J. and Putnam, J. 2010. The Last Glacial Termination. *Hemisphere*. **1652**(June), pp.1652–1657.

Depetris, P.J. and Griffin, J.J. 1968. Suspended Load in the Rio De La Plata Drainage Basin. *Sedimentology*. **11**(1/2), pp.53–60.

Dickson, A.J., Leng, M.J., Maslin, M.A. and Röhl, U. 2010. Oceanic, atmospheric and ice-sheet forcing of South East Atlantic Ocean productivity and South African monsoon intensity during MIS-12 to 10. *Quaternary Science Reviews*. **29**(27–28), pp.3936–3947.

Doyle, M.E. and Barros, V.R. 2002. Midsummer low-level circulation and precipitation in subtropical South America and related sea surface temperature anomalies in the South Atlantic. *Journal of Climate*. **15**(23), pp.3394–3410.

Eguchi, N.O., KAWAHATA, H. and TAIRA, A. 1999. Seasonal Response of Planktonic Foraminifera to Surface Ocean Condition: Sediment Trap Results from the Central North Pacific Ocean. *Journal of Oceanography*. **55**, pp.681–691.

Emery, W.J. 2015. Oceanographic Topics: Water Types and Water Masses. *Encyclopedia of Atmospheric Sciences: Second Edition*., pp.329–337.

Ezard, T.H.G., Edgar, K.M. and Hull, P.M. 2015. Environmental and biological controls on size-specific ^{13}C and ^{18}O in recent planktonic foraminifera.

Paleoceanography. **30**(3), pp.151–173.

Fabel, D. 2015. "…[samples were] reduced to graphite before AMS 14C analysis at the SUERC AMS Facility ." *Britice-Chrono NERC Consortium*. [Online], p.7. [Accessed 7 April 2020]. Available from: https://briticechronoblog.wordpress.com/2015/09/20/samples-were-reduced-to-graphite-before-ams-14c-analysis-at-the-suerc-ams-facility/.

Fairbanks, R.G. 1989. A 17,000-year glacio-eustatic sea level record: influence of glacial melting rates on the Younger Dryas event and deep-ocean circulation. *Nature*. **342**, pp.637–642.

Fairbanks, R.G. and Wiebe, P.H. 1980. Foraminifera and chlorophyll maximum: Vertical distribution, seasonal succession, and paleoceanographic significance. *Science*. **209**(4464), pp.1524–1526.

Flores, J.-A., Santarosa, A.C.A., Quadros, J.P., Camillo, E., Toledo, F.A.L. and Costa, K.B. 2016. Plankton biochronology for the last 772,000 years from the western South Atlantic Ocean. *Marine Micropaleontology*. **127**, pp.50–62.

Franco-Fraguas, P., Burone, L., Mahiques, M., Ortega, L., Urien, C., Muñoz, A., López, G., Marin, Y., Carranza, A., Lahuerta, N. and de Mello, C. 2014. Hydrodynamic and geomorphological controls on surface sedimentation at the Subtropical Shelf Front / Brazil-Malvinas Confluence transition off Uruguay (Southwestern Atlantic Continental Margin). *Marine Geology*. **349**, pp.24–36.

Frozza, C.F., Pivel, M.A.G., Suárez-Ibarra, J.Y., Ritter, M.N. and Coimbra, J.C. 2020. Bioerosion on Late Quaternary Planktonic Foraminifera Related to Paleoproductivity in the Western South Atlantic. *Paleoceanography and Paleoclimatology*. **35**(8), pp.1–16.

Gaines, W.L., Harrod, R.J. and Lehmkuhl, J.F. 1999. Monitoring Biodiversity: Quantification and Interpretation. *USDA Forest Service - General Technical Report PNW*. (PNW-GTR-443).

Garcia, C.A.E., Sarma, Y.V.B., Mata, M.M. and Garcia, V.M.T. 2004. Chlorophyll variability and eddies in the Brazil-Malvinas Confluence region. *Deep-Sea Research Part II: Topical Studies in Oceanography*. **51**(1–3), pp.159–172.

García Chapori, N. and Laprida, C. 2021. Planktonic foraminifera assemblages from the Brazil–Malvinas Confluence: palaeoceanographic implications of sub-surface temperature reconstructions in the western South Atlantic. *Lethaia*. **54**(4), pp.477–494.

Garcia, S.R. and Kayano, M.T. 2010. Some evidence on the relationship between the South American monsoon and the Atlantic ITCZ. *Theoretical and Applied Climatology*. **99**(1–2), pp.29–38.

Garreaud, R.D. 2007. Precipitation and circulation covariability in the extratropics. *Journal of Climate*. **20**(18), pp.4789–4797.

Garreaud, R.D., Vuille, M., Compagnucci, R. and Marengo, J. 2009. Present-day South American climate. *Palaeogeography, Palaeoclimatology, Palaeoecology*. **281**(3–4), pp.180–195.

Garzoli, S.L. and Gordon, A.L. 1996. Origins and variability of the Benguela Current. *Journal of Geophysical Research: Oceans*. **101**(C1), pp.897–906.

Gibson, T.G. 1989. Planktonic benthonic foraminiferal ratios: Modern patterns and Tertiary applicability. *Marine Micropaleontology*. **15**(1–2), pp.29–52.

Giosan, L., Flood, R.D. and Aller, R.C. 2002. Paleoceanographic significance of sediment color on western North Atlantic drifts: I. Origin of color. *Marine Geology*. **189**(1–2), pp.25–41.

Giraudeau, J. 1993. Planktonic foraminiferal assemblages in surface sediments from the southwest African continental margin. *Marine Geology*. **110**(1–2), pp.47–62.

Gordon, A.L. 1981. South Atlantic thermocline ventilation. *Deep Sea Research Part A, Oceanographic Research Papers*. **28**(11), pp.1239–1264.

Govin, A., Holzwarth, U., Heslop, D., Ford Keeling, L., Zabel, M., Mulitza, S., Collins, J.A. and Chiessi, C.M. 2012. Distribution of major elements in Atlantic surface sediments (36°N-49°S): Imprint of terrigenous input and continental weathering. *Geochemistry, Geophysics, Geosystems*. **13**(1), pp.1–23.

Groeneveld, J. and Chiessi, C.M. 2011. Mg/Ca of Globorotalia inflata as a recorder of permanent thermocline temperatures in the South Atlantic. *Paleoceanography*. **26**(2), pp.1–12.

Gu, F., Chiessi, C.M., Zonneveld, K.A.F. and Behling, H. 2018a. Late Quaternary environmental dynamics inferred from marine sediment core GeoB6211-2 off southern Brazil. *Palaeogeography, Palaeoclimatology, Palaeoecology*. **496**(January), pp.48–61.

Gu, F., Chiessi, C.M., Zonneveld, K.A.F. and Behling, H. 2018b. *Late Quaternary vegetation , climate and ocean dynamics inferred from marine sediment cores off southeastern South America*. Georg-August-Universität Göttingen.

Gu, F., Chiessi, C.M., Zonneveld, K.A.F. and Behling, H. 2018c. Shifts of the Brazil-Falklands/Malvinas Confluence in the western South Atlantic during the latest Pleistocene–Holocene inferred from dinoflagellate cysts. *Palynology*. **0**(0), pp.1–11.

Gu, F., Zonneveld, K.A.F., Chiessi, C.M., Arz, H.W., Pätzold, J. and Behling, H. 2017. Long-term vegetation, climate and ocean dynamics inferred from a 73,500 years old marine sediment core (GeoB2107-3) off southern Brazil. *Quaternary Science Reviews*. **172**, pp.55–71.

Guerrero, R.A., Piola, A.R., Fenco, H., Matano, R.P., Combes, V., Chao, Y., James, C., Palma, E.D., Saraceno, M. and Strub, P.T. 2014. The salinity signature of the cross-shelf exchanges in the Southwestern Atlantic Ocean: Satellite observations. *Journal of Geophysical Research: Oceans*. **119**(11), pp.7794–7810.

Guilderson, T.P., Burckle, L., Hemming, S. and Peltier, W.R. 2000. Late Pleistocene sea level variations derived from the Argentine Shelf. *Geochemistry, Geophysics, Geosystems*. **1**(12).

Sen Gupta, B.K. 2003. Modern Foraminifera B. K. Sen Gupta, ed. *Modern Foraminifera*. **36**(4), p.384.

Gyldenfeldt, A.-B. V, Carstens, J. and Meincke, J. 2000. Estimation of the catchment area of a sediment trap by means of current meters and foraminiferal tests. *Deep-Sea Research Part II: Topical Studies in*

Oceanography. **47**(9–11), pp.1701–1717.

Gyllencreutz, R., Mahiques, M.M., Alves, D.V.P. and Wainer, I.K.C. 2010. Mid- to late-Holocene paleoceanographic changes on the southeastern Brazilian shelf based on grain size records. *Holocene*. **20**(6), pp.863–875.

Haddam, N.A., Michel, E., Siani, G., Cortese, G., Bostock, H.C., Duprat, J.M. and Isguder, G. 2016. Improving past sea surface temperature reconstructions from the Southern Hemisphere oceans using planktonic foraminiferal census data. *Paleoceanography*. **31**(6), pp.822–837.

Hajdas, I., Ivy-Ochs, S., Pickering, R. and Preusser, F. 2008. Recent developments in quaternary dating methods. *Geographica Helvetica*. **63**(3), pp.176–180.

Hammer, Ø. and Harper, D.A.T. 2007. *Paleontological Data Analysis*.

Hanebuth, T.J.J., Voris, H.K., Yokoyama, Y., Saito, Y. and Okuno, J. 2011. Formation and fate of sedimentary depocentres on Southeast Asia's Sunda Shelf over the past sea-level cycle and biogeographic implications. *Earth-Science Reviews*. **104**(1–3), pp.92–110.

Harrison, S., Smith, D.E. and Glasser, N.F. 2019. Late Quaternary meltwater pulses and sea level change. *Journal of Quaternary Science*. **34**(1), pp.1–15.

Heaton, T.J., Köhler, P., Butzin, M., Bard, E., Reimer, R.W., Austin, W.E.N., Bronk Ramsey, C., Grootes, P.M., Hughen, K.A., Kromer, B., Reimer, P.J., Adkins, J., Burke, A., Cook, M.S., Olsen, J. and Skinner, L.C. 2020. Marine20 - The Marine Radiocarbon Age Calibration Curve (0-55,000 cal BP). *Radiocarbon*. **62**(4), pp.779–820.

Hecht, a. D. 1976. An ecologic model for test size variation in Recent planktonic foraminifera; applications to the fossil record. *The Journal of Foraminiferal Research*. **6**(4), pp.295–311.

Help, C.H.R., Herman, P.M.J. and Soetaert, K. 1998. Indices of diversity and evenness *. . **24**(2459), pp.61–87.

Hernández-Molina, F.J., Paterlini, M., Somoza, L., Violante, R.A., Arecco, M.A., de Isasi, M., Rebesco, M., Uenzelmann-Neben, G., Neben, S. and Marshall, P. 2010. Giant mounded drifts in the Argentine Continental Margin: Origins, and global implications for the history of thermohaline circulation. *Marine and Petroleum Geology*. **27**(7), pp.1508–1530.

Hernández-Molina, F.J., Paterlini, M., Violante, R.A., Marshall, P., de Isasi, M., Somoza, L. and Rebesco, M. 2009. Contourite depositional system on the Argentine slope: An exceptional record of the influence of Antarctic water masses. *Geology*. **37**(6), pp.507–510.

Hernández-Molina, F.J., Soto, M., Piola, A.R., Tomasini, J., Preu, B., Thompson, P., Badalini, G., Creaser, A., Violante, R.A., Morales, E., Paterlini, M. and De Santa Ana, H. 2016. A contourite depositional system along the Uruguayan continental margin: Sedimentary, oceanographic and paleoceanographic implications. *Marine Geology*. **378**, pp.333–349.

Hinz, K., Neben, S., Schreckenberger, B., Roeser, H.A., Block, M., Souza, K.G. De and Meyer, H. 1999. The Argentine continental margin north of 48°S: Sedimentary successions, volcanic activity during breakup. *Marine and Petroleum Geology*. **16**(1), pp.1–25.

Hodell, D.A., Channeil, J.E.T., Curtis, J.H., Romero, O.E. and Röhl, U. 2008. Onset of 'Hudson Strait' Heinrich events in the eastern North Atlantic at the end of the middle Pleistocene transition (~640 ka)? *Paleoceanography*. **23**(4).

Isla, F.I. 1989. Holocene sea-level fluctuation in the southern hemisphere. *Quaternary Science Reviews*. **8**(4), pp.359–368.

Jansen, E., Overpeck, J., Briffa, K.R., Duplessy, J.-C., Joos, F., Masson-Delmotte, V., Olago, D., Otto-Bliesner, B.L., Peltier, W.R., Rahmstorf, S., Ramesh, R., Raynaud, D., Rind, D., Solomina, O., Villalba, R. and Zhang, D. 2007. Paleoclimate *In*: *Climate Change 2007: The Physical Science Basis. Contribution of Working Group I to the Fourth Assessment Report of the Intergovernmental Panel on Climate Change* [Online]., pp.433–497. Available from: http://scholar.google.com/scholar?hl=en&btnG=Search&q=intitle:Agriculture.+In+Climate+Change+2007:+Mitigation.+Contribution+of+Working+Group+III+to+the+Fourth+Assessment+Report+of+the+Intergovernmental+Panel+on+Climate+Change+[B.#0.

Jones, C. and Carvalho, L.M.V. 2013. Climate change in the South American monsoon system: Present climate and CMIP5 projections. *Journal of Climate*. **26**(17), pp.6660–6678.

Jonkers, L., Gopalakrishnan, A., Weßel, L., Chiessi, C.M., Groeneveld, J., Monien, P., Lessa, D. and Morard, R. 2021. Morphotype and Crust Effects on the Geochemistry of Globorotalia inflata. *Paleoceanography and Paleoclimatology*. **36**(4), pp.1–16.

Jonkers, L., Van Heuven, S., Zahn, R. and Peeters, F.J.C. 2013. Seasonal patterns of shell flux, δ18O and δ13C of small and large N. pachyderma (s) and G. bulloides in the subpolar North Atlantic. *Paleoceanography*. **28**(1), pp.164–174.

Jonkers, L. and Kučera, M. 2015. Global analysis of seasonality in the shell flux of extant planktonic Foraminifera. *Biogeosciences*. **12**(7), pp.2207–2226.

Jullion, L., Heywood, K.J., Naveira Garabato, A.C. and Stevens, D.P. 2010. Circulation and Water Mass Modification in the Brazil–Malvinas Confluence. *Journal of Physical Oceanography*. **40**(5), pp.845–864.

Kanner, L.C., Burns, S.J., Cheng, H., Edwards, R.L. and Vuille, M. 2013. High-resolution variability of the South American summer monsoon over the last seven millennia: Insights from a speleothem record from the central Peruvian Andes. *Quaternary Science Reviews*. **75**, pp.1–10.

Kaufman, D., McKay, N., Routson, C., Erb, M., Dätwyler, C., Sommer, P.S., Heiri, O. and Davis, B. 2020. Holocene global mean surface temperature, a multi-method reconstruction approach. *Scientific Data*. **7**(1), p.201.

Kaufman, D., McKay, N., Routson, C., Erb, M., Davis, B., Heiri, O., Jaccard, S., Tierney, J., Dätwyler, C., Axford, Y., Brussel, T., Cartapanis, O., Chase, B., Dawson, A., de Vernal, A., Engels, S., Jonkers, L., Marsicek, J., Moffa-Sánchez, P., Morrill, C., Orsi, A., Rehfeld, K., Saunders, K., Sommer, P.S., Thomas, E., Tonello, M., Tóth, M., Vachula, R., Andreev, A., Bertrand, S., Biskaborn, B., Bringué, M., Brooks, S., Caniupán, M., Chevalier, M., Cwynar, L., Emile-Geay, J., Fegyveresi, J., Feurdean, A., Finsinger, W., Fortin, M.-C., Foster, L., Fox, M., Gajewski, K., Grosjean, M., Hausmann,

S., Heinrichs, M., Holmes, N., Ilyashuk, B., Ilyashuk, E., Juggins, S., Khider, D., Koinig, K., Langdon, P., Larocque-Tobler, I., Li, J., Lotter, A., Luoto, T., Mackay, A., Magyari, E., Malevich, S., Mark, B., Massaferro, J., Montade, V., Nazarova, L., Novenko, E., Pařil, P., Pearson, E., Peros, M., Pienitz, R., Płóciennik, M., Porinchu, D., Potito, A., Rees, A., Reinemann, S., Roberts, S., Rolland, N., Salonen, S., Self, A., Seppä, H., Shala, S., St-Jacques, J.-M., Stenni, B., Syrykh, L., Tarrats, P., Taylor, K., van den Bos, V., Velle, G., Wahl, E., Walker, I., Wilmshurst, J., Zhang, E. and Zhilich, S. 2020. A global database of Holocene paleotemperature records. *Scientific Data*. **7**(1), p.115.

Kennett, J.P. and Srinivasan, M.S. 1983. *Neogene planktonic foraminifera: A Phylogenetic Atlas*. Stroudsburg, Pa. : Hutchinson Ross ; New York, NY.

Khan, N.S., Horton, B.P., Engelhart, S., Rovere, A., Vacchi, M., Ashe, E.L., Törnqvist, T.E., Dutton, A., Hijma, M.P. and Shennan, I. 2019. Inception of a global atlas of sea levels since the Last Glacial Maximum. *Quaternary Science Reviews*. **220**, pp.359–371.

Kilian, R. and Lamy, F. 2012. A review of Glacial and Holocene paleoclimate records from southernmost Patagonia (49-55°S). *Quaternary Science Reviews*. **53**(C), pp.1–23.

Kim, S.-T. and O'Neil, J.R. 1997. Equilibrium and nonequilibrium oxygen isotope effects in synthetic carbonates. *Geochimica et Cosmochimica Acta*. **61**(16), pp.3461–3475.

King, B.A., Moat, B., McLean, L., Brearley, A., Gramcianinov, C., Hamersley, D., McCarthy, G., Torres Valdes, S., Chambers, L., Darroch, L., Posada-Gonzalez, A., Moore, M., Schuster, U., De Boer, A., Scally, S., Cooper, D., Woodward, S., Brousseau, A., Silvera, N. and De Araujo, P. 2010. *RSS James Cook Cruise JC032, 07 Mar – 21 Apr 2009. Hydrographic sections across the Brazil Current and at 24°S in the Atlantic.* (B. A. King & D. Hamersley, eds.).

Knutz, P.C. 2008. Chapter 24 Palaeoceanographic Significance of Contourite Drifts. *Developments in Sedimentology*. **60**(08), pp.511–535.

Krastel, S., Wefer, G., Anasetti, A., Andreula, R., Arnold, G.L., Beck, A., Bender, V.B., Bergenthal, M., Bogus, K., Bozzano, G., Chiessi, C.M., Collins, J., Dekeyzer, S., Diekamp, V., Domnia, Y., Düßmann, R., Esteban, F.D., Fekete, N., Fink, C., Formolo, M., Freudenthal, T., Greif, G., Hanebuth, T.J.J., Henkel, S., Hilgenfeld, C., Hohnberg, H.-J., Huppertz, T., Kasten, S., Klein, T., Könnecker, H.-O., Kokisch, B., Lange, M., Lantzsch, H., Lindhorst, K., Meyer, M., Mill, S., Müller, H., Mund, O., Ochsenhirt, W.-T., Preu, B., Raeke, A., Razik, S., Renken, J., Riedinger, N., Rosiak, U., Sawicka, J.E., Schmidt, W., Schwenk, T., Seiter, C., Strasser, M., Tomasini, J., Truscheit, T., Violante, R.A., Vossmeyer, A. and Winkelmann, D. 2001. Sediment transport off Uruguay and Argentina: From the shelf to the deep sea. *Berichte Fachbereich Geowissenschaften Universit□t Bremen*. (170), p.114.

Krastel, S., Wefer, G., Hanebuth, T.J.J., Antobreh, A.A., Freudenthal, T., Preu, B., Schwenk, T., Strasser, M., Violante, R. and Winkelmann, D. 2011. Sediment dynamics and geohazards off Uruguay and the de la Plata River region (northern Argentina and Uruguay). *Geo-Marine Letters*. **31**(4), pp.271–283.

Kretschmer, K., Jonkers, L., Kucera, M. and Schulz, M. 2018. Modeling seasonal and vertical habitats of planktonic foraminifera on a global scale. *Biogeosciences*. **15**(14), pp.4405–4429.

Kroon, D., Steens, T., Troelstra, S.R. and Kingdom, U. 1991. ONSET OF MONSOONAL RELATED UPWELLING IN THE WESTERN ARABIAN SEA AS REVEALED BY PLANKTONIC FORAMINIFERS 1 Quantitative analysis of the late Cenozoic planktonic foraminiferal record from western Arabian Sea Site 722 re- vealed long term trends in the h. *Proceedings of Ocean Drilling Program, Scientific Result*. **117**, pp.257–263.

Kruijt, A. 2019. *Transport of planktic foraminifera by ocean currents in the Uruguayan margin*.[Online] Utrecht University. Available from: http://dspace.library.uu.nl/handle/1874/394873.

Kucera, M. 2007. Chapter Six Planktonic Foraminifera as Tracers of Past Oceanic Environments. *Developments in Marine Geology*. **1**(07), pp.213–262.

Kucera, M., Rosell-Melé, A., Schneider, R., Waelbroeck, C. and Weinelt, M. 2005. Multiproxy approach for the reconstruction of the glacial ocean surface (MARGO). *Quaternary Science Reviews*. **24**(7-9 SPEC. ISS.), pp.813–819.

Lachniet, M.S., Johnson, L., Asmerom, Y., Burns, S.J., Polyak, V., Patterson, W.P., Burt, L. and Azouz, A. 2009. Late Quaternary moisture export across Central America and to Greenland: evidence for tropical rainfall variability from Costa Rican stalagmites. *Quaternary Science Reviews*. **28**(27–28), pp.3348–3360.

Lambeck, K., Rouby, H., Purcell, A., Sun, Y. and Sambridge, M. 2014. Sea level and global ice volumes from the Last Glacial Maximum to the Holocene. *Proceedings of the National Academy of Sciences*. **111**(43), pp.15296–15303.

Lamy, F., Hebbeln, D., Röhl, U. and Wefer, G. 2001. Holocene rainfall variability in Southern Chile: A marine record of latitudinal shifts of the Southern Westerlies. *Earth and Planetary Science Letters*. **185**(3–4), pp.369–382.

Lamy, F., Kilian, R., Arz, H.W., Francois, J.P., Kaiser, J., Prange, M. and Steinke, T. 2010. Holocene changes in the position and intensity of the southern westerly wind belt. *Nature Geoscience*. **3**(10), pp.695–699.

Lange, M. and Sebille, E. Van 2017. Parcels v0.9: Prototyping a Lagrangian ocean analysis framework for the petascale age. *Geoscientific Model Development*. **10**(11), pp.4175–4186.

Lantzsch, H., Hanebuth, T.J.J., Chiessi, C.M., Schwenk, T. and Violante, R.A. 2014. The high-supply, current-dominated continental margin of southeastern South America during the late quaternary. *Quaternary Research (United States)*. **81**(2), pp.339–354.

Laprida, C., García Chapori, N., Chiessi, C.M., Violante, R.A., Watanabe, S. and Totah, V. 2011. Middle Pleistocene sea surface temperature in the Brazil-Malvinas Confluence Zone : Paleoceanographic implications based on planktonic foraminifera. *Micropaleontology*. **57**(2), pp.183–195.

Lastras, G., Acosta, J., Muñoz, A. and Canals, M. 2011. Submarine canyon formation and evolution in the Argentine Continental Margin between

44°30'S and 48°S. *Geomorphology*. **128**(3–4), pp.116–136.

Leckie, R.M. and Olson, H.C. 2003. Foraminifera as proxies for sea-level change on siliciclastic margins. *SEPM (Society for Sedimentary Geology) Special Publication*. (75), pp.5–19.

Lee, S.Y., Chiang, J.C.H., Matsumoto, K. and Tokos, K.S. 2011. Southern Ocean wind response to North Atlantic cooling and the rise in atmospheric CO2: Modeling perspective and paleoceanographic implications. *Paleoceanography*. **26**(1), pp.1–16.

LeGrande, A.N. and Schmidt, G.A. 2006. Global gridded data set of the oxygen isotopic composition in seawater. *Geophysical Research Letters*. **33**(12), pp.1–5.

Lessa, D.V.O., Santos, T.P., Venancio, I.M., Santarosa, A.C.A., dos Santos Junior, E.C., Toledo, F.A.L., Costa, K.B. and Albuquerque, A.L.S. 2019. Eccentricity-induced expansions of Brazilian coastal upwelling zones. *Global and Planetary Change*. **179**(May), pp.33–42.

Li, J. and Heap, A.D. 2008. A Review of Spatial Interpolation Methods for Environmental Scientists. *Australian Geological Survey Organisation*. **GeoCat# 68**(2008/23), p.154.

Li, Q. and McGowran, B. 1998. Oceanographic implications of recent planktonic foraminifera along the southern Australian margin. *Marine and Freshwater Research*. **49**(5), pp.439–445.

Lin, Q., Wang, J., Algeo, T.J., Su, P. and Hu, G. 2016. Formation mechanism of authigenic gypsum in marine methane hydrate settings: Evidence from the northern South China Sea. *Deep-Sea Research Part I: Oceanographic Research Papers*. **115**, pp.210–220.

Liu, Z., Zhu, J., Rosenthal, Y., Zhang, X., Otto-Bliesner, B.L., Timmermann, A., Smith, R.S., Lohmann, G., Zheng, W. and Timm, O.E. 2014. The Holocene temperature conundrum. *Proceedings of the National Academy of Sciences of the United States of America*. **111**(34).

Ljung, K., Björck, S., Renssen, H. and Hammarlund, D. 2008. South Atlantic island record reveals a South Atlantic response to the 8.2 kyr event. *Climate of the Past*. **4**(1), pp.35–45.

Locarnini, R.A., Mishonov, A. V., Baranova, O.K., Boyer, T.P., Zweng, M.M., Garcia, H.E., Reagan, J.R., Seidov, D., Weathers, K.W., Paver, C.R. and Smolyar, I. V. 2019. *World Ocean Atlas 2018, Volume 1: Temperature.* (A. V. Mishonov, ed.).

Locarnini, R.A., Mishonov, A. V, Antonov, J.I., Boyer, T.P., Garcia, H.E., Baranova, O.K., Zweng, M.M., Paver, C.R., Reagan, J.R., Johnson, D.R., Hamilton, M. and Seidov, D. 2013. *WORLD OCEAN ATLAS 2013, Volume 1: Temperature* (S. Levitus & A. Mishonov, eds.).

Lončarić, N., van Iperen, J., Kroon, D. and Brummer, G.J.A. 2007. Seasonal export and sediment preservation of diatomaceous, foraminiferal and organic matter mass fluxes in a trophic gradient across the SE Atlantic. *Progress in Oceanography*. **73**(1), pp.27–59.

Lončarić, N., Peeters, F.J.C., Kroon, D. and Brummer, G.J.A. 2006. Oxygen isotope ecology of recent planktic foraminifera at the central Walvis Ridge (SE Atlantic). *Paleoceanography*. **21**(3), pp.1–18.

Lumpkin, R. and Garzoli, S. 2011. Interannual to decadal changes in the western South Atlantic's surface circulation. *Journal of Geophysical Research: Oceans*. **116**(1), pp.1–10.

Magurran, A. 2004. *Measuring Biological Diversity*. Blackwell Publishing.

de Mahiques, M.M., Coaracy Wainer, I.K., Burone, L., Nagai, R., de Mello e Sousa, S.H., Lopes Figueira, R.C., Almeida da Silveira, I.C., Bícego, M.C., Vicente Alves, D.P. and Hammer, Ø. 2009. A high-resolution Holocene record on the Southern Brazilian shelf: Paleoenvironmental implications. *Quaternary International*. **206**(1–2), pp.52–61.

Marcott, S. a., Shakun, J.D., Clark, P.U. and Mix, A.C. 2013. A Reconstruction of Regional. *Science (New York, N.Y.)*. **339**(6124), pp.1198–1201.

Marcott, S.A. and Shakun, J.D. 2015. *Holocene climate change and its context for the future*.

Marengo, J.A., Liebmann, B., Grimm, A.M., Misra, V., Silva Dias, P.L., Cavalcanti, I.F.A., Carvalho, L.M.V., Berbery, E.H., Ambrizzi, T., Vera, C.S., Saulo, A.C., Nogues-Paegle, J., Zipser, E., Seth, A. and Alves, L.M. 2012. Recent developments on the South American monsoon system. *International Journal of Climatology*. **32**(1), pp.1–21.

Marsh, R., Mills, R.A., Green, D.R.H., Salter, I. and Taylor, S. 2007. Controls on sediment geochemistry in the Crozet region. *Deep-Sea Research Part II: Topical Studies in Oceanography*. **54**(18–20), pp.2260–2274.

Martínez, S. and Rojas, A. 2013. Relative sea level during the Holocene in Uruguay. *Palaeogeography, Palaeoclimatology, Palaeoecology*. **374**, pp.123–131.

Masson-Delmotte, V., Schulz, M., Abe-Ouchi, A., Beer, J., Ganopolski, A., Gonzalez Rouco, J.F., Jansen, E., Lambeck, K., Luterbacher, J., Naish, T., Osborn, T., Otto-Bliesner, B., Quinn, T., Ramesh, R., Rojas, M., Shao, X. and Timmermann, A. 2014. Information from Paleoclimate Archives *In*: *Climate Change 2013 – The Physical Science Basis* [Online]. Cambridge University Press, pp.383–464. Available from: https://www.cambridge.org/core/product/identifier/CBO9781107415324A021/type/book_part.

Masson-Delmotte, V., Schulz, M., Abe-Ouchi, A., Beer, J., Ganopolski, A., Rouco, J.F.G., Jansen, E., Lambeck, K., Luterbacher, J., Naish, T., Osborn, T., Otto-Bliesner, B., Quinn, T., Ramesh, R., Rojas, M., Shao, X. and Timmermann, and A. 2013. Information from Paleoclimate Archives *In*: Intergovernmental Panel on Climate Change, ed. *Climate Change 2013 - The Physical Science Basis* [Online]. Cambridge: Cambridge University Press, pp.383–464. Available from: http://ebooks.cambridge.org/ref/id/CBO9781107415324A021.

Matano, R.P., Combes, V., Piola, A.R., Guerrero, R., Palma, E.D., Ted Strub, P., James, C., Fenco, H., Chao, Y. and Saraceno, M. 2014. The salinity signature of the cross-shelf exchanges in the Southwestern Atlantic Ocean: Numerical simulations. *Journal of Geophysical Research: Oceans*. **119**(11), pp.7949–7968.

Matano, R.P. and Palma, E.D. 2008. On the upwelling of downwelling currents. *Journal of Physical Oceanography*. **38**(11), pp.2482–2500.

Matano, R.P., Palma, E.D. and Piola, A.R. 2010. The influence of the Brazil and Malvinas Currents on the Southwestern Atlantic Shelf circulation. *Ocean Science*. **6**(4), pp.983–995.

Mayewski, P.A., Rohling, E.E., Stager, J.C., Karlén, W., Maasch, K.A., Meeker, L.D., Meyerson, E.A., Gasse, F., van Kreveld, S., Holmgren, K., Lee-Thorp, J., Rosqvist, G., Rack, F., Staubwasser, M., Schneider, R.R. and Steig, E.J. 2004. Holocene climate variability. *Quaternary Research*. **62**(3), pp.243–255.

McGuire, C.J., Rogerson, M., Parsons, D. and Herringshaw, L. 2019. *Late Pleistocene to Holocene Sedimentology, Palaeoceanography and Micropalaeontology of the Uruguayan Continental Slope*.[Online] University of Hull. Available from: https://hydra.hull.ac.uk/assets/hull:18324a/content.

McKinney, M.L. 1990. Trends in body-size evolution *In*: *Evolutionary Trends*., pp.75–118.

McPhaden, M.J., Zebiak, S.E. and Glantz, M.H. 2006. ENSO as an integrating concept in earth science. *Science*. **314**(5806), pp.1740–1745.

Milne, G.A., Long, A.J. and Bassett, S.E. 2005. Modelling Holocene relative sea-level observations from the Caribbean and South America. *Quaternary Science Reviews*. **24**(10–11), pp.1183–1202.

Mitas, L. and Mitasova, H. 2005. Spatial interpolation *In*: P. A. Longley, M. F. Goodchild, D. J. Maguire and D. W. Rhind, eds. *Geographical Information Systems: Principles, Techniques, Management and Applications*., pp.481–492.

Mohiuddin, M.M., Nishimura, A., Tanaka, Y. and Shimamoto, A. 2002. Regional and interannual productivity of biogenic components and planktonic foraminiferal fluxes in the northwestern Pacific Basin. *Marine Micropaleontology*. **45**(1), pp.57–82.

Mojtahid, M., Jorissen, F.J., Garcia, J., Schiebel, R., Michel, E., Eynaud, F., Gillet, H., Cremer, M., Diz Ferreiro, P., Siccha, M. and Howa, H. 2013. High resolution holocene record in the southeastern bay of biscay: Global versus regional climate signals. *Palaeogeography, Palaeoclimatology, Palaeoecology*. **377**, pp.28–44.

Morales, E., Chang, H.K., Soto, M., Corrêa, F.S., Veroslavsky, G., Ana, H. de S., Conti, B., Daners, G., Santos Corrêa, F., Veroslavsky, G., De Santa Ana, H., Conti, B. and Daners, G. 2017. Tectonic and stratigraphic evolution of the Punta del Este and Pelotas basins (offshore Uruguay). *Petroleum Geoscience*. **23**, pp.415–426.

Morales, E., Chang, H.K., Soto, M., Veroslavsky, G., Conti, B., Ana, H. de S. and Corrêa, F.S. 2017. Speculative petroleum systems of the Punta del Este Basin (offshore Uruguay). *Brazilian Journal of Geology*. **47**(4), pp.645–656.

Morard, R., Quillévéré, F., Douady, C.J., de Vargas, C., de Garidel-Thoron, T. and Escarguel, G. 2011. Worldwide genotyping in the planktonic foraminifer globoconella inflata: Implications for life history and paleoceanography. *PLoS ONE*. **6**(10).

Morard, R., Quillévéré, F., Escarguel, G., de Garidel-Thoron, T., de Vargas, C. and Kucera, M. 2013. Ecological modeling of the temperature dependence

of cryptic species of planktonic Foraminifera in the Southern Hemisphere. *Palaeogeography, Palaeoclimatology, Palaeoecology*. **391**, pp.13–33.

Morard, R., Reinelt, M., Chiessi, C.M., Groeneveld, J. and Kucera, M. 2016. Tracing shifts of oceanic fronts using the cryptic diversity of the planktonic foraminifera Globorotalia inflata. *Paleoceanography*. **31**(9), pp.1193–1205.

Moreno, A., Giralt, S., Valero-Garcés, B., Sáez, A., Bao, R., Prego, R., Pueyo, J.J., González-Sampériz, P. and Taberner, C. 2007. A 14 kyr record of the tropical Andes: The Lago Chungará sequence (18°S, northern Chilean Altiplano). *Quaternary International*. **161**(1), pp.4–21.

Mörner, N.A. 1996. Global change and interaction of earth rotation, ocean circulation and paleoclimate. *Anais da Academia Brasileira de Ciencias*. **68**(SUPPL. 1), pp.91–94.

Morrill, C., Anderson, D.M., Bauer, B.A., Buckner, R., Gille, E.P., Gross, W.S., Hartman, M. and Shah, A. 2013. Proxy benchmarks for intercomparison of 8.2 ka simulations. *Climate of the Past*. **9**(1), pp.423–432.

Moulin, M., Aslanian, D., Olivet, J.L., Contrucci, I., Matias, L., Géli, L., Klingelhoefer, F., Nouzé, H., Réhault, J.P. and Unternehr, P. 2005. Geological constraints on the evolution of the Angolan margin based on reflection and refraction seismic data (ZaïAngo project). *Geophysical Journal International*. **162**(3), pp.793–810.

Moy, C.M., Seltzer, G.O., Rodbell, D.T. and Anderson, D.M. 2002. Variability of El Niño/Southern Oscillation activity at millennial timescales during the Holocene epoch. *Nature*. **420**(6912), pp.162–165.

Mulitza, S., Chiessi, C.M., Schefuß, E., Lippold, J., Wichmann, D., Antz, B., Mackensen, A., Paul, A., Prange, M., Rehfeld, K., Werner, M., Bickert, T., Frank, N., Kuhnert, H., Lynch-Stieglitz, J., Portilho-Ramos, R.C., Sawakuchi, A.O., Schulz, M., Schwenk, T., Tiedemann, R., Vahlenkamp, M. and Zhang, Y. 2017. Synchronous and proportional deglacial changes in Atlantic meridional overturning and northeast Brazilian precipitation. *Paleoceanography*. **32**(6), pp.622–633.

Münnich, M. and Neelin, J.D. 2005. Seasonal influence of ENSO on the Atlantic ITCZ and equatorial South America. *Geophysical Research Letters*. **32**(21), pp.1–4.

Nagai, R.H., Sousa, S.H.M., Burone, L. and Mahiques, M.M. 2009. Paleoproductivity changes during the Holocene in the inner shelf of Cabo Frio, southeastern Brazilian continental margin: Benthic foraminifera and sedimentological proxies. *Quaternary International*. **206**(1–2), pp.62–71.

Nelson, C.S. and Cooke, P.J. 2001. History of oceanic front development in the New Zealand sector of the southern ocean during the cenozoic - A synthesis. *New Zealand Journal of Geology and Geophysics*. **44**(4), pp.535–553.

Nooteboom, P.D., Bijl, P.K., Sebille, E., Heydt, A.S. and Dijkstra, H.A. 2019. Transport Bias by Ocean Currents in Sedimentary Microplankton Assemblages: Implications for Paleoceanographic Reconstructions. *Paleoceanography and Paleoclimatology*. **34**(7), pp.1178–1194.

Novello, V.F., Cruz, F.W., Vuille, M., Stríkis, N.M., Edwards, R.L., Cheng, H., Emerick, S., De Paula, M.S., Li, X., Barreto, E.D.S., Karmann, I. and

Santos, R. V. 2017. A high-resolution history of the South American Monsoon from Last Glacial Maximum to the Holocene. *Scientific Reports*. **7**(March), pp.1–8.

Nürnberg, D., Müller, R.D., N&-Berg, D., Miiller, R.D. and M??ller, R.D. 1991. The tectonic evolution of the South Atlantic from Late Jurassic to present. *Tectonophysics*. **191**(1–2), pp.27–53.

de Oliveira Lessa, D.V., Ramos, R.P., Barbosa, C.F., da Silva, A.R., Belem, A., Turcq, B. and Albuquerque, A.L. 2014. Planktonic foraminifera in the sediment of a western boundary upwelling system off Cabo Frio, Brazil. *Marine Micropaleontology*. **106**, pp.55–68.

Olson, D.B., Podestá, G.P., Evans, R.H. and Brown, O.B. 1988. Temporal variations in the separation of Brazil and Malvinas Currents. *Deep Sea Research Part A, Oceanographic Research Papers*. **35**(12), pp.1971–1990.

Olson, H.C. and Leckie, R.M. 2003. *Micropaleontologic Proxies for Sea-Level Change and Stratigraphic Discontinuities* [Online] (H. C. OLSON & R. M. LECKIE, eds.). SEPM (Society for Sedimentary Geology). Available from: https://pubs.geoscienceworld.org/books/book/1384/.

Olsson, R.K., Hemleben, C., Berggren, W.A. and Huber, B.T. 1999. *Atlas of Paleocene Planktonic Foraminifera*.

Palma, E.D., Matano, R.P. and Piola, A.R. 2008. A numerical study of the Southwestern Atlantic Shelf circulation: Stratified ocean response to local and offshore forcing. *Journal of Geophysical Research: Oceans*. **113**(11), pp.1–22.

Paniagua, G.F., Saraceno, M., Piola, A.R., Guerrero, R., Provost, C., Ferrari, R., Lago, L.S. and Artana, C.I. 2018. Malvinas Current at 40°S–41°S: First Assessment of Temperature and Salinity Temporal Variability. *Journal of Geophysical Research: Oceans*. **123**(8), pp.5323–5340.

Passier, H.F., Middelburg, J.J., De Lange, G.J. and Böttcher, M.E. 1999. Modes of sapropel formation in the eastern Mediterranean: Some constraints based on pyrite properties. *Marine Geology*. **153**(1–4), pp.199–219.

Patterson, R.T. and Fishbein, E. 1989. Re-examination of the statistical methods used to determine the number of point counts needed for micropaleontological quantitative research. *Journal of Paleontology*. **63**(2), pp.245–248.

Pearson, P.N. 2012. Oxygen Isotopes in Foraminifera : Overview and Historical Review R = 18 O 16 O. *The Paleontological Society Papers*. **18**, pp.1–38.

Pearson, P.N., Olsson, R.K., Huber, B.T., Hemleben, C. and Berggren, W.A. 2006. Atlas of Eocene planktonic foraminifera. *Cushman Foundation Special Publication*. **41**(41), p.513.

Pereira, L.S., Arz, H.W., Pätzold, J. and Portilho-Ramos, R.C. 2018. Productivity Evolution in the South Brazilian Bight During the Last 40,000 Years. *Paleoceanography and Paleoclimatology*. **33**(12), pp.1339–1356.

Pérez, E.M. 2013. *Evolução Tectônica E Estratigráfica das bacias da margem continental do Uruguay*.[Online] Universidade Estadual Paulista. Available from: http://hdl.handle.net/11449/138385.

Pérez, L.F., Hernández-Molina, F.J., Esteban, F.D., Tassone, A., Piola, A.R., Maldonado, A., Preu, B., Violante, R.A. and Lodolo, E. 2015. Erosional and depositional contourite features at the transition between the western Scotia Sea and southern South Atlantic Ocean: links with regional water-mass circulation since the Middle Miocene. *Geo-Marine Letters*. **35**(4), pp.271–288.

Peterson, R.G. and Stramma, L. 1991. Upper-level circulation in the South Atlantic Ocean. *Progress in Oceanography*. **26**(1), pp.1–73.

Pielou, E.C. 1966. The measurement of diversity in different types of biological collections. *Journal of Theoretical Biology*. **13**(C), pp.131–144.

Piola, A.R., Campos, E.J.D., Möller, O.O., Charo, M. and Martinez, C. 2000. Subtropical shelf front off eastern South America. *Journal of Geophysical Research: Oceans*. **105**(C3), pp.6565–6578.

Piola, A.R., Franco, B.C., Palma, E.D. and Saraceno, M. 2013. Multiple jets in the Malvinas current. *Journal of Geophysical Research: Oceans*. **118**(4), pp.2107–2117.

Piola, A.R. and Matano, R.P. 2008. Brazil and Falklands (Malvinas) Currents. *Encyclopedia of Ocean Sciences: Second Edition*. (June), pp.422–430.

Piola, A.R. and Matano, R.P. 2019. Ocean Currents: Atlantic Western Boundary—Brazil Current/Falkland (Malvinas) Current *In*: *Encyclopedia of Ocean Sciences* [Online]. Elsevier, pp.414–420. Available from: http://dx.doi.org/10.1016/B978-0-12-409548-9.10541-X.

Piola, A.R., Möller, O.O., Guerrero, R.A. and Campos, E.J.D. 2008. Variability of the subtropical shelf front off eastern South America: Winter 2003 and summer 2004. *Continental Shelf Research*. **28**(13), pp.1639–1648.

Pirazzoli, P.A. 1993. Global sea-level changes and their measurement. *Global and Planetary Change*. **8**(3), pp.135–148.

Piva, A., Asioli, A., Schneider, R.R., Trincardi, F., Andersen, N., Colmenero-Hidalgo, E., Dennielou, B., Flores, J.A. and Vigliotti, L. 2008. Climatic cycles as expressed in sediments of the PROMESSI borehole PRAD1-2, central Adriatic, for the last 370 ka: 1. Integrated stratigraphy. *Geochemistry, Geophysics, Geosystems*. **9**(1).

Pivel, M.A.G., de Lima Toledo, F.A. and Costa, K.B. 2010. Foraminiferal record of changes in summer monsoon precipitation at the southeastern Brazilian continental margin since the Last Glacial Maximum. *Revista Brasileira de Paleontologia*. **13**(2), pp.79–88.

Pivel, M.A.G., Santarosa, A.C.A., Toledo, F.A.L. and Costa, K.B. 2013. The Holocene onset in the southwestern South Atlantic. *Palaeogeography, Palaeoclimatology, Palaeoecology*. **374**, pp.164–172.

Portilho-Ramos, R. da C., Ferreira, F., Calado, L., Frontalini, F. and de Toledo, M.B. 2015. Variability of the upwelling system in the southeastern Brazilian margin for the last 110,000 years. *Global and Planetary Change*. **135**, pp.179–189.

Portilho-Ramos, R. da C., Pinho, T.M.L., Chiessi, C.M. and Barbosa, C.F. 2019. Understanding the mechanisms behind high glacial productivity in the southern Brazilian margin. *Climate of the Past*. **15**(3), pp.943–955.

Portilho-Ramos, R.C., Cruz, A.P.S., Barbosa, C.F., Rathburn, A.E., Mulitza, S., Venancio, I.M., Schwenk, T., Rühlemann, C., Vidal, L., Chiessi, C.M. and Silveira, C.S. 2018. Methane release from the southern Brazilian margin during the last glacial. *Scientific Reports*. **8**(1), p.5948.

Preu, B., Hernández-Molina, F.J., Violante, R.A., Piola, A.R., Paterlini, M., Schwenk, T., Voigt, I., Krastel, S. and Spieß, V. 2013. Morphosedimentary and hydrographic features of the northern Argentine margin: The interplay between erosive, depositional and gravitational processes and its conceptual implications. *Deep-Sea Research Part I: Oceanographic Research Papers*. **75**, pp.157–174.

Preu, B., Schwenk, T., Hernández-Molina, F.J., Violante, R.A., Paterlini, M., Krastel, S., Tomasini, J. and Spieß, V. 2012. Sedimentary growth pattern on the northern Argentine slope: The impact of North Atlantic Deep Water on southern hemisphere slope architecture. *Marine Geology*. **329**–**331**, pp.113–125.

Prieto, A.R., Mourelle, D., Peltier, W.R., Drummond, R., Vilanova, I. and Ricci, L. 2017. Relative sea-level changes during the Holocene in the Río de la Plata, Argentina and Uruguay: A review. *Quaternary International*. **442**, pp.35–49.

Raggio, F., Gerster, R. and Welsink, H. 2011. Cuencas del Salado y Punta del Este. *VIII Congreso de Exploración y Desarrollo de Hidrocarburos Simposio Cuencas Argentinas: visión actual*., pp.80–87.

Ramsey, C.B. 2009. Bayesian analysis of radiocarbon dates. *Radiocarbon*. **51**(1), pp.337–360.

Ramsey, C.B. 2008. Deposition models for chronological records. *Quaternary Science Reviews*. **27**(1–2), pp.42–60.

Razik, S., Chiessi, C.M., Romero, O.E. and von Dobeneck, T. 2013. Interaction of the South American Monsoon System and the Southern Westerly Wind Belt during the last 14kyr. *Palaeogeography, Palaeoclimatology, Palaeoecology*. **374**, pp.28–40.

Razik, S., Govin, A., Chiessi, C.M. and von Dobeneck, T. 2015. Depositional provinces, dispersal, and origin of terrigenous sediments along the SE South American continental margin. *Marine Geology*. **363**, pp.261–272.

Rebesco, M., Hernández-Molina, F.J., Van Rooij, D. and Wåhlin, A. 2014. Contourites and associated sediments controlled by deep-water circulation processes: State-of-the-art and future considerations. *Marine Geology*. **352**, pp.111–154.

Rebotim, A., Helga Luise Voelker, A., Jonkers, L., Waniek, J.J., Schulz, M. and Kucera, M. 2019. Calcification depth of deep-dwelling planktonic foraminifera from the eastern North Atlantic constrained by stable oxygen isotope ratios of shells from stratified plankton tows. *Journal of Micropalaeontology*. **38**(2), pp.113–131.

Rebotim, A., Voelker, A.H.L., Jonkers, L., Waniek, J.J., Meggers, H., Schiebel, R., Fraile, I., Schulz, M. and Kucera, M. 2017. Factors controlling the depth habitat of planktonic foraminifera in the subtropical eastern North Atlantic. *Biogeosciences*. **14**(4), pp.827–859.

Reimer, P.J., Bard, E., Bayliss, A., Beck, J.W., Blackwell, P.G., Ramsey, C.B.,

Buck, C.E., Cheng, H., Edwards, R.L., Friedrich, M., Grootes, P.M., Guilderson, T.P., Haflidason, H., Hajdas, I., Hatté, C., Heaton, T.J., Hoffmann, D.L., Hogg, A.G., Hughen, K.A., Kaiser, K.F., Kromer, B., Manning, S.W., Niu, M., Reimer, R.W., Richards, D.A., Scott, E.M., Southon, J.R., Staff, R.A., Turney, C.S.M. and van der Plicht, J. 2013. IntCal13 and Marine13 Radiocarbon Age Calibration Curves 0–50,000 Years cal BP. *Radiocarbon*. **55**(4), pp.1869–1887.

Renaud, S. and Schmidt, D.N. 2003. Habitat tracking as a response of the planktic foraminifer Globorotalia truncatulinoides to environmental fluctuations during the last 140 kyr. *Marine Micropaleontology*. **49**(1–2), pp.97–122.

Retailleau, S., Eynaud, F., Mary, Y., Abdallah, V., Schiebel, R. and Howa, H. 2012. Canyon heads and river plumes: How might they influence neritic planktonic foraminifera communities in the se bay of biscay? *Journal of Foraminiferal Research*. **42**(3), pp.257–269.

Retailleau, S., Schiebel, R. and Howa, H. 2011. Population dynamics of living planktic foraminifers in the hemipelagic southeastern Bay of Biscay. *Marine Micropaleontology*. **80**(3–4), pp.89–100.

Reynolds, C.E., Richey, J.N., Fehrenbacher, J.S., Rosenheim, B.E. and Spero, H.J. 2018. Environmental controls on the geochemistry of Globorotalia truncatulinoides in the Gulf of Mexico: Implications for paleoceanographic reconstructions. *Marine Micropaleontology*. **142**(June), pp.92–104.

Robertson, A. and Mechoso, C. 2000. Interannual and Interdecadal Variability of the South Atlantic Convergence Zone *. *Monthly weather review*. **128**, pp.2947–2957.

Rogerson, M., Rohlin, E.J. and Weaver, P.P.E. 2006. Promotion of meridional overturning by Mediterranean-derived salt during the last deglaciation. *Paleoceanography*. **21**(4), pp.1–8.

Rogerson, M., Weaver, P.P.E., Rohling, E.J., Lourens, L.J., Murray, J.W. and Hayes, A. 2006. Colour logging as a tool in high-resolution palaeoceanography. *Geological Society Special Publication*. **267**, pp.99–112.

Rohling, E.J. 2013. Oxygen Isotope Composition of Seawater. *Encyclopedia of Quaternary Science*. **2**, pp.915–922.

Rothwell, R.G., Hoogakker, B., Thomson, J., Croudace, I.W. and Frenz, M. 2006. Turbidite emplacement on the southern Balearic Abyssal Plain (western Mediterranean Sea) during Marine Isotope Stages 1-3: An application of ITRAX XRF scanning of sediment cores to lithostratigraphic analysis. *Geological Society Special Publication*. **267**(Haschke), pp.79–98.

Rothwell, R.G. and Rack, F.R. 2006. New techniques in sediment core analysis: an introduction. *Geological Society, London, Special Publications*. **267**(1), pp.1–29.

Rovere, A., Stocchi, P. and Vacchi, M. 2016. Eustatic and Relative Sea Level Changes. *Current Climate Change Reports*. **2**(4), pp.221–231.

Rühlemann, C., Mulitza, S., Müller, P.J., Wefer, G. and Zahn, R. 1999. Warming of the tropical Atlantic Ocean and slowdown of thermohaline circulation during the last deglaciation. *Nature*. **402**(December), pp.511–514.

Sakko, A.L. 1998. The influence of the Benguela upwelling system on Namibia's marine biodiversity. *Biodiversity and Conservation*. **7**(4), pp.419–433.

Santos, T.P., Lessa, D.O., Venancio, I.M., Chiessi, C.M., Mulitza, S., Kuhnert, H., Govin, A., Machado, T., Costa, K.B., Toledo, F.A.L., Dias, B.B. and Albuquerque, A.L.S. 2017. Prolonged warming of the Brazil Current precedes deglaciations. *Earth and Planetary Science Letters*. **463**(April), pp.1–12.

Saraceno, M., Provost, C. and Piola, A.R. 2005. On the relationship between satellite-retrieved surface temperature fronts and chlorophyll a in the western South Atlantic. *Journal of Geophysical Research: Oceans*. **110**(11), pp.1–16.

Saraceno, M., Provost, C., Piola, A.R., Bava, J. and Gagliardini, A. 2004. Brazil Malvinas Frontal System as seen from 9 years of advanced very high resolution radiometer data. *Journal of Geophysical Research C: Oceans*. **109**(5).

Schiebel, R. and Hemleben, C. 2017. *Planktic Foraminifers in the Modern Ocean* [Online]. Available from: http://link.springer.com/10.1007/978-3-662-50297-6.

Schiebel, R., Smart, S.M., Jentzen, A., Jonkers, L., Morard, R., Meilland, J., Michel, E., Coxall, H.K., Hull, P.M., de Garidel-Thoron, T., Aze, T., Quillévéré, F., Ren, H., Sigman, D.M., Vonhof, H.B., Martínez-García, A., Kučera, M., Bijma, J., Spero, H.J. and Haug, G.H. 2018. Advances in planktonic foraminifer research: New perspectives for paleoceanography. *Revue de Micropaleontologie*. **61**(3–4), pp.113–138.

Schiebel, R., Waniek, J., Bork, M. and Hemleben, C. 2001. Planktic foraminiferal production stimulated by chlorophyll redistribution and entrainment of nutrients. *Deep-Sea Research Part I: Oceanographic Research Papers*. **48**(3), pp.721–740.

Schlitzer, R. and Mieruch-Schnülle, S. 2021. webODV Explore.

Schmid, C. and Garzoli, S.L. 2009. New observations of the spreading and variability of the Antarctic intermediate water in the Atlantic. *Journal of Marine Research*. **67**(6), pp.815–843.

Schmidt, D.N., Elliott, T. and Kasemann, S.A. 2008. The influences of growth rates on planktic foraminifers as proxies for palaeostudies - A review. *Geological Society Special Publication*. **303**, pp.73–85.

Schmidt, D.N., Lazarus, D., Young, J.R. and Kucera, M. 2006. Biogeography and evolution of body size in marine plankton. *Earth-Science Reviews*. **78**(3–4), pp.239–266.

Schmidt, D.N., Renaud, S. and Bollmann, J. 2003. Response of planktic foraminiferal size to late Quaternary climate change. *Paleoceanography*. **18**(2), pp.1–12.

Schmidt, D.N., Renaud, S., Bollmann, J., Schiebel, R. and Thierstein, H.R. 2004. Size distribution of Holocene planktic foraminifer assemblages: Biogeography, ecology and adaptation. *Marine Micropaleontology*. **50**(3–4), pp.319–338.

Van Sebille, E., Scussolini, P., Durgadoo, J. V., Peeters, F.J.C., Biastoch, A., Weijer, W., Turney, C., Paris, C.B. and Zahn, R. 2015. Ocean currents

generate large footprints in marine palaeoclimate proxies. *Nature Communications*. **6**(Ivm), pp.1–8.

Shakun, J.D. and Carlson, A.E. 2010. A global perspective on Last Glacial Maximum to Holocene climate change. *Quaternary Science Reviews*. **29**(15–16), pp.1801–1816.

Shepard D 1968. Two- dimensional interpolation function for irregularly- spaced data *In*: *Proc 23rd Nat Confer*., pp.517–524.

Shi, X., Yao, Z., Liu, Q., Larrasoaña, J.C., Bai, Y., Liu, Y., Liu, J., Cao, P., Li, X., Qiao, S., Wang, K., Fang, X. and Xu, T. 2016. Sedimentary architecture of the Bohai Sea China over the last 1 Ma and implications for sea-level changes. *Earth and Planetary Science Letters*. **451**, pp.10–21.

Siccha, M. and Kucera, M. 2017. Data Descriptor: ForCenS, a curated database of planktonic foraminifera census counts in marine surface sediment samples. *Scientific Data*. **4**, pp.1–12.

Silveira, I.C.A. da, Schmidt, A.C.K., Campos, E.J.D., Godoi, S.S. de and Ikeda, Y. 2000. A Corrente do Brasil ao Largo da Costa Leste Brasileira (The Brazil Current off the Eastern Brazilian Coast). *Revista Brasileira de Oceanografia*. **48**(2), pp.171–183.

Simpson, E.H. 1949. Measurement of diversity. *Nature*. **163**(1943), p.688.

Solomon, S., Dahe, Q. and Manning, M. 2007. *Climate Change 2007: impacts, adaptation and vulnerability: contribution of Working Group II to the fourth assessment report of the Intergovernmental Panel* [Online]. Available from: http://books.google.com/books?hl=en&lr=&id=TNo-SeGpn7wC&oi=fnd&pg=PA81&dq=Climate+Change+2007:+Impacts,+Adaptation+and+Vulnerability.+Contribution+of+Working+Group+II+to+the+Fourth+Assessment+Report+of+the+Intergovernmental+Panel+on+Climate+Change&ots=vP2.

Soto, M., Morales, E., Veroslavsky, G., de Santa Ana, H., Ucha, N. and Rodríguez, P. 2011. The continental margin of uruguay: Crustal architecture and segmentation. *Marine and Petroleum Geology*. **28**(9), pp.1676–1689.

Stanford, J.D., Hemingway, R., Rohling, E.J., Challenor, P.G., Medina-Elizalde, M. and Lester, A.J. 2011. Sea-level probability for the last deglaciation: A statistical analysis of far-field records. *Global and Planetary Change*. **79**(3–4), pp.193–203.

Stoakes, F.A., Campbell, C. V., Cass, R. and Ucha, N. 1991. Seismic Stratigraphic Analysis of the Punta del Este Basin, Offshore Uruguay, South America. *American Association of Petroleum Geologists Bulletin*. **75**(2), pp.219–240.

Storz, D., Schulz, H., Waniek, J.J., Schulz-Bull, D.E. and Kučera, M. 2009. Seasonal and interannual variability of the planktic foraminiferal flux in the vicinity of the Azores Current. *Deep-Sea Research Part I: Oceanographic Research Papers*. **56**(1), pp.107–124.

Stramma, L. and England, M. 1999. On the water masses and mean circulation of the South Atlantic Ocean. *Journal of Geophysical Research: Oceans*. **104**(C9), 20,863-30,883.

Stríkis, N.M., Cruz, F.W., Cheng, H., Karmann, I., Edwards, R.L., Vuille, M.,

Wang, X., de Paula, M.S., Novello, V.F. and Auler, A.S. 2011. Abrupt variations in South American monsoon rainfall during the Holocene based on a speleothem record from central-eastern Brazil. *Geology*. **39**(11), pp.1075–1078.

Sylvester, F. 2009. Past Climate Variability in South America and Surrounding Regions *In*: F. Vimeux, F. Sylvestre and M. Khodri, eds. *Developments in Paleoenvironmental Research* [Online]. Developments in Paleoenvironmental Research. Dordrecht: Springer Netherlands, pp.1–418. Available from: http://link.springer.com/10.1007/978-90-481-2672-9.

Takahashi, K. and Be, A.W.H. 1984. Planktonic foraminifera: factors controlling sinking speeds. *Deep Sea Research Part A. Oceanographic Research Papers*. **31**(12), pp.1477–1500.

Thompson, D.W.J. and Solomon, S. 2002. Interpretation of recent Southern Hemisphere climate change. *Science*. **296**(5569), pp.895–899.

Thomson, J., Croudace, I.W. and Rothwell, R.G. 2006. A geochemical application of the ITRAX scanner to a sediment core containing eastern Mediterranean sapropel units. *Geological Society Special Publication*. **267**, pp.65–77.

Toledo, F.A.L. 2008. Tracing past circulation changes in the western South Atlantic based on planktonic foraminifera. *Revista Brasileira de Paleontologia*. **11**(3), pp.169–178.

Ujiié, Y. and Asami, T. 2014. Temperature is not responsible for left-right reversal in pelagic unicellular zooplanktons. *Journal of Zoology*. **293**(1), pp.16–24.

Ujiié, Y., de Garidel-Thoron, T., Watanabe, S., Wiebe, P. and de Vargas, C. 2010. Coiling dimorphism within a genetic type of the planktonic foraminifer Globorotalia truncatulinoides. *Marine Micropaleontology*. **77**(3–4), pp.145–153.

de Vargas, C., Renaud, S., Hilbrecht, H. and Pawlowski, J. 2001. Pleistocene adaptive radiation in Globorotalia truncatulinoides : genetic, morphologic, and environmental evidence . *Paleobiology*. **27**(1), pp.104–125.

Varma, V., Prange, M., Merkel, U., Kleinen, T., Lohmann, G., Pfeiffer, M., Renssen, H., Wagner, A., Wagner, S. and Schulz, M. 2012. Holocene evolution of the Southern Hemisphere westerly winds in transient simulations with global climate models. *Climate of the Past*. **8**(2), pp.391–402.

Vera, C., Higgins, W., Amador, J., Ambrizzi, T., Garreaud, R., Gochis, D., Gutzler, D., Lettenmaier, D., Marengo, J., Mechoso, C.R., Nogues-Paegle, J., Silva Dias, P.L. and Zhang, C. 2006. Toward a unified view of the American monsoon systems. *Journal of Climate*. **19**(20), pp.4977–5000.

Viana, A.R. 2002. Seismic expression of shallow- to deep-water contourites along the south-eastern Brazilian margin. *Marine Geophysical Researches*. **22**(5–6), pp.509–521.

Viana, A.R. and Faugères, J.-C. 1998. Upper slope sand deposits: the example of Campos Basin, a latest Pleistocene-Holocene record of the interaction between alongslope and downslope currents. *Geological Society, London, Special Publications*. **129**(1), pp.287–316.

Viana, A.R., Hercos, C.M., De Almeida, W., Magalhaes, J.L. and De Andrade, S.B. 2002. Evidence of bottom current influence on the Neogene to Quaternary sedimentation along the northern Campos Slope, SW Atlantic Margin. *Geological Society, London, Memoirs*. **22**(1), pp.249–259.

Viana, A.R., Jr, W.D.E.A. and Almeida, C.W.D.E. 2002. Upper slope sands : late Quaternary shallow-water sandy contourites of Campos Basin , SW Atlantic Margin. *Atlantic*., pp.261–270.

Villela, R.J. 2017. The south Atlantic convergence zone: A critical view and overview. *Revista do Instituto Geologico*. **38**(2), pp.1–19.

Voigt, I., Chiessi, C.M., Prange, M., Mulitza, S., Groeneveld, J., Varma, V. and Henrich, R. 2015. Holocene shifts of the southern westerlies across the South Atlantic. *Paleoceanography*. **30**(2), pp.39–51.

Voigt, I., Henrich, R., Preu, B., Piola, A.R., Hanebuth, T., Schwenk, T. and Chiessi, C.M. 2013. A submarine canyon as a climate archive - Interaction of the antarctic intermediate water with the mar del plata canyon (southwest atlantic). *Marine Geology*. **341**, pp.46–57.

Vuille, M., Burns, S.J., Taylor, B.L., Cruz, F.W., Bird, B.W., Abbott, M.B., Kanner, L.C., Cheng, H. and Novello, V.F. 2012. A review of the South American monsoon history as recorded in stable isotopic proxies over the past two millennia. *Climate of the Past*. **8**(4), pp.1309–1321.

Wade, B.S., Olsson, R.K., Pearson, P.N., Huber, B.T. and Berggren, W.A. 2018. *Atlas of Oligocene Planktonic Foraminifera* (B. S. Wade, R. K. Olsson, P. N. Pearson, B. T. Huber, & W. A. Berggren, eds.). Cushman Foundation for Foraminiferal Research.

Wainer, I., Gent, P. and Goni, G. 2000. Annual cycle of the Brazil-Malvinas confluence region in the National Center for Atmospheric Research Climate System Model Maximun vector is 35. *Journal of Geophysical Research*. **105**(1999), 26,167-26,177.

Wainer, I. and Venegas, S.A. 2002. South Atlantic multidecadal variability in the climate system model. *Journal of Climate*. **15**(12), pp.1408–1420.

Wanner, H., Beer, J., Bütikofer, J., Crowley, T.J., Cubasch, U., Flückiger, J., Goosse, H., Grosjean, M., Joos, F., Kaplan, J.O., Küttel, M., Müller, S.A., Prentice, I.C., Solomina, O., Stocker, T.F., Tarasov, P., Wagner, M. and Widmann, M. 2008. Mid- to Late Holocene climate change: an overview. *Quaternary Science Reviews*. **27**(19–20), pp.1791–1828.

Wanner, H., Wanner, H., Mercolli, L., Mercolli, L., Grosjean, M., Grosjean, M. and Ritz, S.P. 2015. Holocene climate variability and change; a data-based review. *Journal of the Geological Society*. **172**(2), pp.254–263.

Warratz, G., Henrich, R., Voigt, I., Chiessi, C.M., Kuhn, G. and Lantzsch, H. 2017. Deglacial changes in the strength of deep southern component water and sediment supply at the Argentine continental margin. *Paleoceanography*., pp.796–812.

Weltje, G.J. and Tjallingii, R. 2008. Calibration of XRF core scanners for quantitative geochemical logging of sediment cores: Theory and application3. *Earth and Planetary Science Letters*. **274**(3–4), pp.423–438.

Wilke, I., Meggers, H. and Bickert, T. 2009. Depth habitats and seasonal distributions of recent planktic foraminifers in the Canary Islands region

(29°N) based on oxygen isotopes. *Deep-Sea Research Part I: Oceanographic Research Papers*. **56**(1), pp.89–106.

Woodhouse, A., Jackson, S.L., Jamieson, R.A., Newton, R.J., Sexton, P.F. and Aze, T. 2021. Adaptive ecological niche migration does not negate extinction susceptibility. *Scientific Reports*. (June).

Wycech, J.B., Kelly, D.C., Kozdon, R., Orland, I.J., Spero, H.J. and Valley, J.W. 2018. Comparison of δ18O analyses on individual planktic foraminifer (Orbulina universa) shells by SIMS and gas-source mass spectrometry. *Chemical Geology*. **483**(February), pp.119–130.

Zhou, J. and Lau, K.M. 1998. Does a monsoon climate exist over South America? *Journal of Climate*. **11**(5), pp.1020–1040.

Ziegler, M., Jilbert, T., De Lange, G.J., Lourens, L.J. and Reichart, G.J. 2008. Bromine counts from XRF scanning as an estimate of the marine organic carbon content of sediment cores. *Geochemistry, Geophysics, Geosystems*. **9**(5), pp.1–6.

van der Zwaan, G.J., Jorissen, F.J. and de Stigter, H.C. 1990. The depth dependency of planktonic/benthic foraminiferal ratios: Constraints and applications. *Marine Geology*. **95**(1), pp.1–16.

Zweng, M.M., Reagan, J.R., Seidov, D., Boyer, T.P., Antonov, J.I., Locarnini, R.A., Garcia, H.E., Mishonov, A. V., Baranova, O.K., Weathers, K.W., Paver, C.R. and Smolyar, I. V. 2019. World Ocean Atlas 2018 Volume 2: Salinity. *NOAA Atlas NESDIS*. **82**(July), p.50pp.

Appendices

Appendix A

A.1 Core top sample list

A.2 Downcore sample list

Appendix B

B.1 Core top assemblage counts

B.2 Downcore assemblage counts

Appendix C

C.1 Core top stable isotopes

C.2 Downcore stable isotopes

Appendix D

D.1 Acquired Radiocarbon dates

D.2 Interpolated Radiocarbon dates

Appendix E

E.1 K-means analysis R script

Appendix F

F.1 UPC 023 ITRAX data

F.2 UPC 028 ITRAX data

F.3 UPC 122 ITRAX data

Appendix G

G.1 *Gs. ruber Pink* interpolated assemblage

G.2 *Gs. ruber White* interpolated assemblage

G.3 *Gr. hirsuta Pink* interpolated assemblage

G.4 *O. universa* interpolated assemblage

G.5 *T. sacculifer* interpolated assemblage

G.6 *Gc. inflata* interpolated assemblage

G.7 *Gg. bulloides* interpolated assemblage

G.8 *Gt. glutinata* interpolated assemblage

G.9 *N. incompta* interpolated assemblage

G.10 *N. pachyderma* interpolated assemblage

Appendix H

H.1 Core photos. Sections one to six

Appendix I

I.1-7 SEM plates

For raw data see:
Mair_AM_Earth_And_Environment_PhD_2022_Summary_Appendices.xls

Core top samples																		
Sample Number	Core number	Section number	Sample interval	Water depth	Latitude	Longitude	Recovery	Total sections	Wet Weight (g)	Dry Weight (g)	Date received	Split counted	Weight *Split	Total foram numbers	Forams /gram	Assemblage counts	Stable Isotopes	C14 dating
1	UPC 125	1	Core top	-1121.22	-36.848	-53.633	4.22	5	14.12	4.54	29/03/2018	1/2	2.27	852	375.33	Yes	No	No
2	UPC 001	1	Core top	-2053.05	-36.924	-53.4084	5.3	6	20.5	1.27	17/09/2018	1	1.27	1031	811.81	Yes	Yes	No
3	UPC 102	1	Core top	-2933.09	-37.122	-53.0946	0.6	1	27.52	5.45	17/09/2018	Barren	2.73	5	1.83	N/A	N/A	No
4	UPC 081	1	Core top	-1895.64	-36.833	-53.3178	5.52	6	30.58	0.64	29/03/2018	1/2	0.32	1574	4918.75	Yes	Yes	No
5	UPC 003	1	Core top	-2205.15	-36.869	-53.2626	1.18	1	36.5	3.27	17/09/2018	Barren	3.27	75	22.94	N/A	N/A	No
6	UPC 155	1	Core top	-2557.21	-36.931	-53.158	4.86	6	26.07	2.92	17/09/2018	1/2	1.46	569	389.73	Yes	No	No
7	UPC 153	1	Core top	-3046.37	-37.021	-53.0067	5.09	6	33.6	5.3	17/09/2018	1/4	1.33	623	470.19	Yes	No	No
8	UPC 124	1	Core top	-1710.71	-36.633	-53.4146	5.25	6	33.2	7.48	29/03/2018	1/4	1.87	1746	933.69	Yes	No	No
9	UPC 058	1	Core top	-2255.28	-36.725	-53.2086	5.36	6	27.67	0.24	29/03/2018	1/2	0.12	945	7875.00	Yes	Yes	No
10	UPC 091	1	Core top	-2644.1	-36.879	-53.0244	5.72	6	30.31	3.21	17/09/2018	1/8	0.40	520	1295.95	Yes	No	No
11	UPC 035	1	Core top	-3026.75	-36.917	-52.9112	2.23	4	28.28	0.94	29/03/2018	Barren	0.47	0	0.00	N/A	N/A	No
12	UPC 143	1	Core top	-1356.17	-36.599	-53.237	5.27	6	34	3.64	29/03/2018	1/4	0.91	1214	1334.07	Yes	No	No
13	UPC 142	1	Core top	-2682.11	-36.764	-52.9812	5.64	6	32.82	5.42	17/09/2018	1/4	1.36	584	431.00	Yes	Yes	No
14	UPC 141	1	Core top	-2431.08	-36.702	-53.039	4.96	6	38.2	4.97	17/09/2018	1/2	2.49	852	342.86	Yes	Yes	No
15	UPC 063	1	Core top	-1255	-36.54	-53.1697	5.4	3	32.36	7.52	29/03/2018	1/8	0.94	679	722.34	Yes	Yes	No
16	UPC 066	1	Core top	-1257	-36.549	-53.1781	4.66	6	29.57	7.14	29/03/2018	1/8	0.89	717	803.36	Yes	Yes	No
17	UPC 122	1	Core top	-1154.19	-36.504	-53.211	4.25	5	39.37	9.23	29/03/2018	1/8	1.15	946	819.93	Yes	Yes	No
18	UPC 123	1	Core top	-1194.3	-36.456	-53.1629	5.75	6	22.57	4.56	29/03/2018	1/8	0.57	734	1287.72	Yes	No	No
19	UPC 053	1	Core top	-2115.24	-36.539	-53.0234	5.63	6	31.65	0.79	29/03/2018	1	0.79	978	1237.97	Yes	Yes	No
20	UPC 032	1	Core top	-2513.29	-36.619	-52.9211	5.6	6	21.97	2.73	17/09/2018	1	2.73	842	308.42	Yes	No	No
21	UPC 161	1	Core top	-1241.64	-36.42	-53.1285	5.35	6	37.72	9.19	17/09/2018	1/16	0.57	679	1182.15	Yes	No	No
22	UPC 033	1	Core top	-2582.33	-36.597	-52.8997	5.3	6	28.15	0.79	29/03/2018	1/4	0.20	529	2678.48	Yes	Yes	No
23	UPC 145	1	Core top	-1595.39	-36.494	-52.9822	5.43	6	35.49	3.39	29/03/2018	1/8	0.42	596	1406.49	Yes	Yes	No
24	UPC 022	1	Core top	-2027.53	-36.461	-52.8823	5.74	6	33.69	2.95	17/09/2018	1/2	1.48	860	583.05	Yes	Yes	No
25	UPC 013	1	Core top	-1574.92	-36.332	-53.0063	4.26	5	29.72	4.09	17/09/2018	1/4	1.02	834	815.65	Yes	No	No
26	UPC 139	1	Core top	-2499	-36.529	-52.7062	4.08	5	35.21	5.96	17/09/2018	1/4	1.49	712	477.85	Yes	No	No
27	UPC 023	1	Core top	-2046.34	-36.394	-52.8172	5.28	6	30.77	1.07	29/03/2018	1/4	0.27	785	2934.58	Yes	Yes	No
28	UPC 024	1	Core top	-2252.95	-36.326	-52.7493	5.16	6	28.14	5.04	17/09/2018	1/2	2.52	584	231.75	Yes	No	No
29	UPC 093	1	Core top	-2572.48	-36.322	-52.5819	5.6	6	35.25	4.16	17/09/2018	1/4	1.04	638	613.46	Yes	Yes	No
30	UPC 134	1	Core top	-2731	-36.407	-52.4773	5.66	6	39.05	4.61	17/09/2018	1	4.61	630	136.66	Yes	No	No
31	UPC 025	1	Core top	-2445.71	-36.223	-52.5319	5.2	6	32.2	3.37	17/09/2018	1/4	0.84	362	429.67	Yes	No	No
32	UPC 176	1	Core top	-2351	-36.175	-52.5402	4.83	6	37.36	4.6	17/09/2018	1/2	2.30	529	230.00	Yes	No	No
33	UPC 170	1	Core top	-2535	-36.232	-52.4126	4.45	5	33.35	4.51	17/09/2018	1/8	0.56	427	757.43	Yes	No	No
34	UPC 180	1	Core top	-2433	-36.192	-52.4345	5.53	6	28.71	3.82	17/09/2018	1/2	1.91	362	189.53	Yes	No	No
35	UPC 028	1	Core top	-2353	-36.151	-52.4627	3.48	6	27.84	0.57	29/03/2018	1/2	0.29	551	1933.33	Yes	Yes	No

Downcore samples																		
Sample Number	Core number	Section number	Sample interval	Water depth	Latitude	Longitude	Recovery	Total sections	Wet Weight (g)	Dry Weight (g)	Date received	Split counted	Weight *Split	Total foram numbers	Forams /gram	Assemblage counts	Stable Isotopes	C14 dating
36	UPC 028	2	27-29cm	-2353	-36.151	-52.4627	3.48	6	16.76	0.70	17/09/2018	1/2	0.35	738	2108.57	Yes	No	No
37	UPC 028	2	34-36cm	-2353	-36.151	-52.4627	3.48	6	14.87	1.23	17/09/2018	1/4	0.31	325	1056.91	Yes	No	No
38	UPC 028	2	41-43cm	-2353	-36.151	-52.4627	3.48	6	15.40	1.15	17/09/2018	1/2	0.58	363	631.30	Yes	Yes	No
39	UPC 028	2	48-50cm	-2353	-36.151	-52.4627	3.48	6	18.38	0.58	17/09/2018	1/4	0.15	339	2337.93	Yes	No	No
40	UPC 028	2	55-57cm	-2353	-36.151	-52.4627	3.48	6	15.39	1.43	17/09/2018	1/2	0.72	534	746.85	Yes	No	No
41	UPC 028	2	62-64cm	-2353	-36.151	-52.4627	3.48	6	16.20	1.00	17/09/2018	1/2	0.50	400	800.00	Yes	No	No
42	UPC 028	2	69-71cm	-2353	-36.151	-52.4627	3.48	6	18.71	1.65	17/09/2018	1/2	0.83	555	672.73	Yes	No	No
43	UPC 028	2	76-78cm	-2353	-36.151	-52.4627	3.48	6	15.61	0.74	17/09/2018	1/2	0.37	407	1100.00	Yes	No	No
44	UPC 028	2	83-85cm	-2353	-36.151	-52.4627	3.48	6	14.96	1.04	17/09/2018	1/2	0.52	355	682.69	Yes	Yes	No
45	UPC 028	2	90-92cm	-2353	-36.151	-52.4627	3.48	6	14.18	1.20	17/09/2018	1/2	0.60	363	605.00	Yes	No	No
46	UPC 028	2	97-99cm	-2353	-36.151	-52.4627	3.48	6	13.42	0.70	17/09/2018	1/2	0.35	336	960.00	Yes	No	Yes
47	UPC 028	2	104-106cm	-2353	-36.151	-52.4627	3.48	6	14.61	1.18	17/09/2018	1/2	0.59	431	730.51	Yes	No	No
48	UPC 028	2	111-113cm	-2353	-36.151	-52.4627	3.48	6	17.53	0.97	17/09/2018	1/2	0.48	482	993.81	Yes	No	No
49	UPC 028	2	118-120cm	-2353	-36.151	-52.4627	3.48	6	19.99	1.75	17/09/2018	1/4	0.44	392	896.00	Yes	Yes	No
50	UPC 028	3	120-122cm	-2353	-36.151	-52.4627	3.48	6	11.11	0.92	17/09/2018	1/2	0.46	387	841.30	Yes	No	No
51	UPC 028	3	127-129cm	-2353	-36.151	-52.4627	3.48	6	14.65	1.22	17/09/2018	1/2	0.61	355	581.97	Yes	No	No
52	UPC 028	3	134-136cm	-2353	-36.151	-52.4627	3.48	6	16.41	0.75	17/09/2018	1/2	0.38	438	1168.00	Yes	No	No
53	UPC 028	3	141-143cm	-2353	-36.151	-52.4627	3.48	6	16.74	0.61	17/09/2018	1/2	0.31	495	1622.95	Yes	No	No
54	UPC 028	3	148-150cm	-2353	-36.151	-52.4627	3.48	6	18.41	1.45	17/09/2018	1/2	0.72	544	750.34	Yes	Yes	No
55	UPC 028	3	155-157cm	-2353	-36.151	-52.4627	3.48	6	21.29	1.24	17/09/2018	1/4	0.31	533	1719.35	Yes	No	No
56	UPC 028	3	162-164cm	-2353	-36.151	-52.4627	3.48	6	22.10	1.25	17/09/2018	1/4	0.31	530	1696.00	Yes	No	No
57	UPC 028	3	169-171cm	-2353	-36.151	-52.4627	3.48	6	18.38	0.70	17/09/2018	1/4	0.18	466	2662.86	Yes	No	No
58	UPC 028	3	176-178cm	-2353	-36.151	-52.4627	3.48	6	17.86	1.01	17/09/2018	1/2	0.50	945	1871.29	Yes	Yes	No
59	UPC 028	3	183-185cm	-2353	-36.151	-52.4627	3.48	6	17.92	1.11	17/09/2018	1/4	0.28	622	2241.44	Yes	No	No
60	UPC 028	3	190-192cm	-2353	-36.151	-52.4627	3.48	6	21.42	1.67	17/09/2018	1/8	0.21	328	1571.26	Yes	No	No
61	UPC 028	3	197-199cm	-2353	-36.151	-52.4627	3.48	6	24.59	1.40	17/09/2018	1/4	0.35	676	1931.43	Yes	No	Yes
62	UPC 028	4	240-242cm	-2353	-36.151	-52.4627	3.48	6	16.92	0.93	17/09/2018	1/4	0.23	484	2081.72	Yes	No	No
63	UPC 028	4	247-249cm	-2353	-36.151	-52.4627	3.48	6	21.91	1.94	17/09/2018	1/4	0.48	616	1270.10	Yes	No	No
64	UPC 028	4	254-256cm	-2353	-36.151	-52.4627	3.48	6	15.12	0.57	17/09/2018	1/4	0.14	428	3003.51	Yes	Yes	No
65	UPC 028	4	261-263cm	-2353	-36.151	-52.4627	3.48	6	15.41	0.71	17/09/2018	1/4	0.18	432	2433.80	Yes	No	No
66	UPC 028	4	268-270cm	-2353	-36.151	-52.4627	3.48	6	17.81	0.69	17/09/2018	1/4	0.17	699	4052.17	Yes	No	No
67	UPC 028	4	275-277cm	-2353	-36.151	-52.4627	3.48	6	18.07	0.77	17/09/2018	1/4	0.19	485	2519.48	Yes	No	No
68	UPC 028	4	282-284cm	-2353	-36.151	-52.4627	3.48	6	21.82	0.92	17/09/2018	1/4	0.23	734	3191.30	Yes	Yes	No
69	UPC 028	4	289-291cm	-2353	-36.151	-52.4627	3.48	6	22.36	1.48	17/09/2018	1/8	0.19	337	1821.62	Yes	No	No

Downcore samples continued

Sample Number	Core number	Section number	Sample interval	Water depth	Latitude	Longitude	Recovery	Total sections	Wet Weight (g)	Dry Weight (g)	Date received	Split counted	Weight *Split	Total foram numbers	Forams /gram	Assemblage counts	Stable Isotopes	C14 dating
70	UPC 028	4	296-298cm	-2353	-36.151	-52.4627	3.48	6	16.74	1.03	17/09/2018	1/4	0.26	708	2749.51	Yes	No	No
71	UPC 028	4	303-305cm	-2353	-36.151	-52.4627	3.48	6	16.86	0.97	17/09/2018	1/4	0.24	592	2441.24	Yes	Yes	No
72	UPC 028	4	310-312cm	-2353	-36.151	-52.4627	3.48	6	16.70	1.24	17/09/2018	1/2	0.62	509	820.97	Yes	No	Yes
73	UPC 028	4	317-319cm	-2353	-36.151	-52.4627	3.48	6	16.28	1.15	17/09/2018	1/4	0.29	402	1398.26	Yes	No	No
74	UPC 028	4	324-326cm	-2353	-36.151	-52.4627	3.48	6	17.99	1.06	17/09/2018	1/4	0.27	524	1977.36	Yes	Yes	No
75	UPC 028	4	331-333cm	-2353	-36.151	-52.4627	3.48	6	18.69	1.19	17/09/2018	1/4	0.30	505	1697.48	Yes	No	No
76	UPC 028	4	338-340cm	-2353	-36.151	-52.4627	3.48	6	19.94	1.05	17/09/2018	1/8	0.13	296	2255.24	Yes	No	No
77	UPC 028	5	340-342cm	-2353	-36.151	-52.4627	3.48	6	15.77	0.94	17/09/2018	1/4	0.23	389	1655.32	Yes	No	No
78	UPC 028	5	347-349cm	-2353	-36.151	-52.4627	3.48	6	17.89	0.93	17/09/2018	1/4	0.23	383	1647.31	Yes	Yes	No
79	UPC 028	5	354-356cm	-2353	-36.151	-52.4627	3.48	6	15.49	0.83	17/09/2018	1/4	0.21	391	1884.34	Yes	No	No
80	UPC 028	5	361-363cm	-2353	-36.151	-52.4627	3.48	6	17.11	1.32	17/09/2018	1/4	0.33	407	1233.33	Yes	Yes	No
81	UPC 028	5	368-370cm	-2353	-36.151	-52.4627	3.48	6	19.85	0.91	17/09/2018	1/4	0.23	495	2175.82	Yes	No	No
82	UPC 028	5	375-377cm	-2353	-36.151	-52.4627	3.48	6	15.52	0.55	17/09/2018	1/4	0.14	593	4312.73	Yes	No	No
83	UPC 028	5	382-384cm	-2353	-36.151	-52.4627	3.48	6	17.69	0.80	17/09/2018	1/8	0.10	384	3840.00	Yes	Yes	No
84	UPC 028	5	389-391cm	-2353	-36.151	-52.4627	3.48	6	19.28	0.80	17/09/2018	1/4	0.20	754	3770.00	Yes	No	No
85	UPC 028	5	396-398cm	-2353	-36.151	-52.4627	3.48	6	16.71	0.92	17/09/2018	1/4	0.23	641	2786.96	Yes	Yes	No
86	UPC 028	6	400-402cm	-2353	-36.151	-52.4627	3.48	6	17.68	1.12	17/09/2018	1/4	0.28	352	1257.14	Yes	No	Yes
87	UPC 028	6	407-409cm	-2353	-36.151	-52.4627	3.48	6	14.39	0.50	17/09/2018	1/8	0.06	503	8048.00	Yes	No	No
88	UPC 028	6	412-415cm	-2353	-36.151	-52.4627	3.48	6	13.85	0.51	17/09/2018	1/4	0.13	511	4007.84	Yes	No	No
89	UPC 028	6	417-419cm	-2353	-36.151	-52.4627	3.48	6	12.41	0.38	17/09/2018	1/4	0.10	530	5578.95	Yes	No	No
90	UPC 028	6	422-424cm	-2353	-36.151	-52.4627	3.48	6	10.60	0.67	17/09/2018	1/4	0.17	537	3205.97	Yes	Yes	No
91	UPC 028	6	427-429cm	-2353	-36.151	-52.4627	3.48	6	14.50	0.68	17/09/2018	1/4	0.17	715	4205.88	Yes	No	No
92	UPC 028	6	432-434cm	-2353	-36.151	-52.4627	3.48	6	15.89	0.99	17/09/2018	1/4	0.25	791	3195.96	Yes	No	No
93	UPC 028	6	437-439cm	-2353	-36.151	-52.4627	3.48	6	14.50	0.91	17/09/2018	1/8	0.11	366	3217.58	Yes	No	No
94	UPC 028	6	442-444cm	-2353	-36.151	-52.4627	3.48	6	13.35	0.64	17/09/2018	1/4	0.16	448	2800.00	Yes	No	No
95	UPC 028	6	447-449cm	-2353	-36.151	-52.4627	3.48	6	19.48	1.15	17/09/2018	1/8	0.14	387	2692.17	Yes	Yes	No
96	UPC 028	6	452-454cm	-2353	-36.151	-52.4627	3.48	6	16.70	0.45	17/09/2018	1/4	0.11	703	6248.89	Yes	No	No
97	UPC 028	6	457-459cm	-2353	-36.151	-52.4627	3.48	6	16.50	0.78	17/09/2018	1/4	0.20	633	3246.15	Yes	No	No
98	UPC 028	6	462-464cm	-2353	-36.151	-52.4627	3.48	6	16.92	0.76	17/09/2018	1/8	0.09	501	5273.68	Yes	No	No
99	UPC 028	6	467-469cm	-2353	-36.151	-52.4627	3.48	6	16.29	0.72	17/09/2018	1/8	0.09	422	4688.89	Yes	Yes	No
100	UPC 028	6	472-474cm	-2353	-36.151	-52.4627	3.48	6	14.25	0.99	17/09/2018	1/4	0.25	503	2032.32	Yes	No	No
101	UPC 028	6	477-479cm	-2353	-36.151	-52.4627	3.48	6	20.16	1.05	17/09/2018	1/4	0.26	900	3428.57	Yes	No	No
102	UPC 028	6	482-484cm	-2353	-36.151	-52.4627	3.48	6	15.80	0.96	17/09/2018	1/4	0.24	710	2958.33	Yes	Yes	No
103	UPC 028	6	487-489cm	-2353	-36.151	-52.4627	3.48	6	18.17	1.88	17/09/2018	1/4	0.47	482	1025.53	Yes	No	Yes

Appendix B.1 Core top assemblage counts

Core number	*Gs. ruber (p)*	*T. sacculifer*	*Gr. tumida*	*Gr. crassaformis*	*Gr. menardii*	*Gs. ruber (w)*	*Ge. siphonifera*	*O. universa*	*Gs. conglobatus*	*G. falconensis*	*Ge. calida*	*N. dutertrei*	*Gr. hirsuta*	*Tn. parkerae*	*Gtr. rubescens*	*Tb. clarkei*	*Gt. minuta*	*C. nitida*	*Gc. inflata*	*Gt. glutinata*	*Gy. bulloides*	*Gr. scitula*	*Gr. truncatulinoides*	*N. incompta*	*Tb. quinqueloba*	*N. pachyderma*	Number of PF	Number of BF	Total foram	If barren	Tropical (%)	Sub-tropical (%)	Warm groupings (%)	Transitional (%)	Cold groupings (%)	Sub-polar (%)	Polar (%)
UPC 125	0	3	0	6	0	2	0	0	0	0	0	0	0	0	0	0	0	0	63	44	7	6	6	38	5	146	326	526	852	NO	2.76	0.61	3.37	38.65	57.98	13.19	44.79
UPC 001	2	4	7	2	0	13	4	5	0	0	0	10	1	7	2	0	0	0	82	97	30	5	12	95	17	84	479	552	1031	NO	3.13	8.77	11.90	47.18	40.92	23.38	17.54
UPC 102	0	0	0	0	0	0	0	0	0	0	0	0	0	0	0	0	0	0	0	1	0	0	0	0	0	2	3	2	5	YES	0.00	0.00	0.00	33.33	66.67	0.00	66.67
UPC 081	3	3	7	0	0	16	0	1	3	3	0	5	22	2	0	0	0	0	343	52	74	3	54	59	14	176	840	734	1574	NO	1.55	6.19	7.74	62.62	29.64	8.69	20.95
UPC 003	0	0	0	0	0	0	0	0	0	0	0	1	6	0	0	0	0	0	22	1	0	0	0	0	0	1	31	44	75	YES	0.00	22.58	22.58	74.19	3.23	0.00	3.23
UPC 155	2	4	3	3	0	21	1	1	1	2	0	2	6	0	0	0	0	0	62	45	23	2	13	38	7	35	271	298	569	NO	4.43	12.55	16.97	53.51	29.52	16.61	12.92
UPC 153	2	4	5	0	0	18	0	0	0	0	0	1	13	0	2	0	0	0	147	47	18	4	21	20	7	53	362	261	623	NO	3.04	9.39	12.43	65.47	22.10	7.46	14.64
UPC 124	0	0	1	14	0	0	0	0	0	0	0	0	0	0	0	0	0	0	375	16	10	4	6	10	3	52	491	1255	1746	NO	3.05	0.00	3.05	83.71	13.24	2.65	10.59
UPC 058	1	4	2	0	0	7	0	0	0	0	0	1	2	4	1	0	0	0	76	61	38	9	14	57	17	78	372	573	945	NO	1.88	4.03	5.91	53.23	40.86	19.89	20.97
UPC 091	1	3	1	2	0	26	1	5	3	4	0	7	11	5	5	0	0	0	84	46	49	4	13	47	9	69	395	125	520	NO	1.77	16.96	18.73	49.62	31.65	14.18	17.47
UPC 035	0	0	0	0	0	0	0	0	0	0	0	0	0	0	0	0	0	0	0	0	0	0	0	0	0	0	0	0	0	YES	0.00	0.00	0.00	0.00	0.00	0.00	0.00
UPC 143	0	2	3	12	0	4	1	1	0	0	0	0	0	0	0	0	0	0	145	55	16	7	16	40	4	152	456	758	1214	NO	3.73	1.32	5.04	51.97	42.98	9.65	33.33
UPC 142	2	4	1	3	0	15	0	0	0	0	0	3	5	1	1	0	0	0	102	79	27	5	20	70	19	77	434	150	584	NO	2.30	5.76	8.06	53.69	38.25	20.51	17.74
UPC 141	2	7	3	2	0	16	0	5	3	0	0	3	8	0	0	0	0	0	188	73	11	2	8	23	7	54	415	437	852	NO	3.37	8.43	11.81	67.95	20.24	7.23	13.01
UPC 063	0	1	1	1	0	2	1	0	0	3	0	4	10	0	0	0	0	0	131	29	13	0	16	30	1	144	387	292	679	NO	0.78	5.17	5.94	48.84	45.22	8.01	37.21
UPC 066	1	1	3	0	0	6	1	0	0	0	0	1	6	0	0	0	0	0	159	31	13	0	26	23	2	101	374	343	717	NO	1.34	3.74	5.08	61.23	33.69	6.68	27.01
UPC 122	1	0	2	12	0	9	0	0	0	0	0	3	9	1	0	0	0	0	169	30	15	4	19	37	3	172	473	473	946	NO	3.17	1.90	5.07	50.11	44.82	8.46	36.36
UPC 123	0	3	3	11	0	3	0	1	0	0	0	0	10	3	1	0	0	0	136	37	18	0	20	26	12	99	383	351	734	NO	4.44	4.70	9.14	55.09	35.77	9.92	25.85
UPC 053	2	5	6	3	0	33	3	0	1	4	0	5	10	3	1	0	0	0	115	66	47	5	14	55	10	69	457	521	978	NO	3.50	13.13	16.63	54.05	29.32	14.22	15.10
UPC 032	3	4	7	4	0	22	1	2	2	8	0	2	18	2	0	0	0	0	167	56	47	2	21	28	16	69	481	361	842	NO	3.74	11.85	15.59	60.91	23.49	9.15	14.35
UPC 161	0	2	10	6	0	4	0	3	0	0	0	1	5	0	0	0	0	0	142	62	18	4	17	45	13	142	474	205	679	NO	3.80	2.74	6.54	51.27	42.19	12.24	29.96
UPC 033	3	4	3	0	0	27	1	2	2	2	0	6	13	3	0	0	0	0	79	54	40	2	14	42	14	59	370	159	529	NO	2.70	15.14	17.84	51.08	31.08	15.14	15.95
UPC 145	0	1	2	0	0	6	0	0	1	0	0	0	8	0	1	0	0	0	116	26	8	1	26	11	9	55	271	325	596	NO	1.11	5.90	7.01	65.31	27.68	7.38	20.30
UPC 022	0	7	6	0	1	16	1	0	1	6	0	9	10	4	0	1	0	0	124	32	48	5	15	56	14	75	431	429	860	NO	3.25	11.14	14.39	51.97	33.64	16.24	17.40
UPC 013	2	1	9	2	0	6	0	0	0	0	0	1	7	0	0	0	0	0	141	27	10	0	11	11	4	64	296	538	834	NO	4.73	4.73	9.46	63.85	26.69	5.07	21.62
UPC 139	4	12	1	4	0	34	3	8	1	9	0	8	17	0	1	0	0	0	119	84	36	10	23	37	13	60	484	228	712	NO	4.34	16.74	21.07	56.20	22.73	10.33	12.40
UPC 023	4	7	5	3	0	21	6	3	2	9	0	9	6	1	0	0	0	0	103	48	24	3	6	32	11	85	388	397	785	NO	4.90	14.69	19.59	47.42	32.99	11.08	21.91
UPC 024	2	8	4	9	0	16	0	5	3	7	0	4	10	1	0	0	0	0	147	46	24	1	15	23	7	41	373	211	584	NO	6.17	12.33	18.50	62.47	19.03	8.04	10.99
UPC 093	16	15	5	2	0	76	4	6	2	12	2	10	11	2	0	0	0	0	90	96	41	24	14	41	26	60	561	77	638	NO	6.77	23.35	30.12	47.24	22.64	11.94	10.70
UPC 134	3	2	5	0	0	20	4	1	3	10	0	0	14	1	0	0	0	0	115	51	13	4	21	7	5	22	302	328	630	NO	3.31	17.88	21.19	67.55	11.26	3.97	7.28
UPC 025	5	7	4	0	0	57	2	0	0	8	0	3	5	0	0	0	0	0	55	58	14	10	11	37	5	32	318	44	362	NO	5.03	25.16	30.19	46.54	23.27	13.21	10.06
UPC 176	7	12	5	2	0	56	1	2	1	23	3	3	10	5	2	0	0	0	85	81	40	14	20	41	11	28	452	77	529	NO	5.75	23.45	29.20	53.10	17.70	11.50	6.19
UPC 170	6	9	1	0	0	44	1	3	0	6	0	3	7	2	1	0	0	0	76	61	40	3	17	40	16	43	379	48	427	NO	4.22	17.68	21.90	51.98	26.12	14.78	11.35
UPC 180	3	8	8	0	0	15	3	2	1	4	0	1	7	2	0	0	0	0	92	53	21	2	14	9	13	17	275	87	362	NO	6.91	12.73	19.64	66.18	14.18	8.00	6.18
UPC 028	9	21	7	2	0	38	6	4	1	1	0	2	5	0	0	0	0	0	98	61	24	6	14	41	11	58	409	142	551	NO	9.54	13.94	23.47	49.63	26.89	12.71	14.18

For raw data see sheet UPC028 Core top assemblages in Mair_AM_Earth_And_Environment_PhD_2022_Summary_Appendices.xls

Appendix B.2 Downcore assemblages counts

Sample	*Gs. ruber (p)*	*T. saccullifer*	*Gr. tumida*	*Gr. crassaformis*	*Gr. menardii*	*Gs. ruber (w)*	*Ge. siphonifera*	*O. universa*	*Gs. conglobatus*	*G. falconensis*	*Ge. calida*	*N. dutertrei*	*Gr. hirsuta*	*Tn. parkerae*	*Gtr. rubescens*	*Tb. clarkei*	*Gt. minuta*	*C. nitida*	*Gc. inflata*	*Gt. glutinata*	*Gg. bulloides*	*Gr. scitula*	*Gr. truncatulinoides L*	*Gr. truncatulinoides R*	*Gr. truncatulinoides SUM*	*N. incompta*	*Tb. quinqueloba*	*N. pachyderma*	Total Planktonic Foraminifera	Total Benthic Foraminifera	Tropical %	Sub-tropical %	Warm %	Transitional %	Sub-polar%	Polar %	Cold %	Warm vs Cold (%)	Sample Interpolated C14 date (BP)
Core Top	9	21	7	2	0	38	6	4	1	1	0	2	5	0	0	0	0	0	98	61	24	6	NA	NA	14	41	11	58	409	142	9.5	13.9	23.5	49.6	12.7	14.2	26.9	46.6	0.0
27-29 cm	19	25	11	7	0	117	3	1	4	12	0	4	16	2	5	0	0	0	124	119	34	29	17	13	30	54	15	57	688	50	9.0	23.8	32.8	48.8	10.0	8.3	18.3	64.2	361.3
34-36 cm	3	2	3	0	0	30	0	0	2	11	0	4	5	2	3	0	0	0	57	51	24	9	12	2	14	28	13	25	286	39	2.8	19.9	22.7	54.2	14.3	8.7	23.1	49.6	454.9
41-43 cm	5	11	6	0	2	38	5	4	2	16	0	3	16	2	2	0	0	0	65	48	25	4	7	1	8	19	12	19	312	51	7.7	28.2	35.9	48.1	9.9	6.1	16.0	69.1	548.6
48-50 cm	3	1	2	3	0	49	1	4	2	0	0	0	6	0	0	0	0	0	80	61	15	12	NA	NA	20	21	4	26	310	29	2.9	20.0	22.9	60.6	8.1	8.4	16.5	58.2	642.3
55-57 cm	5	11	9	5	1	40	4	1	2	25	0	1	9	2	9	0	0	0	92	84	52	4	9	3	12	36	19	44	467	67	6.6	19.9	26.6	52.2	11.8	9.4	21.2	55.6	735.9
62-64 cm	5	2	7	0	1	31	2	0	1	13	0	3	6	2	9	0	0	0	73	60	41	1	10	6	16	22	11	37	343	57	4.4	19.5	23.9	55.7	9.6	10.8	20.4	53.9	829.6
69-71 cm	12	4	3	2	0	47	4	0	2	18	0	5	14	4	12	0	0	1	70	73	64	6	14	7	21	55	14	45	476	79	4.4	22.5	26.9	49.2	14.5	9.5	23.9	52.9	923.3
76-78 cm	5	6	5	1	0	25	3	3	2	12	0	3	9	0	3	0	0	0	70	71	35	6	12	9	21	21	8	29	338	69	5.0	17.8	22.8	60.1	8.6	8.6	17.2	57.0	1016.9
83-85 cm	3	3	2	0	0	23	2	2	0	13	0	2	7	3	6	0	0	0	58	49	31	3	5	8	13	24	5	46	295	60	2.7	19.7	22.4	52.2	9.8	15.6	25.4	46.8	1110.6
90-92 cm	5	2	5	3	0	20	3	2	0	18	0	0	9	1	4	0	0	1	69	44	28	1	9	4	13	19	12	31	290	73	5.2	20.0	25.2	53.4	10.7	10.7	21.4	54.1	1204.2
97-99 cm	10	2	5	12	1	33	1	2	2	0	0	0	5	0	0	0	0	0	59	53	15	5	NA	NA	14	19	5	43	286	50	10.5	15.0	25.5	51.0	8.4	15.0	23.4	52.1	1297.9
104-106 cm	8	6	3	2	0	19	1	2	1	14	0	2	11	2	5	0	0	0	76	55	44	5	17	3	20	21	11	69	377	54	5.0	15.1	20.2	53.1	8.5	18.3	26.8	42.9	1441.0
111-113 cm	7	2	3	0	0	33	0	1	1	15	0	0	10	0	1	0	0	0	109	57	41	6	15	4	19	20	13	57	395	87	3.0	15.4	18.5	58.7	8.4	14.4	22.8	44.8	1584.2
118-120 cm	13	4	2	1	0	33	5	1	0	11	0	0	3	2	4	0	0	0	75	46	25	8	16	1	17	30	9	40	329	63	6.1	17.9	24.0	52.0	11.9	12.2	24.0	50.0	1727.3
120-122 cm	7	4	7	2	0	34	1	0	1	4	0	3	16	1	1	0	0	0	84	44	25	6	16	3	19	31	8	44	342	45	5.8	17.8	23.7	52.0	11.4	12.9	24.3	49.4	1768.2

Sample	*Gs. ruber (p)*	*T. sacculifer*	*Gr. tumida*	*Gr. crassaformis*	*Gr. menardii*	*Gs. ruber (w)*	*Ge. siphonifera*	*O. universa*	*Gs. conglobatus*	*G. falconensis*	*Ge. calida*	*N. dutertrei*	*Gr. hirsuta*	*Tn. parkerae*	*Gtr. rubescens*	*Tb. clarkei*	*Gt. minuta*	*C. nitida*	*Gc. inflata*	*Gt. glutinata*	*Gg. bulloides*	*Gr. scitula*	*Gr. truncatulinoides L*	*Gr. truncatulinoides R*	*Gr. truncatulinoides SUM*	*N. incompta*	*Tb. quinqueloba*	*N. pachyderma*	Total Planktonic Foraminifera	Total Benthic Foraminifera	Tropical %	Sub-tropical %	Warm %	Transitional %	Sub-polar%	Polar %	Cold %	Warm vs Cold (%)	Sample Interpolated C14 date (BP)
127-129 cm	5	3	3	3	0	17	0	0	1	5	0	2	4	0	3	0	0	0	73	44	35	2	10	3	13	13	15	32	273	82	5.1	11.7	16.8	61.2	10.3	11.7	22.0	43.4	1911.3
134-136 cm	4	5	2	2	1	29	2	2	1	13	0	2	3	5	0	0	0	0	80	51	24	7	12	4	16	4	62	339	99	4.1	16.8	20.9	52.5	8.3	18.3	26.5	44.1	2054.5
141-143 cm	8	6	2	1	0	43	1	3	0	15	0	2	13	1	0	0	0	0	90	52	29	3	14	3	17	12	53	392	103	4.3	20.2	24.5	48.7	13.3	13.5	26.8	47.8	2197.6
148-150 cm	19	8	3	8	0	56	0	2	2	0	0	1	4	0	0	0	0	0	109	83	19	5	NA	NA	12	15	79	461	83	8.2	14.1	22.3	49.5	11.1	17.1	28.2	44.2	2340.7
155-157 cm	8	7	1	0	0	67	3	1	1	20	0	1	13	1	7	0	0	1	84	65	37	7	11	8	19	13	72	459	74	3.5	25.1	28.5	46.2	9.6	15.7	25.3	53.0	2483.9
162-164 cm	3	8	1	0	1	53	4	4	0	14	0	1	6	5	10	0	0	0	135	57	44	3	22	4	26	18	54	487	43	2.7	19.9	22.6	54.4	11.9	11.1	23.0	49.5	2627.0
169-171 cm	5	6	2	0	0	50	1	3	3	17	0	1	9	0	7	0	0	0	68	59	54	19	12	3	15	9	52	410	56	3.2	22.2	25.4	52.4	9.5	12.7	22.2	53.3	2770.1
176-178 cm	13	27	3	3	0	111	5	3	3	18	0	3	30	1	19	0	0	0	179	143	88	22	24	1	25	31	108	892	53	5.2	21.6	26.8	51.2	9.9	12.1	22.0	54.9	2913.3
183-185 cm	5	3	1	1	0	72	1	2	1	30	0	1	6	9	19	0	0	0	86	76	78	9	13	4	17	45	71	554	68	1.8	25.5	27.3	48.0	11.9	12.8	24.7	52.4	3056.4
190-192 cm	2	0	1	0	0	29	4	2	0	16	0	1	8	2	7	0	0	0	62	37	25	11	13	0	13	19	14	52	305	23	1.0	22.6	23.6	48.5	10.8	17.0	27.9	45.9	3199.5
197-199 cm	18	8	2	1	0	56	3	0	1	4	0	0	11	0	4	1	0	0	103	137	59	13	NA	NA	23	57	19	113	633	43	4.6	12.6	17.2	52.9	12.0	17.9	29.9	36.6	3342.7
240-242 cm	10	7	1	0	0	44	3	3	1	15	0	2	9	5	7	0	1	0	91	51	58	11	8	3	11	22	13	63	428	56	4.2	21.0	25.2	51.9	8.2	14.7	22.9	52.4	4132.9
247-249 cm	21	6	3	9	0	57	3	1	3	7	0	2	5	0	11	1	2	0	111	106	24	15	NA	NA	20	35	21	101	564	52	6.9	16.3	23.2	48.9	9.9	17.9	27.8	45.5	4261.9
254-256 cm	12	2	5	0	0	29	1	4	1	16	0	0	8	3	6	0	0	0	75	54	50	4	13	3	16	6	71	383	45	5.0	17.8	22.7	52.0	6.8	18.5	25.3	47.3	4390.5
261-263 cm	12	3	3	0	0	44	2	6	1	15	0	0	8	0	7	0	0	0	78	52	26	2	16	1	17	13	62	381	51	4.7	21.8	26.5	45.9	11.3	16.3	27.6	49.0	4520.0

Sample	*Gs. ruber (p)*	*T. sacculifer*	*Gr. tumida*	*Gr. crassaformis*	*Gr. menardii*	*Gs. ruber (w)*	*Ge. siphonifera*	*O. universa*	*Gs. conglobatus*	*G. falconensis*	*Ge. calida*	*N. dutertrei*	*Gr. hirsuta*	*Tn. parkerae*	*Gtr. rubescens*	*Tb. clarkei*	*Gt. minuta*	*C. nitida*	*Gc. inflata*	*Gt. glutinata*	*Gg. bulloides*	*Gr. scitula*	*Gr. truncatulinoides L*	*Gr. truncatulinoides R*	*Gr. truncatulinoides SUM*	*N. incompta*	*Tb. quinqueloba*	*N. pachyderma*	Total Planktonic Foraminifera	Total Benthic Foraminifera	Tropical %	Sub-tropical %	Warm %	Transitional %	Sub-polar%	Polar %	Cold %	Warm vs Cold (%)	Sample Interpolated C14 date (BP)
268-270 cm	10	6	3	1	0	40	3	7	2	22	0	3	13	2	7	0	0	0	94	81	57	12	22	0	22	50	13	127	575	124	3.5	17.2	20.7	46.3	11.0	22.1	33.0	38.5	4648.0
275-277 cm	9	6	1	0	0	53	4	6	1	13	0	1	7	2	7	0	0	0	57	56	37	9	7	3	10	41	20	85	425	60	3.8	22.1	25.9	39.8	14.4	20.0	34.4	43.0	4776.7
282-284 cm	15	6	2	3	0	95	1	0	1	21	0	5	12	10	8	0	0	0	118	80	53	17	30	4	34	69	23	110	683	51	3.8	22.4	26.2	44.2	13.5	16.1	29.6	47.0	4905.9
289-291 cm	6	7	6	0	0	33	1	3	1	11	0	3	4	1	5	0	0	0	41	22	28	5	14	3	17	40	7	51	292	45	6.5	21.2	27.7	38.7	16.1	17.5	33.6	45.3	5034.8
296-298 cm	25	7	3	3	1	71	9	5	2	0	0	2	9	3	7	0	0	0	94	122	34	20	NA	NA	59	59	32	100	667	41	5.8	16.2	22.0	49.3	13.6	15.0	28.6	43.5	5163.4
303-305 cm	10	9	5	2	0	35	7	3	0	13	0	5	10	4	6	0	0	0	81	65	61	12	22	0	22	77	14	89	530	62	4.9	15.7	20.6	45.5	17.2	16.8	34.0	37.7	5292.5
310-312 cm	10	7	7	1	0	35	4	3	0	9	0	6	12	3	5	0	0	0	75	61	31	10	20	0	20	88	12	70	469	40	5.3	16.4	21.7	42.0	21.3	14.9	36.2	37.5	5421.4
317-319 cm	9	5	2	3	0	34	6	3	1	13	1	4	4	2	3	0	0	0	42	39	25	8	13	1	14	64	16	44	342	60	5.6	20.8	26.3	37.4	23.4	12.9	36.3	42.1	5612.4
324-326 cm	14	7	3	0	0	72	1	8	1	14	1	16	14	4	5	0	0	0	53	39	38	19	9	3	12	73	20	80	494	30	4.9	27.5	32.4	32.6	18.8	16.2	35.0	48.0	5803.7
331-333 cm	16	4	2	3	0	34	4	3	0	15	2	7	3	3	12	0	0	0	36	37	40	6	7	1	8	98	28	91	452	53	5.5	18.4	23.9	28.1	27.9	20.1	48.0	33.2	5995.6
338-340 cm	5	5	1	0	0	23	1	2	2	9	0	4	7	1	6	0	0	0	51	26	15	7	5	1	6	61	8	37	277	19	4.0	19.9	23.8	37.9	24.9	13.4	38.3	38.4	6186.9
340-342 cm	10	10	6	0	0	44	7	2	2	16	0	4	3	3	9	0	0	3	44	27	30	9	6	0	6	68	8	47	358	31	7.3	26.0	33.2	32.4	21.2	13.1	34.4	49.2	6242.0
347-349 cm	8	4	3	1	0	39	1	5	1	0	0	12	5	4	2	0	0	0	40	66	11	6	NA	NA	14	79	8	45	354	29	4.5	19.5	24.0	38.7	24.6	12.7	37.3	39.2	6433.7
354-356 cm	8	7	1	1	0	29	3	3	0	24	0	7	5	6	12	0	0	1	40	28	41	7	6	0	6	90	5	34	358	33	4.7	25.1	29.9	34.1	26.5	9.5	36.0	45.3	6623.8
361-363 cm	8	8	1	0	0	39	3	3	0	8	0	8	8	5	4	0	0	0	29	39	34	4	7	2	9	98	13	45	366	41	4.6	21.3	26.0	31.4	30.3	12.3	42.6	37.8	6815.3

Sample	*Gs. ruber (p)*	*T. sacculifer*	*Gr. tumida*	*Gr. crassaformis*	*Gr. menardii*	*Gs. ruber (w)*	*Ge. siphonifera*	*O. universa*	*Gs. conglobatus*	*G. falconensis*	*Ge. calida*	*N. dutertrei*	*Gr. hirsuta*	*Tn. parkerae*	*Gtr. rubescens*	*Tb. clarkei*	*Gt. minuta*	*C. nitida*	*Gc. inflata*	*Gt. glutinata*	*Gg. bulloides*	*Gr. scitula*	*Gr. truncatulinoides L*	*Gr. truncatulinoides R*	*Gr. truncatulinoides SUM*	*N. incompta*	*Tb. quinqueloba*	*N. pachyderma*	Total Planktonic Foraminifera	Total Benthic Foraminifera	Tropical %	Sub-tropical %	Warm %	Transitional %	Sub-polar%	Polar %	Cold %	Warm vs Cold (%)	Sample Interpolated C14 date (BP)
368-370 cm	19	5	1	1	0	41	3	3	1	9	0	5	7	1	4	0	0	0	64	38	42	7	9	0	9	87	8	47	402	93	6.5	18.4	24.9	39.8	23.6	11.7	35.3	41.3	7006.7
375-377 cm	12	12	4	1	1	50	12	15	1	15	3	20	8	3	7	0	0	0	61	61	37	17	11	0	11	69	26	59	505	88	5.9	26.5	32.5	37.0	18.8	11.7	30.5	51.6	7197.8
382-384 cm	3	10	4	1	0	34	3	5	1	14	0	3	4	2	8	0	0	0	17	37	35	3	5	1	6	53	10	71	324	60	5.6	22.8	28.4	30.2	19.4	21.9	41.4	40.7	7390.1
389-391 cm	13	16	10	0	0	48	1	7	3	16	0	5	15	8	7	0	0	0	71	75	68	15	21	3	24	135	16	104	657	97	5.9	16.7	22.7	38.5	23.0	15.8	38.8	36.9	7581.6
396-398 cm	9	12	4	3	0	47	5	5	0	18	1	4	10	1	6	0	0	0	79	48	60	6	14	0	14	58	10	97	497	144	5.6	19.5	25.2	41.6	13.7	19.5	33.2	43.1	7772.2
400-402 cm	6	6	1	0	0	27	2	2	0	1	0	2	3	3	5	0	0	0	23	68	21	3	NA	NA	10	36	11	62	292	60	4.5	15.4	19.9	42.8	16.1	21.2	37.3	34.7	7881.9
407-409 cm	9	6	1	0	0	31	2	3	0	9	0	1	7	2	8	0	0	0	30	56	51	5	4	3	7	66	18	85	397	106	4.0	15.9	19.9	37.5	21.2	21.4	42.6	31.9	8053.5
412-415 cm	8	2	1	1	0	24	6	0	0	7	0	6	8	3	7	0	0	0	49	49	38	14	7	2	9	69	19	65	385	126	3.1	15.8	19.0	41.3	22.9	16.9	39.7	32.3	8175.4
417-419 cm	9	6	0	0	0	30	7	1	1	10	0	5	7	3	7	0	0	0	34	49	61	1	8	2	10	80	17	107	445	85	3.4	16.0	19.3	34.8	21.8	24.0	45.8	29.7	8297.4
422-424 cm	8	4	1	0	0	34	4	1	0	9	0	14	4	7	3	1	0	0	44	50	45	13	NA	NA	3	81	29	118	473	64	2.7	16.3	19.0	32.8	23.3	24.9	48.2	28.3	8419.5
427-429 cm	14	9	0	2	0	75	6	2	1	17	1	7	6	3	6	0	0	1	48	43	61	12	9	5	14	101	18	155	602	113	4.2	20.8	24.9	29.6	19.8	25.7	45.5	35.4	8542.0
432-434 cm	17	9	1	2	0	84	0	2	0	22	0	10	7	5	13	0	0	0	65	68	50	12	12	9	21	119	20	118	645	146	4.5	22.2	26.7	33.5	21.6	18.3	39.8	40.1	8664.3
437-439 cm	2	2	0	0	0	21	1	2	0	9	0	3	5	1	2	0	0	0	7	21	42	4	4	0	4	79	4	106	315	51	1.3	14.0	15.2	24.8	26.3	33.7	60.0	20.3	8786.1
443-444 cm	6	4	0	0	0	36	9	0	0	8	1	4	11	3	5	0	0	0	42	41	43	5	10	8	18	67	6	47	354	94	2.8	21.2	24.0	42.1	20.6	13.3	33.9	41.5	8931.9
447-449 cm	7	3	0	1	0	16	2	0	1	0	0	8	6	2	5	0	0	0	31	69	18	14	NA	NA	9	67	11	63	334	53	3.3	12.3	15.6	42.2	23.4	18.9	42.2	26.9	9029.8

Sample	*Gs. ruber (p)*	*T. sacculifer*	*Gr. tumida*	*Gr. crassaformis*	*Gr. menardii*	*Gs. ruber (w)*	*Ge. siphonifera*	*O. universa*	*Gs. conglobatus*	*G. falconensis*	*Ge. calida*	*N. dutertrei*	*Gr. hirsuta*	*Tn. parkerae*	*Gtr. rubescens*	*Tb. clarkei*	*Gt. minuta*	*C. nitida*	*Gc. inflata*	*Gt. glutinata*	*Gg. bulloides*	*Gr. scitula*	*Gr. truncatulinoides L*	*Gr. truncatulinoides R*	*Gr. truncatulinoides SUM*	*N. incompta*	*Tb. quinqueloba*	*N. pachyderma*	Total Planktonic Foraminifera	Total Benthic Foraminifera	Tropical %	Sub-tropical %	Warm %	Transitional %	Sub-polar%	Polar %	Cold %	Warm vs Cold (%)	Sample Interpolated C14 date (BP)
452-454 cm	3	7	0	1	0	48	3	1	0	12	0	3	7	5	5	0	0	0	43	40	56	11	11	7	18	116	5	122	506	197	2.2	16.6	18.8	33.2	23.9	24.1	48.0	28.1	9151.8
457-459 cm	4	7	0	3	0	37	5	2	1	14	0	3	6	7	13	0	1	0	33	44	54	6	6	7	13	97	20	118	488	145	2.9	18.2	21.1	30.7	24.0	24.2	48.2	30.5	9274.3
462-464 cm	2	5	1	1	0	27	7	0	1	7	1	6	4	7	6	0	1	1	45	40	40	8	7	5	12	67	9	97	395	106	2.3	17.2	19.5	36.7	19.2	24.6	43.8	30.8	9396.6
462-467 cm	8	7	0	0	0	33	9	2	0	7	0	3	5	3	16	0	0	0	14	48	40	3	3	5	8	39	4	65	314	108	4.8	24.8	29.6	36.0	13.7	20.7	34.4	46.3	9518.3
472-474 cm	2	5	0	0	0	25	1	1	1	4	0	8	5	3	3	0	0	0	54	45	24	6	16	5	21	48	10	91	357	146	2.0	14.3	16.2	42.0	16.2	25.5	41.7	28.0	9640.5
477-479 cm	4	2	0	4	0	23	4	0	0	10	0	0	3	4	6	0	0	0	81	50	54	7	16	6	22	85	8	157	524	376	1.9	9.5	11.5	40.8	17.7	30.0	47.7	19.4	9761.9
482-484 cm	3	2	0	0	0	26	0	0	0	2	0	3	6	3	1	0	0	0	49	30	46	2	17	4	21	75	10	138	417	293	1.2	9.8	11.0	35.5	20.4	33.1	53.5	17.1	9884.5
487-489 cm	2	2	0	0	0	20	3	0	0	3	0	3	3	3	4	0	0	0	43	45	20	4	4	1	5	70	13	76	319	163	1.3	12.2	13.5	36.7	26.0	23.8	49.8	21.3	10006

For raw data see sheet UPC028 downcore assemblages in Mair_AM_Earth_And_Environment_PhD_2022_Summary_Appendices.xls

Appendix C.1 Core top stable isotopes

Sample ID	Core	Core Top/ Downcore	Depth (mbsf)	Latitude	Longitude	Sample Depth (cm)	Radiocarbon Age (cal BP)	δ13C VPDB	δ18O VPDB	Converted Temperature (°C)	Species	Encrustation Classification (A-D)/ Coiling Direction (L-R)
2021-02-04 UPC053CTGI1	UPC053	CT	-2115.2	-36.54	-53.02	0	0	0.614946944	0.383579794	13.11	*Gc. inflata*	A
2021-02-04 UPC001CTGI2	UPC001	CT	-2053.1	-36.92	-53.41	0	0	1.84135302	1.426166829	8.49	*Gc. inflata*	B
2021-02-04 UPC001CTGI3	UPC001	CT	-2053.1	-36.92	-53.41	0	0	2.599643261	0.923406066	10.69	*Gc. inflata*	B
2021-02-11 UPC028CTGI1	UPC028	CT	-2353	-36.15	-52.46	0	0	0.604772194	1.559378236	7.91	*Gc. inflata*	B
2021-02-04 UPC053CTGI4	UPC053	CT	-2115.2	-36.54	-53.02	0	0	0.754715108	0.484491763	12.65	*Gc. inflata*	B
2021-02-04 UPC058CTGI5	UPC058	CT	-2255.3	-36.73	-53.21	0	0	1.465445597	1.370803626	8.73	*Gc. inflata*	B
2021-02-04 UPC001CTGI5	UPC001	CT	-2053.1	-36.92	-53.41	0	0	2.916906913	1.532072701	8.03	*Gc. inflata*	C
2021-02-04 UPC022CTGI3	UPC022	CT	-2027.5	-36.46	-52.88	0	0	1.362570262	1.422041501	8.51	*Gc. inflata*	C
2021-02-04 UPC022CTGI4	UPC022	CT	-2027.5	-36.46	-52.88	0	0	1.312384224	1.782385573	6.96	*Gc. inflata*	C
2021-02-04 UPC023CTGI2	UPC023	CT	-2046.3	-36.39	-52.82	0	0	2.830894202	1.980390479	6.11	*Gc. inflata*	C
2021-02-04 UPC023CTGI5	UPC023	CT	-2046.3	-36.39	-52.82	0	0	2.781863004	1.606370987	7.71	*Gc. inflata*	C
2021-02-11 UPC028CTGI3	UPC028	CT	-2353	-36.15	-52.46	0	0	0.743312345	1.225823997	9.36	*Gc. inflata*	C
2021-02-11 UPC028CTGI5	UPC028	CT	-2353	-36.15	-52.46	0	0	0.837099536	1.203178914	9.46	*Gc. inflata*	C
2021-02-11 UPC033CTGI1	UPC033	CT	-2582.3	-36.60	-52.90	0	0	1.046569339	1.175696318	9.58	*Gc. inflata*	C
2021-02-11 UPC033CTGI5	UPC033	CT	-2582.3	-36.60	-52.90	0	0	1.153933103	1.444172703	8.41	*Gc. inflata*	C
2021-02-04 UPC053CTGI5	UPC053	CT	-2115.2	-36.54	-53.02	0	0	1.503196349	1.23680495	9.31	*Gc. inflata*	C
2021-02-04 UPC058CTGI1	UPC058	CT	-2255.3	-36.73	-53.21	0	0	1.402970991	1.069947457	10.04	*Gc. inflata*	C
2021-02-04 UPC058CTGI3	UPC058	CT	-2255.3	-36.73	-53.21	0	0	1.215017354	1.118866261	9.83	*Gc. inflata*	C
2021-02-04 UPC063CTGI1	UPC063	CT	-1255	-36.54	-53.17	0	0	1.016465755	1.207745303	9.44	*Gc. inflata*	C
2021-02-04 UPC066CTGI1	UPC066	CT	-1257	-36.55	-53.18	0	0	0.852913893	1.032161569	10.21	*Gc. inflata*	C
2021-02-04 UPC081CTGI1	UPC081	CT	-1895.6	-36.83	-53.32	0	0	1.959312461	1.456134457	8.36	*Gc. inflata*	C
2021-02-04 UPC081CTGI2	UPC081	CT	-1895.6	-36.83	-53.32	0	0	2.604173652	1.514985253	8.10	*Gc. inflata*	C
21_02_22_UPC093CTGI2R	UPC093	CT	-2572.5	-36.32	-52.58	0	0	1.003936789	1.510940182	8.12	*Gc. inflata*	C
21_02_25 UPC093CTGI3R	UPC093	CT	-2572.5	-36.32	-52.58	0	0	1.233319479	1.572579129	7.86	*Gc. inflata*	C
2021-02-11 UPC141CTGI1	UPC141	CT	-2431.1	-36.70	-53.04	0	0	2.694012739	1.681725798	7.39	*Gc. inflata*	C
2021-02-11 UPC141CTGI4	UPC141	CT	-2431.1	-36.70	-53.04	0	0	2.485637818	1.286143457	9.10	*Gc. inflata*	C
2021-02-11 UPC142CTGI1	UPC142	CT	-2682.1	-36.76	-52.98	0	0	2.440977329	1.394804824	8.62	*Gc. inflata*	C
2021-02-11 UPC142CTGI2	UPC142	CT	-2682.1	-36.76	-52.98	0	0	0.696085996	1.098433199	9.92	*Gc. inflata*	C
2021-02-11 UPC145CTGI2	UPC145	CT	-1595.4	-36.49	-52.98	0	0	2.691256546	1.857547204	6.64	*Gc. inflata*	C
2021-02-11 UPC145CTGI4	UPC145	CT	-1595.4	-36.49	-52.98	0	0	0.947633958	0.883866109	10.87	*Gc. inflata*	C
2021-02-11 UPC145CTGI5	UPC145	CT	-1595.4	-36.49	-52.98	0	0	1.309027181	1.74437285	7.12	*Gc. inflata*	C
2021-02-04 UPC001CTGI1	UPC001	CT	-2053.1	-36.92	-53.41	0	0	2.983659283	1.488018528	8.22	*Gc. inflata*	D
2021-02-04 UPC001CTGI4	UPC001	CT	-2053.1	-36.92	-53.41	0	0	2.810852684	1.519125614	8.09	*Gc. inflata*	D
2021-02-04 UPC022CTGI2	UPC022	CT	-2027.5	-36.46	-52.88	0	0	0.219848989	0.548201381	12.36	*Gc. inflata*	D
2021-02-04 UPC022CTGI5	UPC022	CT	-2027.5	-36.46	-52.88	0	0	2.757175722	1.691287469	7.35	*Gc. inflata*	D
2021-02-04 UPC023CTGI3	UPC023	CT	-2046.3	-36.39	-52.82	0	0	1.577558623	1.863517422	6.61	*Gc. inflata*	D

Sample ID	Core	Core Top/ Downcore	Depth (mbsf)	Latitude	Longitude	Sample Depth (cm)	Radiocarbon Age (cal BP)	δ13C VPDB	δ18O VPDB	Converted Temperature (°C)	Species	Encrustation Classification (A-D)/ Coiling Direction (L-R)
2021-02-04 UPC023CTGI4	UPC023	CT	-2046.3	-36.39	-52.82	0	0	2.793557726	1.555964855	7.93	*Gc. inflata*	D
21_02_25 UPC023CTGI2R	UPC023	CT	-2046.3	-36.39	-52.82	0	0	1.19279949	1.224882683	9.36	*Gc. inflata*	D
2021-02-11 UPC028CTGI2	UPC028	CT	-2353	-36.15	-52.46	0	0	2.623686814	1.801881449	6.87	*Gc. inflata*	D
2021-02-11 UPC028CTGI4	UPC028	CT	-2353	-36.15	-52.46	0	0	2.464426343	1.807314083	6.85	*Gc. inflata*	D
21_02_25 UPC028CTGI2R	UPC028	CT	-2353	-36.15	-52.46	0	0	1.511985857	1.216196538	9.40	*Gc. inflata*	D
2021-02-11 UPC033CTGI2	UPC033	CT	-2582.3	-36.60	-52.90	0	0	1.045030571	1.804816555	6.86	*Gc. inflata*	D
2021-02-11 UPC033CTGI3	UPC033	CT	-2582.3	-36.60	-52.90	0	0	1.687308702	1.796637746	6.90	*Gc. inflata*	D
2021-02-11 UPC033CTGI4	UPC033	CT	-2582.3	-36.60	-52.90	0	0	2.658814093	1.473650743	8.28	*Gc. inflata*	D
2021-02-04 UPC053CTGI3	UPC053	CT	-2115.2	-36.54	-53.02	0	0	1.205757121	0.704579919	11.66	*Gc. inflata*	D
2021-02-04 UPC058CTGI2	UPC058	CT	-2255.3	-36.73	-53.21	0	0	2.714139032	1.709376147	7.27	*Gc. inflata*	D
2021-02-04 UPC058CTGI4	UPC058	CT	-2255.3	-36.73	-53.21	0	0	0.948735661	1.193655133	9.50	*Gc. inflata*	D
2021-02-04 UPC063CTGI2	UPC063	CT	-1255	-36.54	-53.17	0	0	2.65633694	1.683827327	7.38	*Gc. inflata*	D
2021-02-04 UPC063CTGI3	UPC063	CT	-1255	-36.54	-53.17	0	0	2.881602287	1.646030411	7.54	*Gc. inflata*	D
2021-02-04 UPC063CTGI4	UPC063	CT	-1255	-36.54	-53.17	0	0	2.594157564	1.440170847	8.43	*Gc. inflata*	D
2021-02-04 UPC063CTGI5	UPC063	CT	-1255	-36.54	-53.17	0	0	2.711836269	1.687686153	7.36	*Gc. inflata*	D
2021-02-04 UPC066CTGI2	UPC066	CT	-1257	-36.55	-53.18	0	0	2.604612133	1.656381137	7.50	*Gc. inflata*	D
2021-02-04 UPC066CTGI3	UPC066	CT	-1257	-36.55	-53.18	0	0	1.373798037	1.739236428	7.14	*Gc. inflata*	D
2021-02-04 UPC066CTGI4	UPC066	CT	-1257	-36.55	-53.18	0	0	2.687793464	1.331087623	8.90	*Gc. inflata*	D
2021-02-04 UPC066CTGI5	UPC066	CT	-1257	-36.55	-53.18	0	0	2.467419246	1.895226324	6.48	*Gc. inflata*	D
2021-02-04 UPC081CTGI3	UPC081	CT	-1895.6	-36.83	-53.32	0	0	2.917368843	1.679298203	7.40	*Gc. inflata*	D
2021-02-04 UPC081CTGI4	UPC081	CT	-1895.6	-36.83	-53.32	0	0	2.641580513	1.709971464	7.27	*Gc. inflata*	D
2021-02-04 UPC081CTGI5	UPC081	CT	-1895.6	-36.83	-53.32	0	0	0.706346782	0.931806784	10.65	*Gc. inflata*	D
21_02_25 UPC093CTGI4R	UPC093	CT	-2572.5	-36.32	-52.58	0	0	0.514118091	1.103401764	9.90	*Gc. inflata*	D
21_02_25 UPC093CTGI5R	UPC093	CT	-2572.5	-36.32	-52.58	0	0	0.797478486	1.310074181	8.99	*Gc. inflata*	D
2021-02-11 UPC122CTGI1	UPC122	CT	-1154.2	-36.50	-53.21	0	0	2.733176493	1.698610391	7.31	*Gc. inflata*	D
2021-02-11 UPC122CTGI2	UPC122	CT	-1154.2	-36.50	-53.21	0	0	2.710327112	1.732015951	7.17	*Gc. inflata*	D
2021-02-11 UPC122CTGI3	UPC122	CT	-1154.2	-36.50	-53.21	0	0	2.646884135	1.76348447	7.04	*Gc. inflata*	D
2021-02-11 UPC122CTGI4	UPC122	CT	-1154.2	-36.50	-53.21	0	0	2.656507358	1.77341419	6.99	*Gc. inflata*	D
2021-02-11 UPC122CTGI5	UPC122	CT	-1154.2	-36.50	-53.21	0	0	2.667012162	1.693175373	7.34	*Gc. inflata*	D
2021-02-11 UPC141CTGI2	UPC141	CT	-2431.1	-36.70	-53.04	0	0	2.831593363	1.787527747	6.93	*Gc. inflata*	D
2021-02-11 UPC141CTGI3	UPC141	CT	-2431.1	-36.70	-53.04	0	0	2.550815259	1.821918166	6.79	*Gc. inflata*	D
2021-02-11 UPC141CTGI5	UPC141	CT	-2431.1	-36.70	-53.04	0	0	2.762935982	1.665721922	7.46	*Gc. inflata*	D
2021-02-11 UPC142CTGI3	UPC142	CT	-2682.1	-36.76	-52.98	0	0	1.052815367	1.724432364	7.20	*Gc. inflata*	D
2021-02-11 UPC142CTGI4	UPC142	CT	-2682.1	-36.76	-52.98	0	0	2.438884836	1.618565586	7.66	*Gc. inflata*	D

Sample ID	Core	Core Top/ Downcore	Depth (mbsf)	Latitude	Longitude	Sample Depth (cm)	Radiocarbon Age (cal BP)	δ13C VPDB	δ18O VPDB	Converted Temperature (°C)	Species	Encrustation Classification (A-D)/ Coiling Direction (L-R)
2021-02-11 UPC142CTGI5	UPC142	CT	-2682.1	-36.76	-52.98	0	0	2.756134423	1.672536423	7.43	*Gc. inflata*	D
2021-02-11 UPC145CTGI1	UPC145	CT	-1595.4	-36.49	-52.98	0	0	2.917529886	1.636484074	7.58	*Gc. inflata*	D
2021-02-11 UPC145CTGI3	UPC145	CT	-1595.4	-36.49	-52.98	0	0	2.817647188	1.829040229	6.76	*Gc. inflata*	D
2021_03_08_UPC145CTGI2R	UPC145	CT	-1595.4	-36.49	-52.98	0	0	1.818733314	1.400156445	8.60	*Gc. inflata*	D
2021-02-11 UPC093CTGI1	UPC093	CT	-2572.5	-36.32	-52.58	0	0	0.117695912	0.202027766	13.93	*Gc. inflata*	B
2021-02-11 UPC093CTGI3	UPC093	CT	-2572.5	-36.32	-52.58	0	0	0.769827186	1.363173395	8.76	*Gc. inflata*	D
2021-02-11 UPC093CTGI4	UPC093	CT	-2572.5	-36.32	-52.58	0	0	0.911535272	0.779931288	11.33	*Gc. inflata*	D
2021-02-11 UPC093CTGI5	UPC093	CT	-2572.5	-36.32	-52.58	0	0	0.852479028	1.430073651	8.47	*Gc. inflata*	D
21_02_25 UPC022CTGI1R	UPC022	CT	-2027.5	-36.46	-52.88	0	0	2.257680229	2.996650214	1.90	*Gc. inflata*	D
2021_03_08_UPC022CTGI2R	UPC023	CT	-2046.3	-36.39	-52.82	0	0	1.65169682	2.750090991	2.91	*Gc. inflata*	D
21_02_25 UPC023CTGI1R	UPC023	CT	-2046.3	-36.39	-52.82	0	0	1.949103134	3.021344977	1.80	*Gc. inflata*	D
21_02_25 UPC023CTGI3R	UPC023	CT	-2046.3	-36.39	-52.82	0	0	1.795258058	2.972212249	2.00	*Gc. inflata*	D
21_02_25 UPC023CTGI4R	UPC023	CT	-2046.3	-36.39	-52.82	0	0	1.693646237	2.896023359	2.31	*Gc. inflata*	D
21_02_25 UPC028CTGI1R	UPC028	CT	-2353	-36.15	-52.46	0	0	2.124603449	2.770641199	2.82	*Gc. inflata*	D
21_02_25 UPC028CTGI3R	UPC028	CT	-2353	-36.15	-52.46	0	0	1.775243655	3.066742685	1.62	*Gc. inflata*	D
21_02_25 UPC053CTGI1R	UPC053	CT	-2115.2	-36.54	-53.02	0	0	1.321040412	3.216755979	1.02	*Gc. inflata*	D
21_02_25 UPC053CTGI2R	UPC053	CT	-2115.2	-36.54	-53.02	0	0	1.271496909	2.913894699	2.24	*Gc. inflata*	D
21_02_25 UPC053CTGI4R	UPC053	CT	-2115.2	-36.54	-53.02	0	0	1.470739961	3.043347988	1.71	*Gc. inflata*	D
2021_03_08_UPC145CTGI1R	UPC145	CT	-1595.4	-36.49	-52.98	0	0	1.760661269	2.622568007	3.43	*Gc. inflata*	D
2021_03_08_UPC145CTGI3R	UPC145	CT	-1595.4	-36.49	-52.98	0	0	1.765584219	2.638498864	3.37	*Gc. inflata*	D
2021_02_17 UPC022CTGT1	UPC022	CT	-2027.5	-36.46	-52.88	0	0	1.826076106	1.178690435	9.57	*Gr. truncatulinoides L*	NA
2021_02_17 UPC022CTGT2	UPC022	CT	-2027.5	-36.46	-52.88	0	0	1.808433342	2.663418254	3.26	*Gr. truncatulinoides L*	NA
2021_02_17 UPC033CTGT1	UPC033	CT	-2582.3	-36.60	-52.90	0	0	1.83887115	1.959654228	6.20	*Gr. truncatulinoides L*	NA
2021_02_17 UPC033CTGT3	UPC033	CT	-2582.3	-36.60	-52.90	0	0	1.537001665	0.996833403	10.37	*Gr. truncatulinoides L*	NA
2021_02_17 UPC063CTGT3	UPC063	CT	-1255	-36.54	-53.17	0	0	1.57053941	1.231226443	9.34	*Gr. truncatulinoides L*	NA
21_02_22_UPC066CTGT1	UPC066	CT	-1257	-36.55	-53.18	0	0	1.685871533	1.130830465	9.78	*Gr. truncatulinoides L*	NA
21_02_22_UPC093CTGT2	UPC093	CT	-2572.5	-36.32	-52.58	0	0	1.235864489	1.752948926	7.08	*Gr. truncatulinoides L*	NA
21_02_22_UPC141CTGT1	UPC141	CT	-2431.1	-36.70	-53.04	0	0	1.508970752	1.625476876	7.63	*Gr. truncatulinoides L*	NA
21_02_22_UPC141CTGT3	UPC141	CT	-2431.1	-36.70	-53.04	0	0	1.178256789	2.727856566	3.00	*Gr. truncatulinoides L*	NA
21_02_25 UPC145CTGT1	UPC145	CT	-1595.4	-36.49	-52.98	0	0	1.081224811	1.107109495	9.88	*Gr. truncatulinoides L*	NA
2021_02_17 UPC001CTGT1	UPC001	CT	-2053.1	-36.92	-53.41	0	0	1.35345704	2.656170207	3.29	*Gr. truncatulinoides R*	NA
2021_02_17 UPC001CTGT2	UPC001	CT	-2053.1	-36.92	-53.41	0	0	1.515348712	2.486683356	3.99	*Gr. truncatulinoides R*	NA
2021_02_17 UPC001CTGT3	UPC001	CT	-2053.1	-36.92	-53.41	0	0	1.358354252	2.359126306	4.52	*Gr. truncatulinoides R*	NA
2021_02_17 UPC023CTGT1	UPC023	CT	-2046.3	-36.39	-52.82	0	0	0.572421993	1.181903521	9.55	*Gr. truncatulinoides R*	NA

Sample ID	Core	Core Top/ Downcore	Depth (mbsf)	Latitude	Longitude	Sample Depth (cm)	Radiocarbon Age (cal BP)	δ13C VPDB	δ18O VPDB	Converted Temperature (°C)	Species	Encrustation Classification (A-D)/ Coiling Direction (L-R)
2021_02_17 UPC023CTGT2	UPC023	CT	-2046.3	-36.39	-52.82	0	0	1.753747728	2.773008996	2.81	*Gr. truncatulinoides R*	NA
2021_02_17 UPC023CTGT3	UPC023	CT	-2046.3	-36.39	-52.82	0	0	1.581232382	2.729459425	2.99	*Gr. truncatulinoides R*	NA
2021_02_17 UPC023CTGT4	UPC023	CT	-2046.3	-36.39	-52.82	0	0	1.915984223	2.621508076	3.44	*Gr. truncatulinoides R*	NA
2021_02_17 UPC028CTGT2	UPC028	CT	-2353	-36.15	-52.46	0	0	0.750431933	0.910138835	10.75	*Gr. truncatulinoides R*	NA
2021_02_17 UPC028CTGT3	UPC028	CT	-2353	-36.15	-52.46	0	0	0.844198179	2.737760108	2.96	*Gr. truncatulinoides R*	NA
2021_02_17 UPC033CTGT2	UPC033	CT	-2582.3	-36.60	-52.90	0	0	1.3367747	2.901822719	2.29	*Gr. truncatulinoides R*	NA
2021_02_17 UPC033CTGT4	UPC033	CT	-2582.3	-36.60	-52.90	0	0	0.937702814	2.982349143	1.96	*Gr. truncatulinoides R*	NA
2021_02_17 UPC033CTGT5	UPC033	CT	-2582.3	-36.60	-52.90	0	0	1.300243392	2.597444249	3.54	*Gr. truncatulinoides R*	NA
2021_02_17 UPC053CTGT2	UPC053	CT	-2115.2	-36.54	-53.02	0	0	0.864462098	2.359363694	4.52	*Gr. truncatulinoides R*	NA
2021_02_17 UPC058CTGT2	UPC058	CT	-2255.3	-36.73	-53.21	0	0	1.570514832	2.754889821	2.89	*Gr. truncatulinoides R*	NA
2021_02_17 UPC058CTGT3	UPC058	CT	-2255.3	-36.73	-53.21	0	0	1.475476727	2.95341206	2.08	*Gr. truncatulinoides R*	NA
2021_02_17 UPCO63CTGT1	UPC063	CT	-1255	-36.54	-53.17	0	0	1.349343071	2.428203063	4.24	*Gr. truncatulinoides R*	NA
2021_02_17 UPCO63CTGT2	UPC063	CT	-1255	-36.54	-53.17	0	0	1.812782558	2.719152541	3.03	*Gr. truncatulinoides R*	NA
21_02_22_UPCO63CTGT5	UPC063	CT	-1255	-36.54	-53.17	0	0	1.410519885	3.048656759	1.69	*Gr. truncatulinoides R*	NA
21_02_22_UPCO66CTGT2	UPC066	CT	-1257	-36.55	-53.18	0	0	1.515034205	2.906031875	2.27	*Gr. truncatulinoides R*	NA
21_02_22_UPCO66CTGT3	UPC066	CT	-1257	-36.55	-53.18	0	0	1.58344513	2.527350112	3.82	*Gr. truncatulinoides R*	NA
21_02_22_UPCO66CTGT4	UPC066	CT	-1257	-36.55	-53.18	0	0	1.392897043	2.544001109	3.76	*Gr. truncatulinoides R*	NA
21_02_22_UPCO66CTGT5	UPC066	CT	-1257	-36.55	-53.18	0	0	1.289668342	2.680053575	3.20	*Gr. truncatulinoides R*	NA
21_02_22_UPC081CTGT3	UPC081	CT	-1895.6	-36.83	-53.32	0	0	1.709095728	2.600664027	3.52	*Gr. truncatulinoides R*	NA
21_02_22_UPC081CTGT4	UPC081	CT	-1895.6	-36.83	-53.32	0	0	1.457404489	1.768545421	7.02	*Gr. truncatulinoides R*	NA
21_02_22_UPC081CTGT5	UPC081	CT	-1895.6	-36.83	-53.32	0	0	1.52951003	3.048167939	1.69	*Gr. truncatulinoides R*	NA
21_02_22_UPC081CTGT1	UPC081	CT	-1895.6	-36.83	-53.32	0	0	1.689332687	2.776301656	2.80	*Gr. truncatulinoides R*	NA
21_02_22_UPC093CTGT1	UPC093	CT	-2572.5	-36.32	-52.58	0	0	1.148817	2.796819978	2.72	*Gr. truncatulinoides R*	NA
21_02_22_UPC093CTGT3	UPC093	CT	-2572.5	-36.32	-52.58	0	0	1.474064086	2.93384583	2.16	*Gr. truncatulinoides R*	NA
21_02_22_UPC093CTGT5	UPC093	CT	-2572.5	-36.32	-52.58	0	0	1.397659309	1.848718493	6.67	*Gr. truncatulinoides R*	NA
21_02_22_UPC122CTGT1	UPC122	CT	-1154.2	-36.50	-53.21	0	0	1.290397921	2.660903497	3.27	*Gr. truncatulinoides R*	NA
21_02_22_UPC122CTGT2	UPC122	CT	-1154.2	-36.50	-53.21	0	0	1.575828736	2.826471374	2.60	*Gr. truncatulinoides R*	NA
21_02_22_UPC122CTGT3	UPC122	CT	-1154.2	-36.50	-53.21	0	0	1.530617485	2.727772712	3.00	*Gr. truncatulinoides R*	NA
21_02_22_UPC122CTGT4	UPC122	CT	-1154.2	-36.50	-53.21	0	0	1.519625708	2.820975306	2.62	*Gr. truncatulinoides R*	NA
21_02_22_UPC122CTGT5	UPC122	CT	-1154.2	-36.50	-53.21	0	0	1.695018696	2.733118725	2.98	*Gr. truncatulinoides R*	NA
21_02_22_UPC141CTGT2	UPC141	CT	-2431.1	-36.70	-53.04	0	0	1.438846802	2.932732571	2.16	*Gr. truncatulinoides R*	NA
21_02_22_UPC141CTGT5	UPC141	CT	-2431.1	-36.70	-53.04	0	0	1.467829945	2.679934888	3.20	*Gr. truncatulinoides R*	NA
21_02_25 UPC142CTGT1	UPC142	CT	-2682.1	-36.76	-52.98	0	0	0.897584876	1.225785535	9.36	*Gr. truncatulinoides R*	NA
21_02_25 UPC142CTGT2	UPC142	CT	-2682.1	-36.76	-52.98	0	0	1.596417142	1.688844088	7.36	*Gr. truncatulinoides R*	NA

Sample ID	Core	Core Top/ Downcore	Depth (mbsf)	Latitude	Longitude	Sample Depth (cm)	Radiocarbon Age (cal BP)	δ13C VPDB	δ18O VPDB	Converted Temperature (°C)	Species	Encrustation Classification (A-D)/ Coiling Direction (L-R)
21_02_25 UPC142CTGT3	UPC142	CT	-2682.1	-36.76	-52.98	0	0	1.697840124	2.74446999	2.93	*Gr. truncatulinoides R*	NA
21_02_25 UPC142CTGT4	UPC142	CT	-2682.1	-36.76	-52.98	0	0	1.456231638	1.529945241	8.04	*Gr. truncatulinoides R*	NA
21_02_25 UPC142CTGT5	UPC142	CT	-2682.1	-36.76	-52.98	0	0	1.40700019	1.311653209	8.99	*Gr. truncatulinoides R*	NA
21_02_25 UPC145CTGT2	UPC145	CT	-1595.4	-36.49	-52.98	0	0	1.586583104	3.264002742	0.83	*Gr. truncatulinoides R*	NA
21_02_25 UPC145CTGT3	UPC145	CT	-1595.4	-36.49	-52.98	0	0	1.976026748	3.035574363	1.75	*Gr. truncatulinoides R*	NA
21_02_25 UPC145CTGT4	UPC145	CT	-1595.4	-36.49	-52.98	0	0	1.37567736	3.329039497	0.57	*Gr. truncatulinoides R*	NA
21_02_25 UPC145CTGT5	UPC145	CT	-1595.4	-36.49	-52.98	0	0	1.535700316	2.964508307	2.03	*Gr. truncatulinoides R*	NA
2021_03_04_UPC028CTGT6	UPC028	CT	-2353	-36.15	-52.46	0	0	1.174722482	2.862125384	2.45	*Gr. truncatulinoides R*	NA
2021_03_04_UPC033CTGT6	UPC033	CT	-2582.3	-36.60	-52.90	0	0	1.016940956	3.214684912	1.02	*Gr. truncatulinoides R*	NA
2021_03_04_UPC033CTGT7	UPC033	CT	-2582.3	-36.60	-52.90	0	0	1.715689308	2.679169992	3.20	*Gr. truncatulinoides R*	NA
2021_03_04_UPC033CTGT8	UPC033	CT	-2582.3	-36.60	-52.90	0	0	0.815944519	1.500070051	8.17	*Gr. truncatulinoides R*	NA
2021_03_04_UPC063CTGT6	UPC063	CT	-1255	-36.54	-53.17	0	0	1.226033653	2.716398251	3.05	*Gr. truncatulinoides R*	NA
2021_03_04_UPC063CTGT7	UPC063	CT	-1255	-36.54	-53.17	0	0	1.135588987	2.096612297	5.62	*Gr. truncatulinoides R*	NA
2021_03_04_UPC063CTGT8	UPC063	CT	-1255	-36.54	-53.17	0	0	1.52439579	2.796435362	2.72	*Gr. truncatulinoides R*	NA
2021_03_04_UPC066CTGT6	UPC066	CT	-1257	-36.55	-53.18	0	0	1.611800155	2.859810044	2.46	*Gr. truncatulinoides R*	NA
2019-03-22 UPC 023 CT GT	UPC023	CT	-2046.3	-36.39	-52.82	0	0	1.462817749	2.498221783	3.95	*Gr. truncatulinoides U*	NA
2019-03-22 UPC 028 CT GT	UPC028	CT	-2353	-36.15	-52.46	0	0	1.283018484	2.964654208	2.03	*Gr. truncatulinoides U*	NA
2019-03-22 UPC 122 CT GT	UPC122	CT	-1154.2	-36.50	-53.21	0	0	1.76609233	2.338408223	4.61	*Gr. truncatulinoides U*	NA
2021_03_02_UPC001CTGR1	UPC001	CT	-2053.1	-36.92	-53.41	0	0	1.771923159	-0.422140207	16.81	*Gs. ruber white*	NA
2021_03_02_UPC022CTGR1	UPC022	CT	-2027.5	-36.46	-52.88	0	0	2.470394373	-0.772505253	18.45	*Gs. ruber white*	NA
2021_03_02_UPC022CTGR2	UPC022	CT	-2027.5	-36.46	-52.88	0	0	1.955365004	0.214745278	13.87	*Gs. ruber white*	NA
2021_03_02_UPC022CTGR3	UPC022	CT	-2027.5	-36.46	-52.88	0	0	0.922621832	-0.061952727	15.14	*Gs. ruber white*	NA
2021_03_02_UPC023CTGR1	UPC023	CT	-2046.3	-36.39	-52.82	0	0	1.65903913	-0.873776127	18.93	*Gs. ruber white*	NA
2021_03_02_UPC023CTGR2	UPC023	CT	-2046.3	-36.39	-52.82	0	0	1.69925664	-0.73092646	18.26	*Gs. ruber white*	NA
2021_03_02_UPC023CTGR3	UPC023	CT	-2046.3	-36.39	-52.82	0	0	0.404939072	-0.339084454	16.42	*Gs. ruber white*	NA
2021_03_02_UPC023CTGR4	UPC023	CT	-2046.3	-36.39	-52.82	0	0	0.547689063	-0.408350327	16.74	*Gs. ruber white*	NA
2021_03_02_UPC053CTGR1	UPC053	CT	-2115.2	-36.54	-53.02	0	0	0.679669589	-0.249403205	16.00	*Gs. ruber white*	NA
2021_03_02_UPC058CTGR1	UPC058	CT	-2255.3	-36.73	-53.21	0	0	0.221405281	-0.305040203	16.26	*Gs. ruber white*	NA
2021_03_02_UPC066CTGR1	UPC066	CT	-1257	-36.55	-53.18	0	0	1.308906223	0.378944775	13.13	*Gs. ruber white*	NA
2021_03_02_UPC093CTGR1	UPC093	CT	-2572.5	-36.32	-52.58	0	0	0.871524586	-0.110919483	15.36	*Gs. ruber white*	NA
2021_03_02_UPC093CTGR2	UPC093	CT	-2572.5	-36.32	-52.58	0	0	0.610674346	-0.434268084	16.86	*Gs. ruber white*	NA
2021_03_02_UPC093CTGR3	UPC093	CT	-2572.5	-36.32	-52.58	0	0	1.191016117	-0.690339478	18.07	*Gs. ruber white*	NA
2021_03_02_UPC093CTGR4	UPC093	CT	-2572.5	-36.32	-52.58	0	0	0.574611185	-0.773170953	18.46	*Gs. ruber white*	NA
2021_03_02_UPC122CTGR1	UPC122	CT	-1154.2	-36.50	-53.21	0	0	1.092759066	-1.469293023	21.79	*Gs. ruber white*	NA

Sample ID	Core	Core Top/ Downcore	Depth (mbsf)	Latitude	Longitude	Sample Depth (cm)	Radiocarbon Age (cal BP)	δ13C VPDB	δ18O VPDB	Converted Temperature (°C)	Species	Encrustation Classification (A-D)/ Coiling Direction (L-R)
2021_03_02_UPC141CTGR1	UPC141	CT	-2431.1	-36.70	-53.04	0	0	0.847565958	-0.656744785	17.91	*Gs. ruber white*	NA
2021_03_02_UPC141CTGR2	UPC141	CT	-2431.1	-36.70	-53.04	0	0	0.680487873	-1.145355669	20.23	*Gs. ruber white*	NA
2021_03_02_UPC142CTGR1	UPC142	CT	-2682.1	-36.76	-52.98	0	0	1.481466923	-0.853802628	18.84	*Gs. ruber white*	NA
2021_03_02_UPC142CTGR2	UPC142	CT	-2682.1	-36.76	-52.98	0	0	1.64690512	0.051132429	14.62	*Gs. ruber white*	NA
2021_03_02_UPC142CTGR3	UPC142	CT	-2682.1	-36.76	-52.98	0	0	2.213713285	-0.468010483	17.02	*Gs. ruber white*	NA
2021_03_02_UPC142CTGR4	UPC142	CT	-2682.1	-36.76	-52.98	0	0	2.475423917	-0.367133379	16.55	*Gs. ruber white*	NA
2021_03_02_UPC145CTGR1	UPC145	CT	-1595.4	-36.49	-52.98	0	0	1.998012661	-1.224556591	20.61	*Gs. ruber white*	NA
2021_03_02_UPC145CTGR2	UPC145	CT	-1595.4	-36.49	-52.98	0	0	1.918112571	-0.315766086	16.31	*Gs. ruber white*	NA
2021_03_02_UPC145CTGR3	UPC145	CT	-1595.4	-36.49	-52.98	0	0	2.563926916	-0.1388154	15.49	*Gs. ruber white*	NA
2021_03_04_UPC028CTGR1	UPC028	CT	-2353	-36.15	-52.46	0	0	2.017197165	-0.643271512	17.84	*Gs. ruber white*	NA
2021_03_04_UPC028CTGR2	UPC028	CT	-2353	-36.15	-52.46	0	0	0.807897388	-0.228433678	15.91	*Gs. ruber white*	NA
2021_03_04_UPC028CTGR3	UPC028	CT	-2353	-36.15	-52.46	0	0	0.106607056	-0.367086174	16.55	*Gs. ruber white*	NA
2021_03_04_UPC028CTGR4	UPC028	CT	-2353	-36.15	-52.46	0	0	0.095426894	-0.044345403	15.06	*Gs. ruber white*	NA
2021_04_27_UPC001CTNP1	UPC001	CT	-2053.1	-36.92	-53.41	0	0	0.190467444	1.972891568	6.15	*N. pachyderma*	NA
2021_04_27_UPC001CTNP2	UPC001	CT	-2053.1	-36.92	-53.41	0	0	0.363939929	1.215120514	9.41	*N. pachyderma*	NA
2021_04_27_UPC001CTNP3	UPC001	CT	-2053.1	-36.92	-53.41	0	0	0.368896494	1.430086261	8.47	*N. pachyderma*	NA
2021_04_27_UPC001CTNP4	UPC001	CT	-2053.1	-36.92	-53.41	0	0	0.471925236	1.685600002	7.37	*N. pachyderma*	NA
2021_04_27_UPC001CTNP5	UPC001	CT	-2053.1	-36.92	-53.41	0	0	0.653988089	2.066779204	5.75	*N. pachyderma*	NA
2021_04_27_UPC022CTNP1	UPC022	CT	-2027.5	-36.46	-52.88	0	0	0.566885498	1.644068784	7.55	*N. pachyderma*	NA
2021_04_27_UPC022CTNP2	UPC022	CT	-2027.5	-36.46	-52.88	0	0	0.531349042	1.302283341	9.03	*N. pachyderma*	NA
2021_04_27_UPC022CTNP3	UPC022	CT	-2027.5	-36.46	-52.88	0	0	0.7214981	1.838220316	6.72	*N. pachyderma*	NA
2021_04_27_UPC022CTNP4	UPC022	CT	-2027.5	-36.46	-52.88	0	0	0.341909055	1.894943937	6.48	*N. pachyderma*	NA
2021_04_27_UPC022CTNP5	UPC022	CT	-2027.5	-36.46	-52.88	0	0	0.781960828	1.948590135	6.25	*N. pachyderma*	NA
2021_04_27_UPC023CTNP1	UPC023	CT	-2046.3	-36.39	-52.82	0	0	0.14730746	1.546801276	7.97	*N. pachyderma*	NA
2021_04_27_UPC023CTNP2	UPC023	CT	-2046.3	-36.39	-52.82	0	0	0.037965419	1.450075292	8.39	*N. pachyderma*	NA
2021_03_04_UPC023CTNP3	UPC023	CT	-2046.3	-36.39	-52.82	0	0	1.300225998	2.048603805	5.83	*N. pachyderma*	NA
2021_04_27_UPC023CTNP3	UPC023	CT	-2046.3	-36.39	-52.82	0	0	0.668250904	1.678087806	7.40	*N. pachyderma*	NA
2021_04_27_UPC023CTNP4	UPC023	CT	-2046.3	-36.39	-52.82	0	0	0.250774635	1.259625201	9.21	*N. pachyderma*	NA
2021_04_27_UPC023CTNP5	UPC023	CT	-2046.3	-36.39	-52.82	0	0	-0.124407509	1.150405767	9.69	*N. pachyderma*	NA
2021_03_04_UPC028CTNP1	UPC028	CT	-2353	-36.15	-52.46	0	0	0.857869369	2.567772008	3.66	*N. pachyderma*	NA
2021_04_27_UPC028CTNP1	UPC028	CT	-2353	-36.15	-52.46	0	0	0.426320297	1.95655533	6.21	*N. pachyderma*	NA
2021_04_27_UPC028CTNP2	UPC028	CT	-2353	-36.15	-52.46	0	0	0.099961449	1.646466	7.54	*N. pachyderma*	NA
2021_04_27_UPC028CTNP3	UPC028	CT	-2353	-36.15	-52.46	0	0	-0.29677381	1.041642371	10.17	*N. pachyderma*	NA
2021_04_27_UPC028CTNP4	UPC028	CT	-2353	-36.15	-52.46	0	0	-0.45771958	1.121179523	9.82	*N. pachyderma*	NA

Sample ID	Core	Core Top/ Downcore	Depth (mbsf)	Latitude	Longitude	Sample Depth (cm)	Radiocarbon Age (cal BP)	δ13C VPDB	δ18O VPDB	Converted Temperature (°C)	Species	Encrustation Classification (A-D)/ Coiling Direction (L-R)
2021_04_27_UPC028CTNP5	UPC028	CT	-2353	-36.15	-52.46	0	0	-0.16618245	1.32865575	8.91	*N. pachyderma*	NA
2021_03_04_UPC033CTNP1	UPC033	CT	-2582.3	-36.60	-52.90	0	0	0.618204568	2.310659341	4.73	*N. pachyderma*	NA
2021_04_27_UPC033CTNP1	UPC033	CT	-2582.3	-36.60	-52.90	0	0	0.642886836	1.58687018	7.79	*N. pachyderma*	NA
2021_03_04_UPC033CTNP2	UPC033	CT	-2582.3	-36.60	-52.90	0	0	1.11635786	1.631712844	7.60	*N. pachyderma*	NA
2021_04_27_UPC033CTNP2	UPC033	CT	-2582.3	-36.60	-52.90	0	0	-0.051400844	1.570784527	7.86	*N. pachyderma*	NA
2021_04_27_UPC033CTNP3	UPC033	CT	-2582.3	-36.60	-52.90	0	0	0.72199547	2.027185186	5.92	*N. pachyderma*	NA
2021_04_27_UPC033CTNP4	UPC033	CT	-2582.3	-36.60	-52.90	0	0	-0.093019677	1.239879138	9.30	*N. pachyderma*	NA
2021_04_27_UPC033CTNP5	UPC033	CT	-2582.3	-36.60	-52.90	0	0	0.608494992	2.148198019	5.41	*N. pachyderma*	NA
2021_04_21_UPC053CTNP1	UPC053	CT	-2115.2	-36.54	-53.02	0	0	0.474665703	2.185162605	5.25	*N. pachyderma*	NA
2021_04_21_UPC053CTNP2	UPC053	CT	-2115.2	-36.54	-53.02	0	0	0.458622748	2.232631879	5.05	*N. pachyderma*	NA
2021_04_21_UPC053CTNP3	UPC053	CT	-2115.2	-36.54	-53.02	0	0	0.639678851	2.180726909	5.27	*N. pachyderma*	NA
2021_04_21_UPC053CTNP4	UPC053	CT	-2115.2	-36.54	-53.02	0	0	0.462598661	1.881897614	6.53	*N. pachyderma*	NA
2021_03_15_UPC058CTNP1	UPC058	CT	-2255.3	-36.73	-53.21	0	0	0.857524572	1.493522953	8.20	*N. pachyderma*	NA
2021_04_21_UPC058CTNP1	UPC058	CT	-2255.3	-36.73	-53.21	0	0	0.554009013	1.762206524	7.04	*N. pachyderma*	NA
2021_03_15_UPC058CTNP3	UPC058	CT	-2255.3	-36.73	-53.21	0	0	0.502906455	1.638094078	7.57	*N. pachyderma*	NA
2021_04_21_UPC058CTNP3	UPC058	CT	-2255.3	-36.73	-53.21	0	0	0.41204052	1.905750197	6.43	*N. pachyderma*	NA
2021_04_21_UPC058CTNP4	UPC058	CT	-2255.3	-36.73	-53.21	0	0	0.414819475	1.513765904	8.11	*N. pachyderma*	NA
2021_04_21_UPC058CTNP5	UPC058	CT	-2255.3	-36.73	-53.21	0	0	0.383297713	1.69334359	7.34	*N. pachyderma*	NA
2021_04_21_UPC063CTNP1	UPC063	CT	-1255	-36.54	-53.17	0	0	0.679903191	2.161324545	5.35	*N. pachyderma*	NA
2021_04_21_UPC063CTNP2	UPC063	CT	-1255	-36.54	-53.17	0	0	0.843424225	1.776536328	6.98	*N. pachyderma*	NA
2021_04_21_UPC063CTNP3	UPC063	CT	-1255	-36.54	-53.17	0	0	0.648484374	1.94713693	6.25	*N. pachyderma*	NA
2021_04_21_UPC063CTNP4	UPC063	CT	-1255	-36.54	-53.17	0	0	0.688396818	2.000420811	6.03	*N. pachyderma*	NA
2021_04_21_UPC063CTNP5	UPC063	CT	-1255	-36.54	-53.17	0	0	0.486531963	1.83522952	6.73	*N. pachyderma*	NA
2021_04_21_UPC066CTNP1	UPC066	CT	-1257	-36.55	-53.18	0	0	0.861729507	2.078593489	5.70	*N. pachyderma*	NA
2021_04_21_UPC066CTNP2	UPC066	CT	-1257	-36.55	-53.18	0	0	0.857685024	1.854619009	6.65	*N. pachyderma*	NA
2021_04_21_UPC066CTNP3	UPC066	CT	-1257	-36.55	-53.18	0	0	0.911830407	2.044353247	5.84	*N. pachyderma*	NA
2021_03_15_UPC066CTNP4	UPC066	CT	-1257	-36.55	-53.18	0	0	1.022871927	1.796458948	6.90	*N. pachyderma*	NA
2021_04_21_UPC066CTNP4	UPC066	CT	-1257	-36.55	-53.18	0	0	0.937208094	2.033541383	5.89	*N. pachyderma*	NA
2021_04_21_UPC066CTNP5	UPC066	CT	-1257	-36.55	-53.18	0	0	0.885958082	2.01047923	5.99	*N. pachyderma*	NA
2021_03_10_UPC081CTNP1	UPC081	CT	-1895.6	-36.83	-53.32	0	0	1.0519635	1.793029088	6.91	*N. pachyderma*	NA
2021_04_21_UPC081CTNP1	UPC081	CT	-1895.6	-36.83	-53.32	0	0	0.544953647	1.885206597	6.52	*N. pachyderma*	NA
2021_04_21_UPC081CTNP2	UPC081	CT	-1895.6	-36.83	-53.32	0	0	0.445488678	1.798341513	6.89	*N. pachyderma*	NA
2021_04_21_UPC081CTNP3	UPC081	CT	-1895.6	-36.83	-53.32	0	0	1.049772324	2.023930186	5.93	*N. pachyderma*	NA
2021_04_21_UPC081CTNP4	UPC081	CT	-1895.6	-36.83	-53.32	0	0	0.630454431	2.106864859	5.58	*N. pachyderma*	NA

Sample ID	Core	Core Top/ Downcore	Depth (mbsf)	Latitude	Longitude	Sample Depth (cm)	Radiocarbon Age (cal BP)	δ13C VPDB	δ18O VPDB	Converted Temperature (°C)	Species	Encrustation Classification (A-D)/ Coiling Direction (L-R)
2021_04_21_UPC081CTNP5	UPC081	CT	-1895.6	-36.83	-53.32	0	0	0.679159426	1.969959696	6.16	*N. pachyderma*	NA
2021_03_04_UPC093CTNP1	UPC093	CT	-2572.5	-36.32	-52.58	0	0	0.411403779	1.61871846	7.66	*N. pachyderma*	NA
2021_03_10_UPC093CTNP1	UPC093	CT	-2572.5	-36.32	-52.58	0	0	0.701327496	1.450253325	8.38	*N. pachyderma*	NA
2021_04_19_UPC093CTNP1	UPC093	CT	-2572.5	-36.32	-52.58	0	0	0.968970792	1.445518056	8.40	*N. pachyderma*	NA
2021_03_10_UPC093CTNP2	UPC093	CT	-2572.5	-36.32	-52.58	0	0	0.311307818	1.41943032	8.52	*N. pachyderma*	NA
2021_04_19_UPC093CTNP2	UPC093	CT	-2572.5	-36.32	-52.58	0	0	0.014015346	1.064621001	10.07	*N. pachyderma*	NA
2021_03_10_UPC093CTNP3	UPC093	CT	-2572.5	-36.32	-52.58	0	0	0.158155147	1.177244041	9.57	*N. pachyderma*	NA
2021_04_19_UPC093CTNP3	UPC093	CT	-2572.5	-36.32	-52.58	0	0	-0.401083277	0.926786663	10.68	*N. pachyderma*	NA
2021_03_10_UPC093CTNP4	UPC093	CT	-2572.5	-36.32	-52.58	0	0	0.541013668	1.749585712	7.10	*N. pachyderma*	NA
2021_04_19_UPC093CTNP4	UPC093	CT	-2572.5	-36.32	-52.58	0	0	-0.731561718	0.722948685	11.58	*N. pachyderma*	NA
2021_04_19_UPC093CTNP5	UPC093	CT	-2572.5	-36.32	-52.58	0	0	0.142012358	0.971626991	10.48	*N. pachyderma*	NA
2021_03_10_UPC122CTNP1	UPC122	CT	-1154.2	-36.50	-53.21	0	0	0.418264761	1.275313718	9.14	*N. pachyderma*	NA
2021_04_19_UPC122CTNP1	UPC122	CT	-1154.2	-36.50	-53.21	0	0	1.037632451	1.761843005	7.04	*N. pachyderma*	NA
2021_03_10_UPC122CTNP2	UPC122	CT	-1154.2	-36.50	-53.21	0	0	1.087047409	1.736462325	7.15	*N. pachyderma*	NA
2021_04_19_UPC122CTNP2	UPC122	CT	-1154.2	-36.50	-53.21	0	0	0.816755763	1.711219717	7.26	*N. pachyderma*	NA
2021_04_19_UPC122CTNP3	UPC122	CT	-1154.2	-36.50	-53.21	0	0	1.07574773	1.848181621	6.68	*N. pachyderma*	NA
2021_03_10_UPC122CTNP4	UPC122	CT	-1154.2	-36.50	-53.21	0	0	0.389456041	1.562991074	7.90	*N. pachyderma*	NA
2021_04_19_UPC122CTNP4	UPC122	CT	-1154.2	-36.50	-53.21	0	0	0.750592825	1.635052349	7.59	*N. pachyderma*	NA
2021_03_10_UPC122CTNP5	UPC122	CT	-1154.2	-36.50	-53.21	0	0	0.89738836	1.785612018	6.94	*N. pachyderma*	NA
2021_04_19_UPC122CTNP5	UPC122	CT	-1154.2	-36.50	-53.21	0	0	0.904084269	1.65039217	7.52	*N. pachyderma*	NA
2021_03_10_UPC122CTNP6	UPC122	CT	-1154.2	-36.50	-53.21	0	0	0.674074163	1.982225652	6.11	*N. pachyderma*	NA
2021_04_19_UPC122CTNP6	UPC122	CT	-1154.2	-36.50	-53.21	0	0	1.017743048	1.777574358	6.98	*N. pachyderma*	NA
2021_03_10_UPC141CTNP1	UPC141	CT	-2431.1	-36.70	-53.04	0	0	0.724134049	1.075572368	10.02	*N. pachyderma*	NA
2021_04_19_UPC141CTNP1	UPC141	CT	-2431.1	-36.70	-53.04	0	0	0.794263777	1.530454444	8.04	*N. pachyderma*	NA
2021_03_10_UPC141CTNP2	UPC141	CT	-2431.1	-36.70	-53.04	0	0	0.513655189	1.586686289	7.80	*N. pachyderma*	NA
2021_04_19_UPC141CTNP2	UPC141	CT	-2431.1	-36.70	-53.04	0	0	0.741422057	1.554033918	7.94	*N. pachyderma*	NA
2021_04_19_UPC141CTNP3	UPC141	CT	-2431.1	-36.70	-53.04	0	0	0.707058472	1.547030525	7.97	*N. pachyderma*	NA
2021_04_19_UPC141CTNP4	UPC141	CT	-2431.1	-36.70	-53.04	0	0	0.46064162	1.637099437	7.58	*N. pachyderma*	NA
2021_03_10_UPC142CTNP1	UPC142	CT	-2682.1	-36.76	-52.98	0	0	0.09054567	1.454879468	8.36	*N. pachyderma*	NA
2021_04_19_UPC142CTNP1	UPC142	CT	-2682.1	-36.76	-52.98	0	0	0.614664796	1.357886089	8.79	*N. pachyderma*	NA
2021_03_10_UPC142CTNP2	UPC142	CT	-2682.1	-36.76	-52.98	0	0	0.851173341	1.876626401	6.55	*N. pachyderma*	NA
2021_04_19_UPC142CTNP2	UPC142	CT	-2682.1	-36.76	-52.98	0	0	0.646634572	1.670912622	7.43	*N. pachyderma*	NA
2021_03_10_UPC142CTNP3	UPC142	CT	-2682.1	-36.76	-52.98	0	0	0.407556512	1.933251258	6.31	*N. pachyderma*	NA
2021_04_19_UPC142CTNP3	UPC142	CT	-2682.1	-36.76	-52.98	0	0	0.774701881	1.42612203	8.49	*N. pachyderma*	NA

Sample ID	Core	Core Top/ Downcore	Depth (mbsf)	Latitude	Longitude	Sample Depth (cm)	Radiocarbon Age (cal BP)	δ13C VPDB	δ18O VPDB	Converted Temperature (°C)	Species	Encrustation Classification (A-D)/ Coiling Direction (L-R)
2021_03_10_UPC142CTNP4	UPC142	CT	-2682.1	-36.76	-52.98	0	0	0.705558004	1.301432103	9.03	*N. pachyderma*	NA
2021_04_19_UPC142CTNP4	UPC142	CT	-2682.1	-36.76	-52.98	0	0	0.582151404	1.823595885	6.78	*N. pachyderma*	NA
2021_03_10_UPC142CTNP5	UPC142	CT	-2682.1	-36.76	-52.98	0	0	0.454978446	1.755395105	7.07	*N. pachyderma*	NA
2021_04_19_UPC142CTNP5	UPC142	CT	-2682.1	-36.76	-52.98	0	0	0.590771545	1.16575536	9.62	*N. pachyderma*	NA
2021_03_04_UPC145CTNP1	UPC145	CT	-1595.4	-36.49	-52.98	0	0	1.191765833	1.955824696	6.22	*N. pachyderma*	NA
2021_03_10_UPC145CTNP1	UPC145	CT	-1595.4	-36.49	-52.98	0	0	0.969867318	2.165254315	5.33	*N. pachyderma*	NA
2021_04_19_UPC145CTNP1	UPC145	CT	-1595.4	-36.49	-52.98	0	0	0.94833583	1.522267868	8.07	*N. pachyderma*	NA
2021_04_19_UPC145CTNP2	UPC145	CT	-1595.4	-36.49	-52.98	0	0	0.921025719	1.725723423	7.20	*N. pachyderma*	NA
2021_03_10_UPC145CTNP3	UPC145	CT	-1595.4	-36.49	-52.98	0	0	0.987469477	1.932484583	6.32	*N. pachyderma*	NA
2021_04_19_UPC145CTNP3	UPC145	CT	-1595.4	-36.49	-52.98	0	0	0.868582672	1.771648468	7.00	*N. pachyderma*	NA
2021_03_10_UPC145CTNP4	UPC145	CT	-1595.4	-36.49	-52.98	0	0	0.750590043	1.952339507	6.23	*N. pachyderma*	NA
2021_04_19_UPC145CTNP4	UPC145	CT	-1595.4	-36.49	-52.98	0	0	0.831467734	1.650100006	7.52	*N. pachyderma*	NA
2021_03_10_UPC145CTNP5	UPC145	CT	-1595.4	-36.49	-52.98	0	0	0.859815677	2.08558607	5.67	*N. pachyderma*	NA
2021_04_19_UPC145CTNP5	UPC145	CT	-1595.4	-36.49	-52.98	0	0	0.588837313	1.827270594	6.76	*N. pachyderma*	NA
2021_03_08_UPC001CTGG1	UPC001	CT	-2053.1	-36.92	-53.41	0	0	1.066397704	2.337756123	4.61	*Gt. glutinata*	NA
2021_03_08_UPC022CTGG1	UPC022	CT	-2027.5	-36.46	-52.88	0	0	0.563152629	0.932736708	10.65	*Gt. glutinata*	NA
2021_03_08_UPC033CTGG1	UPC033	CT	-2582.3	-36.60	-52.90	0	0	-0.63361267	1.730171419	7.18	*Gt. glutinata*	NA
2021_03_08_UPC033CTGG2	UPC033	CT	-2582.3	-36.60	-52.90	0	0	0.010620578	1.345108781	8.84	*Gt. glutinata*	NA
2021_03_08_UPC033CTGG3	UPC033	CT	-2582.3	-36.60	-52.90	0	0	0.311091068	1.720138825	7.22	*Gt. glutinata*	NA
2021_03_08_UPC063CTGG1	UPC063	CT	-1255	-36.54	-53.17	0	0	0.250528055	2.816062681	2.64	*Gt. glutinata*	NA
2021_03_08_UPC066CTGG1	UPC066	CT	-1257	-36.55	-53.18	0	0	0.583451409	2.150483134	5.40	*Gt. glutinata*	NA
2021_03_08_UPC081CTGG1	UPC081	CT	-1895.6	-36.83	-53.32	0	0	1.315145575	2.737537862	2.96	*Gt. glutinata*	NA
2021_03_08_UPC093CTGG1	UPC093	CT	-2572.5	-36.32	-52.58	0	0	0.45227636	0.099248874	14.40	*Gt. glutinata*	NA
2021_03_08_UPC093CTGG2	UPC093	CT	-2572.5	-36.32	-52.58	0	0	0.871375841	0.256596392	13.68	*Gt. glutinata*	NA
2021_03_08_UPC093CTGG3	UPC093	CT	-2572.5	-36.32	-52.58	0	0	0.250675398	-0.111241792	15.37	*Gt. glutinata*	NA
2021_03_08_UPC122CTGG1	UPC122	CT	-1154.2	-36.50	-53.21	0	0	0.731190977	2.396423397	4.37	*Gt. glutinata*	NA
2021_03_08_UPC122CTGG2	UPC122	CT	-1154.2	-36.50	-53.21	0	0	1.193689734	2.444433058	4.17	*Gt. glutinata*	NA
2021_03_08_UPC028CTGG1	UPC028	CT	-2353	-36.15	-52.46	0	0	1.532080535	0.538079029	12.41	*Gt. glutinata*	NA
2021_03_08_UPC028CTGG2	UPC028	CT	-2353	-36.15	-52.46	0	0	1.807216477	1.835483669	6.73	*Gt. glutinata*	NA
2021_03_08_UPC028CTGG3	UPC028	CT	-2353	-36.15	-52.46	0	0	1.029173414	0.477700684	12.68	*Gt. glutinata*	NA
2021_03_08_UPC141CTGG1	UPC141	CT	-2431.1	-36.70	-53.04	0	0	2.636822595	0.512708319	12.52	*Gt. glutinata*	NA
2021_03_08_UPC141CTGG2	UPC141	CT	-2431.1	-36.70	-53.04	0	0	3.918081764	2.154894017	5.38	*Gt. glutinata*	NA
2021_03_08_UPC142CTGG1	UPC142	CT	-2682.1	-36.76	-52.98	0	0	1.673875253	0.758707414	11.42	*Gt. glutinata*	NA
2021_03_08_UPC142CTGG2	UPC142	CT	-2682.1	-36.76	-52.98	0	0	3.086605308	3.030019738	1.77	*Gt. glutinata*	NA
2021_03_08_UPC145CTGG1	UPC145	CT	-1595.4	-36.49	-52.98	0	0	5.139050916	2.725955623	3.01	*Gt. glutinata*	NA
2021_03_08_UPC145CTGG2	UPC145	CT	-1595.4	-36.49	-52.98	0	0	2.792747358	2.916963477	2.23	*Gt. glutinata*	NA

Appendix C.2 Downcore stable isotopes

Sample ID	Core	Core Top/ Downcore	Depth (mbsf)	Latitude	Longitude	Sample Depth (cm)	Radiocarbon Age (cal BP)	δ13C VPDB	δ18O VPDB	Converted Temperature (°C)	Species	Encrustation Classification (A-D)/ Coiling Direction (L-R)
2021_07_12_UPC028 _41-43cm_GR1	UPC028	DC	-2353	-36.2	-52.46	41	548.6	1.129704154	-1.073447674	19.89	*Gs. ruber white*	NA
2021_07_12_UPC028 _41-43cm_GR2	UPC028	DC	-2353	-36.2	-52.46	41	548.6	0.775538357	-0.701152646	18.12	*Gs. ruber white*	NA
2021_07_12_UPC028 _41-43cm_GR3	UPC028	DC	-2353	-36.2	-52.46	41	548.6	0.667223109	-0.103619587	15.33	*Gs. ruber white*	NA
2021_07_12_UPC028 _41-43cm_GR4	UPC028	DC	-2353	-36.2	-52.46	41	548.6	0.274915457	-1.010878511	19.59	*Gs. ruber white*	NA
2021_07_12_UPC028 _41-43cm_GR5	UPC028	DC	-2353	-36.2	-52.46	41	548.6	1.35375772	-1.24362196	20.70	*Gs. ruber white*	NA
2021_07_14_UPC028_83-85cm_GR1	UPC028	DC	-2353	-36.2	-52.46	83	1110.6	1.46360044	-0.918488099	19.15	*Gs. ruber white*	NA
2021_07_14_UPC028_83-85cm_GR2	UPC028	DC	-2353	-36.2	-52.46	83	1110.6	-0.043813442	-0.671112447	17.98	*Gs. ruber white*	NA
2021_07_14_UPC028_83-85cm_GR3	UPC028	DC	-2353	-36.2	-52.46	83	1110.6	0.896315129	-0.540584084	17.36	*Gs. ruber white*	NA
2021_07_14_UPC028_83-85cm_GR4	UPC028	DC	-2353	-36.2	-52.46	83	1110.6	0.874313873	-0.3829986	16.63	*Gs. ruber white*	NA
2021_07_12_UPC028 _118-120cm_GR1	UPC028	DC	-2353	-36.2	-52.46	118	1727.3	1.696816875	-0.266643682	16.08	*Gs. ruber white*	NA
2021_07_12_UPC028 _118-120cm_GR2	UPC028	DC	-2353	-36.2	-52.46	118	1727.3	1.047689153	-1.214542221	20.56	*Gs. ruber white*	NA
2021_07_12_UPC028 _118-120cm_GR3	UPC028	DC	-2353	-36.2	-52.46	118	1727.3	1.434211272	-0.559720641	17.45	*Gs. ruber white*	NA
2021_07_12_UPC028 _118-120cm_GR4	UPC028	DC	-2353	-36.2	-52.46	118	1727.3	1.162576197	-1.105215945	20.04	*Gs. ruber white*	NA
2021_07_12_UPC028 _118-120cm_GR5	UPC028	DC	-2353	-36.2	-52.46	118	1727.3	1.191358278	-0.653915709	17.89	*Gs. ruber white*	NA
2021_07_14_UPC028_148-150cm_GR1	UPC028	DC	-2353	-36.2	-52.46	148	2340.7	1.12599083	-1.083244688	19.93	*Gs. ruber white*	NA
2021_07_14_UPC028_148-150cm_GR2	UPC028	DC	-2353	-36.2	-52.46	148	2340.7	0.73820118	-1.184116381	20.42	*Gs. ruber white*	NA
2021_07_14_UPC028_148-150cm_GR3	UPC028	DC	-2353	-36.2	-52.46	148	2340.7	0.744317085	-0.461747963	16.99	*Gs. ruber white*	NA
2021_07_14_UPC028_148-150cm_GR4	UPC028	DC	-2353	-36.2	-52.46	148	2340.7	1.622414286	-1.149830593	20.25	*Gs. ruber white*	NA
2021_07_12_UPC028_176-178cm_GR1	UPC028	DC	-2353	-36.2	-52.46	176	2913.3	0.848578087	-0.84257506	18.79	*Gs. ruber white*	NA
2021_07_12_UPC028_176-178cm_GR2	UPC028	DC	-2353	-36.2	-52.46	176	2913.3	0.864007292	-0.568815724	17.49	*Gs. ruber white*	NA
2021_07_12_UPC028_176-178cm_GR3	UPC028	DC	-2353	-36.2	-52.46	176	2913.3	1.072390737	-0.613828223	17.71	*Gs. ruber white*	NA
2021_07_12_UPC028_176-178cm_GR4	UPC028	DC	-2353	-36.2	-52.46	176	2913.3	0.714237591	-0.617655739	17.72	*Gs. ruber white*	NA
2021_07_12_UPC028_176-178cm_GR5	UPC028	DC	-2353	-36.2	-52.46	176	2913.3	1.351725953	-0.815976158	18.66	*Gs. ruber white*	NA
2021_07_14_UPC028_254-256cm_GR1	UPC028	DC	-2353	-36.2	-52.46	254	4390.5	1.101169651	-0.751428152	18.35	*Gs. ruber white*	NA
2021_07_14_UPC028_254-256cm_GR2	UPC028	DC	-2353	-36.2	-52.46	254	4390.5	1.229228957	-0.514229714	17.24	*Gs. ruber white*	NA
2021_07_14_UPC028_254-256cm_GR3	UPC028	DC	-2353	-36.2	-52.46	254	4390.5	1.08321737	-0.801176809	18.59	*Gs. ruber white*	NA
2021_07_14_UPC028_254-256cm_GR4	UPC028	DC	-2353	-36.2	-52.46	254	4390.5	0.9778628	-0.857259086	18.86	*Gs. ruber white*	NA
2021_07_14_UPC028_254-256cm_GR5	UPC028	DC	-2353	-36.2	-52.46	254	4390.5	0.966630082	-1.112976204	20.08	*Gs. ruber white*	NA
2021_07_12_UPC028_282-284cm_GR1	UPC028	DC	-2353	-36.2	-52.46	282	4905.9	1.485177567	-0.455358434	16.96	*Gs. ruber white*	NA
2021_07_12_UPC028_282-284cm_GR2	UPC028	DC	-2353	-36.2	-52.46	282	4905.9	1.19295403	-0.080230199	15.22	*Gs. ruber white*	NA
2021_07_12_UPC028_282-284cm_GR3	UPC028	DC	-2353	-36.2	-52.46	282	4905.9	1.18969164	-0.502739618	17.18	*Gs. ruber white*	NA
2021_07_12_UPC028_282-284cm_GR4	UPC028	DC	-2353	-36.2	-52.46	282	4905.9	0.936831876	-0.872024127	18.93	*Gs. ruber white*	NA
2021_07_12_UPC028_282-284cm_GR5	UPC028	DC	-2353	-36.2	-52.46	282	4905.9	1.154002639	-0.470500699	17.03	*Gs. ruber white*	NA
2021_07_16_UPC028_303-305cm_GR1	UPC028	DC	-2353	-36.2	-52.46	303	5292.5	1.036353986	-0.053241017	15.10	*Gs. ruber white*	NA
2021_07_16_UPC028_303-305cm_GR2	UPC028	DC	-2353	-36.2	-52.46	303	5292.5	1.243158774	-0.275924461	16.13	*Gs. ruber white*	NA
2021_07_16_UPC028_303-305cm_GR3	UPC028	DC	-2353	-36.2	-52.46	303	5292.5	0.851376466	-1.180330072	20.40	*Gs. ruber white*	NA

Sample ID	Core	Core Top/ Downcore	Depth (mbsf)	Latitude	Longitude	Sample Depth (cm)	Radiocarbon Age (cal BP)	δ13C VPDB	δ18O VPDB	Converted Temperature (°C)	Species	Encrustation Classification (A-D)/ Coiling Direction (L-R)
2021_07_16_UPC028_303-305cm_GR4	UPC028	DC	-2353	-36.2	-52.46	303	5292.5	1.152051058	-0.467597713	17.02	*Gs. ruber white*	NA
2021_07_16_UPC028_303-305cm_GR5	UPC028	DC	-2353	-36.2	-52.46	303	5292.5	1.268351728	-0.144694747	15.52	*Gs. ruber white*	NA
2021_07_12_UPC028_324-326cm_GR1	UPC028	DC	-2353	-36.2	-52.46	324	5803.7	2.131434662	-0.680608086	18.02	*Gs. ruber white*	NA
2021_07_12_UPC028_324-326cm_GR3	UPC028	DC	-2353	-36.2	-52.46	324	5803.7	1.485713786	-0.488085988	17.12	*Gs. ruber white*	NA
2021_07_12_UPC028_324-326cm_GR4	UPC028	DC	-2353	-36.2	-52.46	324	5803.7	1.219634226	-0.497501858	17.16	*Gs. ruber white*	NA
2021_07_12_UPC028_324-326cm_GR5	UPC028	DC	-2353	-36.2	-52.46	324	5803.7	1.755043119	-0.472572075	17.04	*Gs. ruber white*	NA
2021_07_16_UPC028_347-349cm_GR1	UPC028	DC	-2353	-36.2	-52.46	347	6433.7	1.078796074	0.140598301	14.21	*Gs. ruber white*	NA
2021_07_16_UPC028_347-349cm_GR2	UPC028	DC	-2353	-36.2	-52.46	347	6433.7	1.683721717	-0.44530213	16.92	*Gs. ruber white*	NA
2021_07_16_UPC028_347-349cm_GR3	UPC028	DC	-2353	-36.2	-52.46	347	6433.7	1.557478434	-0.176232648	15.67	*Gs. ruber white*	NA
2021_07_16_UPC028_347-349cm_GR4	UPC028	DC	-2353	-36.2	-52.46	347	6433.7	1.286327761	-0.477420794	17.07	*Gs. ruber white*	NA
2021_07_12_UPC028_361-363cm_GR1	UPC028	DC	-2353	-36.2	-52.46	361	6815.3	1.7256931	-0.927645988	19.19	*Gs. ruber white*	NA
2021_07_12_UPC028_361-363cm_GR2	UPC028	DC	-2353	-36.2	-52.46	361	6815.3	1.146262025	-0.591003473	17.60	*Gs. ruber white*	NA
2021_07_12_UPC028_361-363cm_GR4	UPC028	DC	-2353	-36.2	-52.46	361	6815.3	1.135108496	-0.535124915	17.34	*Gs. ruber white*	NA
2021_07_12_UPC028_361-363cm_GR5	UPC028	DC	-2353	-36.2	-52.46	361	6815.3	0.672009652	-0.887272407	19.00	*Gs. ruber white*	NA
2021_07_16_UPC028_382-384cm_GR1	UPC028	DC	-2353	-36.2	-52.46	382	7390.1	1.340740469	0.196873597	13.95	*Gs. ruber white*	NA
2021_07_16_UPC028_382-384cm_GR2	UPC028	DC	-2353	-36.2	-52.46	382	7390.1	1.380428292	-0.34994089	16.47	*Gs. ruber white*	NA
2021_07_16_UPC028_382-384cm_GR3	UPC028	DC	-2353	-36.2	-52.46	382	7390.1	1.397349147	-0.419195368	16.79	*Gs. ruber white*	NA
2021_07_16_UPC028_382-384cm_GR4	UPC028	DC	-2353	-36.2	-52.46	382	7390.1	1.661019358	-0.703301249	18.13	*Gs. ruber white*	NA
2021_07_16_UPC028_382-384cm_GR5	UPC028	DC	-2353	-36.2	-52.46	382	7390.1	1.584440924	-0.423456969	16.81	*Gs. ruber white*	NA
2021_07_14_UPC028_396-398cm_GR1	UPC028	DC	-2353	-36.2	-52.46	396	7772.2	0.983995296	-0.589998336	17.59	*Gs. ruber white*	NA
2021_07_14_UPC028_396-398cm_GR2	UPC028	DC	-2353	-36.2	-52.46	396	7772.2	1.433549363	-0.476132905	17.06	*Gs. ruber white*	NA
2021_07_14_UPC028_396-398cm_GR3	UPC028	DC	-2353	-36.2	-52.46	396	7772.2	1.204260571	-0.011000854	14.90	*Gs. ruber white*	NA
2021_07_14_UPC028_396-398cm_GR4	UPC028	DC	-2353	-36.2	-52.46	396	7772.2	0.787518589	-0.27257444	16.11	*Gs. ruber white*	NA
2021_07_14_UPC028_396-398cm_GR5	UPC028	DC	-2353	-36.2	-52.46	396	7772.2	1.924492758	-0.745337837	18.33	*Gs. ruber white*	NA
2021_07_16_UPC028_422-424cm_GR2	UPC028	DC	-2353	-36.2	-52.46	422	8419.5	0.55725566	-0.320566969	16.33	*Gs. ruber white*	NA
2021_07_16_UPC028_422-424cm_GR3	UPC028	DC	-2353	-36.2	-52.46	422	8419.5	0.630886153	-0.477434169	17.07	*Gs. ruber white*	NA
2021_07_16_UPC028_422-424cm_GR4	UPC028	DC	-2353	-36.2	-52.46	422	8419.5	0.824926832	0.139290947	14.22	*Gs. ruber white*	NA
2021_07_14_UPC028_447-449cm_GR1	UPC028	DC	-2353	-36.2	-52.46	447	9029.8	0.684113372	-0.047814714	15.07	*Gs. ruber white*	NA
2021_07_14_UPC028_447-449cm_GR2	UPC028	DC	-2353	-36.2	-52.46	447	9029.8	0.143188059	-0.590085844	17.59	*Gs. ruber white*	NA
2021_07_14_UPC028_447-449cm_GR3	UPC028	DC	-2353	-36.2	-52.46	447	9029.8	0.293425874	0.352919236	13.24	*Gs. ruber white*	NA
2021_07_14_UPC028_447-449cm_GR4	UPC028	DC	-2353	-36.2	-52.46	447	9029.8	1.132339058	-0.416794231	16.78	*Gs. ruber white*	NA
2021_07_14_UPC028_447-449cm_GR5	UPC028	DC	-2353	-36.2	-52.46	447	9029.8	1.263399284	-0.364054039	16.54	*Gs. ruber white*	NA
2021_07_16_UPC028_467-469cm_GR1	UPC028	DC	-2353	-36.2	-52.46	467	9518.3	1.224239843	-0.244981167	15.98	*Gs. ruber white*	NA
2021_07_16_UPC028_467-469cm_GR2	UPC028	DC	-2353	-36.2	-52.46	467	9518.3	1.206526259	-0.838308962	18.77	*Gs. ruber white*	NA
2021_07_16_UPC028_467-469cm_GR3	UPC028	DC	-2353	-36.2	-52.46	467	9518.3	0.594629581	-0.454166365	16.96	*Gs. ruber white*	NA
2021_07_16_UPC028_467-469cm_GR4	UPC028	DC	-2353	-36.2	-52.46	467	9518.3	1.36881173	-0.4676018	17.02	*Gs. ruber white*	NA

Sample ID	Core	Core Top/ Downcore	Depth (mbsf)	Latitude	Longitude	Sample Depth (cm)	Radiocarbon Age (cal BP)	δ13C VPDB	δ18O VPDB	Converted Temperature (°C)	Species	Encrustation Classification (A-D)/ Coiling Direction (L-R)
2021_07_16_UPC028_467-469cm_GR6	UPC028	DC	-2353	-36.2	-52.46	467	9518.3	0.987167299	-0.863264239	18.88	*Gs. ruber white*	NA
2021_07_14_UPC028_482-484cm_GR1	UPC028	DC	-2353	-36.2	-52.46	482	9884.5	-0.062582432	-0.609861472	17.69	*Gs. ruber white*	NA
2021_07_14_UPC028_482-484cm_GR2	UPC028	DC	-2353	-36.2	-52.46	482	9884.5	0.109961506	-0.155905157	15.57	*Gs. ruber white*	NA
2021_07_14_UPC028_482-484cm_GR3	UPC028	DC	-2353	-36.2	-52.46	482	9884.5	0.171816001	0.16132476	14.12	*Gs. ruber white*	NA
2021_08_27_UPC028 41-43cmDCNP1	UPC028	DC	-2353	-36.2	-52.46	41	548.6	1.035516621	1.566907524	7.88	*N. pachyderma*	NA
2021_08_27_UPC028 41-43cmDCNP3	UPC028	DC	-2353	-36.2	-52.46	41	548.6	-0.073133684	1.02782699	10.23	*N. pachyderma*	NA
2021_08_27_UPC028 83-85cmDCNP1	UPC028	DC	-2353	-36.2	-52.46	83	1110.6	0.194301548	1.571855858	7.86	*N. pachyderma*	NA
2021_08_27_UPC028 83-85cmDCNP2	UPC028	DC	-2353	-36.2	-52.46	83	1110.6	0.817793907	2.077558526	5.70	*N. pachyderma*	NA
2021_08_30_UPC028_118-120cmDCNP3	UPC028	DC	-2353	-36.2	-52.46	118	1727.3	0.564019578	1.351680065	8.81	*N. pachyderma*	NA
2021_08_30_UPC028_118-120cmDCNP4	UPC028	DC	-2353	-36.2	-52.46	118	1727.3	0.893647832	1.773098004	7.00	*N. pachyderma*	NA
2021_08_30_UPC028_118-120cmDCNP5	UPC028	DC	-2353	-36.2	-52.46	118	1727.3	0.878032024	1.652358173	7.51	*N. pachyderma*	NA
2021_08_27_UPC028 148-150cmDCNP1	UPC028	DC	-2353	-36.2	-52.46	148	2340.7	0.633502997	1.355766909	8.79	*N. pachyderma*	NA
2021_08_30_UPC028_176-178cmDCNP1	UPC028	DC	-2353	-36.2	-52.46	176	2913.3	1.10407782	1.951630903	6.24	*N. pachyderma*	NA
2021_08_30_UPC028_176-178cmDCNP2	UPC028	DC	-2353	-36.2	-52.46	176	2913.3	0.892228833	1.228600159	9.35	*N. pachyderma*	NA
2021_08_30_UPC028_176-178cmDCNP3	UPC028	DC	-2353	-36.2	-52.46	176	2913.3	0.510742095	0.498414617	12.59	*N. pachyderma*	NA
2021_08_30_UPC028_176-178cmDCNP4	UPC028	DC	-2353	-36.2	-52.46	176	2913.3	0.885322581	1.776619611	6.98	*N. pachyderma*	NA
2021_08_30_UPC028_176-178cmDCNP5	UPC028	DC	-2353	-36.2	-52.46	176	2913.3	0.767992734	1.48749198	8.22	*N. pachyderma*	NA
2021_08_27_UPC028 254-256cmDCNP1	UPC028	DC	-2353	-36.2	-52.46	254	4390.5	0.867029496	1.72792243	7.19	*N. pachyderma*	NA
2021_08_27_UPC028 254-256cmDCNP2	UPC028	DC	-2353	-36.2	-52.46	254	4390.5	0.466324869	1.776502906	6.98	*N. pachyderma*	NA
2021_08_27_UPC028 254-256cmDCNP3	UPC028	DC	-2353	-36.2	-52.46	254	4390.5	0.949653475	1.668935898	7.44	*N. pachyderma*	NA
2021_08_27_UPC028 254-256cmDCNP4	UPC028	DC	-2353	-36.2	-52.46	254	4390.5	0.578050179	1.578578524	7.83	*N. pachyderma*	NA
2021_08_27_UPC028 254-256cmDCNP5	UPC028	DC	-2353	-36.2	-52.46	254	4390.5	0.808223286	1.530375145	8.04	*N. pachyderma*	NA
2021_08_30_UPC028_282-284cmDCNP1	UPC028	DC	-2353	-36.2	-52.46	282	4905.9	0.939255016	1.712875209	7.25	*N. pachyderma*	NA
2021_08_30_UPC028_282-284cmDCNP2	UPC028	DC	-2353	-36.2	-52.46	282	4905.9	0.354903585	1.639806574	7.57	*N. pachyderma*	NA
2021_08_30_UPC028_282-284cmDCNP3	UPC028	DC	-2353	-36.2	-52.46	282	4905.9	0.854136055	1.62602129	7.63	*N. pachyderma*	NA
2021_08_30_UPC028_282-284cmDCNP4	UPC028	DC	-2353	-36.2	-52.46	282	4905.9	0.676979518	1.794982526	6.90	*N. pachyderma*	NA
2021_08_30_UPC028_282-284cmDCNP5	UPC028	DC	-2353	-36.2	-52.46	282	4905.9	0.648484999	1.273491737	9.15	*N. pachyderma*	NA
2021_08_27_UPC028 303-305cmDCNP1	UPC028	DC	-2353	-36.2	-52.46	303	5292.5	0.840280151	1.473428474	8.28	*N. pachyderma*	NA
2021_08_27_UPC028 303-305cmDCNP2	UPC028	DC	-2353	-36.2	-52.46	303	5292.5	0.713032215	1.634686754	7.59	*N. pachyderma*	NA
2021_08_27_UPC028 303-305cmDCNP3	UPC028	DC	-2353	-36.2	-52.46	303	5292.5	0.833735901	1.648752631	7.53	*N. pachyderma*	NA
2021_08_27_UPC028 303-305cmDCNP4	UPC028	DC	-2353	-36.2	-52.46	303	5292.5	0.267424717	1.192400861	9.51	*N. pachyderma*	NA
2021_08_27_UPC028 303-305cmDCNP5	UPC028	DC	-2353	-36.2	-52.46	303	5292.5	0.57908517	1.366901213	8.75	*N. pachyderma*	NA
2021_08_30_UPC028_324-326cmDCNP1	UPC028	DC	-2353	-36.2	-52.46	324	5803.7	0.765939861	0.435677584	12.87	*N. pachyderma*	NA
2021_08_30_UPC028_324-326cmDCNP2	UPC028	DC	-2353	-36.2	-52.46	324	5803.7	0.995262339	1.471110349	8.29	*N. pachyderma*	NA
2021_08_30_UPC028_324-326cmDCNP3	UPC028	DC	-2353	-36.2	-52.46	324	5803.7	0.633567111	0.968896052	10.49	*N. pachyderma*	NA
2021_08_30_UPC028_324-326cmDCNP4	UPC028	DC	-2353	-36.2	-52.46	324	5803.7	0.836656245	1.008749452	10.31	*N. pachyderma*	NA

Sample ID	Core	Core Top/ Downcore	Depth (mbsf)	Latitude	Longitude	Sample Depth (cm)	Radiocarbon Age (cal BP)	δ13C VPDB	δ18O VPDB	Converted Temperature (°C)	Species	Encrustation Classification (A-D)/ Coiling Direction (L-R)
2021_08_30_UPC028_324-326cmDCNP5	UPC028	DC	-2353	-36.2	-52.46	324	5803.7	0.483227754	1.058736378	10.09	*N. pachyderma*	NA
2021_08_27_UPC028 347-349cmDCNP1	UPC028	DC	-2353	-36.2	-52.46	347	6433.7	0.314507188	1.197567681	9.48	*N. pachyderma*	NA
2021_08_27_UPC028 347-349cmDCNP2	UPC028	DC	-2353	-36.2	-52.46	347	6433.7	0.718981212	1.183283319	9.55	*N. pachyderma*	NA
2021_09_01_UPC028_361-363cm_DCNP1	UPC028	DC	-2353	-36.2	-52.46	361	6815.3	0.536799305	1.422873777	8.50	*N. pachyderma*	NA
2021_09_01_UPC028_361-363cm_DCNP3	UPC028	DC	-2353	-36.2	-52.46	361	6815.3	0.368550747	1.188972224	9.52	*N. pachyderma*	NA
2021_08_27_UPC028 382-384cmDCNP1	UPC028	DC	-2353	-36.2	-52.46	382	7390.1	0.56899864	1.353275028	8.81	*N. pachyderma*	NA
2021_08_27_UPC028 382-384cmDCNP2	UPC028	DC	-2353	-36.2	-52.46	382	7390.1	0.683619889	1.710642759	7.26	*N. pachyderma*	NA
2021_08_27_UPC028 382-384cmDCNP3	UPC028	DC	-2353	-36.2	-52.46	382	7390.1	0.597180156	1.393685139	8.63	*N. pachyderma*	NA
2021_08_27_UPC028 382-384cmDCNP4	UPC028	DC	-2353	-36.2	-52.46	382	7390.1	0.498932372	1.242206576	9.29	*N. pachyderma*	NA
2021_09_01_UPC028_396-398cm_DCNP1	UPC028	DC	-2353	-36.2	-52.46	396	7772.2	-0.297049712	0.980325701	10.44	*N. pachyderma*	NA
2021_09_01_UPC028_396-398cm_DCNP2	UPC028	DC	-2353	-36.2	-52.46	396	7772.2	0.309464893	1.130001694	9.78	*N. pachyderma*	NA
2021_08_27_UPC028 422-424cmDCNP1	UPC028	DC	-2353	-36.2	-52.46	422	8419.5	0.495860834	1.525594278	8.06	*N. pachyderma*	NA
2021_08_27_UPC028 422-424cmDCNP2	UPC028	DC	-2353	-36.2	-52.46	422	8419.5	0.502622106	1.999297982	6.03	*N. pachyderma*	NA
2021_08_27_UPC028 422-424cmDCNP3	UPC028	DC	-2353	-36.2	-52.46	422	8419.5	0.573102383	1.821713611	6.79	*N. pachyderma*	NA
2021_08_27_UPC028 422-424cmDCNP4	UPC028	DC	-2353	-36.2	-52.46	422	8419.5	0.447037873	1.845997225	6.68	*N. pachyderma*	NA
2021_08_27_UPC028 422-424cmDCNP5	UPC028	DC	-2353	-36.2	-52.46	422	8419.5	0.311060853	1.611889209	7.69	*N. pachyderma*	NA
2021_09_01_UPC028_447-449cm_DCNP1	UPC028	DC	-2353	-36.2	-52.46	447	9029.8	0.322314377	1.882890289	6.53	*N. pachyderma*	NA
2021_09_01_UPC028_447-449cm_DCNP2	UPC028	DC	-2353	-36.2	-52.46	447	9029.8	0.520079679	1.778140998	6.97	*N. pachyderma*	NA
2021_09_01_UPC028_447-449cm_DCNP3	UPC028	DC	-2353	-36.2	-52.46	447	9029.8	0.431727374	1.550534503	7.95	*N. pachyderma*	NA
2021_09_01_UPC028_447-449cm_DCNP4	UPC028	DC	-2353	-36.2	-52.46	447	9029.8	0.323482895	1.606091509	7.71	*N. pachyderma*	NA
2021_09_01_UPC028_447-449cm_DCNP5	UPC028	DC	-2353	-36.2	-52.46	447	9029.8	0.561170539	1.61035415	7.69	*N. pachyderma*	NA
2021_09_01_UPC028_447-449cm_DCNP6	UPC028	DC	-2353	-36.2	-52.46	447	9029.8	0.413292979	1.861991012	6.62	*N. pachyderma*	NA
2021_09_01_UPC028_467-469cm_DCNP1	UPC028	DC	-2353	-36.2	-52.46	467	9518.3	0.282025288	1.574149234	7.85	*N. pachyderma*	NA
2021_09_01_UPC028_467-469cm_DCNP2	UPC028	DC	-2353	-36.2	-52.46	467	9518.3	0.739325572	2.878128647	2.38	*N. pachyderma*	NA
2021_09_01_UPC028_467-469cm_DCNP3	UPC028	DC	-2353	-36.2	-52.46	467	9518.3	0.577377448	1.799748392	6.88	*N. pachyderma*	NA
2021_09_01_UPC028_467-469cm_DCNP4	UPC028	DC	-2353	-36.2	-52.46	467	9518.3	0.423951638	1.574346667	7.85	*N. pachyderma*	NA
2021_09_01_UPC028_482-484cm_DCNP1	UPC028	DC	-2353	-36.2	-52.46	482	9884.5	0.6048949	2.139612197	5.44	*N. pachyderma*	NA
2021_09_01_UPC028_482-484cm_DCNP2	UPC028	DC	-2353	-36.2	-52.46	482	9884.5	0.489957216	1.899305563	6.46	*N. pachyderma*	NA
2021_09_01_UPC028_482-484cm_DCNP3	UPC028	DC	-2353	-36.2	-52.46	482	9884.5	0.384303412	1.527032294	8.05	*N. pachyderma*	NA
2021_09_01_UPC028_482-484cm_DCNP4	UPC028	DC	-2353	-36.2	-52.46	482	9884.5	0.6945345	1.899077376	6.46	*N. pachyderma*	NA
2021_09_01_UPC028_482-484cm_DCNP5	UPC028	DC	-2353	-36.2	-52.46	482	9884.5	0.185899677	1.59701948	7.75	*N. pachyderma*	NA
2021_09_01_UPC028_482-484cm_DCNP6	UPC028	DC	-2353	-36.2	-52.46	482	9884.5	0.533363348	1.863778808	6.61	*N. pachyderma*	NA
2021_04_15_UPC028_447-449cmGI2	UPC028	DC	-2353	-36.2	-52.46	447	9029.8	0.707610363	0.833355851	11.09	*Gc. inflata*	A
2021_04_13_UPC028_382-384cmGI3	UPC028	DC	-2353	-36.2	-52.46	382	7390.1	1.31318171	1.168531152	9.61	*Gc. inflata*	B
2021_04_13_UPC028_422-424cmGI1	UPC028	DC	-2353	-36.2	-52.46	422	8419.5	0.67787856	0.639040012	11.96	*Gc. inflata*	B
2021_04_13_UPC028_422-424cmGI2	UPC028	DC	-2353	-36.2	-52.46	422	8419.5	1.404806694	1.021554306	10.26	*Gc. inflata*	B

Sample ID	Core	Core Top/ Downcore	Depth (mbsf)	Latitude	Longitude	Sample Depth (cm)	Radiocarbon Age (cal BP)	δ13C VPDB	δ18O VPDB	Converted Temperature (°C)	Species	Encrustation Classification (A-D)/ Coiling Direction (L-R)
2021_03_29_UPC028_41-43cmGI3	UPC028	DC	-2353	-36.2	-52.46	41	548.6	1.121413645	0.985146564	10.42	*Gc. inflata*	C
2021_03_19_UPC028_83-85cmGI4	UPC028	DC	-2353	-36.2	-52.46	83	1110.6	1.510712857	2.836806898	2.55	*Gc. inflata*	C
2021_03_19_UPC028_83-85cmGI5	UPC028	DC	-2353	-36.2	-52.46	83	1110.6	1.60701947	1.272702326	9.16	*Gc. inflata*	C
2021_03_26_UPC028_118-120cmGI3	UPC028	DC	-2353	-36.2	-52.46	118	1727.3	1.660459566	0.420623004	12.94	*Gc. inflata*	C
2021_03_19_UPC028_148-150cmGI1	UPC028	DC	-2353	-36.2	-52.46	148	2340.7	1.49708391	1.223990226	9.37	*Gc. inflata*	C
2021_03_19_UPC028_148-150cmGI2	UPC028	DC	-2353	-36.2	-52.46	148	2340.7	1.574974827	1.160250868	9.65	*Gc. inflata*	C
2021_03_19_UPC028_148-150cmGI4	UPC028	DC	-2353	-36.2	-52.46	148	2340.7	1.451643373	1.005013419	10.33	*Gc. inflata*	C
2021_03_19_UPC028_254-256cmGI2	UPC028	DC	-2353	-36.2	-52.46	254	4390.5	1.709442995	2.955064916	2.07	*Gc. inflata*	C
2021_03_19_UPC028_254-256cmGI3	UPC028	DC	-2353	-36.2	-52.46	254	4390.5	1.430258415	1.490483651	8.21	*Gc. inflata*	C
2021_03_23_UPC028_282-284cmGI1	UPC028	DC	-2353	-36.2	-52.46	282	4905.9	1.93935575	1.018398437	10.27	*Gc. inflata*	C
2021_03_23_UPC028_303-305cmGI1	UPC028	DC	-2353	-36.2	-52.46	303	5292.5	1.343237882	1.042003337	10.17	*Gc. inflata*	C
2021_04_13_UPC028_324-326cmGI4	UPC028	DC	-2353	-36.2	-52.46	324	5803.7	1.91745085	0.82972403	11.11	*Gc. inflata*	C
2021_04_13_UPC028_324-326cmGI5	UPC028	DC	-2353	-36.2	-52.46	324	5803.7	1.821828554	0.806845564	11.21	*Gc. inflata*	C
2021_03_29_UPC028_347-349cmGI3	UPC028	DC	-2353	-36.2	-52.46	347	6433.7	1.384918585	0.327571056	13.36	*Gc. inflata*	C
2021_03_29_UPC028_347-349cmGI4	UPC028	DC	-2353	-36.2	-52.46	347	6433.7	1.477088499	0.756727194	11.43	*Gc. inflata*	C
2021_03_29_UPC028_347-349cmGI5	UPC028	DC	-2353	-36.2	-52.46	347	6433.7	1.275254447	1.142643234	9.72	*Gc. inflata*	C
2021_04_13_UPC028_382-384cmGI2	UPC028	DC	-2353	-36.2	-52.46	382	7390.1	1.263195078	0.610681433	12.08	*Gc. inflata*	C
2021_03_26_UPC028_396-398cmGI2	UPC028	DC	-2353	-36.2	-52.46	396	7772.2	1.516706779	1.247437921	9.27	*Gc. inflata*	C
2021_03_26_UPC028_396-398cmGI4	UPC028	DC	-2353	-36.2	-52.46	396	7772.2	1.607894127	2.458183105	4.11	*Gc. inflata*	C
2021_04_13_UPC028_422-424cmGI3	UPC028	DC	-2353	-36.2	-52.46	422	8419.5	0.848844799	1.253199485	9.24	*Gc. inflata*	C
2021_04_15_UPC028_447-449cmGI4	UPC028	DC	-2353	-36.2	-52.46	447	9029.8	0.653034241	0.599658697	12.13	*Gc. inflata*	C
2021_03_26_UPC028_467-469cmGI3	UPC028	DC	-2353	-36.2	-52.46	467	9518.3	1.489288667	0.894338507	10.82	*Gc. inflata*	C
2021_03_26_UPC028_467-469cmGI4	UPC028	DC	-2353	-36.2	-52.46	467	9518.3	0.822360695	0.908241411	10.76	*Gc. inflata*	C
2021_03_29_UPC028_41-43cmGI1	UPC028	DC	-2353	-36.2	-52.46	41	548.6	1.067567985	0.929173642	10.67	*Gc. inflata*	D
2021_03_29_UPC028_41-43cmGI2	UPC028	DC	-2353	-36.2	-52.46	41	548.6	1.378365778	0.855277955	10.99	*Gc. inflata*	D
2021_03_29_UPC028_41-43cmGI4	UPC028	DC	-2353	-36.2	-52.46	41	548.6	1.680934439	0.708061486	11.65	*Gc. inflata*	D
2021_03_29_UPC028_41-43cmGI5	UPC028	DC	-2353	-36.2	-52.46	41	548.6	1.605382545	2.705751711	3.09	*Gc. inflata*	D
2021_03_19_UPC028_83-85cmGI1	UPC028	DC	-2353	-36.2	-52.46	83	1110.6	1.525468113	2.891985412	2.33	*Gc. inflata*	D
2021_03_19_UPC028_83-85cmGI2	UPC028	DC	-2353	-36.2	-52.46	83	1110.6	1.660330961	2.80406783	2.69	*Gc. inflata*	D
2021_03_19_UPC028_83-85cmGI3	UPC028	DC	-2353	-36.2	-52.46	83	1110.6	1.487728737	2.942371677	2.12	*Gc. inflata*	D
2021_03_26_UPC028_118-120cmGI1	UPC028	DC	-2353	-36.2	-52.46	118	1727.3	1.362112728	0.761148779	11.41	*Gc. inflata*	D
2021_03_26_UPC028_118-120cmGI2	UPC028	DC	-2353	-36.2	-52.46	118	1727.3	1.585580623	2.631072043	3.40	*Gc. inflata*	D
2021_03_26_UPC028_118-120cmGI4	UPC028	DC	-2353	-36.2	-52.46	118	1727.3	1.738930085	2.447820118	4.15	*Gc. inflata*	D
2021_03_26_UPC028_118-120cmGI5	UPC028	DC	-2353	-36.2	-52.46	118	1727.3	1.525445862	2.797187794	2.71	*Gc. inflata*	D
2021_03_19_UPC028_148-150cmGI3	UPC028	DC	-2353	-36.2	-52.46	148	2340.7	1.858529792	2.820908137	2.62	*Gc. inflata*	D
2021_03_19_UPC028_148-150cmGI5	UPC028	DC	-2353	-36.2	-52.46	148	2340.7	1.762316492	2.859134889	2.46	*Gc. inflata*	D

Sample ID	Core	Core Top/ Downcore	Depth (mbsf)	Latitude	Longitude	Sample Depth (cm)	Radiocarbon Age (cal BP)	δ13C VPDB	δ18O VPDB	Converted Temperature (°C)	Species	Encrustation Classification (A-D)/ Coiling Direction (L-R)
2021_03_29_UPC028_176-178cmGI1	UPC028	DC	-2353	-36.2	-52.46	176	2913.3	1.538556901	1.069010504	10.05	*Gc. inflata*	D
2021_03_29_UPC028_176-178cmGI2	UPC028	DC	-2353	-36.2	-52.46	176	2913.3	1.814402962	1.371034577	8.73	*Gc. inflata*	D
2021_03_29_UPC028_176-178cmGI3	UPC028	DC	-2353	-36.2	-52.46	176	2913.3	1.276296648	0.925432358	10.68	*Gc. inflata*	D
2021_03_29_UPC028_176-178cmGI4	UPC028	DC	-2353	-36.2	-52.46	176	2913.3	1.640030171	1.187207401	9.53	*Gc. inflata*	D
2021_03_29_UPC028_176-178cmGI5	UPC028	DC	-2353	-36.2	-52.46	176	2913.3	1.389829503	0.802996161	11.22	*Gc. inflata*	D
2021_03_19_UPC028_254-256cmGI1	UPC028	DC	-2353	-36.2	-52.46	254	4390.5	1.69152315	2.733475019	2.98	*Gc. inflata*	D
2021_03_19_UPC028_254-256cmGI4	UPC028	DC	-2353	-36.2	-52.46	254	4390.5	1.812806406	2.539033727	3.78	*Gc. inflata*	D
2021_03_19_UPC028_254-256cmGI5	UPC028	DC	-2353	-36.2	-52.46	254	4390.5	1.52598647	1.196877506	9.49	*Gc. inflata*	D
2021_03_23_UPC028_282-284cmGI2	UPC028	DC	-2353	-36.2	-52.46	282	4905.9	1.324810867	0.695186351	11.71	*Gc. inflata*	D
2021_03_23_UPC028_282-284cmGI3	UPC028	DC	-2353	-36.2	-52.46	282	4905.9	1.660274576	2.478290885	4.03	*Gc. inflata*	D
2021_03_23_UPC028_282-284cmGI4	UPC028	DC	-2353	-36.2	-52.46	282	4905.9	1.518458334	2.672082471	3.23	*Gc. inflata*	D
2021_03_23_UPC028_282-284cmGI5	UPC028	DC	-2353	-36.2	-52.46	282	4905.9	1.449747339	2.556959565	3.70	*Gc. inflata*	D
2021_03_23_UPC028_303-305cmGI2	UPC028	DC	-2353	-36.2	-52.46	303	5292.5	1.379619515	2.589895354	3.57	*Gc. inflata*	D
2021_03_23_UPC028_303-305cmGI4	UPC028	DC	-2353	-36.2	-52.46	303	5292.5	1.132584083	0.94268473	10.61	*Gc. inflata*	D
2021_03_23_UPC028_303-305cmGI5	UPC028	DC	-2353	-36.2	-52.46	303	5292.5	1.543810647	0.68850966	11.74	*Gc. inflata*	D
2021_04_13_UPC028_324-326cmGI1	UPC028	DC	-2353	-36.2	-52.46	324	5803.7	1.62901663	2.378347709	4.44	*Gc. inflata*	D
2021_04_13_UPC028_324-326cmGI2	UPC028	DC	-2353	-36.2	-52.46	324	5803.7	1.637477103	1.144607153	9.72	*Gc. inflata*	D
2021_04_13_UPC028_324-326cmGI3	UPC028	DC	-2353	-36.2	-52.46	324	5803.7	1.427575897	0.841663407	11.05	*Gc. inflata*	D
2021_03_29_UPC028_347-349cmGI1	UPC028	DC	-2353	-36.2	-52.46	347	6433.7	1.662636601	2.784407494	2.77	*Gc. inflata*	D
2021_03_29_UPC028_347-349cmGI2	UPC028	DC	-2353	-36.2	-52.46	347	6433.7	1.334689047	0.992727686	10.38	*Gc. inflata*	D
2021_03_23_UPC028_361-363cmGI1	UPC028	DC	-2353	-36.2	-52.46	361	6815.3	1.467956965	2.503835826	3.92	*Gc. inflata*	D
2021_03_23_UPC028_361-363cmGI3	UPC028	DC	-2353	-36.2	-52.46	361	6815.3	1.206118702	0.310932086	13.43	*Gc. inflata*	D
2021_03_23_UPC028_361-363cmGI4	UPC028	DC	-2353	-36.2	-52.46	361	6815.3	1.116496561	0.841429498	11.05	*Gc. inflata*	D
2021_04_13_UPC028_382-384cmGI1	UPC028	DC	-2353	-36.2	-52.46	382	7390.1	1.470340115	2.670062507	3.24	*Gc. inflata*	D
2021_04_13_UPC028_382-384cmGI4	UPC028	DC	-2353	-36.2	-52.46	382	7390.1	1.743034174	2.635451989	3.38	*Gc. inflata*	D
2021_04_13_UPC028_382-384cmGI5	UPC028	DC	-2353	-36.2	-52.46	382	7390.1	1.339552869	0.94390169	10.60	*Gc. inflata*	D
2021_03_26_UPC028_396-398cmGI1	UPC028	DC	-2353	-36.2	-52.46	396	7772.2	1.605111863	2.526917355	3.83	*Gc. inflata*	D
2021_03_26_UPC028_396-398cmGI3	UPC028	DC	-2353	-36.2	-52.46	396	7772.2	1.662833385	2.774235255	2.81	*Gc. inflata*	D
2021_03_26_UPC028_396-398cmGI5	UPC028	DC	-2353	-36.2	-52.46	396	7772.2	1.559209958	2.727061151	3.00	*Gc. inflata*	D
2021_04_13_UPC028_422-424cmGI4	UPC028	DC	-2353	-36.2	-52.46	422	8419.5	1.482887693	2.967304699	2.02	*Gc. inflata*	D
2021_04_13_UPC028_422-424cmGI5	UPC028	DC	-2353	-36.2	-52.46	422	8419.5	1.159296885	0.931364939	10.66	*Gc. inflata*	D
2021_04_15_UPC028_447-449cmGI1	UPC028	DC	-2353	-36.2	-52.46	447	9029.8	1.406509185	2.881504286	2.37	*Gc. inflata*	D
2021_04_15_UPC028_447-449cmGI3	UPC028	DC	-2353	-36.2	-52.46	447	9029.8	1.17169499	0.851677166	11.01	*Gc. inflata*	D
2021_04_15_UPC028_447-449cmGI5	UPC028	DC	-2353	-36.2	-52.46	447	9029.8	1.320092117	2.741452236	2.94	*Gc. inflata*	D
2021_03_26_UPC028_467-469cmGI1	UPC028	DC	-2353	-36.2	-52.46	467	9518.3	1.138249391	2.761291943	2.86	*Gc. inflata*	D
2021_03_26_UPC028_467-469cmGI2	UPC028	DC	-2353	-36.2	-52.46	467	9518.3	1.443575716	2.558807483	3.69	*Gc. inflata*	D

Sample ID	Core	Core Top/ Downcore	Depth (mbsf)	Latitude	Longitude	Sample Depth (cm)	Radiocarbon Age (cal BP)	δ13C VPDB	δ18O VPDB	Converted Temperature (°C)	Species	Encrustation Classification (A-D)/ Coiling Direction (L-R)
2021_03_26_UPC028_467-469cmGI5	UPC028	DC	-2353	-36.2	-52.46	467	9518.3	1.523826506	2.680756021	3.19	*Gc. inflata*	D
2021_04_15_UPC028_482-484cmGI1	UPC028	DC	-2353	-36.2	-52.46	482	9884.5	1.359868828	2.734155313	2.97	*Gc. inflata*	D
2021_04_15_UPC028_482-484cmGI2	UPC028	DC	-2353	-36.2	-52.46	482	9884.5	1.152316369	2.661630669	3.27	*Gc. inflata*	D
2021_04_15_UPC028_482-484cmGI3	UPC028	DC	-2353	-36.2	-52.46	482	9884.5	1.606538472	2.899843647	2.30	*Gc. inflata*	D
2021_04_15_UPC028_482-484cmGI4	UPC028	DC	-2353	-36.2	-52.46	482	9884.5	1.199074403	2.899680359	2.30	*Gc. inflata*	D
2021_04_15_UPC028_482-484cmGI5	UPC028	DC	-2353	-36.2	-52.46	482	9884.5	1.488299282	2.838207876	2.55	*Gc. inflata*	D
2019-03-22 UPC 028 CT GI	UPC028	DC	-2353	-36.2	-52.46	0	0	1.098536944	1.229784627	9.34	*Gc. inflata*	U
2019-03-22 UPC 028 148-150 cm GI	UPC028	DC	-2353	-36.2	-52.46	148	2340.7	1.484263038	1.178849588	9.57	*Gc. inflata*	U
2019-03-22 UPC 028 176-178 cm GI	UPC028	DC	-2353	-36.2	-52.46	176	2913.3	1.411295205	1.1340444	9.76	*Gc. inflata*	U
2019-03-25 UPC 028 324-326 cm GI	UPC028	DC	-2353	-36.2	-52.46	324	5803.7	1.502788002	1.093706271	9.94	*Gc. inflata*	U
2019-03-25 UPC 028 347-349 cm GI	UPC028	DC	-2353	-36.2	-52.46	347	6433.7	1.300109475	1.008724679	10.31	*Gc. inflata*	U
2019-03-25 UPC 028 422-424 cm GI	UPC028	DC	-2353	-36.2	-52.46	422	8419.5	0.86566339	1.022188069	10.25	*Gc. inflata*	U
2019-03-25 UPC 028 447-449 cm GI	UPC028	DC	-2353	-36.2	-52.46	447	9029.8	0.881343487	1.549779112	7.95	*Gc. inflata*	U
2021_03_29_UPC028_41-43cmGT1	UPC 028	DC	-2353	-36.2	-52.46	41	548.6	1.677835746	0.82651207	11.12	*Gr. truncatulinoides L*	L
2021_03_29_UPC028_41-43cmGT2	UPC 028	DC	-2353	-36.2	-52.46	41	548.6	1.453417616	0.661678784	11.86	*Gr. truncatulinoides L*	L
2021_03_29_UPC028_41-43cmGT5	UPC 028	DC	-2353	-36.2	-52.46	41	548.6	1.62397248	1.105510306	9.89	*Gr. truncatulinoides L*	L
2021_03_19_UPC028_83-85cmGT1	UPC 028	DC	-2353	-36.2	-52.46	83	1110.6	1.700347401	1.073140188	10.03	*Gr. truncatulinoides L*	L
2021_03_19_UPC028_83-85cmGT2	UPC 028	DC	-2353	-36.2	-52.46	83	1110.6	1.369747538	0.935273077	10.64	*Gr. truncatulinoides L*	L
2021_03_19_UPC028_83-85cmGT3	UPC 028	DC	-2353	-36.2	-52.46	83	1110.6	1.203782006	0.82421972	11.13	*Gr. truncatulinoides L*	L
2021_03_19_UPC028_83-85cmGT4BROKEN	UPC 028	DC	-2353	-36.2	-52.46	83	1110.6	1.855359903	1.383487598	8.67	*Gr. truncatulinoides L*	L
2021_03_29_UPC028_118-120cm_GT3	UPC 028	DC	-2353	-36.2	-52.46	118	1727.3	1.781560602	2.703668994	3.10	*Gr. truncatulinoides L*	L
2021_03_29_UPC028_118-120cm_GT4	UPC 028	DC	-2353	-36.2	-52.46	118	1727.3	1.345145321	0.382378565	13.11	*Gr. truncatulinoides L*	L
2021_03_19_UPC028_148-150cmGT1	UPC 028	DC	-2353	-36.2	-52.46	148	2340.7	1.529474802	1.16475199	9.63	*Gr. truncatulinoides L*	L
2021_03_29_UPC028_176-178cmGT1	UPC 028	DC	-2353	-36.2	-52.46	176	2913.3	1.703143111	0.979838363	10.44	*Gr. truncatulinoides L*	L
2021_03_29_UPC028_176-178cmGT3	UPC 028	DC	-2353	-36.2	-52.46	176	2913.3	1.74848983	0.879616604	10.88	*Gr. truncatulinoides L*	L
2021_03_29_UPC028_176-178cmGT5	UPC 028	DC	-2353	-36.2	-52.46	176	2913.3	1.048092532	0.741124435	11.50	*Gr. truncatulinoides L*	L
2021_03_23_UPC028_254-256cmGT2	UPC 028	DC	-2353	-36.2	-52.46	254	4390.5	1.538236603	0.757452405	11.43	*Gr. truncatulinoides L*	L
2021_03_23_UPC028_254-256cmGT3	UPC 028	DC	-2353	-36.2	-52.46	254	4390.5	1.439801661	0.873836431	10.91	*Gr. truncatulinoides L*	L
2021_03_23_UPC028_303-305cmGT4	UPC 028	DC	-2353	-36.2	-52.46	303	5292.5	1.558079353	2.859408404	2.46	*Gr. truncatulinoides L*	L
2021_03_26_UPC028_361-363cmGT1	UPC 028	DC	-2353	-36.2	-52.46	361	6815.3	1.577377024	1.01563879	10.28	*Gr. truncatulinoides L*	L
2021_03_26_UPC028_361-363cmGT5	UPC 028	DC	-2353	-36.2	-52.46	361	6815.3	1.261356802	0.782944191	11.31	*Gr. truncatulinoides L*	L
2021_04_15_UPC028_422-424cmGT2	UPC 028	DC	-2353	-36.2	-52.46	422	8419.5	0.861800148	0.337076984	13.32	*Gr. truncatulinoides L*	L
2021_04_15_UPC028_422-424cmGT3	UPC 028	DC	-2353	-36.2	-52.46	422	8419.5	1.390085449	1.288615391	9.09	*Gr. truncatulinoides L*	L
2021_04_15_UPC028_447-449cmGT1	UPC 028	DC	-2353	-36.2	-52.46	447	9029.8	1.29109293	0.789024679	11.29	*Gr. truncatulinoides L*	L
2021_04_15_UPC028_447-449cmGT2	UPC 028	DC	-2353	-36.2	-52.46	447	9029.8	0.799805874	0.749771607	11.46	*Gr. truncatulinoides L*	L
2021_04_15_UPC028_447-449cmGT4	UPC 028	DC	-2353	-36.2	-52.46	447	9029.8	1.39384091	1.037446015	10.19	*Gr. truncatulinoides L*	L

Sample ID	Core	Core Top/ Downcore	Depth (mbsf)	Latitude	Longitude	Sample Depth (cm)	Radiocarbon Age (cal BP)	δ13C VPDB	δ18O VPDB	Converted Temperature (°C)	Species	Encrustation Classification (A-D)/ Coiling Direction (L-R)
2021_04_15_UPC028_447-449cmGT5	UPC028	DC	-2353	-36.2	-52.46	447	9029.8	1.336292407	0.82294733	11.14	*Gr. truncatulinoides L*	L
2021_03_26_UPC028_467-469cmGT1	UPC028	DC	-2353	-36.2	-52.46	467	9518.3	1.156737543	0.895986725	10.81	*Gr. truncatulinoides L*	L
2021_03_26_UPC028_467-469cmGT2	UPC028	DC	-2353	-36.2	-52.46	467	9518.3	0.96936968	0.698802465	11.69	*Gr. truncatulinoides L*	L
2021_03_26_UPC028_467-469cmGT3	UPC028	DC	-2353	-36.2	-52.46	467	9518.3	1.089508916	0.825266366	11.13	*Gr. truncatulinoides L*	L
2021_03_26_UPC028_467-469cmGT5	UPC028	DC	-2353	-36.2	-52.46	467	9518.3	1.182803205	0.726447197	11.57	*Gr. truncatulinoides L*	L
2021_04_15_UPC028_482-484cmGT3	UPC028	DC	-2353	-36.2	-52.46	482	9884.5	1.629894545	1.14272161	9.72	*Gr. truncatulinoides L*	L
2021_04_15_UPC028_482-484cmGT5	UPC028	DC	-2353	-36.2	-52.46	482	9884.5	1.417963823	1.18984647	9.52	*Gr. truncatulinoides L*	L
2021_03_29_UPC028_41-43cmGT3	UPC028	DC	-2353	-36.2	-52.46	41	548.6	1.111902409	2.893616795	2.32	*Gr. truncatulinoides R*	R
2021_03_29_UPC028_41-43cmGT4	UPC028	DC	-2353	-36.2	-52.46	41	548.6	1.330265037	2.825369744	2.60	*Gr. truncatulinoides R*	R
2021_03_19_UPC028_83-85cmGT5BROKEN	UPC028	DC	-2353	-36.2	-52.46	83	1110.6	1.615315171	2.700089191	3.11	*Gr. truncatulinoides R*	R
2021_03_29_UPC028_118-120cm_GT1	UPC028	DC	-2353	-36.2	-52.46	118	1727.3	1.798494678	2.821149415	2.62	*Gr. truncatulinoides R*	R
2021_03_29_UPC028_118-120cm_GT5	UPC028	DC	-2353	-36.2	-52.46	118	1727.3	1.335568429	2.174066474	5.30	*Gr. truncatulinoides R*	R
2021_03_19_UPC028_148-150cmGT2	UPC028	DC	-2353	-36.2	-52.46	148	2340.7	1.54974261	2.77286543	2.81	*Gr. truncatulinoides R*	R
2021_03_19_UPC028_148-150cmGT3	UPC028	DC	-2353	-36.2	-52.46	148	2340.7	1.25914564	1.450427432	8.38	*Gr. truncatulinoides R*	R
2021_03_19_UPC028_148-150cmGT4	UPC028	DC	-2353	-36.2	-52.46	148	2340.7	1.212293818	2.98313241	1.96	*Gr. truncatulinoides R*	R
2021_03_19_UPC028_148-150cmGT5	UPC028	DC	-2353	-36.2	-52.46	148	2340.7	1.57500999	2.915018133	2.23	*Gr. truncatulinoides R*	R
2021_03_29_UPC028_176-178cmGT2	UPC028	DC	-2353	-36.2	-52.46	176	2913.3	1.570791787	2.749594929	2.91	*Gr. truncatulinoides R*	R
2021_03_29_UPC028_176-178cmGT4	UPC028	DC	-2353	-36.2	-52.46	176	2913.3	1.481011164	2.823371441	2.61	*Gr. truncatulinoides R*	R
2021_03_23_UPC028_254-256cmGT4	UPC028	DC	-2353	-36.2	-52.46	254	4390.5	1.574153658	2.851900205	2.49	*Gr. truncatulinoides R*	R
2021_03_23_UPC028_254-256cmGT5	UPC028	DC	-2353	-36.2	-52.46	254	4390.5	1.5756125	2.673094653	3.22	*Gr. truncatulinoides R*	R
2021_03_23_UPC028_282-284cmGT1	UPC028	DC	-2353	-36.2	-52.46	282	4905.9	1.163417102	1.227211824	9.35	*Gr. truncatulinoides R*	R
2021_03_23_UPC028_282-284cmGT2	UPC028	DC	-2353	-36.2	-52.46	282	4905.9	0.2310447	0.78918996	11.29	*Gr. truncatulinoides R*	R
2021_03_23_UPC028_282-284cmGT3	UPC028	DC	-2353	-36.2	-52.46	282	4905.9	1.642649459	2.707751216	3.08	*Gr. truncatulinoides R*	R
2021_03_23_UPC028_282-284cmGT4	UPC028	DC	-2353	-36.2	-52.46	282	4905.9	1.629227722	2.885150699	2.36	*Gr. truncatulinoides R*	R
2021_03_23_UPC028_282-284cmGT5	UPC028	DC	-2353	-36.2	-52.46	282	4905.9	1.29527921	2.718647217	3.04	*Gr. truncatulinoides R*	R
2021_03_23_UPC028_303-305cmGT1	UPC028	DC	-2353	-36.2	-52.46	303	5292.5	1.510212275	2.57972966	3.61	*Gr. truncatulinoides R*	R
2021_03_23_UPC028_303-305cmGT2	UPC028	DC	-2353	-36.2	-52.46	303	5292.5	1.547548931	2.330515509	4.64	*Gr. truncatulinoides R*	R
2021_03_23_UPC028_303-305cmGT3	UPC028	DC	-2353	-36.2	-52.46	303	5292.5	1.084552303	0.966349247	10.50	*Gr. truncatulinoides R*	R
2021_03_23_UPC028_303-305cmGT5	UPC028	DC	-2353	-36.2	-52.46	303	5292.5	0.918403478	0.720640154	11.59	*Gr. truncatulinoides R*	R
2021_04_13_UPC028_324-326cmGT1	UPC028	DC	-2353	-36.2	-52.46	324	5803.7	1.355978022	2.530945107	3.81	*Gr. truncatulinoides R*	R
2021_04_13_UPC028_324-326cmGT2	UPC028	DC	-2353	-36.2	-52.46	324	5803.7	1.541647032	1.041558409	10.17	*Gr. truncatulinoides R*	R
2021_04_13_UPC028_324-326cmGT3	UPC028	DC	-2353	-36.2	-52.46	324	5803.7	1.475975708	2.595196139	3.54	*Gr. truncatulinoides R*	R
2021_04_13_UPC028_324-326cmGT4	UPC028	DC	-2353	-36.2	-52.46	324	5803.7	1.681374236	2.502277312	3.93	*Gr. truncatulinoides R*	R
2021_04_13_UPC028_324-326cmGT5	UPC028	DC	-2353	-36.2	-52.46	324	5803.7	1.580934732	1.427337528	8.48	*Gr. truncatulinoides R*	R
2021_04_13_UPC028_347-349cmGT1	UPC028	DC	-2353	-36.2	-52.46	347	6433.7	0.806339175	1.096029057	9.93	*Gr. truncatulinoides R*	R
2021_04_13_UPC028_347-349cmGT3	UPC028	DC	-2353	-36.2	-52.46	347	6433.7	1.396459512	2.852139168	2.49	*Gr. truncatulinoides R*	R

Sample ID	Core	Core Top/ Downcore	Depth (mbsf)	Latitude	Longitude	Sample Depth (cm)	Radiocarbon Age (cal BP)	δ13C VPDB	δ18O VPDB	Converted Temperature (°C)	Species	Encrustation Classification (A-D)/ Coiling Direction (L-R)
2021_04_13_UPC028_347-349cmGT4	UPC 028	DC	-2353	-36.2	-52.46	347	6433.7	0.306613006	1.298184579	9.04	*Gr. truncatulinoides R*	R
2021_04_13_UPC028_347-349cmGT5	UPC 028	DC	-2353	-36.2	-52.46	347	6433.7	1.091499419	3.038159248	1.74	*Gr. truncatulinoides R*	R
2021_03_26_UPC028_361-363cmGT2	UPC 028	DC	-2353	-36.2	-52.46	361	6815.3	0.75373607	0.681133193	11.77	*Gr. truncatulinoides R*	R
2021_03_26_UPC028_361-363cmGT3	UPC 028	DC	-2353	-36.2	-52.46	361	6815.3	1.016308158	1.03456016	10.20	*Gr. truncatulinoides R*	R
2021_03_26_UPC028_361-363cmGT4	UPC 028	DC	-2353	-36.2	-52.46	361	6815.3	1.076048456	2.489542093	3.98	*Gr. truncatulinoides R*	R
2021_04_13_UPC028_382-384cmGT1	UPC 028	DC	-2353	-36.2	-52.46	382	7390.1	1.169187247	2.937635823	2.14	*Gr. truncatulinoides R*	R
2021_04_13_UPC028_382-384cmGT2	UPC 028	DC	-2353	-36.2	-52.46	382	7390.1	0.602736315	1.025566778	10.24	*Gr. truncatulinoides R*	R
2021_04_13_UPC028_382-384cmGT3	UPC 028	DC	-2353	-36.2	-52.46	382	7390.1	1.384848674	1.980692265	6.11	*Gr. truncatulinoides R*	R
2021_04_13_UPC028_382-384cmGT4	UPC 028	DC	-2353	-36.2	-52.46	382	7390.1	1.626165254	1.880326831	6.54	*Gr. truncatulinoides R*	R
2021_04_13_UPC028_382-384cmGT5	UPC 028	DC	-2353	-36.2	-52.46	382	7390.1	1.495915941	1.575811395	7.84	*Gr. truncatulinoides R*	R
2021_03_26_UPC028_396-398cmGT1	UPC 028	DC	-2353	-36.2	-52.46	396	7772.2	1.603361684	1.661440796	7.47	*Gr. truncatulinoides R*	R
2021_03_26_UPC028_396-398cmGT3	UPC 028	DC	-2353	-36.2	-52.46	396	7772.2	1.16649232	3.001388489	1.88	*Gr. truncatulinoides R*	R
2021_03_26_UPC028_396-398cmGT4	UPC 028	DC	-2353	-36.2	-52.46	396	7772.2	1.582981527	1.891510427	6.49	*Gr. truncatulinoides R*	R
2021_03_26_UPC028_396-398cmGT5	UPC 028	DC	-2353	-36.2	-52.46	396	7772.2	1.319291102	3.076193899	1.58	*Gr. truncatulinoides R*	R
2021_04_15_UPC028_422-424cmGT1	UPC 028	DC	-2353	-36.2	-52.46	422	8419.5	1.114420537	2.637128088	3.37	*Gr. truncatulinoides R*	R
2021_04_15_UPC028_422-424cmGT4	UPC 028	DC	-2353	-36.2	-52.46	422	8419.5	0.871864114	2.709376978	3.07	*Gr. truncatulinoides R*	R
2021_04_15_UPC028_422-424cmGT5	UPC 028	DC	-2353	-36.2	-52.46	422	8419.5	1.040633804	2.743561038	2.93	*Gr. truncatulinoides R*	R
2021_04_15_UPC028_447-449cmGT3	UPC 028	DC	-2353	-36.2	-52.46	447	9029.8	1.0002675	1.123239296	9.81	*Gr. truncatulinoides R*	R
2021_04_15_UPC028_482-484cmGT1	UPC 028	DC	-2353	-36.2	-52.46	482	9884.5	1.310601114	3.068435579	1.61	*Gr. truncatulinoides R*	R
2021_04_15_UPC028_482-484cmGT2	UPC 028	DC	-2353	-36.2	-52.46	482	9884.5	0.945550084	3.160681186	1.24	*Gr. truncatulinoides R*	R
2021_04_15_UPC028_482-484cmGT4	UPC 028	DC	-2353	-36.2	-52.46	482	9884.5	1.086738834	2.950536604	2.09	*Gr. truncatulinoides R*	R
2019-03-25 UPC 028 148-150 cm GT	UPC 028	DC	-2353	-36.2	-52.46	148	2340.7	1.619419407	2.456593357	4.12	*Gr. truncatulinoides U*	U
2019-03-25 UPC 028 176-178 cm GT	UPC 028	DC	-2353	-36.2	-52.46	176	2913.3	1.628388035	1.72828756	7.19	*Gr. truncatulinoides U*	U
2019-03-25 UPC 028 324-326 cm GT	UPC 028	DC	-2353	-36.2	-52.46	324	5803.7	1.500866288	2.005725554	6.01	*Gr. truncatulinoides U*	U
2019-03-27_UPC 028 347-349 cm GT	UPC 028	DC	-2353	-36.2	-52.46	347	6433.7	1.132937686	2.085623533	5.67	*Gr. truncatulinoides U*	U
2019-03-27_UPC 028 422-424 cm GT	UPC 028	DC	-2353	-36.2	-52.46	422	8419.5	1.120276576	1.283840842	9.11	*Gr. truncatulinoides U*	U
2019-03-27_UPC 028 447-449 cm GT	UPC 028	DC	-2353	-36.2	-52.46	447	9029.8	1.223840426	1.5011493	8.16	*Gr. truncatulinoides U*	U

For raw data see sheet ISOTOPES in
Mair_AM_Earth_And_Environment_PhD_2022_Summary_Appendices.xls

Appendix D.1 Acquired Radiocarbon dates

Radiocarbon dates							
Publication code	Sample identifier	Depth (cm)	C14 Radiocarbon Age (years BP ± 1 σ)	Marine20 Calibrated Age range (cal BP)	1 σ error (years)	2 σ error (years)	Assumed vs Measured
-	UPC028 CT	0-2 cm	-62 ± 10	-62	10	10	Assumed
UCIAMS-228257	UPC028 97-99 cm	97-99	1830 ± 25	1235.9	119	248	Measured
UCIAMS-228258	UPC028 197-199 cm	197-199	3560 ± 30	3280.7	150	301	Measured
UCIAMS-228259	UPC028 310-312 cm	310-312	5170 ± 40	5359.4	160	355	Measured
UCIAMS-228260	UPC028 400-402 cm	400-402	7550 ± 60	7819.9	177	338	Measured
UCIAMS-228261	UPC028 487-489 cm	487-489	9340 ± 70	9,944.30	280	503	Measured

Appendix D.2 Interpolated Radiocarbon date

See sheet UPC028RADIOCARBON in Mair_AM_Earth_And_Environment_PhD_2022_Summary_Appendices.xls

Appendix E.1 K-means analysis R script

```
#K means analysis of Gc. inflata data for k-means cluster analysis
#Load a visualisation package factoextra
#Following steps on statology.org/k-means-clustering-in-r/
library(factoextra)
library(dplyr)
library(farver)
library(ggplot2)
library(tidyverse)
library(cluster)
#import data sets csv
InflataAll = read.csv("~/Desktop/Leeds PhD/Isotopes/Chapter 6/InflataRKSimp.csv")
#View the data table
View(InflataAll)
#Summary of all data stats
summary(InflataAll)
#attach database so values can be searched
attach(InflataAll)
#Rename InflataAll
df <- InflataAll
df <- na.omit(df)
df <- scale(df)
#Attempt to find optimal number of clusters for the data set through production of an elbow plot
fviz_nbclust(df, kmeans, method = "wss")
#Alternative method to find optimal number of clusters is to use gap statistic, comparing total intra-cluster variation
gap_stat <- clusGap(df,
```

```
            FUN=kmeans,
            nstart=25,
            K.max = 15,
            B = 50)
#plot number of clusters vs. gap statistic
fviz_gap_stat(gap_stat)
#Info from towardsdatascience.com/10-tips-for-choosing-the-optimal-number-of-clusters-277e93d72d92
#And now the silhouette method
fviz_nbclust(df, kmeans, method = "silhouette", k.max = 24)
#Still not sure which to use so lets see what cValid suggests for number of clusters
library(clValid)
clusterValidation <- clValid(df, nClust = 2:35,
                    clMethods = c("hierarchical","kmeans","pam"), validation = "internal")
#Get a summary, from this Pam method suggests 2 clusters, hierarchical 33 and kmeans 3
summary(clusterValidation)
#Sum of squares method attempt
#Additional packages
library(tidyverse)
library(magrittr)
library(cluster)
library(cluster.datasets)
library(cowplot)
library(NbClust)
library(clValid)
library(ggfortify)
library(clustree)
library(dendextend)
library(factoextra)
library(FactoMineR)
library(corrplot)
library(GGally)
library(ggiraphExtra)
library(knitr)
library(kableExtra)
#kmeans for 2-7 for sum of squares
kmean_calc <- function(df, ...){
  kmeans(df, scaled = ..., nstart = 30)
}
```

```
km2 <- kmean_calc(InflataAll, 2)
km3 <- kmean_calc(InflataAll, 3)
km4 <- kmeans(InflataAll, 4)
km5 <- kmeans(InflataAll, 5)
km6 <- kmeans(InflataAll, 6)
km7 <- kmeans(InflataAll, 7)
p1 <- fviz_cluster(km2, data = InflataAll, ellipse.type = "convex") + theme_minimal() +
ggtitle("k = 2")
p2 <- fviz_cluster(km3, data = InflataAll, ellipse.type = "convex") + theme_minimal() +
ggtitle("k = 3")
p3 <- fviz_cluster(km4, data = InflataAll, ellipse.type = "convex") + theme_minimal() +
ggtitle("k = 4")
p4 <- fviz_cluster(km5, data = InflataAll, ellipse.type = "convex") + theme_minimal() +
ggtitle("k = 5")
p5 <- fviz_cluster(km6, data = InflataAll, ellipse.type = "convex") + theme_minimal() +
ggtitle("k = 6")
p6 <- fviz_cluster(km7, data = InflataAll, ellipse.type = "convex") + theme_minimal() +
ggtitle("k = 7")
plot_grid(p1, p2, p3, p4, p5, p6, labels = c("k2", "k3", "k4", "k5", "k6", "k7"))
#Actual Sum of squares bit
ssc <- data.frame(
  kmeans = c(2,3,4,5,6,7),
  within_ss = c(mean(km2$withinss), mean(km3$withinss), mean(km4$withinss),
mean(km5$withinss),
            mean(km6$withinss), mean(km7$withinss)),
  between_ss = c(km2$betweenss, km3$betweenss, km4$betweenss,
km5$betweenss,
             km6$betweenss, km7$betweenss)
)
ssc%<>% gather(., key = "measurement", value = value, -kmeans)
#ssc$value <- log10(ssc$value)
ssc%>% ggplot(., aes(x=kmeans, y=log10(value), fill = measurement))+
  geom_bar(stat="identity", position = "dodge")+ ggtitle("Cluster Model
  Comparison") + xlab("Number of Clusters")+ ylab("Log10 Total Sum of Squares")+
  scale_x_discrete(name="Number of Clusters", limits = c("0", "2", "3", "4", "5", "6", "7"))
#Still not sure what number of clusters to use, lets try NbClust
res.nbclust <- NbClust(InflataAll, distance = "euclidean",
                       min.nc = 2, max.nc = 15,
                       method = "complete", index = "all")
factoextra::fviz_nbclust(res.nbclust)+ theme_minimal()+
  ggtitle("NbClust's optimal number of clusters")
```

```
#From this result going to use 2 clusters as suggested by 8 indices in nbclust
#and significantly fewer than 13 or 15 which were the other suggestions
#First to make repeatable/reproducible
set.seed(1)
#perform k-means clustering with 3 clusters
Inflatakm <- kmeans(InflataAll, centers = 2, nstart = 50)
#See results
Inflatakm
#Plot results of final k-means model
fviz_cluster(Inflatakm, data = InflataAll)
#Add cluster assignment to original data
FinalInflata <- cbind(InflataAll,cluster=Inflatakm$cluster)
#View final data
head(FinalInflata)
View(FinalInflata)
#Attach data
detach(InflataAll)
attach(FinalInflata)
#Try plotting
ggplot(FinalInflata)+
  (aes(x=d13C.VPDB, y=d18O.VPDB, colour=factor(cluster)))+
  geom_point()+
  scale_colour_manual(values=c("red2","blue2"))+
  scale_y_reverse(limits=c(3.5,0))+
  xlim(0,2.5)+
  labs(x=expression(delta^13*"C"["(VPDB)"]*"
(\u2030)"),y=expression(delta^18*"O"["(VPDB)"]*" (\u2030)"))+
  theme(plot.title = element_blank(), panel.grid.minor =
element_blank(),panel.grid.major = element_blank(),panel.background =
element_rect(colour = "black", fill = "NA"), strip.background = element_blank(),
strip.text = element_blank(), axis.text = element_text(colour = "black",size = 10),
legend.position = "right", axis.title = element_text(size=15))+
  guides(colour=guide_legend("Cluster"))
```

Appendix F.1 UPC 023 ITRAX data. See sheet UPC023ITRAXRAW in Mair_AM_Earth_And_Environment_PhD_2022_Summary_Appendices.xls

Appendix F.2 UPC 028 ITRAX data See sheet UPC028ITRAXRAW in Mair_AM_Earth_And_Environment_PhD_2022_Summary_Appendices.xls

Appendix F.3 UPC 122 ITRAX data See sheet UPC0122ITRAXRAW in Mair_AM_Earth_And_Environment_PhD_2022_Summary_Appendices.xls

Appendix G.1 *Gs. ruber White* interpolated assemblage

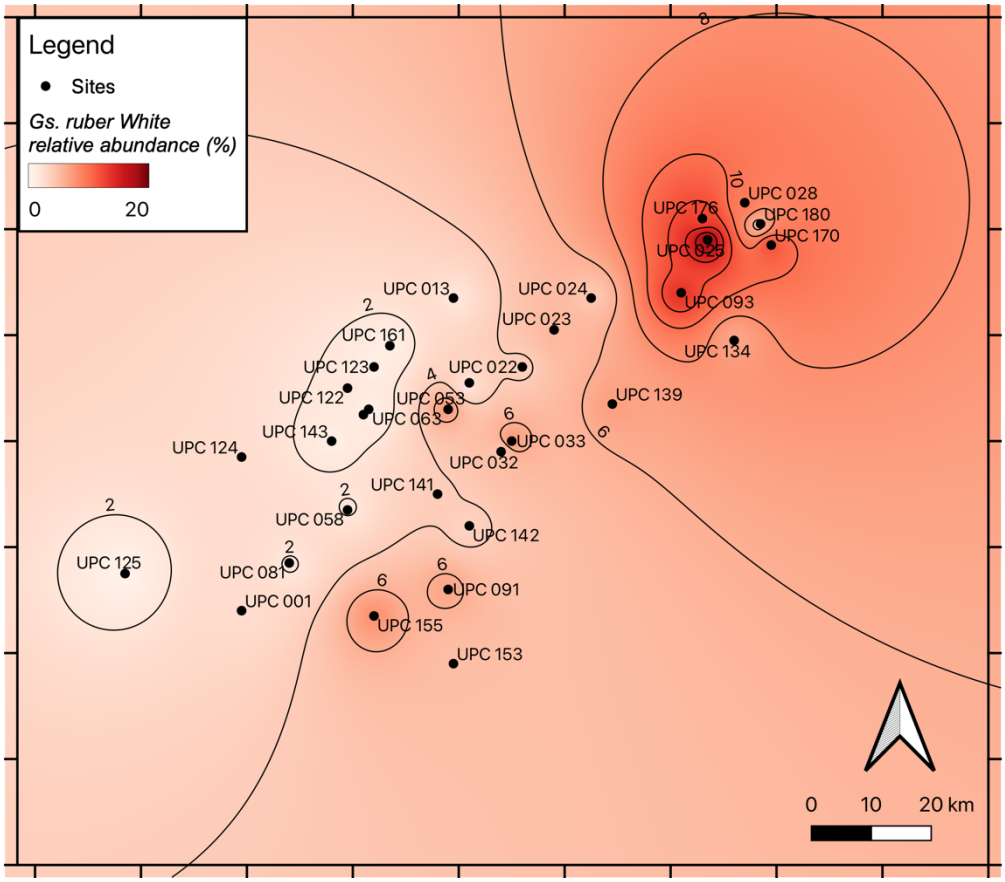

Appendix G.2 *Gs. ruber Pink* interpolated assemblage

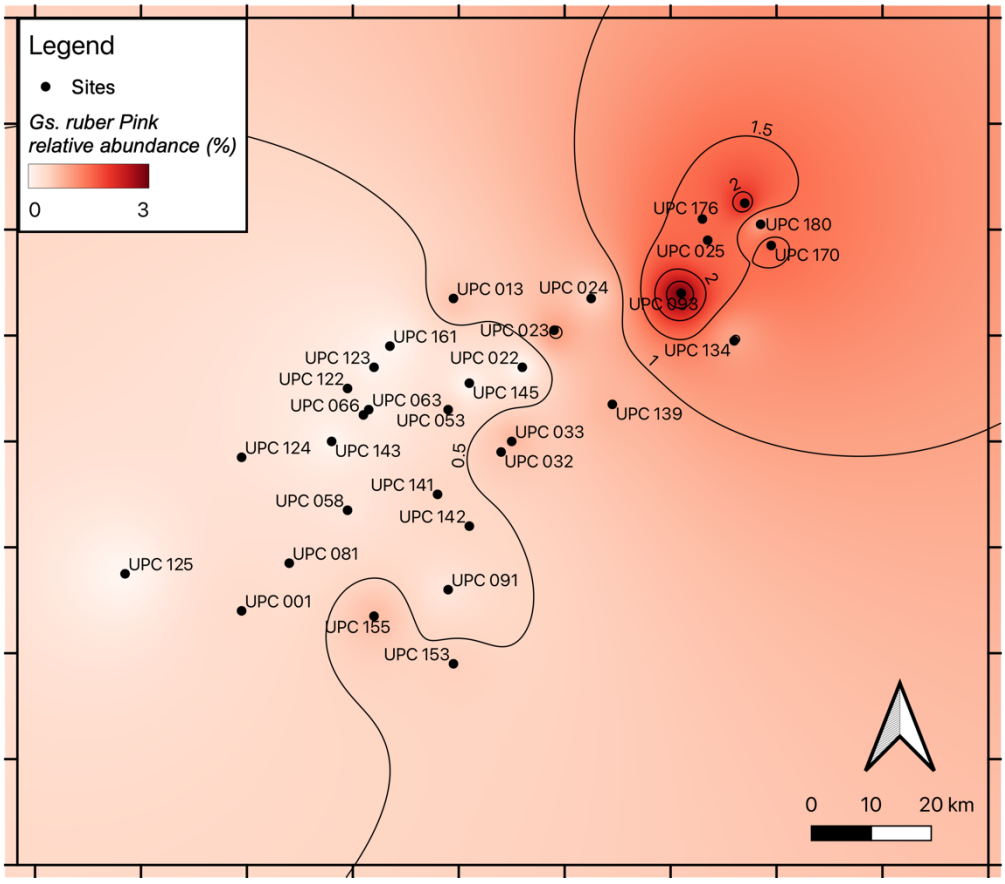

Appendix G.3 *Gr. hirsuta* interpolated assemblage

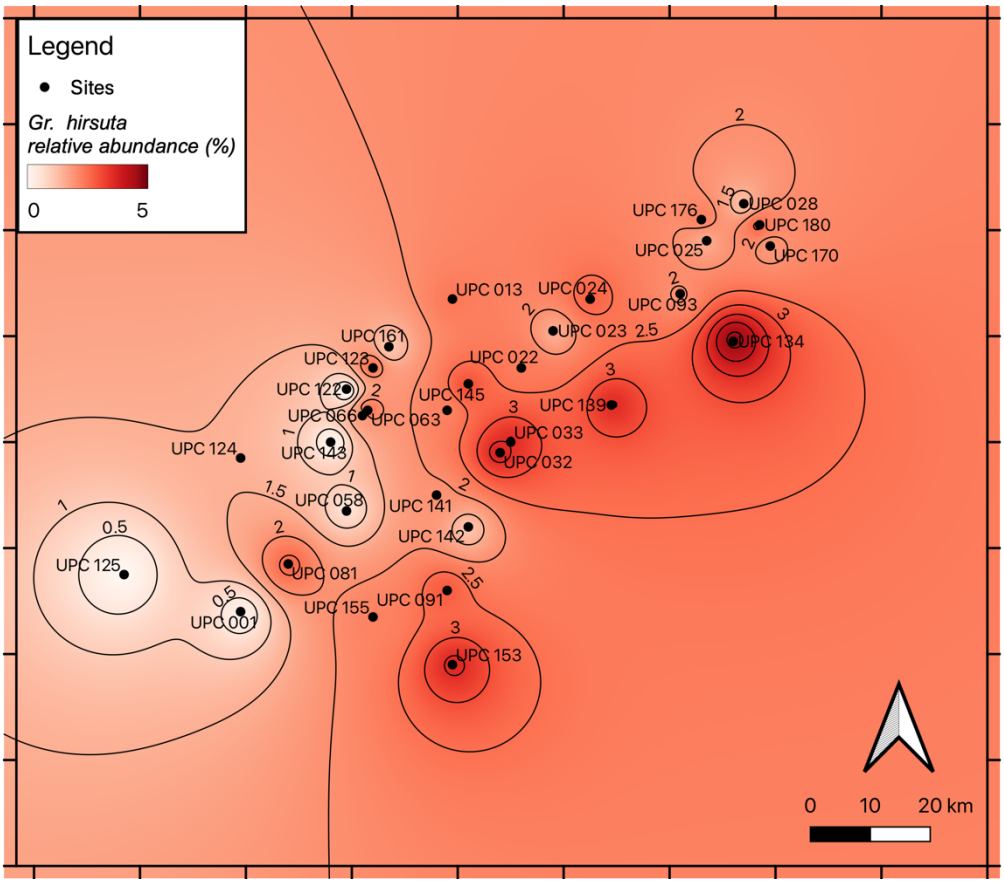

Appendix G.4 *O. universa* interpolated assemblage

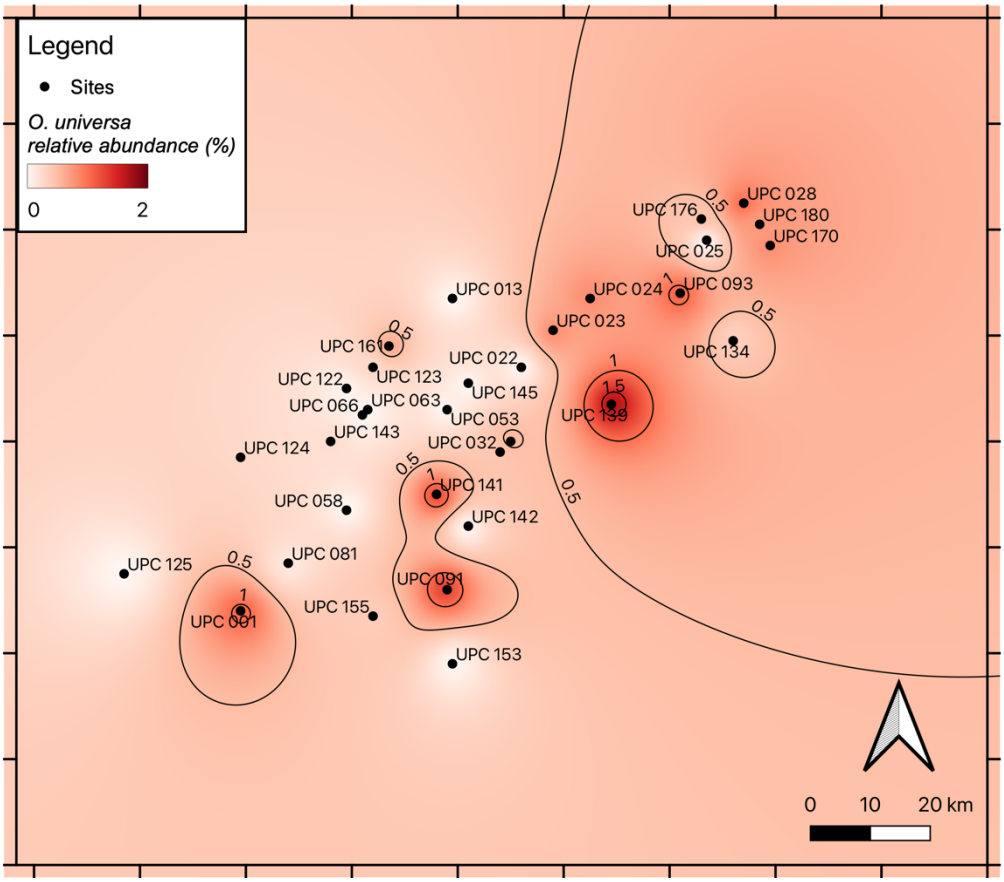

Appendix G.5 *T. sacculifer* interpolated assemblage

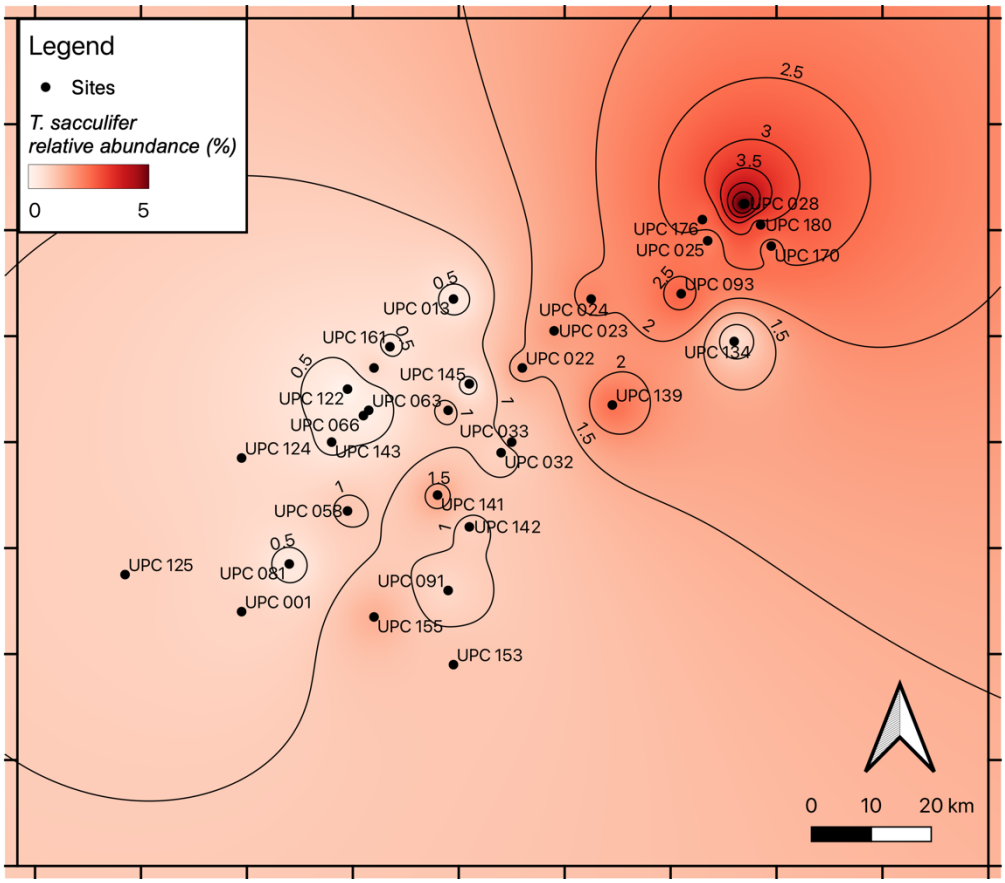

Appendix G.6 *Gc. inflata* interpolated assemblage

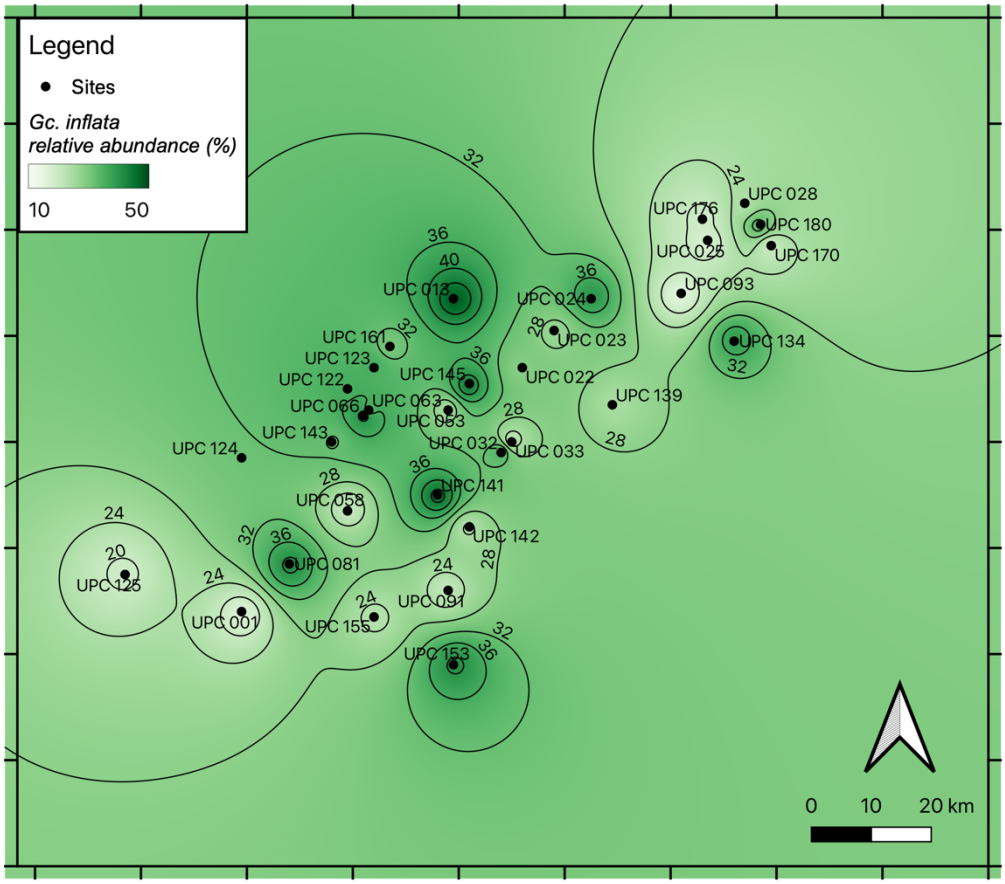

Appendix G.7 *Gg. bulloides* interpolated assemblage

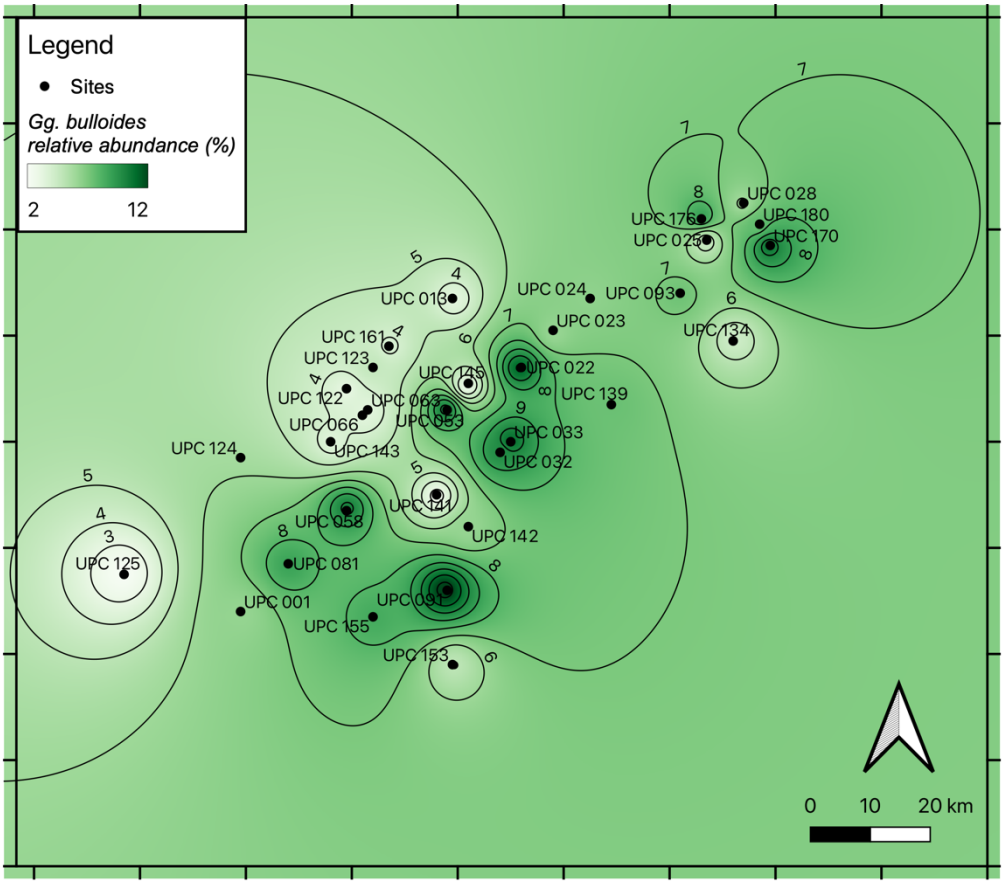

Appendix G.8 *Gt. glutinata* interpolated assemblage

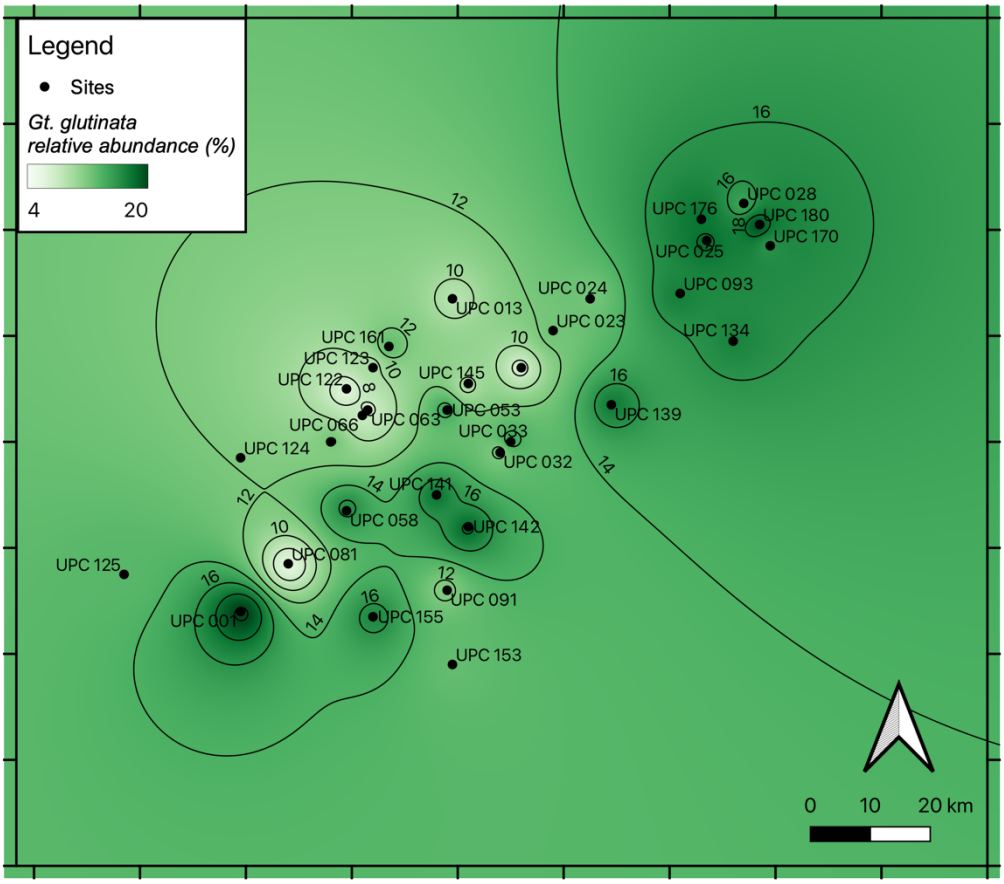

Appendix G.9 *N. incompta* interpolated assemblage

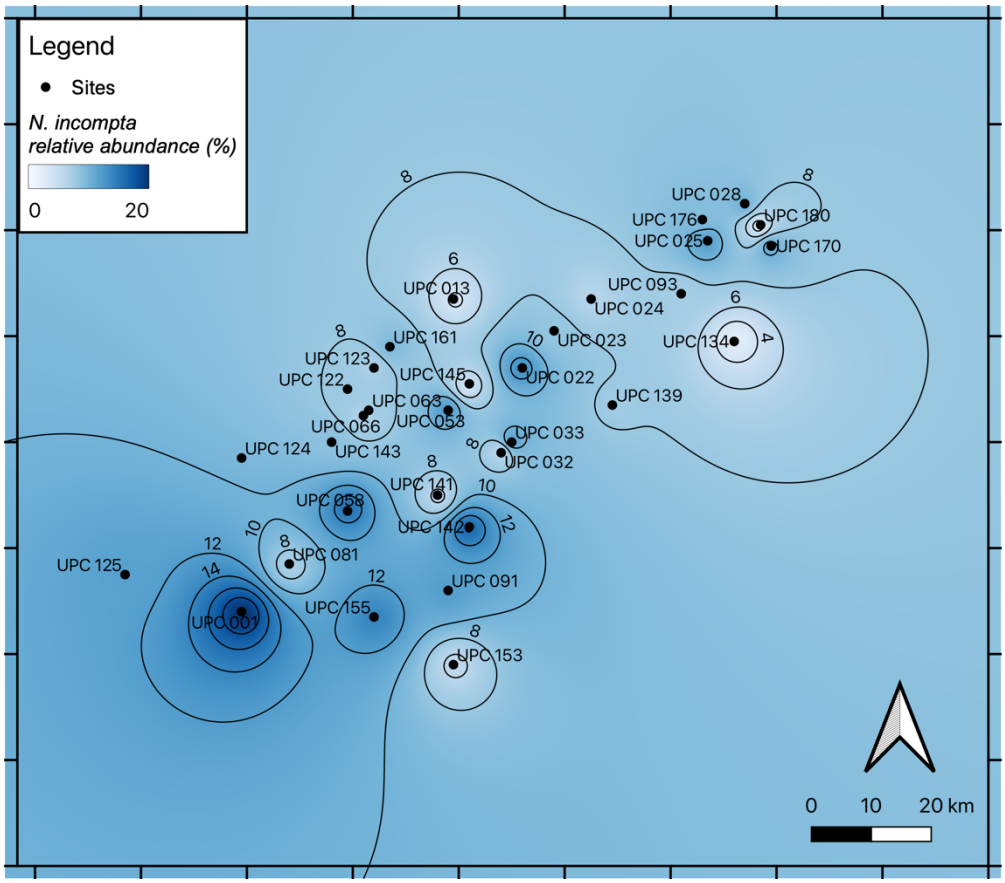

Appendix G.10 *N. pacyderma* interpolated assemblage

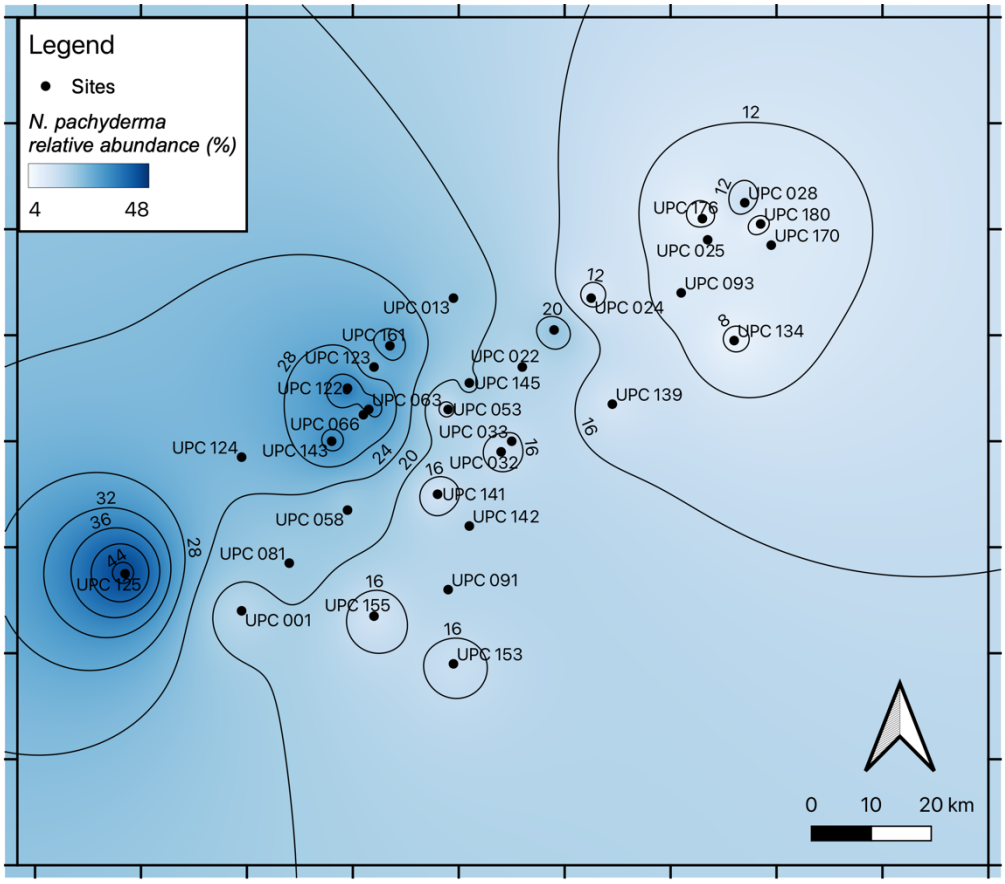

Appendix H.1 Core photos. Sections one to six

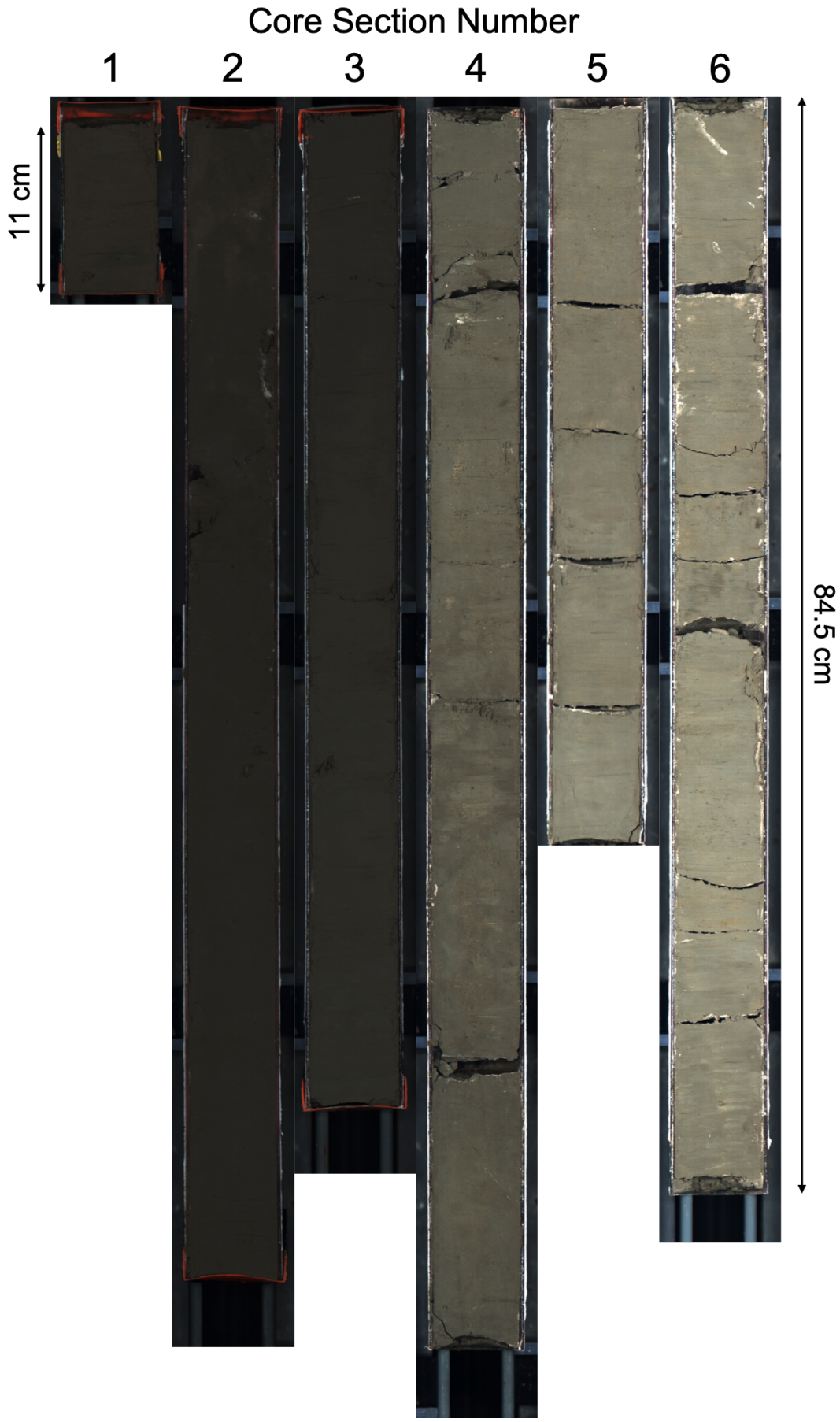

Appendix I SEM Plate 1

Species are listed in order of downcore assemblage record. See Appendix B.2 for listing.

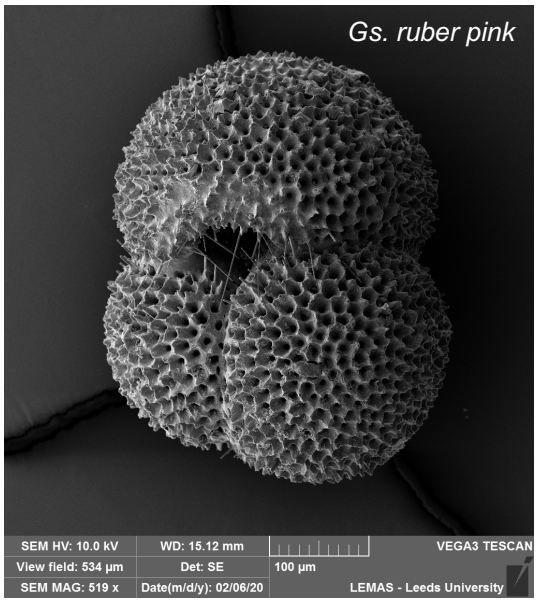

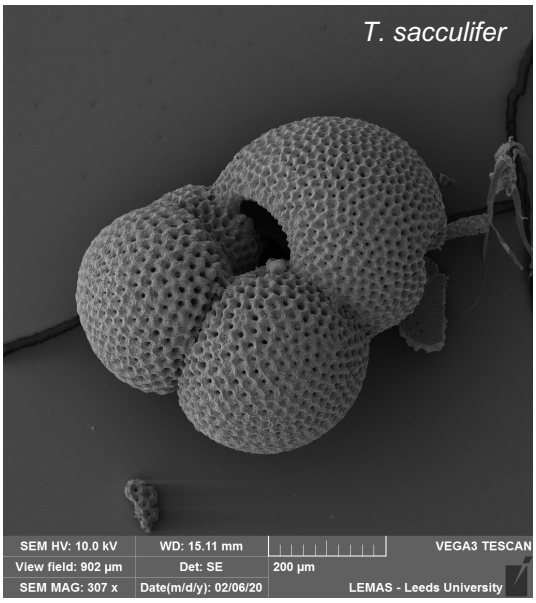

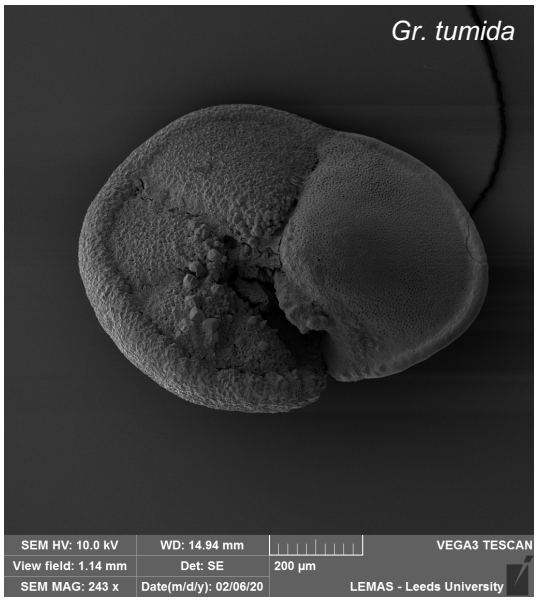

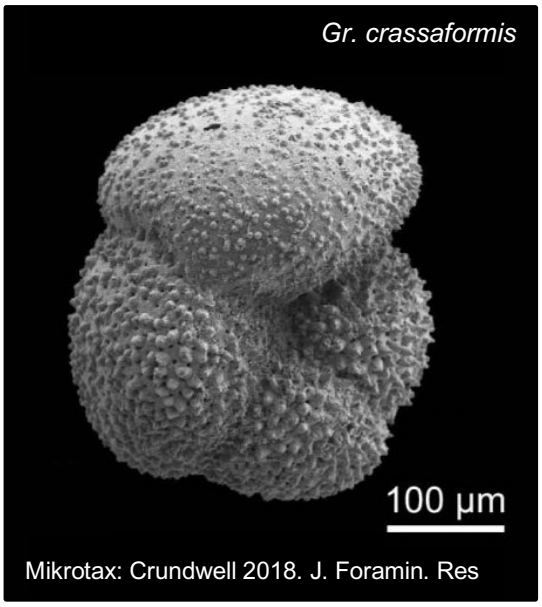

Gs. ruber pink, T. sacculifer, Gr. tumida **and** ***Gr. crassaformis.*** **Scale bars are specific to image, where images were not collected using the SEM at the University of Leeds the reference for the image source is provided.**

Appendix I SEM Plate 2

Species are listed in order of downcore assemblage record. See Appendix B.2 for listing. Follows on from Plate 2.

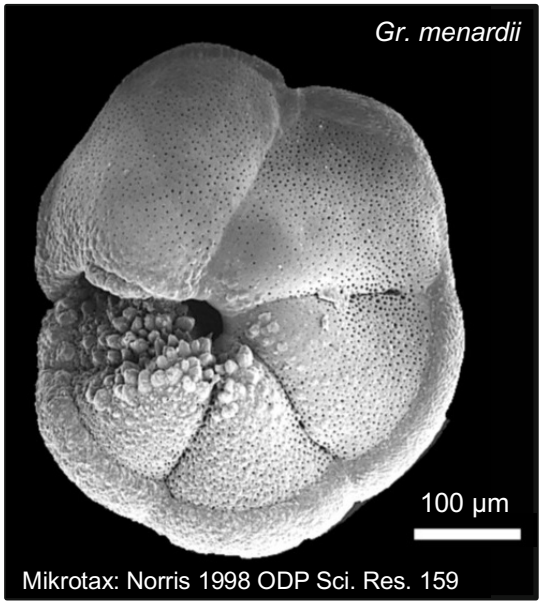

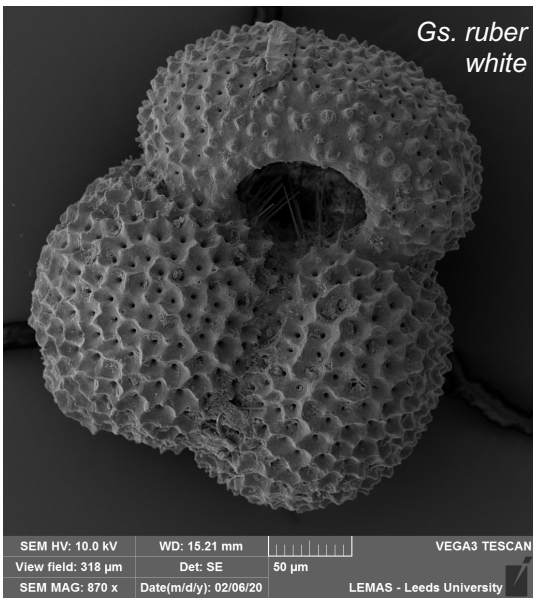

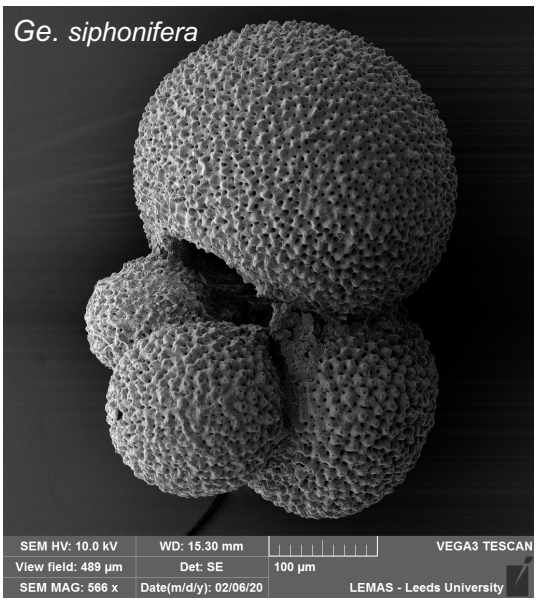

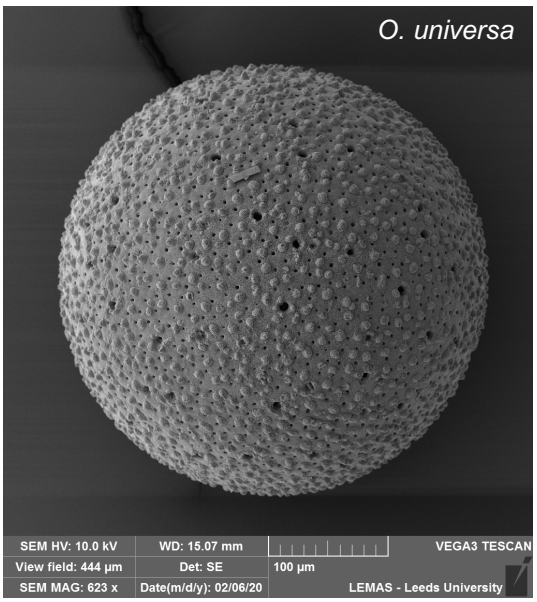

***Gr. menardii, Gs. ruber white, Ge. siphonifera* and *O. universa.* Scale bars are specific to image, where images were not collected using the SEM at the University of Leeds the reference for the image source is provided.**

Appendix I SEM Plate 3

Species are listed in order of downcore assemblage record. See Appendix B.2 for listing. Follows on from Plate 2.

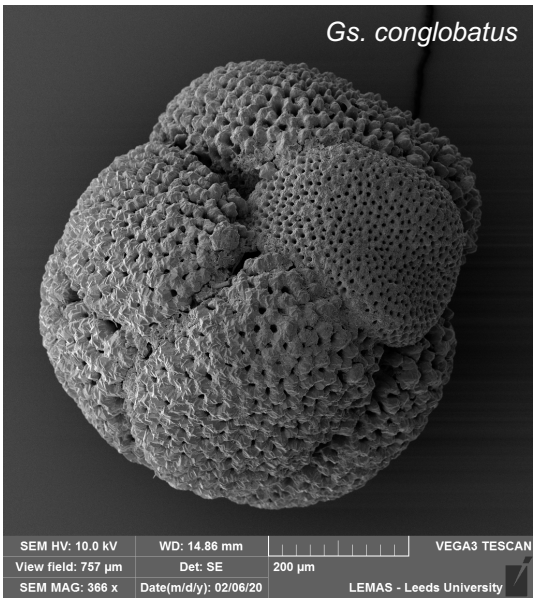

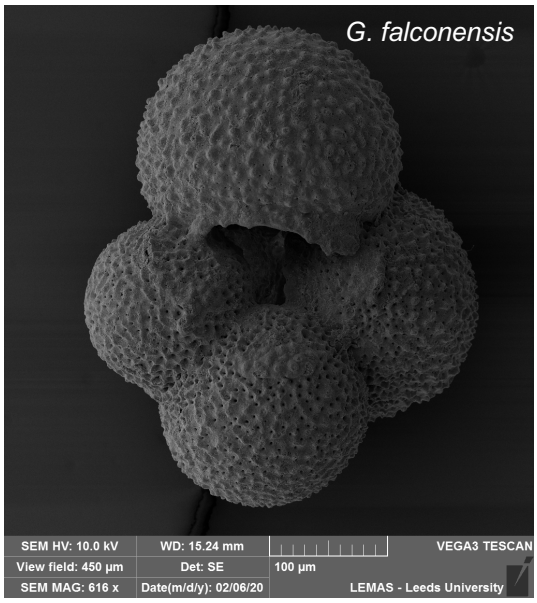

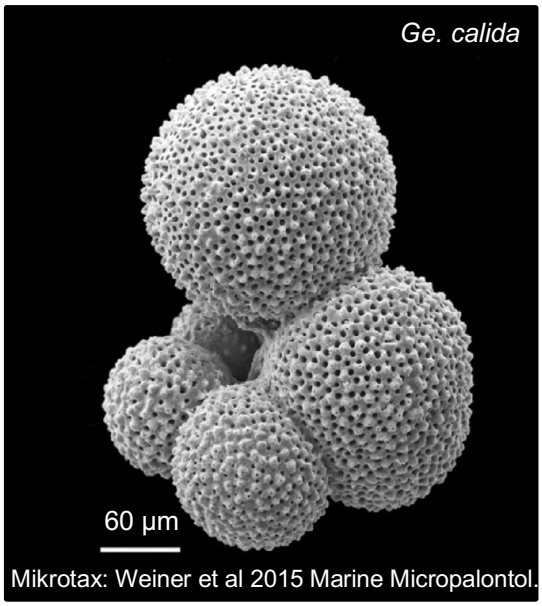

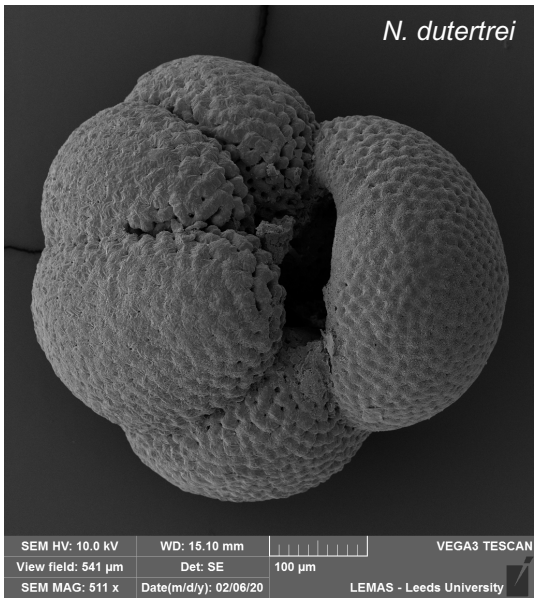

Gs. conglobatus, G. falconensis, Ge. calida **and** ***N. dutertrei.*** **Scale bars are specific to image, where images were not collected using the SEM at the University of Leeds the reference for the image source is provided.**

Appendix I SEM Plate 4

Species are listed in order of downcore assemblage record. See Appendix B.2 for listing. Follows on from Plate 3.

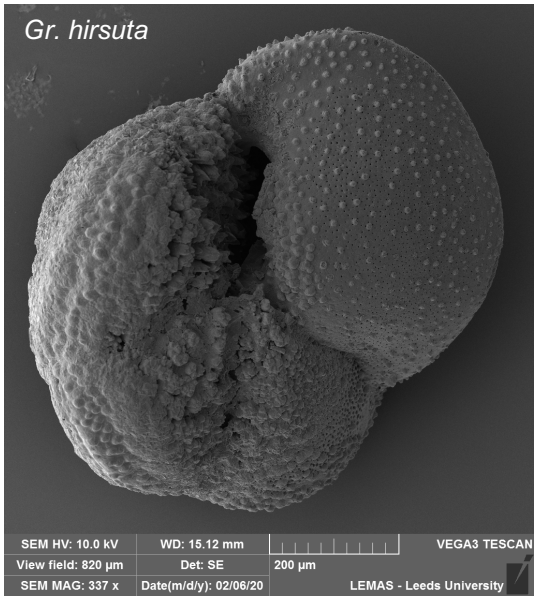

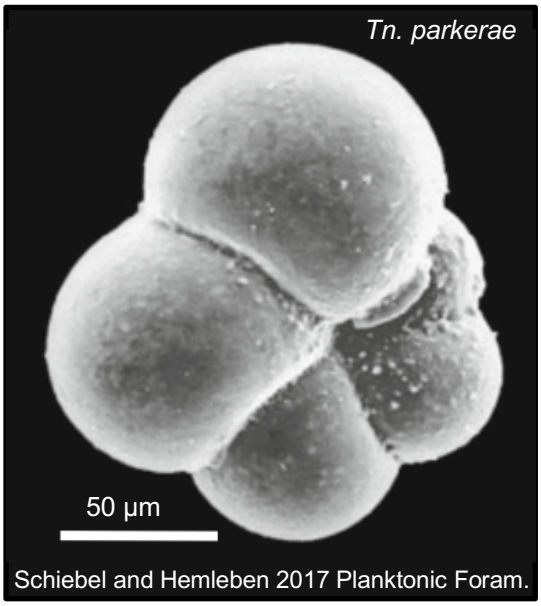

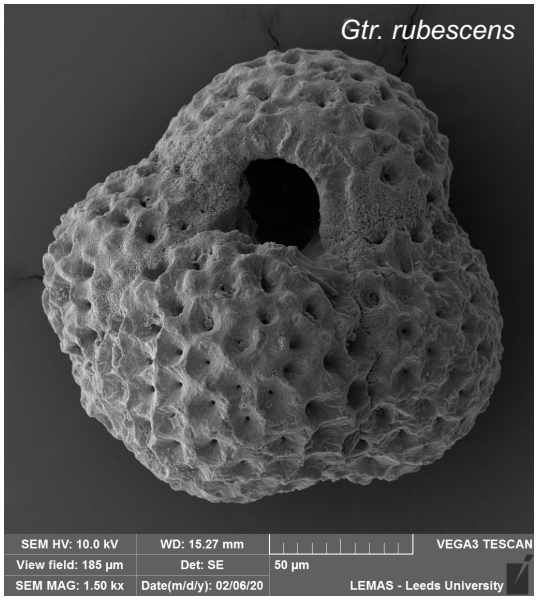

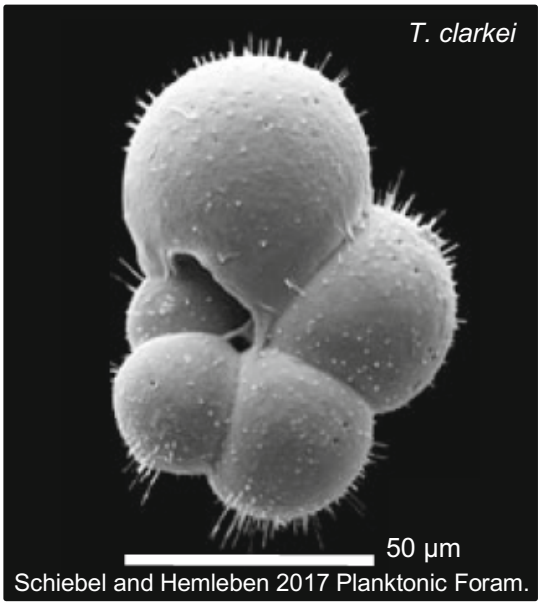

***Gr. hirsuta, Tn. parkerae, Gtr. rubescens* and *T. clarkei.* Scale bars are specific to image, where images were not collected using the SEM at the University of Leeds the reference for the image source is provided.**

Appendix I SEM Plate 5

Species are listed in order of downcore assemblage record. See Appendix B.2 for listing. Follows on from Plate 4.

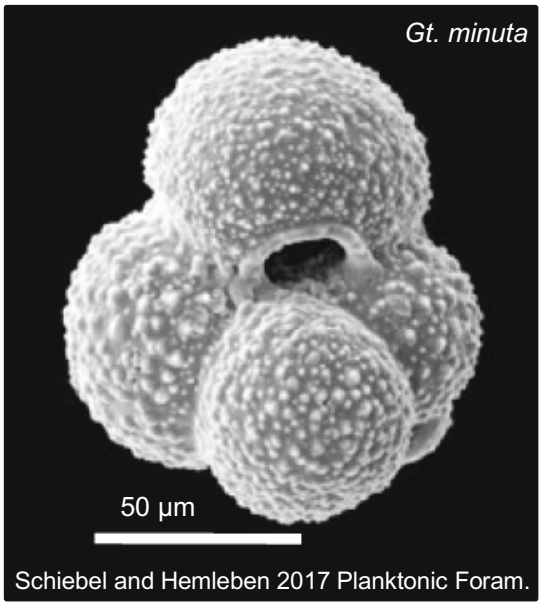

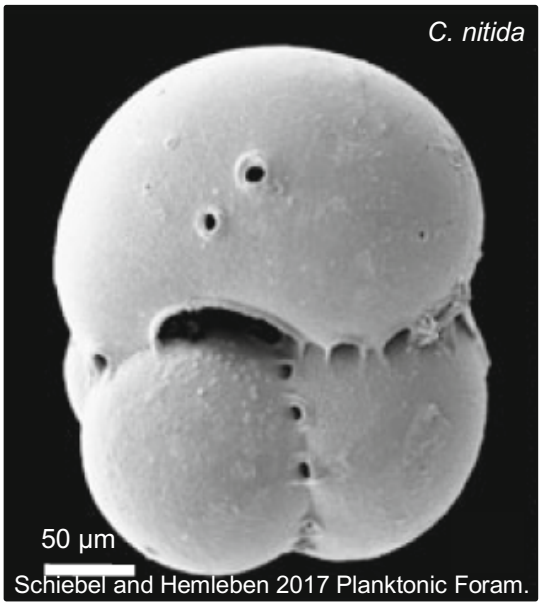

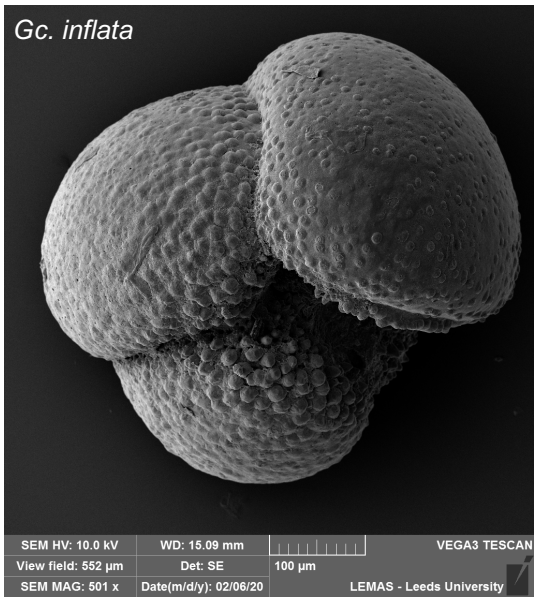

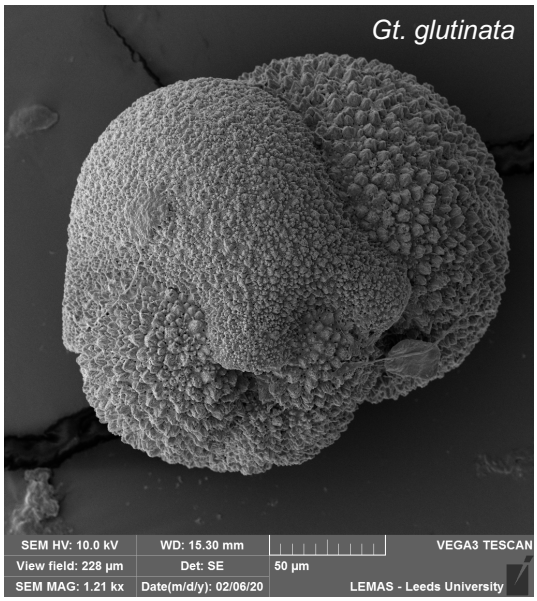

***Gt. minuta, C. nitida, Gc. inflata* and *Gt. glutinata.* Scale bars are specific to image, where images were not collected using the SEM at the University of Leeds the reference for the image source is provided.**

Appendix I SEM Plate 6

Species are listed in order of downcore assemblage record. See Appendix B.2 for listing. Follows on from Plate 5.

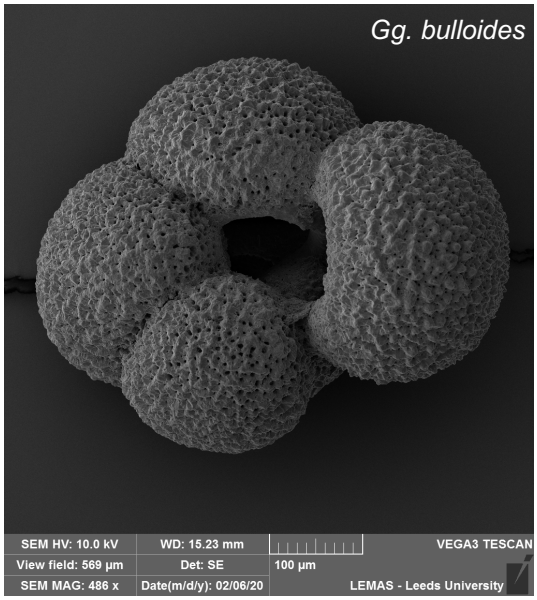

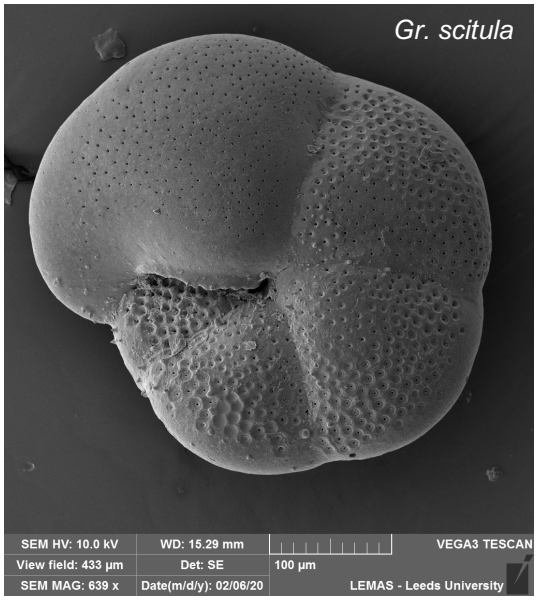

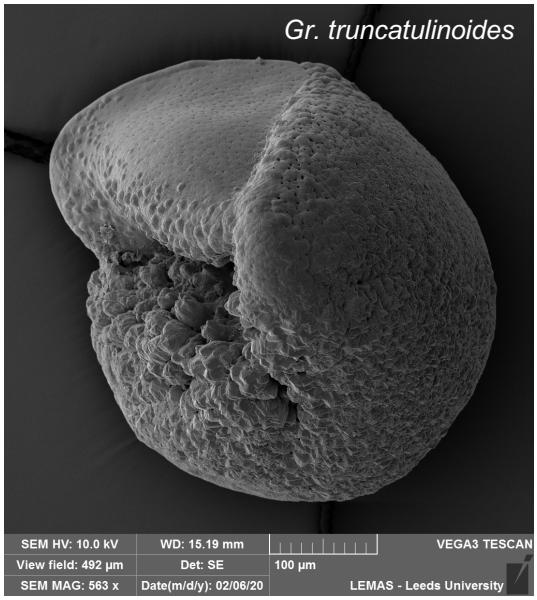

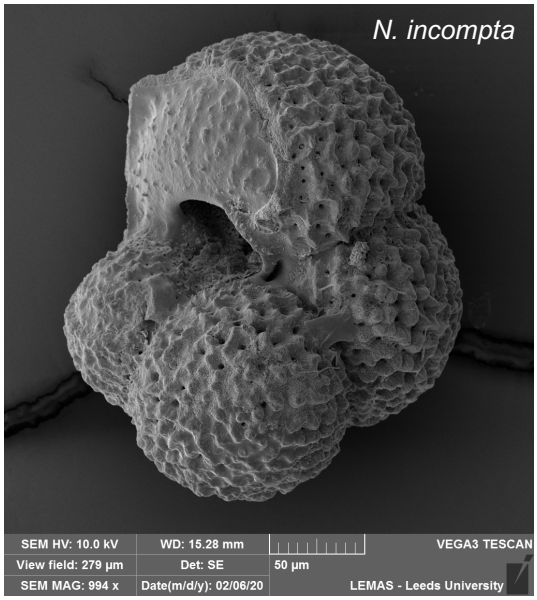

***Gg. bulloides, Gr. scitula, Gr. truncatulinoides* and *N. incompta.* Scale bars are specific to image, where images were not collected using the SEM at the University of Leeds the reference for the image source is provided.**

Appendix I SEM Plate 7

Species are listed in order of downcore assemblage record. See Appendix B.2 for listing. Follows on from Plate 6.

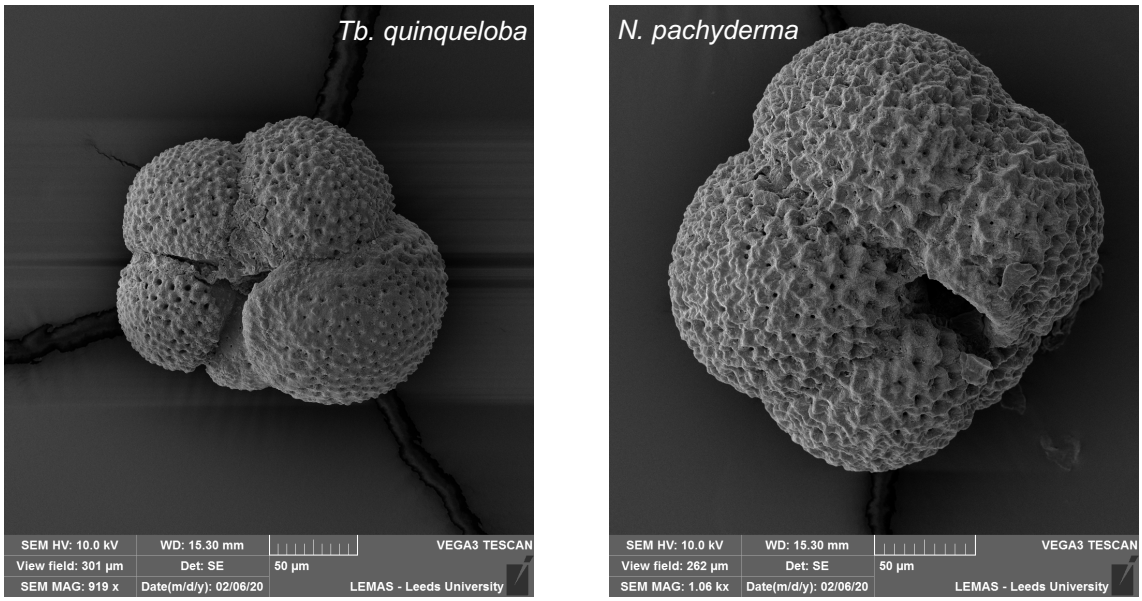

***Tb. quinqueloba* and *N. pachyderma.* Scale bars are specific to image, where images were not collected using the SEM at the University of Leeds the reference for the image source is provided.**